Dissertation zur Erlangung des Doktorgrades
der Fakultät für Chemie und Pharmazie
der Ludwig-Maximilians-Universität München

Use of styrylbenzothiazole photoswitches in drugs for spatiotemporal control over microtubule-dependent biology

Li Gao

aus

Xi'an (Shaanxi), China

2021

Erklärung

Diese Dissertation wurde im Sinne von § 7 der Promotionsordnung vom 28. November 2011 von Herrn Dr. Oliver Thorn-Seshold betreut.

Eidesstattliche Versicherung

Diese Dissertation wurde eigenständig und ohne unerlaubte Hilfe erarbeitet.

München, 05.07.2021

Li Gao .....

Dissertation eingereicht am 09.07.2021

1. Gutachter: Dr. Oliver Thorn-Seshold

2. Gutachter: Prof. Dr. Ivan Huc

Mündliche Prüfung am 08.10.2021

Parts of this work have been published in peer-reviewed journals:

Li Gao, Joyce C.M. Meiring, Yvonne Kraus, Maximilian Wranik, Tobias Weinert, Stefanie D. Pritzl, Rebekkah Bingham, Evangelia Ntouliou, Klara I. Jansen, Natacha Olieric, Jörg Standfuss, Lukas C. Kapitein, Theobald Lohmüller, Julia Ahlfeld, Anna Akhmanova, Michel O. Steinmetz, Oliver Thorn-Seshold; A Robust, GFP-Orthogonal Photoswitchable Inhibitor Scaffold Extends Optical Control over the Microtubule Cytoskeleton, *Cell Chemical Biology* **2021**, 28 (2), 228-241.

Parts of this work have been deposited on preprint servers and are currently in review process:

Li Gao, Joyce C.M. Meiring, Adam Varady, Iris E. Ruider, Constanze Heise, Maximilian Wranik, Cecilia D. Velasco, Jennifer A. Taylor, Beatrice Terni, Jörg Standfuss, Clemens C. Cabernard, Artur Llobet, Michel O. Steinmetz, Andreas R. Bausch, Martin Distel, Julia Thorn-Seshold, Anna Akhmanova, Oliver Thorn-Seshold; In vivo photocontrol of microtubule dynamics and integrity, migration and mitosis, by the potent GFP-imaging-compatible photoswitchable reagents SBTubA4P and SBTub2M, bioRxiv 2021.03.26.437160.

Li Gao[†], Joyce C. M. Meiring[†], Constanze Heise, Ankit Rai, Adrian Müller-Deku, Anna Akhmanova, Julia Thorn-Seshold, Oliver Thorn-Seshold; Photoswitchable epothilone-based microtubule stabilisers allow GFP-imaging-compatible, optical control over the microtubule cytoskeleton, bioRxiv 2021.03.31.437838.

[†] these authors contributed equally to this work

1. Abstract

1.1. The challenge at hand – the discrepancy between modern technology and classic drugs when used as research tools

Thousands of biological processes take place within a single cell, every second of its existence. These processes are meticulously orchestrated and highly regulated in order to guarantee proper functioning and homeostasis within the organism. Multiple proteins assemble to form highly sophisticated molecular machines and structures to carry out certain tasks at exact timepoints, such as the microtubule-based mitotic spindle apparatus, which separates the chromosomes during mitosis; or the replisome that performs DNA replication with an unprecedented level of precision and reliability.

The visualization of cells, their biological processes, and our understanding of the biomolecular function of proteins, have grown rapidly with the invention of groundbreaking new technologies and continuous improvement of existing instruments. Cryo-electron microscopy, high-speed or super-resolution microscopy have considerably pushed the limits of temporal and spatial resolution past the micron spatial scale and millisecond time scale, opening new frontiers in modern biology. Small molecule drugs which can modulate, inhibit or amplify these machineries and their functions, have been a key factor to explore the molecular dynamics of proteins and cellular systems. Consequently, while selective small molecule inhibitors for certain protein targets have garnered much interest in drug discovery, as promising drug candidates to treat diseases, they have also become crucial research tools in order to perturb and study protein and network function.

However, the technological leap has created a discrepancy between modern technology and classic drugs when used as research tools. With high-precision instruments able to observe highly dynamic cellular systems, it is the current set of molecular tools available to researchers that lack the spatiotemporal precision to control these dynamic cellular systems on a submicron and millisecond scale. Influencing or controlling biological processes with classic small molecule inhibitors without spatiotemporal specificity is a poor method to investigate a finely tuned machine.

Part One of this work will focus on the introduction of innovative molecular tools that allow simple control over a highly dynamic cellular system: the microtubule cytoskeleton. This is intended to optimally utilize, and in return further develop, state of the art imaging techniques and to expand biologists arsenal of molecular tools that can help to answer key questions in

neuroscience, embryology, and cytoskeleton research, by using light as a non-invasive, high-precision, biorthogonal regulator for biological application.

I introduce the styrylbenzothiazole (SBT) photoswitch as a research tool in cell biology, with initial application to reliably enable fast and reversible *in situ* optical control over the microtubule cytoskeleton. To situate this application I will discuss the problems of current state-of-the-art photoswitchable microtubule destabilizers, in particular azobenzene based PST-1, and showcase the **SBTubs** as an SBT-based alternative. We confirm their biological utility as photoswitchable tubulin inhibitors, compare their (photo)chemical & metabolic robustness, and test their compatibility to common fluorescent imaging tags over the azobenzene scaffold.

Part Two will focus on consolidating the newly introduced SBTs as a powerful alternative photoswitch scaffold with complementary features to azobenzenes. I perform an SAR study and identify two lead compounds **SBTub2M** and **SBTubA4P** as low nanomolar and water-soluble photoswitchable antimitotics that enable photocontrol over microtubule dynamics and structure in 3D systems and animal models (*D. rerio*, *X. tropicalis*), thus bringing *in vivo* photopharmacology one step closer to realization. Furthermore, I report the first photopharmacology study of a styrylthiazole (ST) photoswitch.

In the final part of my thesis I will apply this ST photoswitch scaffold instead to address the taxane binding site, showing its applicability and general features. I design and synthesize the first ever reported photoswitchable epothilones (**STEpos**) and offer proof of principle of their light-dependent stabilization of microtubules.

Taken together, this research makes a contribution towards (a) spatiotemporal control of microtubule research, helping antimitotic photopharmaceuticals advance beyond 2D cell culture and (b) reshaping the field of photopharmacology by introducing a focus on photoswitches like the SBTs which respond to biologists' technological needs & capacities, which will contribute to new SBT-based photopharmaceuticals both in microtubule research and beyond.

1.1. Das gegenwärtige Problem - die Diskrepanz zwischen moderner Technologie und klassischen Medikamenten zu Forschungszwecken

Innerhalb einer einzelnen Zelle finden jederzeit hunderttausende Prozesse statt. Diese sind akribisch genau reguliert, um die einwandfreie Funktion und das Gleichgewicht innerhalb eines Organismus zu gewährleisten. Mehrere Proteine schließen sich zu komplexen molekularen Maschinen und Strukturen zusammen um eine bestimmte Aufgabe zu einem bestimmten Zeitpunkt auszuführen, wie zum Beispiel der aus Mikrotubuli bestehende Spindelapparat, der die Chromosomen während Mitose trennt., oder das Replisom, das die DNA Vervielfältigung mit höchster Präzision und Zuverlässigkeit durchführt.

Die Visualisierung von Zellen, deren biologischen Prozesse und unser Verständnis der biomolekularen Funktion von Proteinen hat sich mit der Erfindung bahnbrechender neuer Technologien und der kontinuierlichen Verbesserung bestehender Messinstrumente rasant weiterentwickelt.

Kryoelektronenmikroskopie, Hochgeschwindigkeits- oder Superauflösungsmikroskopie haben die Grenzen der zeitlichen und räumlichen Auflösung deutlich bis unter den Mikrometer- und Millisekunden Bereich hinaus geschoben. Dieser Fortschritt führte zur Begründung neuer Felder in der modernen Biologie, um molekulare Dynamiken von Proteinen zu erforschen.

Wirkstoffe, die diese Mechanismen und ihre Funktionen modulieren, hemmen oder verstärken können, sind ein Schlüsselfaktor für die Erforschung der molekularen Dynamik von Proteinen und zellulären Systemen geworden. Während selektive Inhibitoren für bestimmte Proteine als vielversprechende Wirkstoffkandidaten zur Behandlung von Krankheiten großes Interesse in der Arzneimittelforschung geweckt haben, sind sie auch zu wichtigen Forschungsinstrumenten geworden, um Proteinfunktionen zu stören und zu untersuchen.

Der gewaltige Technologiesprung hat jedoch eine Diskrepanz zwischen der modernen Technologie und den klassischen Medikamenten als Forschungswerkzeuge geschaffen. Während hochpräzise Instrumente in der Lage sind, ebenso dynamische zelluläre Systeme zu beobachten, mangelt es den aktuellen molekularen Werkzeugen, die den Forschern zur Verfügung stehen, an räumlicher und zeitlicher Präzision um solch dynamischen zellulären Systeme aufs genaueste kontrollieren zu können. Klassische Inhibitoren sind daher nicht ideal um biologische Prozesse zu untersuchen.

Der erste Teil konzentriert sich auf die Einführung innovativer molekularer Werkzeuge, die eine einfache Kontrolle des hochdynamischen Mikrotubuli Zytoskeletts ermöglicht, um modernste bildgebende Verfahren optimal zu nutzen. Im Gegenzug erweitern sich die Auswahlmöglichkeiten an molekularen Werkzeugen für Biologen um Schlüsselfragen in den

Neurowissenschaften, der Embryologie und der Zytoskelett-Forschung beantworten zu können. Dabei wird Licht als nicht-invasiver, hochpräziser, bio-orthogonaler Regulator für biologische Anwendungen eingesetzt.

Ich stelle Styrylbenzothiazol (SBT) als Photoschalter in der Zellbiologie vor, um eine schnelle und zuverlässige lichtabhängige Kontrolle über das Mikrotubuli-Zytoskelett zu ermöglichen. Ich diskutiere die Probleme der aktuellen Mikrotubuli destabilisierenden Photoschalter, insbesondere des Azobenzols PST-1, und stelle eine neue Lösung vor: **SBTubs**. Wir bestätigen den Tubulin inhibierenden Wirkmechanismus und betonen ihre Überlegenheit gegenüber dem Azobenzol Gerüst in Bezug auf (photo)chemische Robustheit und Kompatibilität zu gängigen Fluorophoren

Der zweite Teil konzentriert sich auf die weitere Etablierung der neu eingeführten SBTs als praktische und sich gegenseitig ergänzende Photoschalteralternative zum Azobenzol. Ich führe eine SAR-Studie durch und identifiziere zwei Leitstrukturen **SBTub2M** und **SBTubA4P** als niedrige nanomolare und wasserlösliche anitimitotische Photoschalter, die eine lichtabhängige Kontrolle über Mikrotubulidynamik und -struktur in 3D Zellsystemen und Tiermodellen ermöglichen und den Traum von *in vivo* Photopharmakologie einen Schritt näher an die Realisierung bringen. Darüber hinaus berichte ich über die erste Photopharmakologie-Studie eines Styrylthiazol (ST) Photoschalters.

Im letzten Teil meiner Arbeit wende ich den ST-Photoschalter an, um die Taxan-Bindungsstelle zu adressieren, und demonstriere die allgemeine Anwendbarkeit des Photoschalters außerhalb der gut etablierten Colchicin-Bindungsstelle. Ich entwerfe und synthetisiere die ersten jemals berichteten photoschaltbaren Epothilone (**STEpos**) und beweise, dass STEpos Mikrotubuli lichtabhängig stabilisieren können.

Alles in allem hat meine Forschung einen bedeutenden Beitrag zur lichtäbhängigen Kontrolle von Mikrotubuli geleistet und damit den Weg geebnet, Photopharmazeutika außerhalb von 2D-Zellkultur hinaus zu verwenden. Meine innovative Anwendung des SBT-Photoschalter Konzepts als alternative zum Azobenzol hat das Feld der Photopharmakologie revolutioniert und wird sicherlich neue SBT-Photopharmazeutika hervorbringen sowohl für die Mikrotubuli-Forschung als auch auf anderen Gebieten der Biologie.

Table of Contents

2. Introduction

2.1. Light can trigger chemical processes in biology with unrivaled spatiotemporal precision

The concept of light as an external trigger to control biological activity is present throughout all domains of life. Nature uses light as an energy source to drive chemical processes, most prominently the fixation of carbon dioxide during photosynthesis where the absorption of a photon by chlorophyll initiates an electron transport chain. But light is also used as a carrier to transfer information with pinpoint accuracy in order to see and to perceive time.

The ability to focus light with a defined wavelength and intensity for a precise duration onto a specific point makes it an ideal tool in chemical and biological research settings to noninvasively exert a desired effect at a precise location and timepoint with unrivalled spatiotemporal precision.

2.2. Optogenetics - optical control on the protein level

Genetically engineered, light-responsive proteins are used in the field of optogenetics to install optical control over various biological systems and processes, since their introduction as tools by Miesenböck, Boyden, and Deisseroth, around the early 2000s.[1–3] Channelrhodopsin[4] and Halorhodopsin are blue- and yellow-light responsive membrane proteins that can be encoded in DNA and be expressed selectively in neurons of other organisms or whole animals by genetic manipulation to allow multiple-color optical excitation and inhibition of neuronal signal conduction with spatiotemporal precision (Fig 1a).[5] When a photon is absorbed by these proteins, a conformational change of an all-*E*-retinal complex to 13-*Z*-retinal, causes a structural change of the transmembrane protein pore that allows specific ions to cross the membrane (Fig 1b).

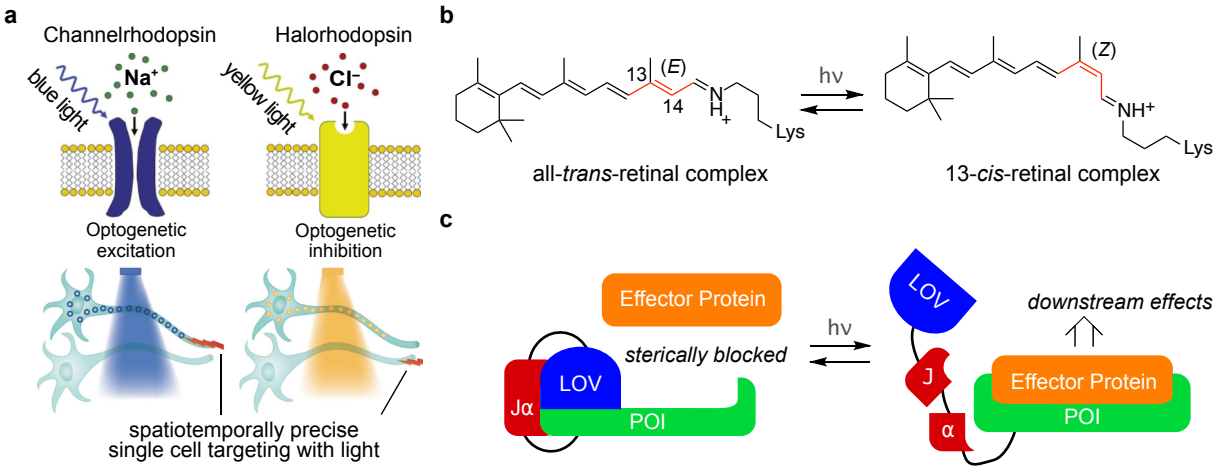

Figure 1: **(a)** Channelrhodopsins are blue-light responsive sodium channels and Halorhodopsins are yellow-light responsive chloride pumps, respectively. They can be expressed in neurons of other organisms to allow excitation

and inhibition of neuronal signal conduction by illuminating a selected single cell with spatiotemporally precise light pulses. (Adapted and modified from Deisseroth et al.[6]) **(b)** A protein bound retinal chromophore absorbs light to isomerize a double bond and consequently changes the protein structure to allow ions to pass through the transmembrane protein. **(c)** The light-oxygen-voltage (LOV) domain is composed by a "core" and a Jα helix. In the dark the LOV domain sterically blocks an effector protein from docking to the protein of interest (POI). Upon light activation the Jα helix undocks to allow downstream effectors to bind.

Instead of causing a structural change in the protein structure like Channelrhodopsin, light-oxygen-voltage (LOV) domains, first discovered by Huala et al. in 1997,[7] sterically block access of downstream effectors to a protein of interest (POI) (Fig 1c). In Hahn's landmark paper a genetically-encoded photoactivatable Rac1 (pa-Rac1) controls the motility of living cells using a LOV domain. On blue light stimulation, pa-Rac1 stimulates lamellipodia F-actin polymerization and cell migration is directed towards the illuminated area.[8] Even though optogenetics has made major contributions to the understanding of biological processes, there are also drawbacks to the 2010 "Nature method of the year". Since optogenetics operates on the protein level by expression of a genetically engineered gene sequence within the organism, it requires a substantial amount of time and resources to successfully install optical control over a protein target. Optogenetics are tailored to a specific model system and are therefore difficult to transfer onto other model systems without having to undergo the time-consuming genetic engineering process again.

Instead of genetic engineering, it would be more convenient to systemically apply a small molecule drug that allows spatiotemporal photoactivation of any model system.

2.3. Photopharmacology - putting a light-switch on small molecule drugs

The field of photopharmacology controls biological activity with synthetic photoresponsive small molecules (photopharmaceuticals, photodrugs) that respond to light.[9,10]

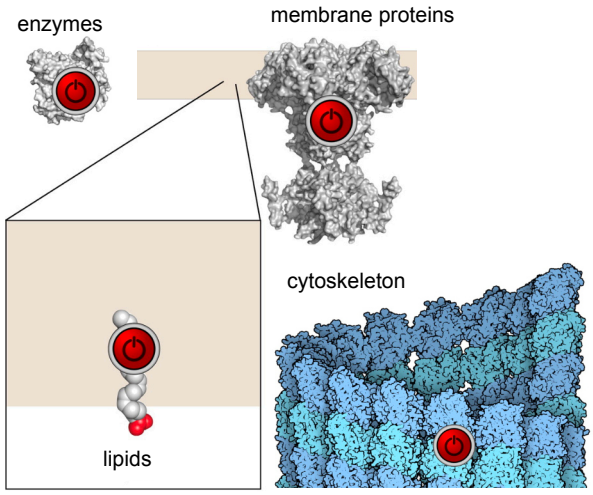

Figure 2: Targets of photopharmacology include enzymes, membrane bound proteins, lipids and components of the cytoskeleton (adapted from Trauner et al.[10]).

First reports regulating enzyme activity using photoswitchable effectors date back to Erlanger's work in 1969[11], when a series of photochromic inhibitors of the nicotinic acetylcholine receptor were shown to have different activities under different lighting regimes. Today several targets can be controlled with photochromic ligands - enzymes, membrane proteins, lipid membranes, and components of the cytoskeleton (Fig 2, cf. chapter 2.3.4).[10,12] Upon irradiation these photopharmaceuticals can absorb a photon to undergo a distinct structural and physicochemical change, that typically then affects a molecule's binding affinity towards a specific POI.[12] Similar to nature, which relies on just a small number of chromophores (retinals, flavins and tetrapyrroles), the toolbox of photopharmacology is also limited to a relatively small set of structure motifs that are categorized into irreversibly photoactivated photocages and reversible photoswitches.

2.3.1. Photouncageable drugs are photoactivatable prodrugs

A photocleavable protecting group ("photocage")[13] can be a straightforward prodrug strategy to modify a drug into an inactive state, that can then be followed by photo-triggered activation. Photocaged compounds are designed to block binding of the drug by attachment of a photolabile group.

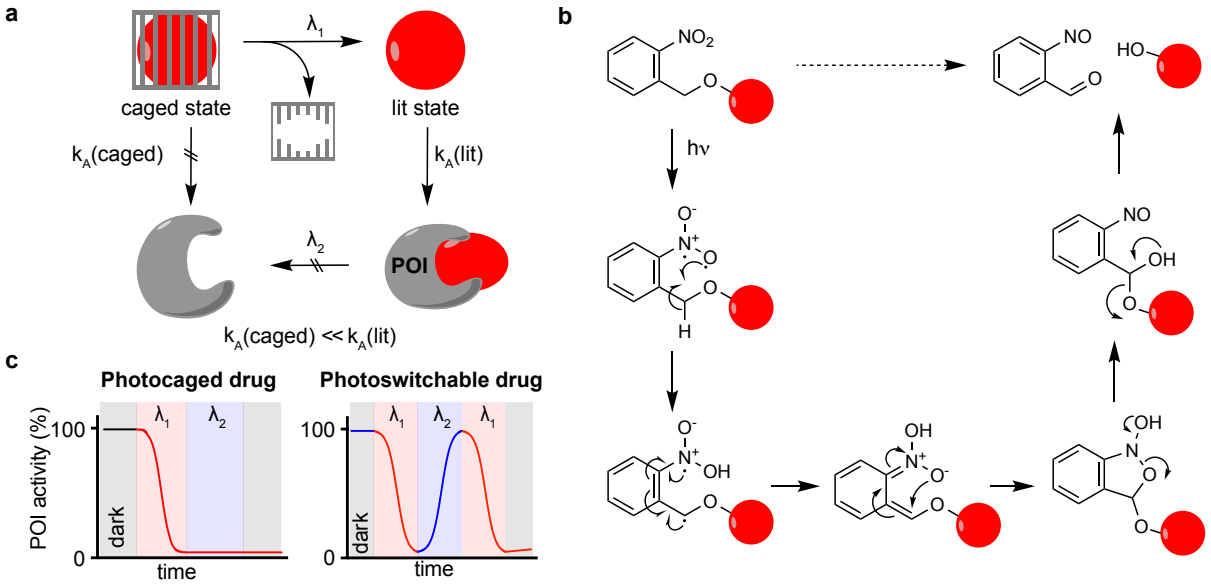

Figure 3: **(a)** The concept of a photocaged drug: In photocaged compounds binding of the drug is blocked by a photolabile group, when activated by light of a certain wavelength λ_1 the photocage is irreversibly cleaved and the drug is released. **(b)** Photocleavage mechanism of an *o*-nitrobenzyl-based photocage to release the active drug (red ball) and an *o*-nitrosobenzaldehyde.[14] **(c)** Compared to a photocaged drug, a photoswitchable drug allows reversible inhibition and restoration of biological function using a two-wavelength protocol.

When activated by light with a certain wavelength λ_1, the photocage is irreversibly cleaved and the drug is released (Fig 3a). Among the most commonly used photocages are the *ortho*-nitrobenzyl groups (Fig 3b), which are attached to a crucial functional group within the pharmacophore (e.g. OH or NH_2-groups). After illumination with UV light intramolecular

abstraction of a γ-hydrogen forms a 1,4-diradical which undergoes irreversible cyclization to a five membered ring followed by hemiacetal formation. The active drug is released with its full potency after rate determining hydrolysis of the hemiacetal.[14,15]

Most photocaged drugs are lit-active by design and their irreversible cleaving mechanism makes them effective single illumination "turn-ON" probes. Compared to a photocaged drug that can only be activated once, a photoswitchable drug allows reversible photoswitching of a drug between an active and an inactive state (Fig 3c).

2.3.2. Photoswitchable drugs and their design strategies

Photoswitches are two-state molecules, that can switch between these states using light (Fig 4a). Ideally, an inactive photoswitchable drug with no specific protein interaction undergoes a structural change that allows specific binding to the desired POI upon irradiation with light of a specific wavelength λ_1. The protein activity can be reversibly restored by photoswitching of the photopharmaceutical back to its inactive state with light of another wavelength λ_2 or by thermal relaxation.

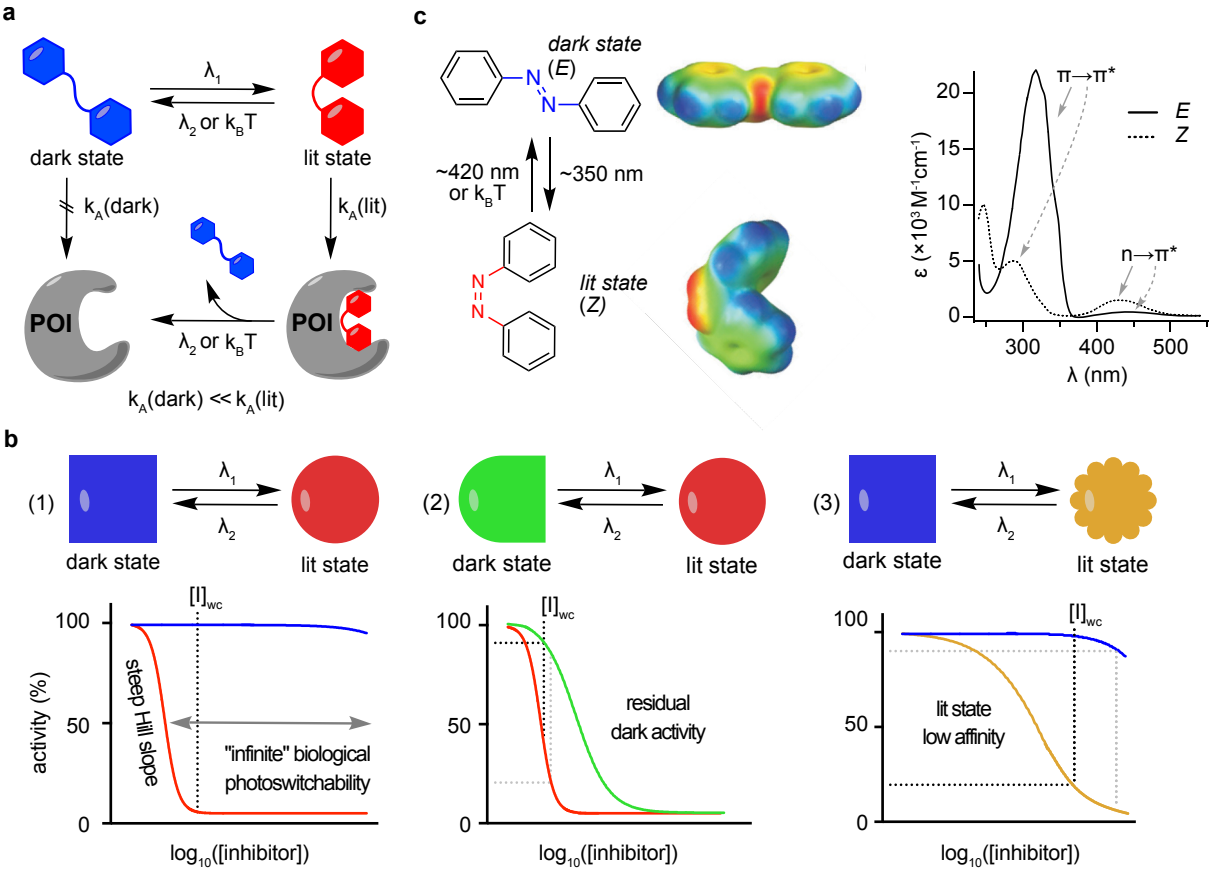

Figure 4: **(a)** The concept of a photoswitchable drug: The photodrug has no binding affinity towards the active site of a POI when applied in the dark state but displays high selectivity and affinity when the compound is switched to the lit state by illumination with light of a certain wavelength λ_1. If irradiated with another wavelength λ_2 or by thermal relaxation the photoswitch reverts back to the thermodynamically favored dark state and the ligand dissociates out of the binding pocket. **(b)** Different scenarios of photoswitch design (1) the ideal photopharmaceutical displays complete photoswitchable bioactivity between lit and dark states. $[I]_{WC}$ is the lowest concentration with full inhibition

in the lit state. (2) residual dark activity is observed if the dark state still resembles the active lit state, $[I]_{WC}$ is set by the 10% dark state inhibition threshold. (3) low binding affinity of the lit state requires higher concentrations to observe similar grades of inhibition as compared to (1), $[I]_{WC}$ is set by the 80% lit state inhibition threshold. **(c)** The azobenzene photoswitch can be photoisomerized between the thermodynamically stable *E*-isomer to the metastable *Z*-isomer. The *E*-isomer is almost planar and has no dipole moment, whereas the *Z*- isomer adopts a bent and polarized conformation with its phenyl rings twisted out of the plane from the azo group. *E*-azobenzene shows a strong $\pi \rightarrow \pi^*$ transition near 320 nm and a weak $n \rightarrow \pi^*$ band near 440 nm, whereas *Z*-azobenzene has a stronger $n \rightarrow \pi^*$ band near 440 nm and a weak $\pi \rightarrow \pi^*$ transition near 300 nm (adapted from Beharry and Woolley[16]).

However, the idealized scenario (Fig 4b(1)) is rarely achieved in practice because the structural differences between the lit and dark state are too small, resulting in either residual dark activity (Fig 4b(2)) or low activity (low K_A, flat Hill slope) of the photopharmaceutical in the lit state (Fig 4b(3)). Therefore, compromises are usually made when choosing a practical working concentration $[I]_{WC}$. In my work, I will define the $[I]_{WC}$ as the concentration where either the lit efficacy reaches >80% of its plateau, or treatment in the dark causes <10% difference of biological effect compared to the untreated control: whichever is the lower concentration.

The most common photoswitch in photopharmacology is the azobenzene scaffold and its photoswitching behavior has been very well studied (Fig 4c).[17] Azobenzenes photoisomerize between a thermodynamically stable *E*-isomer and the metastable *Z*-isomer when irradiated in their $\pi \rightarrow \pi^*$ or $n \rightarrow \pi^*$ bands. Irradiating into the $\pi \rightarrow \pi^*$ band where *E*-azobenzene and *Z*-azobenzene have the largest difference in extinction coefficients (in Fig 4c at 350 nm) typically gives an *E*/*Z* ratio of roughly 20:80. When irradiating into the $n \rightarrow \pi^*$ band where *Z*-azobenzenes and *E*-azobenzene have the largest difference in extinction coefficients a 90:10 *E*/*Z* ratio is obtained. Additionally, the thermodynamically stable *E*-azobenzene can be quantitatively regained by thermal relaxation.[16] Due to its high quantum yields and fast, bidirectional switching, photostable over thousands of cycles, azobenzene is the most applied photoswitch in photopharmacology.

Choosing the right attachment site of a photoswitch is often a non-trivial challenge in photoswitch design and design strategies have been described to increase chances of success.[10] The different sterics of the *E*- and *Z*-azobenzene are often exploited in photodrug design to change the ligand's fit into the binding pocket. The synthesis of photoswitchable Δ^9-tetrahydrocannabinol derivatives (*azo*-THC)[18] by extending an azobenzene off the side of a parent drug's core structure exemplifies how molecular docking, structure-activity relationship tables and X-ray/Cryo-EM structures help to design photopharmaceuticals that interact differently with secondary structure motifs and key residues of the protein depending on the isomer (Fig 5a).

The azobenzene scaffold can also replace various structure motifs found throughout medicinal chemistry to introduce a photoswitch into a drug scaffold. Common azobenzene-analogs

(azologs) include stilbenes, *N*-phenyl benzamides, benzyl phenyl (thio)ethers, benzyl anilines, 1,2-diaryl ethanes and biaryl sulphonamides.[19,20] But azologization can also replace aliphatic chains to mimic less obvious motifs such as (un)saturated fatty acids to study lipid signaling and membrane organization in lipid bilayer vesicles (Fig 5b).[21–23]

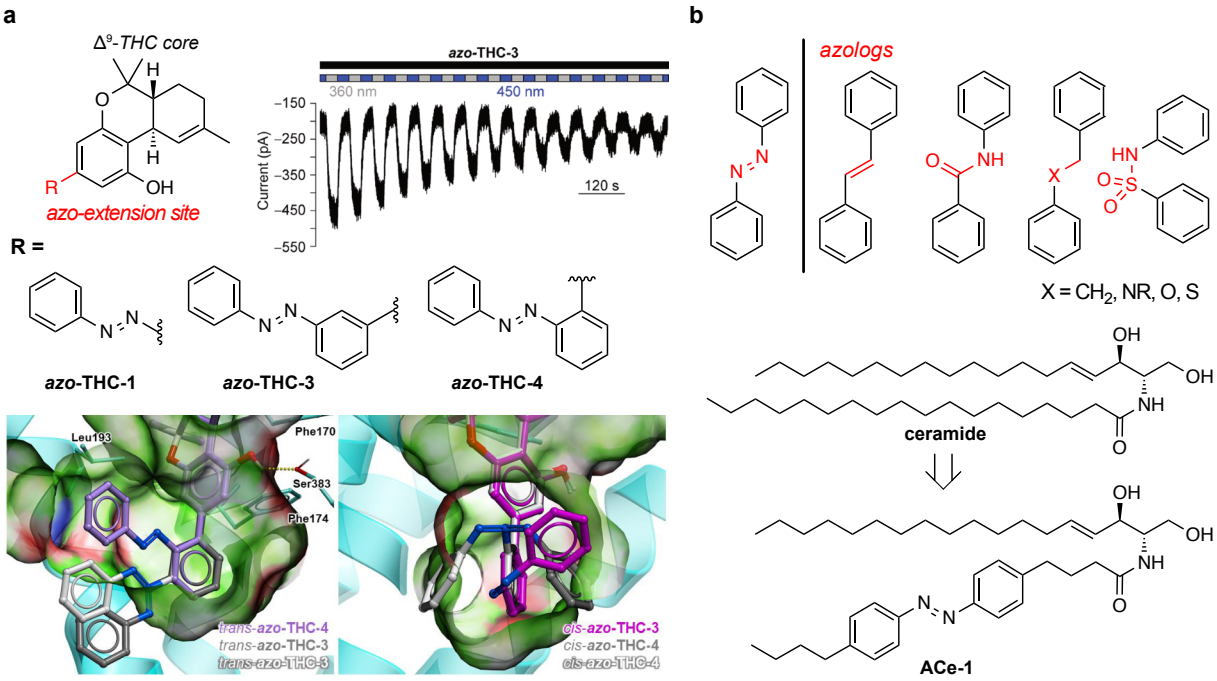

Figure 5: **(a)** Azo-extension from Δ9-THC core allows optical control over a cannabinoid receptor. The design rational was supported by molecular docking based on previous structure-activity relationship studies and X-ray/Cryo-EM data of the protein-ligand complex and offers an explanation how *E*- and *Z*-azobenzene fill out the binding pocket or clash with secondary structure motifs of the protein. (adapted from Westphal et al.[18]) **(b)** the azobenzene scaffold can replace various structure motifs (so called azologs) found throughout medicinal chemistry to introduce a photoswitch into a drug scaffold. Because of azobenzene's lipophilic nature they can even replace the fatty acid side chains of glycerides.[24]

The azobenzene photoswitch has been highly successful in photopharmacology to install optical control over a large range of proteins and biological processes, not only because azobenzenes have high quantum yields and fast bidirectional photoswitching over thousands of cycles but also because design principles to obtain azobenzene photodrugs are well documented and straightforward to implement.

2.3.3. Non-azobenzene photoswitches used in photopharmacology

Non-azobenzene photoswitches are starting to gain more attention, because the azobenzene scaffold only covers parts of the chemical space in drug design and photoswitching properties of azobenzenes can be impractical in certain situations. Consequently, the toolbox of photoswitches has been expanded continuously in the recent years with each photoswitch having their own unique strengths and weaknesses over the other.

Stilbenes (Fig 6a) undergo an *E*→*Z* photoisomerization process similar to azobenzenes under lower UV-A light (UV-A region: 400-320 nm, lower UV-A < 350 nm). However, the *Z*→*E*

photoisomerization is much harder and less efficient, because of the missing n→π* band. Due to the higher thermal barrier in stilbenes compared to azobenzenes[25,26], thermal relaxation to the thermodynamically favored *E*-isomer is also significantly slower.

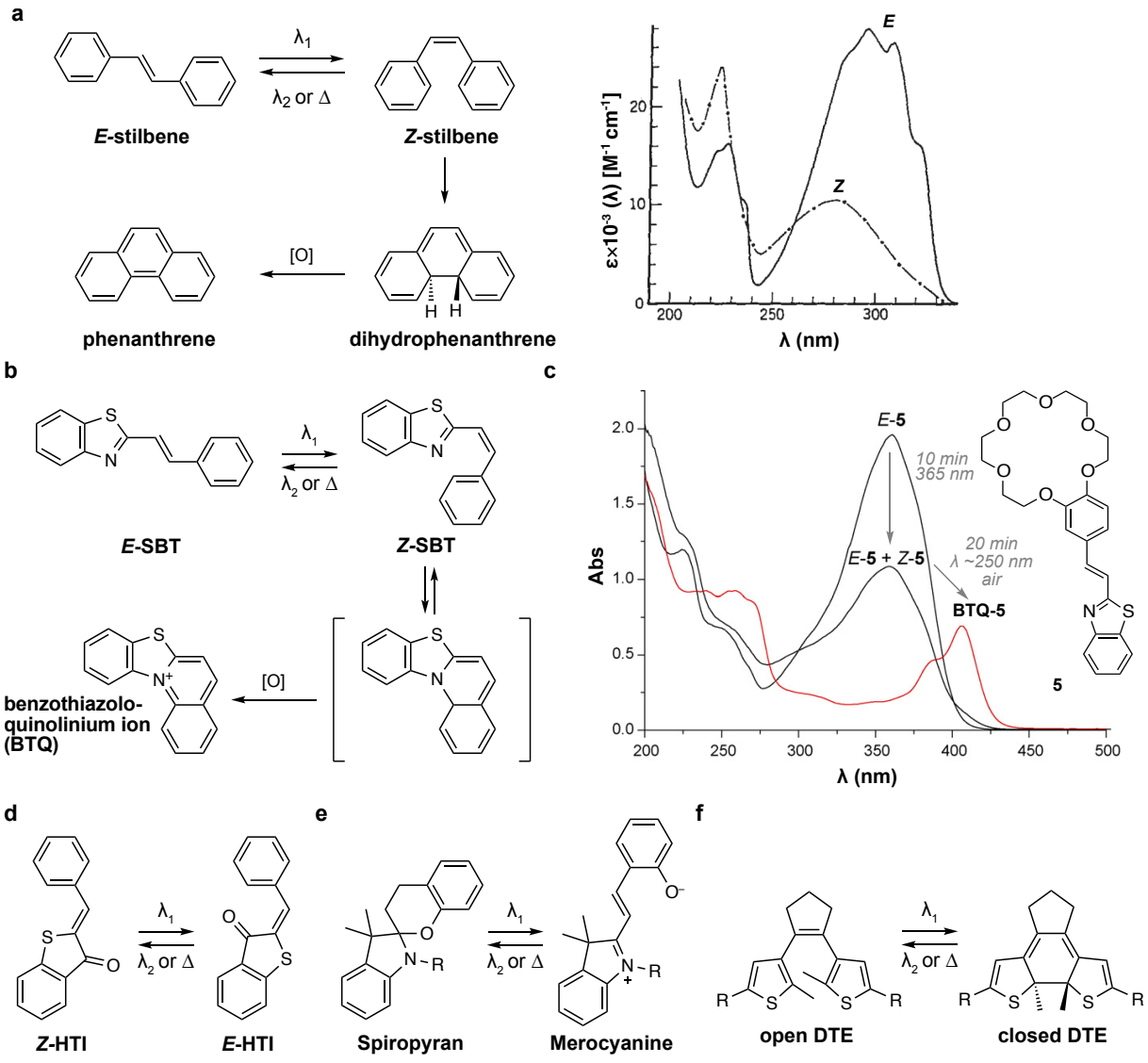

Figure 6: Examples of non-azobenzene photoswitches in photopharmacology **(a)** Stilbenes undergo *E*→*Z* photoisomerisation at switching wavelength $\lambda_{E\rightarrow Z}$ = 300-350 nm, further photocyclization to dihydrophenanthrene followed by oxidation leads to phenanthrene. UV spectra of *E*- and *Z*-stilbene in hexane, adapted from Meier et al.[25] **(b-c)** Styrylbenzothiazole (SBT) photoswitch with red-shifted absorption wavelength compared to normal stilbenes ($\lambda_{E\rightarrow Z}$ = 350-410 nm) of the *E*-isomer that undergoes *E*→*Z* photoisomerisation **(c)** UV spectra of SBT **5** (40 μM in acetonitrile), before (*E*-5) and after photoequilibration (mixture of *E*- + *Z*-5) at 365 nm for 10 minutes, shows SBT's photostability at cell culture relevant photon fluxes. The BTQ ion is observed after illumination with λ ~255 nm for 20 minutes (adapted from Fedorova et al.)[27] **(d)** Hemithioindigo (HTI) shows bistable photoswitching, the structural difference between both isomers is less pronounced than it is in azobenzenes. **(e)** Spiropyran-merocyanine photoswitches can switch between an uncharged lipophilic and a charged hydrophilic form. **(f)** Dithienylethenes (DTE) photoswitch with little change of geometry but large color and electronic changes.

Furthermore, *Z*-stilbenes can undergo various side reactions such as a 6 π-electrocyclic rearrangement to form a dihydrophenanthrene, that readily oxidizes to phenanthrene under air[28], or intermolecular [2+2] photocycloaddition.[25] Because they are structurally close to azobenzenes they are often replaced by azobenzenes ("azologization") to red-shift the photoswitching wavelength out of the phototoxic low UV-A region and improve bidirectional

photoswitching as well as photostability. Heteroarylstilbene photoswitches like styrylbenzothiazoles (SBTs)[29] have been developed from classic stilbenes and maintain the C=C double bond character. Because of the benzothiazole heterocycle the E→*Z* isomerization wavelength is slightly red-shifted (Fig 6b, $\lambda_{E\rightarrow Z}$ = 360-410 nm) making their photoisomerization less phototoxic in cell culture settings, where 360 nm is generally considered the lowest applicable wavelength that is not causing significant phototoxicity. Compared to classic stilbenes, SBTs are less prone to the electrocyclization-oxidation side reaction.[30,31] But highly energetic UV light (~ 250 nm) and oxidizing conditions slowly form the benzothiazoloquinolinium ion (Fig 6c).[32,33]

Hemithioindigo (HTI)[34] is an emerging photoswitch with strong absorption bands in the visible, that allow photoisomerization in both *E* and *Z* directions. HTIs show highly fatigue resistant photoswitching and enhanced thermal bistability, however the structural difference between both isomers is less pronounced than it is in azobenzenes (Fig 6d). The spiropyran-merocyanine switches (SPMCs)[35] can be regarded as a polarity switch[36], due to the large difference between the uncharged spiropyran and the zwitterionic merocyanine (Fig 6e). But SPMC's susceptibility to hydrolysis under aqueous conditions limits its applicability in biology.[37] The photo-6π-electrocyclic rearrangement of dithienylethenes and fulgimide photoswitches is associated with little changes of geometry but large color and electronic changes (Fig 6f).

The growing number of non-azobenzene photoswitches opens up photodrug designs with different metabolic profiles and photoswitching properties[38,39] tailor-made for specific purposes and circumstances.

2.3.4. Current state of photopharmacology

Photopharmacology has been particularly successful to install optical control over systems with nonlinear response to ligand concentration, such as the neural network, where a slight change in the activity of a modulator can generate an action potential.[40] There are photopharmaceuticals targeting several transmembrane proteins. Glutamate receptors, voltage and ligand gated ion channels can be controlled with light using photochromic ligands in order to restore visual function to the blind retina.[41,42] The movement behavior of different animal models (*nematode C. elegans*, zebrafish) can be changed through photoregulation of nAChRs[43] or GIRK[44] channels and photoswichtable ligands play an important role to elucidate the molecular mechanisms by which GPCRs modulate biological processes[45–47]. The power of photolipids to study lipid signaling and membrane organization in lipid bilayer vesicles has been demonstrated by recently published photolipids such as FAAzos, azo-PCs or PhoDAGs, a photoswitchable version of the second messenger lipid diacylglycerol which allows optical regulation of protein kinase C and Munc13 to control vesicle release.[21–23]

Carreira[48] and Trauner[49] have both incorporated a photochromic ligand into the PROTAC[50] (*proteolysis targeting chimera*) concept, bifunctional molecules that target proteins for ubiquitylation by an E3 ligase complex and subsequent degradation by the proteasome, to allow optical control over the concentration levels of specific cellular proteins.

Ben Feringa the 2016 Nobel laureate in chemistry has also envisioned that photoswitchable drugs could be used to treat various diseases or disabilities.[9] And photoswitchable ligands for vision restoration developed by Trauner, Iscaoff and Kramer are very promising tools to improve or restore visual function in degenerative retinal diseases.[51] Other therapeutic fields for photoswitchable drugs include photoswitchable antibiotics[52,53] or cytotoxic photopharmaceuticals with defined molecular targets suitable for cancer therapy such as photoswitchable proteasome inhibitors[54], histone deacetylases (HDACs)[55] or cytoskeletal inhibitors[56–59]. Such photodrugs could be systemically applied and then locally activated at the site of the tumor to reduce systemic side effects that occur in conventional chemotherapy.

However, except for vision restoration any currently ongoing *in vivo* application of photopharmaceuticals for therapy has yet to be proven effective in even a preclinical setting and many challenges remain for a photopharmaceutical to enter clinical stages[60]. Nevertheless, it is without question that such two-state molecules have shown to be extraordinary tools in biological research to install optical control over various biological processes and to study highly dynamic cellular systems - such as the microtubule cytoskeleton, which is treated in the next section.

2.4. The microtubule cytoskeleton

The microtubule (MT) cytoskeleton supports an extraordinary range of cellular functions simultaneously, with central roles in nearly all directional processes, such as intracellular transport and cell motility; its crucial function in cell proliferation has also made it a prominent anticancer drug target. Together with actin and intermediate filaments they are part of the cytoskeleton and are permanently remodeled through regulated cycles of growth and shrinkage in order to fulfil their spatiotemporally-regulated functions.

2.4.1. Microtubule structure and dynamics

Microtubules (MTs) are dynamic polymers found in all eukaryotic cells that form long cylindrical structures (Fig 7). They consist of tubulin heterodimers, which themselves are made up of α-tubulin and β-tubulin subunits, to form single stranded tubulin protofilaments in a head-to-tail fashion, i.e. the β-subunits of one tubulin heterodimer attach longitudinal to the α-subunits of the next heterodimer. Around 13 of these protofilaments are bundled in parallel to each other to form hollow MT tubes, with a diameter of ~25 nm and stabilized *via* homotypic lateral

interactions between tubulin subunits.[61] This is only interrupted at the MT lattice seam where α-tubulin subunits from one protofilament make lateral contact to β-tubulin subunits of the adjacent protofilament.[62] The protofilaments and the MT itself is a polar structure due to the head-to-tail assembly of heterodimers. Therefore, both ends can be distinguished from each other as a fast-growing *plus* end (+) and a slow-growing *minus* end (–).

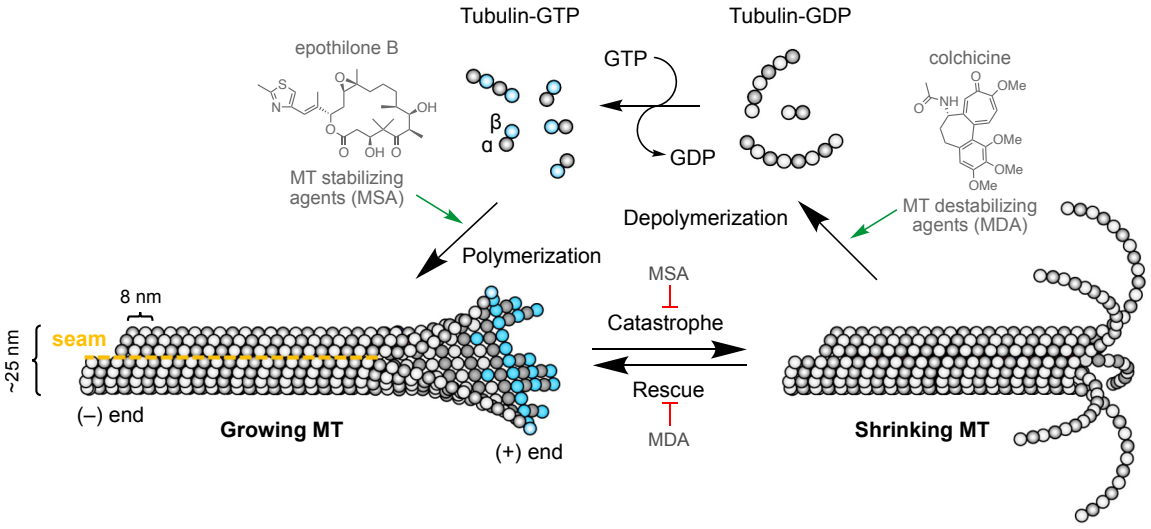

Figure 7: Microtubules (MTs) are in a constant equilibrium of polymerization and depolymerization called dynamic instability. Tubulin-GTP dimers and protofilaments add to growing (+) ends of MTs to form giant tube-like structures that are stabilized by lateral and longitudinal contacts. GTP hydrolysis after polymerization allows the protofilaments to take on a curved shape leading to destabilization of the MT structure and eventual disassembly. Free tubulin-GDP within the "cell cytosol pool" can exchange GDP for GTP to be available again for polymerization. MSAs like epothilones can promote MT polymerization (even of tubulin-GDP) and prevent MT catastrophe, whereas MDAs stop MT polymerization and rescue (adapted from Steinmetz and Prota[63]).

MTs undergo a constant process of polymerization and depolymerization caused by the hydrolysis of GTP on the β-tubulin subunit. Tubulin carrying GTP has a higher tendency to polymerize into straight protofilaments and MTs. When GTP is hydrolyzed after a certain while a slight structural change within the tubulin heterodimer causes the protofilament to bend into a curved shape and the MTs tend to fall apart if not otherwise stabilized, because they lose stability from weakened lateral contacts between the protofilaments.

2.4.2. Microtubule associated proteins and posttranslational modifications

The structure and reorganization of the MT network is crucial to many anisotropic processes such as intracellular transport or cell motility. Spatiotemporally controlled recruitment of MTs within specific regions of the cell[64] form a polarized network that allows cargo transport, organelle and protein movement *via* motor proteins such as kinesins or dyneins. The stability as well as other properties of MTs can be regulated through microtubule-associated proteins (MAPs),[65] such as end-binding protein 1 (EB1) that recruits other microtubule-plus-end tracking proteins (+TIPs) and binds to the GTP-cap of growing microtubules to promote growth.[66] The family of EB proteins have become widely successful in biological research

settings as fluorescent fusion proteins to visualize MT dynamics in living cells.[67,68] MTs play key roles during all stages of mitosis, where MTs coordinate a diverse set of biological processes, including chromosome segregation, correct spindle positioning and cytokinesis (Fig 8a).

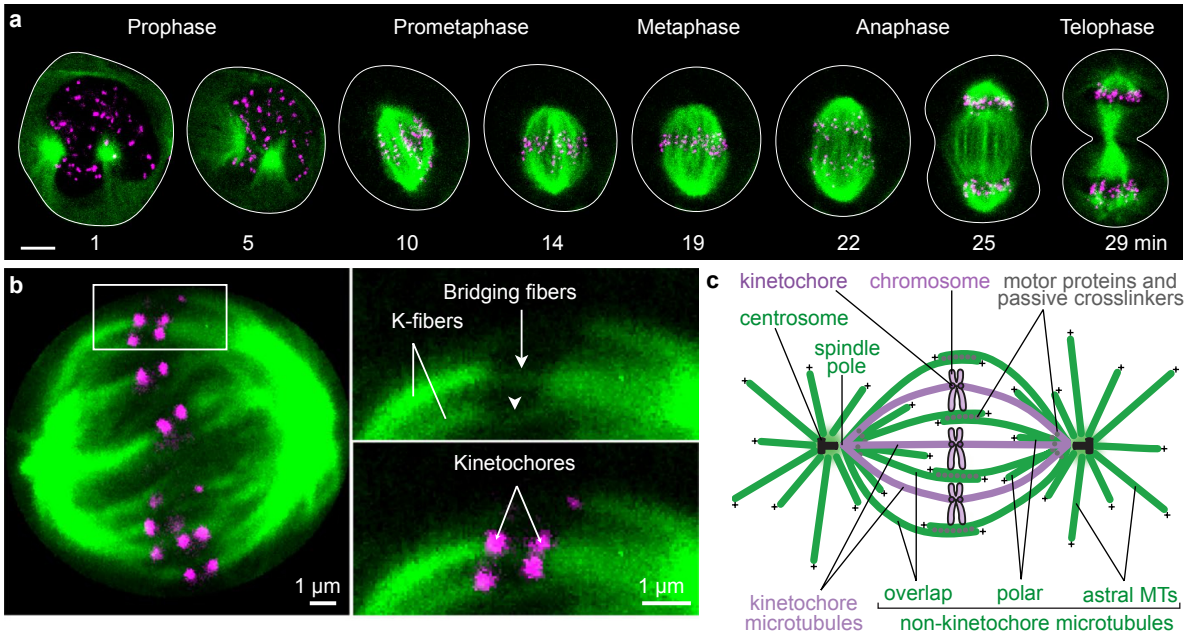

Figure 8: **(a)** Visualization of the MT cytoskeleton network and its remodeling during different stages of mitosis. (Human U2OS cell expressing CENP-A-GFP and mCherry-α-tubulin. green: MTs, magenta: kinetochores, white: cell outline). **(b-c)** To orchestrate these diverse functions, MTs self-organize into distinct structures that span up the spindle apparatus**. (b)** Immunofluorescence staining of a mitotic spindle in a HeLa cell. MTs in green (SiR-tubulin), kinetochores in magenta (eGFP-CENP-A). Enlargements of the boxed region show bridging fibers connecting sister kinetochore fibers (K-fibers). **(c)** schematic view of the MTs in the mitotic spindle apparatus (**a**-**c** taken and adapted from Tolić[69]).

The flawless interplay between MTs, motor proteins and MAPs is essential for the correct assembly of the spindle apparatus during cell proliferation (Fig 8b), where MTs self-organize into distinct structures like kinetochore fibers, astral and interpolar MTs[70] (Fig 8c). The astounding ability of MTs to show different behaviors, properties and functions between species and cell types or even within single cells is owed not only to regulation of MT-binding proteins, but also to the incorporation of different tubulin isotypes and their posttranslational modifications that function as a tubulin code on the MTs themselves.[71]

2.4.3. Inhibitors of microtubules are classified into destabilizers and stabilizers

Despite the functional diversity of MTs, all tubulin proteins are actually similar in structure and the tubulin gene sequence has been highly conserved throughout evolution. This structural homology throughout all species has brought forth a plethora of cytotoxic natural products targeting tubulin which are produced by a large number of plants and animals presumably for self-protection.[72,73] Six known tubulin-binding sites have been identified in great detail by X-ray crystallography and Cryo-EM to date (Fig 9): ligands binding to the colchicine site, the vinca

site, the maytansine site or the pironetin site are considered MT destabilizers (MDAs: **M**icrotubule **D**estabilizing **A**gents) that promote MT shrinkage/catastrophe and ligands that bind to the taxane site or the laulimalide/peloruside site have the ability to promote MT growth/rescue (MSAs: **M**icrotubule **S**tabilizing **A**gents).[63]

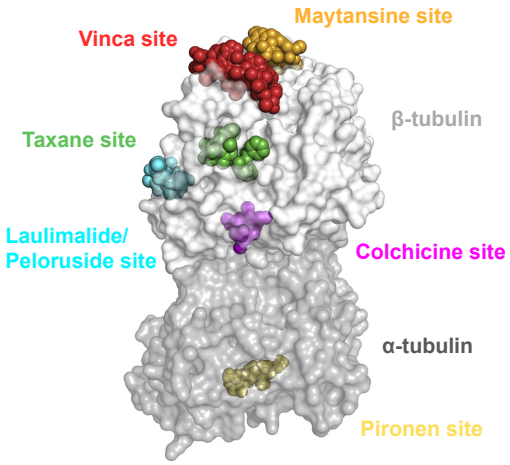

Figure 9: The tubulin heterodimer has six ligand binding sites that influence polymerization behavior by interacting with key secondary structures responsible for lateral and longitudinal contact with neighboring tubulin heterodimers (taken from Steinmetz and Prota[63]).

Because of the crucial role MTs play in almost all directional cellular activities, especially during mitosis and cell division, compounds that interfere with the microtubule cytoskeleton structure and their dynamics have become highly interesting not only for basic biology research to study MT dependent cellular processes, but also therapeutically as pesticides, antiparasitics and most importantly anticancer agents.[74]

2.4.4. The colchicine binding site and colchicine domain inhibitors

There are many structurally diverse colchicine domain inhibitors (CDIs) in literature[75,76]. Among the oldest microtubule inhibitor known as a medication is colchicine (Fig 10). Used to treat rheumatism and swelling as early as 1500 B.C., it is still prescribed today to treat symptoms of gout.[77] Other CDIs include the combretastatins, such as CA4 (Fig 10), a class of natural products originally isolated from the African Bushwillow tree *Combretum caffrum*[78] which have progressed all the way to phase III clinical trials.

The colchicine binding site is a deeply buried, hydrophobic pocket found at the interface of α-tubulin and β-tubulin. It is surrounded by the β-S8 and β-S9 strands, β-H7 and β-H8 helices as well as the β-T7 and α-T5 loop. Colchicine domain inhibitors mainly interact with these secondary structures through hydrophobic contacts with just a few polar interactions. Most characteristic is the movement of the T7 loop and H8 helix (two secondary structural elements that establish key longitudinal tubulin contacts along protofilaments in MTs) that is needed to create enough space to allow the ligand to bind.[79] Upon binding of a ligand to the colchicine

site the MT-stabilizing curved-to-straight transition in tubulin is prevented thus promoting MT breakdown. Additionally, by removing ligand-bound tubulin out of the available "free tubulin pool" further microtubule polymerization is prevented.

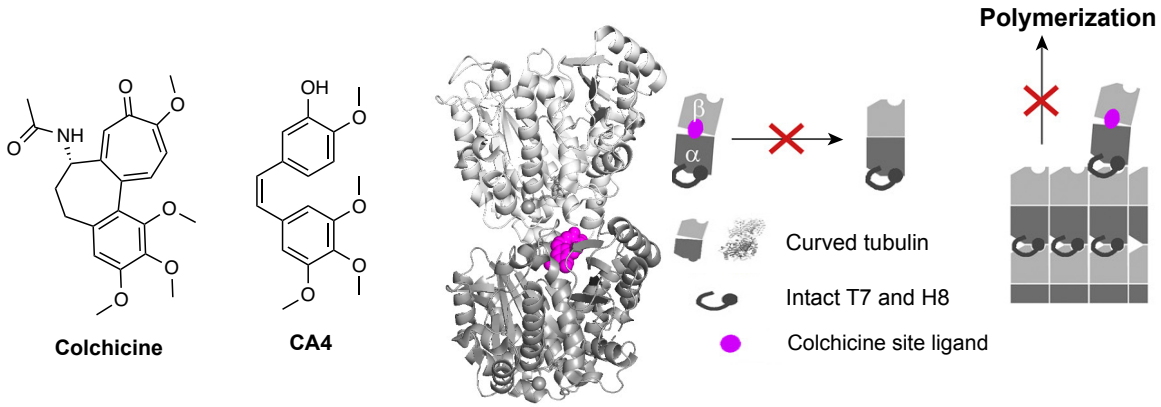

Figure 10: Chemical structures of colchicine and combretastatin A4 (CA4). Colchicine domain inhibitors (magenta) are MT destabilizing agents that bind to the interface of α- and β-tubulin, thereby preventing the curved-to-straight transition of tubulin which is necessary for MT polymerization (taken and adapted from Steinmetz and Prota[63]).

2.4.5. Taxane binding site inhibitors

The taxane site is located on the luminal side of MTs, it is predominantly formed by hydrophobic residues of helix H7, strand S7 and loops H6-H7, S7-S9 and S9-S10 of β-tubulin (Fig 11).[80] All taxane site ligands establish both hydrophobic and polar contacts with several of these secondary structural elements and their ability to shape the otherwise disordered M-loop into a short helix is crucial for the stabilization of lateral contacts in MTs.[81] Paclitaxel (Taxol) was the first MT stabilizing agent to be discovered in 1962 as a result of an NCI screening program for new natural products with antitumor activity (Fig 11). It showed strong antiproliferative activity in HeLa cells, arresting cells in the G2/M phase of the cell cycle[82,83] and was approved by the FDA for the treatment of a wide range of malignancies in the early 1990s.[84] The success of paclitaxel prompted an extensive search for taxol-like natural products that could stabilize microtubules which lead to the discovery and characterization of the epothilones by Höfle et al.;[85,86] isolated from the myxobacterium *Sorangium cellulosum* (Fig 11).[87] The epothilones gained a large amount of interest when their taxol-like MT stabilizing mechanism of action was discovered, yet they showed even higher binding affinities than paclitaxel in competitive binding assays and higher effectiveness against Pgp-expressing multiple drug resistant tumor cells, including taxol-resistant cell lines.[88] Notably, ixabepilone (Ixempra, Bristol-Myers-Squibb) a lactam derivative of epothilone B was the first epothilone approved by FDA for the treatment of aggressive metastatic or locally advanced breast cancer.[89] However, severe side effects have been reported in several clinical trials, including neutropenia, fatigue, mucositis, peripheral toxicity and diarrhea.[90–92]

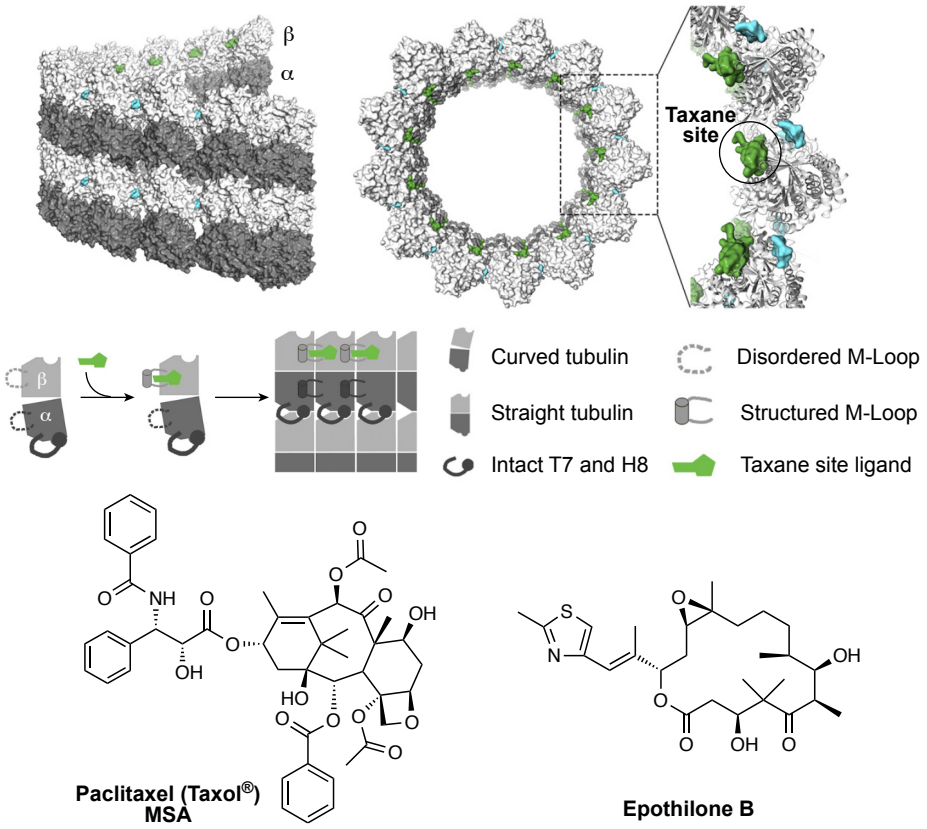

Figure 11: The taxane binding site (green) can be found opposite to the Laulimalide binding site (cyan) at the inner site of MTs. By stabilizing the β-tubulin M-loop, lateral contacts between protofilaments are consolidated, preventing MT catastrophe (taken and adapted from Steinmetz and Prota[63]). Chemical structure of classic taxane site binders paclitaxel and epothilone B.

MT inhibitors have contributed greatly as molecular tools in cytoskeleton research to shine light on some of the structural interactions of tubulin and giving a deeper understanding of the MT cytoskeleton itself and its role in various biological processes and pathologies.[93–95] However, to fully be able to study the dynamic behavior of such a complex system as the MT cytoskeleton will require new *dynamic* research tools with high spatiotemporal precision.

2.5. State of the art in photocontrol over the MT cytoskeleton

Cytoskeleton research typically aims to study a subset of MT-dependent processes that are spatially and/or temporally localized. Nearly all small-molecule inhibitors of MTs (drugs such as paclitaxel, colchicine, epothilone, etc.) cannot be spatiotemporally directed, so they inhibit MT dynamics throughout cells and systems to which they are applied.[58] Recently, the advent of optically targeted tools to manipulate biological systems with increased spatiotemporal precision has revolutionized diverse fields of biological research, particularly for temporally regulated and geometrically complex systems.

While optogenetics has been extremely successful in patterning ion currents and cell signaling with high spatiotemporal precision, no reports are known of optogenetically engineered MTs

that allow direct photomodulation of MT dynamics. However, Wittmann's indirect approach to control MT dynamics *via* a photo-inactivated EB1 variant[67] that upon photodissociation of a LOV2–Zdk1 complex stops the recruitment of +TIPs to the growing ends of MTs has impressively demonstrated the unrivalled subcellular spatial precision that only optogenetic methods can offer.[96]

2.5.1. Photopharmaceuticals targeting the colchicine binding site

By comparison, optically targeted tools to photomodulate MT structure and dynamics are well studied and can be dated back to 1970, just one year after Erlanger's pioneering work, when the antimitotic effect of colcimid (*N*-methyl *N*-desacetyl colchicine) was photoinactivated by UV light (Fig 12a)[97] in fertilized sea urchin eggs[98] and was later used by Hiramoto et al. to study the MT dependent formation and migration of the sperm aster in marine eggs.[99] Almost 25 years later Wühr et al. developed a lit-active photouncageable CA4 (Fig 12b) to study the effect of astral MTs on centrosome positioning in amphibian and fish embryos.[100] Hadfield, Bisby and Scherer investigated the photoinduced isomerization of *trans*-CA4 (Fig 12c).[101,102] *E*-CA4 was shown to be several orders of magnitude less potent than the *Z*-isomer[103,104], making the *E*⇄*Z* photoisomerization highly attractive for photoswitch development. Even though these studies showed that *in situ* photoisomerization of CA4 was possible, the hard UV light that was required to isomerize classic stilbenes (320-340 nm) prevented this first photoswitch approach from being widely used in research settings, due to the high phototoxicity and low tissue penetration of light at that wavelength.

Thorn-Seshold and Trauner replaced the bridging C=C double bond of the stilbenoid combretastatins with an isosteric N=N double bond to give the azo-combretastatin Photostatins (PSTs)[57], which allowed reversible bidirectional photoswitching by low intensity visible light between the biologically inactive *E*-isomer and the antimitotic *Z*-isomer (Fig 12d). Engdahl[105] and Hartman[106] would later confirm PST's ability to act directly as a light-activated tubulin polymerization inhibitor on purified tubulin *in vitro* and a greater than 200-fold increase in cytotoxicity in human cancer cells following photoisomerization, while also hinting at its metabolic susceptibility to glutathione mediated destruction of the azobenzene structure especially for the bioactive *Z*-isomer. Nevertheless, PST photoswitching has enabled noninvasive, reversible, cellularly resolved optical control over MT dynamics and structures in various model systems to photocontrol cell proliferation, cell cycle arrest, and induction of apoptosis (Fig 12e). PSTs were used to reveal a noncentrosomal form of MT organization that directs intracellular transport in early-stage mouse embryos.[107] Matis et al. used PSTs to study the interplay of actin and noncentrosomal MT dependent push-and-pull mechanics responsible for autonomous, individual epithelial cell morphogenesis in early *Drosophila* wing

development.[108] Overall, PSTs have become a viable niche tool in understanding the role of MTs in embryology[109], cargo transport[110], cell motility[111] and neuroscience[112].

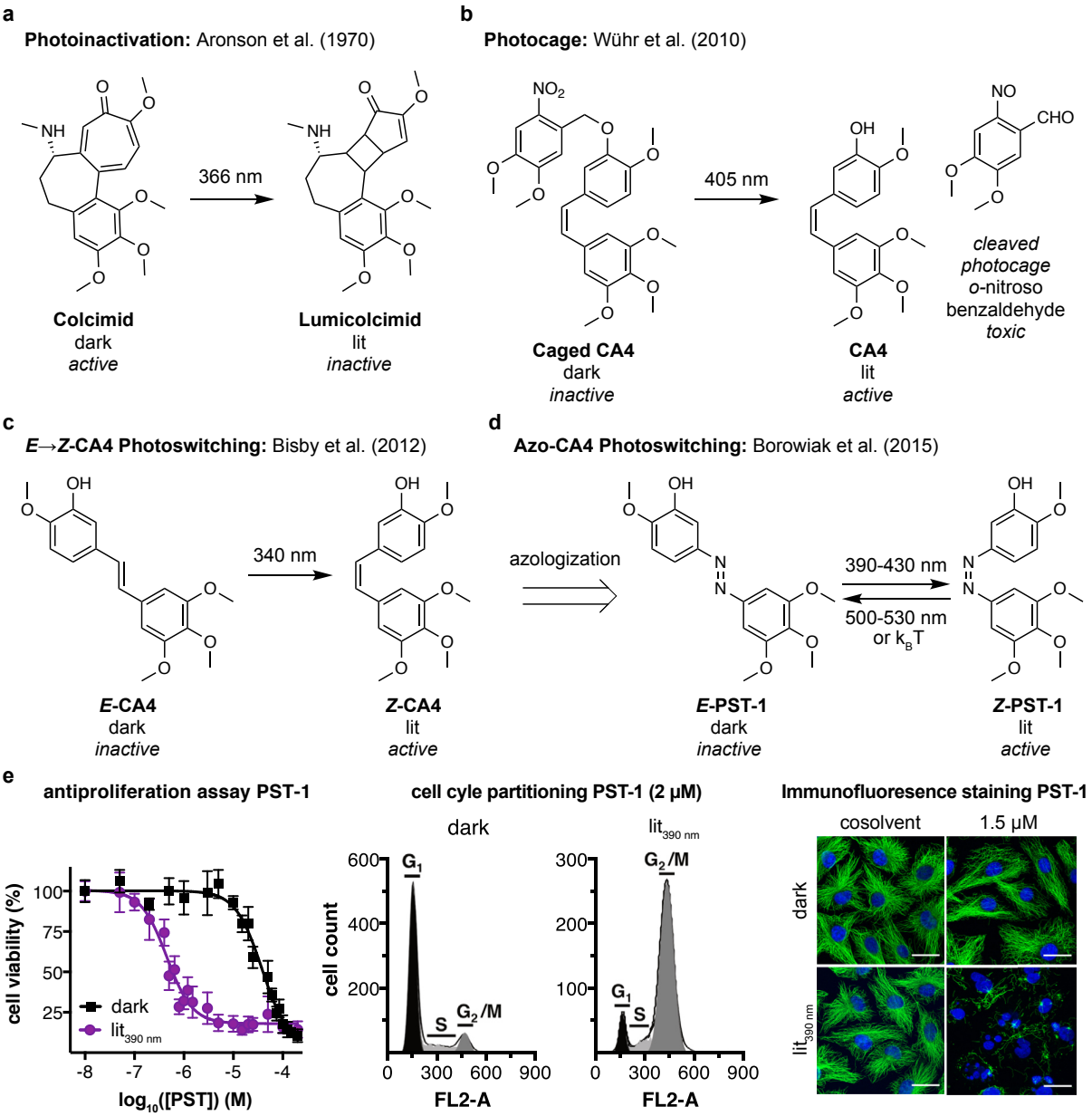

Figure 12: **(a-d)** Small molecule solutions to install optical control over the MT cytoskeleton system and its underlying biological roles have become more sophisticated over the years and the development of **(d)** azo-combretastatin PST-1 has allowed **(e)** light dependent reliable, reversible, cellularly resolved optical control over MT dynamics to photocontrol cell proliferation, cell cycle arrest, and MT structures (taken from Borowiak et al.[57]).

Several light-dependent derivatives of CA4 have been reported in the recent years by derivatization and scaffold-hopping.[113,114] Sailer et al.[115] developed a set of CA4-like photopharmaceuticals based on the HTI photoswitch scaffold (HOTub) which showed near quantitative E→Z photoswitching with green light (510-550 nm). The HOTubs could intentionally be designed to be lit or dark active, depending on the functional group patterning. While the most potent HOTub had a cellular IC_{50} of only 1 µM, Sailer also investigated an HTI

mimic of indanocine, an indanone based colchicine domain inhibitor and structurally more similar to the HTI photoswitch scaffold, to lower cellular potency down to ~100 nM.[116]

2.5.2. Photopharmaceuticals targeting the taxane binding site

In contrast to the MT destabilizers, there are nearly no light-dependent MT stabilizers. This can be partly owed to the success of PSTs in cell biology, the structural simplicity and SAR of parent compound CA4 and its extreme isomer-dependent bioactivity, probably unique in photopharmacology, that almost always guarantees light-dependent cytotoxicity. In comparison, MT stabilizers are large and complex structures that have posed tough challenges for even the biggest groups in classic total synthesis.[88,117,118] Attempts to develop photoresponsive prodrugs of paclitaxel generally suffered from low kinetic release rates of the active drug compound after photouncaging and the problem of additionally decreasing paclitaxel's inherently low water solubility.[119]

Müller-Deku et al. developed the first photoswitchable paclitaxel *via* azo-extension at the sidechain benzamide, the light dependent inhibition of MTs was confirmed both in cell-free tubulin polymerisation assays and in cells, where AzTax would inhibit MT-dependent functions leading to multinucleated cells and cell-cycle arrest in G2/M phase. Cytotoxic potency of the lit state was roughly 6 times higher than the dark state. During live cell imaging AzTax could instantaneously and reversibly inhibit MT polymerization when activated in single selected cells without affecting neighboring cells. In selected dendrite regions of individual rat hippocampal neurons AzTax would also allow a degree of subcellular control over MT dynamics.

The emergence of photoswitchable antimitotics as spatiotemporally precise tools in biology research to study the highly dynamic MT cytoskeleton has been largely successful. While most of the breakthrough findings are based on azo-combretastatin PST-1, it is undeniable that new MT inhibiting photopharmaceuticals are needed that are based on other photoswitches or other parent drug scaffolds, with complementary properties that compensate for the weaknesses of the current photoswitchable antimitotics available.

2.6. Challenges and weaknesses

The number of azobenzene-based photopharmaceuticals that have been used in a biology setting are overwhelmingly high compared to that of non-azobenzene photoswitches; for example, Hüll et al.[12] list only 7 out of 123 (5.7%) non-azobenzene based photopharmaceuticals that were used in a biochemical/biology setting. The success of photopharmacology is greatly owed to the azobenzene photoswitch due to the intuitive ligand design from parent drug scaffolds[120], easy synthetic access,[121] and reliable bidirectional (and optionally bistable) photoswitching performance.[16] This combination has made azobenzene

the preferred photoswitch to install optical control over small molecule drugs, especially if these targets are within lipophilic compartments of a cell. However, focusing solely on the powerful azobenzene scaffold has also limited the progress of photopharmacology in directions where azobenzenes face problems.

2.6.1. Metabolic liabilities in intracellular settings

While azobenzene based photopharmaceuticals are regularly used in live animals to study neuronal signaling[122,123] it has not been possible to achieve the same impact in cytosolic targets; and azobenzene photopharmaceuticals for intracellular targets tend to lose performance when transitioning from cell-free to cellular assays. One key driver seems to be the cellular instability of their electrophilic and abiotic N=N chromophore. For example, PSTs are ~2 orders of magnitude less potent in cells than CA4, despite near-identical potency in cell-free assays. Sheldon et al.[106] have observed fast degradation of *Z*-PST-1 following the addition of glutathione (GSH) to the N=N group[124].

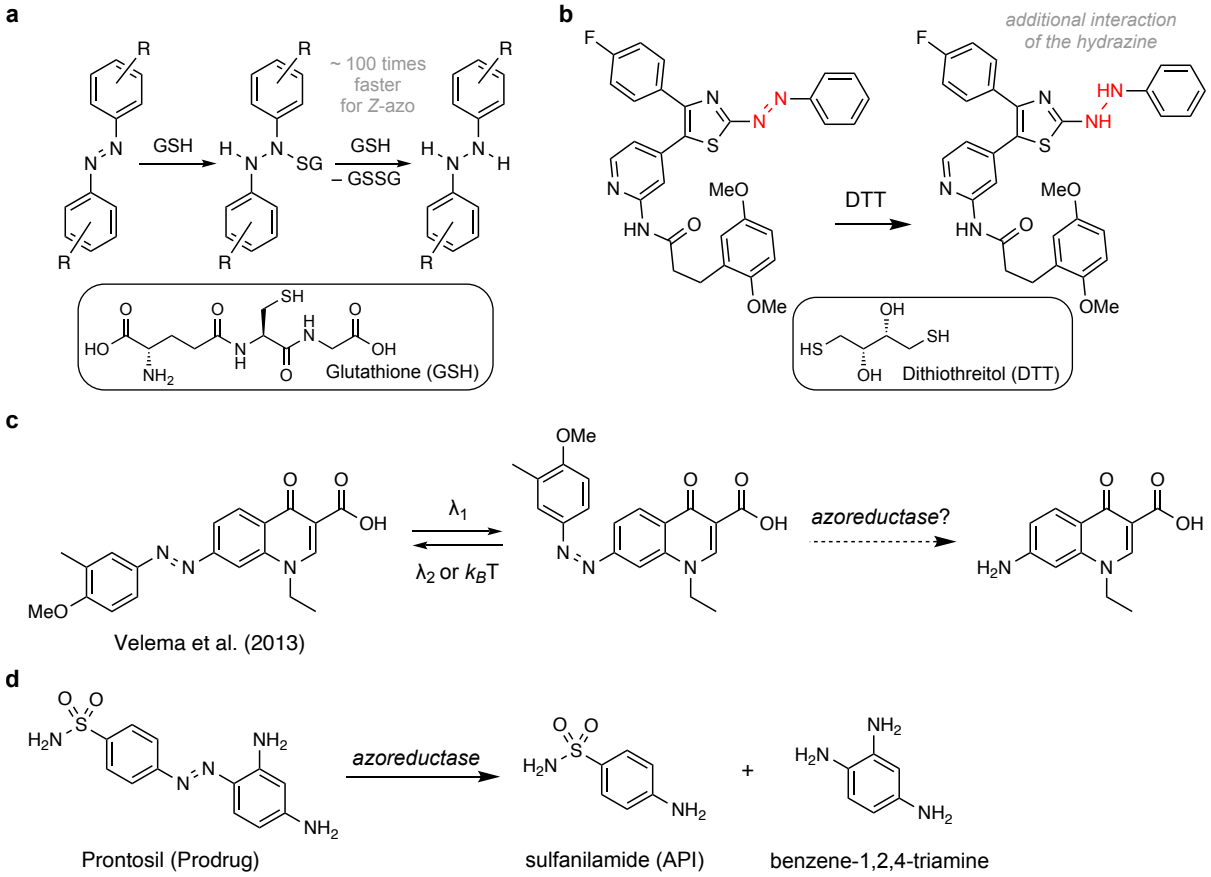

Figure 13: **(a)** GSH is present up to 10 mM in cells. GSH reduction of azobenzene begins with a nucleophilic attack of the thiolate on the diazo bond to form an adduct which reacts further with a second equivalent GSH to form the reduced hydrazine, this two-step process occurs at neutral and basic pH and is ~100 times faster for the *Z*-isomer.[125] **(b)** Photoswitchable kinase inhibitor developed by the Herges group.[126] It turned out that the diarylazo unit was reduced by DTT to a hydrazine moiety under normal assay conditions. **(c)** Photoswitchable antibiotics showed light-dependent antibacterial activity.[53] However, it is not fully clear if the compound is enzymatically cleaved after photoisomerization because the *Z*-isomer is more susceptible to reduction. **(d)** the azobenzene scaffold can be used as an enzymatically cleaved prodrug scaffold as it has been shown in the case of prontosil.[127]

The majority of azobenzenes can be degraded this way (Fig 13a), ultimately giving a range of non-photoswitchable byproducts of N=N bond degradation (e.g. hydrazines)[128–130] and cleavage byproducts (e.g. anilines) that could either be toxic or compete for the target binding site with the intact reagent, which blocks cellular photoswitchability of inhibition.[126] In a study by Schehr et al.[126] an arylazo-containing photoswitchable kinase inhibitor displayed contradicting activity to their design hypothesis and discrepancies across different assay conditions which they could trace back to photoswitch reduction by dithiothreitol, a common reducing agent used in biochemistry, showing that the resulting hydrazine was the most active substance present in their assays (Fig 13b). While it is becoming common practice to test photopharmaceuticals for their resistance against GSH reduction, this is mostly done exclusively for the *E*-isomer, not taking into account that the *Z*-isomer has typically ca. 100-fold higher susceptibility toward GSH reduction (see chapter 5), which can lead to wrongfully misinterpreting isomer-dependent photoswitch reactions as isomer-dependent differences of bioactivity.

The susceptibility of azobenzenes to reduction by azoreductases[131] also restricts the use of azobenzene reagents in the presence of hypoxic tumor microenvironments (slow re-oxidation of the hydrazines)[132] and in bacteria (high azoreductase activity). Although Feringa's landmark papers have shown that azobenzene-based antibiotics can light-dependently inhibit bacterial growth,[52,53] it was not tested and it remains unclear whether the antibacterial activity originates from the photoisomerized *Z*-isomer or from the enzymatically cleaved aniline (Fig 13c): which is the known mechanism for prodrugs like prontosil that use bacterial azobenzene reduction to release the pharmaceutically active aniline (Fig 13d)[127]. Irreversible reduction to an active species is detrimental to the stated aim of most photopharmaceuticals, which is to achieve photoreversibility of bioactivity (either for high-precision applications, or in the case of antibiotics, to avoid buildup of APIs in the environment which can lead to antibiotic resistance).

2.6.2. Non-orthogonality to standard imaging conditions

Secondly, photopharmacology typically relies on imaging-based readouts (particularly for intracellular targets), but the two most commonly used photoswitches, azobenzenes and HTIs, usually feature such a strong uni- or bidirectional photoresponse to standard imaging wavelengths, that isomerization caused by imaging overrides their desired photoswitching and/or limits the scope of experiments (Fig 14). This photoresponse in azobenzenes is due to the low-energy $n \rightarrow \pi^*$ transitions of their N=N chromophore's lone pairs. Regardless of their starting isomer population, azobenzenes, such as PSTs, are rapidly switched to ~3:1 *E*:*Z* under 488 nm (GFP/fluorescein imaging) and to ~4:1 *E*:*Z* under 514 nm (YFP); even 561 nm illumination noticeably affects isomer ratios on the confocal stage. Therefore, due to imaging,

a background of *Z*-azobenzene is created in areas where isomerization away from the stable *E*-isomer is not desired; and in areas where most *Z*-isomer is generated (typically by photoswitching at 405 nm), each imaging frame instead increases the proportion of *E*-isomer. By counteracting any spatiotemporally resolved isomer patterning throughout the sample, non-compatibility to imaging wavelengths limits the azobenzene scaffold's potential for high-precision use in cell biology or transgenic animals (where the most common tags are GFP/YFP-based). Though "normal" azobenzenes are not orthogonal to GFP/YFP imaging, the current focus in azobenzene spectral shifting research is actually on "red-shifting" photoresponse spectra to still longer wavelengths. Since "red-shifting strategies" almost always shift the photoresponse spectra of both isomers, the result of these is that bidirectional photoswitching continues to be stimulated by imaging fluorescent proteins: extending their non-orthogonality with GFP/YFP now strongly to RFP/mCherry imaging too and making the problem worse.

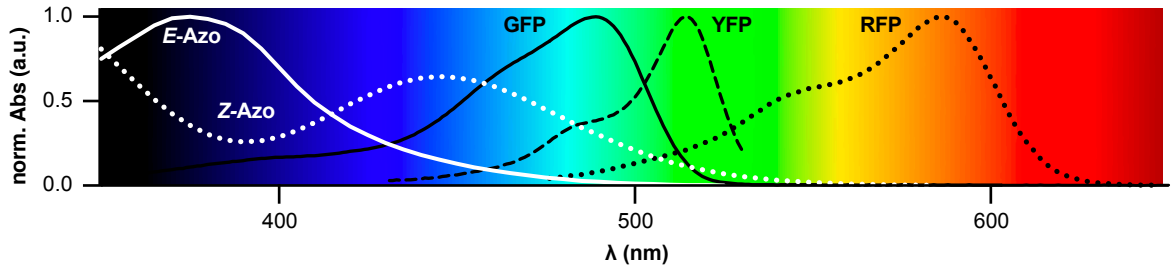

Figure 14: Overlays of excitation spectra of common fluorescent proteins GFP (black line), YFP (dashed black line) and RFP (dotted black line) and *E*- and *Z*-azobenzene (*E*: white line, *Z*: dotted white line) show that λ_{ex} of fluorophores (especially ~480-520 nm) overlaps with the n→π* band of *Z*-azobenzene, driving majority *Z*→*E* isomerization during fluorescence imaging.

2.6.3. Substituent-dependent limits on thermal half-life

Thirdly, azobenzenes undergo spontaneous unidirectional *Z*→*E* isomer relaxation, the rate of which greatly depends on the substituents at the six *ortho* and *para* positions that are in resonance with the N=N double bond. In general, some of the most important functional groups for ligand-protein interactions (including hydroxy, amine, and thiol groups) cause fast relaxation in azobenzenes and HTIs under physiological aqueous conditions if they substitute at any of these positions, typically giving *μ*s-ms half-lives.[133–135] Fast-relaxing azobenzenes cannot practicably be photopatterned to address intracellular targets, since counteracting their uniform relaxation to the *E*-isomer would require biologically unacceptable photon fluxes. Azobenzene photopharmacology is in general limited by the ranges of relaxation half-lives accessible to its tolerated substituent space, which also probably restricts its target scope.

These problems - non-orthogonality to standard imaging conditions, metabolic liabilities in intracellular settings, and strong substituent-dependent limits on thermal half-life - intrinsically derive from azobenzene's N=N double bond and have hindered the translation of azobenzene

photopharmaceuticals for intracellular targets from cell-free to cell culture settings, and essentially block their applications from simple *in vivo* models to higher animals.

3. Aim of the doctoral thesis

The azobenzene has mostly set the direction of photopharmaceutical research in the past decade. Making use of azobenzene's inherent lipophilic nature and its robust bidirectional photoswitching they have been mostly used to install reversible photocontrol over lipid membranes and membrane proteins where readout is not fluorescence-based and azobenzene reduction by GSH can be neglected.[136] However, noninvasive optical tools to modulate microtubule dynamics, structure and function with high spatiotemporal precision have different requirements.

Studying microtubule dynamics and its underlying processes in cells and *in vivo* is highly dependent on live cell imaging using fluorescent imaging tags. Currently available small-molecule inhibitors that offer spatiotemporal control over microtubules interfere with these common imaging tags and do not offer reliable microtubule photocontrol when transitioning out of 2D cell culture due to metabolic liabilities.

When studying long-term downstream effects after MT disruption, metabolically stable photopharmaceuticals with long thermal half-lives are required that reduce the amount of compound and photon fluxes needed to maintain the lit-state.

This thesis aims to synthesize and evaluate new photoswitchable microtubule targeting agents for enhanced spatiotemporal control over microtubule function and dynamics. Therefore, photoswitches based on the metabolically stable, GFP-orthogonal styrylbenzothiazole (SBT) scaffold were assessed for their suitability as highly potent photoswitchable cytotoxins from 2D cell culture to *in vivo* application.

On a general level this thesis should establish an alternative photoswitch scaffold in photopharmacology with complementary features to the well-established azobenzene scaffold. Similar to the azobenzene scaffold, I present a rational design approach strategy based on parent drug scaffold isosterism and structure-photoswitching-activity relationship based on Cryo-EM/X-Ray crystallographic data.

In the following chapters, I present my research towards these aims.

4. Author contributions

Bringing projects like the following ones to fruition would have never been possible on my own. While a summary of each author's contribution can be found within each manuscript, it only reflects part of what each of them have contributed to these projects, not mentioning their constant support, input and passion. I am more than thankful to all my collaborators who have contributed to and supported this research to give me the opportunity to report *our* findings.

In the following I will shortly describe my contribution to each project.

Part One: First generation styrylbenzothiazole SBTubs

I performed chemical synthesis and characterization of the SBTubs and performed one-photon photocharacterization. I compared **SBTub**'s and **PST-1**'s resistance to reduction by glutathione as well as photostability studies of the SBT scaffold. Furthermore, light-dependent antiproliferation studies were done from my side before further mechanistic evaluation by coworkers and collaborators, where I took on an advisory role. I coordinated data assembly and figure preparation during manuscript preparation and wrote the manuscript together with my supervisor Oliver Thorn-Seshold.

Part Two: Second generation styrylbenzothiazole SBTubs

I designed the SAR study and performed chemical synthesis and characterization of the twenty second generation **SBTubs**. I performed light-dependent antiproliferation studies to identify two lead compounds for further mechanistical studies and synthesized a water-soluble **SBTub** prodrug suitable for *in vivo* photopharmacological application. Additionally, I offered conceptual advice on assay development and compound handling for 3D cell culture and *in vivo* studies, as part of four collaborations I coordinated data assembly and wrote the manuscript together with my supervisor Oliver Thorn-Seshold.

Part Three: Photoswitchable epothilone-based microtubule stabilizers

I designed and performed chemical synthesis, photocharacterization and cell viability assays of the **STEpos** and coordinated data assembly during manuscript preparation.

5. Part One: First generation styrylbenzothiazole SBTubs

In the following work we intentionally move away from the overwhelming majority of azobenzene based photopharmacology studies and introduce an in-depth proof of principle for the styrylbenzothiazole scaffold (SBT) as an alternative photoswitch scaffold for photopharmacology for cell biological control.

We show that azobenzene photopharmaceuticals can be redesigned into SBT photopharmaceuticals without losing their mechanism of action or their potency. Therefore, we synthesized SBT-based Tubulin inhibitors (**SBTubs**), mimics of azo-combretastatin PST-1, which allow optical control over MT dynamics and their underlying processes. **SBTubs'** display *Z*-isomer specific cytotoxicity and induce light-dependent G2/M phase cell-cycle arrest and disruption of the MT network architecture in long term cellular assays even after a single photoactivation light pulse.

Additionally, we show that the desymmetrized SBT scaffold allows designed control over ligand orientation within a binding pocket and we describe a scaffold assessment methodology comparing designed-active and designed-inactive regioisomeric permutation control compounds, to verify enzyme-specificity and phototolerability of this new scaffold. SBTs' photoswitching performance is chemocompatible with *o/p*-EDGs such as hydroxyl groups, which are often found in bioactive drug-like compounds but are not well tolerated in intracellular applications, of either azobenzene or hemithioindigo photoswitches, due to their ultrafast relaxation.

We explicitly assay the SBTs for tolerance of intracellular biochemistry and for general metabolic resistance, in comparison to the standard photopharmacology scaffold azobenzene. SBTs are fully inert to cellular thiols (e.g. glutathione) which are highly problematic for intracellular applications of azobenzenes; and SBTs are also substantially resistant to microsomal metabolic processing.

Lastly, *in situ* photoswitching of **SBTubs** quickly and reversibly suppresses MT polymerization dynamics, revealed by live-cell imaging of EB3-GFP comets, with subcellular localization in neurons and fully orthogonal to GFP-imaging wavelengths.

Conceptually, the **SBTubs** can be placed somewhere between the bidirectionally photoswitchable azobenzene PST-1[57], and photocaged CA4 prodrugs[100]. However, the potency of these first generation **SBTubs** (IC_{50} ~1 µM) is less than either previous system (IC_{50} *Z*-PST-1 ~0.5 µM, fully uncaged CA4 ~20 nM); making further structural tuning of **SBTubs** necessary to improve potency. It is the different photoresponse and metabolic stability of **SBTubs** that derives from their C=C double bond which makes them promising for certain

photopharmacological applications not addressable with currently availble tools. The higher thermal stability of their photostationary state equilibria and the increased robustness towards GSH reduction allow **SBTubs** to tackle long time photopharmacological experiments *in vivo*, without photoswitch depletion due to metabolism or thermal back-isomerization, which is a still outstanding challenge for photopharmacological translations *in vivo*. Because SBTs, unlike azobenzenes, have no n→π* band they do not respond to wavelengths above 460 nm making them fully orthogonal to GFP/YFP/RFP imaging. In cells, azobenzenes can undergo *Z*⇄*E* switching by illumination and *Z*→*E* isomerization by spontaneous relaxation, whereas this first generation of **SBTubs** only allows cellular *E*→*Z* switching.

Therefore, the unidirectional photoactivation of **SBTubs** is conceptually somewhat similar to that of photouncageable inhibitors, however their performance differs in four key aspects: (1) typical photocaging groups (e.g. *ortho*-nitrobenzyl) require hydrolysis before cargo release that can take seconds to minutes, which diminishes the spatiotemporal precision of photouncaging approaches. Isomerization, as the SBTs use, is typically orders of magnitude faster (<< ns), and **SBTubs** give reproducibly high precision biological control. (2) Photouncaging byproducts are often unspecifically toxic and may also be phototoxic[14], while SBTubs photochemically robust *E*→*Z* isomerization allows cell-tolerated long-term experimentation. (3) Photouncaging strategies add significant molecular weight which often penalizes bioavailability or biodistribution; they may suffer non-photolytic compound release (enzymatic or spontaneous hydrolysis); and they involve higher synthetic cost[137]. SBT-inclusion in a pharmacophore does not add compound weight or complexity, and avoids any hydrolytic/enzymatic activation mechanisms. (4) While **SBTubs** only allow cellular *E*→*Z* isomerization, they can actually undergo quantitative *Z*→*E* back-isomerization at elevated temperatures (60°C). This “rescue” greatly improves the ease of use in the lab as compared to photocaged CA4, e.g. upon accidental photoactivation of the bio-stocks during handling.

Taken together, these features set SBTs apart from photouncaging approaches and from azobenzene photoswitching, recommending them for reproducible, high-precision, “clean” photopharmacological control particularly in higher-complexity biological systems.

Resource

Cell Chemical Biology

A Robust, GFP-Orthogonal Photoswitchable Inhibitor Scaffold Extends Optical Control over the Microtubule Cytoskeleton

Graphical Abstract

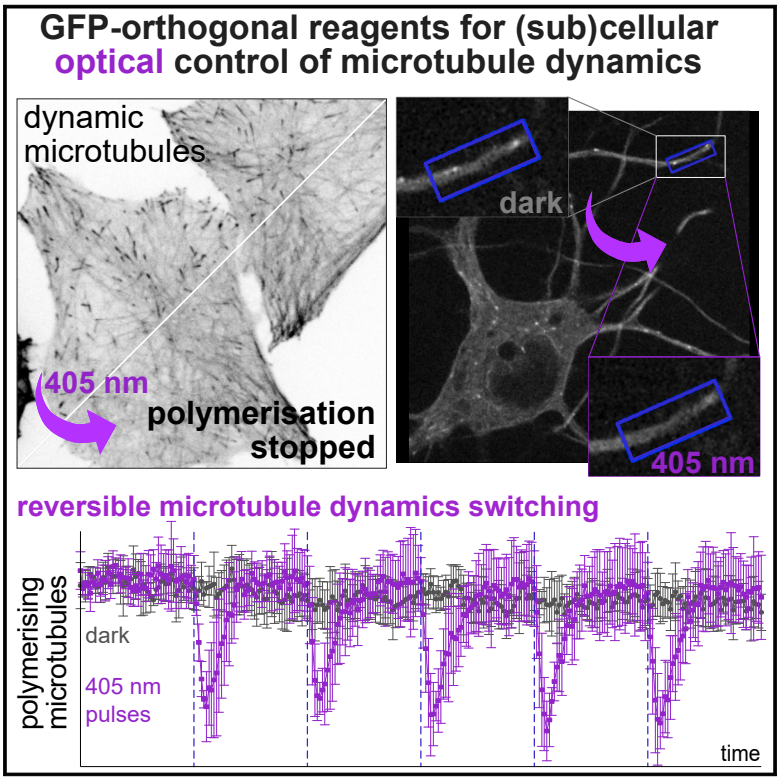

Highlights

- SBTub3 photocontrols microtubule dynamics, organization, and dependent processes
- Microtubule photocontrol is cell and sub-cellularly precise and temporally reversible
- SBT photocontrol is orthogonal to GFP/YFP imaging and SBTs are metabolically stable
- The SBT scaffold is promising for photopharmaceuticals for other protein targets

Authors

Li Gao, Joyce C.M. Meiring, ..., Julia Ahlfeld, Anna Akhmanova, Michel O. Steinmetz, Oliver Thorn-Seshold

Correspondence

oliver.thorn-seshold@cup.lmu.de

In Brief

Photocontrollable reagents have unique potential as high spatiotemporal precision modulators of biological systems. Here, Gao et al. demonstrate a GFP-orthogonal and metabolically stable photoswitch that allows optical control over microtubule dynamics and architecture with subcellular resolution. The photoswitch scaffold also offers new possibilities for photopharmaceutical design against other targets.

Gao et al., 2021, Cell Chemical Biology *28*, 1–14
February 18, 2021
https://doi.org/10.1016/j.chembiol.2020.11.007

CellPress

Please cite this article in press as: Gao et al., A Robust, GFP-Orthogonal Photoswitchable Inhibitor Scaffold Extends Optical Control over the Microtubule Cytoskeleton, Cell Chemical Biology (2020), https://doi.org/10.1016/j.chembiol.2020.11.007

Cell Chemical Biology

CellPress

Resource

A Robust, GFP-Orthogonal Photoswitchable Inhibitor Scaffold Extends Optical Control over the Microtubule Cytoskeleton

Li Gao,[1] Joyce C.M. Meiring,[2] Yvonne Kraus,[1] Maximilian Wranik,[3] Tobias Weinert,[3] Stefanie D. Pritzl,[4] Rebekkah Bingham,[1] Evangelia Ntouliou,[1] Klara I. Jansen,[2] Natacha Olieric,[3] Jörg Standfuss,[3] Lukas C. Kapitein,[2] Theobald Lohmüller,[4] Julia Ahlfeld,[1] Anna Akhmanova,[2] Michel O. Steinmetz,[3,5] and Oliver Thorn-Seshold[1,6,*]

[1]Department of Pharmacy, Ludwig-Maximilians University of Munich, Munich 81377, Germany

[2]Cell Biology, Neurobiology and Biophysics, Department of Biology, Faculty of Science, Utrecht University, Utrecht 3584, Netherlands

[3]Laboratory of Biomolecular Research, Division of Biology and Chemistry, Paul Scherrer Institut, Villigen 5232, Switzerland

[4]Chair for Photonics and Optoelectronics, Nano-Institute Munich, Department of Physics, Ludwig-Maximilians University of Munich, Munich 80539, Germany

[5]Biozentrum, University of Basel, Basel 4056, Switzerland

[6]Lead Contact

*Correspondence: oliver.thorn-seshold@cup.lmu.de

https://doi.org/10.1016/j.chembiol.2020.11.007

SUMMARY

Optically controlled chemical reagents, termed "photopharmaceuticals," are powerful tools for precise spatiotemporal control of proteins particularly when genetic methods, such as knockouts or optogenetics are not viable options. However, current photopharmaceutical scaffolds, such as azobenzenes are intolerant of GFP/YFP imaging and are metabolically labile, posing severe limitations for biological use. We rationally designed a photoswitchable "SBT" scaffold to overcome these problems, then derivatized it to create exceptionally metabolically robust and fully GFP/YFP-orthogonal "SBTub" photopharmaceutical tubulin inhibitors. Lead compound SBTub3 allows temporally reversible, cell-precise, and even subcellularly precise photomodulation of microtubule dynamics, organization, and microtubule-dependent processes. By overcoming the previous limitations of microtubule photopharmaceuticals, SBTubs offer powerful applications in cell biology, and their robustness and druglikeness are favorable for intracellular biological control in *in vivo* applications. We furthermore expect that the robustness and imaging orthogonality of the SBT scaffold will inspire other derivatizations directed at extending the photocontrol of a range of other biological targets.

INTRODUCTION

The microtubule (MT) cytoskeleton supports an extraordinary range of cellular functions simultaneously, with central roles in nearly all directional processes, such as intracellular transport and cell motility; its crucial function in cell proliferation has also made it a prominent anticancer drug target (Dumontet and Jordan, 2010; Peterson and Mitchison, 2002). Although cytoskeleton research typically aims to study a subset of MT-dependent processes that are spatially and/or temporally localized, nearly all small-molecule inhibitors of MTs (drugs such as paclitaxel, colchicine, epothilone, etc.) cannot be spatiotemporally directed, so they inhibit MT dynamics throughout cells and systems to which they are applied (Janke and Steinmetz, 2015). For decades this restricted the scope of inhibition studies of MT biology.

Recently, the advent of optically targeted tools to manipulate biological systems with increased spatiotemporal precision has revolutionized diverse fields of biological research, particularly for temporally regulated and geometrically complex systems. Optogenetics, photouncaging approaches, and photoswitchable small-molecule inhibitors or "photopharmaceuticals," have all been developed as optically targeted tools, with distinct strengths and weaknesses (Wittmann et al., 2020). Photopharmaceuticals offer performance and applications that are quite distinct from the other methods. Unlike photouncaging, they feature near-instantaneous photoresponse without byproduct generation, and can offer reversible switching (Klán et al., 2013). As distinct from optogenetics, they possess the advantages of small-molecule inhibitors: they do not require genetic engineering; they can directly address critical proteins (such as tubulin), which due to their structure may not permit functional control through fusion to optogenetically active domains; they also offer easy transition between model systems as well as potential for therapeutic applications (Hüll et al., 2018; Zenker et al., 2017). Motivated by the spatiotemporal complexity and critical importance of MT cytoskeleton biology, the search for photopharmaceutical MT-modulating reagents has intensified in recent years (Castle and Odde, 2015).

Please cite this article in press as: Gao et al., A Robust, GFP-Orthogonal Photoswitchable Inhibitor Scaffold Extends Optical Control over the Microtubule Cytoskeleton, Cell Chemical Biology (2020), https://doi.org/10.1016/j.chembiol.2020.11.007

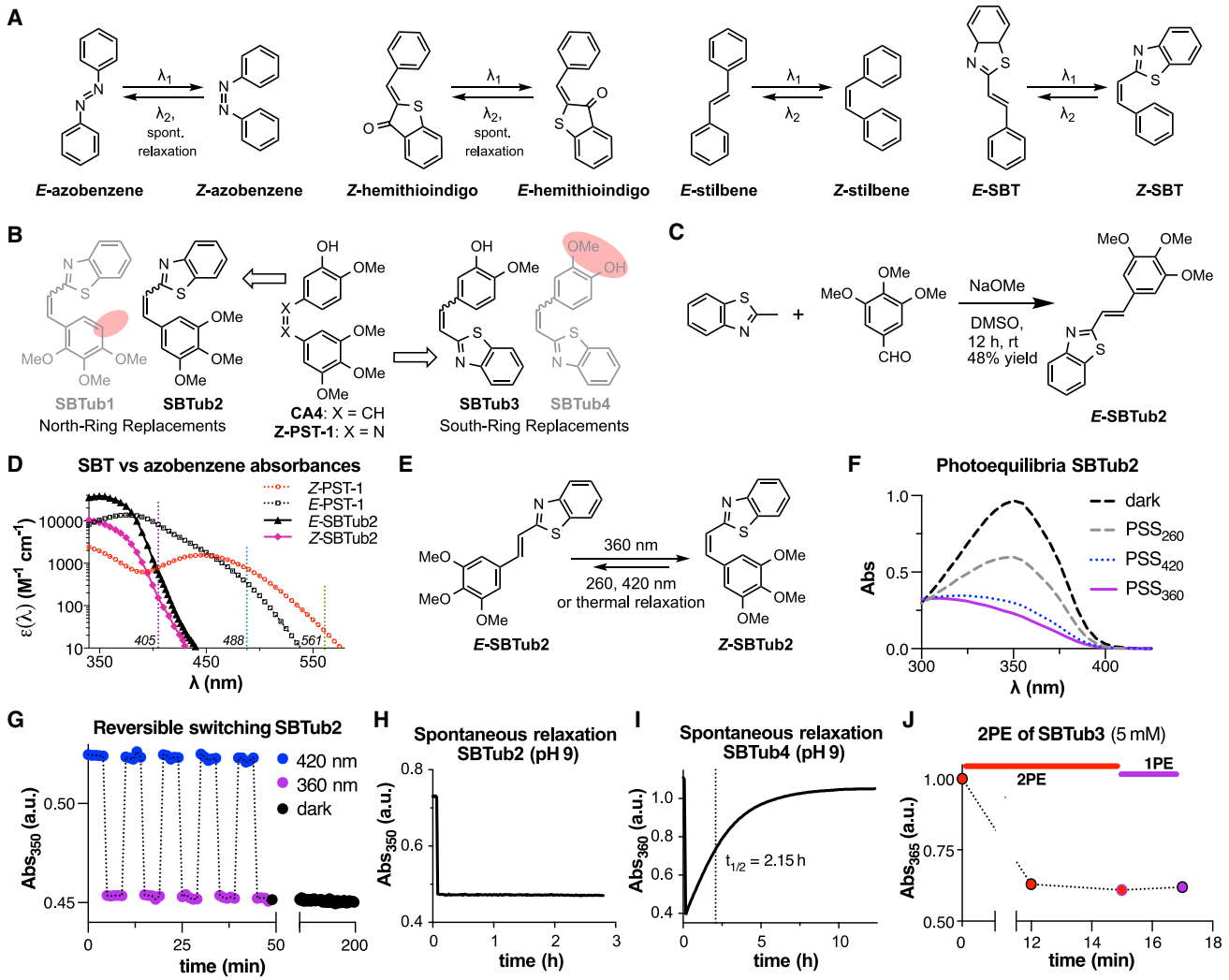

Figure 1. Design, Synthesis and Photoswitching of SBTubs

(A) Photoswitchable molecular scaffolds azobenzene, hemithioindigo, stilbene, and styrylbenzothiazole (SBT).

(B) SBTubs designed by derivatizing SBTs so that their *Z* isomers mimic (SBTub2/3) or mismatch (SBTub1/4) the tubulin-binding pharmacophore of combretastatin A-4 (CA4) and of azobenzene photopharmaceutical PST-1. Mismatches indicated by red shaded ovals.

(C) Synthesis of representative reagent, SBTub2.

(D) Comparison of absorbance spectra of representative SBT and azobenzene scaffolds illustrates the SBT's absorption cutoff above 410 nm, which suits it to orthogonality to GFP, YFP, and RFP imaging.

(E) SBTubs can be photoswitched from all-*E* to majority-*Z* using 360 nm, partially switched back with 420 or 260 nm light, and revert quantitatively to all-*E* by thermally driven spontaneous relaxation.

(F) Absorbance spectra of representative SBTub2 at various photostationary state (PSSs) equilibria.

(G) SBTubs can be photoswitched in aqueous medium under air over multiple cycles without degradation (see also Figures S1B–S1J). At pH ~7 they persist at PSS without appreciable spontaneous relaxation for hours when illumination is stopped.

(H and I) Spontaneous relaxation of (H) SBTub2 and (I) SBTub4 at pH ~9 shows the structure-dependent influence of solvent environment on relaxation rates (see also Figure S1C).

(J) SBTubs can be isomerized via two-photon excitation (2PE) reaching identical PSS as under single-photon excitation (1PE) (2PE at 780 nm, 1PE at 360 nm; compare Figure S1D).

The vast majority of photopharmaceuticals continue to be based on the reversibly photoswitchable azobenzene molecular scaffold, in which an abiotic N=N chromophore underlies photoswitching between the stable *E* and metastable *Z* isomers (Figure 1A) (Broichhagen et al., 2015). The most widely used photopharmaceuticals for optical MT control are also azobenzene based. These "photostatins" (PSTs) (Figure 1B) are analogs of the tubulin depolymerizing agent combretastatin A-4 (CA4) (Figure 1B) (Borowiak et al., 2015; Engdahl et al., 2015; Gaspari et al., 2017; Sheldon et al., 2016). Driven by illuminations with low-intensity visible light, PSTs undergo bidirectional photoswitching between the inactive *E* and the MT-inhibiting *Z* isomer. PST photoswitching has enabled noninvasive, reversible, cellularly resolved optical control over MT dynamics and network

Please cite this article in press as: Gao et al., A Robust, GFP-Orthogonal Photoswitchable Inhibitor Scaffold Extends Optical Control over the Microtubule Cytoskeleton, Cell Chemical Biology (2020), https://doi.org/10.1016/j.chembiol.2020.11.007

structure in cell culture as well as *Drosophila melanogaster* (Singh et al., 2018), *Caenorhabditis elegans* (Borowiak et al., 2015), *Danio rerio* (Vandestadt et al., 2019), and mouse models (Zenker et al., 2017), helping to resolve questions in mammalian development and neuroscience (Eguchi et al., 2017; Zenker et al., 2018). These illustrate the power of photopharmacology to enable previously inaccessible studies of spatiotemporally complex processes. However, azobenzene-based approaches to photocontrol of intracellular biology in general incur three disadvantages.

Firstly, intracellular photopharmacology typically relies on imaging-based readouts, but azobenzenes usually feature such a strong uni- or bidirectional photoresponse to standard imaging wavelengths, that isomerization caused by imaging overrides their desired photoswitching (Borowiak et al., 2015; Hüll et al., 2018) and/or limits the scope of experiments. This photoresponse is due to the low-energy $n \rightarrow \pi^*$ transitions of their N=N chromophore's lone pairs. Regardless of their starting isomer population, azobenzenes, such as PSTs, are rapidly switched to ~3:1 *E*:*Z* under 488 nm (GFP/fluorescein imaging) and to ~4:1 *E*:*Z* under 514 nm (YFP/Cy3); even 561 nm illumination noticeably affects isomer ratios on the confocal stage. Therefore, due to imaging, a background of *Z*-azobenzene is created in areas where isomerization away from the stable *E* isomer is not desired; and in areas where most *Z* isomer is generated (typically by photoswitching at 405 nm), each imaging frame instead increases the proportion of *E* isomer. By counteracting any spatiotemporally resolved isomer patterning throughout the sample, non-orthogonality to imaging wavelengths limits the azobenzene scaffold's potential for high-precision use in cell biology or transgenic animals (where the most common tags are GFP/YFP-based).

Secondly, azobenzene photopharmaceuticals for intracellular targets tend to lose performance when transitioning to cellular assays, which seems to be due to the cellular instability of their electrophilic and abiotic N=N chromophore (Schehr et al., 2019). The majority of azobenzenes can be degraded following the addition of cytoplasmic glutathione (GSH) (ca. 3–10 mM) to the N=N group, ultimately giving a range of non-photoswitchable byproducts of N=N bond degradation (Lei et al., 2019; Samanta et al., 2013a, 2013b; Sheldon et al., 2016). Cleavage byproducts may in many cases be *more* bioactive on target than the intact reagent, which blocks cellular photoswitchability of inhibition (Schehr et al., 2019). This is a major flaw of the prevailing design strategy of "azo-extension," which ensures that only half of the photoswitch is properly accommodated by the protein target, despite the known risks of scission. Even when cellularly photoswitchable reagents are designed by pharmacophore embedding, such that scission byproducts cannot be bioactive on target (such as PSTs), they typically feature losses of apparent potency that are presumably due to such degradation. For example, PSTs are ~2 orders of magnitude less potent in cells than CA4, despite near-identical potency in cell-free assays. Potency loss and potentially problematic metabolites continue to obstruct robust applications of azobenzenes to intracellular targets, especially *in vivo* (Boulègue et al., 2007; Sheldon et al., 2016).

Thirdly, azobenzenes undergo spontaneous unidirectional $Z \rightarrow E$ isomer relaxation, the rate of which depends on the substituents at the six *ortho* and *para* positions that interact strongly with the N=N double bond. In particular, some of the most important functional groups for ligand-protein interactions (including hydroxy, amine, and thiol groups) cause fast relaxation in physiological aqueous medium if they substitute at any of these positions, typically giving μs–ms half-lives (Hüll et al., 2018; Samanta et al., 2013b). Fast-relaxing azobenzenes cannot practicably be photopatterned to address intracellular targets, since counteracting their uniform relaxation to the *E* isomer would require biologically unacceptable photon fluxes. Azobenzene photopharmacology is in general limited by the ranges of relaxation half-lives accessible to its tolerated substituent space, which also probably restricts its target scope.

These problems—non-orthogonality to standard imaging conditions, metabolic liabilities in intracellular settings, and strong substituent-dependent limits on thermal half-life—intrinsically derive from azobenzene's N=N double bond. We perceive that these problems have largely hindered the translation of azobenzene photopharmaceuticals for intracellular targets from cell-free to cell culture settings, and essentially block their applications from simple *in vivo* models to higher animals (for further discussion, see the Supplemental Information). Therefore, we were motivated to develop new photoswitchable scaffolds avoiding these three problems—both for the specific case of photoswitchable MT inhibitors, as well as for general applications to chemical biology—and to examine their performance features that could suit them to more robust, orthogonal, biological photocontrol in complex systems.

In light of these three problems, we here explored the almost-unstudied styrylbenzothiazole (SBT) molecular scaffold as an alternative photoswitch based on a C=C double bond that could avoid these three problems. We evaluated this scaffold for chemical biology by synthesizing a rationally designed series of SBT-based tubulin inhibitors (SBTubs) and assaying them for their performance as biochemically robust, GFP-orthogonal, photoswitchable analogs of CA4. We obtained ligand-protein crystal structures confirming the SBTubs' two modes of tubulin binding, then demonstrated their optical control over MT network integrity, cell division, and cell death. Finally, using their unique photoresponse characteristics, we demonstrate that they enable temporally reversible, optical modulation of MT dynamics independently of ongoing imaging, in live GFP-tagged cells, and demonstrate their capacity for subcellularly spatially resolved and temporally precise inhibition of endogenous MT dynamics in primary hippocampal neurons. This is to our knowledge the first use of SBTs as photopharmaceuticals in chemical biology, and highlights both SBTubs' and the SBT scaffold's promise for use in a range of high spatiotemporal precision biological studies.

RESULTS

Scaffold Selection

To avoid photoresponse to wavelengths above 460 nm, we chose a photoswitch based on a C=C double bond that has no chromophore lone pairs and so no n-π^* bands (Horspool and Lenci, 2004), yet offers substantial geometric change upon isomerization so that bioactivity photoswitching could be possible. Hemithioindigo is the most widely used C=C-based photoswitch, but we excluded it because of its long-wavelength response even at 520 nm, due to the *ipso*-sulfur (Sailer et al.,

Please cite this article in press as: Gao et al., A Robust, GFP-Orthogonal Photoswitchable Inhibitor Scaffold Extends Optical Control over the Microtubule Cytoskeleton, Cell Chemical Biology (2020), https://doi.org/10.1016/j.chembiol.2020.11.007

2020). Stilbenes are barely used in modern photopharmacology since they require UV light below 340 nm for photoswitching, which is not accessible on microscopes, and also degrade when illuminated in the presence of oxygen (Francioso et al., 2014). We instead selected the almost-unstudied SBT scaffold. SBT is a C=C double bond-based photoswitch whose planar *E* and bent *Z* isomers differ substantially in geometric fit and end-to-end distance. They have similar geometry as the azobenzene *E* and *Z* isomers, although they are larger on their benzothiazole side (Figure 1A). We expected that the non-electrophilic C=C double bond (Awad et al., 2013; Hofmann, 1880) would endow them with increased robustness toward GSH reduction as well as slower relaxation of the *Z* isomer, as compared with azobenzenes; while, as compared with stilbenes, the benzothiazole would redshift the π-π^* band enough to be photoswitched with visible light (Mishra et al., 2013) while also blocking photochemical degradation (El-Hendawy et al., 2015).

Reagent Design and Synthesis

Searching for isomer-dependently bioactive tubulin inhibitors based on the SBT scaffold, we designed two SBTubs whose *Z* isomers could be closely isosteric replacements of the MT inhibitor CA4 and whose *E isomer*s would mimic the inactive *trans*-CA4, so aiming at *Z*-SBTub-specific MT inhibition. These became SBTub2 (where the benzothiazole ring replaces the "north," isovanillinyl ring of CA4), and SBTub3 (where the benzothiazole replaces the "south," trimethoxyphenyl ring; Figure 1B). We expected that the benzothiazole would give similar space occupancy, geometry, and polarity intermediate as the replaced rings, and since the colchicine site is somewhat accommodating (Shan et al., 2011; Tron et al., 2006), we expected that both *Z*-SBTubs might bind despite sacrificing some potency-enhancing interactions.

As a key validation step, we also created permutation controls (designed-inactive compounds) to test the tubulin specificity and *Z* isomer specificity of SBTub bioactivity. Permutation controls contain the same number and types of functional groups, but swap the positions of key bioactivity-controlling substituents to intentionally mismatch requirements for target-specific binding. We have previously used this to distinguish effects of molecularly specific binding to the target protein (which should be a feature of the designed-active compounds only) versus "pan-assay interference compounds"-like nonspecific bioactive effects expected for typically hydrophobic photoswitch compounds (e.g., promiscuous binding to or aggregation on proteins, compound precipitation, membrane disruption [Baell and Nissink, 2018]) as well as nonspecific scaffold toxicity or phototoxicity under illumination, since any nonspecific bioactivity should be reproduced by permutation controls (Sailer et al., 2019). We permuted methoxy and hydro groups of SBTub2 to create control SBTub1, and permuted hydroxy and methoxy groups of SBTub3 to create control SBTub4 (Figure 1B). Reagents SBTub1–4 were synthesized in good yields by basic aldol condensations of 2-methylbenzothiazole with the corresponding aldehydes (Figure 1C; see the Supplemental Information).

SBTub Spectral Response in Cuvette Suggests Orthogonality to GFP Imaging

The spectral characteristics of SBTubs were similar, with $\pi \rightarrow \pi^*$ absorption maxima for *E* ($\sim$360 nm) and *Z* isomers ($\sim$305 nm) being well separated, enabling directional photoisomerizations with LEDs at wavelengths $\leq$425 nm (Figures S1A–S1D). Pleasingly, both *E*- and *Z*-SBT isomers' absorptions drop sharply toward zero above 410 nm (Figure 1D). This is crucial for avoiding any $E \leftrightarrow Z$ photoisomerization under 488 nm imaging with intense focused lasers ("GFP-orthogonality") because absorption "tails" that extend far past absorbance maxima can cause substantial photoswitching in microscopy (e.g., 561 nm RFP imaging on the confocal microscope photoisomerizes the azobenzene *Z*-PST, although its absorbance maximum is at 445 nm). Our expectation was therefore, that the SBTubs' absorption cutoff is at the optimum position to permit rapid $E \rightarrow Z$ photoswitching with the common 405 nm microscopy laser line, while potentially allowing GFP-orthogonality.

SBTub Photoswitching Is Robust across a Range of pH and Environments

Under physiological conditions, the SBTubs could be optimally $E \rightarrow Z$ photoisomerized with 360 nm light, giving a photostationary state (PSS) equilibrium with a *Z*:*E* ratio of $\sim$85:15. Applying shorter or longer wavelengths back-isomerized the SBTubs toward more *E*-enriched PSSs (Figures 1E and 1F). We selected "dark" (all-*E*) and "lit" (360 nm, mostly-*Z*) as default illumination conditions for further use (Berdnikova et al., 2012). Pleasingly for our aims, reversible photoisomerizations with high-power illuminations repeatedly traversing the biologically applicable range of 360–420 nm caused no detectable photodegradation under aerobic aqueous conditions (Figure 1G). The SBTub spectra and photoswitching properties were entirely robust to variations of pH and environment (Figures S1C and S1D). The functional performance of this first generation of slow-relaxing SBTubs is turn-on-only, due to the band overlap between *E* and *Z* isomers. However, the metastable *Z* isomers of all SBTubs could be quantitatively relaxed to *E* by warming to 50°C–60°C overnight, although at 25°C they showed no significant thermal relaxation after several hours at pH $\sim$7 in physiological medium (Figure 1G). The *para*-hydroxy group unique to SBTub4 accelerated its relaxation in basic conditions (Figures 1H and 1I), but the stability of *Z*-SBTub4 against relaxation at pH $\sim$7 contrasts favorably to both azobenzene and hemithioindigo photoswitches with *para*- (or *ortho*-) hydroxy or amino substituents that typically feature millisecond (azobenzene) to second (hemithioindigo) half-lives at these conditions. This underlines the broader chemocompatibility of SBTs as a photoswitch scaffold for these functional groups that are so important in ligand design (further discussion in the Supplemental Information).

SBTubs Can Undergo Two-Photon Photoswitching

We tested if SBTubs can be isomerized by two-photon excitation (2PE), which could increase spatial resolution compared with single-photon excitation (1PE) (Moreno et al., 2015). This may especially benefit high spatial precision cell-free studies, such as time-resolved studies of tubulin structural rearrangements following ligand isomerization inside a lattice. We used a mode-locked Ti-sapphire laser at 780 nm to bulk photoisomerize SBTub3 in concentrated (5 mM) DMSO solution, delivering 2PE inside a single voxel and relying on diffusion to establish *Z*/*E*-isomer equilibrium in the whole 8 μL sample. After 12 min of 2PE the isomer equilibrium did not evolve either with additional 2PE or

Please cite this article in press as: Gao et al., A Robust, GFP-Orthogonal Photoswitchable Inhibitor Scaffold Extends Optical Control over the Microtubule Cytoskeleton, Cell Chemical Biology (2020), https://doi.org/10.1016/j.chembiol.2020.11.007

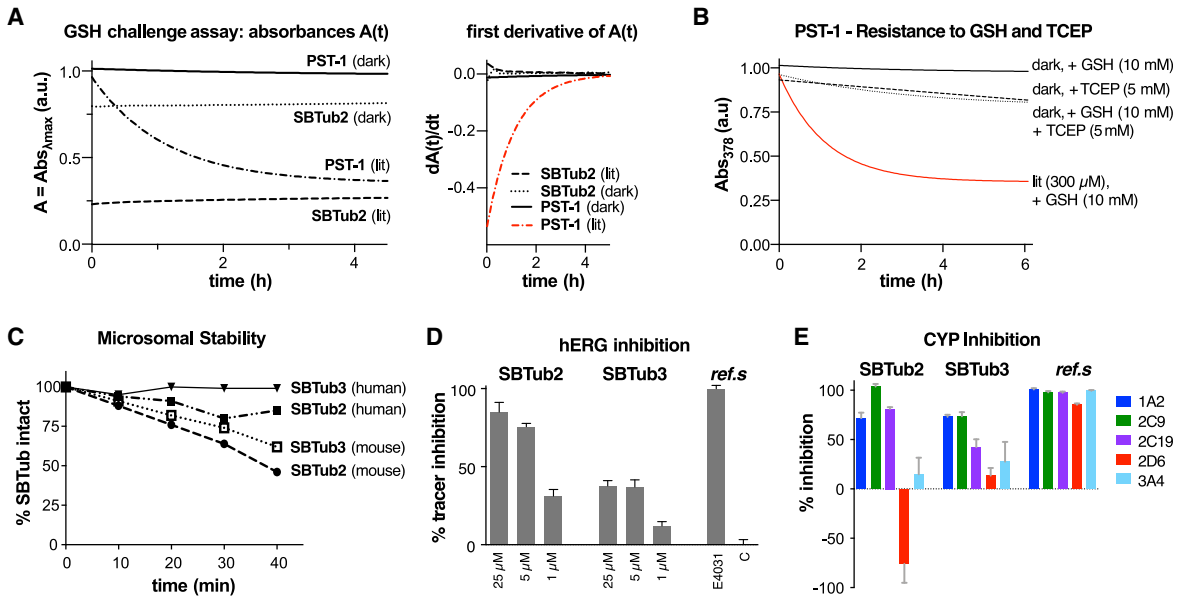

Figure 2. Biochemistry of SBTubs

(A and B) Glutathione (GSH) challenge assays under dark or lit conditions (A) monitoring the change of photoswitch absorbance during incubation with 10 mM GSH of SBT SBTub2 (25 μM) and azobenzene PST-1 (50 μM dark/300 μM lit); decreases indicate molecular degradation. (B) The reducing agent TCEP degrades even the more resistant *E isomer* of PST-1, while *Z*-PST-1 is rapidly degraded by GSH alone (see also Figures S2A–S2F).

(C) SBTub2 and SBTub3 substantially resist metabolism by purified human and mouse liver microsomes (monitored by high-performance liquid chromatography).

(D) hERG binding by SBTub2 and SBTub3, referenced to positive control E4031 (30 μM) and cosolvent-only negative control "C." Data represented as mean with SE, n = 4.

(E) *E*-SBTubs (10 μM) show moderate CYP450 inhibition.

See also Figure S2G.

with 1PE at 360 nm, indicating that 2PE can efficiently photoswitch *E*-SBTub to ~85% *Z* (Figure 1J).

SBTubs Are Highly Robust to Glutathione, and Resist Photobleaching and Metabolism

We next assessed the SBT scaffold's photochemical and biochemical robustness. We monitored *E*- and *Z*-SBTubs under UV irradiation in a Rayonet photochemical reactor. We found them to be stable to 1 h of continuous high-power UV, indicating outstanding photochemical stability (Figures S1E and S1F). We assayed their sensitivity to cellular levels of GSH (10 mM) (Figures 2A and S2A), but detected no degradation, adduct formation, addition-elimination, reduction, or other loss mechanisms. This contrasts strongly to the GSH-mediated destruction of similarly substituted *Z*-azobenzenes, including PST-1 (Figures 2A, 2B, and S2B–S2F; see discussion in the Supplemental Information). We also performed an early *in vitro* metabolic assessment of SBTub2 and SBTub3 for their suitability *in vivo*, examining stability to processing by liver microsomes, inhibition of representative cytochromes, and hERG channel inhibition (Figures 2C–2E). Especially for SBTub3 these assays did not indicate typical drug development problems. As far as we know, only one report has ever considered these crucial biological stability aspects for photoswitches (Babii et al., 2020), and no data are reported for azobenzenes.

We consider the SBT's performance as a photoswitch scaffold, as well as its improved stability and substituent tolerance compared with azobenzenes, promising for further biological applications toward cellular and *in vivo* use. We thus began exploring its applicability as a photopharmaceutical scaffold for cell biology research, through the use of SBTubs as photoswitchable MT inhibitors.

SBTubs Bind to Tubulin and Inhibit Tubulin Polymerization in Their "Lit" State

Since prolonged inhibition of cellular MT dynamics blocks cell proliferation and ultimately results in cell death, we first assayed SBTubs by examining their light-dependent antiproliferative effects on the HeLa cervical cancer cell line (incubation in "lit" conditions via pulsed illuminations with 360 or 420 nm light, or else "dark"). Both SBTub2 and SBTub3 were photoswitchably cytotoxic with ≫20-fold cytotoxicity enhancement when lit at 360 nm (half maximal inhibitory concentration [IC_{50}] ~1–2 μM with ~85% *Z* isomer), as compared with the dark experiments (IC_{50} ≫ 20 μM with ~100% *E* isomer). Crucially, neither permutation control SBTub1/4 displayed significant or light-dependent bioactivity. This supports the suitability of the SBT scaffold for long-term intracellular photopharmacology (Figure 3A). We attribute the weak antiproliferative activity of all SBTubs at high concentrations in the dark, equal to that of permutation controls SBTub1/4 under lit conditions, as aggregation-dependent effects from poor solubility of the compounds at high concentrations (known for similar species [Borowiak et al., 2015; Sailer et al., 2019], and examined further below). The light-dependent

Please cite this article in press as: Gao et al., A Robust, GFP-Orthogonal Photoswitchable Inhibitor Scaffold Extends Optical Control over the Microtubule Cytoskeleton, Cell Chemical Biology (2020), https://doi.org/10.1016/j.chembiol.2020.11.007

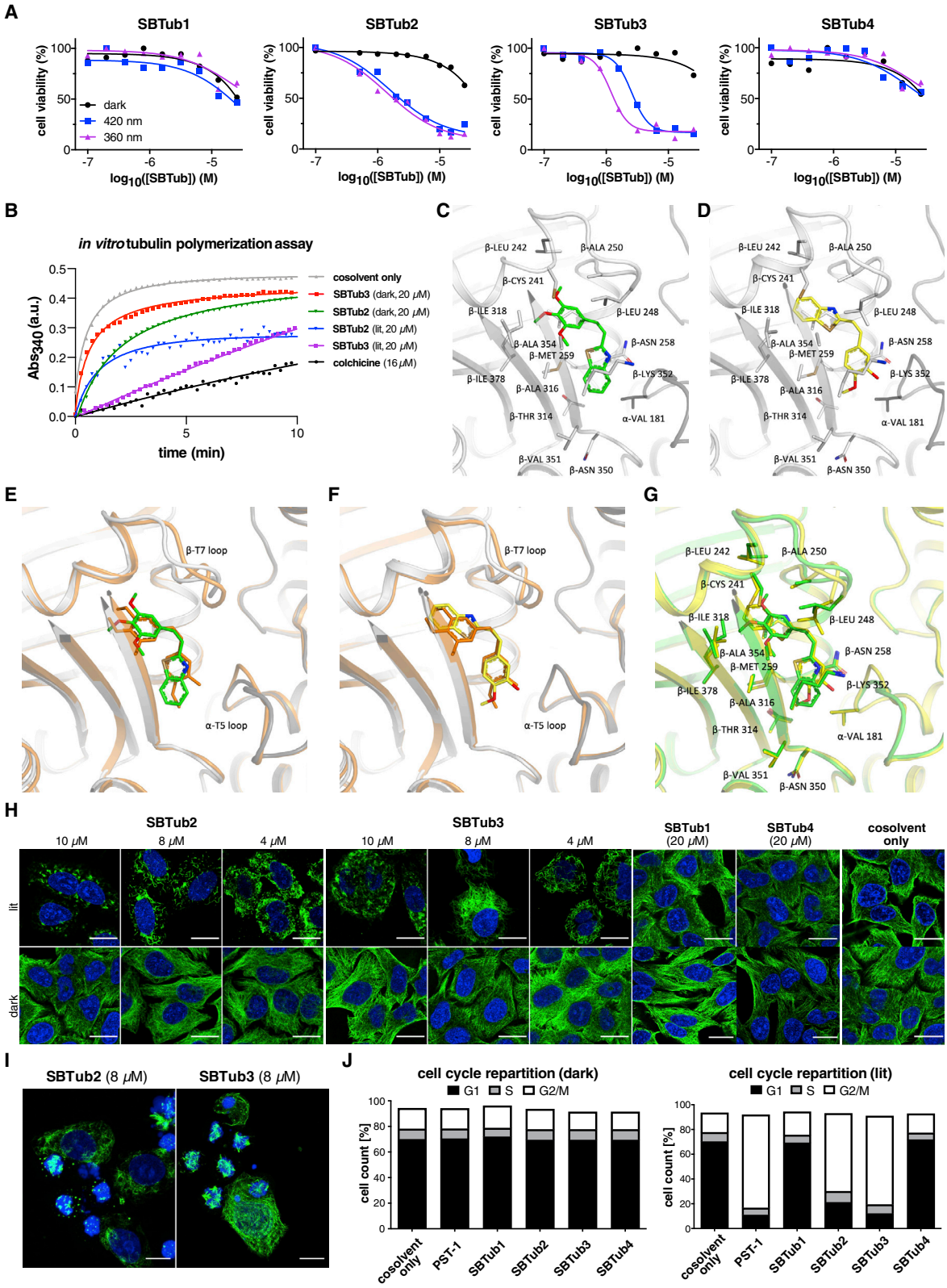

(legend on next page)

Please cite this article in press as: Gao et al., A Robust, GFP-Orthogonal Photoswitchable Inhibitor Scaffold Extends Optical Control over the Microtubule Cytoskeleton, Cell Chemical Biology (2020), https://doi.org/10.1016/j.chembiol.2020.11.007

activity of the designed-active SBTubs, and the low toxicity of their permutation controls, matched expectations that SBTub2/3's cellular antiproliferative potency should be based primarily on MT inhibition exerted only by the *in-situ*-photogenerated *Z isomer*s binding to the colchicine site.

To examine their molecular mechanism of light-dependent cellular bioactivity, we first assayed the photoswitchably cytotoxic SBTub2/3 for light-dependent inhibition of polymerization of purified tubulin in a cell-free system. *E*-SBTub2/3 were essentially inactive, but their *Z* isomers generated in lit conditions (particularly *Z*-SBTub3) were inhibitors, as expected for colchicine-site ligands (Figure 3B).

Testing the assumption of *Z* isomer-specific tubulin binding at the colchicine site by SBTub2/3, we succeeded in crystallizing *Z*-SBTub2 and *Z*-SBTub3 in complex with the tubulin-DARPin D1 complex (Pecqueur et al., 2012) and solved the structures to 2.05 and 1.86 Å resolution by X-ray crystallography, respectively (Table S1). Both *Z*-SBTub2/3 bind to the colchicine site (at the interface of α- and β-tubulin) (Figures 3C–3G and S3A–S3C). As designed in the ring replacement strategy, they bind with their benzothiazoles in opposite poses, despite contacting identical residues in the binding pocket. *Z*-SBTub2 places its trimethoxyphenyl ring in the "bottom" lobe of the pocket, which is characteristic of trimethoxyphenyl-bearing CA4 analogs (Tron et al., 2006), whereas *Z*-SBTub3 binds with its benzothiazole in the "bottom" lobe to maintain polar interactions at the top lobe with its isovanillyl ring (Figure S3D). The benzothiazole can therefore occupy the same space as either the trimethoxyphenyl or the isovanillyl unit of typical colchicine-site inhibitors (Gaspari et al., 2017). This intriguing top-versus-bottom desymmetrization should assist rational design of SBTub-based photopharmaceuticals that project substituents (e.g., functionally diverse side-chain reporters) outward from the colchicine-binding site.

SBTubs Light Dependently Inhibit MT Function in Cells

We began examining the cellular mechanism of isomer-dependent SBTub bioactivity by imaging the endogenous MT network architecture in cells incubated with *E*/*Z*-SBTubs. Dark assays with *E*-SBTub2/3 had no impact on MT network architecture, but SBTub2/3 lit at 360 nm (mostly-*Z* isomer) caused mitotic arrest and MT depolymerization, with similar dose dependency as in the viability assays (Figure 3H). Z-stack images revealed substantial accumulation of rounded, mitotically arrested cells (Figure 3I). These are hallmarks of treatment with MT-inhibiting antimitotics, supporting the conjecture that SBTub2/3's strongly photoswitchable cytotoxicity arises from their *Z* isomers inhibiting MTs in cells. By contrast, the permutation controls SBTub1/4 showed no disruption of MT network architecture under dark or lit conditions, even at high concentrations which do exert antiproliferative effects (Figure 3H), further supporting that MT-binding activity is specific to photoswitched *Z*-SBTub2/3 only. If their major cellular bioactivity mechanism is MT inhibition, *Z*-SBTub2/3 should induce light-dependent G_2/M phase cell-cycle arrest (Tron et al., 2006), and using flow cytometric analysis we observed this for both *Z*-SBTub2 and 3, but not for their *E* isomers or for permutation controls *E*/*Z*-SBTub1/4 (Figure 3J). This further supports that all-*E*-SBTubs have negligible MT-inhibiting effects, while the appropriately substituted *Z*-SBTub2/3 potently inhibit MT function, suiting them to photoswitching-based control of MT-dependent processes. Observing that, from the two active compounds, SBTub3 was both more reliably soluble than SBTub2, and exhibited a sharper dose-response curve which makes it more suited to isomerization-based bioactivity switching, we selected SBTub3 as our preferred lead compound and performed all subsequent assays with it.

We next set out to test some conceptual advantages that the photophysical and biochemical properties of the SBT scaffold should endow upon the SBTubs, when compared with azobenzenes and other major photoswitch types, in their most likely biological applications.

A Single Isomerization of SBTub Enables Long-Term MT Photocontrol

Since *Z*-SBTubs are stable to cell-free biochemical challenge and to spontaneous relaxation (Figures 1 and 2), we first tested whether a single $E \rightarrow Z$ isomerization event could be used to induce long-term impact on cells, without requiring re-illuminations throughout the assay (as is necessary with faster-relaxing azobenzenes, e.g., PSTs) (Borowiak et al., 2015). We applied *E*-SBTub3 to cell culture, isomerized it *in situ* to a majority-*Z* population using 18 s of low-power LED illumination at 360 nm, then shielded the cells from outside light and observed cell viability

Figure 3. SBTubs' Bioactivity is Light Specific and Tubulin Mediated

(A) SBTub2/3 give strong light-specific antiproliferative effects, while controls SBTub1/4 give minor and light-independent effects (HeLa cells, 40 h incubation; all-*E* dark conditions versus mostly-*Z* lit conditions using low-power pulsed LED illuminations [75 ms per 15 s, <1 mW/cm^2]; one representative experiment of three independent experiments shown).

(B) SBTub2/3 light dependently inhibit tubulin polymerization (turbidimetric *in vitro* polymerization assay; greater absorbance corresponds to a greater degree of polymerization).

(C–G) Close-up views at the colchicine-binding site of X-ray crystal structures of tubulin-*Z*-SBTub complexes (see also Figure S3). (C) Tubulin-*Z*-SBTub2 (PDB: 6ZWC) and (D) tubulin-*Z*-SBTub3 (PDB: 6ZWB) complexes (dark gray α-tubulin and light gray β-tubulin in cartoon representation; ligands and interacting residues in stick representation with oxygens red, nitrogens blue, and ligand carbons green [SBTub2] or yellow [SBTub3]). (E–F) Superimpositions of tubulin-CA4 (orange carbons; PDB: 5LYJ) with (E) tubulin-SBTub2 (green carbons) and (F) tubulin-SBTub3 (yellow carbons) structures. (G) Superimposition of tubulin-SBTub2 (green carbons) and tubulin-SBTub3 (yellow carbons) structures.

(H) Immunofluorescence imaging of cells treated with SBTub2/3 shows breakdown of MT architecture under 360 nm pulsing ("lit") but no disorganization in the dark. Scaffold controls SBTub1/4 and cosolvent controls show no scaffold- or light-dependent confounding effects (HeLa cells, 20 h incubation; α-tubulin in green, DNA stained with DAPI in blue). Scale bars, 20 μm.

(I) Maximum intensity projections along the z axis of SBTub2/3 immunofluorescence image stacks show mitotic arrests in illuminated conditions; treatment as in (H).

(J) Cell-cycle analysis of cells treated with SBTub2/3 shows significant G_2/M arrest under 360 nm pulsing ("lit") but not in the dark, as does reference PST-1. Controls SBTub1/4 and cosolvent show no cell-cycle effects (SBTubs at 20 μM, PST-1 at 2.5 μM).

Please cite this article in press as: Gao et al., A Robust, GFP-Orthogonal Photoswitchable Inhibitor Scaffold Extends Optical Control over the Microtubule Cytoskeleton, Cell Chemical Biology (2020), https://doi.org/10.1016/j.chembiol.2020.11.007

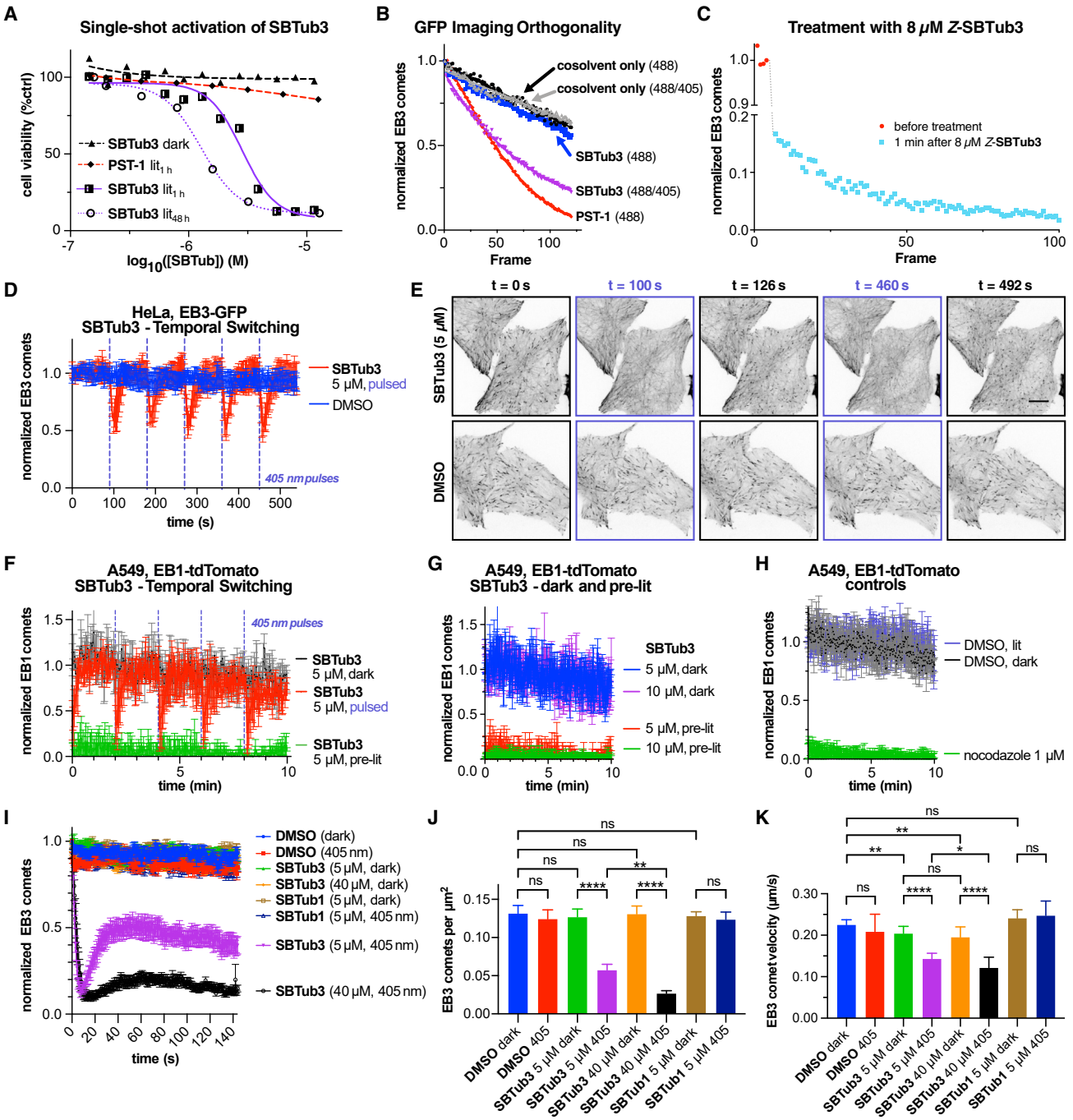

Figure 4. SBTub3 is a GFP-Orthogonal Reagent that When Isomerized Causes Rapidly Reversible Inhibition of MT Dynamics in Live Cells

(A) Antiproliferation assays with single-shot photoactivation ($lit_{1\ h}$) versus with ongoing illumination ($lit_{48\ h}$) show the SBT's sustained pharmacological activity compared with azobenzene PST-1 (HeLa cells, 48 h, pulsing as in Figure 3A; one representative experiment of three independent experiments shown).

(B and C) Live-cell EB3-GFP "comet" counts during GFP imaging with 488 nm (HeLa cells). (B) Imaging in the presence of *E*-SBTub3 does not affect comets, whereas azobenzene PST-1 is isomerized by imaging and stops MT polymerization. Only with additional 405 nm pulses does *E*-SBTub3 isomerize to *Z*-SBTub3 and stop MT polymerization dynamics (10 μM *E*-SBTub3 or *E*-PST-1). (C) Comet count before and after treatment with pre-lit (mostly-*Z*) SBTub3.

(D and E) Data related to Video S1: EB3-GFP-transfected HeLa cells treated with/without SBTub3 were illuminated at 405 nm every 90 s; MT polymerization dynamics were quantified by imaging EB3 comets at 491 nm. (D) EB3 comet counts are reversibly modulated by 405 nm photoactivations with SBTub3 (red) but are unaffected in its absence (blue) (dotted lines indicate 405 nm pulses, n = 5 movies per condition, mean with standard deviation). (E) Representative still images at baseline (t = 0 s); at 10 s/36 s after the first photoactivation (t = 100 s/126 s, comets vanished/recovered); and at 10 s/42 s after the fifth photoactivation (t = 460 s/492 s, comets vanished/recovered). Scale bar, 10 μm.

(legend continued on next page)

Please cite this article in press as: Gao et al., A Robust, GFP-Orthogonal Photoswitchable Inhibitor Scaffold Extends Optical Control over the Microtubule Cytoskeleton, Cell Chemical Biology (2020), https://doi.org/10.1016/j.chembiol.2020.11.007

40 h later. *Z*-SBTub3's antiproliferative potency in this single-shot experiment (Figure 4A) nearly matched that observed under pulsed re-illuminations every 15 s, indicating the stability of the *Z*-SBTubs in cells in the long term (despite the presence of, e.g., cellular thiols). By comparison, azobenzene-based PST-1 was essentially inactive in this single-shot experiment, which was expected since degradative metabolism as well as thermal relaxation should deplete cellular *Z*-PST levels rapidly (reports suggest within an hour [Sheldon et al., 2016]).

SBTubs Enable Photocontrol of Cellular MT Dynamics Independently of GFP/YFP Imaging

To study SBTubs' ability to effect *in situ* photocontrol of MT dynamics in higher spatiotemporal resolution, we imaged live cells transfected with labeled end binding proteins (EBs). EBs, including EB1 and EB3, mark the GTP cap regions of polymerizing MTs. Imaging fluorescent EB fusion proteins by live-cell confocal microscopy reveals the plus ends of polymerizing MTs as dynamic comets (Merriam et al., 2013; Roostalu et al., 2020), and imaging during photoswitching is a spatiotemporally resolved readout for isomerization-dependent inhibition of MT dynamics by photoswitchable inhibitors (Borowiak et al., 2015; Müller-Deku et al., 2020).

We first tested whether SBTubs avoid any isomerization during imaging, which would make them suitable for fully orthogonal imaging and photocontrol: an important unsolved challenge for intracellular photopharmacology. We imaged MT dynamics using GFP-EB3 with excitation at 488 nm and YFP-EB3 with excitation at 514 nm by confocal microscopy. As hoped from their sharp absorption cutoff above 410 nm, neither GFP nor YFP imaging under treatment with *E*-SBTub3 caused inhibition of MT dynamics; but when 405 nm photoactivation pulses were additionally applied, MT dynamics were rapidly suppressed (Figure 4B). By imaging and photoactivation of cosolvent controls, and imaging under treatment with pre-activated *Z*-SBTub3, we showed that this suppression of MT dynamics is not due to photobleaching but is consistent with selective $E \rightarrow Z$ photoisomerization of SBTub3 under 405 nm only (Figures 4B and 4C). As treatment with *Z*-SBTub3 blocks MT dynamics throughout the imaging time course, this shows that both $E \rightarrow Z$ and $Z \rightarrow E$-SBTub isomerization are fully orthogonal to typical imaging conditions (Figures 4C and S4A–S4C; see discussion in the Supplemental Information). We consider this a powerful demonstration that the SBT scaffold may more generally be well suited for use in photopharmaceuticals, against diverse targets, across many biological systems where GFP and YFP reporters are used.

SBTubs Enable Temporally Reversible MT Photocontrol in Cells that Are Orthogonal to Imaging

Achieving temporally reversible, spatially localized cellular applications of photoactivatable compounds is the major goal of both photopharmacology and photouncaging. These first-generation SBTubs were designed for $E \rightarrow Z$ photoisomerization with high spatiotemporal precision. They cannot be substantially $Z \rightarrow E$ photoisomerized in cells, and they are too stable to undergo substantial spontaneous $Z \rightarrow E$ relaxation at physiological temperatures, so neither process can be relied upon to revert *Z*-SBTub to its bioinactive isomer. However, as in photouncaging, temporally reversible and spatially localized inhibition can still be achieved using spatiotemporally localized activating photoisomerization, if two conditions are met: (1) inhibitor-target dissociation and intracellular or transmembrane diffusion must quickly reduce the concentration of the photoactivated species below its inhibitory threshold and (2) protein function must be immediately restored upon inhibitor dissociation (true for colchicine domain inhibitors). If so, and particularly in systems with a highly nonlinear dose response (such as the MT cytoskeleton), localized photoactivation followed by diffusion-based depletion of the photogenerated bioactive isomer may give complete functional recovery in a single cell or region, on the compound's diffusion or transmembrane partitioning timescale. *Z*-SBTub3 did show fast membrane penetration kinetics, since its addition to cell bath solutions quickly stopped MT dynamics (Figure 4C). We therefore assayed the temporal reversibility of SBTub's cell-localized modulation of MT dynamics by an EB3-GFP imaging assay with pulses of 405 nm photoactivation. MT polymerization dynamics were repeatedly paused then rapidly recovered to normal, with quantifications aligning closely over many cells (Video S1; Figures 4D and 4E).

We performed a similar experiment while changing the cell line, biological label, and fluorescent marker, to test the SBTubs' broader applicability and the hypothesis that SBTubs generate readout in these assays by causatively modulating MT polymerization (rather than, e.g., by directly affecting EB3-GFP/YFP). We repeated the temporal reversibility experiments in A549 lung cancer cell line, transfected with the dsRed-derived tdTomato marker fused to the end binding protein EB1. We observed identical temporal modulation (Figures 4F–4K; Video S2), validated by benchmarking against non-405 nm illuminated cells treated with pre-lit *Z*-SBTub3 (Figures 4F and 4G). Comparing dark and pre-lit SBTub3 with DMSO-only controls and the positive control tubulin inhibitor nocodazole confirmed resistance to both $E \rightarrow Z$ and $Z \rightarrow E$ isomerization during imaging (Figures 4I–4K). SBTub photoswitching can therefore drive highly reproducible, GFP-orthogonal, temporally reversible modulation of MT polymerization in live cells, performance which no other tubulin photopharmaceutical has delivered.

SBTub Photoswitching Permits Subcellularly Resolved MT Inhibition in Primary Neurons

Rapid diffusion of small-molecule inhibitors within cells makes subcellular patterning of photopharmaceuticals against cytosolic

(F–H) Data related to Videos S1 and S2: EB1-tdTomato-transfected A549 cells treated with/without SBTub3 were imaged for EB1 comets at 561 nm. Cells exposed to SBTub3 and pulses of 405 nm show temporally precise suppressions of MT polymerization dynamics upon 405 nm applications that reach maximal inhibition similar to positive controls nocodazole or pre-lit SBTub3, but rapidly recovering to similar levels as non-pulsed SBTub3 or cosolvent controls.
(I–K) Controls related to (B–H). EB3-GFP-transfected HeLa cells were treated with SBTub3, scaffold control SBTub1, or DMSO solvent alone, then imaged directly after treatment, optionally with 405 illuminations interleaved. Movies were analyzed for (I) EB3 comet counts, (J) average EB3 comet density, and (K) average EB3 comet velocity. Data shown as mean ± standard deviation; *$p < 0.05$, **$p < 0.01$, ***$p < 0.001$, ****$p < 0.0001$; n.s., not significant; n = 10 cells per condition).

Please cite this article in press as: Gao et al., A Robust, GFP-Orthogonal Photoswitchable Inhibitor Scaffold Extends Optical Control over the Microtubule Cytoskeleton, Cell Chemical Biology (2020), https://doi.org/10.1016/j.chembiol.2020.11.007

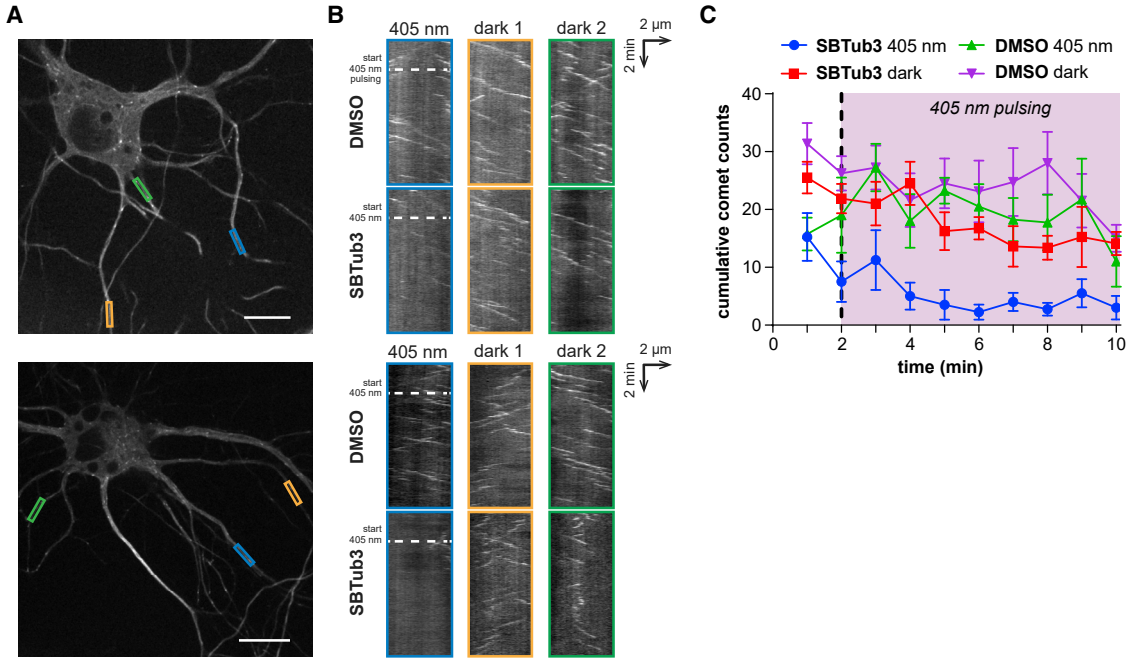

Figure 5. Local SBTub Photoisomerization Inhibits MT Polymerization in Subcellular Regions of Primary Hippocampal Neurons

(A–C) Data related to Video S3: cultured primary neurons (10 days *in vitro*) transfected with EB3-GFP and treated with 1% DMSO were imaged for EB3 for 10 min while an ROI (blue box) was pulsed with 405 nm commencing 2 min into the acquisition (indicated by dotted lines). Baseline EB3 dynamics in the cell and the ROI were shown to be light independent. The same neurons were then exposed to 1 µM SBTub3 and immediately imaged for another 10 min; during this time the same ROI was again pulsed with 405 nm from 2 min onward. (A) Cell images with regions marked, and (B) EB3 kymographs of these regions. The ROI pulsed with 405 nm is boxed in blue; the regions not pulsed with 405 nm are boxed in orange and green. Scale bars, 10 µm. (C) EB3 comet counts accumulated over 20 frame (1 min) intervals (±SEM) plotted over time, for regions treated with or without SBTub3 and 405 nm pulsing (n = 4 cells).

targets challenging. However, large cells (e.g., embryonic systems) or irregularly shaped cells (e.g., neurons) are targets whose geometry and size may favor subcellular patterning. We cultured isolated primary rat hippocampal neurons until neurites developed, then transfected them with EB3-GFP for imaging (Kapitein et al., 2010). For each neuron, we selected several equal-sized areas along independent neurites and monitored the dynamics of EB3 comets before and during SBTub3 treatment, with repetitive ROI-localized 405 nm applications to one of the areas, aiming to locally block MT polymerization in the selected neuronal process area (Figure 5; Video S3). For SBTub3-treated cells, kymographs of 405 nm illuminated neurites showed localized reductions in EB3 comet number and lifetime, while non-illuminated neurites showed no significant changes from baseline; and controls before/after SBTub3 application showed no photobleaching by 405 nm illumination (Figure 5B). Comet counts (Figure 5C) indicated likewise that SBTub3 photoswitching induces subcellularly localized inhibition of MT polymerization.

DISCUSSION

Photopharmacological approaches to high spatiotemporal precision reagents for noninvasive studies of endogenous protein function have made significant progress in the last decade. From original applications in neuroscience (Lester et al., 1980; Volgraf et al., 2005), they now impact membrane and cytoskeleton biology (Borowiak et al., 2015, 2020; Frank et al., 2016; Urban et al., 2018); and recent advances in long-wavelength photoswitches offer prospects for *in vivo* photopharmacology (Bléger et al., 2012; Konrad et al., 2016; Samanta et al., 2013b). However, the scope of targets and assays accessible to photopharmacology has been restricted by its chemistry. The overwhelming majority of photopharmaceutical designs employ azobenzenes as the photoswitch moiety and so inherit their functional limitations: (1) the diazene's nucleophilic and metabolic susceptibility is problematic for addressing intracellular targets or for long-term, systemic *in vivo* applications; (2) its n-π^* absorption in the blue-green spectral region is triggered by imaging standard biological tags (e.g., GFP/YFP); and (3) azobenzenes for cytosolic targets have restricted substituent scope since *ortho*/*para*-electron-donating groups that are key to strong ligand-protein interactions (OH, NH_2, etc.) cause microsecond relaxation rates, so are not bulk photoisomerizable under physiological conditions. Only recently have non-azobenzene photoswitches, such as dithienylethenes and hemithioindigos, been used in bioactive pharmacophores (Sailer et al., 2019; Simeth et al., 2017); and the development of novel photoswitch scaffolds is recognized as a valuable milestone even before reaching cellular applications (Hoorens et al., 2019).

Here, we have demonstrated the design and testing of a novel concept for a GFP-orthogonal metabolically resistant SBT photoswitch scaffold. The SBT scaffold has comparable chemical simplicity with that of azobenzene and delivers spatiotemporally precise photoswitching-based biological control, while also

Please cite this article in press as: Gao et al., A Robust, GFP-Orthogonal Photoswitchable Inhibitor Scaffold Extends Optical Control over the Microtubule Cytoskeleton, Cell Chemical Biology (2020), https://doi.org/10.1016/j.chembiol.2020.11.007

addressing all three challenges by bringing: (1) biochemical/metabolic robustness; (2) orthogonality to common imaging conditions; and (3) an alternative range of isomerization-tolerant substituents (e.g., including *para*-OH). Thus, SBT expands the scope of intracellular targets and of biological assays (toward *in vivo* use) accessible to photopharmacology.

The reagents conceptually nearest to the SBTubs are the fully photoswitchable (but non-GFP-orthogonal and metabolically labile) PST-1, and (irreversibly) photouncageable inhibitors, such as nitrobenzylether-capped CA4 (Wuhr et al., 2010). A minor issue is that the potency of these SBTubs ($IC_{50} \sim 1$ μM) is less than either previous system (IC_{50} PST-1 ~ 0.5 μM, fully uncaged CA4 ~20 nM); however, further structural tuning of SBTubs may improve potency. It is the different photoresponse of SBTubs that brings them more important advantages and disadvantages. In cells, azobenzenes can undergo $Z \leftrightarrow E$ switching by illumination and $Z \rightarrow E$ isomerization by spontaneous relaxation, whereas this first generation of SBTubs only allows cellular $E \rightarrow Z$ switching (unidirectional activation). Spontaneous $Z \rightarrow E$ relaxation could improve their performance in spatiotemporally localized activation assays, by passively counteracting the build-up of photoactivated but diffused reagent; and bidirectional $Z \leftrightarrow E$ photoswitching would allow active control over the spatiotemporal localization of both *E* and *Z* isomers.

The unidirectional photoactivation of SBTubs is conceptually somewhat similar to that of photouncageable inhibitors; however, their performance differs in five respects (1) typical photocaging groups (e.g., *ortho*-nitrobenzyls) require hydrolysis before cargo release that can take seconds to minutes, which diminishes the spatiotemporal precision of photouncaging (off-to-on) and diffusion (on-to-off). Isomerization, as the SBTs use, is typically orders of magnitude faster (<< ns), and SBTubs give reproducibly high-precision biological control. (2) Photouncaging byproducts are often unspecifically toxic and may also be phototoxic (Klán et al., 2013), while SBTub's photochemically robust $E \rightarrow Z$ isomerization allows cell-tolerated long-term experimentation. (3) Photouncaging strategies add significant molecular weight, which often penalizes bioavailability or biodistribution; they may suffer non-photolytic compound release (enzymatic or spontaneous hydrolysis); and they involve higher synthetic cost (Klán et al., 2013; Reeβing and Szymanski, 2017). SBT inclusion in a pharmacophore does not add compound weight or complexity, and avoids any activation mechanisms except photoactivation. (4) The photocages that are orthogonal to 488 nm imaging (e.g., nitrobenzyls) have low uncaging yield at 405 nm and thus require high photon fluxes to uncage, which can cause phototoxicity problems and also photodegrade the released reagent; whereas SBT can efficiently exploit this common microscopy line with high yield and excellent photostability. (5) Photouncageable probes must be protected from irreversible ambient light-induced photodegradation during synthesis, storage, and use; SBTs are easier to handle and use because accidentally light-exposed stocks can be relaxed quantitatively back to the inactive *E* isomer by warming.

Taken together, these features set SBTs apart from photouncaging approaches and from azobenzene photoswitching, recommending them for reproducible, high-precision, "clean" photopharmacological control particularly in higher-complexity biological systems. We therefore expect that the SBTubs may contribute to high-precision MT cytoskeleton studies and manipulation in neuroscience, motility, and embryology. If SBTubs can also be applied *in vivo* beyond small embryonic systems, it could offer exciting research potential. In larger animals, colchicine domain inhibitors are most often used as vascular disrupting agents and studied *in situ* by microscopy in one- or two-photon mode (Tozer et al., 2001). These are both feasible methods to isomerize SBTubs, and in superficial tissue settings the penetration of UV/violet light can be sufficient for photoswitching (Morstein et al., 2019). So far only one report of systemic pharmacokinetics of a photopharmaceutical has been published (Babii et al., 2020). If SBTubs or their derivatives do have favorable pharmacokinetics, their biochemical stability may enable powerful *in vivo* translation of MT photopharmacology.

We also believe that the development of the SBT scaffold itself is promising for photopharmaceutical development. The SBT scaffold unites photochemical and biochemical robustness with GFP-orthogonality, and tolerates drug-important polar functional groups. These characteristics recommend SBT for research applications that are inaccessible to current photopharmaceuticals, e.g., for intracellular photocontrol in embryos and primary cell isolates of GFP/YFP animal models, both of which are important in development and neurodegeneration. More broadly, it is significant that "scaffold hopping" from azobenzene (PST-1) to SBT (SBTub) has been successful. Novel photoswitches that can substitute typical azobenzenes without requiring total redesign, while offering new performance, are already impacting the hitherto azobenzene-based field of photopharmacology. In this context, diazocines (Reynders et al., 2020; Siewertsen et al., 2009), tetra-*ortho*-substitutions (Bléger et al., 2012), and azoniums (Samanta et al., 2013a) are rapidly garnering applications for spectral shifting. Our work suggests that SBT may be used more generally to substitute azobenzene in photopharmaceutical designs to improve performance on intracellular targets or for optically orthogonal use in live-imaging studies. SBT may thus drive the development of new generations of more powerful photopharmaceuticals against a broader range of biological targets.

SIGNIFICANCE

Photocontrollable reagents have unique potential as high spatiotemporal precision modulators of endogenous biological systems: in particular, systems—such as the microtubule cytoskeleton—where rapid dynamics and tight spatial organization are key to function. Lead compound SBTub3 provides spatiotemporally precise control over endogenous microtubule dynamics in live cells, to a level that has not previously been possible. Subcellularly localized SBTub3 photoswitching can even modulate MT polymerization dynamics in individual neurites: a level of precision manipulation that will motivate a range of highly resolved inhibition studies in neurobiology and beyond. More generally, the practical utility of SBTub3 and of SBT-based photoswitches in biological research is significantly greater than that of previous photopharmaceuticals based on azobenzenes, because the rational design of the SBT photoswitch scaffold solves the three outstanding problems

Please cite this article in press as: Gao et al., A Robust, GFP-Orthogonal Photoswitchable Inhibitor Scaffold Extends Optical Control over the Microtubule Cytoskeleton, Cell Chemical Biology (2020), https://doi.org/10.1016/j.chembiol.2020.11.007

hampering their biological use. Firstly, photocontrollable inhibitors must be light responsive, but not to the wavelengths used for imaging; the strong isomerization of the azobenzene scaffold under GFP and YFP (even RFP) excitation, can restrict the channels available for imaging and cause significant background activity. Secondly, azobenzenes can be metabolically unstable in the cytosol after illumination, and release intrinsically bioactive products upon degradation. Thirdly, azobenzenes have poor tolerance of key functional groups that drive ligand binding (OH, NH_2, etc.). By contrast, the SBT scaffold's C=C double bond chromophore gives SBT-based photopharmaceuticals (such as SBTub3) outstanding performance in practical biological uses. SBTs are metabolically stable, allowing robust application to cytosolic targets; they tolerate tautomerizable groups without instability of the *cis* isomer; and they are orthogonal to GFP imaging, allowing background-free photoswitching and easy translation between models. Importantly, we show that azobenzene photopharmaceuticals can be redesigned into SBT photopharmaceuticals without losing their mechanism of action or their potency. SBTs are thus a promising advance for high-precision microtubule biology, and for the development of high-performance photopharmaceuticals against other protein targets.

STAR★METHODS

Detailed methods are provided in the online version of this paper and include the following:

SUPPLEMENTAL INFORMATION

Supplemental Information can be found online at https://doi.org/10.1016/j.chembiol.2020.11.007.

ACKNOWLEDGMENTS

This research was supported by funds from the German Research Foundation (DFG: SFB1032 Nanoagents for Spatiotemporal Control project B09 to O.T.-S. and project A08 to T.L.; Emmy Noether grant no. 400324123, SFB TRR 152 project P24 no. 239283807, and SPP 1926 project no. 426018126 to O.T.-S.); the Swiss National Science Foundation (31003A_166608 to M.O.S.); and the Munich Centre for NanoScience initiative (CeNS). J.C.M.M. acknowledges support from an EMBO Long-Term Fellowship. X-ray diffraction data were collected at the beamline X06SA at the Swiss Light Source (Paul Scherrer Institut, Villigen PSI, Switzerland). We thank S. Schmidt (LMU) for help with synthesis; K.T. Wanner (LMU) for collegial discussions; H. Harz, I. Solvei, and C. Jung (LMU microscopy platforms), K. Bartel, A. Vollmar, H. Leonhardt, and S. Zahler (LMU) for access to general biology and microscopy facilities; and D. Hörl (LMU) for measuring microscope laser power. We dedicate this paper to GFP's discoverer Osamu Shimomura,whose devoted research has made modern chemical biology possible.

AUTHOR CONTRIBUTIONS

L.G. performed synthesis, single-photon photocharacterization, *in vitro* studies, figure preparation, coordinated data assembly, and wrote the manuscript. J.C.M.M. performed characterization of EB3 dynamics, temporally reversible live-cell imaging studies, and subcellularly localized photoswitching. Y.K. performed *in vitro* studies. M.W. performed tubulin protein production, purification, crystallization, crystal handling, and X-ray data collection, processing, and refinement. T.W. performed tubulin crystal handling, data collection, and data processing and refinement. S.D.P. performed two-photon photocharacterization. R.B. performed cell-free tubulin polymerization assays. E.N. performed live-cell imaging on A549 cell lines. K.I.J. and L.C.K. performed primary neuron isolation and culture. N.O. performed tubulin protein production, purification, and crystallization. T.L. supervised two-photon photocharacterization. J.S. and M.O.S. supervised protein crystallography. A.A. supervised characterization of EB3 dynamics, temporally reversible cell imaging and subcellularly localized photoswitching. J.A. performed *in vitro* studies, coordinated data assembly and figure preparation, and supervised all other cell biology. O.T.-S. designed the concept and experiments, supervised all other experiments, coordinated data assembly, and wrote the manuscript with input from all authors.

DECLARATION OF INTERESTS

The authors declare no competing interests.

Received: October 21, 2020
Revised: November 10, 2020
Accepted: November 13, 2020
Published: February 18, 2021

REFERENCES

Adams, P.D., Afonine, P.V., Bunkoczi, G., Chen, V.B., Davis, I.W., Echols, N., Headd, J.J., Hung, L.-W., Kapral, G.J., Grosse-Kunstleve, R.W., et al. (2010). PHENIX: a comprehensive Python-based system for macromolecular structure solution. Acta Crystallogr. Section D *66*, 213–221.

Awad, M.K., El-Hendawy, M.M., Fayed, T.A., Etaiw, S.E.H., and English, N.J. (2013). Aromatic ring size effects on the photophysics and photochemistry of styrylbenzothiazole. Photochem. Photobiol. Sci. *12*, 1220–1231.

Babii, O., Afonin, S., Schober, T., Garmanchuk, L.V., Ostapchenko, L.I., Yurchenko, V., Zozulya, S., Tarasov, O., Pishel, I., Ulrich, A.S., et al. (2020). Peptide drugs for photopharmacology: how much of a safety advantage can be gained by photocontrol? Future Drug Discov. *2*, FDD28.

Baell, J.B., and Nissink, J.W.M. (2018). Seven year itch: pan-assay interference compounds (PAINS) in 2017—utility and limitations. ACS Chem. Biol. *13*, 36–44.

Berdnikova, D., Fedorova, O., Gulakova, E., and Ihmels, H. (2012). Photoinduced in situ generation of a DNA-binding benzothiazoloquinolinium derivative. Chem. Commun. *48*, 4603–4605.

Bléger, D., Schwarz, J., Brouwer, A.M., and Hecht, S. (2012). o-Fluoroazobenzenes as readily synthesized photoswitches offering nearly quantitative two-way isomerization with visible light. J. Am. Chem. Soc. *134*, 20597–20600.

Borowiak, M., Küllmer, F., Gegenfurtner, F., Peil, S., Nasufovic, V., Zahler, S., Thorn-Seshold, O., Trauner, D., and Arndt, H.-D. (2020). Optical manipulation of F-actin with photoswitchable small molecules. J. Am. Chem. Soc. *142*, 9240–9249.

Borowiak, M., Nahaboo, W., Reynders, M., Nekolla, K., Jalinot, P., Hasserodt, J., Rehberg, M., Delattre, M., Zahler, S., Vollmar, A., et al. (2015). Photoswitchable inhibitors of microtubule dynamics optically control mitosis and cell death. Cell *162*, 403–411.

Boulègue, C., Löweneck, M., Renner, C., and Moroder, L. (2007). Redox potential of azobenzene as an amino acid residue in peptides. ChemBioChem *8*, 591–594.

Broichhagen, J., Frank, J.A., and Trauner, D. (2015). A roadmap to success in photopharmacology. Acc. Chem. Res. *48*, 1947–1960.

Castle, B.T., and Odde, D.J. (2015). Optical control of microtubule dynamics in time and space. Cell *162*, 243–245.

Dumontet, C., and Jordan, M.A. (2010). Microtubule-binding agents: a dynamic field of cancer therapeutics. Nat. Rev. Drug Discov. *9*, 897.

Eguchi, K., Taoufiq, Z., Thorn-Seshold, O., Trauner, D., Hasegawa, M., and Takahashi, T. (2017). Wild-type monomeric α-synuclein can impair vesicle endocytosis and synaptic fidelity via tubulin polymerization at the calyx of Held. J. Neurosci. *37*, 6043–6052.

El-Hendawy, M.M., Fayed, T.A., Awad, M.K., English, N.J., Etaiw, S.E.H., and Zaki, A.B. (2015). Photophysics, photochemistry and thermal stability of diarylethene-containing benzothiazolium species. J. Photochem. Photobiol. *301*, 20–31.

Emsley, P., and Cowtan, K. (2004). Coot: model-building tools for molecular graphics. Acta Crystallogr. Section D *60*, 2126–2132.

Engdahl, A.J., Torres, E.A., Lock, S.E., Engdahl, T.B., Mertz, P.S., and Streu, C.N. (2015). Synthesis, characterization, and bioactivity of the photoisomerizable tubulin polymerization inhibitor azo-combretastatin A4. Org. Lett. *17*, 4546–4549.

Francioso, A., Boffi, A., Villani, C., Manzi, L., D'Erme, M., Macone, A., and Mosca, L. (2014). Isolation and identification of 2,4,6-trihydroxyphenanthrene as a byproduct of trans-resveratrol photochemical isomerization and electrocyclization. J. Org. Chem. *79*, 9381–9384.

Frank, J.A., Franquelim, H.G., Schwille, P., and Trauner, D. (2016). Optical control of lipid rafts with photoswitchable ceramides. J. Am. Chem. Soc. *138*, 12981–12986.

Gaspari, R., Prota, A.E., Bargsten, K., Cavalli, A., and Steinmetz, M.O. (2017). Structural basis of *cis*- and *trans*-combretastatin binding to tubulin. Chem *2*, 102–113.

Hofmann, A.W. (1880). Zimmtsäurederivat des Amidophenylmercaptans. Chem. Ber. 1235–1238.

Hoorens, M.W.H., Medved', M., Laurent, A.D., Di Donato, M., Fanetti, S., Slappendel, L., Hilbers, M., Feringa, B.L., Jan Buma, W., and Szymanski, W. (2019). Iminothioindoxyl as a molecular photoswitch with 100 nm band separation in the visible range. Nat. Comm. *10*, 2390.

Horspool, W.M., and Lenci, F. (2004). CRC Handbook of Organic Photochemistry and Photobiology, 2nd ed. edn (CRC Press).

Hüll, K., Morstein, J., and Trauner, D. (2018). In vivo photopharmacology. Chem. Rev. *118*, 10710–10747.

Janke, C., and Steinmetz, M.O. (2015). Optochemistry to control the microtubule cytoskeleton. EMBO J. *34*, 2114–2116.

Kabsch, W. (2010). XDS. Acta Crystallographica Section D, Biol. Crystallogr. *66*, 125–132.

Kapitein, L.C., Yau, K.W., and Hoogenraad, C.C. (2010). Chapter 7. Microtubule dynamics in dendritic spines. In Methods in Cell Biology, L. Cassimeris and P. Tran, eds. (Academic Press), pp. 111–132.

Klán, P., Šolomek, T., Bochet, C.G., Blanc, A., Givens, R., Rubina, M., Popik, V., Kostikov, A., and Wirz, J. (2013). Photoremovable protecting groups in chemistry and biology: reaction mechanisms and efficacy. Chem. Rev. *113*, 119–191.

Kleele, T., Marinković, P., Williams, P.R., Stern, S., Weigand, E.E., Engerer, P., Naumann, R., Hartmann, J., Karl, R.M., Bradke, F., et al. (2014). An assay to image neuronal microtubule dynamics in mice. Nat. Commun. *5*, 4827.

Konrad, D.B., Frank, J.A., and Trauner, D. (2016). Synthesis of redshifted azobenzene photoswitches by late-stage functionalization. Chem. Eur. J. *22*, 4364–4368.

La Sala, G., Olieric, N., Sharma, A., Viti, F., de Asis Balaguer Perez, F., Huang, L., Tonra, J.R., Lloyd, G.K., Decherchi, S., Díaz, J.F., et al. (2019). Structure, thermodynamics, and kinetics of plinabulin binding to two tubulin isotypes. Chem *5*, 2969–2986.

Lei, H., Mo, M., He, Y., Wu, Y., Zhu, W., and Wu, L. (2019). Bioactivatable reductive cleavage of azobenzene for controlling functional dumbbell oligodeoxynucleotides. Bioorg. Chem. *91*, 103106.

Lester, H.A., Krouse, M.E., Nass, M.M., Wassermann, N.H., and Erlanger, B.F. (1980). A covalently bound photoisomerizable agonist: comparison with reversibly bound agonists at electrophorus electroplaques. J. Gen. Physiol. *75*, 207–232.

Lin, C.M., Singh, S.B., Chu, P.S., Dempcy, R.O., Schmidt, J.M., Pettit, G.R., and Hamel, E. (1988). Interactions of tubulin with potent natural and synthetic analogs of the antimitotic agent combretastatin: a structure-activity study. Mol. Pharmacol. *34*, 200–208.

Meijering, E., Dzyubachyk, O., and Smal, I. (2012). Chapter 9. Methods for cell and particle tracking. In Methods in Enzymology, P.M. conn, ed. (Academic Press), pp. 183–200.

Merriam, E.B., Millette, M., Lumbard, D.C., Saengsawang, W., Fothergill, T., Hu, X., Ferhat, L., and Dent, E.W. (2013). Synaptic regulation of microtubule dynamics in dendritic spines by calcium, F-actin, and drebrin. J. Neurosci. *33*, 16471.

Mishra, A., Thangamani, A., Chatterjee, S., Chipem, F.A.S., and Krishnamoorthy, G. (2013). Photoisomerization of *trans*-2-[4'-(dimethylamino)styryl]benzothiazole. Photochem. Photobiol. *89*, 247–252.

Moreno, J., Gerecke, M., Dobryakov, A.L., Ioffe, I.N., Granovsky, A.A., Bléger, D., Hecht, S., and Kovalenko, S.A. (2015). Two-photon-induced versus one-photon-induced isomerization dynamics of a bistable azobenzene derivative in solution. J. Phys. Chem. B *119*, 12281–12288.

Morstein, J., Hill, R.Z., Novak, A.J.E., Feng, S., Norman, D.D., Donthamsetti, P.C., Frank, J.A., Harayama, T., Williams, B.M., Parrill, A.L., et al. (2019). Optical control of sphingosine-1-phosphate formation and function. Nat. Chem. Biol. *15*, 623–631.

Müller-Deku, A., Meiring, J.C.M., Loy, K., Kraus, Y., Heise, C., Bingham, R., Jansen, K.I., Qu, X., Bartolini, F., Kapitein, L.C., et al. (2020). Photoswitchable paclitaxel-based microtubule stabilisers allow optical control over the microtubule cytoskeleton. Nat Commun *11*, 4640.

Pecqueur, L., Duellberg, C., Dreier, B., Jiang, Q., Wang, C., Plückthun, A., Surrey, T., Gigant, B., and Knossow, M. (2012). A designed ankyrin repeat protein selected to bind to tubulin caps the microtubule plus end. Proc. Natl. Acad. Sci. U S A *109*, 12011.

Peterson, J.R., and Mitchison, T.J. (2002). Small molecules, big impact. Chem. Biol. *9*, 1275–1285.

Reeßing, F., and Szymanski, W. (2017). Beyond photodynamic therapy: light-activated cancer chemotherapy. Curr. Med. Chem. *24*, 4905–4950.

Reynders, M., Matsuura, B.S., Bérouti, M., Simoneschi, D., Marzio, A., Pagano, M., and Trauner, D. (2020). PHOTACs enable optical control of protein degradation. Sci. Adv. *6*, eaay5064.

Roostalu, J., Thomas, C., Cade, N.I., Kunzelmann, S., Taylor, I.A., and Surrey, T. (2020). The speed of GTP hydrolysis determines GTP cap size and controls microtubule stability. eLife *9*, e51992.

Sailer, A., Ermer, F., Kraus, Y., Bingham, R., Lutter, F.H., Ahlfeld, J., and Thorn-Seshold, O. (2020). Potent hemithioindigo-based antimitotics photocontrol the microtubule cytoskeleton in cellulo. Beilstein J. Org. Chem. *16*, 125–134.

Sailer, A., Ermer, F., Kraus, Y., Lutter, F., Donau, C., Bremerich, M., Ahlfeld, J., and Thorn-Seshold, O. (2019). Hemithioindigos for cellular photopharmacology: desymmetrised molecular switch scaffolds enabling design control over the isomer-dependency of potent antimitotic bioactivity. ChemBioChem *20*, 1305–1314.

Samanta, S., Babalhavaeji, A., Dong, M.-x., and Woolley, G.A. (2013a). Photoswitching of ortho-substituted azonium ions by red light in whole blood. Angew. Chem. Int. Ed. *52*, 14127–14130.

Samanta, S., Beharry, A.A., Sadovski, O., McCormick, T.M., Babalhavaeji, A., Tropepe, V., and Woolley, G.A. (2013b). Photoswitching azo compounds in vivo with red light. J. Am. Chem. Soc. *135*, 9777–9784.

Schehr, M., Ianes, C., Weisner, J., Heintze, L., Müller, M.P., Pichlo, C., Charl, J., Brunstein, E., Ewert, J., Lehr, M., et al. (2019). 2-Azo-, 2-diazocine-thiazols and 2-azo-imidazoles as photoswitchable kinase inhibitors: limitations and pitfalls of the photoswitchable inhibitor approach. Photochemical Photobiological Sci. *18*, 1398–1407.

Schindelin, J., Arganda-Carreras, I., Frise, E., Kaynig, V., Longair, M., Pietzsch, T., Preibisch, S., Rueden, C., Saalfeld, S., Schmid, B., et al. (2012). Fiji: an open-source platform for biological-image analysis. Nat. Methods *9*, 676–682.

Shan, Y.S., Zhang, J., Liu, Z., Wang, M., and Dong, Y. (2011). Developments of combretastatin A-4 derivatives as anticancer agents. Curr. Med. Chem. *18*, 523–538.

Sheldon, J.E., Dcona, M.M., Lyons, C.E., Hackett, J.C., and Hartman, M.C.T. (2016). Photoswitchable anticancer activity via *trans-cis* isomerization of a combretastatin A-4 analog. Org. Biomol. Chem. *14*, 40–49.

Siewertsen, R., Neumann, H., Buchheim-Stehn, B., Herges, R., Näther, C., Renth, F., and Temps, F. (2009). Highly efficient reversible Z-E photoisomerization of a bridged azobenzene with visible light through resolved S1($n\pi^*$) absorption bands. J. Am. Chem. Soc. *131*, 15594–15595.

Simeth, N.A., Kneuttinger, A.C., Sterner, R., and König, B. (2017). Photochromic coenzyme Q derivatives: switching redox potentials with light. Chem. Sci. *8*, 6474–6483.

Singh, A., Saha, T., Begemann, I., Ricker, A., Nüsse, H., Thorn-Seshold, O., Klingauf, J., Galic, M., and Matis, M. (2018). Polarized microtubule dynamics directs cell mechanics and coordinates forces during epithelial morphogenesis. Nat. Cell Biol *20*, 1126–1133.

Smart, O.S., Womack, T.O., Flensburg, C., Keller, P., Paciorek, W., Sharff, A., Vonrhein, C., and Bricogne, G. (2012). Exploiting structure similarity in refinement: automated NCS and target-structure restraints in BUSTER. Acta Cryst. D *68*, 368–380.

Stepanova, T., Slemmer, J., Hoogenraad, C.C., Lansbergen, G., Dortland, B., De Zeeuw, C.I., Grosveld, F., van Cappellen, G., Akhmanova, A., and Galjart, N. (2003). Visualization of microtubule growth in cultured neurons via the use of eb3-GFP (end-binding protein 3-green fluorescent protein). J. Neurosci. *23*, 2655–2664.

Strzyz, P.J., Lee, H.O., Sidhaye, J., Weber, I.P., Leung, L.C., and Norden, C. (2015). Interkinetic nuclear migration is centrosome independent and ensures apical cell division to maintain tissue integrity. Dev. Cell *32*, 203–219.

Tickle, I.J., Flensburg, C., Keller, P., Paciorek, W., Sharff, A., Smart, O., Vonrhein, C., and Bricogne, G. (2018). STARANISO Anisotropy and Bayesian Estimation Server (Global Phasing Ltd).

Tseng, Q., Duchemin-Pelletier, E., Deshiere, A., Balland, M., Guillou, H., Filhol, O., and Thery, M. (2012). Spatial organization of the extracellular matrix regulates cell-cell junction positioning. Proc. Natl. Acad. Sci. U S A *109*, 1506–1511.

Tozer, G.M., Prise, V.E., Wilson, J., Cemazar, M., Shan, S., Dewhirst, M.W., Barber, P.R., Vojnovic, B., and Chaplin, D.J. (2001). Mechanisms associated with tumor vascular shut-down induced by combretastatin A-4 phosphate: intravital microscopy and measurement of vascular permeability. Cancer Res. *61*, 6413–6422.

Tron, G.C., Pirali, T., Sorba, G., Pagliai, F., Busacca, S., and Genazzani, A.A. (2006). Medicinal chemistry of combretastatin A4: present and future directions. J. Med. Chem. *49*, 3033–3044.

Urban, P., Pritzl, S.D., Konrad, D.B., Frank, J.A., Pernpeintner, C., Roeske, C.R., Trauner, D., and Lohmüller, T. (2018). Light-controlled lipid interaction and membrane organization in photolipid bilayer vesicles. Langmuir *34*, 13368–13374.

Vandestadt, C., Vanwalleghem, G.C., Castillo, H.A., Li, M., Schulze, K., Khabooshan, M., Don, E., Anko, M.-L., Scott, E.K., and Kaslin, J. (2019). Early migration of precursor neurons initiates cellular and functional regeneration after spinal cord injury in zebrafish. bioRxiv, 539940.

Volgraf, M., Gorostiza, P., Numano, R., Kramer, R.H., Isacoff, E.Y., and Trauner, D. (2005). Allosteric control of an ionotropic glutamate receptor with an optical switch. Nat. Chem. Biol. *2*, 47.

Weinert, T., Olieric, N., Cheng, R., Brünle, S., James, D., Ozerov, D., Gashi, D., Vera, L., Marsh, M., Jaeger, K., et al. (2017). Serial millisecond crystallography for routine room-temperature structure determination at synchrotrons. Nat. Commun. *8*, 542.

Wittmann, T., Dema, A., and van Haren, J. (2020). Lights, cytoskeleton, action: optogenetic control of cell dynamics. Curr. Opin. Cell Biol. *66*, 1–10.

Wuhr, M., Tan, E.S., Parker, S.K., Detrich, H.W., 3rd, and Mitchison, T.J. (2010). A model for cleavage plane determination in early amphibian and fish embryos. Curr. Biol. *20*, 2040–2045.

Zenker, J., White, M.D., Gasnier, M., Alvarez, Y.D., Lim, H.Y.G., Bissiere, S., Biro, M., and Plachta, N. (2018). Expanding actin rings zipper the mouse embryo for blastocyst formation. Cell *173*, 776–791.

Zenker, J., White, M.D., Templin, R.M., Parton, R.G., Thorn-Seshold, O., Bissiere, S., and Plachta, N. (2017). A microtubule-organizing center directing intracellular transport in the early mouse embryo. Science *357*, 925–928.

Please cite this article in press as: Gao et al., A Robust, GFP-Orthogonal Photoswitchable Inhibitor Scaffold Extends Optical Control over the Microtubule Cytoskeleton, Cell Chemical Biology (2020), https://doi.org/10.1016/j.chembiol.2020.11.007

CellPress

STAR★METHODS

KEY RESOURCES TABLE

REAGENT or RESOURCE	SOURCE	IDENTIFIER
Antibodies		
rabbit α-tubulin primary antibody	Abcam	Cat#ab18251; RRID: AB_2210057
goat-anti-rabbit Alexa fluor 488 secondary antibody	Abcam	Cat#ab150077, RRID: AB_2630356
Chemicals, Peptides, and Recombinant Proteins		
SBTub1	this paper	N/A
SBTub2	this paper	N/A
SBTub3	this paper	N/A
SBTub4	this paper	N/A
PST-1	Borowiak et al., 2015	N/A
Glutathione (GSH)	TCI	Cat#G0073; CAS:27025-41-8
99% tubulin (porcine brain)	Cytoskeleton Inc.	Cat#T240
tubulin (bovine brain)	Centro de Investigaciones Biológicas (Microtubule Stabilizing Agents Group), CSIC, Madrid, Spain	N/A
Human liver microsomes	XenoTech	Cat#H0630 lot#1610016
Critical Commercial Assays		
Vivid™ CYP450 Screening Kit	Thermo Fisher Scientific	Cat#P2871, P3027, P2980, P2954
Predictor™ hERG Fluorescence Polarization Assay	Invitrogen/ Thermo Fisher Scientific	Cat#PV5365
Deposited Data		
tubulin-DARPin D1-*Z*-**SBTub2**	this paper	6ZWC
tubulin-DARPin D1-*Z*-**SBTub3**	this paper	6ZWB
Tubulin Darpin room-temperature structure	Weinert et al., 2017	5NQT
Tubulin-Combretastatin A4 complex	Gaspari et al., 2017	5LYJ
Experimental Models: Cell Lines		
HeLa cell line	DSMZ (German Collection of Microorganisms and Cell Cultures)	ACC 57d
A549 cell line	ATCC	CCL-185
Experimental Models: Organisms/Strains		
Rattus norvegicus (Wistar; HanRj:WI)	RGD, Janvier labs	Cat# 13792727; RRID: RGD_13792727
Recombinant DNA		
EB3-GFP (used with neurons)	Stepanova et al., 2003	N/A
EB3-GFP (used with HeLa cells)	Strzyz et al., 2015	Addgene Plasmid #105948; RRID: Addgene_105948
EB3-YFP	Kleele et al., 2014	N/A
EB1-tdTomato	Dent et al., unpublished	Addgene Plasmid #50825; RRID:Addgene_50825
Software and Algorithms		
Fiji (ImageJ)	Schindelin et al., 2012	https://imagej.net/Fiji
ComDet plugin to ImageJ	E. Katrukha, University of Utrecht	https://github.com/ekatrukha/ComDet
MTrackJ plugin to ImageJ	Meijering et al., 2012	https://imagescience.org/meijering/software/mtrackj/

(*Continued on next page*)

Please cite this article in press as: Gao et al., A Robust, GFP-Orthogonal Photoswitchable Inhibitor Scaffold Extends Optical Control over the Microtubule Cytoskeleton, Cell Chemical Biology (2020), https://doi.org/10.1016/j.chembiol.2020.11.007

Continued

REAGENT or RESOURCE	SOURCE	IDENTIFIER
Template Matching plugin in ImageJ	Tseng et al., 2012	https://sites.google.com/site/qingzongtseng/template-matching-ij-plugin
"Flowing" FACS analysis software	P. Terho, Turku Centre for Biotechnology	https://bioscience.fi/services/cell-imaging/flowing-software/
X-ray: Data processing (XDS)	Kabsch, 2010	http://xds.mpimf-heidelberg.mpg.de/
X-ray: Data correction (Staraniso)	Tickle et al., 2018	http://staraniso.globalphasing.org/
X-ray: ligands and restraints (Grade server)	Smart et al., 2012	http://grade.globalphasing.org
X-ray: refinement (PHENIX)	Adams et al., 2010	https://www.phenix-online.org/download/
X-ray: refinement (COOT)	Emsley and Cowtan, 2004	https://www2.mrc-lmb.cam.ac.uk/personal/pemsley/coot/

RESOURCE AVAILABILITY

Lead Contact

Requests for further information and requests for reagents and resources should be directed to and will be fulfilled by Lead Contact, Oliver Thorn-Seshold (oliver.thorn-seshold@cup.lmu.de).

Materials Availability

All unique reagents generated in this study are available from the Lead Contact without restriction for non-commercial applications, or with a completed Materials Transfer Agreement if there is potential for commercial applications; requestors are required to handle all shipping and customs costs.

Data and Code Availability

The X-Ray datasets generated are available at the Protein Data Bank as tubulin-DARPin D1-*Z*-**SBTub2** (PDB 6ZWC) and tubulin-DARPin D1-*Z*-**SBTub3** (PDB 6ZWB).

EXPERIMENTAL MODEL AND SUBJECT DETAILS

HeLa Human Cervical Carcinoma Cells

HeLa human cervical carcinoma cells (female) were maintained in Dulbecco's modified Eagle's medium (DMEM, PAN-Biotech) supplemented with 10% fetal calf serum (FCS), 100 U/mL penicillin and 100 U/mL streptomycin, at 37°C in a 5% CO_2 atmosphere. Cell line was last authenticated via STR-typing by the distributer (DSMZ (German Collection of Microorganisms and Cell Cultures) and ATCC) and are regularly replaced with new working stocks from our master cell bank.

A549 Human Lung Cancer Cells

A549 human lung cancer cells (male) were maintained in Dulbecco's modified Eagle's medium (DMEM, PAN-Biotech) supplemented with 10% fetal calf serum (FCS), 100 U/mL penicillin and 100 U/mL streptomycin, at 37°C in a 5% CO_2 atmosphere. Cell line was last authenticated via STR-typing by the distributer (DSMZ (German Collection of Microorganisms and Cell Cultures) and ATCC) and are regularly replaced with new working stocks from our master cell bank.

Rat Primary Hippocampal Neurons

All animal experiments were performed in accordance with Dutch law (Wet op de Dierproeven, 1996) and European regulations (Directive 2010/63/EU) under animal licence AVD1080020173404. All animal experiments were approved by the Dutch Animal Experiments Committee (DEC, Dier Experimenten Commissie) and were in line with the institutional guidelines of Utrecht University. Primary hippocampal neurons were derived from hippocampi of embryonic day 18 pups (male and female) from pregnant Wistar rats (Janvier; at least 10 weeks of age and not involved in any previous experiments).

Mouse Hepatic Microsomes

Mouse hepatic microsomes were isolated from pooled, perfused livers of male Balb/c mice (n=50) by Bienta Biology Services (Kiev, Ukraine) under the ethics guidelines of Enamine/Bienta.

Please cite this article in press as: Gao et al., A Robust, GFP-Orthogonal Photoswitchable Inhibitor Scaffold Extends Optical Control over the Microtubule Cytoskeleton, Cell Chemical Biology (2020), https://doi.org/10.1016/j.chembiol.2020.11.007

CellPress

Human Hepatic Microsomes

Human hepatic microsomes were purchased from XenoTech (Cat#H0630, lot#1610016, n=50), no available information how samples were allocated to experimental groups.

Transfection

Transient transfections were performed with *EB3-GFP* (Stepanova et al., 2003; Strzyz et al., 2015), *EB3*-YFP (Kleele et al., 2014). or *EB1-tdTomato* plasmids using jetPRIME (Polyplus), FuGENE 6 (Promega) or Lipofectamine 2000 (Invitrogen) reagents according to the manufacturers' instructions and cells were imaged 24 h later (HeLa, A549) or 3 days later (neurons).

METHODS DETAILS

Compound Synthesis and Characterisation

All reactions and characterisations were performed with unpurified, undried, non-degassed solvents and reagents from commercial suppliers (Sigma-Aldrich, TCI Europe N.V., Fisher Scientific etc.), used as obtained, under closed air atmosphere without special precautions. Manual flash column chromatography was performed on Merck silica gel Si-60 (40–63 μm). MPLC flash column chromatography performed on a Biotage Isolera Spektra system, using Biotage prepacked silica cartridges. Thin-layer chromatography (TLC) was run on 0.25 mm Merck silica gel plates (60, F-254), with UV light (254 nm and 365 nm) as visualizing agents. NMR characterisation was performed on a Bruker Ascend 400 (400 MHz & 100 MHz for ^{1}H and ^{13}C respectively). HRMS was carried out by the Zentrale Analytik of the LMU Munich. Analytical HPLC-MS was performed on an Agilent 1100 SL coupled HPLC-MS system with H_2O:MeCN eluent gradients through a Thermo Scientific Hypersil GOLD™ C18 column (1.9 μm; 3 × 50 mm) maintained at 25°C, detected on an Agilent 1100 series diode array detector and a Bruker Daltonics HCT-Ultra spectrometer (ESI mode, unit m/z). IR spectra were recorded on a PerkinElmer Spectrum BX II FT-IR system. Full experimental details are given in the Data S1 Part C.

Photocharacterisation

UV-Vis absorption spectra measurements in cuvette were acquired on an Agilent CaryScan 60 (1 cm pathlength) at room temperature (25°C) with default compound concentrations of 25 μM and default solvents of PBS at pH ~7.4 with 10 % of DMSO as cosolvent. "Star" LEDs (H2A1-models spanning 360–435 nm Roithner Lasertechnik; FWHM ~25 nm and 260 nm HP-LED Sahlmann Photochemical Solutions) were used for photoisomerisations in cuvette that were also predictive of what would be obtained in LED-illuminated cell culture. Spectra of pure *E* and *Z* isomers were acquired from the HPLC's inline Agilent 1100 series diode array detector (DAD) over the range 200–550 nm, manually baselining across each elution peak of interest to correct for eluent composition. Two-photon excitation was performed using a mode-locked Ti-Sapphire Laser operating at 780 nm (Spectra Physics, Tsunami) with a pulse repetition frequency of 80 MHz (pulse with <100 fs) and an output power of 0.65 W, coupled into an upright Zeiss Axiotech 100 microscope and focused with a 40× reflective objective (Thorlabs, LMM-40X-UVV, measuring sample transmittance using a HAL 100 illuminator (Carl Zeiss) and a SP300i spectrograph equipped with a MicroMAX CCD camera for signal recording (both Princeton Instruments), between 360 nm and 380 nm. For more information on *in vitro* photocharacterization see Data S1 Part D

Stability towards Glutathione (GSH)

Samples of both all-*E* ("dark") and mostly-*Z* ("pre-lit") **SBTub2** and **PST-1** were prepared in PBS pH ~7.4 with 10% DMSO, containing GSH (10 mM), in UV-Vis cuvettes that were sealed under air atmosphere (gas head volume <2 mL) with parafilm and maintained at 37°C, during absorbance measurements over several hours in a Agilent Cary 60 spectrophotometer. "Dark" assays were performed with the *E*-isomers of the test compounds; "pre-lit" **SBTub2** had been pre-illuminated to reach PSS under 360 nm light; while "lit" **PST-1** was maintained under continuous illumination from above with a 390 nm LED to maintain **PST-1** in a mostly-*cis* state. **SBTub2** was monitored at 345 nm, while **PST-1** was monitored at 378 nm and 440 nm for dark and lit states, respectively. For detailed experimental procedure and discussion on the GSH stability of **SBTub2** and **PST-1** see Data S1 Part E.

Microsomal Stability, CYP Inhibition and hERG Inhibition

SBTubs' stability to degradation by liver microsomes was assessed by *in vitro* studies using isolated mouse and human liver microsomes, performed by Bienta Biology Services (Kiev, Ukraine) over a 40 min timecourse at 37°C following standard practice. Mouse hepatic microsomes were isolated from pooled, perfused livers of male Balb/c mice (n=50); human hepatic microsomes were supplied by XenoTech. Microsomal incubations were performed in duplicates and control incubations were performed replacing the NADPH-cofactor system with PBS. Supernatants were analyzed using HPLC-MS. The potential for CYP450 inhibition was assessed by *in vitro* inhibition studies using fluorogenic CYP450 substrates with the corresponding CYP450 enzymes and NADPH regeneration system (Vivid CYP450 Screening Kits) performed by Bienta Biology Services. hERG inhibition experiments were performed by Bienta Biology Services using Invitrogen PredictorTM hERG Fluorescence Polarization Assay in accordance with the manufacturer's protocol (Protocol PV5365). Please see Data S1 Part E for more information.

Please cite this article in press as: Gao et al., A Robust, GFP-Orthogonal Photoswitchable Inhibitor Scaffold Extends Optical Control over the Microtubule Cytoskeleton, Cell Chemical Biology (2020), https://doi.org/10.1016/j.chembiol.2020.11.007

Tubulin Polymerisation *In Vitro*

99% purity tubulin from porcine brain was obtained from Cytoskeleton Inc. (cat. #T240) and polymerisation assays run according to manufacturer's instructions. Tubulin was pre-incubated for 10 min at 37°C with "lit"- (after 360 nm illumination) or "dark" (all-*E* conditions) **SBTub** (20 μM) in buffer (with 3% DMSO, 10% glycerol); at time zero, GTP (1 mM) was added and the change in absorbance at 340 nm was monitored over 15 mins at 37°C (Lin et al., 1988).

Protein Production, Crystallisation and Soaking

The DARPin D1 was prepared as previously described (Pecqueur et al., 2012). Tubulin from bovine brain was purchased from the Centro de Investigaciones Biológicas (Microtubule Stabilizing Agents Group), CSIC, Madrid, Spain. The tubulin-DARPin D1 (TD1; (La Sala et al., 2019; Pecqueur et al., 2012; Weinert et al., 2017)) complex was formed by mixing the respective components in a 1:1.1 molar ratio. The TD1 complex was crystallised overnight by the hanging drop vapor diffusion method (drop size 2 μL, drop ratio 1:1) at a concentration of 15.9 mg/mL and at 20°C with a precipitant solution containing 18% PEG 3350, 0.2 M ammonium sulfate and 0.1 M bis-tris methane, pH 5.5. All drops were subsequently hair-seeded with crystalline material obtained in previous PEG-screening, which resulted in single and large (0.5 μm) TD1 complex crystals. The crystals were fished and transferred into new precipitant solution drops containing 10% DMSO and compounds (*E*-**SBTub2**/*E*-**SBTub3**) at final concentrations 2 mM, then 360 nm LED illumination was applied for 5 min to generate *Z*-**SBTub**s *in situ*. After 4 h of soaking in the dark, the crystals were mounted for X-ray diffraction data collection.

X-ray Diffraction Data Collection, Processing and Refinement

Data were collected at beamline X06SA at the Swiss Light Source (Paul Scherrer Institute, Villigen, Switzerland). The beam was focused to 30 × 30 μm, the flux was 3 × 10^{10} photons/s and the data collection speed was 2°/s at an oscillation range of 0.2° per frame (see Table S1). For TD1-**SBTub2** and TD1-**SBTub3**, 210° and 220° of data were collected, respectively. Data processing was done with XDS (Kabsch, 2010). Due to anisotropy, the data were corrected using the Staraniso server (Tickle et al., 2018) (http://staraniso.globalphasing.org/). The structures were solved by molecular replacement using PDB ID 5NQT as a search model (Weinert et al., 2017). The ligands and restraints were generated with the grade server (Smart et al., 2012) (http://grade.globalphasing.org/) using their SMILES annotation. The structures were then refined iteratively in PHENIX (Adams et al., 2010) with manual editing cycles in COOT (Emsley and Cowtan, 2004). For more information please see Data S1 Part F

MTT Antiproliferation Assay

Cells seeded in 96-well plates at 5,000 cells/well and left to adhere for 24 h were treated with *E*-**SBTub**s under the indicated lighting conditions for 48 h (1% DMSO; six technical replicates). Compounds and cosolvent were added *via* a D300e digital dispenser (Tecan) and cells were either incubated under "dark" (light-excluded) or "lit" conditions (where pulsed illuminations were applied by multi-LED arrays to create and maintain the wavelength-dependent photostationary state isomer ratios throughout the experiment, as previously described (Borowiak et al., 2015)). Cells were then treated with 0.5 mg/mL (3-(4,5-dimethylthiazol-2-yl)-2,5-diphenyl tetrazolium bromide (MTT) for 3 h; the medium was aspirated and formazan crystals were re-dissolved in DMSO (100 μL) before measuring absorbance at 550 nm using a FLUOstar Omega microplate reader (BMG Labtech). Absorbance was averaged over the technical replicates, and normalised as viability by reference to the cosolvent-only control (set as 100%) and to zero absorbance (set as 0%).

Cell Cycle Analysis

E-**SBTub**s were added to HeLa cells in 24-well plates (seeding density: 50,000 cells/well) and incubated under "dark" or "lit" conditions for 24 h. Cells were collected, permeabilised and stained with 2 μg/mL propidium iodide (PI) at 4°C for 30 min. Following PI staining, cells were analysed by flow cytometry using a FACS Canto II flow cytometer (Becton Dickinson) run by BD FACSDiva software. 30,000 cells were measured per condition and the data were transferred to *Flowing* software for cell cycle analysis. Cells were sorted into sub-G1, G1, S and G_2/M phase according to DNA content (PI signal).

Immunofluorescence Staining

HeLa cells seeded on glass coverslips in 24-well plates (50,000 cells/well) were left to adhere for 18 h then treated for 24 h with **SBTub**s under "dark" or "lit" conditions as described above. Cover slips were washed then fixed with 0.5% glutaraldehyde, quenched with 0.1% $NaBH_4$, blocked with PBS + 10% FCS, and treated with rabbit alpha-tubulin primary antibody (abcam ab18251; 1:400 in PBS + 10% FCS) for 1 h; after washing with PBS, cells were incubated with goat-anti-rabbit Alexa fluor 488 secondary antibody (Abcam, ab150077; 1:400 in PBS + 10% FCS) for 1 h. After washing with PBS, coverslips were mounted onto glass slides using Roti-Mount FluorCare DAPI (Roth) and imaged with a Zeiss LSM Meta confocal microscope. Images were processed using Fiji software (Schindelin et al., 2012). Postprocessing was performed only to improve visibility. For maximum intensity projections, images were recorded at different focal planes by incrementally stepping through the sample (step size 1-2 μm) and maximum intensity projections were obtained using Fiji software.

EB1/EB3 Comet Assays with Whole-Sample Photoisomerisation

HeLa or A549 cells (12,000 or 40,000 cells/well, respectively) were seeded on 8-well ibiTreat μ slides (ibidi) 24 h prior to transfection with fluorescently-labeled end binding protein (Kleele et al., 2014). Cells were transiently transfected with *EB3-GFP*, *EB3-YFP* or

Please cite this article in press as: Gao et al., A Robust, GFP-Orthogonal Photoswitchable Inhibitor Scaffold Extends Optical Control over the Microtubule Cytoskeleton, Cell Chemical Biology (2020), https://doi.org/10.1016/j.chembiol.2020.11.007

EB1-tdTomato plasmids using jetPRIME (Polyplus) or FuGENE 6 (Promega) reagents according to the manufacturers' instructions. Cells were imaged 24 h later, under 37°C and 5% CO_2 atmosphere. HeLa cells were imaged using an UltraVIEW Vox spinning disc confocal microscope (PerkinElmer) equipped with an EMCCD camera (Hammamatsu, Japan) and operated with *Volocity* software. A549 cells were imaged using a Nikon TiE microscope equipped with a Yokogawa CSU-W1 spinning disk confocal unit (50 μm pinhole size), an Andor Borealis illumination unit, Andor ALC600 laser beam combiner (405/488/561/640 nm), Andor IXON 888 Ultra EMCCD camera, and a Nikon 100× NA 1.45 oil immersion objective. The microscope was controlled by Nikon NIS Elements software (v.5.02.00). **SBTub** was added cautiously after focussing on cells on the microscope stage, and the compound was incubated for 5-10 min before imaging; this avoided exposure of the **SBTub** to any white focusing light, preventing unwanted isomerisation prior to imaging that could falsify results when testing for GFP/YFP orthogonality. Cells were imaged either at 488 nm (GFP; 23% laser power, 400 ms exposure time, 45 frames/min), 514 nm (YFP; similar parameters), or 561 nm (tdTomato; 20% laser power, 300 ms exposure time, 30 frames/min). Optionally for EB3 imaging, cells were additionally exposed, once per two minutes, to four consecutive frames (4×250 ms) of **SBTub**-isomerizing 405 nm light for compound activation. Optionally for EB1 imaging, 405 nm illuminations (10% laser power, 175 μs pixel dwell time) were re-applied at 2 min intervals during acquisition as indicated. For EB3 comet statistics, 6 cells per condition from three independent trials were taken; for EB1 statistics, 3 cells per condition. For photobleaching/orthogonality experiments, first-order exponential decay curves were fitted to each cell's comet count timecourses. EB3 count values were normalised to 100% at time zero, and EB1 counts were treated similarly or else normalised to 100% at the first return to plateau as appropriate; this enables intercomparison of cells with different starting comet counts (depending on their size, the position of the focal plane, etc). EB3 comets were counted with a *Fiji* software plugin based on the "Find maxima" function from the NIH; EB1 comets were counted in ImageJ using the ComDet plugin (E. Katrukha, University of Utrecht, https://github.com/ekatrukha/ComDet). Data are represented as mean comet count over time, with standard deviation, and scalebars in EB1 Videos are 10 μm.

Quantification of the Impact of SBTub3 on Live Cell MT Dynamics

HeLa cells were transfected with EB3-GFP using FuGENE 6 (Promega) according to manufacturer's instructions. Cells were imaged on a Nikon Eclipse Ti microscope equipped with a perfect focus system (Nikon), a spinning disk-based confocal scanner unit (CSU-X1-A1, Yokogawa) and an Evolve 512 EMCCD camera (Photometrics) with a stage top incubator INUBG2E-ZILCS (Tokai Hit) and lens heating calibrated for incubation at 37°C with 5% CO_2. Microscope image acquisition was controlled using MetaMorph 7.7. GFP was imaged at 491 nm (0.2 mW, 100 ms every 0.6 s) and full frame SBTub3 photoactivation was performed using 405 (0.1 mW, 100ms every 1.2 s), and images were acquired using a Plan Apo VC 60× NA 1.4 oil objective. Comet count analysis was performed in ImageJ using the ComDet plugin (E. Katrukha, University of Utrecht, Netherlands, https://github.com/ekatrukha/ComDet). Velocity analysis was performed in ImageJ using the MTrackJ plugin (Meijering et al., 2012).

EB3 Comet Assay with Cell-Specific Photoisomerisation

HeLa cells were transfected with *EB3-GFP* using FuGENE 6 (Promega) according to manufacturer's instructions. Cells were imaged on a Nikon Eclipse Ti microscope equipped with a perfect focus system (Nikon), a spinning disk-based confocal scanner unit (CSU-X1-A1, Yokogawa) and an Evolve 512 EMCCD camera (Photometrics) with a stage top incubator INUBG2E-ZILCS (Tokai Hit) and lens heating calibrated for incubation at 37°C with 5% CO_2. Microscope image acquisition was controlled using MetaMorph 7.7, with GFP imaging at 491 nm (0.17 mW, 300 ms every 2 s) and compound activation at 405 nm (77 μW, 100 ms every 90 s), and images were acquired using a Plan Apo VC 60× NA 1.4 oil objective. Comet count analysis performed in ImageJ using the ComDet plugin (E. Katrukha, University of Utrecht, https://github.com/ekatrukha/ComDet). Please see Data S1 Part G for more information.

EB3 Comet Assay in Rat Primary Hippocampal Neurons

All animal experiments were performed in accordance with Dutch law (Wet op de Dierproeven, 1996) and European regulations (Directive 2010/63/EU) under animal licence AVD1080020173404. All animal experiments were approved by the Dutch Animal Experiments Committee (DEC, Dier Experimenten Commissie) and were in line with the institutional guidelines of Utrecht University. Primary hippocampal neurons were derived from hippocampi of embryonic day 18 pups (male and female) from pregnant Wistar rats, cultured at 37°C and 5% CO_2 in supplemented NB, transfected with EB3-GFP at the 7th day *in vitro* (DIV 7) using Lipofectamine 2000 (Invitrogen), and imaged at DIV 10 in conditioned NB with 1% DMSO cosolvent (Kapitein et al., 2010, further details in the Supplementary Information). Cells were imaged on the Nikon Eclipse Ti system used for cell-specific photoisomerisation assays with similar conditions, except in that GFP was imaged at 491 nm (0.1 mW, 500 ms every 3 s). Neurons were initially imaged for EB3 for 10 min while a ROI (blue box) was pulsed with 405 nm light commencing 2 min into the acquisition, establishing baselines for EB3 activity in the cell and in the ROI (areas not pulsed with 405 nm but analysed in kymographs are boxed in orange and green); the ROI-pulsing protocol was to illuminate the ROI at 405 nm (95 μW, 7 ms per trace) tracing over the ROI 5 times every 3 s with imaging frames interleaved. The same neurons were then exposed to 1 μM **SBTub3** and immediately imaged for another 10 min using the same protocol. Images were processed in ImageJ, XY drift or movement was automatically compensated using the Template Matching plugin (Tseng et al., 2012) https://sites.google.com/site/qingzongtseng/template-matching-ij-plugin), comet count analysis was performed using the ComDet plugin (E. Katrukha, University of Utrecht, https://github.com/ekatrukha/ComDet).

Please cite this article in press as: Gao et al., A Robust, GFP-Orthogonal Photoswitchable Inhibitor Scaffold Extends Optical Control over the Microtubule Cytoskeleton, Cell Chemical Biology (2020), https://doi.org/10.1016/j.chembiol.2020.11.007

QUANTIFICATION AND STATISTICAL ANALYSIS

All relevant assays were done in independent biological replicates. All attempts at replication were successful and no data were excluded from analysis. Blinding was not performed as assay readout is mostly unbiased (plate reader, flow cytometry, Fiji/ImageJ plugins). Microscopic evaluation was performed independently by two separate scientists. Data were analysed using Prism 8 software (GraphPad). Two-tailed unpaired t tests were used in pairwise group comparisons; * was used for $P < 0.05$, ** for $P < 0.01$, *** for $P < 0.001$, **** for $P < 0.0001$.

Cell Chemical Biology, Volume *28*

Supplemental Information

A Robust, GFP-Orthogonal Photoswitchable Inhibitor Scaffold Extends Optical Control over the Microtubule Cytoskeleton

Li Gao, Joyce C.M. Meiring, Yvonne Kraus, Maximilian Wranik, Tobias Weinert, Stefanie D. Pritzl, Rebekkah Bingham, Evangelia Ntouliou, Klara I. Jansen, Natacha Olieric, Jörg Standfuss, Lukas C. Kapitein, Theobald Lohmüller, Julia Ahlfeld, Anna Akhmanova, Michel O. Steinmetz, and Oliver Thorn-Seshold

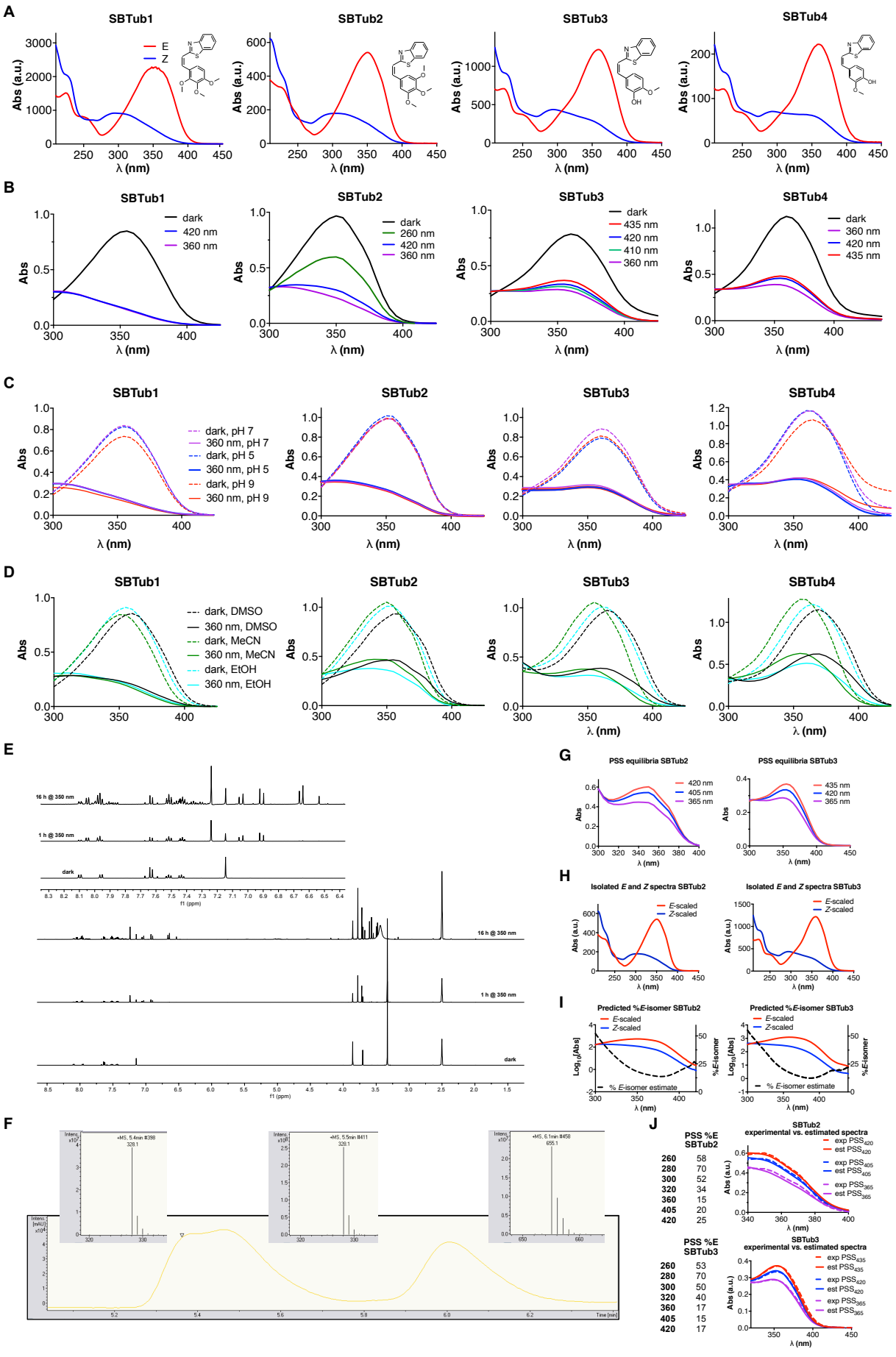
A
SBTub1
SBTub2
SBTub3
SBTub4
E
Z
Abs (a.u.)
λ (nm)
B
dark
420 nm
360 nm
260 nm
435 nm
410 nm
Abs
C
dark, pH 7
360 nm, pH 7
dark, pH 5
360 nm, pH 5
dark, pH 9
360 nm, pH 9
D
dark, DMSO
360 nm, DMSO
dark, MeCN
360 nm, MeCN
dark, EtOH
360 nm, EtOH
E
16 h @ 350 nm
1 h @ 350 nm
dark
f1 (ppm)
F
G
PSS equilibria SBTub2
PSS equilibria SBTub3
405 nm
365 nm
H
Isolated E and Z spectra SBTub2
Isolated E and Z spectra SBTub3
E-scaled
Z-scaled
I
Predicted %E-isomer SBTub2
Predicted %E-isomer SBTub3
% E-isomer estimate
J
PSS %E SBTub2
260 58
280 70
300 52
320 34
360 15
405 20
420 25
SBTub2 experimental vs. estimated spectra
exp PSS420
est PSS420
exp PSS405
est PSS405
exp PSS365
est PSS365
PSS %E SBTub3
260 53
280 70
300 50
320 40
360 17
405 15
420 17
SBTub3 experimental vs. estimated spectra
exp PSS435
est PSS435

Figure S1. Photoswitching of SBTubs, Related to Figure 1

(A) all-*E* and all-*Z* spectra of SBTub1-4 from inline HPLC-DAD. (B) Absorption spectra of SBTub samples under saturating illumination at different wavelengths generating the given photostationary state (PSS) equilibria for SBTub1-4, from UV-Vis spectrophotometry, in 90% PBS:10% DMSO (SBTubs at 25 μM).

(C-D) Absorption spectra of SBTub1-4 (25 μM) in the dark (dashed lines) and at 360 nm PSS (solid lines), in (C) 90% PBS+10% DMSO at different buffer pH values and (D) different solvent environments.

(E) H-NMR spectra of SBTub2 in the dark (all-trans) and after exposure to 350 nm UV in Rayonet photoreactor for 1 h / 16 h, with zoom-ins on the aromatic region that illustrates isomerisation/cycloaddition.

(F) HPLC-MS trace of SBTub2 after irradiation with 350 nm in the UV photoreactor for 16 h displaying all three major peaks, with zoom panels showing mass spectra at 5.4 min (*Z*-SBTub2), 5.5 min (*E*-SBTub2), and 6.1 min (the [2+2] cycloaddition product).

(G-J) Procedure for determining PSS composition (see details in Supplemental Information): (G) PSS absorption spectra acquired in biological media are used to scale (H) HPLC spectra of pure *E* and *Z* isomers, which are then used to calculate (I) predicted *E*-isomer percentages at PSS under a range of illumination wavelengths (black dotted line scaling to the right axis, and accompanying tables). (J) The correspondence of simulated PSS ("est. PSS") to measured PSS ("exp. PSS") absorption spectra is checked, to confirm whether PSS interpolation is valid. PSS interpolation is shown to be closely valid for SBTub2 and SBTub3.

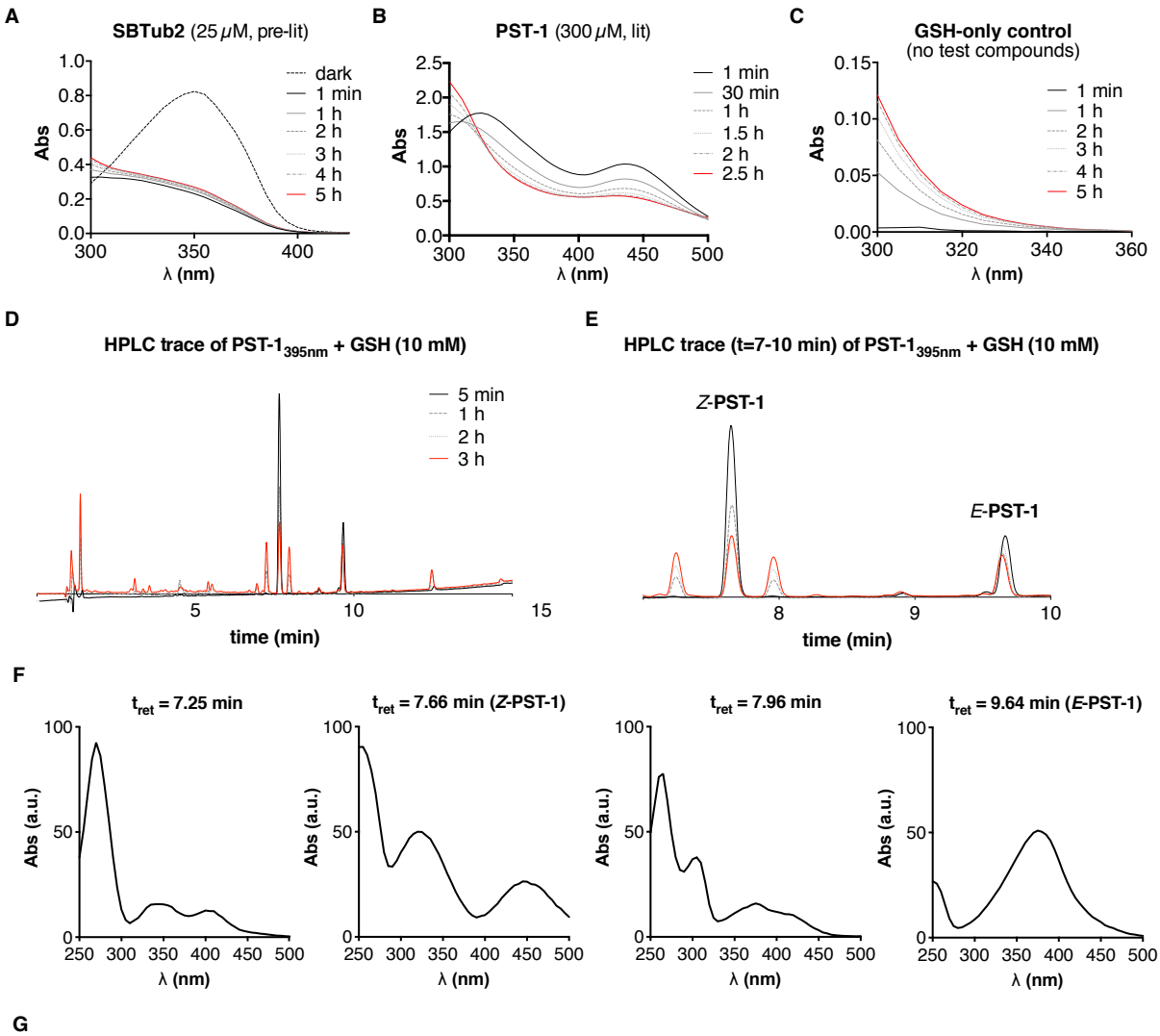

G

CYP	Reference inhibitor	Ref. inhibitor conc. (μM)	% Inhibition
1A2	α-naphthoflavone	2	100.8
2C9	sulfaphenazole	5	97.9
2C19	ticlopidine	25	97.3
2D6	quinidine	0.5	85.2
3A4	ketoconazole	2	99.0

Figure S2. Biochemistry of SBTubs, Related to Figure 2

(A-F) GSH resistance assays, incubating test compounds with 10 mM GSH, data corresponding to Figure 2A. (A-B) Absorbance spectra of SBTub2 and PST-1 over time during GSH challenge. (C) Absorption spectrum of no-compound control sample (dark, 10 mM GSH only) presumably showing disulfide-formation-based absorption change underlying the profile changes in Figure S2A-B, which does not substantially affect results when taking the intercept at 360 nm or above. (D-E) 254 nm HPLC trace timecourse of PST-1 (0.5 mM) incubated with 10 mM GSH, with (D) the full-scale panel also shown as (*E*) zoom on the region of interest from t_{ret} = 7–10 min, showing *Z*-PST-1 (t_{ret} 7.66 min), *E*-PST-1 (t_{ret} 9.64 min) and the two new unidentified signals that increase over time (t_{ret} 7.25 min and t_{ret} 7.96 min). (F) DAD absorption spectra at the four major peaks. (All assays conducted with 10% DMSO for solubilisation). (G) Reference compounds used to benchmark CYP inhibition (see Figure 2E).

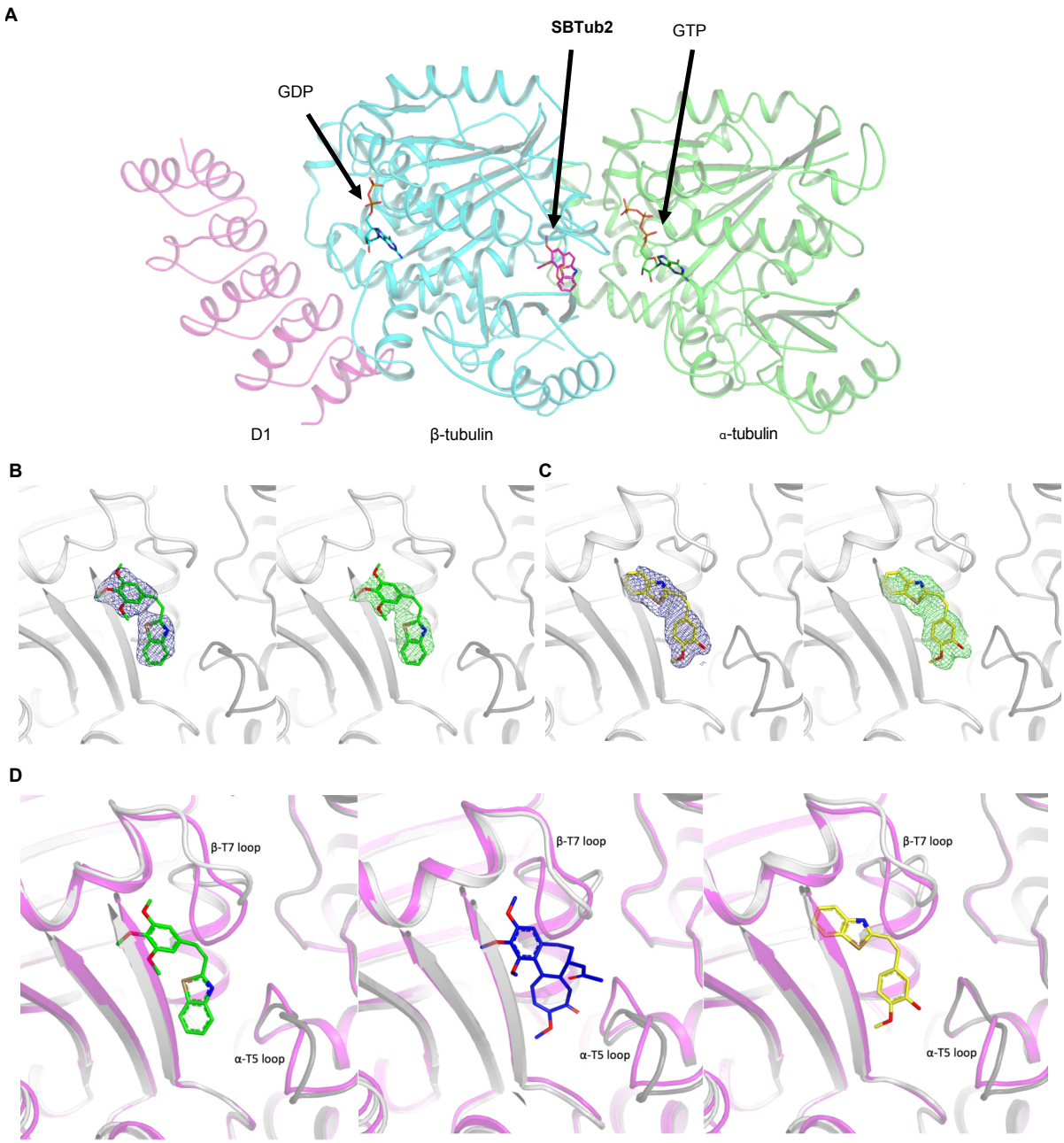

Figure S3. Cell-Free Crystal Structures of Tubulin-SBTub Complexes Support Their Light-Specific Tubulin-Mediated Mechanism of Action, Related to Figure 3

(A) Overall view of the TD1-Z-SBTub2 complex structure shown in cartoon representation with the different ligands shown in sticks representation.

(B) Colchicine site of tubulin-Z-SBTub2 with 2FoFc map contoured at 1σ shown in blue (left) and simulated annealing omit map at 2.5σ shown in green (right) mesh representation.

(C) Colchicine site of tubulin-Z-SBTub3 with 2FoFc map contoured at 1σ shown in blue (left) and simulated annealing omit map at 2.5σ shown in green (right) mesh representation.

(D) Side-by-side comparison of the colchicine sites of the tubulin-colchicine (middle; PDB ID 5NM5), tubulin-Z-SBTub2 (left) and tubulin-Z-SBTub3 (right) complex structures. On each structure, the ligand-free protein structure (PDB ID 5NQT) has been superimposed (shown in pink), to highlight structural rearrangements induced upon complexation.

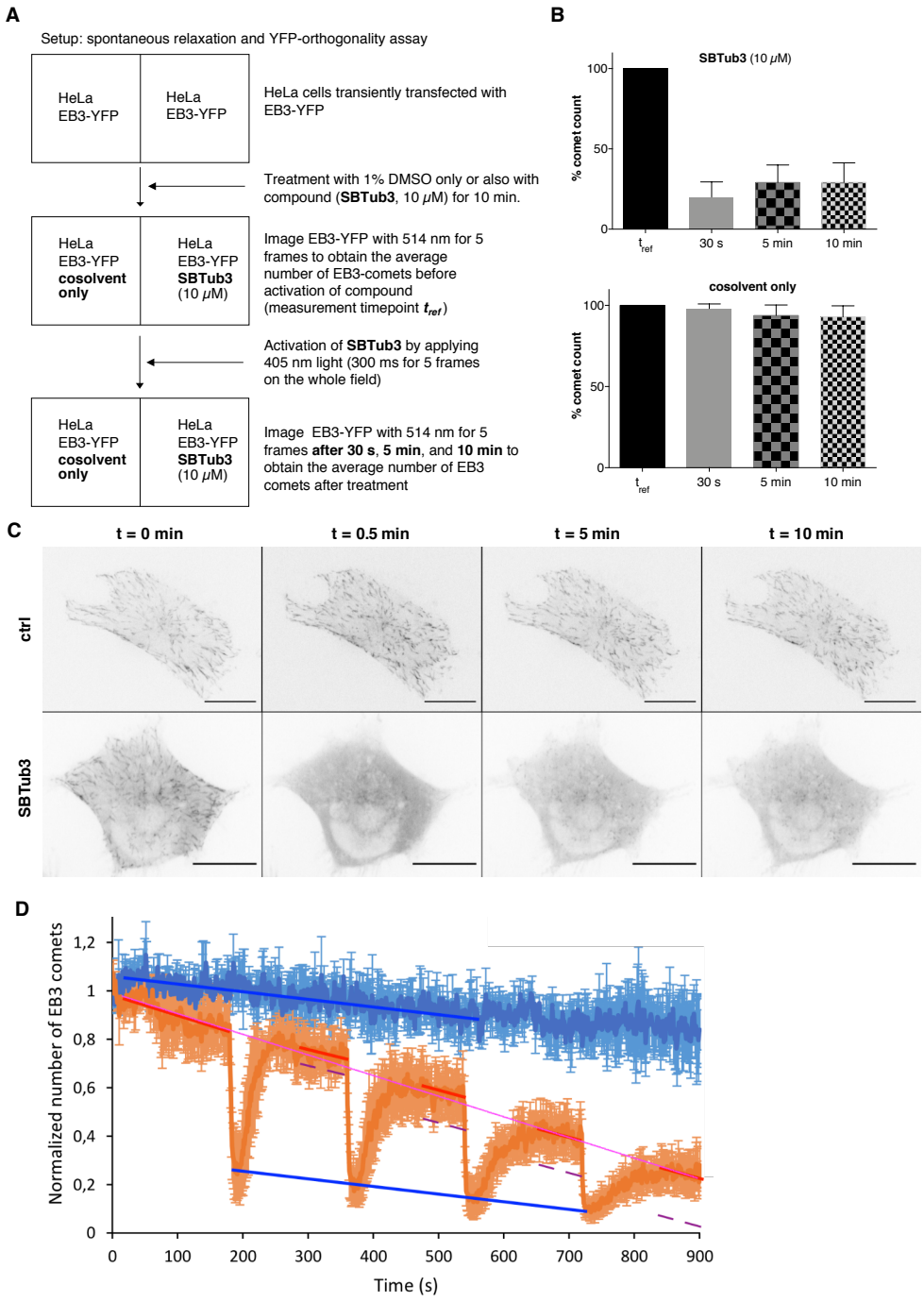

Figure S4. EB imaging protocol and troubleshooting, Related to Figure 4

(A) Experimental setup for photoswitching during live cell imaging of SBTub3 to evaluate orthogonality to YFP imaging (similar protocol used for evaluating GFP orthogonality) and resistance to relaxation on the stage.

(B) Quantification of EB3-YFP comets at different timepoints upon photoswitching during live cell imaging, normalised relative to comet count at t_{ref}.

(C) Stills of SBTub3 live cell imaging experiment corresponding to Figure S4B. (Cells have similar surface areas but stills are differently scaled in order to fill the fields of view; an inverted color scheme is used (black=bright signal, white=no signal) to highlight EB3 comets, which here appear as black dots; scale bar represents 20 μm).

(D) Example EB3-imaging experiment where the starting choice of imaging parameters did not allow temporally reversible MT control and also caused fluorescent protein marker (FP) photobleaching. Blue statistics: DMSO control. Orange statistics: an SBTub-treated sample (40 μM) where 405 nm photoactivation was applied for ca. 5 seconds every 180 seconds. Dotted purple and solid blue, red and pink fitlines are discussed in the Practical User Guide section of the Supplemental Information.

Table S1. Crystallographic Data for *Z*-SBTub2 bound to tubulin-DARPin D1 (TD1) complex and for *Z*-SBTub3 bound to TD1 complex, Related to Star Methods X-ray diffraction data collection, processing and refinement.

Data Statistics	TD1-*Z*-**SBTub2**	TD1-*Z*-**SBTub3**
Space group	P 2_1	P 2_1
Unit cell (a; b; c; β)	73.90 91.85 82.81 96.58	73.87 91.72 83.00 97.06
Wavelength (Å)	1.0	1.0
Resolution (Å)	45.18 – 2.05 (2.33 – 2.05)	45.85 – 1.86
R_{pim} (%)	7.4 (59.1)	5.5 (50.0)
I/σI	7.1 (1.6)	9.3 (1.7)
Spherical completeness (%)	59.5 (9.3)	68.4 (12.9)
Ellipsoidal completeness (%)	88.2 (53.1)	91.2 (59.9)
Ellipsoidal truncation resolution limits (Å)	2.04, 2.50, 2.55	1.84, 2.23, 2,12
Multiplicity	4.1 (4.7)	4.2 (4.3)
$CC_{1/2}$	0.992 (0.951)	0.997 (0.526)
Refinement Statistics		
Resolution	45.18 – 2.05	45.04 – 1.75
No. reflections	40926	68146
R_{work} / R_{free}	22.5 / 28.1	18.5 / 23.3
Ramachandran favoured	94.98%	97.15%
Ramachandran outliers	0.79%	0.1%
R.m.s.d. bond length (Å)	0.002	0.003
R.m.s.d. bond angles (°)	0.463	0.627
PDB code	6ZWC	6ZWB

Data S1. Detailed information on synthesis, characterization, handling and usage of photoswitchable SBTubs, Related to STAR Methods

Part H: NMR Spectra

Supplementary Information Bibliography

Part A: Practical User Guide

SBTub - User Introduction

- **SBTubs** are light-triggered tubulin depolymerisers. They can be used to switch cells and organisms from a state of ordinary MT polymerisation dynamics to an inhibited state.
- Light illumination changes **SBTub**s from their inactive ***trans*** [*E*] to their bioactive ***cis*** [*Z*] isomer. Upon reaching a **threshold concentration of the *cis* state** inside a cell, tubulin polymerisation will slow then stop (and microtubules start to depolymerise); when the *cis* concentration drops below this threshold, tubulin polymerisation restarts. The threshold is usually reached at an applied extracellular *cis*-concentration of ~ 2-4 μM.
- The **SBTub**s' *cis* state has similar biological effects to known tubulin inhibitors colchicine, combretastatin or nocodazole but is somewhat less potent than these inhibitors, so **SBTub**s have to be used at higher concentrations to achieve comparable biological effects. Titrate for your system! The **SBTub**s' inactive *trans* state does not affect tubulin at all.
- The inhibitory threshold concentration of *cis*-**SBTub** may typically be reached by applying a low concentration of **SBTub** and converting most of it to *cis* using light: e.g. converting 85% of a total dose of 2-4 μM **SBTub3** to *cis* by applying light at any wavelengths from 360 to 405 nm (aiming to arrest tubulin polymerisation dynamics).

Storage Notes

For **SBTub2**, **SBTub3** (or controls like **PST-1**): stocks (as powder or as 100%-DMSO stocks) can be stored at room temperature (shielded from light in a cardboard box or wrapped in aluminum foil) or at 4°C; freeze-thaw cycles are no problem. Warm up any cold DMSO stock to room temp before using; there should be no solids and the solutions should be optically clear (otherwise sonicate). Adjust your pure-DMSO stocks to 100X and then dilute them straight into buffer for assays (see cosolvent instructions below). **Do not cold store diluted samples in buffer-DMSO mixtures** as the compounds will precipitate out of solution and won't redissolve – keep any buffer-DMSO samples at room temperature or at 37°C, shielded from light. Ideally, only store DMSO/powder stocks and make all working dilutions fresh. Compound lifetime > 2 years.

SBTub - Photoisomerisation: How to do it

- Short answer: Applying UV/violet light isomerises the **SBTub** to its bioactive isomer.
- **Illumination** with a given wavelength of light shifts the balance between *cis* and *trans* forms toward a "photoequilibrium ratio" that is dictated by the wavelength used. Relatively low light intensities are sufficient, even unfocussed LEDs; lasers are NOT required. Slow isomerisation under light that has a UV/blue component (e.g. sunlight) takes place when the compound is in solution; stocks should therefore always be stored protected from light and/or in brown glass vials if you want to keep them as *E*-isomer (inactive isomer), e.g. to establish baseline behaviour before local switching.
- The equilibrium percentage of *cis* and *trans* that illumination eventually establishes at photoequilibrium [the "PSS"] depends on what wavelength is used for illumination. **When the equilibrium ratio has been reached in a certain location or sample** (by passing enough

photons through that location/sample), **then applying any more light to that location/sample will not change the *cis*/*trans* ratio in that location/sample any more** (i.e. no further activation will be achieved). This is very different performance to "photouncageable" compounds such as photocaged Taxol or combretastatin.

- After photoisomerisations that push the **SBTub** population mainly into the bioactive *Z* isomer state, the typical **SBTub**s **can not be substantially photoreverted** back towards the *trans* isomer with biologically acceptable light wavelengths (>300 nm). Spontaneous relaxation (unidirectional spontaneous process, from *cis* to all-*trans*) is the only way this can be achieved (see below). Consequence: **photopatterned SBTub**s **can be imaged with any wavelengths of light above 470 nm without optically disrupting the photopattern of MT inhibition**. That offers different performance compared to our previous light-responsive tubulin polymerisation inhibitors the "**photostatins**" [**PST**s].

SBTub - Recovering the inactive state by relaxation and/or diffusion

- **SBTub** molecules that have been illuminated into the *cis* state show **negligeable spontaneous change** ["relaxation"] back towards the all-*trans* (inactive) state under standard usage conditions [<38°C, DMSO or DMSO-water solvent systems]. Therefore a cell that has been exposed to enough **SBTub** with enough illumination *applied throughout the whole well* such that MT dynamics slow/stop, will remain with slowed/stopped MT dynamics for >24 h (one-shot activation). If a whole tissue has been illuminated, then MT dynamics will not recover until the *cis*-**SBTub** inside the cells of that tissue diffuse out into naïve or fresh surrounding media. **However, if only a single cell within a larger well or tissue has been illuminated** by photoisomerising UV light, this diffusion can extremely rapid ("diffusion-based temporal reversibility") - **it is typically complete within much less than 60 s**, and diffusion-based reversibility kinetics can be substantially tuned by choice of concentration, photoisomerisation ROI, photoisomerisation pulse photon flux, etc. These are all different performance features compared to **PST**s [**PST**s do spontaneously relax back to the non-inhibiting state with halflives of minutes to hours].
- Under standard *biological usage* conditions there is <1% relaxation after 24 h, but **SBTub** relaxation does however occur. Its relaxation halflife τ depends strongly on the temperature, and also on the compound used, the pH, the solvent, etc.
- **In case of unwanted photoactivation of a SBTub stock solution**, one can exploit relaxation to recover a stock of **SBTub** into its fully bioinactive state before an assay by storing it (capped tightly) overnight in an oven set to 60 °C. This speeds up relaxation of the *cis* form to the *trans* form, reaching ~100%-*trans* (with first-order kinetics) typically after 12 h, which we call a "fully dark" stock. An experiment run with a fully dark stock under dark or redlight conditions will therefore contain 100% of the biologically inactive *trans* form and should show no MT inhibition (*cis* compound control experiment). This recoverability is another difference to photouncageable compounds.

Generic Details

- **SBTub3** (M = 283 g/mol) is usually provided as a **10 mM stock in DMSO**, or can be sent as a solid to be dissolved in any other polar organic solvent if needed (MeOH, EtOH, MeCN, DMF, EtOAc, CH_2Cl_2). **SBTub3** is **not soluble** in pure aqueous buffers.

- For biological testing, it should be assumed that **SBTub3** is *irreversibly activated*, once exposed to near-UV light. However see the note about recovering unwanted photoactivation of a stock (above).
- A final factor to consider in choosing a **SBTub** is its **solubility**. Most **SBTub**s are almost insoluble in pure media/buffers, unless a cosolvent is used. A good cosolvent stops compound invisibly precipitating/aggregating out of solution and allows to perform experiments reliably. Typical good cosolvent choices are preferably 1% DMSO (this is usually acceptable for cell culture and is recommended for all cell extract work); ethanol or DMSO, *at least* 0.1% are required. We recommend to spike directly from a 100% DMSO solution adjusted to 100X concentration, into the aqueous media of the test well. **Some SBTubs** are being formulated (ongoing work) as fully water-soluble prodrugs that require no cosolvent and are highly *in vivo* compatible, however the **prodrugs are unsuitable for cell-free use** and may be poorly effective in short-term experiments (<10 min) where cell penetration speed is important. For prodrug formulations of **SBTub**s (experimental) and for reference prodrugs: store the compounds (powder or aqueous stocks) at 20°C. Do not use DMSO cosolvent with the formulations; they are only soluble in buffer. Freeze-thaw cycles are no problem. Store diluted samples frozen. Warm frozen stocks/samples to room temp or 37°C before using; there should be no solids & the solutions should be optically clear (otherwise sonicate). Compound lifetime ~1 year. Contact us for more information.
- **SBTub**s require much less illumination than **PST**s to show a cytotoxic effect since they only need to be illuminated once to provide a long-term effect. This 'single-shot activation' allows easier illumination setups especially for moving cells or animals, since no repetitive re-illuminations or cell/tissue tracking is required. It is also more 'forgiving' in case that illumination is accidentally stopped at some point during the setup, or when model system is not fixed to one location – floating / moving around.

Frequently Asked Questions (FAQ)

When do I need to use an SBTub instead of a PST for MT photocontrol?

SBTub is a highly photostable and much more biostable analogue of **PST**. It showcases longer thermal halflife and total resistance against glutathione (GSH) and has no effects caused by imaging at >450 nm.

We recommend using **SBTub**s **(a)** in **long-term in vivo** experiments to reduce the **PST**s' complications (**PST**s need repeated illuminations & there is GSH/metabolic depletion of cis-**PST**); **(b)** when controlling MTs while **imaging GFP or fluorescein** to avoid worrying about unwanted photoisomerization (full GFP-orthogonality). **SBTub**s switch on best with 360 nm but if working on the microscope, 405 nm also does the job.

How easily are SBTubs activated with ambient room light (e.g. computer monitor light, DIC light used to typically find sample focus, etc.)?

(1) The danger of activation by ambient room light at usual intensities on the work surface (in the era of LEDs and fluorescent lamps, which barely emit below 410 nm) is far lower for **SBTubs** (absorption cutoff: 410 nm) than for their azobenzene counterparts such as **PST**s (absorption cutoff: 490 530 nm, depending on isomer). (2) Monitor light is of too low intensity and has too little UV component to affect **SBTub**s at all, though should not greatly affect **PST**s either. (3) For **PST**s white DIC light on the microscope causes strong isomerisation that has repeatedly complicated

experiments in our and other labs. However under white DIC light conditions we did not observe any induction of inhibitory effects with **SBTub**s. (4) Since we always ship **SBTub** stocks in brown glass vials and since bio/microscope labs are "closed" systems, daylight activation of **SBTubs** should not be expected under ordinary handling. **SBTub**s can be pipetted and handled with ambient light without compound activation. By comparison, **PST** users are advised to keep **PST** in the dark and pipette under redlight.

My dark experiment shows the same (or more!) MT inhibition as my lit experiment!

The stock may have been **accidentally photoactivated**. In this case store an all-DMSO stock solution overnight in a 60°C oven to thermally relax 100% of the compound to the trans form. Redo the experiment using this "baked" stock making sure that there is minimal UV, white light or sunlight applied during the dark experiment (red light work; store in dark box, etc).

Should I expect the same results for a SBTub and its prodrug?

In cells/animals, yes. Any differences are most likely due to different solubility in aqueous media. Prodrugs are more reliably soluble; **SBTub**s require cosolvents (e.g. DMSO), which is not always tolerated by the model system (e.g. zebrafish in our hands go up to 1% DMSO).

How should I store SBTub?

See Storage Note at start of this doc! For **SBTub3** powders and DMSO stocks, you can store them at room temperature prior to diluting them with buffer for your assays. Don't store the diluted samples at 4°C as the compound can crash out of solution and it can't go back in solution. For long-term storage, the DMSO stocks/powders can be stored at –20°C.

I have no way to do 360 nm illumination, is 400 nm or 420 nm also ok?

Any UV wavelength or violet light up to 420 nm still gives satisfactory photoactivation compared to the dark experiment. "UV Blacklight" LEDs or LED-strip-lights can be bought on Amazon and these work fine. We can also provide LED-arrays or single LEDs if needed. *Or we can send a build guide for making a 20€ UV illumination array for cell culture microplates based on sticking together 120 LEDs/m UV Blacklight strip lighting off Amazon, together with a pulse timer that costs 8€.*

Worked example of tuning parameters for cell assay

Figure S4D shows an EB3-imaging experiment where conditions for imaging while photoswitching **SBTub3** (40 μM) did not allow temporally reversible MT control and also caused fluorescent protein marker (FP) photobleaching. This highlights several problems which can be individually tuned by better choice of experimental settings, to allow temporally-reversible **SBTub**-based photocontrol of MT dynamics, as follows:

Problem 1. FP-imaging protocol used (a) directly bleaches 20% of comets in DMSO control over 900 s (blue solid fit line to blue DMSO dataset); and (b) is also making a *cis*-**SBTub** background throughout the cell & relevant-surrounding-volume (e.g. in first 180s cycle, already lost 20% of comets in the orange **SBTub** dataset; the extra **SBTub** background is visible in that the pink solid fit line to the tops of the **SBTub**-data decreases faster than the blue fit line to DMSO, indicating slow buildup of *cis*-**SBTub**).

Diagnosis 1: imaging photon flux is far too high for this high concentration of **SBTub** applied!

Solutions 1a: slow down imaging frame acquisition rate 5-fold and also make each imaging pulse 1/4 of the current acquisition time. This reduces imaging photon flux 20-fold. So you should now see

20-fold less direct photobleaching in the DMSO control; *and* 20-fold less background activation to *cis*-**SBTub** which means better - **more frequent, more complete, and faster** - recoveries.

Theoretically you can also reduce the laser intensity for imaging, so that photon flux per imaging frame is further reduced. But **we do not recommend this** since in many microscopes the photon flux is not linear with "laser power %" over the full range, whereas imaging frame acquisition time is definitely linear to flux, so there you know what you are dealing with. (Or, you could theoretically increase the pixel size, but there can be other pixel size effects, as well as loss of resolution, too so we also do not recommend this).

Check 1: Now retry imaging, with same concentration of **SBTub** for 600 s. How many comets are lost over time in DMSO control? Further reduce flux until it's acceptable.

Check 2: How about (pink) comet loss fit line for the **SBTub**-treated case? Better?

Solutions 1b: If there is still significant loss of comets, **adjust SBTub concentration down** (e.g. to 10 μM) and compare. Keep titrating **SBTub** concentrations such that the 405 nm flash still gets to a desired level of EB inhibition, but there's less *trans*-**SBTub** present in the whole well to get background activated (better recoveries). There will be a concentration that doesn't show significant comet reduction over time.

Observation 2: Comet count at the peak of the 405 nm periods (blue fit to orange data) decreases at same rate as does comet direct FP bleaching by FP imaging, seen in DMSO control, i.e. the max-*cis*-**SBTub** in cell seems not to increase with 405 nm pulsing; conclude: we reach the same concentration of cis-**SBTub** during each 405 nm pulse (just we have some comets getting bleached) despite the fact that there is a background level of cis-**SBTub** which is increasing over time in the whole sample (see Problem 1).

Diagnosis 2a: The 405 flash photon flux being used must be "overkill" since the cell already experiences the highest possible concentration of *cis*-**SBTub** during the first 405 nm flash, despite the low background level of *cis*-**SBTub**. The aim in such an experiment is however not to isomerise all **SBTub** inside the cell (and in the conical light path through the well), but *just enough* of the **SBTub** in the cell to get a substantial block of EB comets. So all that extra 405 nm photon flux can be causing too much off-target photobleaching or photoisomerisation when experiments get more complex.

Solution 2a: Minimise the 405 nm flux before starting difficult experiments. This can make a **faster recovery halflife** too. Modify 405 nm frame flux (total time per 405 nm period), and see if results look similar. If similar, keep halving flux until the inhibition reached is no longer good enough; stop there and use whatever was still OK - the true minimum 405 nm flux.

Diagnosis 2b: There is no significant contribution from 405 nm in-cell isomerisations to the loss of comets over time (if there were, the recovered comet count timecourse would "step" down (dotted purple lines) instead of going smoothly down (red lines) and recovery time kinetics of ~80 s would also lengthen. So if needed, can do at least double the time-density of 405 nm isomerisations eg. one every 90 s (adjust according to the recovery times after all previous improvements).

Ideas: (3) Apply FP imaging to a smaller field of view, to reduce background SBT isomerisation in the whole sample? Assuming the aperture has already been adjusted to minimum! (4) Compare to **PST-1** active photoswitching under similar conditions.

Part B: Photo/Chemical Design

This section is expanded from the main text of the manuscript to provide a more comprehensive introduction to the design motivations behind the development of the **SBTubs**.

Molecular photoswitches for biology reagents and MTs - chemical background

Molecular photoswitches have been used to install optical control over a broad range of phenomena, with applications from material sciences[1,2] through to reversible photocontrol of ligand binding affinities[3] and manipulation of diverse cellular processes in chemical biology[4,5]. For studies of temporally-regulated and spatially anisotropic biological systems, particularly those that simultaneously support several cellular functions, photoswitchable inhibitors ("photopharmaceuticals") conceptually enable a range of powerful studies not accessible with other tool systems.[6-8]

The microtubule (MT) cytoskeleton is a prime example of such a spatiotemporally regulated, multifunctional system where photoswitchable inhibitors have the potential to enable conceptually important and unique studies. Whereas cytoskeleton research typically aims to study a subset of MT-dependent processes that are spatially and/or temporally localised, nearly all MT inhibitors reported as tool compounds for biological research are drugs that are active wherever they are distributed, including at sites and at times where drug activity is not desired.[9] This restricts the scope of applications and utility of these inhibitors for selective research into the various, highly dynamic, anisotropic processes dependent on MTs.[10]

The structure of the colchicine site MT inhibitor combretastatin A-4 (**CA4**; Figure 1B)[11] has recently inspired photoswitchable solutions to the problem of achieving spatiotemporal control over MT inhibition. **CA4** is a stilbene whose *Z*-isomer (*cis*) binds tubulin, acts as a low nanomolar cytotoxin *in cellulo*, and reached Phase III trials as an anticancer drug.[12,13] Crucially, its *E*-isomer (*trans*) is several orders of magnitude less bioactive.[14] An approach to microtubule photocontrol *via* photoisomerisation of its bridging C=C bond has been proposed, whereby bioactive *Z*-combretastatins should be generated *in situ* from inactive *E*-precursors, allowing spatially and temporally precise application of antimitotic bioactivity.[15] However, to the best of our knowledge this concept has not been realised in biology, hindered by the bio-incompatible short-wavelength illumination required ($\lambda_{max} \sim 300$ nm) and the irreversible photochemical degradations that stilbenes undergo in aerobic conditions (e.g. oxidative 6π-electrocyclisation).[16]

Instead, designing **CA4** analogues incorporating the synthetic azobenzene photoswitch scaffold inside their pharmacophore - a design strategy known as “azologisation”[17] - delivered the biocompatibly-switchable, azobenzene-based Photostatins (**PST**s; Figure 1B)[6,18-20], which undergo optically reversible, bidirectional photoswitching between inactive *E* and MT-inhibiting *Z* isomers using low-intensity visible light. The **PST**s have enabled specific optical control over MT structure and dynamics in live cells as well as *D. melanogaster*[21], *C. elegans*[6], zebrafish[22], and mouse[7] and have been used to resolve key biological questions in mammalian development and in neuroscience.[8,23]. These applications illustrate the power of photopharmacology to enable previously inaccessible studies of spatiotemporally anisotropic processes without genetic engineering, which is particularly important for studies of cytoskeletal scaffold proteins, since no optogenetic methods have yet been developed that can control their structure-dependent functions.[7,8,21,24]

Design problems of current photoswitchable reagents that SBTs may solve

Photopharmacology in general has been extensively reviewed in the chemical literature,[25-28] from which it is apparent that (a) the vast majority of all photopharmaceuticals reported are based on the azobenzene photoswitch scaffold, (b) many photopharmaceuticals have a poor dynamic range of photoswitchability (less than 10-fold difference between on-target bioactivities of their "best on-state PSS" and "best off-state PSS" photogenerated equilibrium populations; see also below); (c) most compounds reported as photopharmaceuticals have not been shown to succeed except in cell-free systems, and of those that have been applied to cells the majority act on membrane-bound extracellularly-accessible targets; (d) azobenzene photopharmaceuticals only rarely perform well enough against protein targets in intracellular environments to be serious candidates for research uses (e.g. satisfactory cellular potency of the more-bioactive photogenerated population, >10-fold reduction of potency of the less-active photogenerated population).

In addition to the discussion in the main text, we particularly note the following problems of design and performance:

(1) Though "normal" azobenzenes are not orthogonal to GFP/YFP imaging, the current focus in azobenzene spectral shifting research is actually on "red-shifting" photoresponse spectra to still-longer wavelengths. Since "red-shifting strategies" almost always shift the photoresponse spectra of *both* isomers, the result of these is that bidirectional photoswitching continues to be stimulated by imaging fluorescent proteins: extending their non-orthogonality with GFP/YFP now strongly to RFP/mCherry imaging too and making the problem worse.

(2) almost all azobenzene photopharmaceuticals which display photoswitchable bioactivity on intracellular targets in cell assays, have very poor potency as compared to their parent inhibitor compounds. For example, cellularly photoswitchable **PST**s are ~2 orders of magnitude less potent in cells than **CA4**, despite almost identical potency in cell-free assays; other azobenzenes retain potency but are no longer photoswitchable. The reasons have barely been investigated, but it is known that the majority of azobenzenes can be sequestered and degraded following the addition of cytoplasmic glutathione (GSH; ca. 3-10 mM) to the electrophilic and abiotic N=N group[29-31], which initiates rapid destruction particularly of electron-rich systems[32]. Although other mechanisms are also likely to be relevant, this is sufficient to understand the performance loss described above. For those few "azo-inclusion" designs (such as **PST**s) where the azobenzene must be intact for binding to occur, only the undegraded fraction of reagent is available for binding, so an apparent potency loss may be seen due to sequestration/degradation of a fraction of the applied azobenzene. More commonly, particularly for "azo-extension" designs, the products of cleavage of the N=N bond (such as anilines, which also incur toxicity risks, e.g. carcinogenicity risks through nitrosobenzene intermediates) can often be predicted to be potent on-target binders, yet these will no longer be photoswitchable; therefore cellular metabolic products from a degraded azobenzene may deliver potent *though non-photoswitchable* on-target bioactivity which blocks the utility of the compound. Potency loss and/or problematic metabolites obstruct robust applications of azobenzenes to intracellular targets in general; and especially so *in vivo* where high doses may be required due to partial degradation, so that by-products have to be evaluated, so their toxicity risks are likely to be particularly problematic[19,33].

(3) Azobenzene relaxation halflives span more than 13 orders of magnitude, and compared to timescales of typical biological experiments (seconds to hours) these mainly fall into two clusters: either fast-relaxing (aqueous halflives from microseconds up to 1 second) or slow-relaxing (longer

than 24 h). Fast-relaxing azobenzenes (aqueous halflives from microseconds up to 1 second) typically arise when any of several common polar functional groups (OH, NHR, NH_2, etc: which are often vital in establishing ligand-protein interactions) are used in any of the six *ortho* or *para* positions. These halflives are far too short for reliable isomerisation-based photopatterning in the aqueous intracellular environment, leaving only the four *meta* positions available for these functional groups. The water-solubilisable **PST** derivatives **PST-1** and **PST-2** place these polar groups in *meta* and so did attain favourable halflives for cellular applications (in the range 1 - 60 min), but even this was not optimal for *in vivo* use: they would require re-illuminations during longer *in vivo* studies which are problematic to deliver with spatial precision in motile embryos or animals, and re-illuminations can also cause photobleaching of fluorescent labels on target proteins[6] as well as nonspecific photodamage. (**PST-1** is solubilisable as the phosphorylated **PST-1P**, and **PST-2** as the serinylated **PST-2S**). In comparison, SBT bioactivity persists in the long term after switching on by a single illumination (see Fig 4A). This can reduce both the overall photon flux needed for SBT operation as well as the requirements for repeating illuminations, which can be experimentally problematic, and which more rapidly-relaxing or isomer-dependently metabolically labile photopharmaceutical scaffolds such as azobenzenes require. The SBTs' violet-light operation and their extreme photochemical robustness under biological conditions also differentiates them from previously proposed but still not *in situ*-demonstrated deep-UV-operated stilbene-based probes[15] which are likely to suffer electrocyclisation-oxidation degradation[34].

We perceived however that these three key problems intrinsically associated to the azobenzene's N=N double bond (non-orthogonality to standard GFP / YFP imaging conditions, cellular/metabolic liabilities in intracellular settings, and substituent-dependent limits on thermal halflife scope) which reduce the success of translation of azobenzene photopharmaceuticals for intracellular targets from cell-free into cell culture and thence *in vivo* research applications, could be addressed by moving instead to new photoswitchable scaffolds that avoiding these three chemistry-based problems – both for the specific case of photoswitchable MT inhibitors, as well as for other applications in chemical biology.

Opportunities for SBT photopharmaceuticals: The current vogue of shifting isomerisation wavelengths towards the red wavelengths is intended to allow photopharmaceuticals to be photoswitched *in vivo* in animals, by light sources external to the organism (since red light penetrates biological tissue much deeper because it is not absorbed by chromophores such as hemoglobin; which also raises the problem that non-absorbed light actually loses spatial specificity due to its penetration completely through a subject). However, our ongoing results as well as published reports (Morstein et al., 2019) have shown successful subcutaneous isomerisation of photoswitches even with simple transdermal 360 nm LED illumination. Indeed, *in vivo*, colchicine domain inhibitors are often used as vascular disrupting agents and studied *in situ* in surface tissues using one- and two-photon microscopy (Tozer et al., 2001): which are both feasible approaches to also photoswitch **SBTub**s. In these superficial tissue settings, the penetration of violet light required for single-photon **SBTub** isomerisation is unlikely to be problematic. Rather than light accessibility for tissues, we consider that two compound-specific factors are likely to determine the success of *in situ*-actuated photoswitches for intracellular targets reaching *in vivo* applications. One is systemic pharmacokinetics. Only one pharmacokinetic study of a photopharmaceutical has been published (Babii et al., 2020), and no data are known for azobenzenes; yet the metabolic stability and druglikeness the SBTs feature are positive early signs. The second is the ability to robustly photomodulate intracellular biology, which relies on the intracellular biochemical stability of the

bioactive isomer, and in this respect SBTs show superior performance compared to the cognate azobenzenes. We therefore consider the **SBTub**s to offer exciting potential for *in vivo* translation within the context of MT photopharmacology.

Part C: Chemical Synthesis

Conventions

Abbreviations: The following abbreviations are used: Hex – distilled isohexanes, EA – ethyl acetate, Me – methyl, MeCN – acetonitrile, DMSO – dimethylsulfoxide, PBS – phosphate buffered saline aqueous buffer.

Safety Hazards: no remarkable safety hazards were encountered.

Reagents and Conditions: Unless stated otherwise, (1) all reactions and characterisations were performed with unpurified, undried, non-degassed solvents and reagents, used as obtained, under closed air atmosphere without special precautions; (2) "hexane" used for chromatography was distilled from commercial crude isohexane fraction by rotary evaporation; (3) "column" and "chromatography" refer to manual flash column chromatography on Merck silica gel Si-60 (40–63 µm); (4) "MPLC" refers to flash column chromatography purification on a Biotage Isolera Spektra system, using prepacked silica cartridges purchased from Biotage; (5) procedures and yields are unoptimised; (6) yields refer to isolated chromatographically and spectroscopically pure materials; (7) all eluent and solvent mixtures are given as volume ratios unless otherwise specified, thus "1:1 Hex:EA" indicates a 1:1 mixture (by volume) of hexanes and ethyl acetate; (8) chromatography eluents e.g. "3:1 → 1:1" indicate a stepwise or continual gradient of eluent composition.

Thin-layer chromatography (TLC) was run on 0.25 mm Merck silica gel plates (60, F-254), typically with Hex:EA eluents. UV light (254 nm) was used as a visualising agent, with cross-checking by 365 nm UV lamp for **SBTub** fluorescence. TLC characterisations are abbreviated as $\mathbf{R}_f$ = 0.64 (UV 254 nm, EA:Hex = 1:1).

NMR: Standard NMR characterisation was by ^{1}H- and ^{13}C-NMR spectra on a Bruker Ascend 400 (400 MHz & 100 MHz for ^{1}H and ^{13}C respectively). Chemical shifts (δ) are reported in ppm calibrated to residual non-perdeuterated solvent as an internal reference[35]. Peak descriptions singlet (s), doublet (d), triplet (t), and multiplet (m) are used. NMR spectra are given in Part H.

HRMS: High resolution mass spectrometry (HRMS) was carried out by the Zentrale Analytik of the LMU Munich using ESI ionisation in the positive mode.

IR Spectroscopy: IR spectra were recorded on a PerkinElmer Spectrum BX II FT-IR system. Both solids and liquids were directly applied as thin films of neat substance on the ATR unit. The measured wavenumbers are reported with relative intensities, abbreviated by s (strong), m (medium) and w (weak).

Synthesis procedures

2-(2,3,4-trimethoxystyryl)benzothiazole (SBTub1)

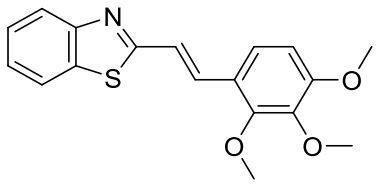

2-methylbenzothiazole (0.12 mL, 1 mmol) and 2,3,4-trimethoxybenzaldehyde (196 mg, 1 mmol, 1 eq) were dissolved in DMSO (2 mL). NaOMe (5.4 M in MeOH, 185 μL, 1 mmol, 1 eq) was added and the reaction was stirred overnight. H_2O (10 mL) was added. The mixture was extracted with ethyl acetate (3 × 15 mL). The combined organic layers were washed with brine (10 mL) and dried over $MgSO_4$. Flash column purification of the crude material (EA:Hex = 3:7) yielded **SBTub1** as light yellowish solid (298 mg, 0.91 mmol, 91%).

R_f = 0.64 (UV 254 nm, EA:Hex = 1:1). **HRMS (ESI$^+$):** 328.10002 calculated for $C_{18}H_{18}NO_3S^+$ $[M+H]^+$, 328.10003 found. **^{1}H-NMR (400 MHz, $CDCl_3$):** δ = 7.98 (d, *J* = 8.1 Hz, 1H), 7.84 (d, *J* = 8.0 Hz, 1H), 7.71 (d, *J* = 16.4 Hz, 1H), 7.45 (t, *J* = 8.3 Hz, 1H), 7.41 (d, *J* = 16.4 Hz, 1H), 7.35 (t, *J* = 8.2 Hz, 1H), 7.35 (d, *J* = 8.8 Hz, 1H), 6.73 (d, *J* = 8.8 Hz, 1H), 3.98 (s, 3H), 3.91 (s, 3H), 3.90 (s, 3H) ppm. **^{13}C-NMR (100 MHz, $CDCl_3$):** δ = 168.2, 155.0, 154.0, 152.8, 142.5, 134.3, 132.9, 126.4, 125.3, 122.9, 122.6, 122.4, 121.6, 121.5, 108.0, 61.6, 61.1, 56.2 ppm. **IR (FT, ATR):** $\tilde{\nu}$ = 2946 (w), 2835 (w), 1619 (w), 1588 (m), 1497 (m), 1455 (m), 1435 (m), 1412 (m), 1288 (s), 1254 (m), 1195 (m), 1093 (s), 1042 (m), 1014 (m), 968 (m), 945 (m), 914 (w), 851 (w), 798 (m), 754 (m) cm^{-1}.

2-(3,4,5-trimethoxystyryl)benzothiazole (SBTub2)

Note that this compound was reported - although only in the *trans* state - as a cytotoxic resveratrol analogue targeting tubulin, in 2014-2015 by Penthala *et al.*, as "Example Compound 4 (Formula (I)(d)" in their patent WO2014/172363[36] and as compound 13 in their paper[37]. In these reports it was synthesised and biologically evaluated for antiproliferative activity in 2D cell culture (patent Table 1, showing growth inhibition $GI_{50} < 1$ μM in almost all reported cell lines (NCI60 panel), down to GI_{50} = 40 nM. Its *trans* (*E)*-geometry was established explicitly and extensive docking simulations were performed to rationalise observed activity[36,37], docking the *trans*-state to the colchicine site of tubulin using Sybyl software. The authors conclude, "[compound 13] exhibited significant growth inhibition against most of the human cancer cells in the 60-cell panel, and the results from the molecular modeling studies are consistent with the *in vitro* anti-cancer activit[y] …being mediated via binding to the colchicine binding site on tubulin… [it was] considered as [an] important lead compound for further development as [an] anti-cancer drug". The authors implicitly argue against the widely-reported requirement[14,38] for colchicine-site binders of this type to be *cis*oid isomers, which has been structurally rationalised by us[39]. We decided therefore to pursue our paper's design logic paying particular attention to experimentally verify the isomer status and binding mode of the compound.

Penthala *et al*'s prior reports of **SBTub2** properties also argue directly against our experience[6,39,40] and literature understanding[13] of the requirements of the colchicine binding site, as well as our present cellular bioactivity assays and our experimental ligand:protein crystallisation results, in which we show that *trans*-**SBTub2** has no specific cytotoxicity whereas *cis*-**SBTub2** is strongly bioactive. We consider that Penthala *et al* may initially have synthesised **SBTub2** purely as its *trans*-isomer, but that the possibility of its photoisomerisation-dependent bioactivity (which has not been reported

before our current work) escaped their attention. This may have led them to perform bioactivity tests without rigorous certainty of what isomer was being tested in what situation; that would nullify the predictive value of their reports and cast doubt on the validity of the docking. We consider that their work has therefore, from conceptual grounds, not delivered an understanding of these compounds' bioactivity, so we here wish to report upon the **SBTub** independently of Penthala *et al.*'s reported cellular activities and docking study, by careful and rationalised studies controlling for isomerisation and experimentally verifying the docking mode of these ligands.

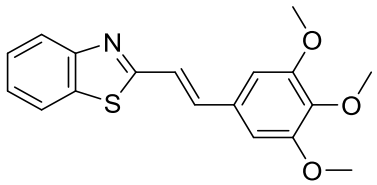

2-methylbenzothiazole (0.12 mL, 1 mmol) and 3,4,5-trimethoxybenzaldehyde (196 mg, 1 mmol, 1 eq) were dissolved in DMSO (2 mL). NaOMe (5.4 M in MeOH, 185 μL, 1 mmol, 1 eq) was added and the reaction mixture was stirred overnight. H_2O (10 mL) was added and the mixture was extracted with ethyl acetate (3 × 15 mL). The combined organic layers were washed with brine (10 mL) and dried over $MgSO_4$. Flash column purification of the crude material (EA:Hex = 3:7) yielded **SBTub2** as faint-yellow solid (158 mg, 0.48 mmol, 48%).

R_f = 0.68 (UV 254 nm, EA:Hex = 1:1). **HRMS (ESI$^+$):** 328.10002 calculated for $C_{18}H_{18}NO_3S^+$ $[M+H]^+$, 328.10002 found. **^{1}H-NMR (400 MHz, $CDCl_3$):** δ = 7.99 (d, *J* = 8.1 Hz, 1H), 7.86 (d, *J* = 8.0 Hz, 1H), 7.47 (t, *J* = 7.1 Hz, 1H), 7.45 (d, *J* = 16.1 Hz, 1H), 7.38 (t, *J* = 7.0 Hz, 1H), 7.33 (d, *J* = 16.1 Hz, 1H), 6.82 (s, 2H), 3.92 (s, 6H), 3.90 (s, 3H) ppm. **^{13}C-NMR (100 MHz, $CDCl_3$):** δ = 167.0, 153.9, 153.7, 139.6, 137.7, 134.4, 131.1, 126.5, 125.5, 123.0, 121.7, 121.7, 104.6, 61.1, 56.3 ppm. **IR (FT, ATR):** $\tilde{\nu}$ = 2997 (w), 2966 (w), 2934 (w), 2833 (w), 1626 (w), 1581 (m), 1504 (m), 1452 (m), 1417 (m), 1329 (m), 1240 (m), 1202 (w), 1155 (w), 1126 (s), 1005 (m), 983 (w), 964 (m), 812 (m), 758 (m), 729 (m) cm^{-1}.

5-(2-(benzothiazol-2-yl)vinyl)-2-methoxyphenol (SBTub3)

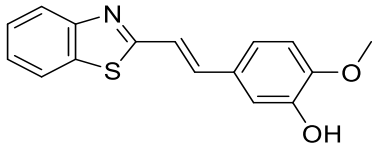

2-methylbenzothiazole (0.25 mL, 2 mmol), 3-hydroxy-4-methoxybenzaldehyde (304 mg, 2 mmol, 1 eq) were dissolved in DMSO (4 mL). NaOMe (5.4 M in MeOH, 741 μL, 4 mmol, 2 eq) was added. After stirring overnight sat. aq. NH_4Cl solution (30 mL) was added and the reaction mixture was extracted with EA (3 × 20 mL). The combined organic layers were washed with water (20 mL), brine (20 mL) and dried over $MgSO_4$. The crude material was purified by normal phase MPLC using gradient elution (EA:Hex = 0:100 → 100:0) to yield **SBTub3** as slightly yellowish solid (502 mg, 1.77 mmol, 89%).

R_f = 0.55 (UV 254 nm, EA:Hex = 1:1). **HRMS (ESI$^+$):** 284.07398 calculated for $C_{16}H_{14}NO_2S^+$ $[M+H]^+$, 284.07384 found. **^{1}H-NMR (400 MHz, $CDCl_3$):** δ = 7.98 (d, *J* = 8.1 Hz, 1H), 7.85 (d, *J* = 8.0 Hz, 1H), 7.46 (t, *J* = 7.1 Hz, 1H), 7.44 (d, *J* = 16.2 Hz, 1H), 7.36 (t, *J* = 7.0 Hz, 1H), 7.26 (d, *J* = 16.1 Hz, 1H), 7.20 (d, *J* = 2.1 Hz, 1H), 7.09 (dd, *J* = 8.3, 2.1 Hz, 1H), 6.88 (d, *J* = 8.3 Hz, 1H), 5.73 (s, 1H, *OH*), 3.93 (s, 3H) ppm. **^{13}C-NMR (100 MHz, $CDCl_3$):** δ = 167.5, 153.9, 148.1, 146.1, 137.7, 134.4, 129.2, 126.4, 125.3, 122.9, 121.6, 120.9, 120.5, 112.7, 110.8, 56.2 ppm. **IR (FT, ATR):** $\tilde{\nu}$ = 3053 (w), 2846

(w), 1626 (w), 1598 (w), 1585 (w), 1522 (m), 1483 (w), 1435 (s), 1358 (w), 1308 (w), 1293 (m), 1245 (m), 1231 (m), 1199 (s), 1164 (s), 1123 (s), 1026 (m), 981 (w), 946 (s), 923 (w), 838 (w), 797 (s), 765 (s), 731 (m) cm^{-1}.

4-(2-(benzothiazol-2-yl)vinyl)-2-methoxyphenol (SBTub4)[41]

E-**SBTub4** has also previously been synthesised in the context of ligands for platinum complexes[41], although its isomerisation to *Z* was not considered. It was reported in the *trans* state by Lozano *et al*. as compound **1i**[41], where it was used as a monodentate ligand in a tribromo platinum(II) complex (**2i**). In that report it was assessed for cytotoxicity as a free ligand and also when complexed, in both cases only in *trans* and without consideration of isomerisation. In this work its role was to serve as a designed inactive biological control compound *in the* cis *state,* being a permutation control of **SBTub3** that is designed to be *cis*-active. Here we require it specifically as a *Z*-isomeric control and accordingly we pursued its synthesis and biological characterisation ourselves, paying particular attention to the isomer state.

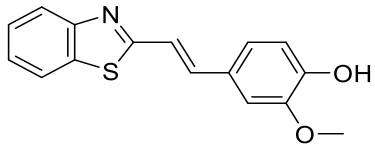

2-methylbenzothiazole (0.41 mL, 3.3 mmol), 4-hydroxy-3-methoxybenzaldehyde (0.5 g, 3.3 mmol, 1.0 eq) and NaOMe (5.4 M solution in MeOH, 1.2 mL, 6.5 mmol, 2 eq) were dissolved in DMSO (6.5 mL). After stirring overnight, sat. aq. NH_4Cl solution (30 mL) was added and the reaction mixture was extracted with EA (3 × 20 mL). The combined organic layers were washed with water (20 mL), brine (20 mL) and dried over $MgSO_4$. The crude material was purified by normal phase MPLC using gradient elution (EA:Hex = 0:100 → 100:0) and $\lambda_{collect}$ = 360 nm to yield **SBTub4** as a yellow solid (256 mg, 0.9 mmol, 28%).

R_f = 0.6 (UV 254 nm, EA:Hex = 1:1). **HRMS (ESI^+):** 284.07398 calculated for $C_{16}H_{14}NO_2S^+$ $[M+H]^+$, 284.07385 found. **^{1}H-NMR (400 MHz, $CDCl_3$):** δ = 7.98 (d, *J* = 8.1 Hz, 1H), 7.85 (d, *J* = 7.9 Hz, 1H), 7.46 (t, *J* = 7.1 Hz, 1H), 7.45 (d, *J* = 15.7 Hz, 1H), 7.36 (t, *J* = 7.1 Hz, 1H), 7.27 (d, *J* = 16.1 Hz, 1H), 7.13 – 7.07 (m, 2H), 6.95 (d, *J* = 8.7 Hz, 1H), 6.02 (s, 1H, *OH*), 3.94 (s, 3H) ppm. **^{13}C-NMR (100 MHz, $CDCl_3$):** δ = 167.5, 153.9, 147.5, 147.1, 138.0, 134.3, 128.1, 126.4, 125.3, 122.9, 122.4, 121.6, 120.0, 115.0, 108.8, 56.1 ppm. **IR (FT, ATR):** ṽ = 3004 (w), 2829 (w), 2643 (w), 1623 (m), 1587 (s), 1518 (s), 1456 (m), 1431 (m), 1399 (m), 1338 (w), 1308 (m), 1286 (s), 1254 (s), 1220 (m), 1197 (w), 1169 (w), 1138 (m), 1112 (s), 1064 (w), 1037 (m), 1014 (w), 967 (m), 922 (w), 908 (w), 829 (m), 802 (m), 781 (w), 751 (s), 722 (m) cm^{-1}.

Part D: Photocharacterisation in vitro

HPLC for UV-Vis spectroscopy on separated isomers

Analytical high-performance liquid chromatography (HPLC) was performed on an Agilent 1100 SL coupled HPLC system with (a) a binary pump to deliver H_2O:MeCN eluent mixtures containing 0.1% formic acid at a 0.4 mL/min flow rate, (b) Thermo Scientific Hypersil GOLD™ C18 column (1.9 µm; 3 × 50 mm) maintained at 25°C, whereby the solvent front eluted at t_{ret} = 0.5 min, (c) an Agilent 1100 series diode array detector, which was used to acquire peak spectra of separated compound isomers in the range 200–550 nm after manually baselining across each elution peak of interest to correct

for eluent composition effects. Run conditions were a linear gradient of H_2O:MeCN eluent composition from 90:10 through to 1:99, applied during the separation phase (first 5 min), then 0:100 for 2 min for flushing; the column was (re)equilibrated with 90:10 eluent mixture for 2 min before each run.

UV-Vis spectrophotometry of bulk samples

Absorption spectra in cuvette ("UV-Vis") were acquired on a Agilent CaryScan 60 (1 cm pathlength). For photoisomerisation measurements, Hellma microcuvettes (108-002-10-40) taking 500 μL volume to top of optical window were used with test solution such that the vertical pathlength of the isomerization light is less than 7 mm to the bottom of the cuvette, with the default test solution concentrations of 25 μM. Measurements were performed by default in PBS at pH ~7.4 with 10–20% of DMSO. Photoisomerisations and relaxation rate measurements were performed at room temperature. "Star" LEDs (H2A1-models spanning 360–435 nm from Roithner Lasertechnik and a 260 nm HP-LED from Sahlmann Photochemical Solutions) were used for photoisomerisations in the cuvette that were also predictive of what would be obtained in LED-illuminated cell culture.

E- *and* **Z-***isomers' absorption spectra and photostationary state equilibria*

Pure *E* and *Z* isomer spectra of **SBTub**s (Figure S1A) were obtained on the HPLC DAD as outlined in *HPLC*. Whole-sample absorption spectra of **SBTub**s at different photostationary state equilibria (Figure S1B) were measured as outlined in *Spectrophotometry*. This illustrates the efficient photoswitching to nearly-all-*Z* that may be achieved by a range of violet/near-UV wavelengths.

SBTubs' absorption spectra and photostationary states

SBTubs feature substantially solvent- and pH-independent absorption spectra and photostationary states (Figure S1C-D). This outlines their robustness of photoresponse with respect to variations of local conditions as may be encountered in biology, with e.g. localisation into different cellular compartments or changes of environmental dielectric constant during partitioning. We feel that this particularly recommends the SBT scaffold as a reproducible photoswitch for biology use.

Thermal relaxation of p-hydroxy SBTub4 differs from non-p-hydroxy SBTubs

para-hydroxy **SBTub4** was the only **SBTub** to show appreciable spontaneous $Z \rightarrow E$ isomerization at 25°C in aqueous media (Figure 1I), and this only under basic aqueous conditions (pH ~9): the non-*para*-hydroxy **SBTub**s did not show relaxation under these conditions (Figure 1H). We presume **SBTub4**'s pH-dependent relaxation rate acceleration results from resonance between the phenolate form (where the bridging bond is a C=C double bond) and its quinoidal form (bridging C-C single bond, for which free rotation to the thermodynamically more stable *transoid* conformation could occur).

In azobenzenes the choice of substituents in *ortho* or *para* to the diazene is restricted, if photoswitching is to be performed in predominantly aqueous environments (e.g. in the cytosol in biological systems) since *o*/*p*-hydroxyl, -thiol or -amine groups give fast thermal relaxation, often complete in under a second, and in many cases their *Z* states cannot even be observed in aqueous environments.[42,43] However these groups are powerful interaction points for docking to proteins, which it would be desirable to be able to place freely around the azobenzene scaffold while maintaining reliable photoswitchability. This can be achieved using SBTs, which we feel is a particular advantage for SBTs as a new photoswitch scaffold for chemical biology.

Complementary relaxation performance of SBTubs compared to azobenzenes

In summary, the metastable *Z*-isomers of all **SBTub**s could be quantitatively relaxed to *E* by warming to 50-60°C in DMSO overnight, although at 25°C they showed no significant thermal relaxation within hours at pH~7 in aqueous media (Figure 1G-H). However, *para*-hydroxy **SBTub4** thermally relaxed at pH~9 with a halflife around 2 h (Figure 1I). This offers two opportunities for future applications of styrylbenzothiazole photopharmaceuticals. Firstly, the *Z*-stability of *para*-hydroxy **SBTub4**'s *Z* isomer at pH~7 contrasts to both azobenzene and hemithioindigo photoswitches with *para*- (or *ortho*-) hydroxy or aniline substituents, that typically feature millisecond (azobenzene) to second (hemithioindigo) aqueous relaxation halflives even at pH~7. This underlines the broader chemocompatibility of styrylbenzothiazoles as a photoswitch scaffold for these functional groups, that are highly prevalent in bioactive molecules for many biological targets due to e.g. their importance in creating high-affinity ligand-protein interactions. Secondly, the pH-sensitivity of *para*-hydroxy **SBTub4**'s relaxation rate suggests that pK_a-modulation could deliver styrylbenzothiazoles relaxing on a second or minute timescale at pH~7, such that local $E \rightarrow Z$ photoswitching could be combined with sample-wide thermal relaxation to improve spatiotemporal localisation of the *Z*-isomer.

Photostability of SBTubs – isomerisation and cycloaddition

To examine whether degradative photochemical side reactions (e.g. 6-π electrocyclisation, [2+2] cycloaddition, etc.) could affect the **SBTub**s during chemical biology use, a sample of **SBTub2** (3.3 mg) in d_6-DMSO (0.5 mL) in a quartz NMR tube capped under air, was irradiated with 350 nm UV within a Rayonet RPR-200 photochemistry reactor (Raynonet RPR-3500A lamps, air cooled with a cooling fan). The NMR tube was mounted to an RMA-500 Merry Go-Round unit to maintain an approximate distance of 2 cm from the UV-lamps. An NMR was taken before and after constant irradiation for 1 h, showing exclusively a mixture of *E*- and *Z*-isomers (no photodegradation or cycloaddition). During standard biological assays, illuminations are conducted with far lower photon fluxes (e.g. < 1 mW/cm^2 pulses from low-power LEDs for total <1 min illuminated time over long-term viability experiments), therefore it can be assumed that negligible photodegradation of the **SBTub**s should occur. Only after constant Rayonet reactor irradiation overnight, was photodegradation (primarily [2+2] cycloaddition product) evidenced by NMR and LC-MS analysis (detected by HPLC coupled to a Bruker Daltonics HCT-Ultra spectrometer used in ESI mode, unit m/z) although the major compound present was still the **SBTub** (as a mixture of *E*- and *Z*-isomers) (Figure S1E-F).

PSS measurements and their comparison to simulated PSS(λ)

For photopharmaceutical assays in biology it is helpful to straightforwardly estimate the *E/Z* ratio at any wavelength's photostationary state (PSS), to choose optimal wavelength conditions for illumination during biological assays or to understand the limits of what is possible on a given setup. The absorption spectrum of a bulk sample at a certain PSS is a linear combination of spectra of the constituent *E* and *Z*-isomers. Therefore we compared experimentally measured UV-spectra from different PSS equilibria, with calculated PSS spectra obtained by assuming (1) that quantum yields for $E \rightarrow Z$ and $Z \rightarrow E$ isomerisations are approximately equal over the measured photoisomerisation region (which is experimentally verifiable by confirming that illumination at the isosbestic point gives an *E*/*Z* ratio approximately 1:1), and that (2) the isomer spectra measured inline in HPLC are approximately identical to those that underlie UV-Vis measurements in biological media in cuvette

(which we verified by solvent indepency measurements, as shown in Figure S1C-D, comparing HPLC eluent solvent to biological media): these assumptions allow us to simulate PSS spectra on the basis of HPLC traces as follows (see also Figure S1G-J):

a) Taking experimental PSS absorption spectra on a UV-Vis spectrometer under different illumination wavelengths, thus also determining the isosbestic point λ_{iso}.
b) Obtaining absorption spectra $\varepsilon E(\lambda)$ and $\varepsilon Z(\lambda)$ of the pure *E* and *Z*-isomers from an inline diode array detector (DAD) of an HPLC system. Absorption spectra of both isomers are scaled by multiplication in order to cross at λ_{iso}, generating data $\varepsilon' E(\lambda)$ and $\varepsilon' Z(\lambda)$ in arbitrary units, such that $\varepsilon' E(\lambda) / \varepsilon' Z(\lambda) = \varepsilon E(\lambda) / \varepsilon Z(\lambda)$ across all wavelengths.
c) Estimation of $\text{Frac}[E]_{PSS}(\lambda)$, the fraction of *E*-isomer that should be generated at photostationary state illumination at wavelength λ (assumes identical quantum yields for *E*→*Z* and *Z*→*E* isomerisations) *via*

$$\text{Frac}[E]_{PSS}(\lambda) = \frac{\varepsilon' Z(\lambda)}{\varepsilon' Z(\lambda) + \varepsilon' E(\lambda)}$$

d) Simulating absorption spectra in arbitrary units *via*

$$Abs_{SIM}(\lambda) = \text{Frac}[E]_{PSS}(\lambda) \times \varepsilon' E(\lambda) + \left(1 - \text{Frac}[E]_{PSS}(\lambda)\right) \times \varepsilon' Z(\lambda)$$

and comparing the predicted-PSS *curve shape* to that of experimental data (more important than comparing single absolute absorption values since more robust to variation). When the curve shapes match across a range of PSS wavelengths, we assume that we can interpolate other PSS *E/Z* ratios under any bracketed illumination wavelength, from the measured isolated-isomer spectra (HPLC). This was found to be exquisitely accurate for **SBTub**s.

Two-photon excitation

Two-photon excitation of **SBTub3** (5 mM in DMSO) was performed using a mode-locked Ti-Sapphire Laser operating at 780 nm (Spectra Physics, Tsunami) with a pulse repetition frequency of 80 MHz (pulse width <100 fs) and an output power of 0.65 W. The laser was coupled into an upright Microscope (Zeiss Axiotech 100) and focused with a 40× reflective objective (**Thorlabs, LMM-40X-UVV**) onto the sample. Transmittance through the sample was measured using a HAL 100 illuminator (Carl Zeiss) and a SP300i spectrograph equipped with a MicroMAX CCD camera for signal recording (both Princeton Instruments), between 360 nm and 380 nm. This spectral range was chosen to be around the absorbance maximum of **SBTub3** in DMSO (~366 nm Figure S1D). Spectra were recorded with low intensity incident light, and an exposure time of only 1 s to prevent any unintended photoisomerization of the molecules during the measurement (and as a control, 12 min of continuous spectral recording produced an *E* to *Z* isomerisation of only 4%). The sample was measured in a home-made microcuvette with optical path length d=0.1 mm and volume ~7.8 µL. Photoisomerization was analyzed by measuring the change in light intensity across the spectral range 360-380 nm (0.5 nm increments) after passing through the sample (I_{SBTub3}) in relation to light passing through a reference sample of only DMSO (I_{DMSO}), smoothing the spectra (Savitsky-Golay) confirming the overlap of the spectra with those acquired under dilute conditions on the UV-Vis (50 μM, 1 cm path length) to rule out concentration-dependent effects on spectra or photoisomerisation, then taking a representative intercept to the smoothed spectra and calculating absorbance of the sample as $\mathbf{A = -\log_{10}(I_{SBTub3} / I_{DMSO})}$.

Part E: Biochemistry

Stability towards glutathione – comparison to an azobenzene photoswitch

In summary, we monitored **SBTub** changes due to GSH adduct formation, thiol addition-elimination (that should return *E*-**SBTub** due to the sp^3 intermediate), reductive degradation (involving a second equivalent of GSH) or other compound loss mechanisms by UV-Vis and HPLC-UV-MS, yet no such changes were observed. This contrasts markedly to the instability in our hands of similar *Z*-azobenzenes when challenged by GSH, including **PST-1** (note however that our GSH challenge assay, which avoided the biologically irrelevant exogenous phosphine nucleophile TCEP, resulted in substantially less adduct formation/photoswitch destruction than literature methods[19] despite using a vast excess of reduced GSH which is elsewhere incorrectly reported as though it were the only active species in GSH+TCEP mixtures; compare also Figure 2B).

Stability towards glutathione (GSH) of samples of both all-*E* ("dark") and mostly-*Z* ("pre-lit") **SBTub2** (Figure 2A) was determined similarly to published methods, and compared to that of **PST-1** (all-*E* "dark", and mostly-*Z* "lit").[19] All solutions were prepared in PBS pH ~7.4 with 10% DMSO, containing GSH (10 mM), in UV-Vis cuvettes that were sealed under air atmosphere (gas head volume <2 mL) with parafilm and maintained at 37°C, during absorbance measurements over several hours in a Agilent Cary 60 spectrophotometer. "Dark" assays were performed with the *E*-isomers of the test compounds; "pre-lit" **SBTub2** (note: relaxation far slower than experiment time) had been pre-illuminated to reach PSS under 360 nm light; while "lit" **PST-1** (note: relaxation faster than experiment time) was maintained under continuous illumination from above with a 390 nm LED to maintain undegraded **PST-1** in a mostly-*cis* state. The π→π* transition was monitored for dark PST-1 and lit/dark SBTub2, (**SBTub2** at 345 nm, **PST-1** at 378 nm) while for lit PST-1, its stronger n→π* band at 440 nm was followed instead for more accurate readout (Figure 2A-B). This is because **SBTub2** has a large enough π→π* absorbance coefficient to be reliably measured at 25 μM in both dark and lit experiments; the smaller absorbance coefficient of *trans*-**PST-1** encouraged us to use it at 50 μM for the dark assay, while we performed the crucial lit assay of **PST-1** (*Z* isomer absorbance ca. 6 times lower still) at 300 μM. The full absorbance spectra and those of a no-compound GSH-only control are shown in Figure S2A-C.

SBTub2 was stable against GSH addition and/or GSH-dependent reduction of the chromophore (which should both decrease its π→π* absorbance at 345 nm towards zero) in both all-*E* and mostly-*Z* assays. *Z*-**SBTub2** did not appear susceptible to significant *Z* to *E* isomerisation catalysed by reversible GSH addition-elimination since if this had continued to completion it would increase the π→π* absorbance for the "lit" solution by a factor of 3; we instead assign the slight absorbance increase at short wavelengths (Figure S2A) primarily to GSH oxidation to GSSG (Figure S2C) with almost negligeable thermal relaxation of *Z*-**SBTub2** over the experimental time course.

We compared the SBT scaffold's GSH stability to that of the widely used photopharmaceutical scaffold azobenzene, using similarly-decorated azobenzene **PST-1** as a comparison.

In our hands *E*-**PST-1** (50 μM) was stable to the GSH challenge (Figure 2A-B) which does not match the "GSH/reductive susceptibility" described in the literature for this as well as other azobenzenes.[19] However, we trust our result to replicate the average cellular situation, and ascribe the discrepancy to literature use of co-reductants such as phosphines which we feel do not well predict the cellular situation. Those literature assays are typically performed with a powerful co-reductant such as TCEP, that is intended to keep GSH in its reduced form, with the non-explicit assumption that the

phosphine should not perform Mitsunobu-type addition to the diazene or otherwise affect the reaction paths available to the photoswitch. When we tested for degradative effects due to 5 mM TCEP (with and without GSH) we found that TCEP alone caused appreciable *E*-**PST-1** degradation, and to an identical degree as the TCEP + GSH combination (Figure 2B). This suggests that TCEP (not GSH) is the agent responsible for degradation of *E*-**PST-1** in such literature "GSH assays", arguing more generally for caution in interpreting prior *in vitro* assessments of azobenzene "bioinstability" against cellular thiol concentrations if non-innocent co-reductants were employed. In our opinion, limiting the amount of oxygen available to a sample (e.g. capping a vial/cuvette under air with a negligible headspace volume) should be sufficient for running such assays reliably: since it seems to us that applying an approx. 10 mM concentration of GSH (i.e. at least 30-fold excess), should allow enough GSH to persist in the reduced state throughout an assay lifetime, despite potential oxidation from dissolved oxygen or from air in the headspace, such that large excesses (with respect to test compound) of additional reductants of a chemically different nature (especially those that are not physiological in nature or in concentration) can be productively avoided. Certainly, a less risky approach to test whether autoxidative GSSG formation precludes biochemically relevant compound reduction in the assay lifetime would be to vary the concentration and/or equivalents of GSH applied.

However, we observed unequivocally that *Z*-**PST-1** (300 μM) evolved rapidly in the absence of TCEP, indicating near-stoichiometric degradation by GSH (Figure 2B, Figure S2B-F). We ruled out addition-elimination-catalysed *Z* to *E* isomerisation as the *major* mechanism of absorbance evolution, since complete *Z* to *E* isomerisation would increase the assay absorbance reading from the starting value of ca. 1 to ca. 6, whereas in fact the absorbance decreases to 0.40 at plateau[6] (Figure 2B). We presumed at this stage that GSH adduct formation, and/or reduction through to the hydrazine or still further to the anilines, is the major cause of loss of absorbance, and explored this in more detail with HPLC as detailed below.

Further exploration of glutathione-induced Z-azobenzene degradation

To further examine the degradation of *Z*-azobenzene by GSH, a timecourse of HPLC analyses of a similar "lit" sample of **PST-1** (0.5 mM, lit at 395 nm) with 10 mM GSH in PBS + 10% DMSO was performed following our standard HPLC conditions (Figure S2D-F). The results showed progressive formation of two major UV-active impurities, which because of their retention time shifts and their *Z*- and *E*-azobenzene-like UV spectra (Figure S2F) it could be tempting to assign as e.g. *ortho*-SG adducts on north and south aryl rings; however we were not able to observe interpretable signals in MS perhaps due to fragmentation in the spray.

The greater susceptibility of *Z*-**PST-1** was to be expected from the literature-known faster kinetics of nucleophile addition to *Z*-azobenzenes, as well as their greater oxidising potential, as compared to the *E* isomers.[33] The stoichiometry and the limiting amount of reduction in the presence of physiological concentrations of thiol reductant can however be questioned; and we prefer not to conclude broadly about the final fate of azobenzenes in cells, nor about the completeness of adduct formation or reduction in general, since while the cell-free model gives a clear result of *Z*-azobenzene degradation with GSH, this is not equivalent to showing *cellular* degradation: (1) Cells are not homogenous aqueous cosolvent environments but have complex compartmentalisation effects controlling compound distribution as well as redox environments[44], e.g. that lipid-environment-bound azobenzenes could very reasonably be expected to be protected from reaction with cytosolic GSH; (2) cellular, embryonic and adult animal assays[7,21,24] have robustly shown photoreversible switching with **PST-1**; and this implies that cells maintain a cellularly-available pool of freely

photoisomerisable, non-adduct-state *E*- and *Z*-**PST-1** at a basal concentration that is above the inhibitory threshold, hence that reduction is by no means complete in the cellular context and certainly does not impact the cellular utility of this cytosol-active azobenzene; (3) the survival of cells treated briefly with high *Z*-**PST-1** concentrations (see one-time-activation assay Figure 4A) argues strongly against cellularly-relevant stoichiometric disturbance of the thiol pool or of thiol-based enzymes through poorly-reversible adduct formation and/or reduction through to the hydrazine and beyond; (4) our results do not exclude a non-innocent role for the dimethylsulfoxide cosolvent which is present at very high equivalence (or its potential contaminants) in modifying the **PST**s' apparent GSH stability. Addressing these azobenzene-centric issues is beyond the scope of this study into styrylbenzothiazoles and will be tackled elsewhere.

Microsomal Stability

The **SBTubs'** stability to degradation by liver microsomes was assessed by *in vitro* studies using isolated mouse and human liver microsomes, performed by Bienta Biology Services (Kiev, Ukraine) over a 40 min timecourse at 37°C following standard practice. Mouse hepatic microsomes were isolated according to a standard protocol; human hepatic microsomes were supplied by XenoTech. Microsomal incubations were performed in duplicates and control incubations were performed replacing the NADPH-cofactor system with PBS. Supernatants were analyzed using HPLC-MS. **SBTub2** and **SBTub3** showed good microsomal stability (Figure 2C).

hERG Inhibition

hERG inhibition experiments were performed by Bienta Biology Services using Invitrogen PredictorTM hERG Fluorescence Polarization Assay in accordance with the manufacturer's protocol (Protocol PV5365). In brief, a fluorescent tracer is incubated with **SBTub** and membranes bearing hERG channel for 2–4 hours in the solution and the polarization of fluorescence emission (higher when bound to hERG, lower in solution due to free tumbling) is assayed with reference to control inhibitor E-4031 to validate assay performance. **SBTubs** were tested in quadruplicates at 1 µM, 5 µM and 25 µM with reference to a positive control (only tracer, fluorescence polarization is maximal when nothing interferes with the reaction of the tracer and hERG membranes - minimal tracer rotation) and a negative control (30 µM of E-4031, i.e. 100% tracer displacement and minimum assay polarization value, due to tested compound competing with the tracer for the hERG channel, the polarization of emitted light).

SBTub2 showed strong and dose dependent hERG binding, while **SBTub3** showed moderate and dose dependent hERG binding (Figure 2D). However, tracer inhibition can be exaggerated if low compound solubility or if promiscuous protein binding are issues. Further evaluations in more sophisticated models are ongoing.

CYP450 inhibition

The potential for CYP450 inhibition was assessed by *in vitro* inhibition studies using fluorogenic CYP450 substrates with the corresponding CYP450 enzymes and NADPH regeneration system (Vivid CYP450 Screening Kits) with some minor changes to the manufacturer's protocols, performed by Bienta Biology Services. The fluorescent signal produced from reaction is directly proportional to the cytochrome P450 activity. In the cases when tested compounds interfere with the CYP450 enzyme-substrate reaction, the fluorescent signal decreases.

In brief, the tested compounds were first dissolved in DMSO at 1 mM, then diluted in aqueous assay buffer to 25 µM, then the dilute solutions were mixed with a pre-mix consisting of human CYP450 + oxidoreductase and $NADP^+$ regeneration system (glucose-6-phosphate and glucose-6-phosphate dehydrogenase). After 10 min pre-incubation, the enzymatic reaction was initiated by the addition of a mix of NADPH and the appropriate CYP450 substrates yielding a test compound concentration of 10 μM. The reaction was incubated for the desired reaction time (25 min for CYP1A2, CYP2C9, CYP2D6, and CYP3A4, 60 min for CYP2C19) after which Stop Reagent was added and fluorescence measured using SpectraMax Paradigm Multi-Mode Microplate Reader. All test points were performed in quadruplicates at concentration 10 µM (1% DMSO). Reference compounds used to benchmark the CYP inhibition under these conditions are listed in Figure S2G.

At 10 µM, **SBTub2** and **SBTub3** showed strong inhibition of 1A2, 2C9 and 2C19 CYP isoforms (Figure 2E). *Higher* fluorescence was detected after incubation of **SBTub2** with CYP2D6 comparing to positive control, which resulted in negative value of inhibition, but we assign that result to assay interference. Further evaluations are ongoing.

SBTubs show light specific inhibition of tubulin polymerisation in vitro

99% tubulin from porcine brain was obtained from Cytoskeleton Inc. (cat. #T240). The polymerisation reaction was performed at 5 mg/mL tubulin, in polymerisation buffer BRB80 (80 mM piperazine-N,N′-bis(2-ethanesulfonic acid) (PIPES) pH = 6.9; 0.5 mM EGTA; 2 mM $MgCl_2$), in a cuvette (120 µL final volume, 1 cm path length) in a Agilent CaryScan 60 with Peltier cell temperature control unit maintained at 37°C; with glycerol (10 μL). Tubulin was first incubated for 10 min at 37°C with "lit"-(360 nm-pre-illuminated; mostly-*Z*-) or dark- (all-*E*) **SBTub** (final **SBTub** concentration 20 μM) in buffer with 3% DMSO, without GTP. Then GTP was added to achieve final GTP concentration 1 mM (with mixing), and the change in absorbance at 340 nm was monitored for 15 min, scanning at 15 s intervals[45]. While **SBTub2** and **SBTub3** in the "dark"-state (20 μM) displayed almost similar MT growth dynamics as the cosolvent-only control, "lit" **SBTub2** and **SBTub3** (20 μM) showed noticeable slowdown of polymerisation kinetics, similar to known microtubule inhibitors such as colchicine (assayed at 16 μM) (Figure 3B). Designed-inactive **SBTub1** and **SBTub4** were not tested for cell-free tubulin polymerization inhibition since they robustly showed no MT inhibiting effects (cytotoxicity, G2/M arrest, MT breakdown in IF) in any other experiments.

Part F: Protein Crystallisation

Protein crystallisation materials and methods

Protein production, crystallization and soaking.

The DARPin D1 was prepared as previously described[46]. Tubulin from bovine brain was purchased from the Centro de Investigaciones Biológicas (Microtubule Stabilizing Agents Group), CSIC, Madrid, Spain.

The tubulin-DARPin D1 (TD1) complex was formed by mixing the respective components in a 1:1.1 molar ratio. The TD1 complex was crystallized overnight by the hanging drop vapor diffusion method (drop size 2 µL, drop ratio 1:1) at a concentration of 15.9 mg/mL and at 20°C with a precipitant solution containing 18% PEG 3350, 0.2 M ammonium sulfate and 0.1 M bis-tris methane, pH 5.5. All drops were subsequently hair-seeded with crystalline material obtained in previous PEG-screening, which resulted in single and large (0.5 µm) TD1 complex crystals. The crystals were

fished and transferred into new precipitant solution drops containing 10% DMSO and respective compounds (**SBTub2**/**SBTub3**) at a final concentration of 2 mM and were pre-switched with 360 nm LEDs for 5 min. After 4 h of soaking in the dark, the **SBTub:**tubulin crystals were mounted for X-ray diffraction data collection.

Data Collection, processing and refinement.

Data were collected at beamline X06SA at the Swiss Light Source (Paul Scherrer Institute, Villigen, Switzerland). The beam was focused to 30 x 30 µm, the flux was 3 x 10^{10} photons/ s and the data collection speed was 2°/s at an oscillation range of 0.2° per frame (see Table S1). For TD1-**SBTub2** and TD1-**SBTub3**, 210° and 220° of data were collected, respectively. Data processing was done with XDS[47]. Due to anisotropy, the data were corrected using the Staraniso server (http://staraniso.globalphasing.org/). The structures were solved by molecular replacement using PDB ID 5NQT as a search model[48]. The ligands and restraints were generated with the grade server (http://grade.globalphasing.org/) using their SMILES annotation. The structures were then refined iteratively in PHENIX[49] with manual editing cycles in COOT[50].

X-ray structural analysis

Both ligands, *Z*-**SBTub2** and *Z*-**SBTub3**, bind to the colchicine site at the interface of α- and β-tubulin (Figure 3C-G, Figure S3A-D; PDB: 6ZWC and 6ZWB respectively). The two ligands bind in exactly opposite poses despite interacting with identical residues in the binding pocket, matching the design goal of this study whereby the poses should be defined by the specific part of the ligand inherited from the combretastatin-A4 archetype (trimethoxyphenyl in case of **SBTub2** and isovanillinyl in case of **SBTub3**). The benzothiazole group is able to bind in both orientations (Figure 3E-F).[39] The β-T7 loop is not well ordered in both tubulin-**SBTub2** and tubulin-**SBTub3** structures, likely due to the influence of the ligands. Despite the weak density for some parts of the loop, it is apparent that the larger trimethoxyphenyl-ring of **SBTub2** occupies more space and pushes β-Leu-248 and the β-T7 loop further out than the smaller flat benzothiazole group in **SBTub3** (Figure 3E-F).

The hydrophilic OH-group at the isovanillyl-ring of **SBTub3** (which binds in the “top-down” pose) appears to stabilize the α-T5 loop in the conformation the ligand-free structure displays (Figure S3D). **SBTub2** binds in the “bottom-up” pose and the α-T5 loop displays an altered conformation similar to that seen with colchicine (Figure S3D). While both ligands, being colchicine site binders, likely interfere with the “curved-to-straight” conformational transition of tubulin during the formation of microtubules[51,52], their difference in disturbing the α-T5 loop conformation may be of pharmacological relevance, given that the archetypical colchicine disturbs the α-T5 loop, while the vascular disrupting agent combretastatin A4 does not.[39]

Part G: Biological Data

Cell assay methods

General cell culture

HeLa and A549 cells were maintained under standard cell culture conditions in Dulbecco’s modified Eagle’s medium (DMEM; PAN-Biotech: P04-035550) supplemented with 10% fetal calf serum (FCS), 100 U/mL penicillin and 100 U/mL streptomycin. Cells were grown and incubated at 37°C in a 5% CO_2 atmosphere. Cells were typically transferred to phenol red free medium prior to assays (DMEM; PAN-Biotech: P04-03591). Substrates and cosolvent (DMSO; 1% final concentration) were

added *via* a D300e digital dispenser (Tecan). Cells were either incubated under "lit" or "dark" conditions; "lit" indicates a pulsed illumination protocol was applied by multi-LED arrays to create the *Z*-isomers of the compounds in *situ* in cells and then maintain the wavelength-dependent PSS isomer ratio throughout the experiment, as described previously.[6] Typical "lit" timing conditions were 75 ms pulses of ~1 mW/cm^2 applied every 15 s. "Dark" indicates that compounds were set to the all-*trans* state by thermal relaxation of the DMSO stocks at 60°C overnight, applied while working under red-light conditions, and cells were then incubated in light-proof boxes to shield from ambient light, thereby maintaining the all-*E*-isomer population throughout the experiment. *Single shot activation* (lit $_{1h}$) indicates, that cells are treated with *E*-**SBTub**s and illuminated *in situ* for a short time (75 ms every 15 s during the first hour only; total illumination time 18 s) before stopping illuminations and incubating for the remaining 47 h without any further illumination.

MTT antiproliferation assay

Cells were seeded in 96-well plates at 5,000 cells/well and left to adhere for 24 h before treating with test compounds. *E*-**SBTub**s were added under the indicated lighting conditions for 48 h (final well volume 100 μL, 1% DMSO; six technical replicates); the "cosolvent control" ("ctrl") indicates treatment with DMSO only. Cells were then treated with 0.5 mg/mL (3-(4,5-dimethylthiazol-2-yl)-2,5-diphenyl tetrazolium bromide (**MTT**) for 3 h. The medium was aspirated and formazan crystals were re-dissolved in DMSO (100 μL); absorbance was measured at 550 nm (Abs_{550}) using a FLUOstar Omega microplate reader (BMG Labtech). Absorbance data was averaged over the technical replicates, then normalized to viable cell count from the cosolvent control cells (%control) as 100%, where 0% viability was assumed to correspond to absorbance zero. Three independent experiments were performed; data are shown from a single representative experiment, as indicated; data were plotted against the log of **SBTub** concentration ($\log_{10}$([**SBTub**]) (M)).

Cell cycle analysis

E-**SBTub**s were added to HeLa cells in 24-well plates (50,000 cells/well; three technical replicates, three biological replicates) and incubated under "dark" or "lit" conditions for 24 h. Cells were collected, permeabilised and stained with 2 μg/mL propidium iodide (PI) in HFS buffer (PBS, 0.1% Triton X-100, 0.1% sodium citrate) at 4°C for 30 min then analysed by flow cytometry using a FACS Canto II flow cytometer (Becton Dickinson) run by BD FACSDiva software. 30,000 events per technical replicate were analysed; the PI signal per event (corresponding to cellular DNA content) was measured and cells were binned into sub-G1, G1, S and G2 phase according to DNA content using *Flowing* software. Results (means of three technical replicates) from one experiment of three independent trials are shown.

Immunofluorescence staining

HeLa cells were seeded on glass coverslips in 24-well plates (50,000 cells/well) and treated with **SBTub**s the next day under "dark" or "lit" conditions for 24 h. Cells were washed with pre-warmed (37°C) MTSB buffer (80 mM PIPES pH 6.8; 1 mM $MgCl_2$, 5 mM ethylene glycol tetraacetic acid (EGTA) dipotassium salt; 0.5% Triton X-100) for 30 s then fixed with 0.5% glutaraldehyde for 10 min. After quenching with 0.1% $NaBH_4$ (7 min), samples were blocked with PBS + 10% FCS (30 min). The cells were treated with primary antibody (1:400 rabbit alpha-tubulin; Abcam ab18251) in PBS containing 10% FCS for 1 h and then washed with PBS. Cells were incubated with secondary antibody (1:400 goat-anti-rabbit Alexa fluor 488; Abcam ab150077) in PBS containing 10% FCS for 1 h. After washing with PBS, the coverslips were mounted onto glass slides using Roti-Mount FluorCare DAPI (Roth) and imaged with a Zeiss LSM Meta confocal microscope (CALM platform,

LMU). Images were processed using the free Fiji software. Postprocessing was only performed to improve visibility. For maximum intensity projections, images were recorded at different focal planes incrementally stepping through the sample (step size 1–2 μm) and maximum intensity projections were obtained using Fiji software.

EB3-comet live cell assays in HeLa cell line: general procedure

HeLa cells (12,000 cells/well) were seeded on 8-well ibiTreat μ ibidi slides (ibidi, Martinsried) 24 h prior to transfection. Cells were transiently transfected with *EB3-GFP* or *EB3-YFP* plasmids using jetPRIME reagent (Polyplus) according to the manufacturer's instructions. Cells were imaged 24 h later, at 37°C under 5% CO_2 atmosphere, using an UltraVIEW Vox spinning disc confocal microscope (PerkinElmer) operated with *Volocity* software equipped with an EMCCD camera (Hammamatsu, Japan), and an environmental chamber kept at 37°C and 5% CO_2 using a 63 × 1.4 NA Plan-Apochromat oil-immersion objective (Zeiss), while applying the specified illumination conditions. EB3-comets[53] were counted with a plugin for the *Fiji* software, based on the "Find maxima" function from the NIH (https://imagej.nih.gov/ij/macros/FindStackMaxima.txt).

Live cell imaging for photobleaching/wavelength orthogonality

For photobleaching/wavelength orthogonality experiments, a suitable focus plane was first chosen on the microscope (white light for focusing). **SBTub** was then added *cautiously* while the cells were still on the microscope stage, and cells incubated for 10 min before imaging. This protocol avoids exposure of the **SBTub** to white focusing light, preventing unwanted isomerization prior to imaging which could falsify results when testing for GFP/YFP orthogonality. Cells were imaged either at 488 nm (GFP; 23% laser power, 400 ms exposure time, 45 frames/min) or 514 nm (YFP; similar parameters; data not shown since GFP orthogonality implies YFP orthogonality); cells were optionally additionally exposed to interleaved dummy frames of **SBTub**-isomerizing 405 nm light for compound activation (250 ms exposure time, 45 frames/min). For analysis statistics, 6 cells per condition from three independent trials were taken. First-order exponential decay curves were fitted to each cell's data with their comet counts normalized to 100% at time zero, enabling intercomparison of cells with different starting comet counts (depending on their size, the position of the focal plane, etc.).

Treatment of live cells with *Z*-SBTub3 under GFP imaging

To show the effect of photoisomerized *Z*-**SBTub3** (as a control for the orthogonality experiment), a suitable focus plane was first chosen on the microscope (white light for focusing) and 5 frames were acquired at 488 nm, to set a reference for basal comet count. An **SBTub3** stock that had been isomerized to PSS with 360 nm was carefully applied on the stage, and after one minute incubation time, 180 frames were taken at 488 nm (400 ms exposure time, 23% laser power, 60 frames/min). The number of remaining comets per frame after treatment was counted and expressed as percentage of the starting reference timepoint.

Temporally reversible MT dynamics modulation with GFP-orthogonality

HeLa cells were transfected with EB3-GFP using FuGENE 6 (Promega) according to manufacturer's instructions. Experiments were imaged on a Nikon Eclipse Ti microscope equipped with a perfect focus system (Nikon), a spinning disk-based confocal scanner unit (CSU-X1-A1, Yokogawa), an Evolve 512 EMCCD camera (Photometrics) attached to a 2.0× intermediate lens (Edmund Optics), a Roper Scientific custom-made set of Stradus 405 nm (100 mW, Vortran) and Calypso 491 nm (100 mW, Cobolt) lasers, a set of ET-BFP2 and ET-GFP filters (Chroma), a motorized stage MS-

2000-XYZ, a stage top incubator INUBG2E-ZILCS (Tokai Hit) and lens heating calibrated for incubation at 37°C with 5% CO_2. Microscope image acquisition was controlled using MetaMorph 7.7 and images were acquired using a Plan Apo VC 60× NA 1.4 oil objective. Comet count analysis was performed in ImageJ using the ComDet plugin (E. Katrukha, University of Utrecht, Netherlands, https://github.com/ekatrukha/ComDet). GFP imaging was performed at 491 nm (0.17 mW; 300 ms every 2 s). In-frame **SBTub** photoactivation was performed at 405 nm (77 μW; 100 ms every 90 s; cell of interest plus in-frame surrounding area). Results were presented in the main text and correspond to Movie M1.

Temporally reversible MT modulation through EB1-comet assays in A549 cell line

A549 cells (40,000 cells/well) were seeded on 8-well ibiTreat μ slides (ibidi) 24 h prior to transfection. Cells were transiently transfected with *EB1-tdTomato* plasmid using jetPRIME reagent (Polyplus) according to the manufacturer's instructions. Cells were imaged 24 h later, under 37°C and 5% CO_2 atmosphere, using a Nikon TiE microscope equipped with a Yokogawa CSU-W1 spinning disk confocal unit (50 µm pinhole size), an Andor Borealis illumination unit, Andor ALC600 laser beam combiner (405/488/561/640 nm), Andor IXON 888 Ultra EMCCD camera, and a Nikon 100× NA 1.45 oil immersion objective. The microscope was controlled by Nikon NIS Elements software (v.5.02.00). Cells were pre-incubated with the indicated compound or cosolvent conditions in the dark for 5 min before acquisition through imaging at 561 nm (20% laser power, 300 ms exposure time, 30 frames/min). Optionally 405 nm illuminations (10% laser power, 175 µs pixel dwell time) were re-applied at 2 min intervals during acquisition as indicated. 3 cells per condition from three independent trials were taken for statistics. EB1 comets were counted in ImageJ using the ComDet plugin (E. Katrukha, University of Utrecht, https://github.com/ekatrukha/ComDet). EB1 count values were normalised to 100% at time zero or else normalised to 100% at the first return to plateau (pulsing experiments) as appropriate; this enables intercomparison of cells with different starting comet counts (depending on their size, the position of the focal plane, etc). Data are represented as mean comet count over time, with standard deviation; scalebars in EB1 movies (Movies M2-M7) are 10 μm.

Live Cell Imaging of EB3 in primary neuronal cultures

Animals: All animal experiments were performed in accordance with Dutch law (Wet op de Dierproeven, 1996) and European regulations (Directive 2010/63/EU) under animal licence AVD1080020173404. All animal experiments were approved by the Dutch Animal Experiments Committee (DEC, Dier Experimenten Commissie) and were in line with the institutional guidelines of Utrecht University. Pregnant Wistar rats (Janvier), which were at least 10 weeks of age and not involved in any previous experiments, were used in this study.

Primary neuronal cultures and transfections: Primary hippocampal neurons were derived from hippocampi of embryonic day 18 pups (male and female). Hippocampi were dissociated into single cells by a combination of enzymatic and mechanical dissociation, as described.[54] After dissociation, neurons were plated in 12-well plates at a density of 100,000 cells per well on coverslips coated with poly-L-lysine (37.5 μg/mL, Sigma-Aldrich) and laminin (1.25 μg/mL, Roche). The primary hippocampal cultures were kept at 37°C and 5% CO_2 in Neurobasal medium (NB, Gibco) supplemented with 2% B27 (Gibco), 0.5 mM glutamine (Gibco), 15.6 μM glutamate (Sigma-Aldrich) and 1% penicillin/streptomycin (Gibco). Neurons were transfected at the 7th day *in vitro* (DIV 7) using Lipofectamine 2000 (Invitrogen) and were imaged at DIV 10. Briefly, for the transfection of each coverslip, 1.8 μg of total DNA (0.4 μg EB3-GFP, 0.2 μg RFP, 1.2 μg empty backbone) was mixed with 3.3 μL of Lipofectamine 2000 in 200 μL non-supplemented NB and incubated for 30 min

at 20°C. Before the DNA/Lipofectamine mix was added to the neurons, half of the volume of supplemented NB in which the neurons had been growing (conditioned NB) was transferred to a new 12-well plate and replaced by NB supplemented with 0.5 mM glutamine. Then, the DNA/Lipofectamine mix was added to the neurons and incubated for 1 h at 37°C and 5% CO_2. After transfection, neurons were rinsed by dipping the coverslips into pre-warmed non-supplemented NB and placed back in conditioned NB that was mixed 50/50 with fresh, supplemented NB.

Live neuronal imaging: Neurons were immersed in conditioned NB with 1% DMSO cosolvent. Cells were imaged similarly to the conditions for ***Temporally reversible MT dynamics modulation with GFP-orthogonality***, except in that GFP was imaged at 491 nm (0.1 mW, 500 ms every 3 s). Neurons were initially imaged for EB3 for 10 min while a ROI (blue box) was pulsed with 405 nm light commencing 2 min into the acquisition, establishing baselines for EB3 activity in the cell and in the ROI (areas not pulsed with 405 nm but analysed in kymographs are boxed in orange and green); the ROI-pulsing protocol was to illuminate the ROI at 405 nm (95 μW, 7 ms per trace) tracing over the ROI 5 times every 3 s with imaging frames interleaved. The same neurons were then exposed to **SBTub3** and immediately imaged for another 10 min using the same protocol.

FACS cell cycle analysis

Results (Figure 3J) show full photoswitching-based control of G2/M-phase cell cycle arresting properties of **SBTub2** and **SBTub3**. Under dark (all-*E*) conditions they give no change of cell cycle repartition while under lit conditions (mostly-*Z*) they show strong G2/M-phase arrest similar to that of the proven photoswitchable colchicine site tubulin inhibitor **PST-1**. Crucially, neither isomer of the permutation control compounds **SBTub1** and **SBTub4** has effects on cell cycle repartition despite low antiproliferative effects at this concentration (see Figure 3A).

Immunofluorescence imaging of microtubule network structure

The results in Figure 3H-I show light- and dose- dependent depolymerisation of microtubule structure by **SBTub2** and **SBTub3**, while **SBTub1** and **SBTub4** have no effect on MT structure under dark and illuminated conditions even at high concentrations of 20 μM. The maximum intensity projection (along the z-axis) of cells treated for 24 h with lit **SBTub2** or lit **SBTub3** shows that most treated cells have been arrested in mitosis and display severe MT depolymerisation and organisational defects, while only a minor population of adherant cells persists albeit with disorganized microtubule networks.

Live cell imaging: GFP/YFP orthogonality via EB3 comet assay

SBTub2 and **SBTub3** inhibit tubulin polymerisation upon photoswitching to their Z-isomers; note that this does not imply that they should depolymerise existing microtubule polymer immediately upon photoswitching (and, at cellularly relevant concentrations over short assay timescales < 30 min, they will not do so). Live cell imaging of EB3-GFP/YFP is a standard assay to monitor microtubule growth dynamics[55] and was therefore used as a readout of in situ generation and cellular retention of these **SBTubs'** bioactive Z-isomers.

Two assays were used, such that taken together, the results show orthogonality of both *E***-** and *Z*-**SBTub**s to GFP/YFP imaging.

Firstly: stability of the *Z*-**SBTub** against *Z*-to-*E* isomerisation under GFP/YFP imaging was assessed. As per the “live cell imaging” methods section, cells were pre-incubated with all-*E* **SBTub3** (10 μM) or with cosolvent only (ctrl) in the dark for 10 min before acquiring uninhibited cellular EB3 comet

count statistics at timepoint t_{ref}. **SBTub3** was then isomerized substantially to *Z* by whole-field illumination at 405 nm (5 × 300 ms) and 5 GFP/YFP imaging frames at time points 30 s, 5 min and 10 min later were acquired (Figure S4A). Three independent trials were performed. For analysis, 8 cells per condition were chosen from the three independent trials. The EB3-comets were counted and each time point's comet count value was set as the average from those of its 5 frames. Each cell's comet counts were normalised with the average of its t = 0 s imaging frames being set to 1. The number of comets at the following timepoints are expressed as fraction or percentage of the initial pre-treatment comet numbers and are represented as mean with SD (Figure S4B).

Comet counts were abruptly and, in this experiment permanently reduced, upon the first global **SBTub3** activation with 405 nm while the cosolvent control showed no effect from this photoswitching, indicating the photostability of the bioactive *Z*-**SBTub3** (Figure S4C).

Secondly: evaluation of *E*-**SBTub**s' photostability ability to effect *in situ* photocontrol over protein dynamics while avoiding interference from the imaging wavelengths of common fluorescent labels GFP and YFP was performed by comparing the EB3 comet count under different lighting and compound conditions (Figure 4B-C). Figure 4B shows the following conditions and conclusions:

neg ctrl: cosolvent-only controls (DMSO) imaged under 488 nm only, or under alternating 488/405 nm lighting protocol as used for **SBTub** photoactivation, are identical, showing the timecourse of "normal" reduction of EB3 comets due to photobleaching only (i.e. in this setup 405 nm pulsing does not result in photobleaching).

SBTub3$_{488}$ (red squares): cells treated with **SBTub3** (10 μM) and imaged at 488 nm only: reduction of EB3 comets was comparable to those of both **neg ctrl**s, indicating that **SBTub3** is not photoactivated by 488 nm light.

SBTub3$_{405}$ (blue triangles): cells treated with **SBTub3** (8 μM) and imaged with 488 nm frames with interleaved 405 nm frames to induce **SBTub** activation. These show a faster decrease of EB3 comet count than of both **neg ctrl**s and of **SBTub3**$_{488}$; decrease is comparable to that of **pos ctrl PST-1** imaged at 488 nm, suggesting comparable inhibition of MT polymerisation.

pos ctrl: known azobenzene based MT depolymerizer **PST-1** (8 μM, non-GFP orthogonal) was imaged at 488 nm, causing compound activation and fast reduction of EB3 comet count (beyond the photobleaching rate).

Additionally, cells were treated with pre-illuminated *Z*-**SBTub3** enriched stock solutions and incubated for 1 min before imaging at 488 nm (Figure 4C). This experimental setup rules out a reduction of EB3 comets due to photobleaching, while also showing that reduction of EB3 comets is caused by exposing cells to *Z*-**SBTub3**.

Taken together, these results show the full orthogonality of both *E*- and *Z*-**SBTub**s to GFP/YFP imaging.

Live cell imaging on A549 lung cancer cell line

To prove a potential broader use for cell biological investigations we assayed the temporal reversibility of **SBTub3**'s cell-localised modulation of MT dynamics using a different cell line, biological label, and fluorescent marker: i.e. performing an EB1-tdTomato "comet" assay on the A549 cell line. A549 cells with or without **SBTub3** were exposed to single pulses of 405 nm every 120 s while imaging EB1-tdTomato comets at 561 nm as described in the main text, achieving temporally reversible MT modulation (Video S1 part B and Figure 4F-H) similar to the results seen in HeLa cells

(Video S1 part A and Figure 4D-E). Particularly, MT polymerisation dynamics were reversibly modulated by cell-localised photoactivations with **SBTub3** (Figure 4F, red trace) but unaffected in the absence of **SBTub3** (Figure 4H, blue trace); MT polymerisation dynamics are not inhibited by unactivated **SBTub3** at 5 and 10 μM (Figure 4G, blue and purple traces), whereas pre-lit **SBTub3** stops MT polymerisation dynamics upon treatment at both concentrations (Figure 4G, red and green traces); and DMSO cosolvent controls under dark and lit regimes (Figure 4H, black and blue traces) show no decrease in comet count, while the positive control colchicine binding site inhibitor nocodazole stops MT polymerisation dynamics at 1 μM (Figure 4H, green trace). See also Video S2 as a representative example of these treatments.

Note that during recovery phases the EB3-GFP "comets" appear to reform and continue their trajectories from their stop positions, which is congruent to the **SBTubs**' design rationale (and results showing) that *Z*-**SBTub** is tubulin-specific and does not directly inhibit EB3.

Detailed quantification of the impact of SBTub3 on live cell MT dynamics

In order to study MT dynamics we used fluorescently labelled EB3 as a marker for the GTP cap of polymerizing microtubules. HeLa cells were transfected with EB3-GFP using FuGENE 6 (Promega) according to manufacturer's instructions. Cells were imaged similarly to the conditions for ***Temporally reversible MT dynamics modulation with GFP-orthogonality***, except here GFP was imaged at 491 nm (0.2 mW, 100 ms every 0.6 s) and full frame SBTub3 photoactivation was performed using 405 nm (0.1 mW, 100ms every 1.2 s). Comet count analysis was performed in ImageJ using the ComDet plugin (E. Katrukha, University of Utrecht, Netherlands, https://github.com/ekatrukha/ComDet). Velocity analysis was performed in Image J using the MTrackJ plugin.[56]

As expected, 405 nm light, **SBTub3** without 405 nm activation, and **SBTub1** inactive control all had no significant impact on EB3 comet numbers or density (Figure 4I-K). However, **SBTub3** with 405 nm activation showed a 90-95% reduction in EB3 comets within the first 5-10 s of 405 nm activation, which subsequently recovered to an equilibrium at ~50% or ~20% of the original comet count for 5 μM or 40 μM of **SBTub3** respectively. It is unclear to us what the cause for this dipped curve is, in particular whether this is an effect resulting from the rate of drug exchange between the inside and outside of the cell or whether this is occuring at the MT level. However, elucidating this mechanism goes beyond the scope of this paper. As expected based on the difference in comet count curves, 40 μM **SBTub3** with 405 nm activation also had a significantly lower EB3 comet density than 405 nm activated 5 μM **SBTub3**. EB3 comet velocities were already very slightly reduced in the **SBTub3** treated cells, prior to photoactivation with 405, though there was no significant difference between 5 μM and 40 μM treated cells. However, activation of **SBTub3** with 405 nm caused a further 30% or 38% decrease in velocity of persisting EB3 comets for 5 μM and 40 μM **SBTub3** respectively (Figure 4K). As expected the permutation control **SBTub1** had no impact on EB3 comet velocity (Figure 4K). We conclude that **SBTub3** can be used effectively in live cells to disrupt MT dynamics in a temporally controlled manner, and that **SBTub3** concentration can be modulated to calibrate the desired level of impact.

Part H: NMR Spectra

2-(2,3,4-trimethoxystyryl)benzothiazole (SBTub1)

^{1}H-NMR:

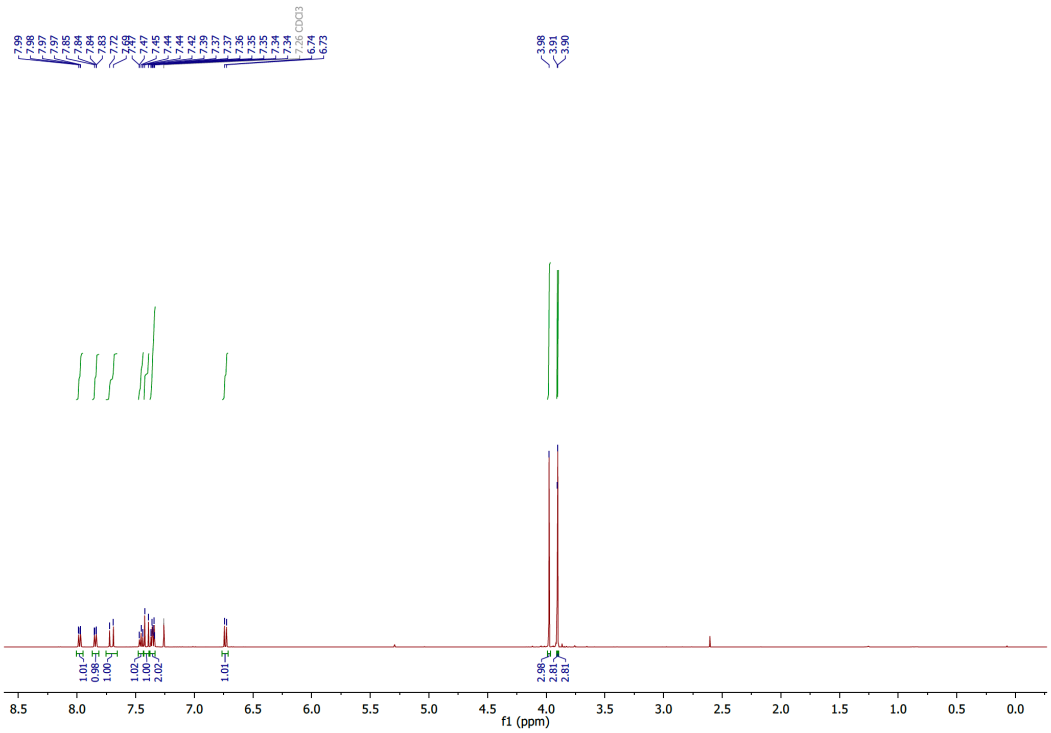

^{13}C-NMR:

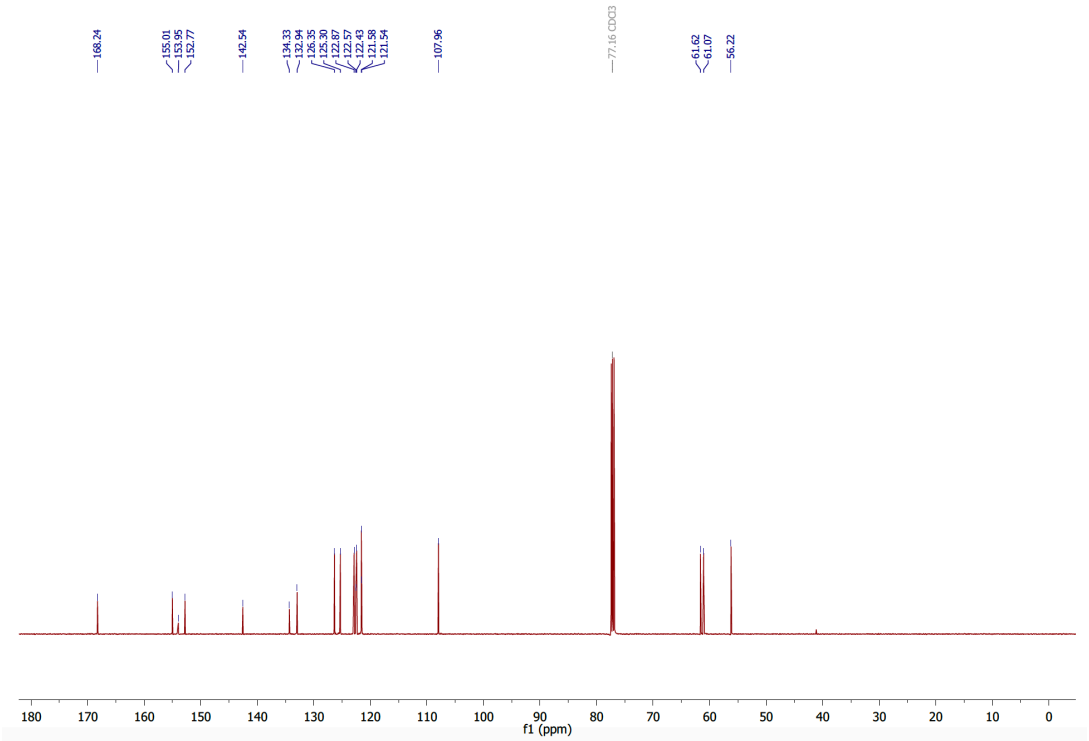

2-(3,4,5-trimethoxystyryl)benzothiazole (SBTub2)

^{1}H-NMR:

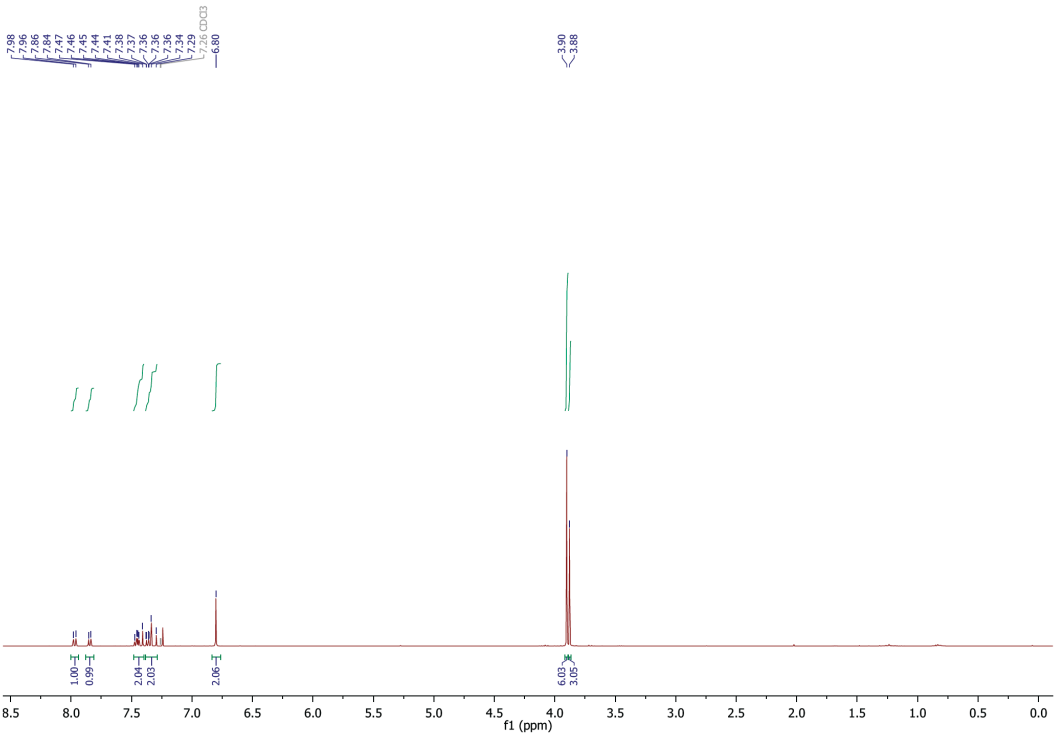

^{13}C-NMR:

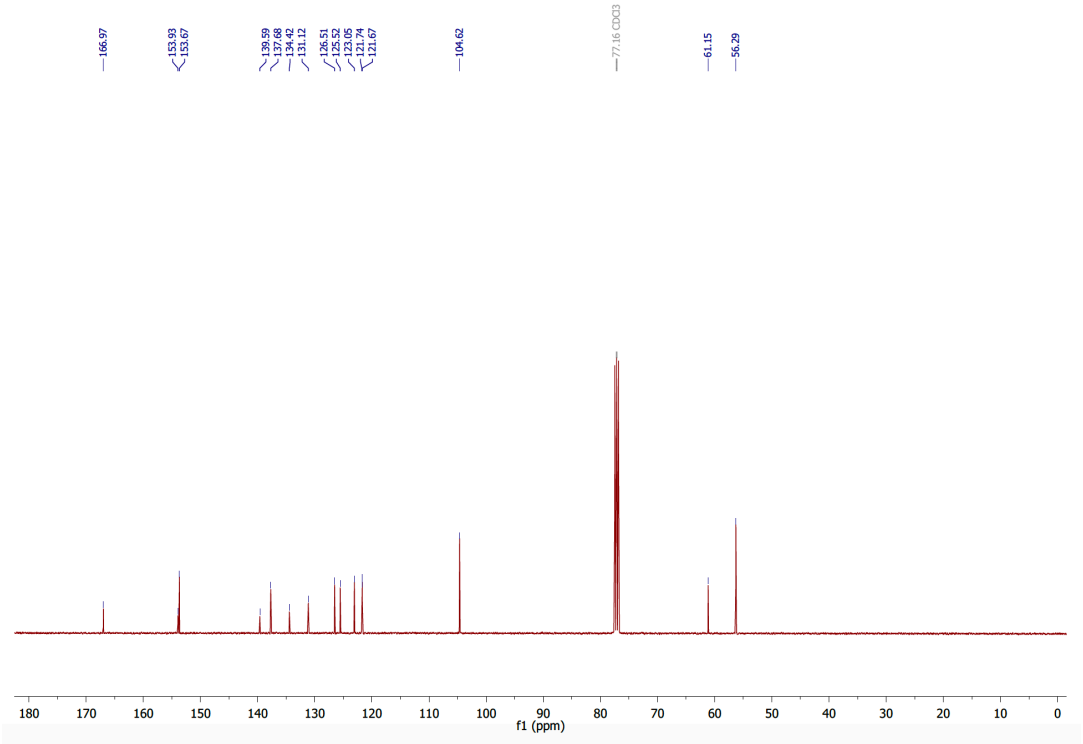

5-(2-(benzothiazol-2-yl)vinyl)-2-methoxyphenol (SBTub3)

^{1}H-NMR:

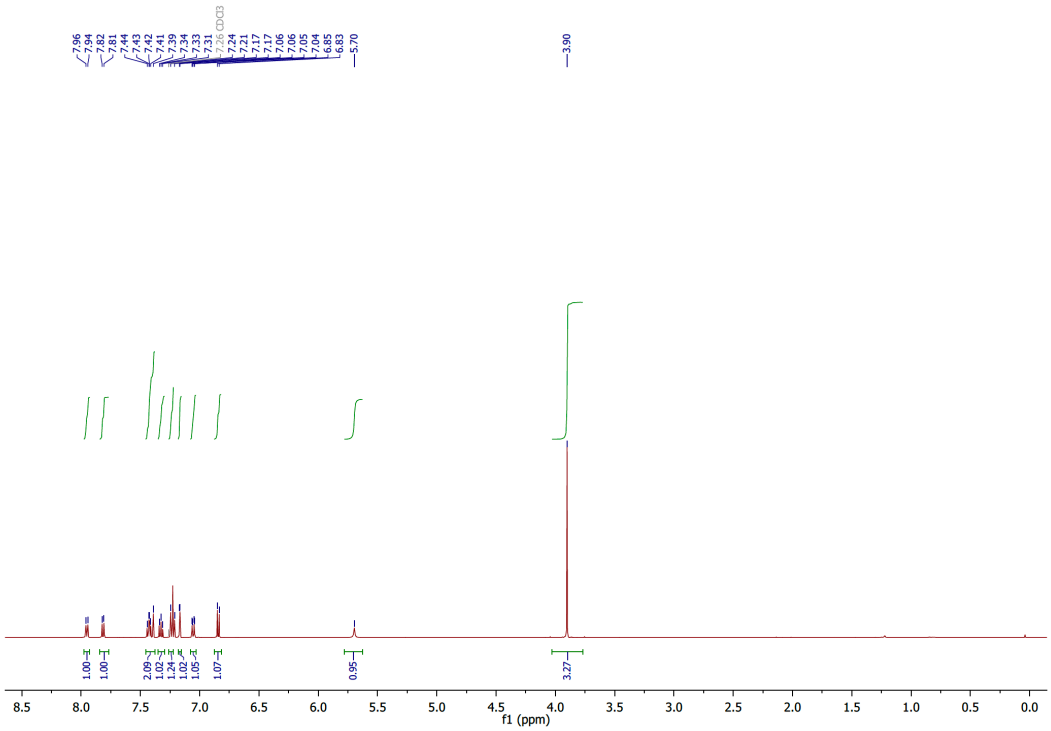

^{13}C-NMR:

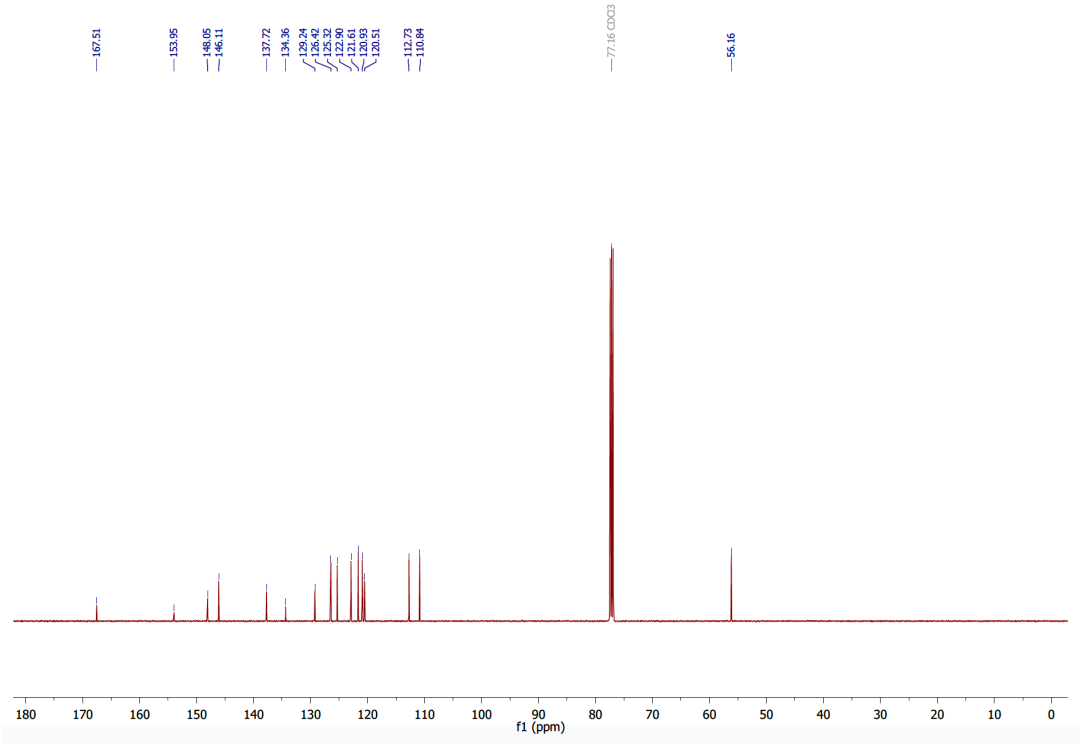

4-(2-(benzothiazol-2-yl)vinyl)-2-methoxyphenol (SBTub4)

^{1}H-NMR:

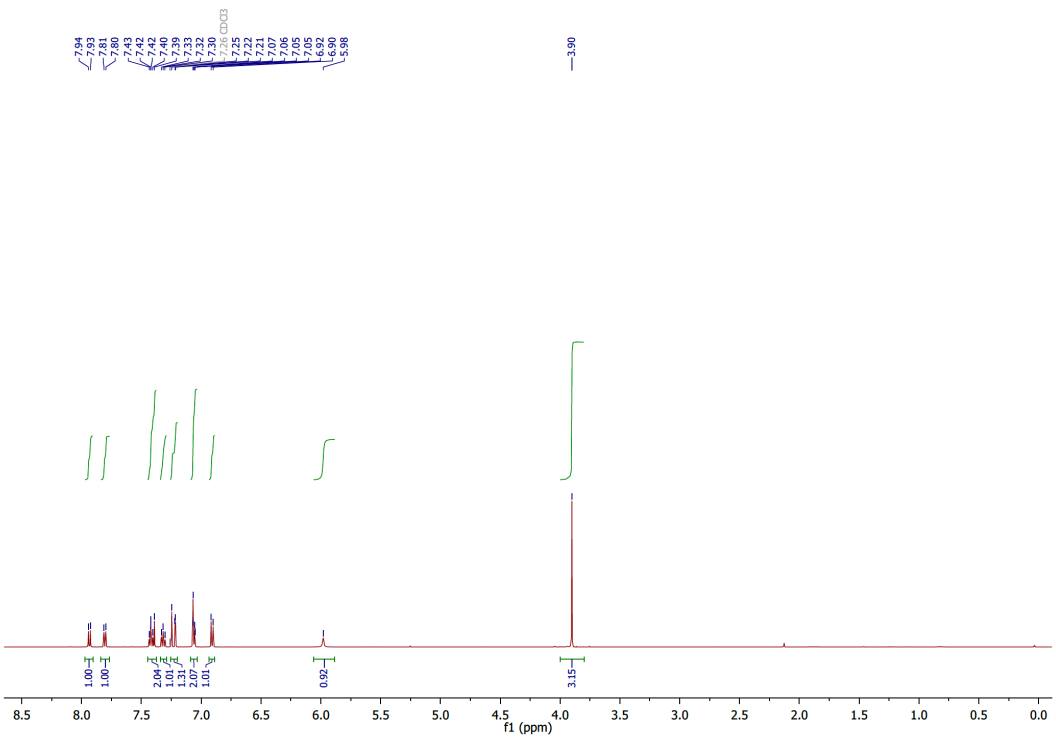

^{13}C-NMR:

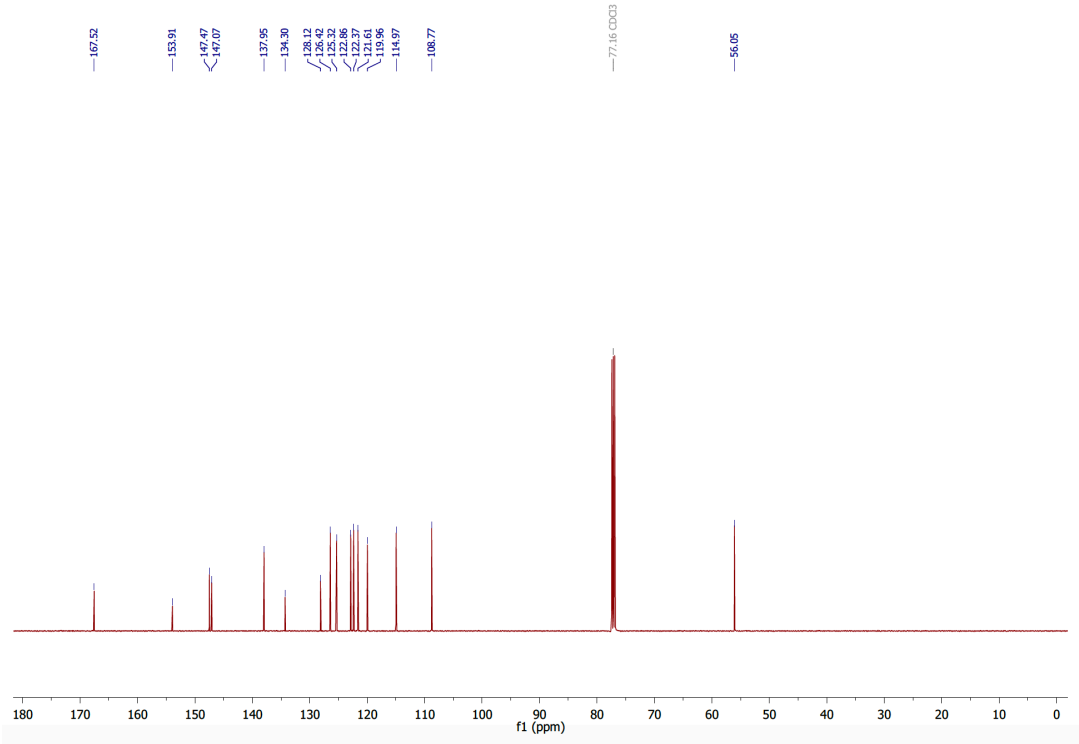

Supplementary Information Bibliography

[1] H. Zhou, C. Xue, P. Weis, Y. Suzuki, S. Huang, K. Koynov, G. K. Auernhammer, R. Berger, H.-J. Butt, S. Wu; *Nat. Chem.* **2017**, *9*, 145 *(10.1038/nchem.2625)*.

[2] G. S. Kumar, D. C. Neckers; *Chem. Rev.* **1989**, *89*, 1915–1925 *(10.1021/cr00098a012)*.

[3] W. A. Velema, J. P. van der Berg, W. Szymanski, A. J. M. Driessen, B. L. Feringa; *ACS Chem. Biol.* **2014**, *9*, 1969–1974 *(10.1021/cb500313f)*.

[4] K. Hüll, J. Morstein, D. Trauner; *Chem. Rev.* **2018**, *118*, 10710–10747 *(10.1021/acs.chemrev.8b00037)*.

[5] M. Dong, A. Babalhavaeji, S. Samanta, A. A. Beharry, G. A. Woolley; *Acc. Chem. Res.* **2015**, *48*, 2662–2670 *(10.1021/acs.accounts.5b00270)*.

[6] M. Borowiak, W. Nahaboo, M. Reynders, K. Nekolla, P. Jalinot, J. Hasserodt, M. Rehberg, M. Delattre, S. Zahler, A. Vollmar, D. Trauner, O. Thorn-Seshold; *Cell* **2015**, *162*, 403-411 *(10.1016/j.cell.2015.06.049)*.

[7] J. Zenker, M. D. White, R. M. Templin, R. G. Parton, O. Thorn-Seshold, S. Bissiere, N. Plachta; *Science* **2017**, *357*, 925-928 *(10.1126/science.aam9335)*.

[8] J. Zenker, M. D. White, M. Gasnier, Y. D. Alvarez, H. Y. G. Lim, S. Bissiere, M. Biro, N. Plachta; *Cell* **2018**, *173*, 776-791 *(10.1016/j.cell.2018.02.035)*.

[9] C. Janke, M. O. Steinmetz; *EMBO J.* **2015**, *34*, 2114–2116 *(10.15252/embj.201592415)*.

[10] B. T. Castle, D. J. Odde; *Cell* **2015**, *162*, 243–245 *(10.1016/j.cell.2015.06.064)*.

[11] G. R. Pettit, S. B. Singh, E. Hamel, C. M. Lin, D. S. Alberts, D. Garcia-Kendall; *Experientia* **1989**, *45*, 209–211.

[12] G. M. Tozer, Kanthou, C., Parkins, C.S., Hill, S.A.; *Int. J. Exp. Pathol.* **2002**, *83*, 21–38 *(10.1046/j.1365-2613.2002.00211.x)*.

[13] G. C. Tron, T. Pirali, G. Sorba, F. Pagliai, S. Busacca, A. A. Genazzani; *J. Med. Chem.* **2006**, *49*, 3033–3044 *(10.1021/jm0512903)*.

[14] J. A. Woods, J. A. Hadfield, G. R. Pettit, B. W. Fox, A. T. McGown; *Br. J. Cancer* **1995**, *71*, 705-711 *(10.1038/bjc.1995.138)*.

[15] K. M. Scherer, R. H. Bisby, S. W. Botchway, J. A. Hadfield, A. W. Parker; *J. Biomed. Opt.* **2015**, *20*, 051004 *(10.1117/1.Jbo.20.5.051004)*.

[16] K. B. Jørgensen; *Molecules* **2010**, *15*, 4334–4358 *(10.3390/molecules15064334)*.

[17] J. Morstein, M. Awale, J.-L. Reymond, D. Trauner; *ACS Central Science* **2019**, *(10.1021/acscentsci.8b00881)*.

[18] A. J. Engdahl, E. A. Torres, S. E. Lock, T. B. Engdahl, P. S. Mertz, C. N. Streu; *Org. Lett.* **2015**, *17*, 4546–4549 *(10.1021/acs.orglett.5b02262)*.

[19] J. E. Sheldon, M. M. Dcona, C. E. Lyons, J. C. Hackett, M. C. T. Hartman; *Org. Biomol. Chem.* **2016**, *14*, 40–49 *(10.1039/c5ob02005k)*.

[20] S. K. Rastogi, Z. Zhao, S. L. Barrett, S. D. Shelton, M. Zafferani, H. E. Anderson, M. O. Blumenthal, L. R. Jones, L. Wang, X. Li, C. N. Streu, L. Du, W. J. Brittain; *Eur. J. Med. Chem.* **2018**, *143*, 1–7 *(10.1016/j.ejmech.2017.11.012)*.

[21] A. Singh, T. Saha, I. Begemann, A. Ricker, H. Nüsse, O. Thorn-Seshold, J. Klingauf, M. Galic, M. Matis; *Nat. Cell Biol.* **2018**, *20*, 1126-1133 *(10.1038/s41556-018-0193-1)*.

[22] C. Vandestadt, G. C. Vanwalleghem, H. A. Castillo, M. Li, K. Schulze, M. Khabooshan, E. Don, M.-L. Anko, E. K. Scott, J. Kaslin; *bioRxiv* **2019**, 539940 *(10.1101/539940)*.

[23] K. Eguchi, Z. Taoufiq, O. Thorn-Seshold, D. Trauner, M. Hasegawa, T. Takahashi; *J. Neurosci.* **2017**, *37*, 6043-6052 *(10.1523/jneurosci.0179-17.2017)*.

[24] K. Eguchi, Z. Taoufiq, O. Thorn-Seshold, D. Trauner, M. Hasegawa, T. Takahashi; *J. Neurosci.* **2017**, *37*, 6043–6052 *(10.1523/jneurosci.0179-17.2017)*.

[25] J. Broichhagen, J. A. Frank, D. Trauner; *Acc. Chem. Res.* **2015**, *48*, 1947-1960 *(10.1021/acs.accounts.5b00129)*.

[26] W. A. Velema, W. Szymanski, B. L. Feringa; *J. Am. Chem. Soc.* **2014**, *136*, 2178-2191 *(10.1021/ja413063e)*.

[27] S. Samanta, A. A. Beharry, O. Sadovski, T. M. McCormick, A. Babalhavaeji, V. Tropepe, G. A. Woolley; *J. Am. Chem. Soc.* **2013**, *135*, 9777-9784 *(10.1021/ja402220t)*.

[28] R. Friederike, S. Wiktor; *Curr. Med. Chem.* **2017**, *24*, 4905-4950 *(10.2174/0929867323666160906103223)*.

[29] S. Samanta, A. A. Beharry, O. Sadovski, T. M. McCormick, A. Babalhavaeji, V. Tropepe, G. A. Woolley; *J. Am. Chem. Soc.* **2013**, *135*, 9777–9784 *(10.1021/ja402220t)*.

[30] J. E. Sheldon, M. M. Dcona, C. E. Lyons, J. C. Hackett, M. C. T. Hartman; *Org. Biomol. Chem.* **2016**, *14*, 40-49 *(10.1039/C5OB02005K)*.

[31] S. Samanta, A. Babalhavaeji, M.-x. Dong, G. A. Woolley; *Angew. Chem., Int. Ed.* **2013**, *52*, 14127–14130 *(10.1002/anie.201306352)*.

[32] H. Lei, M. Mo, Y. He, Y. Wu, W. Zhu, L. Wu; *Bioorg. Chem.* **2019**, 103106 *(10.1016/j.bioorg.2019.103106)*.

[33] C. Boulègue, M. Löweneck, C. Renner, L. Moroder; *ChemBioChem* **2007**, *8*, 591–594 *(10.1002/cbic.200600495)*.

[34] A. Gilbert; *ChemInform* **2004**, *35*, *(10.1002/chin.200418261)*.

[35] H. E. Gottlieb, V. Kotlyar, A. Nudelman; *J. Org. Chem.* **1997**, *62*, 7512-7515 *(10.1021/jo971176v)*.

[36] N. R. Penthala, P. Crooks, V. Sonar; *Combretastatin analogs (US20160068506A1)*, **2016**.

[37] N. R. Penthala, S. Thakkar, P. A. Crooks; *Bioorg. Med. Chem. Lett.* **2015**, *25*, 2763-2767 *(10.1016/j.bmcl.2015.05.019)*.

[38] G. C. Tron, T. Pirali, G. Sorba, F. Pagliai, S. Busacca, A. A. Genazzani; *J. Med. Chem.* **2006**, *49*, 3033-3044 *(10.1021/jm0512903)*.

[39] R. Gaspari, A. E. Prota, K. Bargsten, A. Cavalli, M. O. Steinmetz; *Chem* **2017**, *2*, 102-113 *(10.1016/j.chempr.2016.12.005)*.

[40] A. Sailer, F. Ermer, Y. Kraus, F. Lutter, C. Donau, M. Bremerich, J. Ahlfeld, O. Thorn-Seshold; *ChemBioChem* **2019**, *20*, 1305-1314 *(10.1002/cbic.201800752)*.

[41] C. M. Lozano, O. Cox, M. M. Muir, J. D. Morales, J. L. Rodríguez-Cabán, P. E. Vivas-Mejía, F. A. Gonzalez; *Inorganica Chimica Acta* **1998**, *271*, 137-144 *(doi.org/10.1016/S0020-1693(97)05952-5)*.

[42] A. M. Sanchez, M. Barra, R. H. d. Rossi; *J. Org. Chem.* **1999**, *64*, 1604–1609 *(10.1021/jo982069j)*.

[43] N. J. Dunn, W. H. Humphries, A. R. Offenbacher, T. L. King, J. A. Gray; *J. Phys. Chem. A* **2009**, *113*, 13144–13151 *(10.1021/jp903102u)*.

[44] C. A. Kulkarni, P. Brookes; *Antioxid Redox Signal* **2019**, *(10.1089/ars.2018.7722)*.

[45] C. M. Lin, S. B. Singh, P. S. Chu, R. O. Dempcy, J. M. Schmidt, G. R. Pettit, E. Hamel; *Molecular Pharmacology* **1988**, *34*, 200-208.

[46] L. Pecqueur, C. Duellberg, B. Dreier, Q. Jiang, C. Wang, A. Plückthun, T. Surrey, B. Gigant, M. Knossow; *Proceedings of the National Academy of Sciences* **2012**, *109*, 12011 *(10.1073/pnas.1204129109)*.

[47] W. Kabsch; *Acta crystallographica. Section D, Biological crystallography* **2010**, *66*, 125-132 *(10.1107/S0907444909047337)*.

[48] T. Weinert, N. Olieric, R. Cheng, S. Brünle, D. James, D. Ozerov, D. Gashi, L. Vera, M. Marsh, K. Jaeger, F. Dworkowski, E. Panepucci, S. Basu, P. Skopintsev, A. S. Doré, T. Geng, R. M. Cooke, M. Liang, A. E. Prota, V. Panneels, P. Nogly, U. Ermler, G. Schertler, M. Hennig, M. O. Steinmetz, M. Wang, J. Standfuss; *Nature Communications* **2017**, *8*, 542 *(10.1038/s41467-017-00630-4)*.

[49] P. D. Adams, P. V. Afonine, G. Bunkoczi, V. B. Chen, I. W. Davis, N. Echols, J. J. Headd, L.-W. Hung, G. J. Kapral, R. W. Grosse-Kunstleve, A. J. McCoy, N. W. Moriarty, R. Oeffner, R. J. Read, D. C. Richardson, J. S. Richardson, T. C. Terwilliger, P. H. Zwart; *Acta Crystallographica Section D* **2010**, *66*, 213-221 *(doi:10.1107/S0907444909052925)*.

[50] P. Emsley, K. Cowtan; *Acta Crystallographica Section D* **2004**, *60*, 2126-2132 *(doi:10.1107/S0907444904019158)*.

[51] M. O. Steinmetz, A. E. Prota; *Trends in Cell Biology* **2018**, *28*, 776-792 *(10.1016/j.tcb.2018.05.001)*.

[52] R. B. G. Ravelli, B. Gigant, P. A. Curmi, I. Jourdain, S. Lachkar, A. Sobel, M. Knossow; *Nature* **2004**, *428*, 198-202 *(10.1038/nature02393)*.

[53] T. Kleele, P. Marinković, P. R. Williams, S. Stern, E. E. Weigand, P. Engerer, R. Naumann, J. Hartmann, R. M. Karl, F. Bradke, D. Bishop, J. Herms, A. Konnerth, M. Kerschensteiner, L. Godinho, T. Misgeld; *Nat. Commun.* **2014**, *5*, 4827 *(10.1038/ncomms5827)*.

[54] L. C. Kapitein, K. W. Yau, C. C. Hoogenraad; in *Methods in Cell Biology*, (*Vol. 97*), (Eds.: L. Cassimeris and P. Tran), Academic Press, **2010**, pp. 111-132.

[55] T. Stepanova, J. Slemmer, C. C. Hoogenraad, G. Lansbergen, B. Dortland, C. I. De Zeeuw, F. Grosveld, G. van Cappellen, A. Akhmanova, N. Galjart; *The Journal of Neuroscience* **2003**, *23*, 2655 *(10.1523/JNEUROSCI.23-07-02655.2003)*.

[56] E. Meijering, O. Dzyubachyk, I. Smal; in *Methods in Enzymology*, (*Vol. 504*), (Ed. P. M. conn), Academic Press, **2012**, pp. 183-200.

6. Part Two: Second Generation Styrylbenzothiazole SBTubs

The first generation of **SBTubs** focused on introducing the SBT scaffold as a general photoswitch in cell biology using the MT cytoskeleton and tubulin as our protein of choice for proof of concept experiments. We mainly explored their photoproperties, metabolic stability and compatibility to GFP/YFP imaging tags to demonstrate the SBT scaffolds potential as suitable *in vivo* photopharmaceuticals. Consequently, the potency of these first generation **SBTubs** (IC_{50} ~1 µM) was not fully optimized, which made them relatively weak tubulin inhibitors that would require high volumes of cosolvent and limit their application out of cell culture.

Our goal in the following work was to discover a suitable **SBTub** lead structure with high potency and water solubility that could be used for photocontrol not only in cell culture settings where many photoswitches succeed, but over a range of *in vivo* multi-organ animal models, with temporally-specific and cell-precise *in situ* photoswitching after systemic administration: settings in which no other photoswitchable reagents have so far succeeded.

We performed an SAR study to identify and develop two potent, soluble, metabolically stable, GFP-orthogonal SBT-based photopharmaceuticals **SBTub2M** and **SBTubA4P** and showcase the unprecedented success of both the fully water soluble prodrug **SBTubA4P** and the potent drug **SBTub2M** in allowing systemic administration but local photoactivations to achieve (i) spatiotemporally-specific control over MT dynamics in cell culture, (ii) long-term spatially-resolved photocontrol of migration and proliferation over 24 h in primary mammary organoids, (iii) short-term temporally-resolved photocontrol of neural development in fly brain explant, (iv) photocontrol of embryonic development in the clawed frog, and (v) temporally reversible photocontrol of microtubule dynamics in zebrafish.

These experiments performed with the second generation **SBTubs** are the first to succeed in applying microtubule photocontrol in organisms where the previous "best in class" of 2D-cell-culture-active reagents (PST-1P and **SBTub3**) fail and show that the SBT scaffold allows *in vivo* photopharmacology.

Having shown a proof of concept it will be interesting to see if **SBTubs** can effectively contribute to MT cytoskeleton research and provide actual new insights into MT cytoskeleton research. Another interesting challenge which remains to be tackled is determining **SBTubs**' viability as a potential "turn-ON" photopharmaceutical with improved local precision in tumor xenograft models to test their anticancer effect with reduced systemic side effects.

In vivo photocontrol of microtubule dynamics and integrity, migration and mitosis, by the potent GFP-imaging-compatible photoswitchable reagents SBTubA4P and SBTub2M

Li Gao[1], Joyce C.M. Meiring[2], Adam Varady[3], Iris E. Ruider[4], Constanze Heise[1], Maximilian Wranik[5], Cecilia D. Velasco[6,7], Jennifer A. Taylor[8], Beatrice Terni[6,7], Jörg Standfuss[5], Clemens C. Cabernard[8], Artur Llobet[6,7], Michel O. Steinmetz[5,9], Andreas R. Bausch[4], Martin Distel[3,10], Julia Thorn-Seshold[1], Anna Akhmanova[2], Oliver Thorn-Seshold[1,11,*]

[1] Department of Pharmacy, Ludwig-Maximilians University of Munich; Munich 81377, Germany
[2] Cell Biology, Department of Biology, Faculty of Science, Utrecht University, Utrecht 3584, Netherlands
[3] St. Anna Children's Cancer Research Institute, Vienna 1090, Austria
[4] Physics Department, Technical University of Munich and Center for Protein Assemblies; Garching 85747, Germany
[5] Laboratory of Biomolecular Research, Division of Biology and Chemistry, Paul Scherrer Institut, Villigen 5232, Switzerland
[6] Laboratory of Neurobiology, Department of Pathology and Experimental Therapy, Institute of Neurosciences, University of Barcelona; L'Hospitalet de Llobregat, Barcelona 08907, Spain
[7] Bellvitge Biomedical Research Institute (IDIBELL), L'Hospitalet de Llobregat, Barcelona 08907, Spain
[8] Department of Biology, University of Washington; Seattle 98195, USA
[9] Biozentrum, University of Basel, Basel 4056, Switzerland
[10] Zebrafish Platform Austria for Preclinical Drug Screening, Vienna 1090, Austria
[11] Lead Contact
*Correspondence to oliver.thorn-seshold@cup.lmu.de

ORCID: O.T.-S. 0000-0003-3981-651X

***Keywords**: microtubule dynamics; cytoskeleton; photopharmacology; tubulin polymerisation inhibitor; optical control; colchicine; antimitotic; cell division; cell migration; development; photoswitch.*

Abstract

Photoswitchable reagents to modulate microtubule stability and dynamics are an exciting tool approach towards micron- and millisecond-scale control over endogenous cytoskeleton-dependent processes. When these reagents are globally administered yet locally photoactivated in 2D cell culture, they can exert precise biological control that would have great potential for *in vivo* translation across a variety of research fields and for all eukaryotes. However, photopharmacology's reliance on the azobenzene photoswitch scaffold has been accompanied by a failure to translate this temporally- and cellularly-resolved control to 3D models or to *in vivo* applications in multi-organ animals, which we attribute substantially to the metabolic liabilities of azobenzenes.

Here, we optimised the potency and solubility of metabolically stable, druglike colchicinoid microtubule inhibitors based instead on the styrylbenzothiazole (SBT) photoswitch scaffold, that are non-responsive to the major fluorescent protein imaging channels and so enable multiplexed imaging studies. We applied these reagents to 3D systems (organoids, tissue explants) and classic model organisms (zebrafish, clawed frog) with one- and two-protein imaging experiments. We successfully used systemic treatment plus spatiotemporally-localised illuminations *in vivo* to photocontrol microtubule dynamics, network architecture, and microtubule-dependent processes in these systems with cellular precision and second-level resolution. These nanomolar, *in vivo*-capable photoswitchable reagents can prove a game-changer for high-precision cytoskeleton research in cargo transport, cell motility, cell division and development. More broadly, their straightforward design can also inspire the development

of similarly capable optical reagents for a range of protein targets, so bringing general *in vivo* photopharmacology one step closer to productive realisation.

1. Introduction

Biological instrumentation, methods, and technologies now allow us to observe cellular structures and dynamics on the micron scale, with dynamics resolved to the scale of milliseconds, in settings from *in vitro* cell culture[1] to *in vivo* (multi-organ) animal models[2]. The development of tools to manipulate these processes with matching micrometre spatial precision and millisecond temporal precision has lagged far behind, despite its clear value for research.[3,4] One biological system with particularly urgent need of such tools is the microtubule (MT) cytoskeleton.[5,6] MTs are giant tube-like noncovalent polymers of α/β-tubulin protein heterodimers, that are centrally structured and rapidly remodelled to support hundreds of spatiotemporally-regulated functions in the life of a cell. The most visible roles of MTs include force generation to maintain and change cell shape and position, and in scaffolding the transport of cargos by motor proteins, including chromosomes during cell division.

Tools to noninvasively manipulate MT network structure and remodelling dynamics with high spatiotemporal precision, have great potential to drive biological research. However, to fulfil this potential, tools must succeed in settings from 2D cell culture (e.g. cell migration and division) through to *in vivo*, 3D systems (embryonic development and neuroscience). It is also important that tools be easily transferrable across different models and organisms.[7,8]

Optogenetics has been extremely successful in patterning ion currents and cell signalling with high spatiotemporal precision. However, in MT cytoskeleton studies it has not yet succeeded, with the exception of one photo-inactivated fusion protein that stops promoting MT polymerisation under illumination.[9] Optogenetics also faces difficulties for *in vivo* use that are common to all genetic approaches, including the costs of translating tools across species (time for breeding and validating transgenic lines; optimisation of expression systems; etc).

By comparison, drugs to modulate MT structure and dynamics reliably across all eukaryotes are very well-studied. Taxanes, epothilones, colchicine analogues, and vinca alkaloids are all used for nonspecific suppression of MT-dependent cellular processes, in settings from single-cell studies through to *in vivo* therapeutic use in humans. Photouncaging approaches have for years been applied to these drugs to improve the spatiotemporal precision with which their activity can be applied in cellular research (ideally towards the scale of μm and ms).[10]

Photoisomerisation-based drug analogues or "photopharmaceuticals" elegantly avoid many of the drawbacks that limited the *in vivo* use of typical photouncaging methods:[11] such as toxic and/or phototoxic byproducts, requirements for <360 nm wavelengths and high light intensities, slow post-illumination fragmentation, irreversibly photosensitive stock solutions, and non-optical drug release mechanisms (e.g. enzymatic hydrolysis of cages). In the MT field, recent photoswitchable analogues of taxane[12], epothilone[13] and colchicinoid[5,14–19] MT inhibitors have all been applied to cellular studies. These photopharmaceuticals have enabled noninvasive, reversible optical control over MT dynamics and MT-associated downstream effects, with cell-specific spatial precision and sub-second-scale temporal precision, and have been brought to bear on research in embryology[20], neuroscience[21], and cytoskeleton[5].

However, the typical photoswitch scaffolds introduce problems particularly for *in vivo* application, three of which this paper will focus on: (1) *Metabolic stability*: azobenzenes, particularly as their *Z*-isomers, are reductively degraded by cellular glutathione (GSH).[22–24] This reduces photoswitchability as well as potency, and on timescales typical for *in vivo* studies (> hours) the degradation byproducts are likely to give off-target effects, particularly in metabolically active multiorgan systems (tested below, and also discussed elsewhere[16]). (2) *Orthogonal photocontrol and imaging*: azobenzenes, and the less common hemithioindigos, are isomerised by excitation of the typical imaging labels used in biological studies (GFP/fluorescein at 490 nm, YFP at 514 nm); some also isomerise with RFP/rhodamine imaging at 561 nm (at focussed laser intensities).[16,25] Typically this leaves only the 647 nm laser channel available for orthogonal imaging during photoswitching, yet this laser typically only addresses small molecule probes. These scaffolds' inability to allow orthogonal

fluorescent-protein-based imaging during photocontrol is particularly problematic for *in vivo* research that extensively relies on two- or three-channel imaging with fluorescent protein fusions to resolve processes with biological specificity. (3) *Practical applicability issues*: *in vivo* studies must ensure sufficient delivery of photopharmaceuticals to target tissues without organic cosolvents, as these are far more toxic to animals than they are in cell culture. This either requires high-potency compounds or chemically robust solubilising strategies: neither of which are often seen with typically hydrophobic azobenzene or hemithioindigo drug analogues. To minimise illumination while maximising bioactivity explicitly requires tuning the photoswitch scaffold's photoresponse *at those laser wavelength/s* that are in practice used for photoconversion in the biological study[16] (aim: high efficiency of isomerisation $E(\lambda)^5$ and high photostationary state): since photoswitch performance at optimal but unavailable wavelengths (e.g. 260-380 nm) is irrelevant.

Novel photoswitches that improve practical performance are therefore gaining attention to expand the biological scope of photopharmacology.[26–28] To tackle these three issues in the context of microtubule photocontrol, we introduced styrylbenzothiazoles **SBTub2/3** (**Fig 1a**) as highly metabolically stable, fully GFP/YFP/RFP-orthogonal photoswitchable tubulin inhibitors (**Fig 1b-c**), with excellent photoresponse to the 405 nm laser line that is standard in confocal microscopy. **SBTub3** could photocontrol microtubule dynamics, organization, and MT-dependent processes in live cells with reversible temporal patterning, and with cellular and even sub-cellular spatial precision.[16]

The metabolic stability and imaging-orthogonal photocontrol of **SBTub3** were excellent features towards *in vivo* use, but practical limitations remained, which we determined to address in this study. Primarily, while their parent colchicinoid inhibitor combretastatin A-4 (**CA4**) has ca. 20 nM cellular potency, the slightly larger *Z*-**SBTub2/3** gave only micromolar bioactivity (though note that the **CA4**-isosteric azobenzene analogue *Z*-**PST-1** has only ca. 500 nM potency; **Fig 1a**). The lower the potency, the more compound and the more cosolvent would be needed, which we found blocked animal model applications of both **SBTub2/3** and **PST-1** (see below). Thus we prioritised a structure-activity relationship study to improve the potency of **SBTub**s. Secondly, the **SBTub**s are hydrophobic, so we prioritised fully water-soluble prodrugs for *in vivo* use without cosolvents. Thirdly, while the SBT scaffold is essentially a unidirectional (*E*→*Z*) photoswitch in the biological range because its isomers' absorption bands overlap, we were curious if tautomerisable electron-donating substituents could accelerate its spontaneous thermal *Z*→*E* relaxation, as they do for azobenzenes.[25]

Our goal was then to test whether suitably potent and soluble SBT derivatives could be used for photocontrol not only in cell culture settings where many photoswitches succeed, but over a range of *in vivo* multi-organ animal models, with temporally-specific and cell-precise *in situ* photoswitching after systemic administration: settings in which no other photoswitchable reagents have so far succeeded. We now report the development of these potent, soluble, metabolically stable, GFP-orthogonal SBT-based photopharmaceuticals and characterise the optimal ligand **SBTubA4** with a tubulin:SBT X-ray crystal structure. We then showcase the unprecedented success of its fully water-soluble prodrug **SBTubA4P** in allowing systemic administration but local photoactivations to achieve (i) spatiotemporally-specific control over MT dynamics in cell culture, (ii) long-term spatially-specific control over development and migration in 3D organoid culture, (iii) short-term temporally-resolved photocontrol of neural development in fly brain explant, (iv) photocontrol of embryonic development in the clawed frog, and (v) temporally reversible photocontrol of microtubule dynamics in zebrafish.

2. Results

2.1. Cellular structure-activity optimisation of SBTubs

For a colchicinoid **SBTub** to be cellularly effective, its *Z*-isomer should bind tubulin,[5,29] halting cell proliferation and inducing apoptosis[30]; while the corresponding *E*-isomer should have negligible tubulin binding and no other significant toxicity mechanisms over a wide concentration range where the *Z*-isomer is bioactive, resulting in a high lit/dark bioactivity ratio ("photoswitchability of bioactivity").[16] Thus we performed cellular structure-activity optimisation by comparing the proliferation of cells treated with **SBTub**s under *in situ* pulsed illuminations

with near-UV light ("lit": mostly-*Z*-isomer; aim: nanomolar potency), to their proliferation without illumination ("dark": all-*E*-isomer; aim: no antiproliferative effects up to 100 μM).

Our first priority for *in vivo* use was to increase *Z*-**SBTub** potency. We first tested whether restoring the methoxy groups of the **CA4** pharmacophore would increase potency despite the extra size, with **SBTubA4** (**1**). This, like most **SBTub**s, was synthesised in a short sequence (**Fig 1e**) via basic aldol condensation of the derivatised 2-methylbenzothiazole with the corresponding benzaldehyde, with the 2-methylbenzothiazole obtained *via* Jacobson cyclization[31] of the thioacetanilide using potassium ferricyanide (exceptions were *para*-aniline **7** which was obtained by Horner-Wadsworth-Emmons olefination; and **9** and **11** where the 2,5- and 2,7-dimethylbenzothiazoles were synthesised by Ullmann-type coupling according to Ma[32] since Jacobson cyclization of 3-methyl-thioacetoanilide gave an inseparable mixture; see Suppporting Information for details).

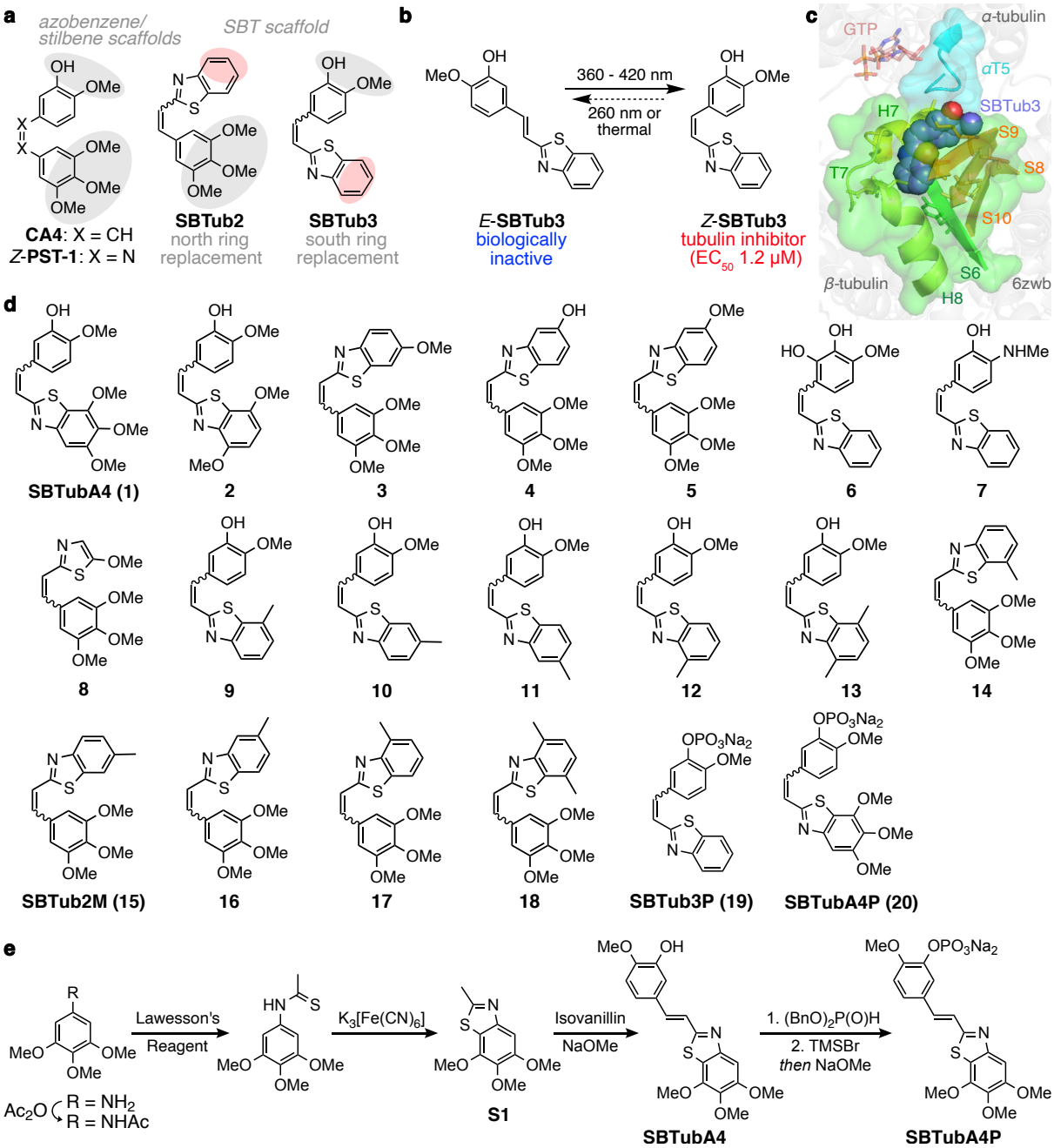

Figure 1: Design and synthesis. (a) The colchicinoid pharmacophore (grey shaded trimethoxyphenyl south ring and isovanillyl north ring) can be applied to various scaffolds, giving photoswitchable azobenzene-based **PST** and SBT-based **SBTub** antimitotics. Previously published **SBTub2/3** lacked key interaction residues (red shaded sites). **(b)** *Z*-**SBTub3** inhibits tubulin polymerisation and MT-dependent processes. **(c)** X-ray structure of tubulin:*Z*-

SBTub3 complex (carbons as purple spheres). The south ring is buried in β-tubulin (green); only the north ring interacts with α-tubulin at the α-T5 loop (cyan). **(d)** Evolved **SBTub** compound library used in this paper. **(e)** Typical synthesis of **SBTub**s proceeds by acetanilide sulfurisation, Jacobson cyclisation, and basic condensation. Phosphate prodrug **SBTubA4P** is further accessed by oxidative phosphoester formation and deprotection.

SBTubA4 was an early hit, with ca. 10-fold more potent *Z*-isomer binding than previous best **SBTub3** and with an excellent dark/lit ratio of 30 (**Table 1**; **Fig 2c**. We then tested if the *Z*-**SBTub**s obey similar structure-activity relationships as known for **CA4**. First, we rearranged the methoxy groups in **2**, reducing the *Z*-potency, which matched literature expectations[33] as the middle methoxy group on the south ring otherwise accepts a hydrogen bond from β-Cys239. We also flipped the SBT scaffold orientation in analogues **3-5**. This was not convenient for installing the hydroxy/methoxy north ring substituent pair, so in **3** and **4** we retained only one of these groups and the compounds suffered a predictable[33] though small loss of potency. The seven-fold potency loss when moving the methoxy group from the spacefilling 6-position to the 5-position which is best occupied by a small polar substituent[33] (compound **5**) was striking and expected. We concluded that indeed *Z*-**SBTub**s obey similar structure-activity relationships as **CA4**, which could guide further development.

At this stage we wished to test if common strategies to accelerate thermal *Z*→*E* relaxation and redshift spectral response in azobenzenes could also be applied to **SBTubs**. We created close steric matches of bioactive **SBTub3** but with tautomerisable *ortho*-catechol **6** and *para*-amino **7** groups. Since *o*-hydroxy derivatives of **CA4** have entered clinical trials[33], we were surprised that **6** gave negligible potency under lit (and dark) conditions; however **7** retained similar light-specific bioactivity as its isostere **SBTub3** (discussed below in section Photoswitch Performance).

Continuing potency optimisation, we also tested whether retaining the **CA4** methoxy groups on a reduced-size photoswitch would be beneficial. We created styrylthiazole (ST) **8** which can be considered a near-perfect isostere of **CA4**/**PST-1** minus the small polar hydroxyl group, or a shrunken analogue of **3**. As far as we know, STs have never been used in photopharmacology before. We considered them interesting as we expected them to retain the metabolic stability and GFP-orthogonality of SBT, while additionally being isosteric to the better-known azobenzene: which offers attractive possibilities for adapting known azobenzenes into potentially biologically more applicable ST-based photopharmaceuticals. **8** was accessed by closing the thiazole, starting from a methyl cinnamoylglycinate (see Supporting Information). Pleasingly, **8** gave strong *Z*-specific cellular bioactivity with ca. 100-fold photoswitchability (**Table 1**), although its 10-fold loss of potency compared to **1** suggested that we should explore **SBTubs** intermediate in size between **SBTub3** and **1**.

Therefore, for potency optimisation, we tested both adding methyl groups to **SBTub3** and "walking" them around the scaffold south ring (**9-13**); and also deleting the north ring hydroxy/methoxy substituent pair from **1** and replacing them with smaller methyls (**14-18**). Note that the SBT *Z*-isomers orient their sulfur towards the inner face of the molecule[16] so we did not rely on rotations around the alkene—benzothiazole single bond to 'reflect' substituents into similar positions (e.g. **9** vs **12**, or **10** vs **11**).

South ring derivatives **9-13** did not approach the potency of **1-5**, although **10-11** still have excellent performance (~1 μM *Z*-potency, ~100-fold photoswitchability of bioactivity). However, north ring derivative **SBTub2M** (**15**) in which the methyl group replaces the spacefilling OMe group, was six times as potent as its methoxy homologue **3** (*Z*-IC_{50} 35 nM) while having excellent photoswitchability of bioactivity (ca. 200-fold; **Fig 2c**). This makes it the most potent *and* the most photoswitchable of the photoswitchable antimitotics known. **16** (methyl at the small polar position) and **14** and **18** (methyl projecting to inner face, clashes with protein) were predictably weaker than **SBTub2M** (though **16** still has submicromolar *Z* activity and ca. 100-fold switching), while **17** that projects the methyl to the outer face (towards the exit tunnel) was well-tolerated (0.2 μM) and retained nearly 200-fold switching. It was highly satisfying that this methyl walk SAR also followed the SAR known for **CA4**, as this supports that their target and binding site are conserved.

Our second priority was to develop soluble **SBTubs** for *in vivo* use in multiorgan animal models, which do not easily tolerate even low amounts of organic cosolvents. We aimed to

formulate water-soluble **SBTub** prodrugs by phenol phosphorylation - an approach that has been generally successful for colchicinoid inhibitors (including clinically-advanced **CA4P**, **BNC105P** etc)[34]. We had initially produced **SBTub3P**, the phosphate prodrug of previous lead compound **SBTub3**, however its aqueous solubility was only moderate (<2 mg/mL) potentially due to aggregate formation by π-stacking of the planar compound. We synthesised **SBTubA4P** hoping that the out-of-plane central methoxy group would reduce π-stacking, which combined with the hydrophilicity of the three extra methoxy groups would give better solubility, as we have seen in other contexts[6,19]. Indeed, **SBTA4P** dissolved to at least 10 mM in water, which was to prove important in later assays. Both prodrugs **SBTubA4P** and **SBTub3P** had similar cellular *Z* and *E* potencies as their drug forms.

In summary, we had developed **SBTubA4** and **SBTub2M** as mid-nanomolar antimitotics with 30-200-fold photoswitchability of bioactivity for cell culture studies (both cross-validated on A549 lung carcinoma cell line, **Fig S5**); and we had further developed **SBTubA4P** as a convenient fully water-soluble prodrug of **SBTubA4** for *in vivo* applications. These became the focus of our further biological evaluations.

Table 1: cytotoxicity EC_{50} values (mostly-*Z* lit (360-450 nm) and all-*E* dark) and dark/lit EC_{50} ratio; and standard photoactivation working concentration $[I]_{WC}$ (defined later), all in HeLa cell line.

	EC_{50} (μM)		**EC_{50} ratio**	**$[I]_{WC}$**
compound	lit	dark	dark / lit	(μM)
SBTub2	1.4	>25	>18	6.0
SBTub3	1.2	>25	>21	3.2
SBTubA4	0.12	3.8	31	0.21
2	0.52	>100	>190	1.6
3	0.20	15	75	0.65
4	0.67	9.3	14	1.5
5	1.4	18	13	3.2
6	23	27	n.d.	n.d.
7	2.6	>35	>13	n.d.
8	1.2	>100	>83	3.0
9	1.0	48	48	2.6
10	3.0	>100	>33	10
11	1.7	>100	>58	4.3
12	0.77	64	83	1.6
13	0.42	8.8	21	1.8
14	1.0	>15	>14	2.7
SBTub2M	0.035	7.0	200	0.06
16	0.52	48	92	1.1
17	0.23	40	174	0.65
18	3.0	>15	5	10
SBTub3P	3.4	>20	**>5**	7.5
SBTubA4P	0.052	0.45	8.7	0.10

2.2. SBTub photoswitch performance studies

The photoresponses of most **SBTub**s (**1-5** and **9-20**) were similar to previously reported SBTs **SBTub2/3**,[16] with absorption maxima and absorption cut-offs being excellently balanced for both efficient *E*→*Z* photoswitching with the common 405 nm microscopy laser, and for full orthogonality to GFP imaging (ca. 488 nm). The separated π→π* absorption maxima for *E*- (~360 nm) and *Z*-isomers (~330 nm) enable efficient directional *E*→*Z* photoisomerisation at 360-420 nm reaching ca. 80% *Z* (**Fig 2a-b**), and extinction coefficients at 405 nm were up to twice those of similar azobenzenes (**Fig 2b**), promising high-efficiency photoactivation on the confocal microscope. Importantly, *E*- and *Z*-SBT absorptions drop sharply towards zero above 410 nm (**Fig 2b**, **Fig S1-S2**) which is crucial for avoiding photoresponse to 488 nm GFP imaging under high-intensity focussed lasers, as well as with broader filtered excitation sources e.g. 490±25 nm: since absorption "tails" extending far beyond band maxima can otherwise cause substantial photoswitching. (For example, 561 nm RFP imaging on the confocal microscope photoisomerises azobenzene **PST-1** despite its extinction coefficients

being < 30 $cm^{-1}M^{-1}$.[21]) However, the **SBTubs**' cutoff suggested they would indeed be GFP-orthogonal: which was later confirmed and found to be crucial for *in vivo* use (see below).

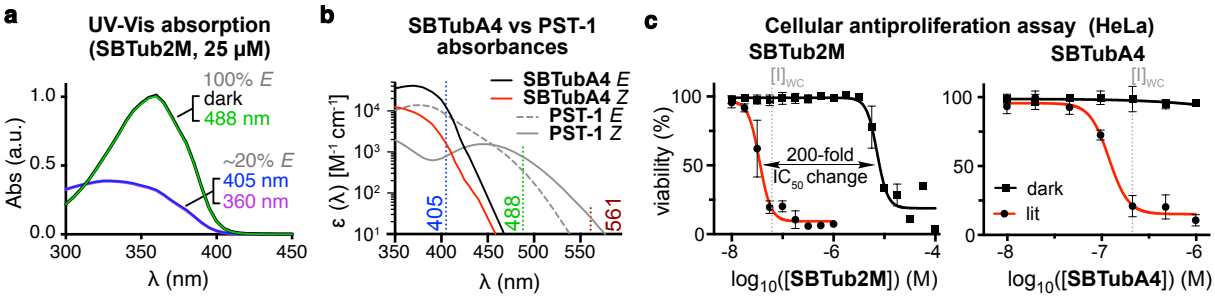

Figure 2: Photocharacterisation. (a) SBTub2M is not isomerised from its all-*E* "dark" state by 488 nm illumination, but is photoswitched to majority-*Z* "lit" states by UV/violet light (78% *Z* at 405 nm by NMR; 50:50 PBS:DMSO). **(b)** Comparison of absorbance spectra of **SBTubA4** and azobenzene **PST-1** illustrates the SBT's ideal match to 405 nm photoactivation, combining stronger 405 nm absorption, with sharper absorption cut-off above 405 nm which makes it orthogonal to GFP (488 nm), YFP (514 nm) and RFP (561 nm) imaging. **(c)** Leads **SBTub2M** and **SBTubA4** have highly nonlinear dose-response profiles, high lit/dark ratio of bioactivity, and mid-nanomolar $[I]_{WC}$ values.

In biological settings (>360 nm) and on the population level, these SBTs act similarly to photoactivation probes: (i) illuminations all give similar majority-*Z* equilibrium photostationary states (PSSs) in the photoresponsive spectral region (360 - ca. <440 nm), and (ii) they show no significant (<2%) *Z*→*E* thermal relaxation after hours in physiological buffers at pH~7 at 25°C (**Fig S3**-**S4**). However, they have all the other practical advantages of photoswitches that are relevant to most research uses[11] (no toxic/phototoxic byproducts, fast illumination response, no non-optical drug activation mechanisms, and stocks can be quantitatively relaxed to *E* by warming to 60°C which is advantageous for stock handling over sequential assays). Their photostability to continuous illumination at >380 nm was excellent. These features are shared with previously-reported **SBTub2/3**.[16]

We used *ortho*-hydroxy **6** and *para*-amino **7** to test if strong electron donor groups that can tautomerise to freely-rotatable quinoids (C-C single bond instead of C=C), can accelerate thermal *Z*→*E* relaxation to make better-reversible **SBTubs**; and if these would induce spectral redshifting. However, in cuvette, *Z*-**6/7** thermally relaxed only slowly (halflives >> hours), and since *Z*-**7** gave similar cytotoxicity in the longterm cellular assay as its isostere **SBTub3**, we concluded that its cellular relaxation was not fast on a biological timescale either. The spectra of **7** were redshifted by nearly 60 nm compared to typical SBTs putting the *E*-**7** absorption maximum exactly at the 405 nm laser line (**Fig S1**), however, as neither **6/7** brought relaxation rate benefits, we did not pursue them.

Styrylthiazoles as in **8** have not yet been studied as scaffolds for photopharmaceuticals[13]. We were pleased that its isomers' spectra were only ca. 25 nm blueshifted compared to the SBTs (giving less efficient isomerisation at 405 nm), and all other properties, such as its completeness of *E*→*Z* photoswitching, were similar to the SBTs. We believe this opens up new possibilities for GFP-orthogonal, metabolically-resistant photoswitches that are isosteric to azobenzenes, and so can replace them for applications where these biologically advantageous properties are required.

Given that each SBTub reached a PSS that was nearly invariant with excitation wavelengths in the range 360-440 nm, we defined a single "typically useful working concentration" **$[I]_{WC}$** for cell culture use in HeLa cell line by closer examination of the dose-response curves (**Fig 2c**, **Table 1**, **Fig S5**). At $[I]_{WC}$, illuminated cells should experience strong inhibition while non-illuminated cells experience insignificant inhibition. We systematically define $[I]_{WC}$ as *either* the lowest concentration where the lit efficacy reaches >80% of its plateau, *or* the highest concentration where treatment in the dark causes <10% difference of biological effect as compared to the untreated control: whichever is the lower. Szymanski has previously proposed an alternative working concentration metric $[I]_{opt}$, to maximise illuminated efficacy, which is based on idealised highly nonlinear dose-response curves[4] that are very rarely obtained in practice. Our empirical $[I]_{WC}$ instead emphasises that baseline/background

inhibition of the system must be minimal for photopharmaceutical control to be biologically useful. For example, even when IC_{50} values are well-separated, $[I]_{WC}$ values are undefined if background bioactivity is too strong for the reagent to be useful (e.g. **7**, **Table 1**). We believe that ranking by $[I]_{WC}$ is the most useful systematic single-value method for early-stage optimisation of photopharmaceuticals' general performance, and that $[I]_{WC}$ will come to find traction in the community.

For all further details, including full discussion of photoswitch performance of **6**/**7** and of *E*-**SBTub** toxicity, see Supporting Information including **Fig S1-S3**.

2.3. SBTubs isomer-dependently target tubulin in cells

To test their cellular mechanism of bioactivity, we first examined the **SBTubs'** isomer-dependent inhibition of polymerisation of purified tubulin protein in a cell-free assay. Both leads **SBTubA4** and **SBTub2M** were non-inhibiting in the all-*E* dark state, permitting tubulin to polymerise as in the cosolvent control (**Fig 3a**). However, in the majority-*Z* illuminated state they were potent inhibitors that suppressed polymerisation entirely to baseline readout levels, comparable to the archetypical colchicinoid nocodazole. Matching the antiproliferation assays, they were significantly stronger inhibitors than first generation **SBTub3** (**Fig 3a**).

If microtubule inhibition is also the main cellular mechanism of action of *Z*-**SBTubs**, we would expect ***Z*-SBTub**-treated cells to show G_2/M-phase cell cycle arrest due to mitotic checkpoint failure.[12] We therefore used flow cytometry-based analysis to quantify cell cycle repartition. *E*-**SBTubs** caused either no change or small changes compared to controls, whereas G_2/M arrest was strongly induced by *in situ*-lit (mostly-*Z*) **SBTubA4P** and **SBTub2M** (**Fig 3b**, **Fig S6**).

As G_2/M-phase arrest is necessary but insufficient to conclude on cellular tubulin inhibition being their major mechanism of action, we next performed confocal microscopy imaging of the MT network architecture in immunofluorescently stained cells, to obtain a direct readout of tubulin-inhibiting effects. *In situ*-illuminated **SBTubA4P** treatment caused microtubules to curve and MT architecture to break down,[35] but *E*-**SBTubs** caused no disorganization at corresponding concentrations in the dark, matching cosolvent controls (**Fig 3c**). This matches the assumption that their photoswitchable cytotoxicity arises from their *Z*-isomers potently inhibiting MT dynamics and stability in cells. While microscopy is a qualitative method that can misrepresent population-level statistics, the quantitative cell cycle data from flow cytometry (10^4 cells per condition) as well as the qualitative match to previous SBTub work[16] give confidence to this result.

Lastly, to check our assumption that *Z*-SBTubs act as colchicinoids, we crystallised the *Z*-**SBTub2M**:tubulin DARPin D1 (TD1) complex. X-ray diffraction studies showed that *Z*-**SBTub2M** indeed directly binds tubulin at the colchicine site (**Fig 3d**) very similarly to **CA4**, even with the same orientation of its substituents (**Fig 3e; Fig S11a-f**). This explains why the **SBTub** SAR determined in this study (**Table 1**) matched to that known for **CA4**. It also highlights the plasticity of the binding site, which accepts such differently-sized inhibitors.

Taken together, these cell-free and cellular assays support that the **SBTubs** act as light-dependent tubulin inhibitors in cells, with their *Z*-isomers binding potently at the colchicine binding site and their *E*-isomers having no effects at the corresponding concentrations.

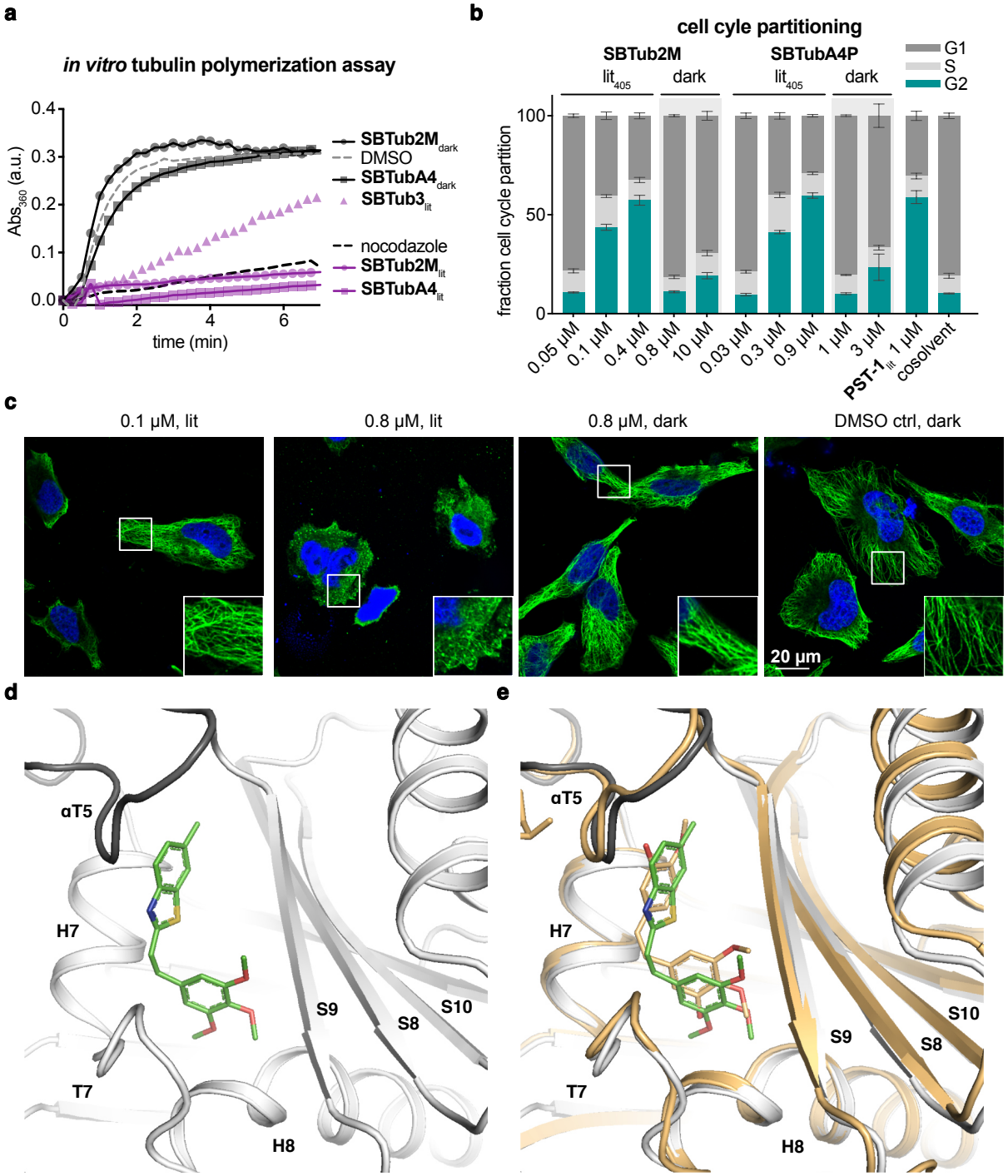

Figure 3: Tubulin-specific cellular mechanism. (a) SBTubs light-dependently inhibit tubulin polymerisation (turbidimetric cell-free assay; absorbance mirrors the degree of polymerisation; "lit" denotes use of **SBTubs** (20 µM) pre-isomerised to majority-*Z* PSS with 405 nm, nocodazole control at 10 µM. **(b)** Cell-cycle analysis of Jurkat cells treated with **SBTub2M** and **SBTubA4P** matches photoswitchable reference **PST-1**: with significant G_2/M arrest under 405 nm pulsing ("lit"), but without cell cycle effects in the dark (matching cosolvent controls). **(c)** Immunofluorescence imaging of cells treated with **SBTubA4P** under pulsed 405 nm illuminations ("lit", mostly-*Z*) and in the dark (all-*E*), compared to cosolvent control (HeLa cells, 20 h incubation; α-tubulin in green, DNA stained with DAPI in blue). **(d)** Close-up views at the colchicine-binding site of X-ray crystal structure of the Darpin D1:tubulin:*Z*-**SBTub2M** complex (dark grey α-tubulin, light grey β-tubulin in cartoon representation; *Z*-**SBTub2M** in stick representation with carbons green, oxygens red, nitrogen blue, and sulfur yellow. **(e)** Superimposition of tubulin:**CA4** (orange carbons; PDB 5LYJ) and TD1:*Z*-**SBTub2M** (green carbons) structures (see also **Fig S11a-f**).

2.4. SBTub photocontrol enables cell-precise, temporally reversible MT inhibition in 2D cell culture

Aiming later to apply **SBTubs** to photocontrol MT dynamics in complex models and *in vivo*, we now switched to using the fully water-soluble prodrug **SBTubA4P**. This is an important step: (i) it avoids cosolvents that can be problematic for *in vivo* toxicity; and (ii) it prevents hydrophobic adsorption onto the matrix materials (PDMS, collagen, agarose) that are used in 2D structured surfaces, 3D cell culture/organoid models, and for embedding motile animals during longterm imaging. Avoiding adsorption is important in our experience, as hydrophobic compounds can exhibit irreproducible apparent potencies or effects in these settings, which is timewise- and ethically prohibitive for resource-intensive low-throughput animal studies.

Before performing animal work, we probed the spatiotemporal resolution that **SBTubs** could achieve for *in situ*-photoswitching-based control over MT dynamics, in 2D cell culture. Using spinning disc confocal live cell microscopy we imaged **SBTubA4P**-treated cells transfected with a fluorescently-labelled fusion of the MT end binding protein EB3, to directly monitor MT polymerisation dynamics during photoswitching.[16] This is possible since EB3 labels the GTP-cap of MTs, so EB3-tdTomato acts as a fluorescent marker revealing the tips of polymerising MT plus ends in cells as hundreds of dynamic "comets" that cascade through the cell at significant velocities (tdTomato excitation at 561 nm).[36] Our protocol for cell-precise photoswitching of MT dynamics, with internal controls for compound application and for photobleaching, was as follows. We imaged transfected cells before **SBTubA4P** application to establish untreated MT dynamics baselines, simultaneously controlling for effects of 405 nm laser pulses on single selected cells (targeted by region of interest (ROI) illumination); then we added *E*-**SBTubA4P** to these same cells, and continued imaging the whole field of view while applying targeted pulses of the 405 nm laser to a single ROI-selected cell.

SBTubA4P enabled repeatable cycles of temporally reversible, photoswitching-induced inhibition of MT dynamics in live cells, with single-cell spatial targeting precision and second-scale onset time precision (**Fig 4a-b**, **Movie S1**). In **SBTubA4P**-treated ROI cells, within seconds upon each single frame 405 nm pulse, polymerising MT tips stop moving and disappear, then more slowly reappear and resume movement (best seen in **Movie S1**). Statistics collected over multiple independent experiments showed these inhibition spikes are highly reproducible; recovery towards uninhibited baseline has a halflife of ca. 25 s, which we attribute to the diffusion of *Z*-**SBTub** out of the ROI cell (**Fig 4a**). There were minor effects on MT dynamics in treated non-ROI neighbour cells as compared to pre-treatment controls; and the 405 nm pulsing protocol alone did not cause any readout changes (**Fig 4a**).

We also modified this protocol to apply single frame 405 nm pulses to the whole field of view instead (**Fig 4c**, **Movie S2**). As expected, this confirmed the temporal precision of onset and the temporal reversibility of the spiking seen with the single-cell-resolved studies; though the video data are easier to interpret as they are even more visually impressive (**Movie S2**). Finally, we performed full-field-of-view imaging while applying a train of 47 frames of 487 nm pulses, to test whether **SBTubA4P** can be used orthogonally to GFP imaging wavelengths. Indeed, even at this high concentration (6 µM, 40×$[I]_{WC}$), there was no induction of MT inhibition, so we concluded that **SBTubA4P** is indeed GFP-orthogonal (unlike azobenzene-based photopharmaceuticals)[16], matching our design and expectations for GFP orthogonality by absorption cut-off (**Movie S3**; **Fig 4c**).

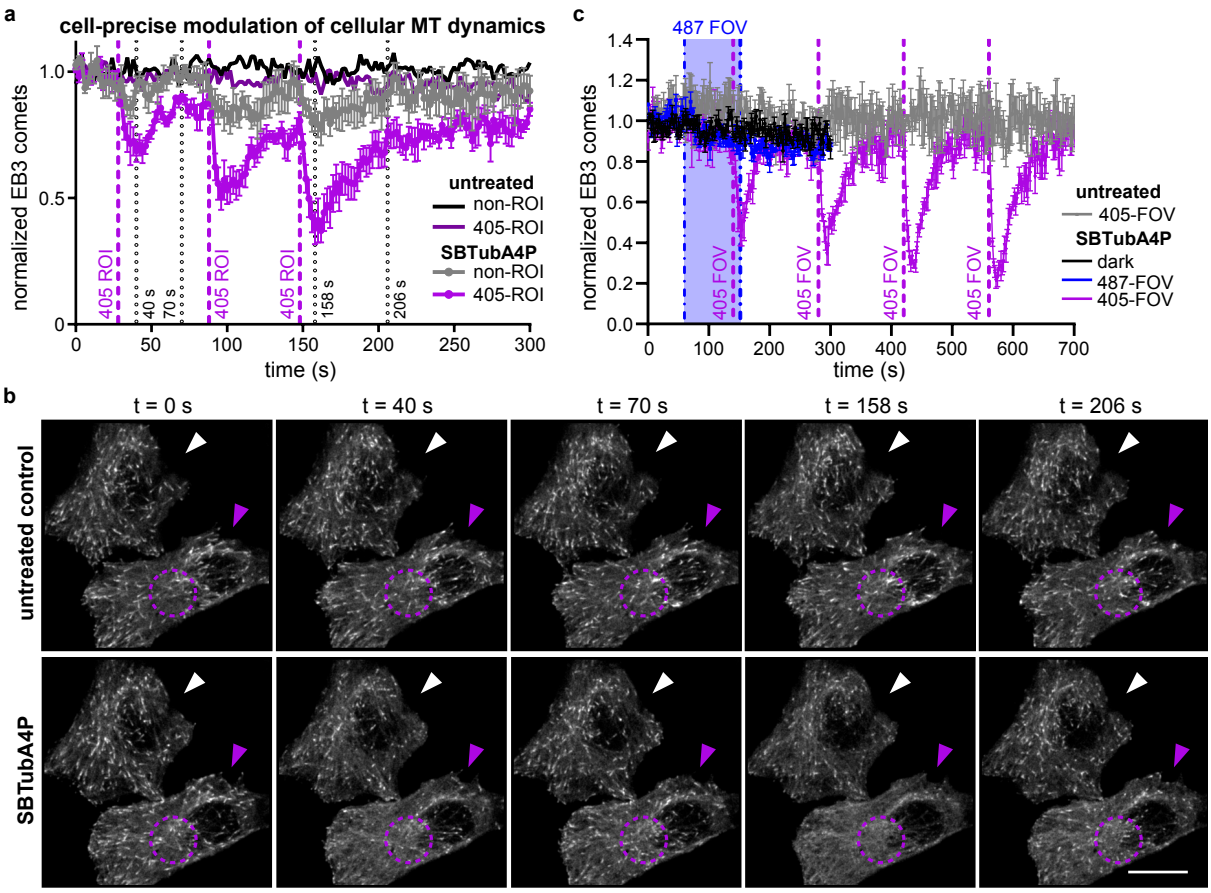

Figure 4: Spatiotemporal control over MT dynamics in 2D-cultured HeLa cells. (a-b) MT inhibition in **SBTubA4P**-treated cells is initiated only upon 405 nm illumination pulses and only in ROI-targeted cells (data related to **Movie S1**; live cell EB3-tdTomato "comets" quantify polymerising MTs). **(a)** Comet count statistics are similar to cosolvent-only baseline in both ROI-pulsed-cosolvent and non-ROI-**SBTubA4P** conditions; ROI-**SBTubA4P** statistics show inhibition spikes. **(b)** Stills from **Movie S1** at the times indicated in **(a)**, initially during the untreated timecourse, then during the **SBTubA4P**-treated timecourse on the same cells. Purple arrowhead indicates the ROI cell, purple dotted circle indicates where the 405 nm ROI is applied at times 26 s, 88 s and 148 s, white arrowhead indicates the non-ROI cell quantified as internal control (scale bar 15 μm). **(c)** EB3 comet counts of cells imaged at 561 nm only ("dark," grey), with 47 frames at 487 nm applied to full field of view during the time span indicated with dashed lines ("487," cyan) and **SBTubA4P** (6 μM), or with single-frame 405 nm pulses, **SBTubA4P** (0.6 μM), applied to full field of view at times indicated with dashed lines ("405," violet) (n = 3 cells). Temporally precise onset and full field diffusional reversibility are shown (data related to **Movies S2-S3**). (a,c: mean ± SEM EB3 comet counts as normalized to the means of the first 5 timepoints; 405 nm ROIs applied at indicated times; for further details see Supporting Information).

From cell culture, to MT photocontrol in 3D models, tissue explants, and animals

By now we had optimised the potency of metabolically stable, GFP-orthogonal photoswitchable **SBTub2M** and fully water-soluble analogue prodrug **SBTubA4P**, clarified the **SBTubs'** tubulin-specific cellular mechanism of action, and shown high-spatiotemporal-resolution photocontrol of MT dynamics in 2D cell culture. We were now primed to tackle the central photopharmacology research challenge, which has so far frustrated essentially all prior approaches: *in vivo* translation using systemic administration but local photocontrol, that clearly and usefully retains a defined cellular mechanism of action. We set out to test if **SBTubs'** performance features would permit this operation across a *range* of complex models from 3D culture, to 3D tissue explant, to two *in vivo* animal models: with spatiotemporally-localised illuminations photocontrolling the full sequence of their bioactivity (from suppressing MT polymerisation, to altering/depolymerising MT network structures, to reducing/stopping microtubule-dependent downstream processes), where appropriate with second-level resolution, but all with cellular precision.

2.5. SBTub photocontrol in 3D organoids enables spatially-targeted blockade of migration and mitosis in the long-term

We first tested **SBTubA4P** in 3D human mammary gland organoids grown from isolated patient tissue embedded in collagen gels. These resemble miniaturized and simplified organs with realistic micro-anatomy, and feature collective motility/invasion behaviour directing cells to migrate and proliferate to form ordered, branched structures.[37,38] Controlling organoid morphology is a sought-after goal, which has been mostly interpreted as requiring spatiotemporal control of gene expression, for which optogenetic approaches have been suggested.[39] Yet, the spatiotemporally-localized application of photochemical compounds offers an alternative, in which the possibility of *instantaneous* cellular response to stimulus is highly attractive for temporally-precise control. Based on the good performance of **SBTubA4P** in 2D cell culture, we assessed whether **SBTubA4P** can be controlled similarly precisely in a 3D organoid model, aiming to manipulate organoid development by locally interfering with the invasion of individual branches during the elongation phase[38].

Though the actin cytoskeleton is the major driver of cell migration, MTs are integral to directional migration and leading edge stabilisation[21,40,41] (as well as to proliferation): so we expected the single-cell motility as well as cell division rates could be locally affected. Therefore, we wished to test if repeated localized photoactivations of **SBTubA4P** (every 7 min) could be used over long timescales (>24 h) to inhibit outgrowth of light-targeted organoid branches, while leaving other branches of the same organoids to develop: so shaping and modulating cell migration and invasion with spatiotemporal control. This aim brings conceptual challenges for photopharmaceuticals: since all cells are exposed to the same drug concentration, and over long timescales the cumulative impacts of scattered photoactivation light, of diffused isomerised compound, and of imaging light itself, may build a spatially-nonspecific background pattern of bioactivity. Organoid morphology does not tolerate >0.1% organic cosolvent either, making full solubility important.

We first determined a suitable working concentration for **SBTubA4P** without spatially resolved activation, by monitoring organoid areas for morphological disruption under lit/dark conditions (**Fig S7a**). We determined an $[I]_{WC}$ of 200 nM for preventing organoid growth over 24 h with UV-lit **SBTubA4P**, whereas organoids looked healthy with no antiproliferative / branch-retracting effects at 500 nM in the dark (**Fig 5a, Fig S7a-b**).

Then, we applied localised UV ROI illuminations to selected organoid branches (ROI_{targ}) every 7 min, comparing to non-UV-illuminated internal control branches (ROI_{ctrl}). This allowed us to noninvasively block cell migration/invasion and proliferation with striking spatial resolution and longterm persistance. With **SBTubA4P**, development of ROI_{targ} branches was totally blocked over > 1 day (**Fig 5b-d**, **Movie S4-S5**); while no-compound controls showed no photo-inhibition of branch development (**Movie S7**, **Fig S7c**). Control branches displayed high motility and matrix invasion (green outline, **Fig 5b**) and their cells freely proliferated (yellow arrowhead, **Fig 5d**), resulting in considerable branch development. Out-directed motion of the collective branch fronts was continuous in ROI_{ctrl} regions (ca. 4.5 µm/h), but was almost completely stopped in ROI_{targ} (ca. 0.2 µm/h; **Fig 5c**). Overall development of branches, only entering ROI_{ctrl} areas, was however clearly visible without any statistical analysis (**Fig 5e, Movie S6**). Thus **SBTubA4P** can be used in 3D matrix cell culture settings to noninvasively control cell motility, invasion and proliferation, allowing photopatterning of branch growth and organoid development down to the spatial scale of individual cells.

2.6. SBTub photocontrol in intact 3D tissue explants allows temporally-precise MT depolymerisation and mitotic control in the short-term

We next tested **SBTub** performance and tubulin-specific mechanism of action when directed against the more complex 3D environment of live intact brain lobes of early third instar larval *Drosophila melanogaster* (fruit fly). Larvae are too motile for long-term imaging and the larval cuticle is largely impermeable, so neurodevelopment studies explant the whole brain. As the explant tolerates cosolvent, we took the opportunity to use **SBTub2M** in these assays to test the broader applicability of the **SBTub** design. Both the whole-organ and explant aspects bring significant challenges. (1) Compounds must permeate through two glia cell

layers to reach mitotically active neural stem cells (neuroblasts). This forces the use of high bath concentrations and potent compounds: however, since surface and surrounding cells are exposed to far higher concentrations than central cells, only potent compounds with *extremely high photoswitchability of bioactivity* ("FDR"; discussed in[19]) can be used: otherwise outer cells die, and morphology and physiology are lost. Indeed, we could use high concentrations of high-FDR **SBTub2M** (30 µM) in brain explants without noticeable toxicity. (2) Using multiple fluorescent protein labels for multiplexed imaging is a typical requirement to achieve useful readouts in biology, but can block chemical photoswitch applications. The most common long-wavelength fluorescent proteins for animal work are excited at 561 nm, which forces the use of GFP (488 nm) or YFP (514 nm) fusions as the next-longest-wavelength markers. For example, to image both MTs and cellular structural elements, we used animals expressing the microtubule-binding protein mCherry::jupiter[42,43], and cortical structure marker sqh::GFP (spaghetti squash, the regulatory light chain of the non-muscle type 2 myosin, fused to eGFP[44]). With hemithioindigo or azobenzene reagents, such two-channel FP imaging would isomerise the photoswitch throughout the sample due to photoresponse at ≤530 nm (Fig 2b), so destroying spatiotemporal specificity in the study zone. In contrast, the non-response of the GFP-orthogonal SBT to 488 nm imaging avoids any photoisomerisation during typical two-channel FP imaging, allowing precise temporal control of activation in our experiments.

We transferred freshly-dissected brain explants into 30 µM **SBTub2M** and started imaging after 30 minutes loading (**Fig S8**). We imaged in both mCherry (ex 561 nm) "red channel" and GFP (ex 488 nm) "green channel" for 15 minutes to establish baseline, then photoactivated **SBTub2M** throughout the imaging stack volume with 405 nm. Photoactivated **SBTub2M** depolymerised centrosome microtubules within 60 s (**Fig 5f** and **Movie S8-9**, MTs shown in white). To control for target specificity, we also used mCherry::tubulin[45] for imaging MTs, and observed similar behavior (**Movie S10-11**). As microtubules are rapidly nucleated in prophase centrosomes, we quantified the loss of centrosomal fluorescence signal after activation as a highly conservative estimate of centrosome MT depolymerisation. We saw dramatic, temporally-resolved signal reduction at the approx. 45 s activation period, while **SBTub** controls were unaffected (**Fig 5g**). We used the second FP channel to image Sqh::GFP, a marker of the cell actomyosin cortex, which plays a key role in neuroblast asymmetric division[46,47]. Normally dividing neuroblasts accumulate Sqh::GFP at the cell cleavage furrow during anaphase. Neuroblasts in which **SBTub2M** was photoactivated retain uniform cortical Myosin, indicating mitotic arrest in the absence of mitotic spindles[46] (cyan arrows, **Fig 5f**).

Previous short-term results imaging EBs at low **SBTub** concentrations in 2D cell culture had illustrated only its capacity to spatiotemporally block MT polymerisation (**Fig 4**). Now, these useful results in the intact brain underlined that **SBTub2M** maintains its *Z*-isomer-specific, MT-depolymerising mechanism of action in live tissue explant, casting **SBTubs** as flexible and powerful tools for cytoskeleton photomanipulation in complex 3D settings.

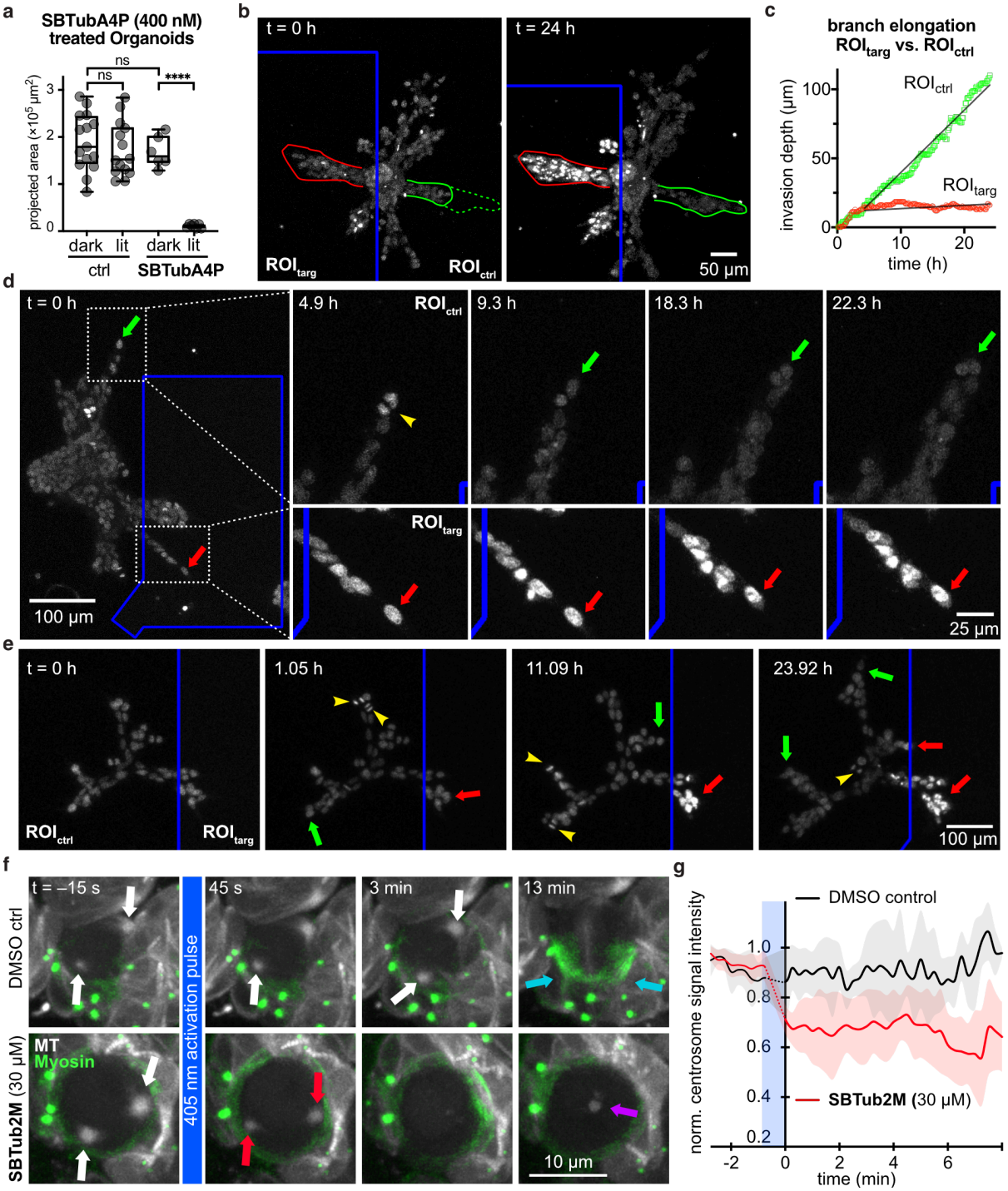

Figure 5: Spatiotemporal control over MT architecture, migration and mitosis in 3D culture and tissue explant. (a) 3D human mammary gland organoids embedded in collagen gels only have inhibited branch outgrowth when treated with both **SBTubA4P** and UV pulses. **(b)** Local applications of UV light to ROI_{targ} regions of **SBTubA4P**-treated organoids (blue boxed zone, one ca. 450 ms pulse per 7 min per z-stack) stops branch proliferation and outgrowth (red outline), while branches in untargeted ROI_{ctrl} regions develop dramatically (start: solid green line, final: dotted green line) (related to **Movie S4**). **(c)** Radial progress of branch tip fronts (directed and collective behaviour) in ROI_{targ} and ROI_{ctrl} regions. **(d)** Still image timecourse, zoomed on a branch tip in the ROI_{ctrl} (blue outline) region, showing cell proliferation (yellow arrowhead) and matrix invasion (one representative of the migrating cells is tracked over time with green arrows); while branch tip of ROI_{targ} region has static non-proliferating cells and even slight branch retraction (red arrows) (data related to **Movie S5**). **(e)** branch progression and proliferation are unimpeded and continuous in ROI_{ctrl} regions, while ROI_{targ} regions are static and branches growing into the ROI_{targ} stop their growth (colour code as in **(e)**, data related to **Movie S6**). (**a-e**: cell location in organoids tracked with siRDNA nuclear stain imaged at 647 nm). **(f)** Whole field of view 405 nm photoactivation of **SBTub2M**-treated intact 3D brain explants of larval *D. melanogaster* (bottom row) causes neuroblast centrosomes (red arrows) to rapidly shrink in size and signal intensity (45 s and 3 min) and prevents the cell from progressing

through division (13 min). Some MT signal accumulates at mid-cell at later time points (purple arrow) (data related to **Movie S8**). In DMSO-only controls (top row), centrosome integrity (white arrows, 45 s and 3 min) and progression through the cell cycle (13 min) are unaffected, indicated by myosin accumulation at the cleavage furrow (cyan arrows) (data related to **Movie S9**). (MTs in white (Jupiter::mCherry imaged at 561 nm), myosin in green (Squash::GFP imaged at 488 nm.) **(g)** Relative mCherry fluorescence intensity of centrosomal ROIs in **SBTub2M**-treated prophase neuroblasts (red) after activation at 405 nm drops notably during the approx. 45 s activation period (blue box) as compared to the DMSO control prophase neuroblasts (black). Signal intensities are shown as the proportion of the per-cell maximum pre-activation signal intensity. (Shading indicates ±1 standard deviation, 1-2 centrosomes quantified from a total of 5 (DMSO) or 5 (**SBTub2M**) neuroblasts from 3 different animals). For details see Supporting Information.

2.7. SBTub photocontrol in live animals enables targeted blockade of embryonic development and cell-precise temporally-reversible inhibition of MT dynamics

Encouraged by performance in 3D models, we evaluated using **SBTubs** for *in vivo* photocontrol. First we studied the effects of *in situ* photoactivations of **SBTubA4P** on the development of *Xenopus tropicalis* clawed frog embryos. During the initial 48 h of development, embryos normally transition over many division cycles from cell spheres through the blastula stage through to multiorgan tadpoles (**Fig S9a**). Initially we tested the effects of **SBTubA4P** in the earliest stages of development, just after embryonic divisions had started, by treating 2-cell stage embryos with *E*-**SBTubA4P** (1 hour loading, then medium exchange and optional *in situ* embryo-localised 410 nm photoactivation pulse during washout; note that this *transient* exposure to the **SBTub** parallels what could be expected for e.g. systemic *i.v.* administration in mammalian models - further discussion in Supporting Information). Embryos only failed to develop morphologically over the subsequent 2 days if they had received the 410 nm photoactivation; embryos without photoactivation developed normally (**Fig 6a-b**). We also tested interfering with development at the later blastula stage (>64 cells) by a similar protocol. While subsequent morphological development was normal under lit and dark conditions (**Fig S9b-c**), sensorimotor responses to mechanical stimulation[48] were suppressed by lit **SBTubA4P** only (**Fig S9e**, **Movie S12**). Interestingly, the tubulin-inhibiting azobenzene photoswitch **PST-1P** (**Fig S9e**) light-*independently* suppresses sensorimotor responses. We believe the SBT's success may reflect its greater metabolic robustness (see Supporting Information); and at any rate, it indicated that **SBTubs** are suitable for *in vivo* use.

Finally, we switched to highly spatiotemporally-resolved *in vivo* MT-imaging studies that would test **SBTubA4P**'s mechanism of action in the zebrafish *Danio rerio*, when systemically applied and maintained in the bath medium.

We first determined useful working concentrations in zebrafish, incubating 24 and 48 hpf (hours post fertilisation) embryos in **SBTubA4P** under lit and dark conditions. While zebrafish morphology remained unaltered in all dark **SBTub** treatments, 24 hpf embryos treated with lit **SBTub** showed major morphological changes even down to 1 µM, whereas more developed 48 hpf embryos showed similar morphological changes only at higher **SBTubA4P** concentrations e.g. 25 µM (**Fig 6c, Fig S10**). Again, we compared these effects to those of azobenzene reagent **PST-1P**, now observing a dramatic difference: even 25 µM lit **PST-1P** did not interfere with development at either the 24 hpf or 48 hpf stage (**Fig 6c, Fig S10**). This argues still more conclusively than **Fig 6b**, that the SBTub scaffold is uniquely suitable for light-controlled biological effects, compared to the previously known azobenzene scaffold. Lastly, we checked the lower-potency soluble prodrug **SBTub3P** in the same assay; matching expectations, it caused only weak changes at 24 hpf and no visible changes at 48 hpf (**Fig S10**), showing the necessity of the potency optimisations we performed in this study.

Aiming to test the MT-modulating effects of **SBTubs** in a challenging live animal system, we therefore decided to proceed with 48 hpf zebrafish embryos, and an **SBTubA4P** working concentration of 25 µM. We took 48 hpf embryos coexpressing EB3-GFP and histone H2B-mRFP as a nuclear marker,[49,50] loaded them with 25 µM *E*-**SBTubA4P** for 4 h, then washed and embedded them in agarose. Imaging at 488 nm caused no suppression of EB3 comets, confirming **SBTubA4P**'s GFP orthogonality *in vivo*. However, photoactivation with the 405 nm laser at a single point caused EB3 comets to vanish rapidly in cells around the targeted region, recovering over ca. 10 minutes. Cells further from the targeted region were predictably less inhibited than those with direct contact to the photoactivation region. The photoactivation-

recovery cycle could be repeated multiple times during imaging (**Fig 6d-e, Movie S13-S16**). Not only microtubule polymerisation dynamics, but also mitotic progression, could be stopped by spatiotemporally-localised **SBTubA4** photoactivation *in vivo* (**Movie S16**). These experiments confirm that the SBT scaffold in general is viable for light-triggered *in vivo* studies, and that **SBTubA4P** when applied *in vivo* retains its mechanism of action as a potent, light-dependent MT inhibitor with excellent spatial specificity and satisfying temporal reversibility.

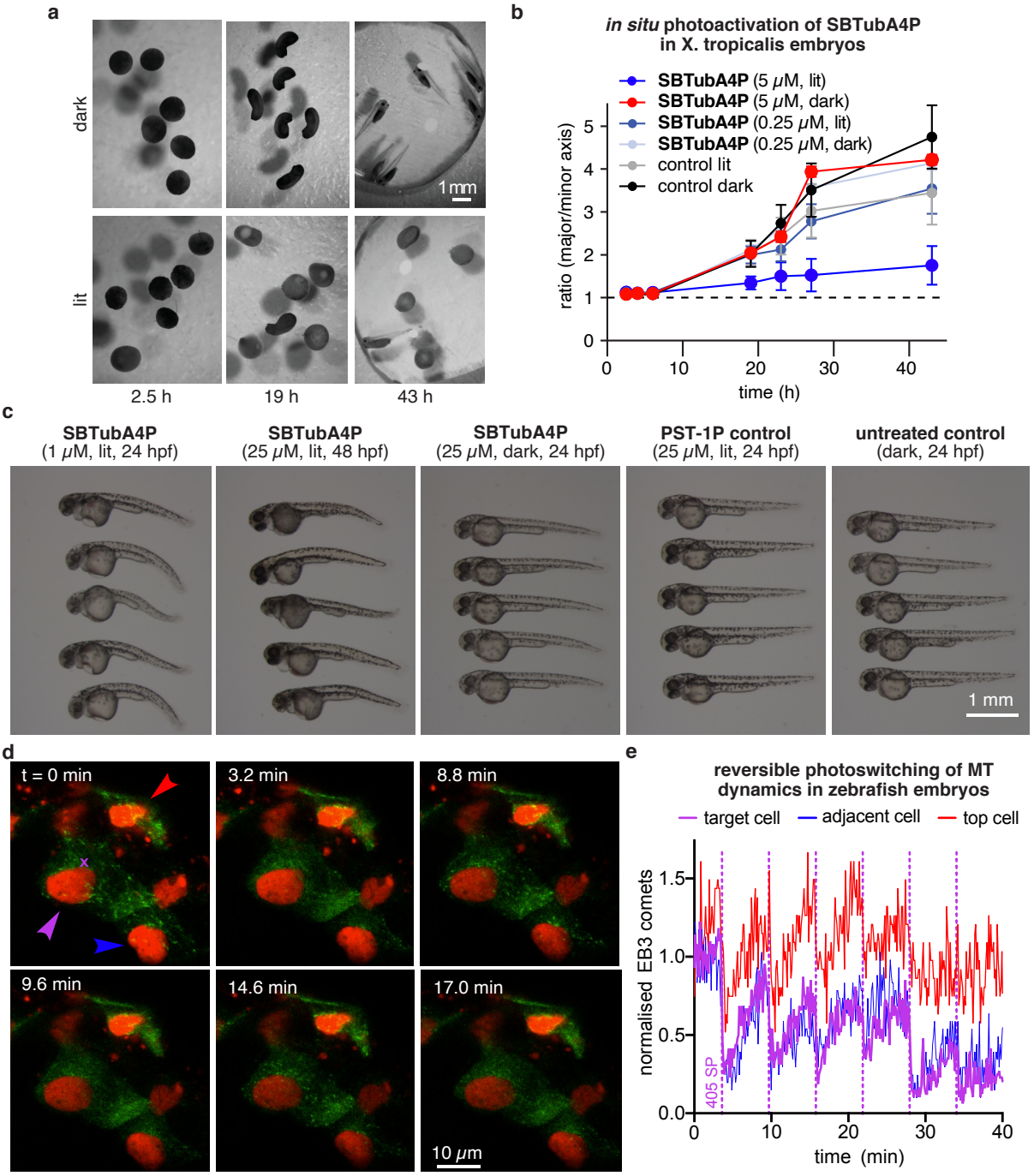

Figure 6: Photoinhibition of *X. tropicalis* development, and *in vivo* photocontrol of MT dynamics in *D. rerio*. **(a-b)** *Xenopus* embryos incubated with compounds for 1 h at the 2-cell-stage, before medium exchange optionally with 410 nm photoactivation. Embryos show irreversible development inhibition by *in situ*-formed *Z*-**SBTubA4** in lit conditions, but had no effects in the dark or with low concentration of **SBTubA4P** (**a**: **SBTubA4P** at 5 μM; **b**: development quantified by the ratio of major to minor embryo axis lengths, 6 embryos per conditions, mean ± SEM). **(c)** Development of *D. rerio* treated at the indicated stages for 24 h with **SBTubA4P** or control compounds under pulsed lit conditions (1 s/5 min) or dark. **SBTubA4P** (1 or 25 μM) causes morphological abnormalities only in the lit state, showing it remains effective *in vivo*. **(d-e)** reversible modulation of MT dynamics in 48 hpf zebrafish embryo. (EB3-GFP in green, histone H2B in red). (data related to **Movies S12-16**; see Supporting Information).

3. Conclusions

Noninvasive optical tools to modulate microtubule dynamics, structure and function with high precision, offer unique potential in the many fields of biology impacted by the spatiotemporally-resolved processes that MTs support: such as cargo transport, cell motility, cell division, development and neuroscience. Photopharmaceutical chemical reagents are conceptually elegant tools, in that they can be rapidly transitioned across models and settings, and they can be rationally designed for photoresponse patterns that interfere minimally with imaging while maximising optical response to a chosen photoactivation wavelength. Locally-applied photopharmaceuticals, particularly intraocularly-applied reagents for action potential control in the retina, have made great progress in adult mammalian disease models.[51,52] However, reaching the true potential of photopharmacology - achieving precisely-targeted *in vivo* applications by localised *in situ* photoactivations following systemic administration - remains an unsolved challenge. This would require combining high photoswitchability of bioactivity, high potency, metabolic robustness, aqueous solubility, and imaging orthogonality. Indeed, very few systemic *in vivo* applications of photopharmaceuticals have been made. As none of those have tested a defined mechanism of drug action, nor explored the optical-scale spatiotemporally-resolved targeting which is the only benefit of photopharmaceutical approaches as compared to conventional drugs,[53–55] the ability of photopharmacology to contribute useful systemically-applicable reagents for organism studies has remained unclear.

In this work we develop highly light-specific tubulin polymerisation inhibitors with unprecedented applicability from 2D cell culture, to 3D culture and whole-organ explant, to systemic *in vivo* administration with local photoactivation. Realising that the metabolic robustness and imaging orthogonality of a photopharmaceutical largely depend on its photoswitch scaffold, we consciously avoided the typical azobenzene photoswitch scaffold. Using the recently-developed SBT photoswitch, we created a panel of twenty **SBTubs**. We optimised potency and photoswitchability of bioactivity in lead **SBTub2M**; and we solubilised another lead to create **SBTubA4P** which does not require organic cosolvents. **SBTubs** are efficiently photoactivated with the common 405 nm laser, but their sharp absorption cutoff leaves GFP, YFP, and RFP channels free for multiplexed imaging of fusion protein markers without risking compound photoactivation. This is a highly desirable feature for areas of research where photopharmacology's optical precision can best contribute unique solutions on the cellular spatial scale (although we note that this runs against the goal of "photoswitch redshifting" that is near-universally cited by chemist photopharmaceutical designers). We cross-validated the **SBTubs'** molecular mechanism of action in cell-free, cellular and *in vivo* settings. **SBTubs** light-dependently interfere with mitosis in cell culture, and depolymerise mitotic spindles and ultimately block development *in vivo*; they can be optically patterned to control motility and branch development in 3D organoid cultures; and their photocontrol allows rapid-response, cell-specific inhibition of microtubule dynamics in cell culture and *in vivo*.

These consistent results across a range of models at different scales of time, length, and biological complexity, recommend the **SBTubs** as excellent and unique general-purpose tools for optically manipulating microtubule dynamics, microtubule structure, and microtubule-dependent processes with high spatiotemporal precision.

The proof-of-concept biological performance of the **SBTubs** has been very satisfying. We believe that the most valuable improvement to this system will now be to extend the temporal reversibility of inhibition (seen in 2D cell culture by diffusion to the medium with ca. 20 s halftime, **Fig 4**) to whole organ / whole animal settings. In these settings, diffusion is slower to achieve reversibility (ca. 10 min), so we seek techniques for *in situ* bidirectional isomerisation of **SBTubs** in our ongoing research. We believe that bidirectional photoswitching may be difficult within the biologically-compatible wavelength range[13]. However, accelerating thermal relaxation to the minute scale, which is probably the most appropriate scale for 3D / *in vivo* applications of interest, may be feasible, and efforts are underway.

In conclusion, the **SBTubs** are excellent photoswitchable microtubule-depolymerising reagents for use in cell culture, 3D culture, small explant, and early-stage animals. Their potency, flexibility and ease of use recommend them for high-spatiotemporal-precision

research across cytoskeleton biology; particularly, we feel, for cell-specific applications to motility and development, but they will also be of great interest in cargo transport, biophysics, cell polarity, neurodegeneration, and cell division. Lastly, we expect that by supporting conceptual innovations in photoswitch scaffold chemistry and rational photopharmaceutical design, and particularly by starting to unlock the applications promise of photopharmacology for globally-administered, locally-targeted *in vivo* use, this **SBTub** research represents a promising advance for high-performance photopharmacology against other protein targets in general, beyond their immediate impact on microtubule biology.

Funding Statement

This research was supported by funds from the German Research Foundation (DFG: Emmy Noether grant number 400324123 to O.T.-S.; SFB 1032 number 201269156 project B09 to O.T.-S. and project A10 to A.R.B.; SFB TRR 152 number 239283807 project P24 to O.T.-S.; and SPP 1926 number 426018126 project XVIII to O.T.-S.). J.C.M.M. acknowledges support from an EMBO Long Term Fellowship. J.T.-S. acknowledges support from a Joachim Herz Foundation Stipend. A.R.B. gratefully acknowledges the financial support of the European Research Council (ERC) through the funding of the grant Principles of Integrin Mechanics and Adhesion (PoINT). A.L. acknowledges funding from the Spanish government (Ministerio de Ciencia e Innovación), grant RTI2018-096948-B-100 (A.L.), co-funded by the European Regional Development Fund (ERDF). M.D.acknowledges funding from the Austrian Research Promotion Agency (FFG) project 7940628 (Danio4Can). C.C.C. is supported by NIH grant 1R01GM126029.

Acknowledgement

We are grateful to Henrietta Lacks, now deceased, and to her surviving family members for their contributions to biomedical research. We thank Monique Preusse for early cell viability testing, and Rebekkah Hammar for performing the tubulin polymerisation assay. We thank Christian Gabka from the Nymphenburg Clinic for Plastic and Aesthetic Surgery, Munich 80637, Germany for providing primary human mammary gland tissue.

Author contributions

L.G. performed synthesis, photocharacterisation, and long-term cellular studies, coordinated data assembly, and wrote the manuscript. J.C.M.M. performed live cell EB3 imaging during photoswitching, and assembled and quantified EB imaging data. A.V. performed zebrafish assays. I.E.R. performed organoid assays. C.H. performed cell viability assays, immunofluorescence staining, and cell cycle analysis. J.A.T. performed *Drosophila* experiments. M.W. performed structural biology. C.D.V. and B.T. performed clawed frog assays. J.S. and M.O.S. supervised structural biology. C.C.C. supervised *Drosophila* experiments. A.L. supervised clawed frog assays. A.R.B. supervised organoid assays. M.D. supervised zebrafish assays. A.A. supervised EB3 imaging. J.T.-S. performed cell cycle analysis, immunofluorescence microscopy, coordinated data assembly and supervised all other cell biology. O.T.-S. designed the concept and experiments, supervised all other experiments, coordinated data assembly and wrote the manuscript with input from all authors.

Declaration of interests

The authors declare no competing interests.

Supplementary Information

(1) PDF containing (i) chemical synthesis and NMR spectra (ii) photocharacterisation in vitro (iii) biochemistry (iv) biological methods and data (v) X-Ray crystallography data.

(2) Supplementary Movies:

Movies S1-S3*: Timestamps in mm:ss, HeLa cells transiently transfected with EB3-tdTomato imaged with 561 nm. Purple dots in* ***Movies S1-S2*** *indicate 405 nm illumination pulses; blue dots in* ***Movie S3*** *indicate 487 nm illumination pulses.*

Movie S1, temporally precise and cell-precise inhibitions of cellular MT polymerisation dynamics by photoactivations of *E*-SBTubA4P at 405 nm, related to

Figure 4a-b: no inhibition of MT polymerisation dynamics unless **SBTubA4P** is present (6 µM) and then 405 nm ROI illumination pulses (indicated by purple dot) are applied to the cell of interest (indicated by purple arrow) with minor impact on non-targeted neighbouring cell (indicated by white arrow) (EB3-tdTomato imaged at 561 nm).

Movie S2, temporally precise full-field-of-view inhibitions of cellular MT polymerisation dynamics by photoactivations of *E*-SBTubA4P at 405 nm, related to Figure 4c: no inhibition of MT polymerisation dynamics unless **SBTubA4P** is present (6 µM) and then 405 nm field of view (FOV) illumination pulses (indicated by purple dot) are applied (EB3-tdTomato imaged at 561 nm).

Movie S3, no inhibition of cellular MT polymerisation dynamics by illumination of *E*-SBTubA4P at 487 nm, related to Figure 4c: cells treated with *E*-**SBTubA4P** (6 µM) then imaged while 487 nm field of view (FOV) illumination pulses (indicated by blue dot) are applied show no inhibition.

Movies S4-S7*: primary human mammary gland organoids, cell nuclei stained with siRDNA and imaged at 674 nm. Blue rectangles in Movies* ***S4-S7*** *indicate the 405 nm* ROI_{targ}.

Movie S4-S6, SBTubA4P blocks branch development light-dependently and with spatiotemporal precision, related to Figure 5b-e: organoids treated with **SBTubA4P** (200 nM) were imaged for 4 h without 405 nm photoactivation (countdown) showing normal proliferation and mitosis, then pulsed 405 nm illumination was begun within the targeted area ROI_{targ} at time t = 0 (1 pulse per 7 min), locally stopping motility and proliferation.

Movie S7, no-compound control shows no photoinhibition of branch development in both ROI_{targ} and ROI_{ctrl}, related to Supporting Figure S7: organoid not treated with any compound was imaged for 4 h without 405 nm photoactivation pulses, then ROI_{targ} illumination with 405 nm pulses was performed as in **Movies S4-S6**. Note that the 405 nm-triggered increase in nuclear fluorescence intensity in the ROI_{targ} (seen in **Movies S4-S6**) is however not accompanied by stoppage of motility or proliferation (unlike in **Movies S4-S6**).

Movies S8-S11: *Timestamps in mm:ss; explanted drosophila brain lobe with focus centred on prophase neuroblast; 2% DMSO final concentration; imaged at 561 nm (mCherry; microtubules; white) and 488 nm (EGFP; spaghetti squash; cortical structure); imaged for 15 min (countdown) prior to 405 nm activation (from t = 0; blue frames; 20 µm stack with 1 µm z-spacing, 2 s/slice at 40% laser power, approx. 45 s total) then for 30 min post-activation.*

Movie S8, temporally precise depolymerization of the mitotic spindle in a prophase Drosophila neuroblast by photoactivation of *E*-SBTub2M (30 µM) at 405 nm, related to Figure 5f-g. Field of view is centred on a prophase neuroblast. White = mCherry::Jupiter; green = Squash::EGFP.

Movie S9, DMSO-only control to Movie S8 shows prophase Drosophila neuroblast undergoing normal mitosis after 405 nm illumination, related to figure 5f-g. Field of view is centred on a prophase neuroblast. White = mCherry::Jupiter; green = Squash::EGFP.

Movie S10, temporally precise depolymerization of the mitotic spindle in a prophase Drosophila neuroblast by photoactivation of *E*-SBTub2M (30 µM) at 405 nm. Field of view is centred on a prophase neuroblast. Compared to Movies S9-S10, a different microtubule marker is used (White = mCherry::Tubulin).

Movie S11, DMSO-only control to Movie S10 shows prophase Drosophila neuroblast undergoing normal mitosis after 405 nm illumination. Field of view is centred on a prophase neuroblast. White = mCherry::Tubulin.

Movie S12, related to Figure 6a-b and Figure S9: Reaction of hatchling embryos to mechanical stimulus depends on temporally precise application of *Z*-SBTubA4 during prior development. Healthy larvae initiate a movement upon mechanical stimulation with the tip of a glass pipette. Comparison of control conditions (dark, water), to 25 µM **SBTubA4P** post-lit and dark.

Movies S13-S16: *Timestamps in mm:ss; wt AB* zebrafish embryos microinjected with pSK_H2B-mRFP:5xUAS:EB3-GFP and pCS_KalTA4 plasmid DNA at the single-cell stage; embryos treated with* ***SBTubA4P*** *from 26-30 hpf then embedded and imaged at 561 nm (RFP; DNA; red) and 488 nm (GFP; microtubule dynamics; green). Photoactivations (405 nm, 7 s) as bleachpoints at the targeted area are indicated with a purple X at the time of application.*

Movie S13-S14, Photoactivation of SBTubA4P (25 µM) in a live zebrafish embryo shows temporally reversible inhibitions of EB3 dynamics over several cycles, related to Figure 6d-e: inhibition of MT polymerisation dynamics at each time when **SBTubA4P** (25 µM) is photoactivated, as repeated over several cycles. Movies show the same field of view, with Movie S13 showing DNA (histones; red) and microtubule plus tips (EB3; green), while Movie S14 shows only the EB3 channel (in white) as can be used for quantification of EB3 dynamics (photoactivations in this movie are temporally indicated by the purple circle).

Movie S15, Inhibition of MT polymerisation dynamics when SBTubA4P (25 µM) is photoactivated. Assay performed as in Movie S13-S14, showing similar effects.

Movie S16, Photoactivation of SBTubA4P (25 µM) stops both EB3 dynamics and cell division in the developing embryo. Assay performed as in Movie S13-S14, showing similar effects; a mitotic cell is also to be seen in the field of view (lower right); photoactivation of **SBTubA4P** stops its EB3 dynamics and after approx. 2.5 minutes the spindle starts to lose integrity; division is not productively continued during the rest of the movie.

References

(1) Stepanova, T.; Slemmer, J.; Hoogenraad, C. C.; Lansbergen, G.; Dortland, B.; De Zeeuw, C. I.; Grosveld, F.; van Cappellen, G.; Akhmanova, A.; Galjart, N. Visualization of Microtubule Growth in Cultured Neurons via the Use of EB3-GFP (End-Binding Protein 3-Green Fluorescent Protein). *J Neurosci* **2003**, *23* (7), 2655–2664. https://doi.org/10.1523/JNEUROSCI.23-07-02655.2003.

(2) Kleele, T.; Marinković, P.; Williams, P. R.; Stern, S.; Weigand, E. E.; Engerer, P.; Naumann, R.; Hartmann, J.; Karl, R. M.; Bradke, F.; Bishop, D.; Herms, J.; Konnerth, A.; Kerschensteiner, M.; Godinho, L.; Misgeld, T. An Assay to Image Neuronal Microtubule Dynamics in Mice. *Nat Commun* **2014**, *5*, 4827. https://doi.org/10.1038/ncomms5827.

(3) Goglia, A. G.; Toettcher, J. E. A Bright Future: Optogenetics to Dissect the Spatiotemporal Control of Cell Behavior. *Curr Opin Chem Biol* **2019**, *48*, 106–113. https://doi.org/10.1016/j.cbpa.2018.11.010.

(4) Hoorens, M. W. H.; Szymanski, W. Reversible, Spatial and Temporal Control over Protein Activity Using Light. *Trends In Biochemical Sciences* **2018**, *43* (8), 567–575. https://doi.org/10.1016/j.tibs.2018.05.004.

(5) Borowiak, M.; Nahaboo, W.; Reynders, M.; Nekolla, K.; Jalinot, P.; Hasserodt, J.; Rehberg, M.; Delattre, M.; Zahler, S.; Vollmar, A.; Trauner, D.; Thorn-Seshold, O. Photoswitchable Inhibitors of Microtubule Dynamics Optically Control Mitosis and Cell Death. *Cell* **2015**, *162* (2), 403–411. https://doi.org/10.1016/j.cell.2015.06.049.

(6) Borowiak, M.; Küllmer, F.; Gegenfurtner, F.; Peil, S.; Nasufovic, V.; Zahler, S.; Thorn-Seshold, O.; Trauner, D.; Arndt, H.-D. Optical Manipulation of F-Actin with Photoswitchable Small Molecules. *JACS* **2020**, *142* (20), 9240–9249. https://doi.org/10.1021/jacs.9b12898.

(7) Glotzer, M. The 3Ms of Central Spindle Assembly: Microtubules, Motors and MAPs. *Nat Rev Mol Cell Biol* **2009**, *10* (1), 9–20. https://doi.org/10.1038/nrm2609.

(8) Kapitein, L. C.; Hoogenraad, C. C. Building the Neuronal Microtubule Cytoskeleton. *Neuron* **2015**, *87* (3), 492–506. https://doi.org/10.1016/j.neuron.2015.05.046.

(9) van Haren, J.; Charafeddine, R. A.; Ettinger, A.; Wang, H.; Hahn, K. M.; Wittmann, T. Local Control of Intracellular Microtubule Dynamics by EB1 Photodissociation. *Nature Cell Biology* **2018**, *20* (3), 252–261. https://doi.org/10.1038/s41556-017-0028-5.

(10) Wühr, M.; Tan, E. S.; Parker, S. K.; Detrich III, H. W.; Mitchison, T. J. A Model for Cleavage Plane Determination in Early Amphibian and Fish Embryos. *Current Biology* **2010**, *20* (22), 2040–2045. https://doi.org/10.1016/j.cub.2010.10.024.

(11) Josa-Culleré, L.; Llebaria, A. In the Search for Photocages Cleavable with Visible Light: An Overview of Recent Advances and Chemical Strategies. *ChemPhotoChem* **2020**, *n/a* (n/a). https://doi.org/10.1002/cptc.202000253.

(12) Müller-Deku, A.; Meiring, J. C. M.; Loy, K.; Kraus, Y.; Heise, C.; Bingham, R.; Jansen, K. I.; Qu, X.; Bartolini, F.; Kapitein, L. C.; Akhmanova, A.; Ahlfeld, J.; Trauner, D.; Thorn-Seshold, O. Photoswitchable Paclitaxel-Based Microtubule Stabilisers Allow Optical Control over the Microtubule Cytoskeleton. *NComm* **2020**, *11* (1), 4640. https://doi.org/10.1038/s41467-020-18389-6.

(13) Gao, L.; Meiring, J. C. M.; Heise, C.; Thorn-Seshold, J.; Akhmanova, A.; Thorn-Seshold, O. Photoswitchable Epothilone-Based Microtubule Stabilisers Allow GFP- Orthogonal, Optical Control over the Microtubule Cytoskeleton. *BioRxiv In Submission* **2021**.

(14) Sailer, A.; Ermer, F.; Kraus, Y.; Lutter, F. H.; Donau, C.; Bremerich, M.; Ahlfeld, J.; Thorn-Seshold, O. Hemithioindigos for Cellular Photopharmacology: Desymmetrised Molecular Switch Scaffolds Enabling Design Control over the Isomer-Dependency of Potent Antimitotic Bioactivity. *CBC* **2019**, *20* (10), 1305–1314. https://doi.org/10.1002/cbic.201800752.

(15) Sailer, A.; Ermer, F.; Kraus, Y.; Bingham, R.; Lutter, F. H.; Ahlfeld, J.; Thorn-Seshold, O. Potent Hemithioindigo-Based Antimitotics Photocontrol the Microtubule Cytoskeleton in Cellulo. *BJOC* **2020**, *16*, 125–134. https://doi.org/10.3762/bjoc.16.14.

(16) Gao, L.; Meiring, J. C. M.; Kraus, Y.; Wranik, M.; Weinert, T.; Pritzl, S. D.; Bingham, R.; Ntouliou, E.; Jansen, K. I.; Olieric, N.; Standfuss, J.; Kapitein, L. C.; Lohmüller, T.; Ahlfeld, J.; Akhmanova, A.; Steinmetz, M. O.; Thorn-Seshold, O. A Robust, GFP-Orthogonal Photoswitchable Inhibitor Scaffold Extends Optical Control over the Microtubule Cytoskeleton. *Cell Chemical Biology* **2021**, *28*, 1–14. https://doi.org/10.1016/j.chembiol.2020.11.007.

(17) Engdahl, A. J.; Torres, E. A.; Lock, S. E.; Engdahl, T. B.; Mertz, P. S.; Streu, C. N. Synthesis, Characterization, and Bioactivity of the Photoisomerizable Tubulin Polymerization Inhibitor Azo-Combretastatin A4. *OL* **2015**, *17* (18), 4546–4549. https://doi.org/10.1021/acs.orglett.5b02262.

(18) Rastogi, S. K.; Zhao, Z.; Gildner, M. B.; Shoulders, B. A.; Velasquez, T. L.; Blumenthal, M. O.; Wang, L.; Li, X.; Hudnall, T. W.; Betancourt, T.; Du, L.; Brittain, W. J. Synthesis, Optical Properties and in Vitro Cell Viability of Novel Spiropyrans and Their Photostationary States. *Tet* **2021**, *80*, 131854. https://doi.org/10.1016/j.tet.2020.131854.

(19) Sailer, A.; Meiring, J.; Heise, C.; Pettersson, L.; Akhmanova, A.; Thorn-Seshold, J.; Thorn-Seshold, O. Pyrrole Hemithioindigo Antimitotics with Near-Quantitative Bidirectional Photoswitching Photocontrol Cellular Microtubule Dynamics with Single-Cell Precision. *ChemArxiv* **2021**. https://doi.org/10.26434/chemrxiv.14130107.v1.

(20) Zenker, J.; White, M. D.; Gasnier, M.; Alvarez, Y. D.; Lim, H. Y. G.; Bissiere, S.; Biro, M.; Plachta, N. Expanding Actin Rings Zipper the Mouse Embryo for Blastocyst Formation. *Cell* **2018**, *173* (3), 776–791. https://doi.org/10.1016/j.cell.2018.02.035.

(21) Theisen, U.; Ernst, A. U.; Heyne, R. L. S.; Ring, T. P.; Thorn-Seshold, O.; Köster, R. W. Microtubules and Motor Proteins Support Zebrafish Neuronal Migration by Directing Cargo. *Journal Of Cell Biology* **2020**, *219* (10), e201908040. https://doi.org/10.1083/jcb.201908040.

(22) Sheldon, J. E.; Dcona, M. M.; Lyons, C. E.; Hackett, J. C.; Hartman, M. C. T. Photoswitchable Anticancer Activity via Trans-Cis Isomerization of a Combretastatin A-4 Analog. *Org Biomol Chem* **2016**, *14* (1), 40–49. https://doi.org/10.1039/c5ob02005k.

(23) An, Y.; Chen, C.; Zhu, J.; Dwivedi, P.; Zhao, Y.; Wang, Z. Hypoxia-Induced Activity Loss of a Photo-Responsive Microtubule Inhibitor Azobenzene Combretastatin A4. *Frontiers Of Chemical Science Engineering* **2020**, *14* (5), 880–888. https://doi.org/10.1007/s11705-019-1864-6.

(24) Gavin, J.; Ruiz, J. F. M.; Kedziora, K.; Windle, H.; Kelleher, D. P.; Gilmer, J. F. Structure Requirements for Anaerobe Processing of Azo Compounds: Implications for Prodrug Design. *BMCL* **2012**, *22* (24), 7647–7652. https://doi.org/10.1016/j.bmcl.2012.10.014.

(25) Hüll, K.; Morstein, J.; Trauner, D. In Vivo Photopharmacology. *Chem Rev* **2018**, *118* (21), 10710–10747. https://doi.org/10.1021/acs.chemrev.8b00037.

(26) Lachmann, D.; Lahmy, R.; König, B. Fulgimides as Light-Activated Tools in Biological Investigations: Fulgimides as Light-Activated Tools in Biological Investigations. *Eur J Org Chem* **2019**, *2019* (31–32), 5018–5024. https://doi.org/10.1002/ejoc.201900219.

(27) Fuchter, M. J. On the Promise of Photopharmacology Using Photoswitches: A Medicinal Chemist's Perspective. *JMC* **2020**, *63* (20), 11436–11447. https://doi.org/10.1021/acs.jmedchem.0c00629.

(28) Welleman, I. M.; Hoorens, M. W. H.; Feringa, B. L.; Boersma, H. H.; Szymanski, W. Photoresponsive Molecular Tools for Emerging Applications of Light in Medicine. *Chem Sci* **2020**, *11* (43), 11672–11691. https://doi.org/10.1039/D0SC04187D.

(29) Gaspari, R.; Prota, A. E.; Bargsten, K.; Cavalli, A.; Steinmetz, M. O. Structural Basis of Cis- and Trans-Combretastatin Binding to Tubulin. *Chem* **2017**, *2* (1), 102–113. https://doi.org/10.1016/j.chempr.2016.12.005.

(30) Tarade, D.; Ma, D.; Pignanelli, C.; Mansour, F.; Simard, D.; van den Berg, S.; Gauld, J.; McNulty, J.; Pandey, S. Structurally Simplified Biphenyl Combretastatin A4 Derivatives Retain in Vitro Anti-Cancer Activity Dependent on Mitotic Arrest. *PLoS One* **2017**, *12* (3), e0171806. https://doi.org/10.1371/journal.pone.0171806.

(31) Jacobson, P. Ueber Bildung von Anhydroverbindungen Des Orthoamidophenylmercaptans Aus Thioaniliden. *Ber D Ch Ges* **1886**, *19* (1), 1067–1077. https://doi.org/10.1002/cber.188601901239.

(32) Ma, D.; Xie, S.; Xue, P.; Zhang, X.; Dong, J.; Jiang, Y. Efficient and Economical Access to Substituted Benzothiazoles: Copper-Catalyzed Coupling of 2-Haloanilides with Metal Sulfides and Subsequent Condensation. *Angewandte Chemie International Edition* **2009**, *48* (23), 4222–4225. https://doi.org/10.1002/anie.200900486.

(33) Tron, G. C.; Pirali, T.; Sorba, G.; Pagliai, F.; Busacca, S.; Genazzani, A. A. Medicinal Chemistry of Combretastatin A4: Present and Future Directions. *JMC* **2006**, *49* (11), 3033–3044. https://doi.org/10.1021/jm0512903.

(34) Kraus, Y.; Glas, C.; Melzer, B.; Gao, L.; Heise, C.; Preuße, M.; Ahlfeld, J.; Bracher, F.; Thorn-Seshold, O. Isoquinoline-Based Biaryls as a Robust Scaffold for Microtubule Inhibitors. *Eur J Med Chem* **2020**, *186*, 111865. https://doi.org/10.1016/j.ejmech.2019.111865.

(35) Florian, S.; Mitchison, T. J. Anti-Microtubule Drugs. In *The Mitotic Spindle: Methods and Protocols*; Chang, P., Ohi, R., Eds.; Springer New York: New York, NY, 2016; pp 403–421.

(36) Roostalu, J.; Thomas, C.; Cade, N. I.; Kunzelmann, S.; Taylor, I. A.; Surrey, T. The Speed of GTP Hydrolysis Determines GTP Cap Size and Controls Microtubule Stability. *eLife* **2020**, *9*. https://doi.org/10.7554/eLife.51992.

(37) Linnemann, J. R.; Miura, H.; Meixner, L. K.; Irmler, M.; Kloos, U. J.; Hirschi, B.; Bartsch, H. S.; Sass, S.; Beckers, J.; Theis, F. J.; Gabka, C.; Sotlar, K.; Scheel, C. H. Quantification of Regenerative Potential in Primary Human Mammary Epithelial Cells. *Development* **2015**, *142* (18), 3239–3251. https://doi.org/10.1242/dev.123554.

(38) Buchmann, B.; Meixner, L. K.; Fernandez, P.; Hutterer, F. P.; Raich, M. K.; Scheel, C. H.; Bausch, A. R. Mechanical Plasticity of the ECM Directs Invasive Branching Morphogenesis in Human Mammary Gland Organoids. *bioRxiv* **2019**, 860015. https://doi.org/10.1101/860015.

(39) Hofer, M.; Lutolf, M. P. Engineering Organoids. *Nature Reviews Materials* **2021**, 1–19. https://doi.org/10.1038/s41578-021-00279-y.

(40) Kopf, A.; Renkawitz, J.; Hauschild, R.; Girkontaite, I.; Tedford, K.; Merrin, J.; Thorn-Seshold, O.; Trauner, D.; Häcker, H.; Fischer, K.-D.; Kiermaier, E.; Sixt, M. Microtubules Control Cellular Shape and Coherence in Amoeboid Migrating Cells. *Journal Of Cell Biology* **2020**, *219* (6), e201907154. https://doi.org/10.1083/jcb.201907154.

(41) Vandestadt, C.; Vanwalleghem, G. C.; Castillo, H. A.; Li, M.; Schulze, K.; Khabooshan, M.; Don, E.; Anko, M.-L.; Scott, E. K.; Kaslin, J. Early Migration of Precursor Neurons Initiates Cellular and Functional Regeneration after Spinal Cord Injury in Zebrafish. *bioRxiv* **2019**, 539940. https://doi.org/10.1101/539940.

(42) Cabernard, C.; Doe, C. Q. Apical/Basal Spindle Orientation Is Required for Neuroblast Homeostasis and Neuronal Differentiation in Drosophila. *Developmental Cell* **2009**, *17* (1), 134–141. https://doi.org/10.1016/j.devcel.2009.06.009.

(43) Karpova, N.; Bobinnec, Y.; Fouix, S.; Huitorel, P.; Debec, A. Jupiter, a New Drosophila Protein Associated with Microtubules. *Cell Motility* **2006**, *63* (5), 301–312. https://doi.org/10.1002/cm.20124.

(44) Royou, A.; Sullivan, W.; Karess, R. Cortical Recruitment of Nonmuscle Myosin II in Early Syncytial Drosophila Embryos : Its Role in Nuclear Axial Expansion and Its Regulation by Cdc2 Activity. *Journal Of Cell Biology* **2002**, *158* (1), 127–137. https://doi.org/10.1083/jcb.200203148.

(45) Rusan, N. M.; Peifer, M. A Role for a Novel Centrosome Cycle in Asymmetric Cell Division. *Journal Of Cell Biology* **2007**, *177* (1), 13–20. https://doi.org/10.1083/jcb.200612140.

(46) Cabernard, C.; Prehoda, K. E.; Doe, C. Q. A Spindle-Independent Cleavage Furrow Positioning Pathway. *Nature* **2010**, *467* (7311), 91–94. https://doi.org/10.1038/nature09334.

(47) Connell, M.; Cabernard, C.; Ricketson, D.; Doe, C. Q.; Prehoda, K. E. Asymmetric Cortical Extension Shifts Cleavage Furrow Position in Drosophila Neuroblasts. *Molecular Biology Of Cell* **2011**, *22* (22), 4220–4226. https://doi.org/10.1091/mbc.e11-02-0173.

(48) Roberts, A.; Borisyuk, R.; Buhl, E.; Ferrario, A.; Koutsikou, S.; Li, W.-C.; Soffe, S. R. The Decision to Move: Response Times, Neuronal Circuits and Sensory Memory in a Simple Vertebrate. *Proceedings Of Royal Society B Biological Sciences* **2019**, *286* (1899), 20190297. https://doi.org/10.1098/rspb.2019.0297.

(49) Distel, M.; Hocking, J. C.; Volkmann, K.; Köster, R. W. The Centrosome Neither Persistently Leads Migration nor Determines the Site of Axonogenesis in Migrating Neurons in Vivo. *Journal Of Cell Biology* **2010**, *191* (4), 875–890. https://doi.org/10.1083/jcb.201004154.

(50) Distel, M.; Wullimann, M. F.; Köster, R. W. Optimized Gal4 Genetics for Permanent Gene Expression Mapping in Zebrafish. *Proceedings Of National Academy Of Sciences* **2009**, *106* (32), 13365–13370. https://doi.org/10.1073/pnas.0903060106.

(51) Fortin, D. L.; Banghart, M. R.; Dunn, T. W.; Borges, K.; Wagenaar, D. A.; Gaudry, Q.; Karakossian, M. H.; Otis, T. S.; Kristan, W. B.; Trauner, D.; Kramer, R. H. Photochemical Control of Endogenous Ion Channels and Cellular Excitability. *Nat Meth* **2008**, *5* (4), 331–338. https://doi.org/10.1038/nmeth.1187.

(52) Laprell, L.; Tochitsky, I.; Kaur, K.; Manookin, M. B.; Stein, M.; Barber, D. M.; Schön, C.; Michalakis, S.; Biel, M.; Kramer, R. H.; Sumser, M. P.; Trauner, D.; Van Gelder, R. N. Photopharmacological Control of Bipolar Cells Restores Visual Function in Blind Mice. *Journal Of Clinical Investigation* **2017**, *127* (7), 2598–2611. https://doi.org/10.1172/JCI92156.

(53) Matera, C.; Gomila, A. M. J.; Camarero, N.; Libergoli, M.; Soler, C.; Gorostiza, P. Photoswitchable Antimetabolite for Targeted Photoactivated Chemotherapy. *JACS* **2018**, *140* (46), 15764–15773. https://doi.org/10.1021/jacs.8b08249.

(54) Babii, O.; Afonin, S.; Schober, T.; Garmanchuk, L. V.; Ostapchenko, L. I.; Yurchenko, V.; Zozulya, S.; Tarasov, O.; Pishel, I.; Ulrich, A. S.; Komarov, I. V. Peptide Drugs for Photopharmacology: How Much of a Safety Advantage Can Be Gained by Photocontrol? *Future Drug Discovery* **2020**, *2* (1), FDD28. https://doi.org/10.4155/fdd-2019-0033.

(55) Afonin, S.; Babii, O.; Reuter, A.; Middel, V.; Takamiya, M.; Strähle, U.; Komarov, I. V.; Ulrich, A. S. Light-Controllable Dithienylethene-Modified Cyclic Peptides: Photoswitching the in Vivo Toxicity in Zebrafish Embryos. *BJOC* **2020**, *16*, 39–49. https://doi.org/10.3762/bjoc.16.6.

Supplemental Information

In vivo photocontrol of microtubule dynamics and integrity, migration and mitosis, by the potent GFP-imaging-compatible photoswitchable reagents SBTubA4P and SBTub2M

Li Gao[1], Joyce C.M. Meiring[2], Adam Varady[3], Iris E. Ruider[4], Constanze Heise[1], Maximilian Wranik[5], Cecilia D. Velasco[6,7], Jennifer A. Taylor[8], Beatrice Terni[6,7], Jörg Standfuss[5], Clemens C. Cabernard[8], Artur Llobet[6,7], Michel O. Steinmetz[5,9], Andreas R. Bausch[4], Martin Distel[3,10], Julia Thorn-Seshold[1], Anna Akhmanova[2], Oliver Thorn-Seshold[1,11,*]

[1] Department of Pharmacy, Ludwig-Maximilians University of Munich; Munich 81377, Germany
[2] Cell Biology, Department of Biology, Faculty of Science, Utrecht University, Utrecht 3584, Netherlands
[3] St. Anna Kinderkrebsforschung Children's Cancer Research Institute, Wien 1090, Austria
[4] Physics Department, Technical University of Munich and Center for Protein Assemblies; Garching 85747, Germany
[5] Laboratory of Biomolecular Research, Division of Biology and Chemistry, Paul Scherrer Institut, Villigen 5232, Switzerland
[6] Laboratory of Neurobiology, Department of Pathology and Experimental Therapy, Institute of Neurosciences, University of Barcelona; L'Hospitalet de Llobregat, Barcelona 08907, Spain
[7] Bellvitge Biomedical Research Institute (IDIBELL), L'Hospitalet de Llobregat, Barcelona 08907, Spain
[8] Department of Biology, University of Washington; Seattle 98195, USA
[9] Biozentrum, University of Basel, Basel 4056, Switzerland
[10] Zebrafish Platform Austria for Preclinical Drug Screening, Vienna 1090, Austria
[11] Lead Contact
*Correspondence to oliver.thorn-seshold@cup.lmu.de

ORCID: O.T.-S. 0000-0003-3981-651X

Keywords*: microtubule dynamics; cytoskeleton; photopharmacology; tubulin polymerisation inhibitor; optical control; colchicine; antimitotic; cell division; cell migration; development; photoswitch.*

Table of Contents

Part A: Chemical Synthesis

Conventions

Abbreviations: The following abbreviations are used: Hex – distilled isohexanes, EA – ethyl acetate, DCM – dichloromethane, Et – ethyl, Ac – acetyl, Me – methyl, MeCN – acetonitrile, DMSO – dimethylsulfoxide, PBS – phosphate buffered saline. TFA – trifluoroacetic acid, DMAP – 4-(dimethylamino)pyridine, TEA – triethylamine.

Safety Hazards: no unexpected or unusually high safety hazards were encountered.

Reagents and Conditions: Unless stated otherwise, (1) all reactions and characterisations were performed with unpurified, undried, non-degassed solvents and reagents, used as obtained, under closed air atmosphere without special precautions; (2) "hexane" used for chromatography was distilled from commercial crude isohexane fraction by rotary evaporation; (3) "column" and "chromatography" refer to manual flash column chromatography on Merck silica gel Si-60 (40–63 μm); (4) MPLC flash column chromatography refers to purification on a Biotage Isolera Spektra, using prepacked silica cartridges from Biotage; (5) procedures and yields are unoptimized; (6) yields refer to isolated chromatographically and spectroscopically pure materials, corrected for residual solvent content; (7) all eluent and solvent mixtures are given as volume ratios unless otherwise specified, thus "1:1 Hex:EA" indicates a 1:1 (v/v) mixture of hexanes and ethyl acetate; (8) chromatography eluents e.g. "0→25% EA:Hex" indicate a linear gradient of eluent composition.

Thin-layer chromatography (TLC) was run on 0.25 mm Merck silica gel plates (60, F-254), typically with Hex:EA eluents, except where indicated. UV light (254 nm) was used as a visualizing agent, with cross-checking by 365 nm UV lamp. TLC characterizations are abbreviated as $\mathbf{R}_f$ = 0.64 (EA:Hex = 1:1).

NMR: Standard NMR characterization was by ^{1}H- and ^{13}C-NMR spectra on a Bruker Ascend 400 (400 **MHz** & 100 **MHz** for ^{1}H and ^{13}C respectively) or a Bruker Ascend 500 (500 **MHz** & 125 **MHz** for ^{1}H and ^{13}C, respectively). Known compounds were checked against literature data and their spectral analysis is not detailed unless necessary. Chemical shifts (δ) are reported in ppm calibrated to residual non-perdeuterated solvent as an internal reference[1]. Peak descriptions singlet (s), doublet (d), triplet (t), quartet (q) and multiplet (m).

Analytical HPLC and Mass Spectra: Analytical HPLC-MS measurements were performed on an Agilent 1100 SL coupled HPLC-MS system with (a) a binary pump to deliver H_2O:MeCN eluent mixtures containing 0.1% formic acid at a 0.4 mL/min flow rate, (b) Thermo Scientific

Hypersil GOLD™ C18 column (1.9 µm; 3 × 50 mm) maintained at 25°C, whereby the solvent front eluted at t_{ret} = 0.5 min, (c) an Agilent 1100 series diode array detector used to acquire peak spectra of separated compounds/isomers in the range 200-550 nm after manually baselining across each elution peak of interest to correct for eluent composition effects, (d) a Bruker Daltonics HCT-Ultra mass spectrometer used in ESI mode at unit mass resolution. Run conditions were a linear gradient of H_2O:MeCN eluent composition from the starting ratio through to 10:90, applied during the separation phase (first 5 min), then 0:100 maintained until all peaks of interest had been observed (typically 2 min more); the column was equilibrated with the H_2O:MeCN eluent mixture for 2 minutes before each run. Unless stated otherwise, all reported peaks in the positive mode were $[M+H]^+$ peaks, and all observed peaks in the negative mode were $[M-H]^-$ peaks. HRMS was carried out by the Zentrale Analytik of the LMU Munich using ESI or EI ionisation as specified. LRMS was carried out on an expression CMS by Advion with either APCI or ESI as ionization source.

General procedures

General procedure 1: Synthesis of SBT *via* Aldol Condensation

Equimolar amounts of the 2-methylbenzothiazole (1 eq) and the benzaldehyde (1 eq) is dissolved in DMSO (1 mL/0.1 mmol) and NaOMe (6 M in MeOH, 2 eq) is added. The reaction mixture is stirred at room temperature overnight. H_2O (15 mL) and sat. aq. NH_4Cl (15 mL) is added and the mixture is extracted with ethyl acetate (3 × 20 mL). The combined organic layers are dried over $MgSO_4$ and concentrated *in vacuo*. The crude product is purified by normal phase MPLC.

General procedure 2: Synthesis of 2-methylbenzothiazoles *via* Jacobsen cyclization

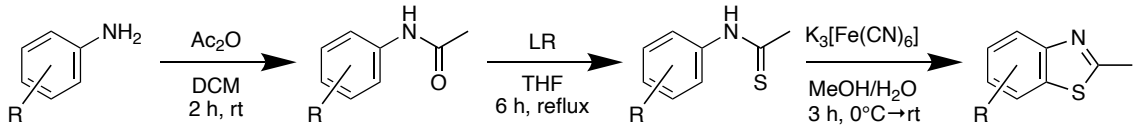

Acetic anhydride (1.2 eq) is slowly added to a solution of the aniline (1 eq) in dry DCM. The reaction mixture is stirred for 2 h at room temperature and reaction progress is monitored by TLC. After completion, the mixture is quenched with sat. aq. $NaHCO_3$ (25 mL) and extracted with DCM. The combined organic layers are dried over $MgSO_4$, filtrated and the solvent is removed under reduced pressure. The unpurified phenyl acetamide is dissolved in THF and Lawesson's reagent (0.7 eq) is added. The reaction mixture is stirred for 6 h at reflux. After the reaction is finished, the solution is cooled down to room temperature and water is added. The suspension is extracted with EA and washed with brine. The combined organic layers are

dried over Na_2SO_4, filtrated and the solvent is removed under reduced pressure. The crude is filtrated through a silica plug and used without further purification. The crude phenyl thioamide is dissolved in MeOH and aq. NaOH (2 M, 2 eq.) is added. After stirring for 1 h at room temperature, MeOH is removed under reduced pressure and a solution of $K_3[Fe(CN)_6]$ (1.2 eq) in H_2O is added at 0°C and warmed up to room temperature. Stirring is continued for another 3 h at room temperature. The reaction mixture is extracted with EA and washed with brine. The combined organic layers are dried over Na_2SO_4, filtrated and concentrated *in vacuo*. The crude is purified by Kugelrohr distillation or normal phase MPLC to give the desired 2-methylbenzothiazole.

General procedure 3: Synthesis of 2-methylbenzothiazoles *via* Cu-catalysis

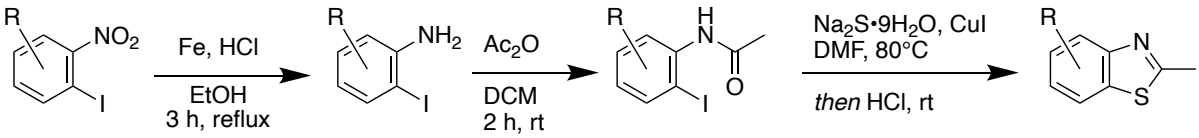

Iron powder (6.2 eq) and conc. HCl (1.2 eq) is added to a solution of *o*-iodo nitrotoluene in ethanol. After 3 h of reflux, the mixture is cooled to room temperature and Na_2CO_3 is added portionwise until gas evolution ceased. After filtration over Celite, the filtrate is extracted with EA and the combined organic fractions are washed with H_2O and brine, dried over $MgSO_4$ and concentrated by rotary evaporation. The crude toluidine is redissolved in dry DCM and acetic anhydride (1.2 eq) is slowly added and stirred at room temperature for 2 h. The suspension is extracted with EA and washed with brine. The combined organic layers are dried over Na_2SO_4, filtrated and the solvent is removed under reduced pressure. Heterocyclic ring closure was performed following a procedure by Ma et al.[2] A mixture of CuI (0.1 mmol), *o*-iodobenzamide (1 mmol), and $Na_2S{\cdot}9H_2O$ (3 mmol) in DMF (2 mL) is stirred at 80°C for 12 h. The reaction mixture is cooled to room temperature before adding 0.8 mL of conc. HCl and the reaction mixture is stirred for another 5-10 h. After adding 10 mL sat. aq. $NaHCO_3$, it is extracted with EA and purified by normal phase MPLC to furnish the desired product.

Experimental data of SBTubs

Synthesis of SBTubA4

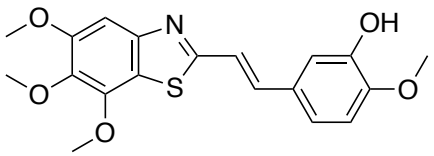

Chemical Formula: $C_{19}H_{19}NO_5S$
Molecular Weight: 373.42

SBTubA4 was synthesized from **S1** (200 mg, 0.84 mmol) and isovanillin (127 mg, 0.84 mmol) following general procedure 1. The crude product was purified by normal phase MPLC (30→100% EA:Hex) to give **SBTubA4** (130 mg, 0.35 mmol, 42%) as yellow solid.

^{1}H-NMR (400 MHz, $CDCl_3$): δ = 7.40 (d, *J* = 16.2 Hz, 1H), 7.26 (s, 1H), 7.21 – 7.15 (m, 2H), 7.06 (dd, *J* = 8.4, 2.0 Hz, 1H), 6.87 (d, *J* = 8.3 Hz, 1H), 5.74 (s, 1H), 4.08 (s, 3H), 3.94 (s, 3H), 3.93 (s, 6H) ppm. **^{13}C-NMR (100 MHz, $CDCl_3$):** δ = 167.3, 154.1, 150.4, 147.9, 146.8, 146.1, 140.0, 136.7, 129.3, 120.8, 120.4, 119.6, 112.6, 110.8, 100.6, 61.6, 60.7, 56.4, 56.2 ppm. $\mathbf{R_f}$ = 0.19 (EA:Hex = 4:6). **HRMS (ESI, positive):** 374.10567 calculated for $C_{19}H_{20}NO_5S^+$ $[M+H]^+$, 374.10521 found.

Synthesis of 2

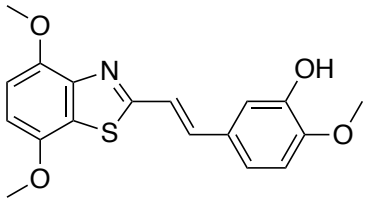

Chemical Formula: $C_{18}H_{17}NO_4S$
Molecular Weight: 343.40

2 was synthesized from **S2** (175 mg, 0.84 mmol) and isovanillin (127 mg, 0.84 mmol) following general procedure 1. The crude product was purified by normal phase MPLC (30→80% EA:Hex) to give **2** (144 mg, 0.42 mmol, 50%) as orange solid.

^{1}H-NMR (400 MHz, DMSO-d_6): δ = 9.25 (s, 1H), 7.56 (d, *J* = 16.2 Hz, 1H), 7.39 (d, *J* = 16.2 Hz, 1H), 7.28 – 7.22 (m, 2H), 7.09 – 6.97 (m, 3H), 3.99 (s, 3H), 3.99 (s, 3H), 3.90 (s, 3H) ppm. **^{13}C-NMR (125 MHz, DMSO-d_6):** δ = 165.6, 149.3, 147.4, 147.4, 146.7, 144.5, 137.5, 128.1, 123.5, 120.3, 119.3, 113.7, 112.1, 108.3, 106.2, 56.1, 56.1, 55.6 ppm. $\mathbf{R_f}$ = 0.21 (EA:Hex = 4:6). **HRMS (ESI, positive):** 344.09511 calculated for $C_{18}H_{18}NO_4S^+$ $[M+H]^+$, 344.09487 found.

Synthesis of 3

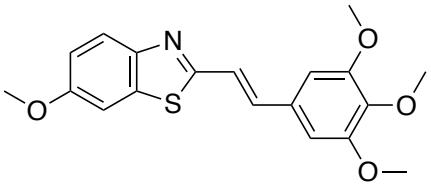

Chemical Formula: $C_{19}H_{19}NO_4S$
Molecular Weight: 357.42

3 was synthesized from 6-methoxy-2-methylbenzothiazole (100 mg, 0.56 mmol) and 3,4,5-trimethoxybenzaldehyde (109 mg, 0.56 mmol) following general procedure 1. The crude product was purified by normal phase MPLC (10→30% EA:Hex) to give **3** (118 mg, 0.33 mmol, 59%) as yellow solid.

^{1}H-NMR (500 MHz, $CDCl_3$): δ = 7.86 (d, *J* = 8.9 Hz, 1H), 7.34 (d, *J* = 16.2 Hz, 1H), 7.32 (d, *J* = 2.5 Hz, 1H), 7.29 (d, *J* = 16.1 Hz, 1H), 7.07 (dd, *J* = 8.9, 2.5 Hz, 1H), 6.80 (s, 2H), 3.91 (s, 6H), 3.89 (s, 6H) ppm. **^{13}C-NMR (125 MHz, $CDCl_3$):** δ = 164.6, 158.1, 153.6, 148.5, 139.4, 136.6, 135.9, 131.3, 123.6, 121.9, 115.8, 104.4, 104.3, 61.1, 56.3, 56.0 ppm. **R_f** = 0.34 (EA:Hex = 3:7). **HRMS (ESI, positive):** 358.11076 calculated for $C_{19}H_{20}NO_4S^+$ $[M+H]^+$, 358.11038 found.

Synthesis of 4

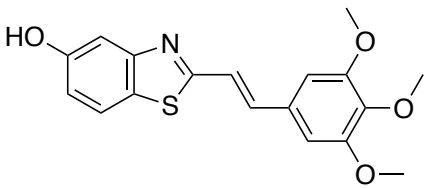

Chemical Formula: $C_{18}H_{17}NO_4S$
Molecular Weight: 343.40

4 was synthesized from 5-hydroxy-2-methylbenzothiazole (50 mg, 0.30 mmol) and 3,4,5-trimethoxybenzaldehyde (59 mg, 0.30 mmol) following general procedure 1. The crude product was purified by normal phase MPLC (10→30% EA:Hex) to give **4** (30 mg, 0.087 mmol, 29%) as yellow solid.

^{1}H-NMR (500 MHz, $CDCl_3$): δ = 7.67 (d, *J* = 8.7 Hz, 1H), 7.47 (d, *J* = 2.4 Hz, 1H), 7.41 (d, *J* = 16.2 Hz, 1H), 7.29 (d, *J* = 16.2 Hz, 1H), 6.98 (dd, *J* = 8.6, 2.5 Hz, 1H), 6.78 (s, 2H), 6.49 (s, 1H), 3.89 (s, 6H), 3.89 (s, 3H) ppm. **^{13}C-NMR (125 MHz, $CDCl_3$):** δ = 168.7, 155.6, 154.8, 153.6, 139.6, 137.7, 131.1, 126.1, 122.2, 121.4, 115.6, 108.3, 104.7, 61.2, 56.3 ppm. **R_f** =

0.44 (EA:Hex = 1:1). **HRMS (ESI, positive):** 344.09511 calculated for $C_{18}H_{18}NO_4S^+$ $[M+H]^+$, 344.09479 found.

Synthesis of 5

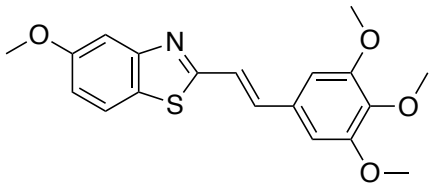

Chemical Formula: $C_{19}H_{19}NO_4S$
Molecular Weight: 357.42

To a solution of **4** (20 mg, 0.058 mmol) in acetone (1 mL) was added potassium carbonate (10 mg, 0.058 mmol, 1.24 eq) and dimethyl sulfate (5.5 μL, .0.059, 1 eq). The reaction mixture was stirred overnight at room temperature. The solvents were removed under reduced pressure. H_2O (3 mL) and DCM (3 mL) was added to the residue. Extraction with DCM (3 × 3 mL). The combined organic layers were dried over $MgSO_4$, filtered and concentrated under reduced pressure. The crude product was purified by normal phase MPLC (10→30% EA:Hex) to give **5** (10 mg, 0.028 mmol, 48%) as yellow solid.

^{1}H-NMR (500 MHz, $CDCl_3$): δ = 7.71 (d, *J* = 8.8 Hz, 1H), 7.48 (d, *J* = 2.5 Hz, 1H), 7.45 (d, *J* = 16.1 Hz, 1H), 7.30 (d, *J* = 16.1 Hz, 1H), 7.03 (dd, *J* = 8.8, 2.5 Hz, 1H), 6.82 (s, 2H), 3.93 (s, 6H), 3.91 (s, 3H), 3.90 (s, 3H) ppm. **^{13}C-NMR (125 MHz, $CDCl_3$):** δ = 168.1, 159.3, 155.2, 153.7, 139.6, 137.2, 131.2, 126.3, 121.9, 121.7, 115.6, 105.4, 104.6, 61.2, 56.3, 55.8 ppm. **R_f** = 0.20 (EA:Hex = 2:8). **HRMS (ESI, positive):** 358.11076 calculated for $C_{19}H_{20}NO_4S^+$ $[M+H]^+$, 358.11040 found.

Synthesis of 6

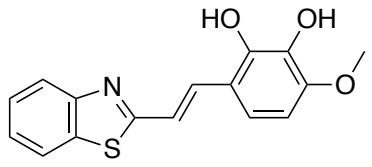

Chemical Formula: $C_{16}H_{13}NO_3S$
Molecular Weight: 299.34

2-methylbenzothiazole (0.07 mL, 0.55 mmol) and **S3** (140 mg, 0.55 mmol, 1 eq) was dissolved in DMSO (5 mL) and NaOMe (5.4 M in MeOH, 0.1 mL, 1 mmol, 1 eq) was added and the reaction mixture was stirred overnight. H_2O (15 mL) was added and the mixture was extracted with ethyl acetate (3 × 10 mL). The combined organic layers were dried over $MgSO_4$ and concentrated *in vacuo*. The residue was redissolved in 3 M HCl/THF (1:1, 10 mL) and

stirred at 40°C for 5 h. H_2O (20 mL) was added and the reaction mixture was extracted with EA (3 × 15 mL) and dried over $MgSO_4$. The crude product was purified by normal phase MPLC (20 → 70% EA:Hex) to give **6** (135 mg, 0.45 mmol, 83%) as brown solids.

^{1}H-NMR (400 MHz, DMSO-*d*$_6$): δ = 8.04 (dd, *J* = 8.0, 1.2 Hz, 1H), 7.92 (d, *J* = 8.0 Hz, 1H), 7.75 (d, *J* = 16.3 Hz, 1H), 7.52 – 7.43 (m, 2H), 7.39 (t, *J* = 8.1 Hz, 1H), 7.19 (d, *J* = 8.8 Hz, 1H), 6.58 (d, *J* = 8.8 Hz, 1H), 3.83 (s, 3H) ppm. **^{13}C-NMR (100 MHz, DMSO-*d*$_6$):** δ = 167.8, 153.6, 149.7, 145.6, 134.0, 133.8, 133.7, 126.4, 125.1, 122.2, 122.1, 119.1, 118.6, 116.2, 103.7, 55.9 ppm. **R_f** = 0.34 (EA:Hex = 1:1). **HRMS (ESI, positive):** 300.06889 calculated for $C_{16}H_{14}NO_3S^+$ $[M+H]^+$, 300.06893 found.

Synthesis of 7

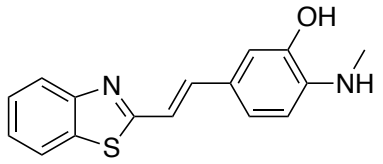

Chemical Formula: $C_{16}H_{14}N_2OS$
Molecular Weight: 282.36

To a cooled solution of **S4** (200 mg, 0.71 mmol) in 3 mL anhydrous THF was added sodium hydride (34 mg, 1.4 mmol, 2 eq) in small portions. After stirring for 10 min at room temperature, aldehyde **S6** (124 mg, 0.71 mmol) in anhydrous THF (3 mL) was added dropwise. The mixture was stirred overnight at room temperature before quenching with water (20 mL) and transferring into a separation funnel. The aqueous layer was extracted with EA (3 × 15 mL) and concentrated *in vacuo*. The crude carbamate was dissolved in 10% aq. NaOH solution (20 mL) and refluxed for 4 h. After cooling, the reaction mixture was transferred into a seperation funnel, EA (30 mL) was added and the organic layer was washed with sat. aq. NH_4Cl (20 mL). The crude mixture was purified by normal phase MPLC (10→100% EA:Hex) and recrystallized from H_2O/MeOH to give compound **7** as brown microneedles (69 mg, 0.24 mmol, 35%).

^{1}H-NMR (400 MHz, DMSO-*d*$_6$): δ = 9.57 (s, 1H), 8.02 (dd, *J* = 7.9, 0.7 Hz, 1H), 7.88 (d, *J* = 7.8 Hz, 1H), 7.50 – 7.39 (m, 2H), 7.36 (ddd, *J* = 8.3, 7.2, 1.2 Hz, 1H), 7.11 – 7.04 (m, 2H), 7.00 (d, *J* = 2.0 Hz, 1H), 6.45 (d, *J* = 8.2 Hz, 1H), 5.46 (q, *J* = 5.1 Hz, 1H), 2.77 (d, *J* = 5.0 Hz, 3H) ppm. **^{13}C-NMR (100 MHz, DMSO-*d*$_6$):** δ = δ 167.5, 153.7, 144.1, 141.2, 139.2, 133.6, 126.3, 124.8, 122.6, 122.2, 121.9, 121.9, 115.4, 110.6, 108.3, 29.5 ppm. **R_f** = 0.62 (EA:Hex = 1:1). **HRMS (ESI, positive):** 283.08996 calculated for $C_{16}H_{15}N_2OS^+$ $[M+H]^+$, 283.08998 found.

Synthesis of 8

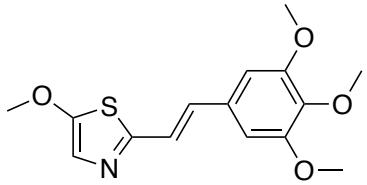

Chemical Formula: $C_{15}H_{17}NO_4S$
Molecular Weight: 307.36

Phosphorus pentasulfide (10 g, 52 mmol) was added portionwise to a solution of **S7** (315 mg, 1 mmol) in chloroform (8 mL), and the suspension was stirred at 80°C overnight. The reaction mixture was poured in 2 M NaOH (15 mL), and extracted with DCM (3 × 10 mL). The organic layer was dried over MgSO4 and concentrated under reduced pressure. The residue was purified by column chromatography (EA:Hex = 3:7) to afford compound **8** as a yellow solid (201 mg, 0.65 mmol, 64%).

^{1}H-NMR (500 MHz, $CDCl_3$): δ = 7.05 (s, 1H), 7.03 (d, *J* = 2.9 Hz, 2H), 6.71 (s, 2H), 3.95 (s, 3H), 3.89 (s, 6H), 3.87 (s, 3H) ppm. **^{13}C-NMR (125 MHz, $CDCl_3$):** δ = 162.3, 155.2, 153.6, 138.9, 132.3, 131.7, 122.3, 121.5, 104.0, 61.5, 61.1, 56.3 ppm. **R_f** = 0.42 (EA:Hex = 1:1). **HRMS (ESI, positive):** 308.09511 calculated for $C_{15}H_{18}NO_4S^+$ $[M+H]^+$, 308.09494 found.

Synthesis of 9

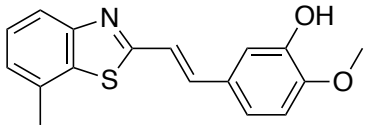

Chemical Formula: $C_{17}H_{15}NO_2S$
Molecular Weight: 297.37

9 was synthesized from **S9** (82 mg, 0.5 mmol) and isovanillin (76 mg, 0.5 mmol) following general procedure 1. The crude product was purified by normal phase MPLC (20→70% EA:Hex) to give **9** (110 mg, 0.37 mmol, 74%) as slightly yellowish solid.

^{1}H-NMR (400 MHz, $CDCl_3$): δ = 7.83 (d, *J* = 8.1 Hz, 1H), 7.46 (d, *J* = 16.2 Hz, 1H), 7.38 (dd, *J* = 8.2, 7.3 Hz, 1H), 7.28 (s, 1H), 7.20 (d, *J* = 2.1 Hz, 1H), 7.16 (d, *J* = 7.3 Hz, 1H), 7.09 (dd, *J* = 8.3, 2.1 Hz, 1H), 6.88 (d, *J* = 8.3 Hz, 1H), 5.68 (s, 1H), 3.94 (s, 3H), 2.58 (s, 3H) ppm. **^{13}C-NMR (100 MHz, $CDCl_3$):** δ = 167.0, 153.9, 148.0, 146.1, 137.5, 134.9, 131.7, 129.3, 126.6, 125.5, 120.9, 120.7, 120.4, 112.7, 110.8, 56.2, 21.6 ppm. **R_f** = 0.31 (EA:Hex = 3:7). **HRMS (ESI, positive):** 298.08963 calculated for $C_{17}H_{16}NO_2S^+$ $[M+H]^+$, 298.08936 found.

Synthesis of 10

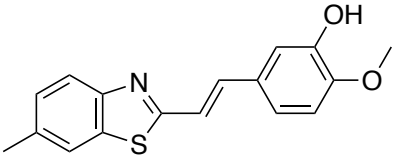

Chemical Formula: $C_{17}H_{15}NO_2S$
Molecular Weight: 297.37

10 was synthesized from **S10** (163 mg, 1 mmol) and isovanillin (152 mg, 1 mmol) following general procedure 1. The crude product was purified by normal phase MPLC (20→70% EA:Hex) to give **10** (183 mg, 0.62 mmol, 62%) as orange solid.

^{1}H-NMR (400 MHz, DMSO-*d*$_6$): δ = 9.17 (s, 1H), 7.85 (dt, *J* = 1.6, 0.7 Hz, 1H), 7.81 (d, *J* = 8.3 Hz, 1H), 7.46 (d, *J* = 16.2 Hz, 1H), 7.35 – 7.25 (m, 2H), 7.20 – 7.13 (m, 2H), 6.98 (d, *J* = 8.9 Hz, 1H), 3.82 (s, 3H), 2.44 (s, 3H) ppm. **^{13}C-NMR (100 MHz, DMSO-*d*$_6$):** δ = 165.8, 151.7, 149.3, 146.7, 137.3, 135.0, 134.0, 128.2, 127.9, 121.9, 121.6, 120.3, 119.4, 113.6, 112.1, 55.7, 21.1. ppm. **R_f** = 0.28 (EA:Hex = 3:7). **HRMS** (EI, positive): 296.0745 calculated for $C_{17}H_{14}NO_2S^{\cdot}$ $[M–H]^{\cdot}$, 296.0740 found.

Synthesis of 11

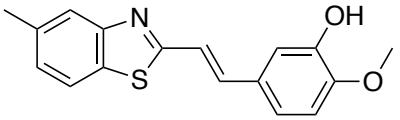

Chemical Formula: $C_{17}H_{15}NO_2S$
Molecular Weight: 297.37

11 was synthesized from **S11** (82 mg, 0.5 mmol) and isovanillin (76 mg, 0.5 mmol) following general procedure 1. The crude product was purified by normal phase MPLC (20→70% EA:Hex) to give **11** (100 mg, 0.34 mmol, 67%) as slightly yellowish solid.

^{1}H-NMR (400 MHz, CDCl$_3$): δ = 7.82 (dt, *J* = 1.5, 0.8 Hz, 1H), 7.75 (d, *J* = 8.1 Hz, 1H), 7.45 (d, *J* = 16.1 Hz, 1H), 7.30 (d, *J* = 0.6 Hz, 1H), 7.25 – 7.20 (m, 2H), 7.11 (dd, *J* = 8.5, 2.1 Hz, 1H), 6.91 (d, *J* = 8.3 Hz, 1H), 5.78 (s, 1H), 3.97 (s, 3H), 2.53 (s, 3H) ppm. **^{13}C-NMR (100 MHz, CDCl$_3$):** δ = 167.6, 154.4, 148.0, 146.1, 137.3, 136.5, 131.3, 129.3, 126.9, 123.0, 121.1, 120.8, 120.7, 112.7, 110.8, 56.2, 21.6 ppm. **R_f** = 0.33 (EA:Hex = 3:7). **HRMS (ESI, positive):** 298.08963 calculated for $C_{17}H_{16}NO_2S^+$ $[M+H]^+$, 298.08932 found.

Synthesis of 12

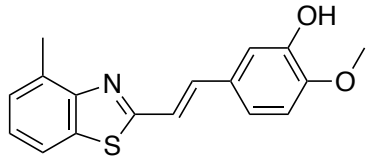

Chemical Formula: $C_{17}H_{15}NO_2S$
Molecular Weight: 297.37

12 was synthesized from **S12** (230 mg, 1.41 mmol) and isovanillin (214 mg, 1.41 mmol) following general procedure 1. The crude product was purified by normal phase MPLC (20→70% EA:Hex) to give **12** (338 mg, 1.14 mmol, 81%) as yellow solid.

^{1}H-NMR (400 MHz, DMSO-*d*$_6$): δ = 9.16 (s, 1H), 7.86 (dd, *J* = 5.3, 3.9 Hz, 1H), 7.46 (d, *J* = 16.2 Hz, 1H), 7.36 (d, *J* = 16.2 Hz, 1H), 7.32 – 7.27 (m, 2H), 7.22 – 7.16 (m, 2H), 6.98 (d, *J* = 8.2 Hz, 1H), 3.82 (s, 3H), 2.66 (s, 3H) ppm. **^{13}C-NMR (100 MHz, DMSO-*d*$_6$):** δ = 165.9, 152.7, 149.3, 146.7, 137.7, 133.6, 131.9, 128.2, 126.8, 125.2, 120.2, 119.6, 119.4, 113.8, 112.1, 55.6, 18.1 ppm. **R_f** = 0.70 (EA:Hex = 1:1). **HRMS (ESI, positive):** 298.08963 calculated for $C_{17}H_{16}NO_2S^+$ $[M+H]^+$, 298.08949 found.

Synthesis of 13

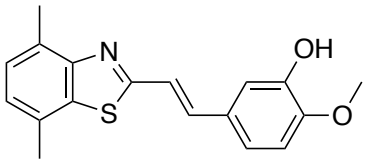

Chemical Formula: $C_{18}H_{17}NO_2S$
Molecular Weight: 311.40

13 was synthesized from **S13** (200 mg, 1.13 mmol) and isovanillin (172 mg, 1.13 mmol) following general procedure 1. The crude product was purified by normal phase MPLC (20→70% EA:Hex) to give **13** (219 mg, 0.70 mmol, 62%) as orange solid.

^{1}H-NMR (500 MHz, $CDCl_3$): δ = 7.40 (d, *J* = 16.1 Hz, 1H), 7.33 (d, *J* = 16.1 Hz, 1H), 7.20 (d, *J* = 2.1 Hz, 1H), 7.18 (d, *J* = 7.4 Hz, 1H), 7.09 (dd, *J* = 8.3, 2.1 Hz, 1H), 7.06 (d, *J* = 7.4 Hz, 1H), 6.87 (d, *J* = 8.3 Hz, 1H), 5.70 (s, 1H), 3.93 (s, 3H), 2.72 (s, 3H), 2.52 (s, 3H). **^{13}C-NMR (125 MHz, $CDCl_3$):** δ = 166.2, 147.9, 146.1, 137.3, 134.5, 130.1, 129.5, 128.8, 127.2, 125.5, 121.2, 120.7, 112.8, 110.8, 56.2, 21.3, 18.4 ppm. **R_f** = 0.21 (EA:Hex = 2:8). **HRMS (ESI, positive):** 312.10528 calculated for $C_{18}H_{18}NO_2S^+$ $[M+H]^+$, 312.10510 found.

Synthesis of 14

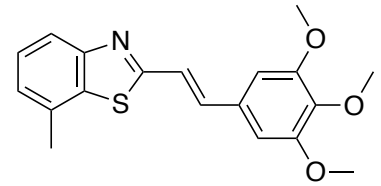

Chemical Formula: $C_{19}H_{19}NO_3S$
Molecular Weight: 341.43

14 was synthesized from **S9** (57 mg, 0.35 mmol) and 3,4,5-trimethoxybenzaldehyde (69 mg, 0.35 mmol) following general procedure 1. The crude product was purified by normal phase MPLC (5→40% EA:Hex) to give **14** (56 mg, 0.16 mmol, 47%) as slightly yellowish solid.

^{1}H-NMR (500 MHz, $CDCl_3$): δ = 7.83 (dt, *J* = 8.0, 0.8 Hz, 1H), 7.46 (d, *J* = 16.1 Hz, 1H), 7.39 (dd, *J* = 8.1, 7.3 Hz, 1H), 7.34 (d, *J* = 16.1 Hz, 1H), 7.18 (dt, *J* = 7.2, 0.9 Hz, 1H), 6.82 (s, 2H), 3.92 (s, 6H), 3.90 (s, 3H), 2.58 (s, 3H) ppm. **^{13}C-NMR (125 MHz, $CDCl_3$):** δ = 166.5, 153.8, 153.7, 139.5, 137.5, 134.9, 131.7, 131.2, 126.7, 125.7, 121.9, 120.5, 104.6, 61.2, 56.3, 21.6 ppm. **R_f** = 0.19 (EA:Hex = 1:9). **HRMS (ESI, positive):** 342.11584 calculated for $C_{19}H_{20}NO_3S^+$ $[M+H]^+$, 342.11547 found.

Synthesis of SBTub2M

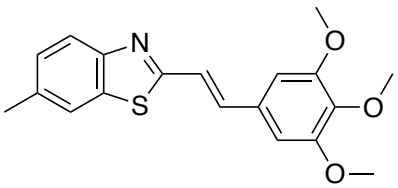

Chemical Formula: $C_{19}H_{19}NO_3S$
Molecular Weight: 341.43

SBTub2M was synthesized from **S10** (69 mg, 0.42 mmol) and 3,4,5-trimethoxybenzaldehyde (83 mg, 0.42 mmol) following general procedure 1. The crude product was purified by normal phase MPLC (5→40% EA:Hex) to give **GAO558** (83 mg, 0.24 mmol, 58%) as yellow solid.

^{1}H-NMR (500 MHz, $CDCl_3$): δ = 7.86 (d, *J* = 8.3 Hz, 1H), 7.65 (dt, *J* = 1.7, 0.8 Hz, 1H), 7.40 (d, *J* = 16.2 Hz, 1H), 7.32 (d, *J* = 16.2 Hz, 1H), 7.28 (ddd, *J* = 8.3, 1.7, 0.8 Hz, 1H), 6.81 (s, 2H), 3.92 (s, 6H), 3.89 (s, 3H), 2.49 (s, 3H) ppm. **^{13}C-NMR (125 MHz, $CDCl_3$):** δ = 165.9, 153.5, 151.9, 139.3, 137.0, 135.7, 134.4, 131.1, 128.0, 122.4, 121.8, 121.3, 104.4, 61.0, 56.2, 21.6 ppm. **R_f** = 0.20 (EA:Hex = 1:9). **HRMS (ESI, positive):** 342.11584 calculated for $C_{19}H_{20}NO_3S^+$ $[M+H]^+$, 342.11565 found.

Synthesis of 16

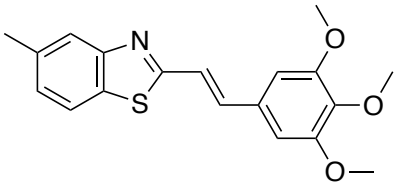

Chemical Formula: $C_{19}H_{19}NO_3S$
Molecular Weight: 341.43

16 was synthesized from **S11** (69 mg, 0.32 mmol) and 3,4,5-trimethoxybenzaldehyde (83 mg, 0.32 mmol) following general procedure 1. The crude product was purified by normal phase MPLC (5→40% EA:Hex) to give **16** (59 mg, 0.17 mmol, 54%) as slightly yellowish solid.

^{1}H-NMR (500 MHz, $CDCl_3$): δ = 7.78 (p, *J* = 0.8 Hz, 1H), 7.73 (d, *J* = 8.1 Hz, 1H), 7.42 (d, *J* = 16.2 Hz, 1H), 7.32 (d, *J* = 16.1 Hz, 1H), 7.21 (ddd, *J* = 8.1, 1.7, 0.7 Hz, 1H), 6.81 (s, 2H), 3.92 (s, 6H), 3.89 (s, 3H), 2.50 (s, 3H) ppm. **^{13}C-NMR (125 MHz, $CDCl_3$):** δ = 167.1, 154.4, 153.7, 139.5, 137.3, 136.6, 131.4, 131.2, 127.2, 123.1, 121.9, 121.1, 104.6, 61.2, 56.3, 21.6 ppm. **R_f** = 0.25 (EA:Hex = 1:9). **HRMS (ESI, positive):** 342.11584 calculated for $C_{19}H_{20}NO_3S^+$ $[M+H]^+$, 342.11581 found.

Synthesis of 17

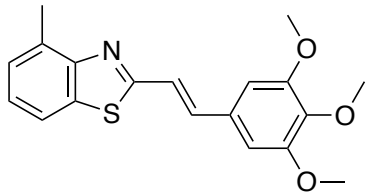

Chemical Formula: $C_{19}H_{19}NO_3S$
Molecular Weight: 341.43

17 was synthesized from **S12** (66 mg, 0.40 mmol) and 3,4,5-trimethoxybenzaldehyde (79 mg, 0.40 mmol) following general procedure 1. The crude product was purified by normal phase MPLC (5→40% EA:Hex) to give **17** (35 mg, 0.10 mmol, 25%) as slightly yellowish solid.

^{1}H-NMR (500 MHz, $CDCl_3$): δ = 7.72 – 7.67 (m, 1H), 7.43 (d, *J* = 16.2 Hz, 1H), 7.38 (d, *J* = 16.1 Hz, 1H), 7.28 – 7.27 (m, 2H), 6.83 (s, 2H), 3.92 (s, 6H), 3.90 (s, 3H), 2.77 (s, 3H) ppm. **^{13}C-NMR (125 MHz, $CDCl_3$):** δ = 166.1, 153.7, 139.5, 137.5, 134.2, 133.0, 131.3, 127.1, 125.5, 122.3, 119.1, 106.3, 104.6, 61.2, 56.3, 18.7. ppm. **R_f** = 0.53 (EA:Hex = 3:7). **HRMS** (ESI, positive): 342.11584 calculated for $C_{19}H_{20}NO_3S^+$ $[M+H]^+$, 342.11552 found.

Synthesis of 18

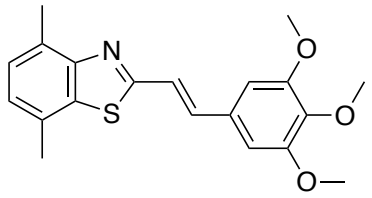

Chemical Formula: $C_{20}H_{21}NO_3S$
Molecular Weight: 355.45

18 was synthesized from **S13** (188 mg, 1.1 mmol) and 3,4,5-trimethoxybenzaldehyde (208 mg, 1.1 mmol) following general procedure 1. The crude product was purified by normal phase MPLC (5→40% EA:Hex) to give **18** (60 mg, 0.17 mmol, 16%) as yellow solid.

^{1}H-NMR (500 MHz, $CDCl_3$): δ = 7.41 (s, 1H), 7.41 (s, 1H), 7.19 (dd, *J* = 7.3, 1.0 Hz, 1H), 7.08 (dd, *J* = 7.3, 1.0 Hz, 1H), 6.83 (s, 2H), 3.92 (s, 6H), 3.90 (s, 3H), 2.72 (s, 3H), 2.53 (s, 3H) ppm. **^{13}C-NMR (125 MHz, $CDCl_3$):** δ = 165.6, 153.5, 152.8, 139.3, 137.2, 134.5, 131.2, 130.1, 128.8, 127.1, 125.6, 122.4, 104.4, 61.0, 56.2, 21.2, 18.3 ppm. **R_f** = 0.36 (EA:Hex = 1:9). **HRMS (ESI, positive):** 356.13149 calculated for $C_{20}H_{22}NO_3S^+$ $[M+H]^+$, 356.13112 found.

Synthesis of SBTub3P

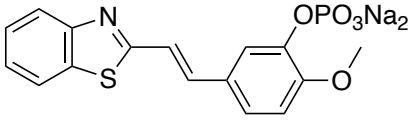

Chemical Formula: $C_{16}H_{12}NNa_2O_5PS$
Molecular Weight: 407.29

To a cooled solution of **SBTub3** (594 mg, 2.1 mmol), TEA (0.58 mL, 4.2 mmol, 2 eq), DMAP (51 mg, 0.42 mmol, 0.2 eq) and CCl_4 (1 mL) in MeCN (20 mL), was slowly added dibenzyl phosphite (770 mg, 2.9 mmol, 1.4 eq) and the resulting mixture was stirred at room temperature until phosphorylation was complete (~15 min). The volatiles were evaporated to give the phenolic (bis)benzyl ester, which was purified by flash column purification (EA:Hex = 4:6) to give 1.14 g of a colourless solid, that was directly redissolved in a mixture of DCM:TFA (14 mL, 1:1) and stirred for 6 h at 40°C. After removing all volatiles under reduced pressure, water (50 mL) was added and the suspension was basified with 2M NaOH until all solids fully dissolved. The clear solution was transferred into a separation funnel and washed with EA (3 × 30 mL). The aqueous layer was set to pH ~2 with 2M HCl and loaded on a C18 solid phase extraction cartridge, washed with water (3 × 10 mL), eluted with MeOH and concentrated *in vacuo*. The crude product was purified by RP-MPLC (0→25% MeCN:H_2O) to give **SBTub3P** (393 mg, 1.1 mmol, 52%) as slightly yellowish powder after lyophilizing.

^{1}H-NMR (400 MHz, D_2O): δ = 7.85 (d, *J* = 7.9 Hz, 1H), 7.79 (d, *J* = 8.0 Hz, 1H), 7.69 (s, 1H), 7.47 – 7.37 (m, 2H), 7.34 (t, *J* = 7.6 Hz, 1H), 7.22 (d, *J* = 16.2 Hz, 1H), 7.15 (dd, *J* = 8.4, 1.6 Hz, 1H), 6.90 (d, *J* = 8.5 Hz, 1H), 3.80 (s, 3H) ppm. **^{13}C-NMR (100 MHz, D_2O):** δ = 169.6, 152.1, 151.2, 143.2, 138.6, 133.5, 128.0, 126.5, 125.3, 123.0, 121.9, 121.3, 118.7, 118.3, 112.3, 55.6 ppm. **HRMS (ESI, negative):** 362.02575 calculated for $C_{16}H_{13}NO_5PS^-$ $[M–H]^-$,362.02566 found.

Synthesis of SBTubA4P

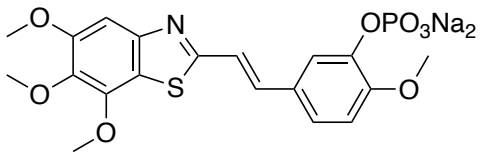

Chemical Formula: $C_{19}H_{18}NNa_2O_8PS$
Molecular Weight: 497.37

A solution of SBTubA4 (1.10 g, 2.95 mmol, 1 eq) in 30 mL MeCN was cooled to 0°C. Dibenzyl diphosphate (1.16 g, 4.42 mmol, 1.5 eq), DIPEA (1 mL, 6.19 mmol, 2.1 eq), DMAP (7 mg, 58.9 µmol, 0.02 eq) and CCl_4 (1 mL). After stirring for 5 min the reaction mixture was allowed to warm to room temperature. After 4 h no further conversion was observed by TLC and HPLC-MS. Water (80 mL) was added and the reaction mixture is extracted with EA (3 x 50 mL) and washed with brine (1 x 50 mL). The combined organic layers were dried over Na_2SO_4, filtrated and concentrated *in vacuo*. The crude was purified by normal phase MPLC to give the bis(benzyl) phosphate of SBTubA4 (1.38 g, 2.17 mmol, 74%) as colourless solid.

^{1}H-NMR (400 MHz, $CDCl_3$): δ = 7.40 – 7.29 (m, 13H), 7.27 (s, 1H), 7.08 (d, *J* = 16.1 Hz, 1H), 6.92 (d, *J* = 8.2 Hz, 1H), 5.20 (dd, *J* = 8.2, 2.0 Hz, 4H), 4.10 (s, 3H), 3.95 (s, 3H), 3.94 (s, 3H), 3.83 (s, 3H) ppm. **^{13}C-NMR (100 MHz, $CDCl_3$):** δ = 166.8, 154.1, 151.8, 150.5, 146.8, 140.2, 135.8, 135.5, 128.8, 128.1, 125.6, 120.8, 120.1, 119.8, 112.8, 100.6, 70.2, 61.6, 60.7, 56.4, 56.1 ppm.

The bis(benzyl)phosphate (1.33 g, 2.1 mmol, 1 eq) was dissolved in dichloromethane (40 mL) at 0°C under nitrogen atmosphere. Bromotrimethylsilane (0.583 µL, 4.42 mmol, 2.1 eq) was added was added dropwise upon which the phosphoric acid intermediate started to precipitate. Methanol (20 mL) was added and stirring was continued for 15 min before concentrating *in vacuo.* The crude mixture was resuspended in EtOH (50 mL) and sodium methoxide (0.77 mL 6M in MeOH, 4.63 mmol, 2.2 eq) was added at 0°C. Stirring was continued overnight at room temperature. The solvent was removed under reduced pressure

and the crude product was purified by RP-MPLC (10→100% MeCN:H_2O) to give **SBTubA4P** (864 mg, 1.74 mmol, 83%) as yellow solid.

^{1}H-NMR (400 MHz, MeOD$_4$): δ = 7.99 (d, *J* = 2.1 Hz, 1H), 7.48 (d, *J* = 16.1 Hz, 1H), 7.34 (d, *J* = 16.1 Hz, 1H), 7.23 (s, 1H), 7.16 (dd, *J* = 8.5, 2.1 Hz, 1H), 6.95 (dd, *J* = 8.5, 1.0 Hz, 1H), 4.05 (s, 3H), 3.93 (s, 3H), 3.88 (s, 3H), 3.87 (s, 3H) ppm. **^{13}C-NMR (100 MHz, MeOD$_4$):** δ = 169.7, 155.6, 153.1, 151.2, 147.9, 145.8, 141.1, 139.3, 129.7, 123.2, 120.2, 120.1, 119.4, 112.9, 101.1, 61.8, 61.1, 56.8, 56.5 ppm. **HRMS (ESI, positive):** 498.0359 calculated for $C_{19}H_{19}NNa_2O_8PS^+$ $[M+H]^+$, 498.03618 found.

Experimental data of synthetic building blocks

Synthesis of S1

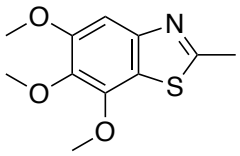

Chemical Formula: $C_{11}H_{13}NO_3S$
Molecular Weight: 239.29

S1 was synthesized from 3,4,5-trimethoxyaniline (3.0 g, 16 mmol) following general procedure 2. The crude product was purified by normal phase MPLC (0→30% EA:Hex) to give **S1** (0.56 g, 2.3 mmol, 14%) as yellow oil.

^{1}H-NMR (400 MHz, CDCl$_3$): δ = 7.23 (s, 1H), 4.05 (s, 3H), 3.92 (s, 3H), 3.90 (s, 3H), 2.78 (s, 3H) ppm. **^{13}C-NMR (100 MHz, CDCl$_3$):** δ = 166.8, 153.7, 149.8, 146.7, 139.3, 120.5, 100.2, 61.4, 60.5, 56.2, 20.0 ppm. **R_f** = 0.23 (EA:Hex = 2:8). **HRMS (ESI, positive):** 240.06889 calculated for $C_{11}H_{14}NO_3S^+$ $[M+H]^+$, 240.06869 found.

Synthesis of S2

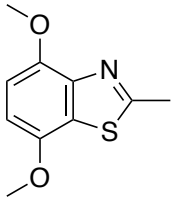

Chemical Formula: $C_{10}H_{11}NO_2S$
Molecular Weight: 209.26

S2 was synthesized from 2,5-dimethoxyaniline (3.0 g, 20 mmol) following general procedure 2. The crude product was purified by normal phase MPLC (5→20% EA:Hex) to give **S2** (0.75 g, 3.6 mmol, 18%) as yellow oil.

^{1}H-NMR (400 MHz, $CDCl_3$): δ = 6.80 (d, *J* = 8.6 Hz, 1H), 6.71 (d, *J* = 8.6 Hz, 1H), 3.99 (s, 3H), 3.93 (s, 3H), 2.85 (s, 3H) ppm. **^{13}C-NMR (100 MHz, $CDCl_3$):** δ = 166.6, 148.1, 147.6, 144.6, 126.1, 106.6, 105.0, 56.3, 56.2, 20.2. ppm. **R_f** = 0.24 (EA:Hex = 2:8). **HRMS (ESI, positive):** 210.05833 calculated for $C_{10}H_{12}NO_2S^+$ $[M+H]^+$, 210.05818 found.

Synthesis of S3 MOM protected benzaldehyde

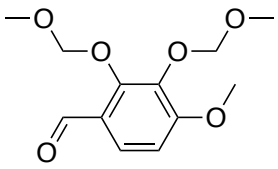

Chemical Formula: $C_{12}H_{16}O_6$
Molecular Weight: 256.25

2,3-dihydroxy-4-methoxybenzaldehyde (100 mg, 0.6 mmol) was dissolved in dry dichloromethane under nitrogen atmosphere and cooled to 0°C. Diisopropylethylamine (0.3 mL, 1.8 mmol, 3 eq) was added dropwise. MOM-Cl (0.09 mL, 1.2 mmol, 2 eq) was added dropwise. The reaction was stirred at 0°C for 2 h, and then warmed to room temperature overnight. Water (30 mL) was added and the aqueous layer was extracted with DCM (3 × 30 mL). The combined organic layers were washed with AcOH (2 × 15 mL, 10%), sat. aq. $NaHCO_3$ (15 mL) and brine (30 mL), dried over $MgSO_4$ and the solvent was removed *in vacuo*. The compound was used without further purification.

^{1}H-NMR (400 MHz, $CDCl_3$): δ = 10.28 (s, 1H), 7.65 (d, *J* = 8.8 Hz, 1H), 6.81 (d, *J* = 8.8 Hz, 1H), 5.26 (s, 2H), 5.13 (s, 2H), 3.93 (s, 3H), 3.60 (s, 3H), 3.57 (s, 3H) ppm. **^{13}C-NMR (100 MHz, $CDCl_3$):** δ = 189.2, 159.1, 154.3, 138.3, 125.0, 124.3, 108.1, 100.5, 98.8, 58.2, 57.7, 56.3 ppm. **R_f** = 0.53 (EA:Hex = 4:6). **LRMS (ESI, positive):** 257.10196 calculated for $C_{12}H_{17}O_6^+$ $[M+H]^+$, 257.1 found.

Synthesis of S4[3]

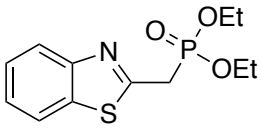

Chemical Formula: $C_{12}H_{16}NO_3PS$
Molecular Weight: 285.30

A mixture of **S5** (0.50 g, 2.19 mmol) in triethyl phosphite (1 mL) was refluxed overnight. The excess $P(OEt)_3$ was removed under a nitrogen flow and the residue was purified by silica gel column chromatography to afford product **S4** in quantitative yield.

^{1}H-NMR (400 MHz, $CDCl_3$): δ = 8.00 (ddt, *J* = 8.1, 1.2, 0.7 Hz, 1H), 7.86 (ddd, *J* = 8.0, 1.2, 0.6 Hz, 1H), 7.47 (ddd, *J* = 8.3, 7.2, 1.3 Hz, 1H), 7.38 (ddt, *J* = 8.2, 7.2, 1.0 Hz, 1H), 4.16 (p, *J* = 7.3 Hz, 4H), 3.76 (s, 1H), 3.71 (s, 1H), 1.32 (t, *J* = 7.1 Hz, 6H) ppm. **R_f** = 0.12 (EA:Hex = 1:1). **LRMS (ESI, positive):** 286.06613 calculated for $C_{12}H_{17}NO_3PS^+$ $[M+H]^+$, 286.2 found.

Synthesis of S5[4]

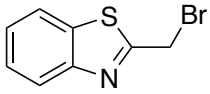

Chemical Formula: C_8H_6BrNS
Molecular Weight: 228.11

2-methylbenzothiazole (1.7 mL, 13.4 mmol), N-bromosuccinimide (2.39 g, 13.40 mmol), and AIBN (0.5 g, 3.04 mmol) was dissolved in CCl_4 (25 mL) and refluxed for overnight. The mixture was cooled and filtered. The filtrate was concentrated *in vacuo* and purified by normal phase MPLC (0→ 10% EA:Hex) to give **S5** (1.29 g, 42%) as a yellow oil.

^{1}H-NMR (400 MHz, $CDCl_3$): δ = 8.03 (dt, *J* = 8.3, 0.9 Hz, 1H), 7.88 (dt, *J* = 8.0, 1.0 Hz, 1H), 7.51 (ddd, *J* = 8.3, 7.2, 1.3 Hz, 1H), 7.43 (ddd, *J* = 8.3, 7.2, 1.3 Hz, 1H), 4.82 (s, 2H) ppm. **R_f** = 0.53 (EA:Hex = 1:9).

Synthesis of S6[5]

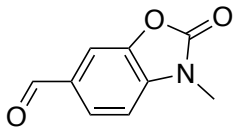

Chemical Formula: $C_9H_7NO_3$
Molecular Weight: 177.16

To 3-Methyl-2-benzoxazolone (0.50 g, 3.35 mmol) and hexamethylenetetramine (1.4 g, 10 mmol, 3 eq) was added TFA (10 mL). The resulting mixture was refluxed overnight at 80°C. The reaction mixture was cooled and poured into ice-water. The solution was neutralized with sat. aq. $NaHCO_3$ and extracted with ethyl acetate (3 × 30 mL). The combined organic layers were dried over Na_2SO_4 and concentrated under reduced pressure to obtain the desired aldehyde **S6** as colorless solid (0.53 mg, 3 mmol, 90%).

^{1}H-NMR (400 MHz, $CDCl_3$): δ = 9.95 (s, 1H), 7.79 (dd, *J* = 8.0, 1.4 Hz, 1H), 7.74 (d, *J* = 1.4 Hz, 1H), 7.11 (d, *J* = 8.0 Hz, 1H), 3.48 (s, 3H) ppm. **R_f** = 0.38 (EA:Hex = 1:1).

Synthesis of S7

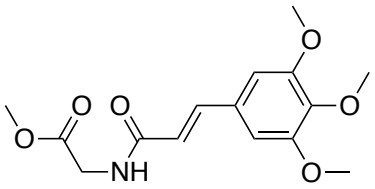

Chemical Formula: $C_{15}H_{19}NO_6$
Molecular Weight: 309.32

To a stirring suspension of cinnamic acid **S8** (0.5 g, 2.1 mmol) was added $SOCl_2$ (1.5 mL, 21 mmol, 10 eq) at 0°C. The mixture was stirred for 3 h at room temperature. The solvent was removed, the cinnamic acid chloride was redissolved in $CHCl_3$ (5 mL) and added to a stirred suspension of glycine methyl ester hydrochloride (290 mg, 2.31 mmol, 1.1 eq) and triethylamine (0.64 mL, 4.62 mmol, 2.2 eq) in chloroform (5 mL). Stirring was continued for 3 h, before the solvent was removed under reduced pressure to afford a yellowish crude, which was purified by flash column chromatography (EA:Hex = 3:7) to afford desired compound **S7** (0.55 g, 1.78 mmol, 85%) as colorless solid.

^{1}H-NMR (500 MHz, $CDCl_3$): δ = 7.56 (d, *J* = 15.5 Hz, 1H), 6.74 (s, 2H), 6.38 (d, *J* = 15.5 Hz, 1H), 6.15 (t, *J* = 4.6 Hz, 1H), 4.20 (d, *J* = 5.0 Hz, 2H), 3.89 (s, 6H), 3.87 (s, 3H), 3.80 (s, 3H) ppm. **^{13}C-NMR (125 MHz, $CDCl_3$):** δ = 170.7, 165.9, 153.6, 142.0, 139.9, 130.3, 119.2, 105.2, 61.1, 56.3, 52.6, 41.6 ppm. **R_f** = 0.42 (EA:Hex = 9:1). **LRMS (ESI, positive):** 310.13 calculated for $C_{15}H_{20}NO_6^+$ $[M+H]^+$, 310.1 found.

Synthesis of cinnamic acid S8

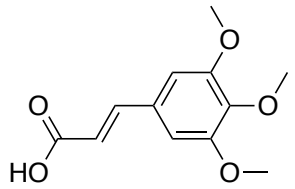

Chemical Formula: $C_{12}H_{14}O_5$
Molecular Weight: 238.24

To a solution of 3,4,5-trimethoxybenzaldehyde (5 g, 25.5 mmol), malonic acid (3.18 g, 30.6 mmol, 1.2 eq) in pyridine (10 mL) was added piperidine (0.25 mL, 2.55 mmol, 0.1 eq) and refluxed for 16 h. The solvent was removed under reduced pressure, redissolved in EA (20 mL) and washed with 2 M HCl (2 × 10 mL), water (10 mL) and brine (10 mL) and recrystallized to afford **S8** as colorless solid (5.19 g, 21.7 mmol, 85%).

^{1}H-NMR (400 MHz, $CDCl_3$): δ = 7.71 (d, *J* = 15.9 Hz, 1H), 6.78 (s, 2H), 6.36 (d, *J* = 15.9 Hz, 1H), 3.90 (s, 6H), 3.90 (s, 3H) ppm. **^{13}C-NMR (100 MHz, $CDCl_3$):** δ =171.4, 153.6, 147.2, 140.7, 129.6, 116.4, 105.7, 61.2, 56.3. ppm. **R_f** = 0.57 (EA:Hex + 0.1% Formic Acid = 1:1). **HRMS (EI, positive):** 238.0836 calculated for $C_{12}H_{14}O_5^+$ $[M]^+$, 238.0836 found.

Synthesis of S9

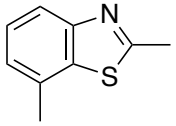

Chemical Formula: C_9H_9NS
Molecular Weight: 163.24

S9 was synthesized following general procedure 3. Starting from 2-Iodo-3-nitrotoluene (1.5 g, 5.7 mmol), obtaining *N*-(2-iodo-3-methylphenyl)acetamide (1.5 g, 5.45 mmol, 96% over two steps). (550 mg, 2 mmol). The crude product from the copper catalysed heteroaromatic ring closure of the acetamide (550 mg, 2 mmol) was purified by normal phase MPLC (10→30% EA:Hex) to give **S9** (244 mg, 1.49 mmol, 75%) as colourless solid.

^{1}H-NMR (500 MHz, $CDCl_3$): δ = 7.80 (d, *J* = 8.1 Hz, 1H), 7.37 (dd, *J* = 8.1, 7.3 Hz, 1H), 7.15 (dt, *J* = 7.3, 0.9 Hz, 1H), 2.85 (s, 3H), 2.54 (s, 3H). **^{13}C-NMR (125 MHz, $CDCl_3$):** δ = 166.6, 153.4, 136.3, 131.7, 126.2, 125.0, 119.9, 21.6, 20.4 ppm. **R_f** = 0.52 (EA:Hex = 2:8). **LRMS** (APCI, positive): 164.05285 calculated for $C_9H_{10}NS^+$ $[M+H]^+$, 164.0 found.

Synthesis of S10[6]

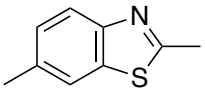

Chemical Formula: C_9H_9NS
Molecular Weight: 163.24

S10 was synthesized from *p*-toluidine (3.1 mL, 28 mmol) following general procedure 2. The crude product was purified by Kugelrohr distillation (50 mbar, 200°C) to give **S10** (2.2 g, 13 mmol, 48%). **^{1}H-NMR (400 MHz, $CDCl_3$):** δ = 7.82 (d, *J* = 8.3 Hz, 1H), 7.60 (dt, *J* = 1.8, 0.8 Hz, 1H), 7.24 (dd, *J* = 8.3, 1.8 Hz, 1H), 2.81 (s, 3H), 2.46 (s, 3H) ppm. **R_f** = 0.20 (EA:Hex = 5:95).

Synthesis of S11

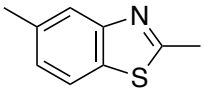

Chemical Formula: C_9H_9NS
Molecular Weight: 163.24

S11 was synthesized following general procedure 3. Starting from 4-Iodo-3-nitrotoluene (1.5 g, 5.7 mmol), first obtaining *N*-(2-iodo-5-methylphenyl)acetamide (1.52 g, 5.5 mmol, 97% over two steps). The crude product from the copper catalysed heteroaromatic ring closure of the acetamide (550 mg, 2 mmol) was purified by normal phase MPLC (10→30% EA:Hex) to give **S11** (185 mg, 1.1 mmol, 57%) as colourless solid.

^{1}H-NMR (500 MHz, $CDCl_3$): δ = 7.75 (s, 1H), 7.68 (d, *J* = 8.2 Hz, 1H), 7.17 (dd, *J* = 8.2, 1.6 Hz, 1H), 2.82 (s, 3H), 2.49 (s, 3H) ppm. **^{13}C-NMR (125 MHz, $CDCl_3$):** δ = 167.2, 153.9, 136.1, 132.7, 126.4, 122.6, 121.0, 21.6, 20.3 ppm. **R_f** = 0.52 (EA:Hex = 2:8). **LRMS** (APCI, positive): 164.05285 calculated for $C_9H_{10}NS^+$ $[M+H]^+$, 164.0 found.

Synthesis of S12

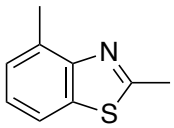

Chemical Formula: C_9H_9NS
Molecular Weight: 163.24

S12 was synthesized from *o*-toluidine (3.6 mL, 34 mmol) following general procedure 2. The crude product was purified by normal phase MPLC (0→20% EA:Hex) to give **S12** (1.93 g, 12 mmol, 35%) as yellow oil.

^{1}H-NMR (400 MHz, $CDCl_3$): δ =7.68 (t, *J* = 4.6 Hz, 1H), 7.29 – 7.25 (m, 2H), 2.88 (s, 3H), 2.78 (s, 3H). ppm. **^{13}C-NMR (100 MHz, $CDCl_3$):** δ = 165.7, 152.8, 135.6, 132.4, 126.6, 124.6, 118.9, 20.3, 18.6 ppm. **R_f** = 0.38 (EA:Hex = 1:40). **HRMS (ESI, positive):** 164.05285 calculated for $C_9H_{10}NS$ $[M+H]^+$, 164.05281 found.

Synthesis of S13

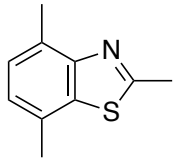

Chemical Formula: $C_{10}H_{11}NS$
Molecular Weight: 177.27

S13 was synthesized from 2,5-dimethylaniline (5 mL, 40 mmol) following general procedure 2. The crude product was purified by Kugelrohr distillation (50 mbar, 200°C) to give **S13** (1.05 g, 6 mmol, 15%) as yellow oil.

^{1}H-NMR (400 MHz, $CDCl_3$): δ = 7.18 (d, *J* = 7.4 Hz, 1H), 7.06 (d, *J* = 7.4 Hz, 1H), 2.89 (s, 3H), 2.71 (s, 3H), 2.49 (s, 3H) ppm. **^{13}C-NMR (100 MHz, $CDCl_3$):** δ = 165.2, 152.1, 135.7, 129.2, 128.5, 126.5, 124.5, 21.1, 20.1, 18.1 ppm. **R_f** = 0.5 (EA:Hex = 1:20). **HRMS (EI, positive):** 177.0612 calculated for $C_{10}H_{11}NS$ $[M]^+$, 177.0603 found.

Part B: Photocharacterisation *in vitro*

Spectrophotometry

Absorption spectra in cuvette ("UV-Vis") were acquired on a Cary 60 UV-Vis Spectrophotometer from Agilent (1 cm pathlength). For photoisomerisation measurements, Hellma microcuvettes (108-002-10-40) taking 500 μL volume to top of optical window were used with the default test solution concentrations of 25 μM. Measurements were performed in PBS at pH~7.4 with 10% of DMSO or 50% DMSO indicated by asterisk (*). Prodrugs SBTubA4P and SBTub3P were measured in PBS only. Photoisomerisations were performed at room temperature. Medium-power LEDs (H2A1-models spanning 360–490 nm from Roithner Lasertechnik) were used to deliver high-intensity and relatively monochromatic light (FWHM ~25 nm) into the cuvette, for rapid PSS determinations that were also predictive of what would be obtained in LED-illuminated cell culture (**Fig S1**). Spectra of pure *E* and *Z* isomers were acquired from the inline Diode Array Detector during analytical separation on the HPLC (injection of 10 μL, 5→100% MeCN:H_2O over 20 min), after injecting DMSO stocks (0.5 – 2.5 mM) that had been irradiated with a 420 nm LED (~ 5 min) (**Fig S2**).

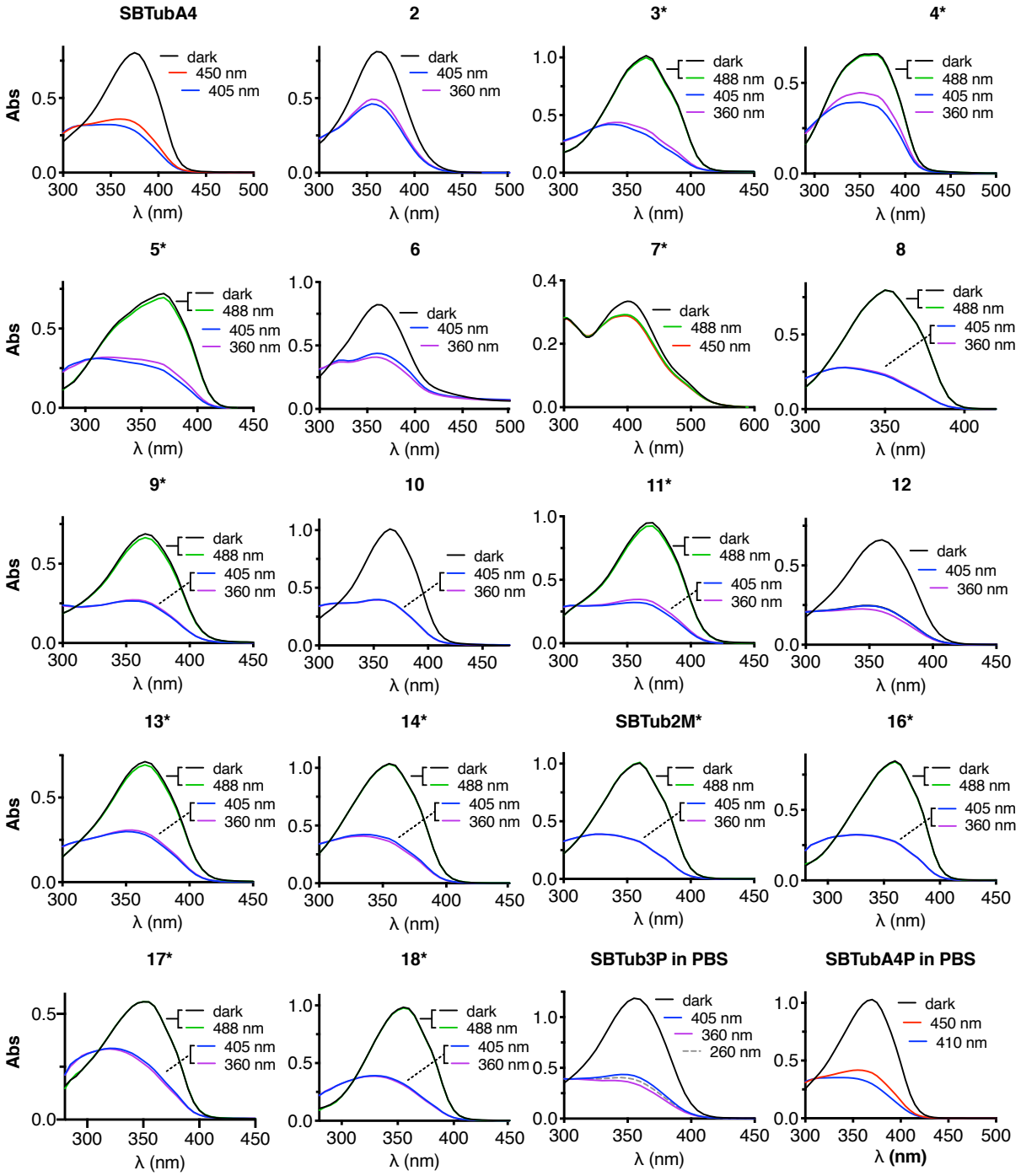

Fig S1: UV-Vis spectra of second generation SBTubs at various photostationary states, shows that the SBT scaffold is relatively unaffected by various functional residues, indicating that most of these newly synthesized SBTubs are also GFP-orthogonal. 25 μM in PBS, pH ~7.4, 10% DMSO unless indicated by asterisk* (50% DMSO) or "in PBS" (0% DMSO), room temperature, under closed air atmosphere.

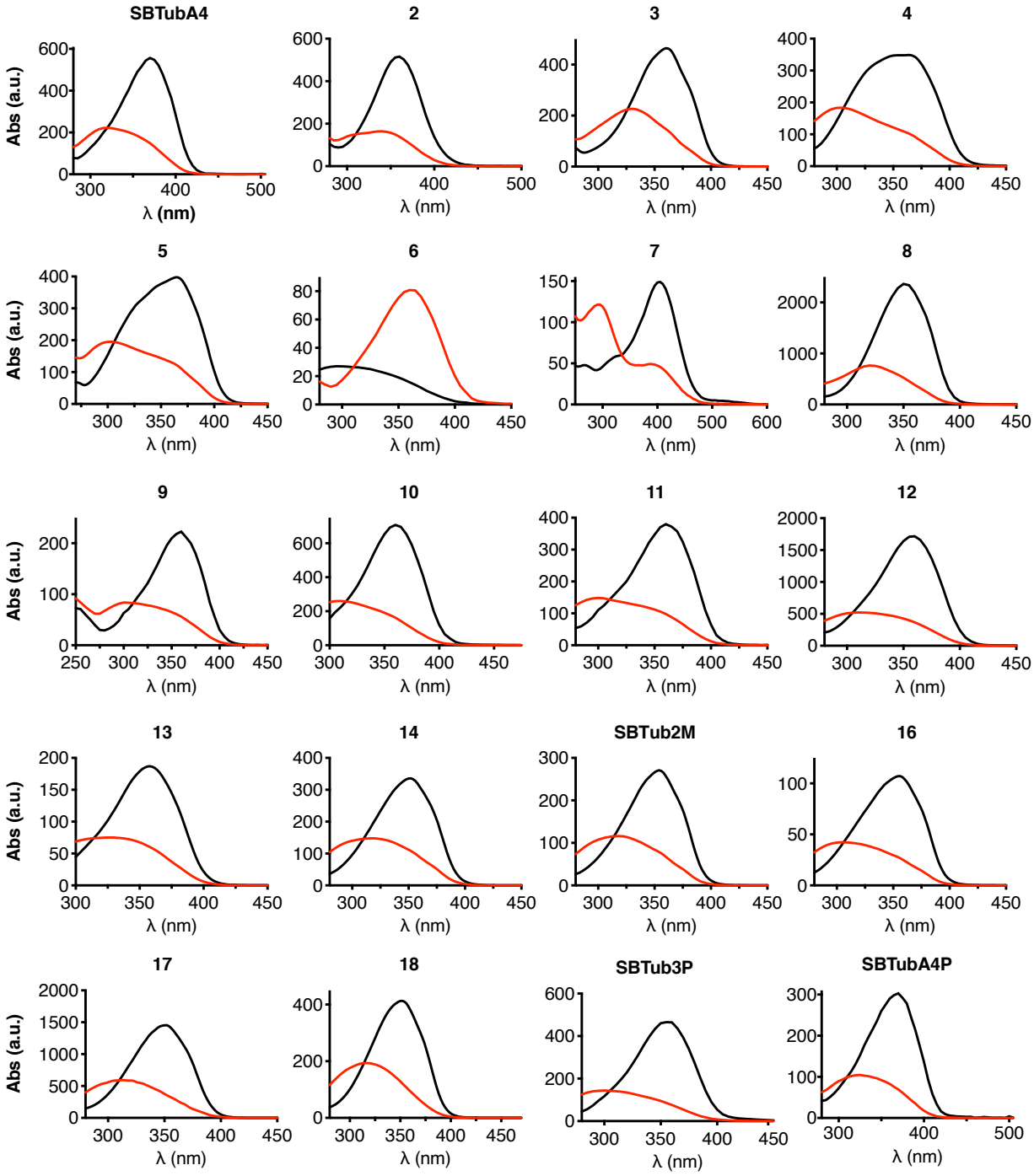

Fig S2: all-*E* and all-*Z* spectra of second generation SBTubs from inline HPLC-DAD

Photoisomerisation: further discussion

Ortho-hydroxy **6** and *para*-amino **7** were designed to test if these strong electron donors, that can also tautomerise to freely-rotatable quinoids (C-C single bond instead of C=C), can accelerate thermal *Z*→*E* relaxation to make better-reversible **SBTub**s, as well as inducing spectral redshifting. On azobenzenes and hemithioindigos, such strong *ortho*/*para*-electron-donating tautomerisable groups typically cause millisecond to second aqueous relaxation rates, often limiting their use on cytosolic targets. However, in cuvette, *Z*-**6/7** thermally relaxed

only slowly compared to the timescales relevant to biological assays (halflives >> hours). *Z*-**7**'s stability was supported by lit-**7**'s appreciable cytotoxicity in cells, which is a remarkable result for the SBT scaffold as an alternative to azobenzenes and hemithioindigos. We had previously shown that a *p*-hydroxy SBT is photoswitchable in cuvette[7] but its design as non-binding control could not test whether its *Z*-isomer would also be stable enough for bioactivity in cells.[8,9] **7** showed that SBT photopharmaceuticals on cytosolic targets indeed tolerate *ortho/para* electron-donating tautomerisable groups. Furthermore, although the spectra of *E/Z*-**6** were similar to normal SBTs, **7** was redshifted by nearly 70 nm (**Fig S1-S2**). This may suit *para*-aminoSBTs as comparably absorbing alternatives to *p*-aminoazobenzenes that retain the often crucial *p*-amino function yet offer bistable isomerisation, which can be of interest in e.g. ion channel photopharmacology (where *p*-aminoazobenzenes are most widely employed). Since **6** was photoswitchable *in cuvette* yet showed no light-dependent cytotoxicity we suppose that it may suffer biochemical problems as known for catechols (e.g. metal complexation, oxidation to the *ortho*-quinone, etc[10]). In this study, as it was clear that neither **6/7** brought relaxation rate benefits, we did not pursue such derivatives further; but these results do showcase the unique compatibility of the SBT scaffold for bistable photopharmaceuticals where small polar hydroxy or amino groups (common groups for high-potency ligand-protein interactions) are needed in the phenyl *ortho* or *para* positions.

Photostability

The SBTubs' photostability to continuous UV illumination at >380 nm was typically excellent.

We also observed that primarily electron-rich SBTubs (**SBTubA4**, **Fig S3**) undergo unwanted photoreactions when short-wavelength irradiation (typically <350 nm) stimulates the S2←S0 transition, a band that is visible as a low-intensity shoulder to the principal S1←S0 band (**Fig S2-S3**; this band is particularly pronounced for aniline **7**). Therefore, for clean *E*→*Z* photoswitching, it is beneficial to use switching wavelengths λ_{lit} that are usually 10-30 nm red-shifted from $\lambda_{max}(E)$. In contrast, continuous illumination with intense < 350 nm light caused slow degradation (ca. 10% lost during 10 min illumination with 360 nm band centre, ca. 25 nm FWHM, LED with nominal 200 mW/cm^2 optical output).

To characterise this photodegradation, electron-rich **SBTubA4** (25 μM in PBS:DMSO = 1:1) was irradiated with LEDs of emission maxima λ > 400 nm until corresponding PSSs were reached (reversible photoswitching; **Fig S3a**). Then applying 100 mW/cm^2 LED illumination with nominal band maximum 360 nm first gave rapid partial bulk *Z*→*E* photoisomerization to the ~360 nm PSS (**Fig S3b**: isosbestic point retained), then slower light-induced side

reactions that destroy the ArC=CAr' chromophore (indicated by the drop of the isosbestic point, **Fig 3c**). Since this photodegradation does not occur at λ > 400 nm it should not pose a problem in biological assays when appropriate pure photoactivation wavelengths are used, such as the standard 405 nm laser (bandwidth < 1 nm) available on standard microscopy setups (see also previously performed photostability studies on SBTubs[7]).

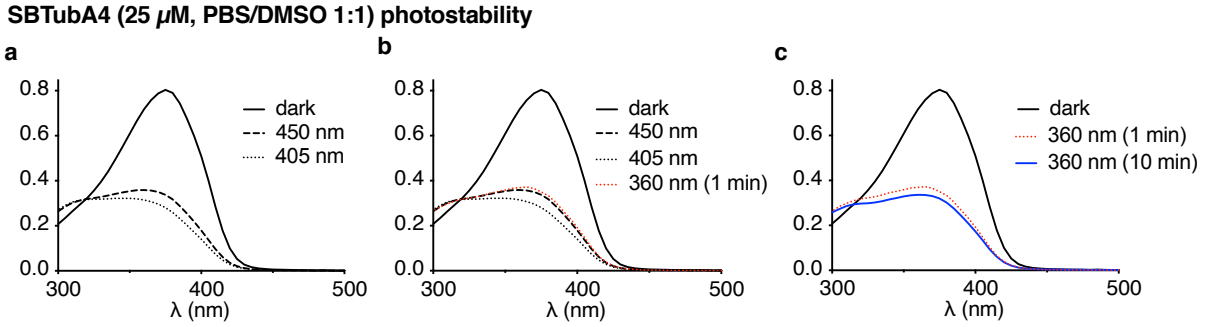

Fig S3: (a) Dark state spectrum, then PSS establishment with LED sources first at 450 nm then at 405 nm (note: LED bandwidth implies that wavelengths below 450 nm are substantially responsible for the photoswitching speed at nominal "450 nm"). (b) From 405 nm PSS, 360 nm LED was applied, reaching new PSS. (c) Under continued 360 nm illumination, the absorption profile drops, indicating side reactions that destroy the ArC=CAr' chromophore.

Spontaneous relaxation of SBTubA4

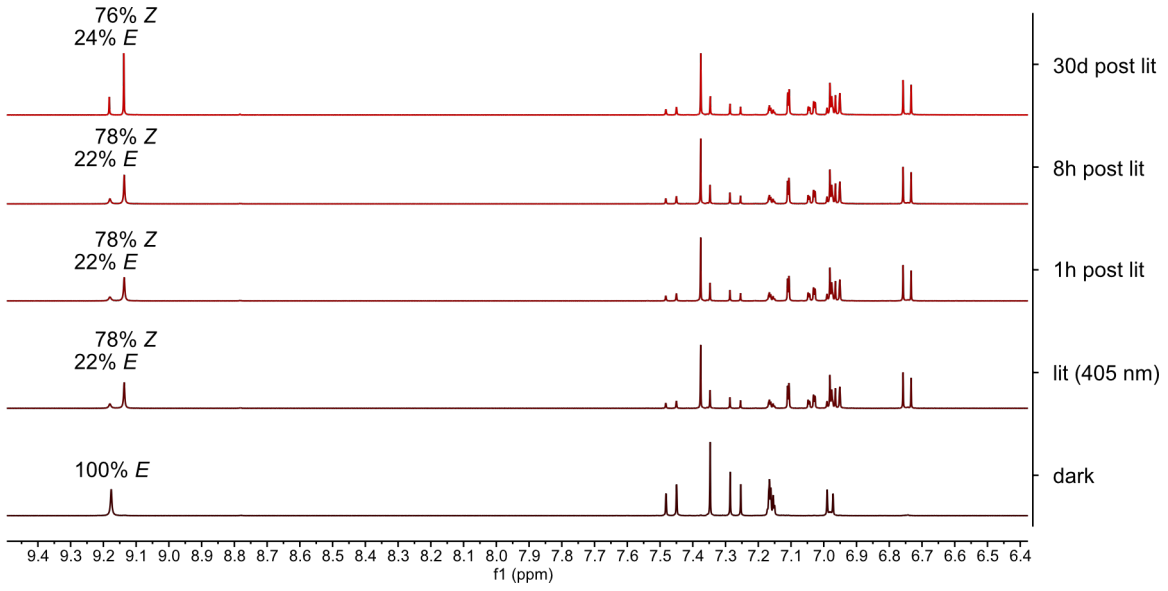

Fig S4: NMR of SBTubA4 showing the aromatic region. Illumination with 405 nm light reaches a PSS of ~80% *Z*-isomer, which is does not relax back over several days.

SBTubA4 (6 mg) was dissolved in deuterated DMSO (0.6 mL) and photoisomerised with a 405 nm LED for 5 minutes to reach a PSS of ~80% *Z*-isomer as measured by NMR, subsequent measurements after storing the NMR tube in the dark for 1 h, 8 h (at 60°C) and 30 days (at room temperature) showed little to none spontaneous relaxation (**Fig S4**). (Side note: a pre-illuminated DMSO stock left in the dark in a fridge at 4°C was found >99% reverted

back to the *E*-isomer after 9 months, giving an upper bound to the relaxation halflife in DMSO). Therefore, DMSO stocks of **SBTubA4** need more careful light-avoiding handling than **SBTub3** or **SBTub2M**, which both thermally revert back to 100% *E* when kept overnight at 60°C.

Part C: Biological Data

Tubulin polymerisation

99% tubulin from porcine brain was obtained from Cytoskeleton Inc. (cat. #T240). The polymerisation reaction was performed at 5 mg/mL tubulin, in polymerisation buffer BRB80 (80 mM piperazine-N,N′-bis(2-ethanesulfonic acid) (PIPES) pH = 6.9; 0.5 mM EGTA; 2 mM $MgCl_2$), in a cuvette (120 µL final volume, 1 cm path length) in a Agilent CaryScan 60 with Peltier cell temperature control unit maintained at 37°C; with glycerol (10 μL). Tubulin was first incubated for 10 min at 37°C with "lit"- (405 nm-pre-illuminated; mostly-*Z*-) or dark- (all-*E*) **SBTub** (final concentration 20 μM) in buffer with 3% DMSO, without GTP. Then GTP was added to achieve final GTP concentration 1 mM (with mixing), and the change in absorbance at 340 nm was monitored for 15 min, scanning at 15 s intervals.

Cell assay methods

General cell culture

HeLa, Jurkat and A549 cells were maintained under standard cell culture conditions in Dulbecco's modified Eagle's medium (DMEM; PAN-Biotech: P04-035550) supplemented with 10% fetal calf serum (FCS), 100 U/mL penicillin and 100 U/mL streptomycin. Cells were grown and incubated at 37°C in a 5% CO_2 atmosphere. Cells were typically transferred to phenol red free medium prior to assays (DMEM; PAN-Biotech: P04-03591). Substrates and cosolvent (DMSO; 1% final concentration) were added *via* a D300e digital dispenser (Tecan). Cells were either incubated under "lit" or "dark" conditions; "lit" indicates a pulsed illumination protocol was applied by multi-LED arrays to create the *Z*-isomers of the compounds in *situ* in cells and then maintain the wavelength-dependent PSS isomer ratio throughout the experiment, as described previously.[11] Typical "lit" timing conditions were 75 ms pulses of ~1 mW/cm^2 applied every 15 s. "Dark" indicates that **SBTub** biostocks were used with an all-*trans* state, as determined by analytical HPLC, kept in the dark at 4°C, applied while working under red-light conditions, and cells were then incubated in light-proof boxes to shield from ambient light, thereby maintaining the all-*E*-isomer population throughout the experiment.

Resazurin antiproliferation assay

HeLa or A549 cells were seeded in 96-well plates at 5,000 cells/well and left to adhere for 24 h before treating with test compounds. *E*-SBTubs were added for 48 h (final well volume 100 µL, 1% DMSO; three technical replicates); the "cosolvent control" ("ctrl") indicates treatment with DMSO only. Cells were then treated with Resazurin 150 mg/mL for 3 h. Fluorescence was measured at 590 nm (excitation 544 nm) using a FLUOstar Omega microplate reader (BMG Labtech). Absorbance data was averaged over the technical replicates, then normalized to viable cell count from the cosolvent control cells (%control) as 100%, where 0% viability was assumed to correspond to fluorescence signal in PBS only with no cells. Three independent experiments were performed. Data were plotted against the log of **SBTub** concentration ($\log_{10}$([**SBTub**]) (M)) with mean and SD. For A549 cell line one experiment out of three is shown. With the exception of **6**, all SBTubs show light dependent cytotoxicity with IC_{50} values ranging from mid nanomolar to mid micromolar concentrations in HeLa cells (**Fig S5**). Lead compounds **SBTub2M** and **SBTubA4** also show light dependent toxicity in A549 cells at low micromolar concentrations (**Fig S5**).

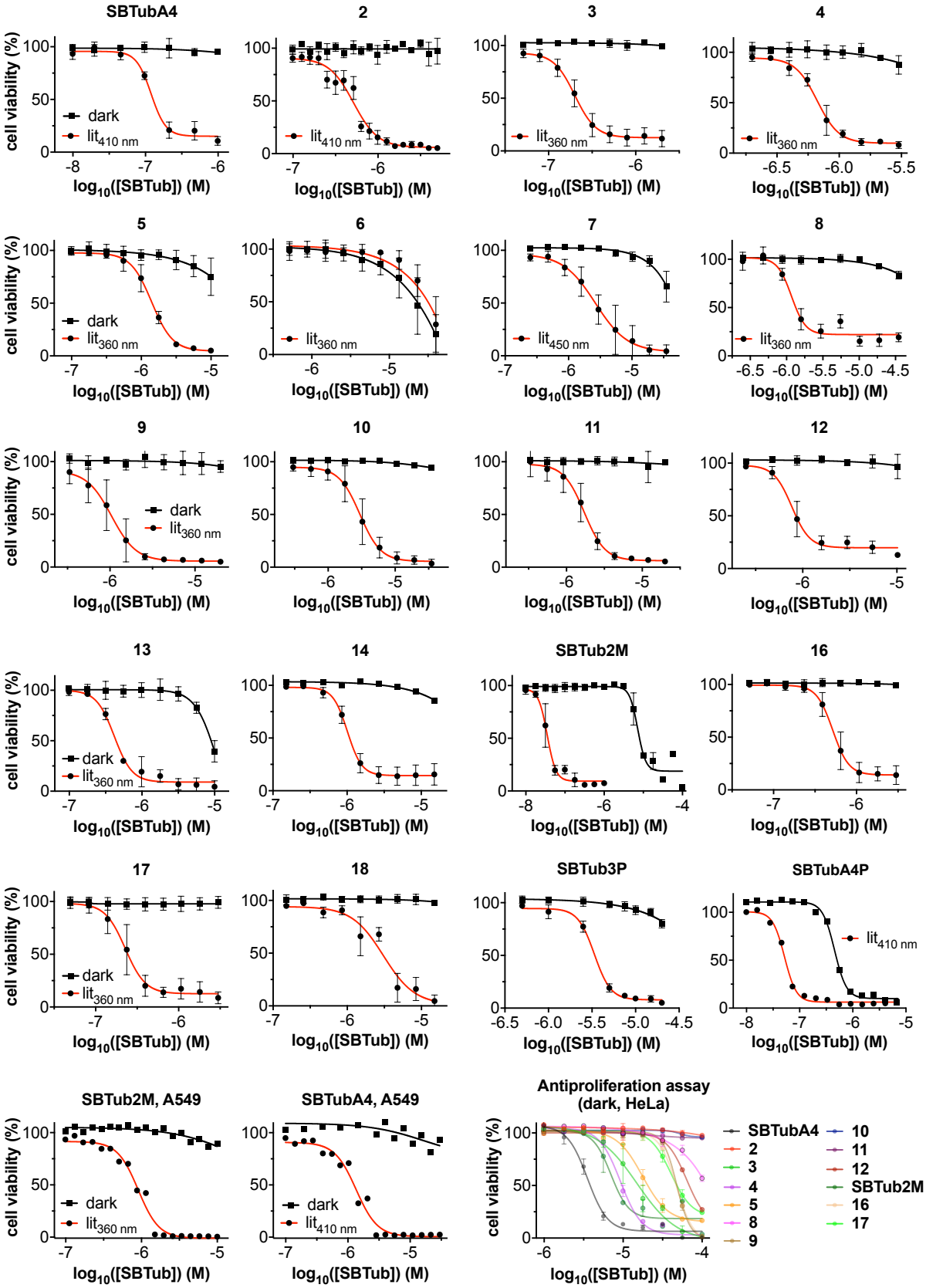

Fig S5: Antiproliferation assay of second generation SBTubs in HeLa cells and A549 cells for selected SBTubs. 40 h incubation; all-*E* dark conditions versus lit conditions with predominantly *Z*-isomer using low-power pulsed LED illuminations (75 ms per 15 s, <1 mW/cm^2); HeLa cells; N = 3; mean ±SD. A549 cells, one representative experiment out of three independent experiments shown. Resazurin antiproliferation assays were run of compounds in the dark up to 100 µM to determine the IC_{50} of SBTubs in the dark.

Cell cycle analysis

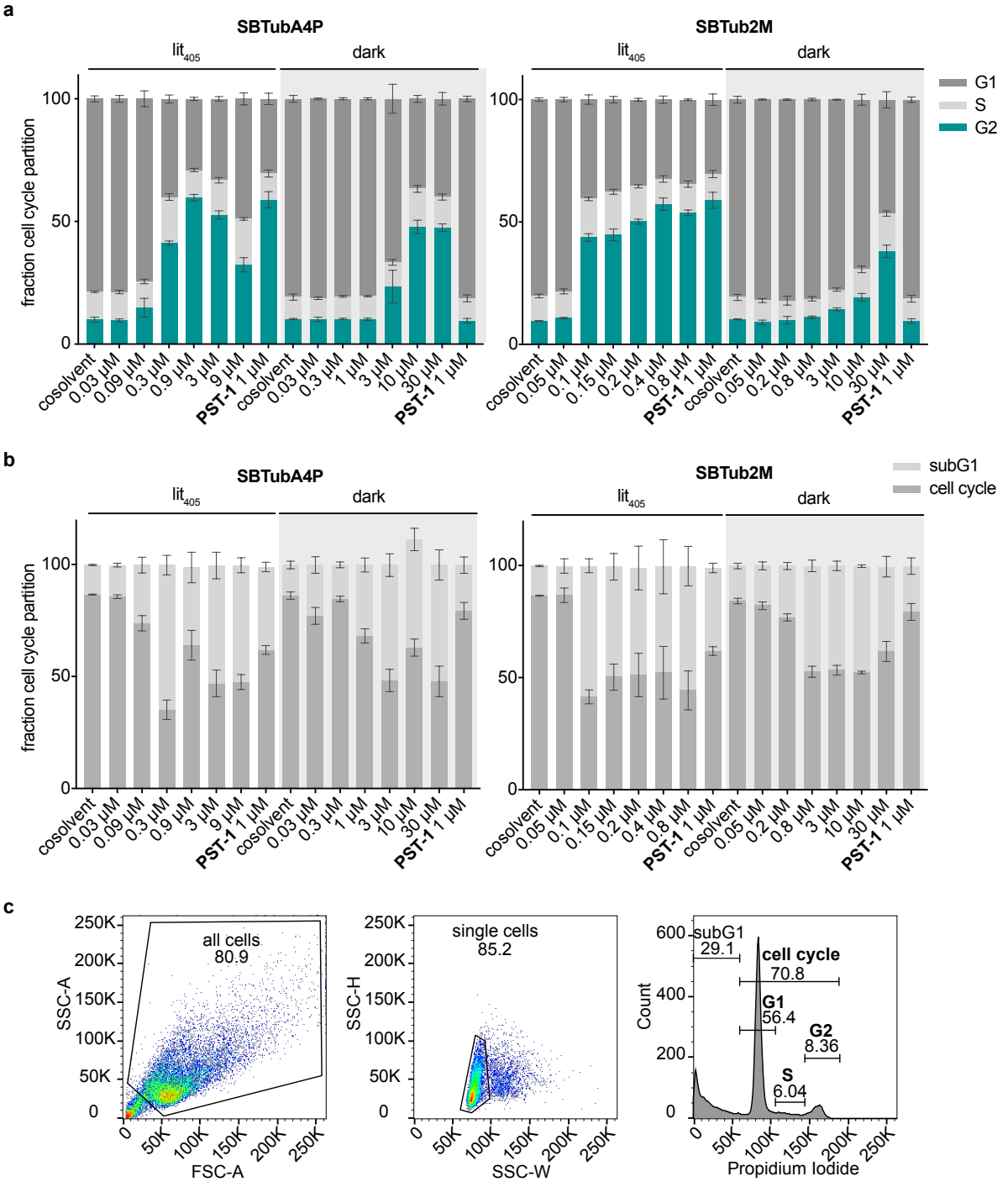

Fig S6: a Cell cycle partitioning of **SBTubA4P** and **SBTub2M** in Jurkat cells shows light dependent G_2/M arrest similar to photoswitchable positive control **PST-1** under lit conditions with 405 nm pulsing but no cell cycle effects when kept in the dark comparable to the DMSO only cosolvent controls. **b** Comparison of cells in subG1 (not shown in **Fig3b** and **Fig S6a**) compared to alive cells which were included in the cell cycle analysis. **c** gating and analysis strategy used in cell cycle quantification on a cosolvent treated sample.

E-**SBTub**s were added to Jurkat cells in 24-well plates (50,000 cells/well; three technical replicates, three biological replicates) and incubated under “dark” or “lit” conditions for 24 h. Cells were collected, permeabilized and stained with 2 µg/mL propidium iodide (PI) in HFS buffer (PBS, 0.1% Triton X-100, 0.1% sodium citrate) at 4°C for 30 min then analysed by flow

cytometry using a LSR Fortessa flow cytometer (Becton Dickinson) run by BD FACSDiva software (version 8.0.1). 10,000 events per technical replicate were analysed; the PI signal per event (corresponding to cellular DNA content) was measured and cells were binned into sub-G1, G1, S and G2 phase according to DNA content using FlowJo software (version 10.7.1). Results (means of three technical replicates) from one experiment of three independent trials are shown (**Fig S6a-b**). Gating strategy shown in **Fig 6c**.

Immunofluorescence staining

HeLa cells were seeded on glass coverslips in 24-well plates (50,000 cells/well) and treated with SBTubs the next day under "dark" or "lit" conditions for 24 h. Cells were fixed and permeabilised in ice-cold methanol for 5 min, then washed and kept in PBS at 4°C until staining. Samples were equilibrated to room temperature and blocked with PBS + 1% BSA for 30 min. Cells were treated with primary antibody (1:200 rabbit alpha-tubulin; Abcam ab18251) in PBS/1% BSA/0.1% Triton X-100 overnight and with secondary antibody (1:500 goat-anti-rabbit Alexa Fluor 488; Abcam ab150077) in PBS/1% BSA/0.1% Triton X-100 for 1 h. Coverslips were mounted onto glass slides using Roti-Mount FluorCare DAPI (Roth) and imaged with a Zeiss LSM710 confocal microscope (CALM platform, LMU). Images were processed using the free Fiji software[12] and Affinity Designer (Serif) for clarification. Postprocessing was only performed to improve visibility.

Live cell imaging

HeLa cells were transfected with EB3-tdTomato using FuGENE 6 (Promega) according to manufacturer's instructions. Experiments were imaged on a Nikon Eclipse Ti microscope equipped with a perfect focus system (Nikon), a spinning disk-based confocal scanner unit (CSU-X1-A1, Yokogawa), an Evolve 512 EMCCD camera (Photometrics) attached to a 2.0× intermediate lens (Edmund Optics), a Roper Scientific custom-made set of Vortran Stradus 405 nm (100 mW), 488 nm (487 nm / 150 mW) and Cobolt Jive 561 nm (110 mW) lasers, a set of ET-DAPI, ET-GFP and ET-mCherry filters (Chroma), a motorized stage MS-2000-XYZ, a stage top incubator INUBG2E-ZILCS (Tokai Hit) and lens heating calibrated for incubation at 37°C with 5% CO_2. Microscope image acquisition was controlled using MetaMorph 7.7 and images were acquired using a Plan Apo VC 40× NA 1.3 oil objective. Imaging conditions were initially optimized to minimize tdTomato bleaching and phototoxicity for untreated cells. For compound treated acquisitions 6 μM **SBTubA4P** diluted in prewarmed cell medium was applied to cells in a dark room with only red ambient light, cells were protected from all ambient light after application of drug. Drug was incubated on cells for at least 1 min before commencing experiment. Comet count analysis was performed in ImageJ using the ComDet

plugin (E. Katrukha, University of Utrecht, Netherlands, https://github.com/ekatrukha/ComDet).

Quantification and statistical analysis.

All relevant assays were done in independent biological replicates. All attempts at replication were successful and no data were excluded from analysis. Blinding was not performed as assay readout is mostly unbiased (plate reader, flow cytometry, Fiji/ImageJ plugins). Microscopic evaluation was performed independently by two separate scientists. Data were analysed using Prism 9 software (GraphPad). Two-tailed unpaired t tests were used in pairwise group comparisons; * was used for $P < 0.05$, ** for $P < 0.01$, *** for $P < 0.001$, **** for $P < 0.0001$.

3D cell culture

Organoid growth conditions:

Organoid culture followed a previously published protocol[13]. Freshly isolated human mammary gland epithelial cells from healthy women undergoing reduction mammoplasty were seeded in a collagen gel (collagen type I from rat tail, Cornings) of final concentration 1.3 mg/ml. The cells were cultured in mammary epithelial growth medium (PromoCell MECGM) with 3 μM Y-27632 (Biomol), 10 μM Forskolin (Biomol) and 0.5% FBS as additives for the first 5 days. Starting from day 5 the medium was replaced by MECGM medium with only 10 μM Forskolin as supplement. The medium was exchanged every second day. Experiments were carried out on organoids prepared from donor M21 (Age: 61 years, Parity: 1).

Dose response curves:

The effect **SBTubA4P** on organoid growth was first assessed in a dilution series (**Fig S7a-b**). Organoids were prepared and cultured based on the afore mentioned protocol up to day 5. On day 5 besides exchanging the medium **SBTubA4P** was added. For the lit culture conditions **SBTubA4P** was supplemented to achieve final concentrations ranging from 10 nM up to 600 nM. **SBTubA4P** was added to yield concentration between 125 nM and 400 nM for dark culture conditions. Medium was exchanged every second day. An additional washing step was carried out to completely remove the old compound from the collagen gel and avoid upconcentration. The organoids cultured under lit conditions were placed on LEDs emitting a 100 ms light pulse at 405 nm every 60 s. The dark control was shielded from light with aluminium foil. After 2 weeks the organoids were fixed with 4% PFA incubation for 15 min. Immunofluorescence staining was performed by permeabilizing cells using a 0.2% Triton X-100 solution followed by incubation with a blocking solution containing 10% donkey serum

and 0.1 %BSA. Cells were stained for the presence of the proliferation marker Ki67 using primary monoclonal mouse antibody (ab238020, 1:200, Abcam) incubation at 4°C overnight succeeded by secondary antibody incubation with donkey anti-mouse IgG (A21202, 1:250, Invitrogen) at 4°C overnight. Cell nuclei were visualized using DAPI. Collagen gels were mounted on microscopy slides using mounting medium (18606-20, Polysciences).

The stained organoids were imaged using a Leica SP8 lightning confocal microscope and a HCX PL APO 10x/0.40 CS dry objective. Z-projections of the DAPI signal were generated to create a mask and determine the projected area of the organoids in the Z-projection (Fig 5a). Images were processed using Fiji software. Data Analysis was carried out using a Python Script. For the dose response curve, the area of the organoids was normalized by using the mean of the area from organoids cultured under normal culture conditions (**Fig S7a**).

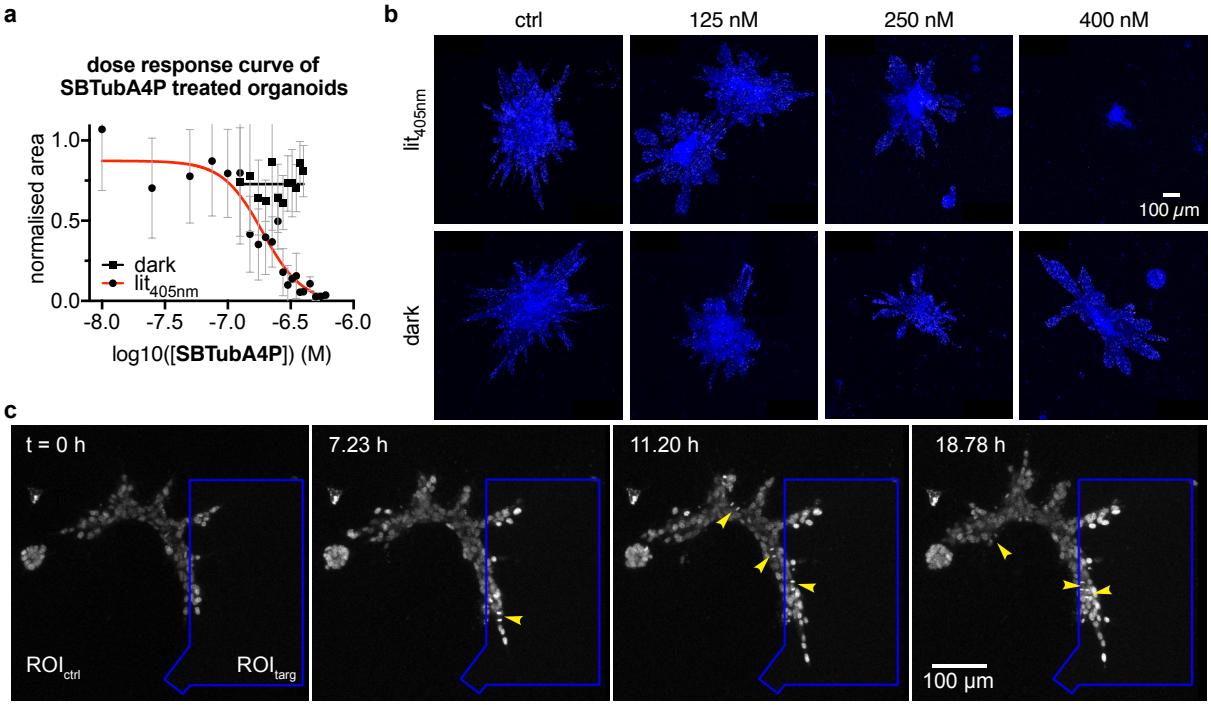

Fig S7: a-b Determination of **SBTubA4P** working concentration $[I]_{wc}$ in human mammary gland epithelial cells. **(c)** Imaging of organoids in the absence of **SBTubA4P** (no compound control) shows that branches are migrating and proliferating (yellow arrowheads) both within and outside the illuminated ROI_{targ}.

Imaging of organoid growth:

Live cell imaging was carried out on a Leica SP8 lightning confocal microscope using a HCX PL APO 10x/0.40 CS dry objective. Laser intensities at full power were as following: 405 nm (0.70 mW), 488 nm (4.50 mW) 552 nm (4.50 mW), 638 nm (0.22 mW). The CO_2 level and humidity were controlled using an ibidi gas incubation chamber. Organoids were imaged 8 to 10 days after seeding to interfere during the branch elongation phase. At this time point substantial branch invasion into the extracellular matrix was reported to take place[14]. Cell

nuclei were labelled by addition of siRDNA (10 μM, Spirochrome AG) 3 h before starting the measurement. **SBTubA4P** was added to the medium to achieve a concentration of 200 nM. After addition of the compound the samples were protected from light to prevent activation of **SBTubA4P**. The excitation wavelength was set to 638 nm and filters were adjusted accordingly to record the emission light peaking at 674 nm for nuclei visualization. To fully capture the whole structure of the organoids several planes in the z-direction were selected. Organoid growth was monitored for 4 h to determine the region of interest in which the cells displayed the most invasive behaviour. Fiji software was used to further process the data. A python script was used to correct for translational drift of the organoids.

Local inhibition of organoid growth:

To locally inhibit organoid growth a region of interest was selected in an area where the cells displayed increased motility. The region of interest was set to be irradiated with light at 405 nm wavelength. The intensity for the 405 nm light was set to 20% (0.14 mW) in the region of interest. The size of the region of interest was varied depending on the cell motility in that area and the translational drift of the organoid observed during the preceding 4 h of measurement. 405 nm light irradiation in the region of interest was active throughout the whole z-stack of the organoids. The pixel dwell time was 2.09 μs/pixel. Therefore, scanning the designated regions of interest took approximately between 390 ms up to 520 ms for each frame of the z-stack. A complete z-stack of the organoids was acquired every 7 min. Cell motility was visualized by imaging the stained nuclei in and outside of the region of interest as described above. Fiji software was used to further process the data. A python script was used to correct for translational drift and to draw the outlines of the region of interest.

Tissue and Animal Assays

Drosophilia melanogaster

Fly strains and culturing

Flies were caged above solid fly nutrient plates and allowed to lay eggs for 2 h. Flies were then removed from the plates as larvae developed. Plates were incubated for a total of 72-96 h at 25°C before larvae were harvested for dissection.

The following transgenes and fluorescent markers were used:
worGal4, *UAS-mCherry*::*Jupiter*, *Sqh*::*GFP*[15]; *worGal4*, *UAS-mCherry*::*tubulin*[16]

Live cell imaging of drosophila neuroblasts and SBTub2M activation

Early third instar (72-96 h) larvae were dissected in Schneider's insect medium (Sigma-Aldrich S0146) supplemented with 1% Bovine Growth Serum (Cytivia SH3054102) and transferred to one well of a μ-slide 8 well (Ibidi 80826) with 200 μL supplemented Schneider's plus 2% DMSO or 30 μM **SBTub2M** (2% final DMSO concentration). Brains were oriented with the lobes facing the coverslip. Once placed, brains were allowed to settle 15 min prior to transferring the slide to the microscope, where the brains were then allowed to settle an additional 15 min prior to the onset of imaging. Experiments with **SBTub2M** were performed in the dark or under red light.

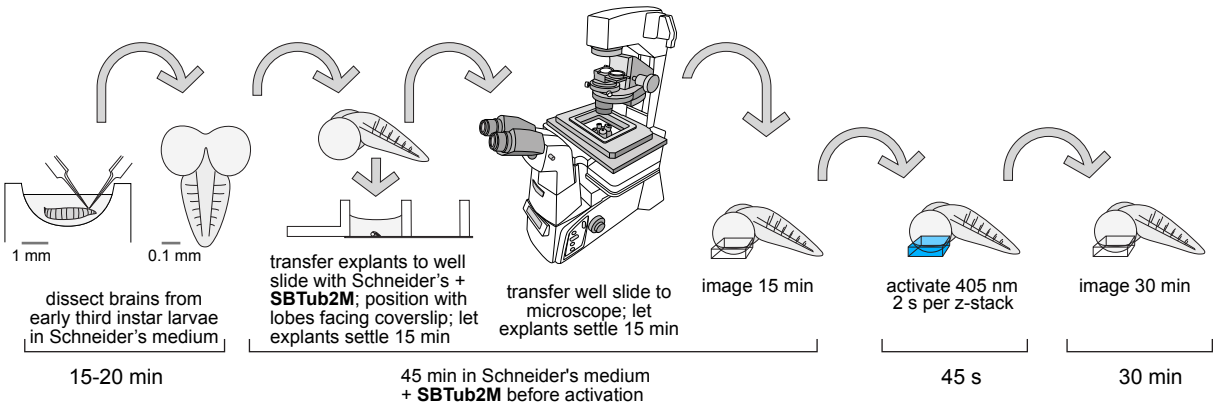

Fig S8: Experimental setup for photoswitching during live cell imaging of **SBTub2M** in fly brain explants.

Brain lobes were imaged with an Intelligent Imaging Innovations (3i) spinning disc confocal system, consisting of a Yokogawa CSU-W1 spinning disc unit and two Prime 95B Scientific CMOS cameras. A 60x/1.4NA oil immersion objective mounted on a Nikon Eclipse Ti microscope was used for imaging. 20 μm stacks with a 1 μm z-spacing at the top of the neural lobe were acquired every 15 s for 15 min before 405 nm activation and for 30 min following activation. mCherry::Jupiter and mCherry::tubulin were imaged for 100 ms at 561 nm (100 mW) with 10% laser power and Sqh::GFP was imaged at 488 nm (150 mW) for 100 ms

with 20% laser power. Activation was performed by imaging the 20 μm stack for 2 s/stack with a 405 nm laser (100 mW) at 40% laser power.

Movies and extended z-stack projections were generated using Imaris v.9.5.1 and 9.2.1. Movies were annotated using FIJI.

Centrosome intensity measurements

Centrosome intensity was calculated with Imaris v.9.5.1 using the median intensity of centrosomes that were manually tracked for 2 min prior to activation and up to 8 min following activation using spots with a 2 μm diameter. Raw data for each track were exported to Microsoft Excel. For each centrosome, the signal intensity for each timepoint was normalized by dividing by the maximum observed signal intensity for each centrosome during the two minutes prior to activation. We used built-in functions in Excel to calculate the average and standard deviation of all of the normalized individual observations per timepoint. These data were plotted in Excel and edited for style in Adobe Illustrator.

Xenopus tropicalis

X. tropicalis embryos were generated according to standard methods by in vitro fertilization.[17] Briefly, a priming step is performed by injecting human chorionic gonadotropin (hCG) into the dorsal lymph sac of sexually mature *X.tropicalis* females (50 μL of a 200 U/mL solution). Frogs are then left for ~20 h in normal housing conditions separated from males. Boosting is completed by injecting 70 μL of a 2000 U/mL hGC solution in female frogs. ~3 h after injection females are gently squeezed to lay eggs, which are collected and fecundated in vitro using frozen sperm. After fecundation, embryos are dejellied with 2% L-cysteine prepared in 0.1x Marc's Modified Ringers (MMR). 1x MMR contains 100 mM NaCl, 2 mM KCl, 1 mM $MgSO_4$, 2 mM $CaCl_2$, 5 mM HEPES, pH 7.8. Embryos are kept in 0.1x MMR in Petri dishes surface-coated with 1% agarose. Temperature is kept constant at 23–25°C. Selection of embryos at 2 cell-stage or at the blastula stage was performed under the stereo microscope.

SBTub4AP incubation/photoactivation: Selected embryos either at the 2-cell or the blastula (>64-cell) stage (spherical shape ca. 1 mm diameter) were incubated with **SBTubA4P** diluted in 0.1x MMR for 1 h in the dark. The manipulation of the compound and embryos were always performed under green light to prevent photoactivation by ambient light. Embryos were selected with a glass pipette and transferred to new dishes (2 mL volume) containing 0.1x MMR without **SBTubA4P** as a washout procedure; the total residual volume of original medium transferred with the embryos was estimated at <50 μL per dish, 10 embryos were

transferred to an imaging RC-25 chamber (Warner Instruments, Hamden, CT) immediately after washout.

For photoactivation, the chamber was mounted on an inverted Olympus IX-50 microscope using a Hg arc lamp (100 W) as light source. Each embryo was illuminated individually *via* the epifluorescence port with 410 nm light (excitation filter D410/40, Chroma) for 5 s. Light was applied through a 20X objective (LCPlanFI 20X/0.4, Olympus, Japan). The diaphragm was fully open to illuminate a zone of diameter ca. 1 mm, i.e. one embryo was fully illuminated, but not the surrounding washout medium. A first round of illumination was followed by a second cycle, which was applied in a time interval of 5 min. Embryos were returned to dishes to monitor their development.

Micrographs of embryos were taken using an AxioCam ERc 5s (Carl Zeiss, Jena, Germany) mounted on a stereo microscope (Leica, Wetzlar, Germany). Movies to assess the movement of hatchling embryos were obtained with a webcam controlled by Image J Webcam Capture Plugin.

Embryonic development was quantified using a morphological (1) and a functional assay (2). (1) Long/short axis ratio: Morphology was evaluated by measuring the ratio between the longest and shortest axis of the embryos. During the initial 48 h of normal development embryos dramatically change their shape and transition from being cell spheres to tadpoles. This characteristic elongation can be quantified by calculating the ratio between the longest and shortest axis of the embryo (Feret's diameter in Image J) (**Fig 6b** from 2-cell-stage treatment, (**Fig S9b-d**) from blastula treatment). The suppression of this elongation reflects a drug's ability to interfere with normal cell divisions and to stop the growth of embryos.

(2) The functional assay was carried out by investigating sensorimotor behaviour. Hatchling tadpoles start to move in reaction to mechanical stimuli with a pipette tip.[18] A qualitative analysis was performed by calculating the proportion of the tadpoles that moved after mechanical stimuli and those that remained still. The ratio of the proportions of tadpoles incubated with the molecule, **SBTubA4P** or **PST-1P**, in lit or dark conditions was used to quantify the light-dependency effect of **SBTubA4P** and **PST-1P** in advanced stages of development (**Fig S9e**).

More than 80% of the tadpoles raised in control conditions or with 5 or 25 μM **SBTubA4P** in the dark consistently showed this behaviour 30 h post-fertilisation (**Movie SXX**). However, the proportion of tadpoles moving in response to mechanical stimulation decreased to about half if 5 or 25 μM **SBTubA4P** was activated at 410 nm light. The defects in the processing of

sensorimotor information might reflect alterations in the nervous system. As this is generated by the ectoderm, the more external layer of the embryo, it is possible that the greater exposure of ectodermic cells to **SBTubA4P** causes defects in the nervous system. The action of **PST-1P** was compared to the effects of **SBTubA4P**. Application of **PST-1P** at 5 or 25 μM did not modify the long/short axis ratio of the embryos. With 25 μM the motion was suppressed both in the dark and after 410nm illumination, while with 5 μM neither lit nor dark suppressed motion.

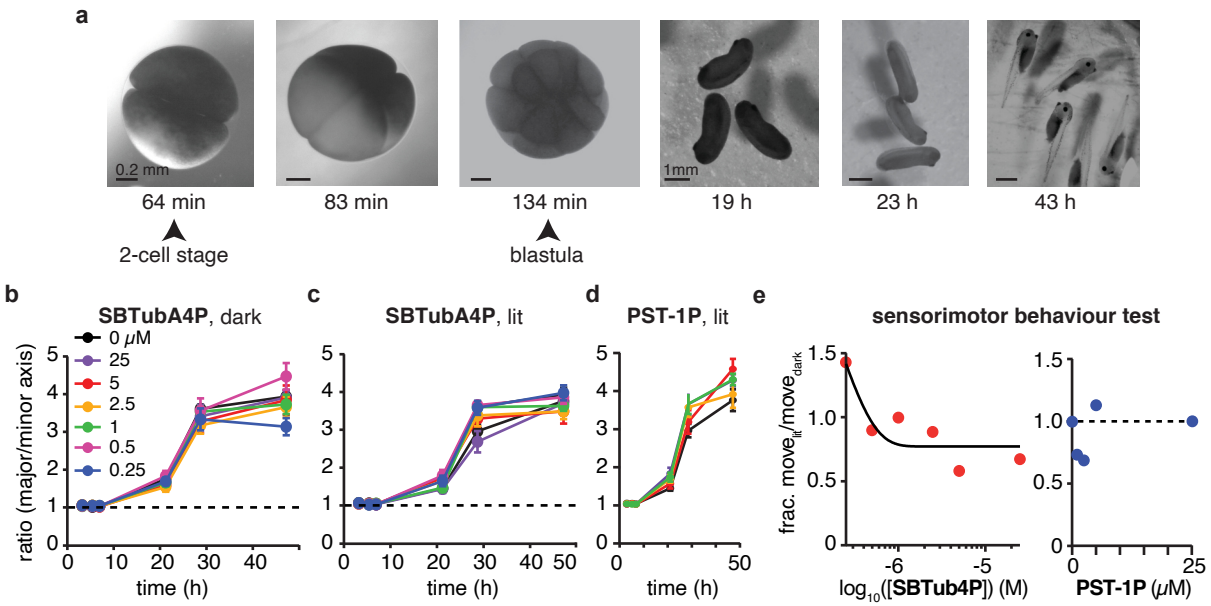

Fig S9: Effect of **SBTubA4P** on the development of *X. tropicalis* tadpoles. **a** Images of *X. tropicalis* embryos at the indicated developmental times post-fertilization. Embryos were exposed to varying **SBTubA4P** concentrations during 1 h, starting at the 2-cell stage (protocol 1) or at the blastula stage (protocol 2). **b-d** Plots evaluating the elongation of embryos during development show that neither **SBTubA4P** or **PST-1P** cause obvious morphological defects. Each dot is the mean of 10 embryos. Bars indicate s.e.m. on embryonic development using protocol 2. **e** The ratio between the proportion of embryos illuminated at 410 nm that moved after mechanical stimulation and the proportion of those kept in the dark is modified as a function of **SBTubA4P** and **PST-1P** concentration. Physiological responses are affected in SBTubA4P treated embryos. For **PST-1P** treated embryos no difference was observed between embryos kept in the dark or exposed to 410 nm light on the physiological level.

This suggests that **PST-1P** did not act light-dependently in the embryos, but can be light-independently toxic (**Fig S9d**). Note that 25 μM is ca. 16× the $[I]_{WC}$ of **PST-1P**[19], and 19× the $[I]_{WC}$ of **SBTubA4P**, so these concentrations could have been thought to deliver roughly equivalent biological effects. Analysing the reasons for azobenzene failure is outside the scope of this paper, but reductive *Z*-diazene degradation[20–22] in this highly metabolically active developing animal seems a likely culprit (which may have inspired the prior *in vivo* use of one azobenzene at 1000× its $[I]_{WC}$[23]); at any rate, the novel SBT photoswitch scaffold is far more robust against such degradation[21].

Danio rerio

Zebrafish strains and maintenance

Zebrafish (Danio rerio) were maintained according to the guidelines of the local authorities under licenses GZ:565304/2014/6 and GZ:534619/2014/4. Zebrafish WT AB* (ZFIN ID: ZDB-GENO-960809-7) embryos were used for all *in vivo* experiments. All embryos were kept in E3 medium (0.63 g/L KCl, 14.0 g/L NaCl, 1.83 g/l $CaCl_2$•$2H_2O$, 1.99 g/l $MgSO_4$•$7H_2O$, pH 7.4) and only for use in confocal microscopy experiments treated with 0.003% Phenylthiourea (PTU, Sigma-Aldrich, St. Louis, MO) before 24 hpf to inhibit melanogenesis. Zebrafish embryos used in all experiments were held at 28°C for upbringing and incubation times.

Determining compound toxicity in zebrafish

For determining toxicity and permeability of **SBTubA4P**, **SBTub3P** and **PST-1P**, zebrafish embryos were dechorionated after 24 hpf or 48 hpf and placed in 12 well tissue culture plates (VWR, Radnor, PA) in 2 mL E3 medium, and treated with either: 25 μM **SBTubA4P**, 1 μM **SBTubA4P**, 25 μM **SBTub3P**, 25 μM **PST-1P**, 0.25% DMSO only, or no treatment (vehicle control). Handling of the compounds was performed in a dark room under red lighting. All treatments were performed as both dark and as illuminated incubations, for 24 h. Global UV illumination was carried out by placing the tissue culture plates on a pulsed 24-LED array (395 nm; previously described[19]), emitting a 1 second UV pulse every five minutes in an otherwise dark incubator. For dark incubation the tissue culture plates containing treated embryos were wrapped in aluminum foil to shield them from light.

For endpoint imaging and evaluation (**Fig S10**), embryos were treated with 0.3 mg/mL Tricaine (ethyl 3-aminobenzoate methanesulfonate 98%, Sigma-Aldrich) for immobilization during the procedure. Imaging and counting of phenotypical abnormalities were performed between 52-54 and 76-78 hpf (for 24 hpf and 48 hpf embryo treatments, respectively). Representative images were recorded using a microscope camera (MC170 HD, Leica Microsystems, Wetzlar, Germany) mounted on a Leica M125 stereomicroscope and the LAS V4 software.

One-day old fish treated with **SBTubA4P** (25 and 1 μM) and **SBTub3P** (25 μM) showed light dependent phenotypical changes from the untreated and vehicle control. Two-day old fish did not show any morphological changes except when treated with **SBTubA4P** (25 μM) under lit conditions. Azobenzene-based tubulin inhibitor **PST-1P** did not show any phenotypical changes up to 25 μM under lit conditions. No phenotypical changes were observed for fish kept in the dark except for slightly curved tails in fish treated with **SBTubA4P** (25 μM).

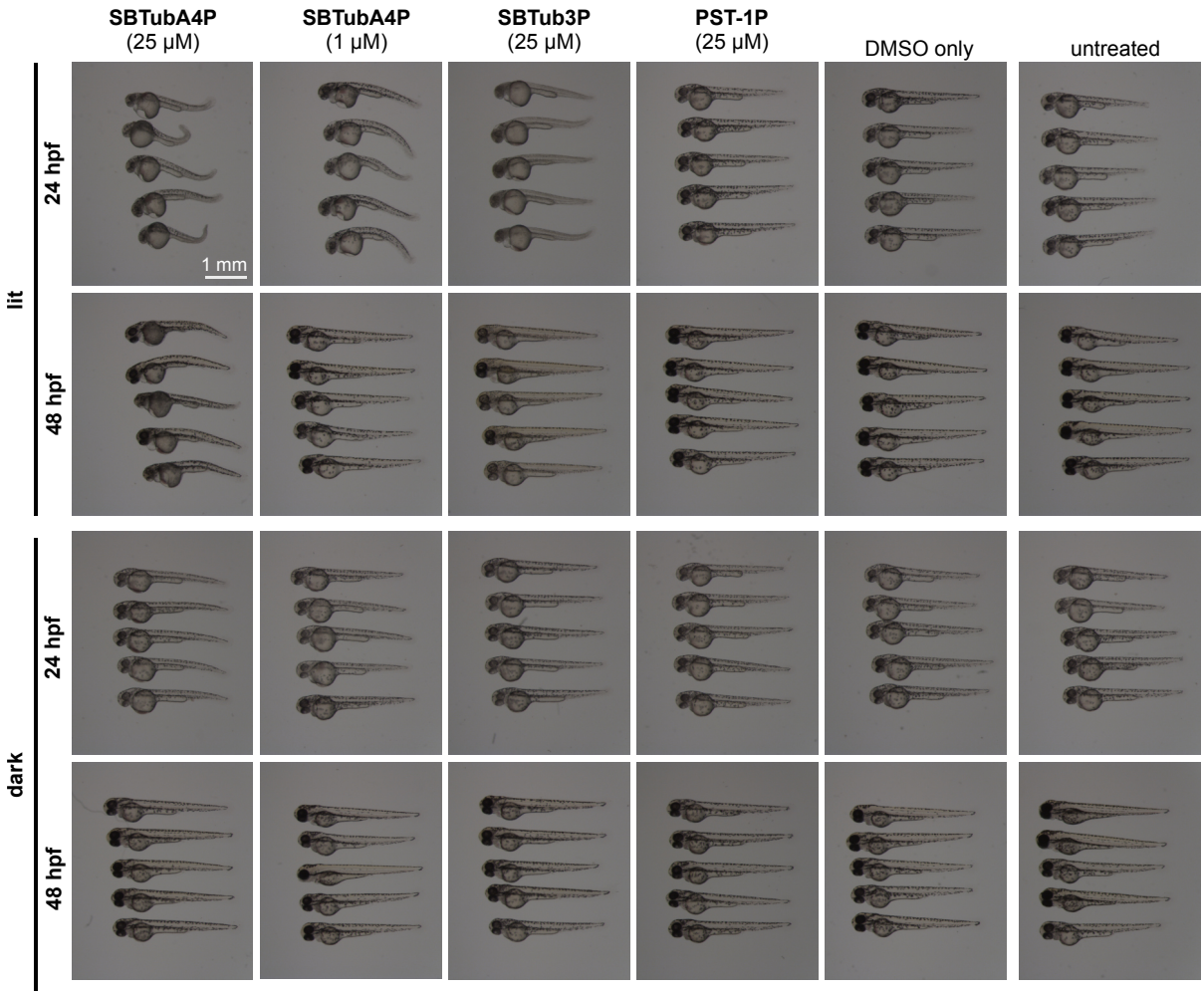

Fig S10: Determining toxicity in zebrafish embryos: 25 µM **SBTubA4P**, 1 µM **SBTubA4P**, 25 µM **SBTub3P**, 25 µM **PST-1P**, 0.25% DMSO (vehicle control) and no treatment.

Targeted inhibition of microtubule dynamics in vivo

For targeted activation of SBTubA4P in embryonic zebrafish to demonstrate inhibition of microtubule dynamics, WT AB* zebrafish embryos were microinjected with 20 pg each of pSK_H2B-mRFP:5xUAS:EB3-GFP[24] and pCS_KalTA4[25] plasmid DNA. Injections were performed with glass capillaries pulled with a needle puller (P97, Sutter Instruments, Novato, CA), mounted onto a micromanipulator (World Precision Instruments Inc., Berlin, Germany) and connected to a microinjector (FemtoJet i4, Eppendorf, Hamburg, Germany). Embryos were dechorionated and incubated with **SBTubA4P** or left untreated as control wrapped in aluminum foil for 4 h, starting from 26 hpf. After the incubation period, embryos were embedded in 1.2% low-melting agarose (Agarose Type IX-A, Ultra-low Gelling Temperature, Sigma-Aldrich) dissolved in E3 medium on #1.5 Glass Bottom Dishes (Cellvis, Mountain View, CA) under red light. Targeted activation of **SBTubA4P** *in situ* and imaging was performed using a SP8 confocal microscope (Leica Microsystems, Wetzlar, Germany). The bleachpoint function was used to target single EB3-GFP positive cells for photoactivation, while time-lapse

imaging was continued to capture inhibition and recovery of microtubule dynamics over time. All photoactivation experiments at the confocal microscope were conducted at 28°C using a temperature control system (The Cube 2, Live Imaging Services, Basel, Switzerland). Images were recorded using the confocal microscope in conjunction with the LAS X software (Leica Microsystems). Videos were edited and labeled with ImageJ. Comet count analysis was performed by J.C.M.M. in ImageJ using the ComDet plugin (E. Katrukha, University of Utrecht, Netherlands, https://github.com/ekatrukha/ComDet).

Laser power and intensity calculations

Laser powers were measured with a 40x water objective (NA 1.1) using a Nova II power meter (Ophir, North Logan, USA). Using a 40x objective the beam diameter was calculated using the following formula: 1.22 x 405 nm/1.1 = 449 nm and the illuminated area of the bleachpoint is 158478 nm^2. Intensity for the bleachpoint experiments was calculated at 18900 W/cm^2.

Part D: Protein Crystallisation

Protein crystallisation materials and methods

Protein production, crystallization and soaking.

The DARPin D1 was prepared as previously described by Pecqueur et al.[26]. Bovine brain tubulin was purchased from the Centro de Investigaciones Biológicas (Microtubule Stabilizing Agents Group, CSIC, Madrid, Spain). The tubulin-DARPin D1 complex (TD1)[26–28] was formed by mixing the respective components in a 1:1.1 molar ratio.

The TD1 complex was crystallized overnight by the hanging drop vapor diffusion method (EasyXTal plates from QIAGEN, drop size 2 µL, drop ratio 1:1), at a complex concentration of 9.8 mg/mL and at 20°C with a precipitant solution containing 21% PEG 3000, 0.2 M ammonium sulfate and 0.1 M bis-tris methane buffer, pH 5.5. All crystallization drops were subsequently hair-seeded with crystalline material obtained from a previous PEG screen. Grown crystals were washed from the plate with precipitant solution and transferred into 0.6 mL centrifuge tubes in order to start batch-crystallization (overnight, 20°C). The average size of obtained batch-crystals (monoclinic needles) was about 120x10x5 µm.

Crystals were transferred into new precipitant solution drops containing 1.7 mM of **SBTub2M** compound (dissolved in DMSO) and 10% Glycerol. Crystals were soaked and illumined for 60 min at 385 nm to generate *cis*-**SBTub2M** *in situ* before being frozen in liquid nitrogen for X-ray diffraction data collection.

Data Collection, processing and refinement.

Data were collected at beamline X10SA (PXII) at the Swiss Light Source (Paul Scherrer Institut, Villigen, Switzerland). The X-ray beam spot was 30 x 15 μm^2, the flux was 7 x 10^{11} photons/s (100% beam intensity, 30 µm aperture). The data were collected with an exposure time of 0.05 s and an oscillation range of 0.1° per frame (see supplementary table S1). For TD1-SBTub2M, the data of three single crystals (210°, 180°, 180°) were merged. Data processing was done with XDS[29]. Due to anisotropy, the data were scaled, merged and corrected using the Staraniso server[30] (http:// staraniso.globalphasing.org/). The structures were solved by molecular replacement using PDB: 5NQT as a search model[27]. The ligands and restraints were generated with the grade server[31] (http://grade.globalphasing.org/) using their SMILES annotation. The structures were then refined iteratively in PHENIX[32] with manual editing cycles in COOT[33].

Supplementary table S1: Crystallographic statistics for *cis*-**SBTub2M** bound to tubulin-DARPin D1 (TD1) complex. Related to Methods X-ray diffraction data collection, processing and refinement.

Data statistics	
Space group	$P2_1$
Unit cell (a b c ß)	73.68 91.61 83.11 97.39
Wavelength (Å)	1.0
Resolution (Å)	45.81 - 2.36
R_{pim} (%)	10.8 (49.1)
I/σI	4.7 (1.6)
Spherical completeness (%)	58.3 (8.7)
Ellipsoidal completeness (%)	92.9 (66.1)
Ellipsoidal truncation resolution limits (Å for a*, b*, c*)	2.36 3.15 2.81
Multiplicity	11.7 (10)
$CC_{1/2}$	0.974 (0.517)
Refinement statistics	
Resolution	45.81 - 2.36
Number of reflections	27889
R_{work} / R_{free}	20.84% / 25.84%
Ramanchandran favoured	93.90%
Ramanchandran outliers	0.1%
R.m.s.d bond lenght (Å)	0.0026
R.m.s.d bond angles (°)	0.572
PDB code	

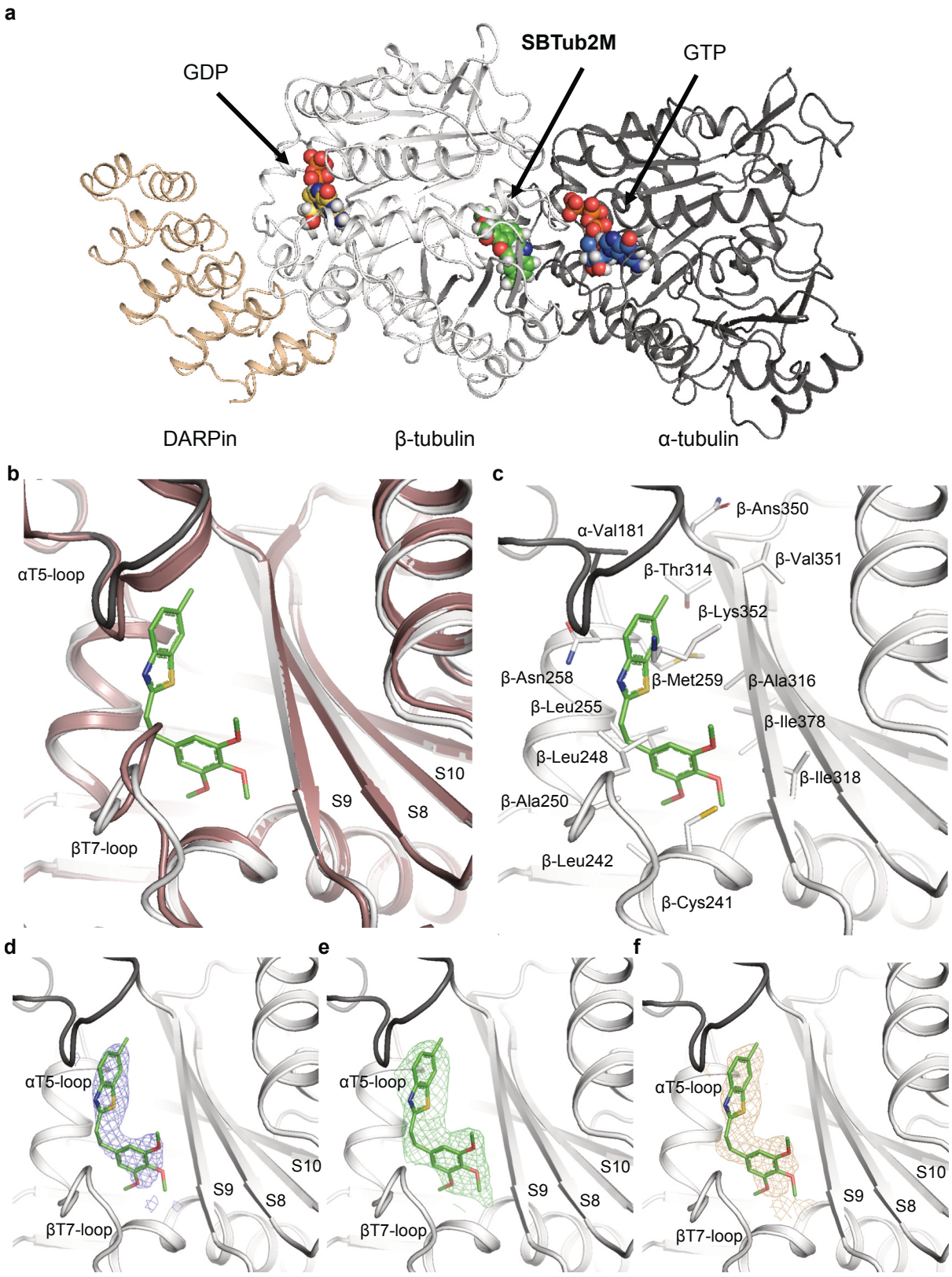

Fig S11: a Structure overview TD1:*Z*-**SBTub2M**. Structures are shown in cartoon representation, ligands shown as sphere. DARPin = wheat, β-tubulin = white, α-tubulin = grey. **b** Overlay of TD1:*Z*-**SBTub2M** and the ligand free structure (red, PDB 5NQU). **c** Close-up view of the colchicine-site showing *Z*-**SBTub2M**. Tubulin shown in cartoon representation; interacting residues are labeled and shown in stick representation. Oxygen = red, nitrogen = blue, sulfur = yellow. **d** *Z*-**SBTub2M** with 2FoFc map at 1.5σ shown in blue **e** *Z*-**SBTub2M** with simple omit map at 3.0σ shown in green **f** *Z*-**SBTub2M** compound with simulated annealing omit map at 2.5σ shown in yellow.

Part E: NMR Spectra

1H-NMR of SBTubA4:

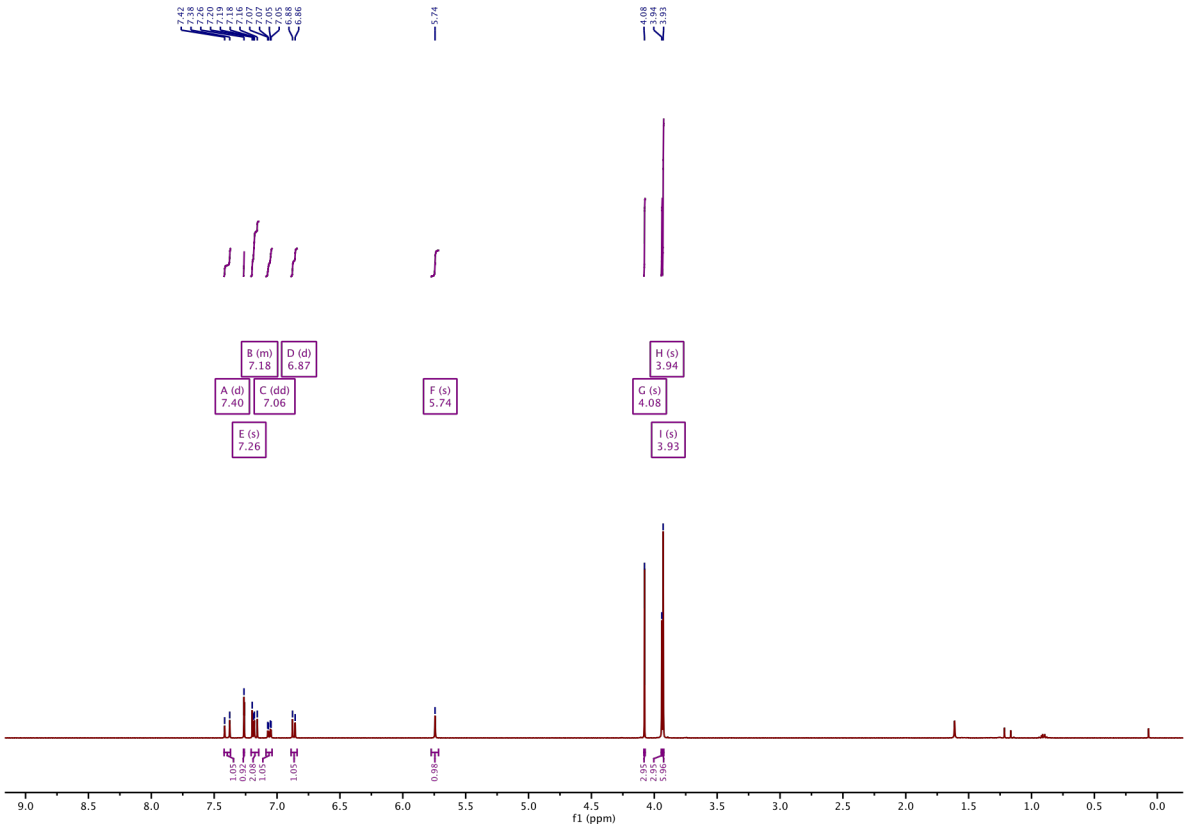

^{13}C-NMR of SBTubA4:

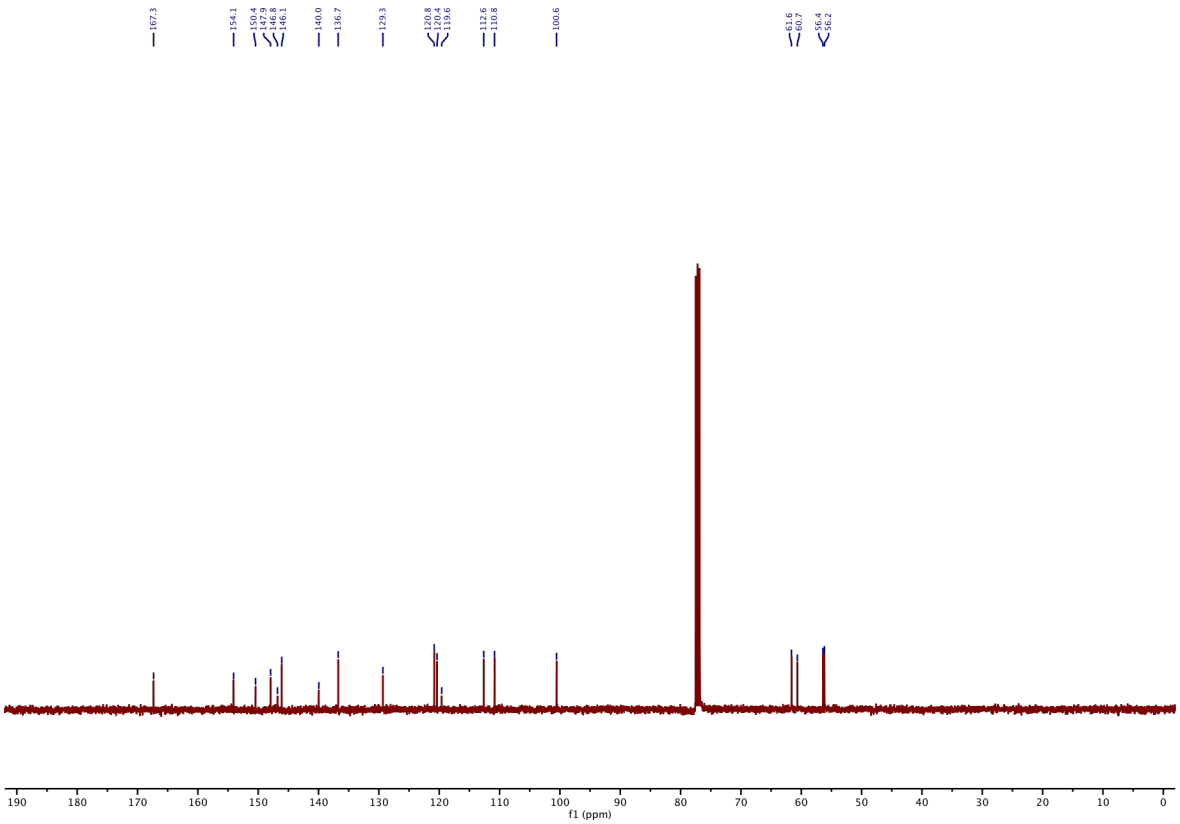

^{1}H-NMR of 2:

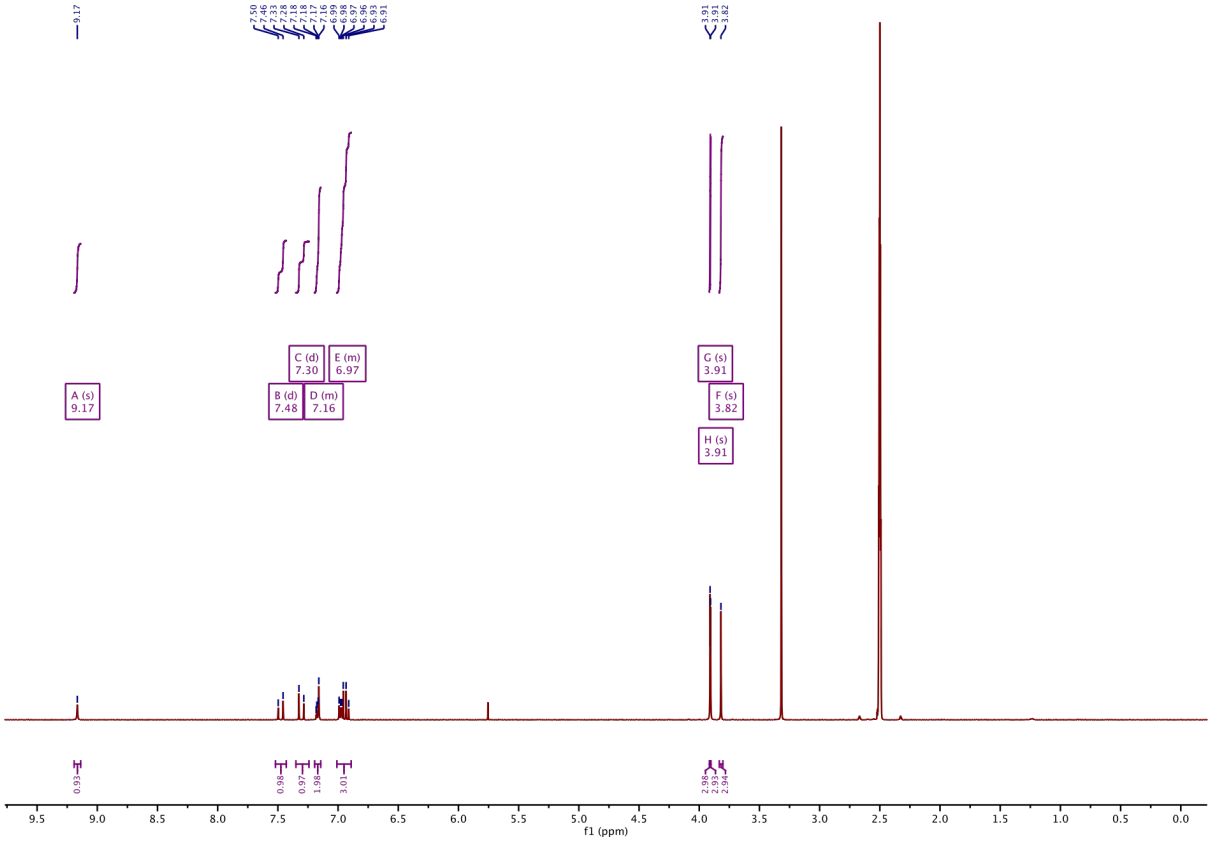

^{13}C-NMR of 2:

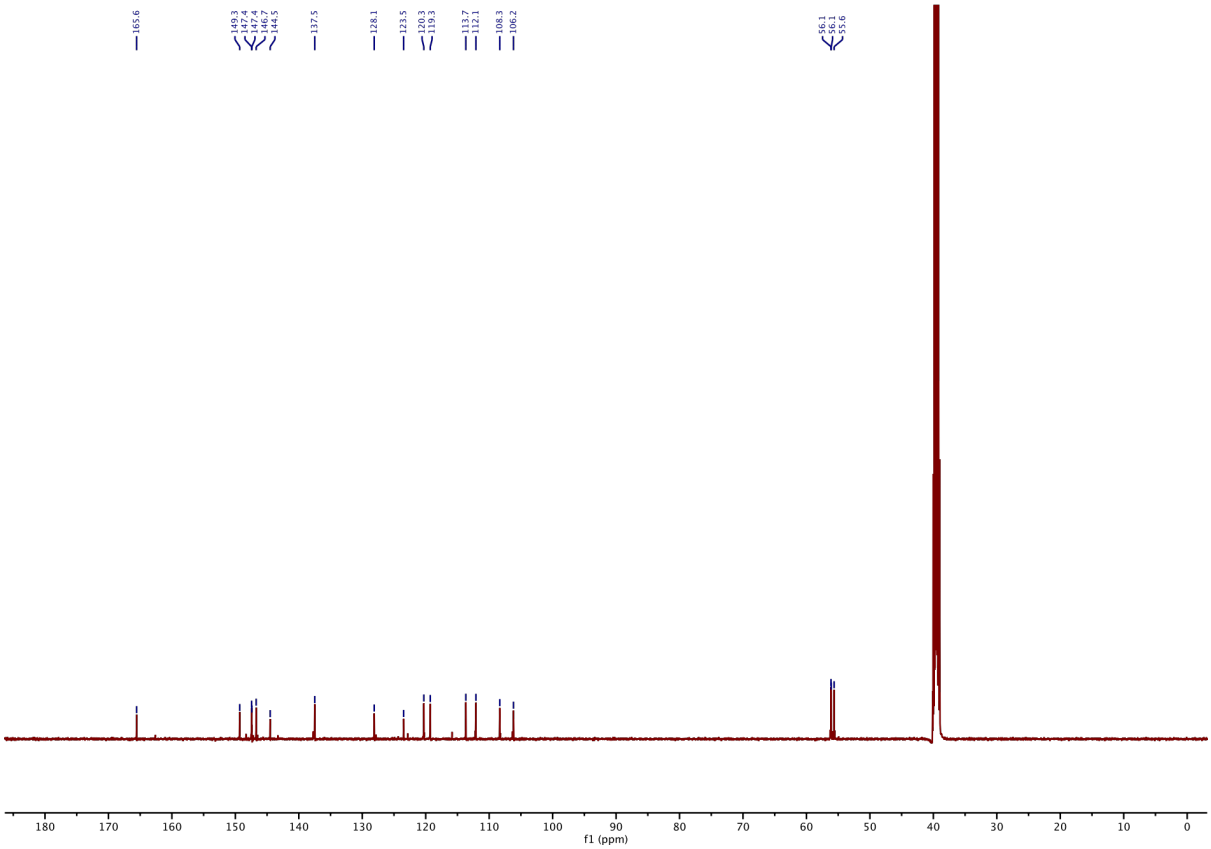

^{1}H-NMR of 3:

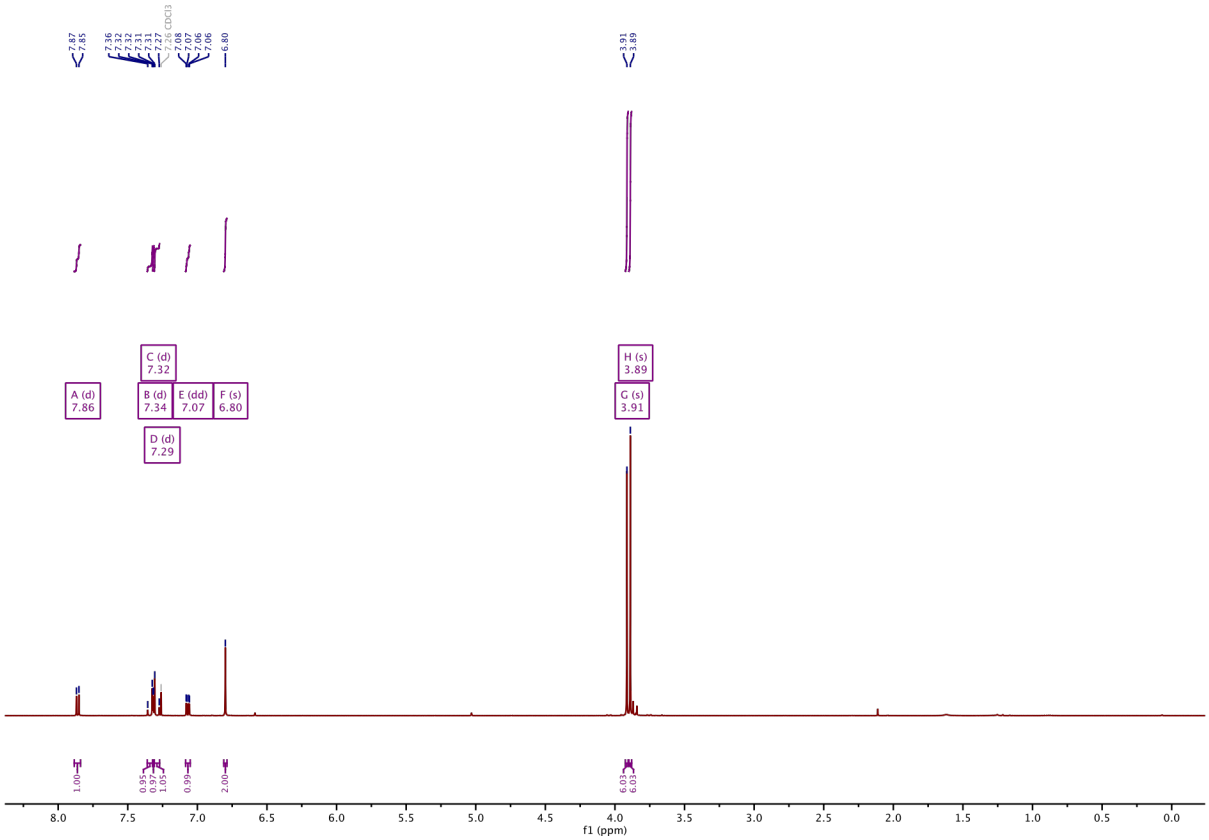

^{13}C-NMR of 3:

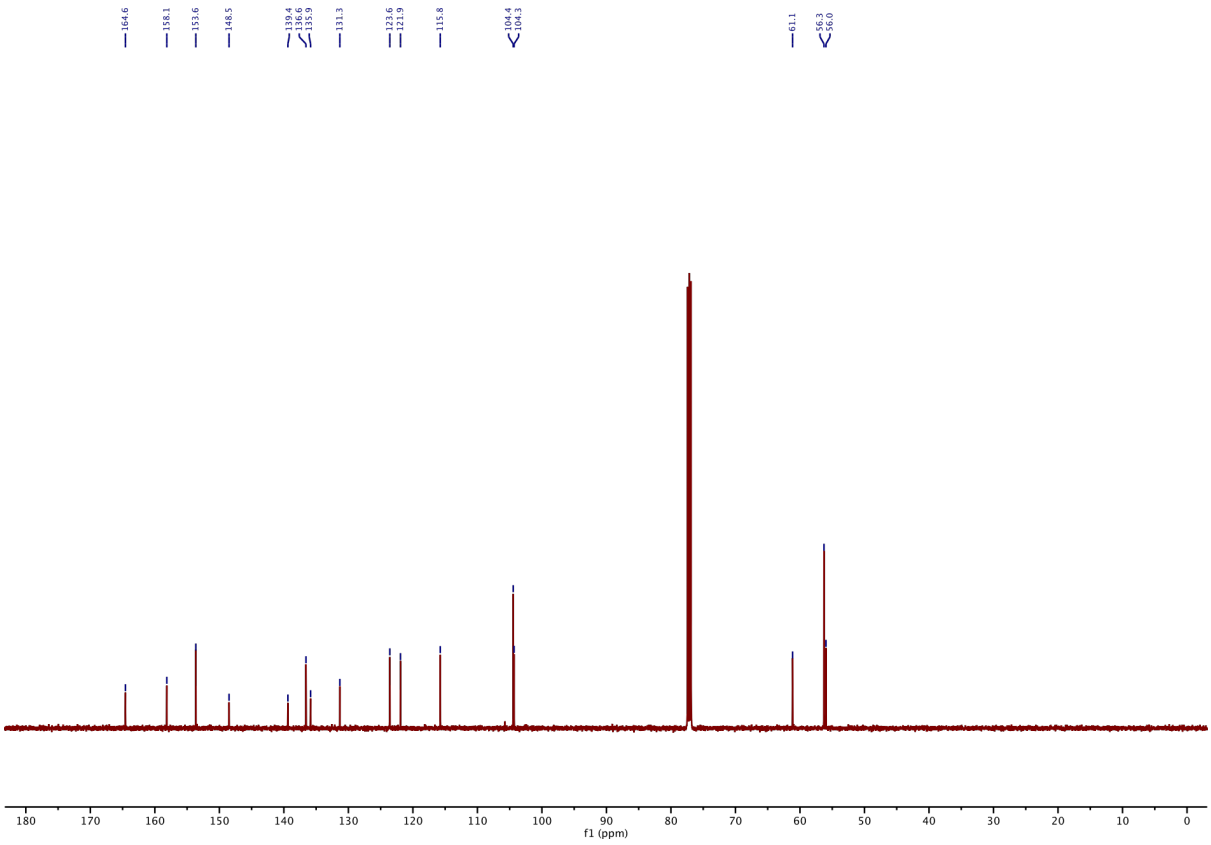

^{1}H-NMR of 4:

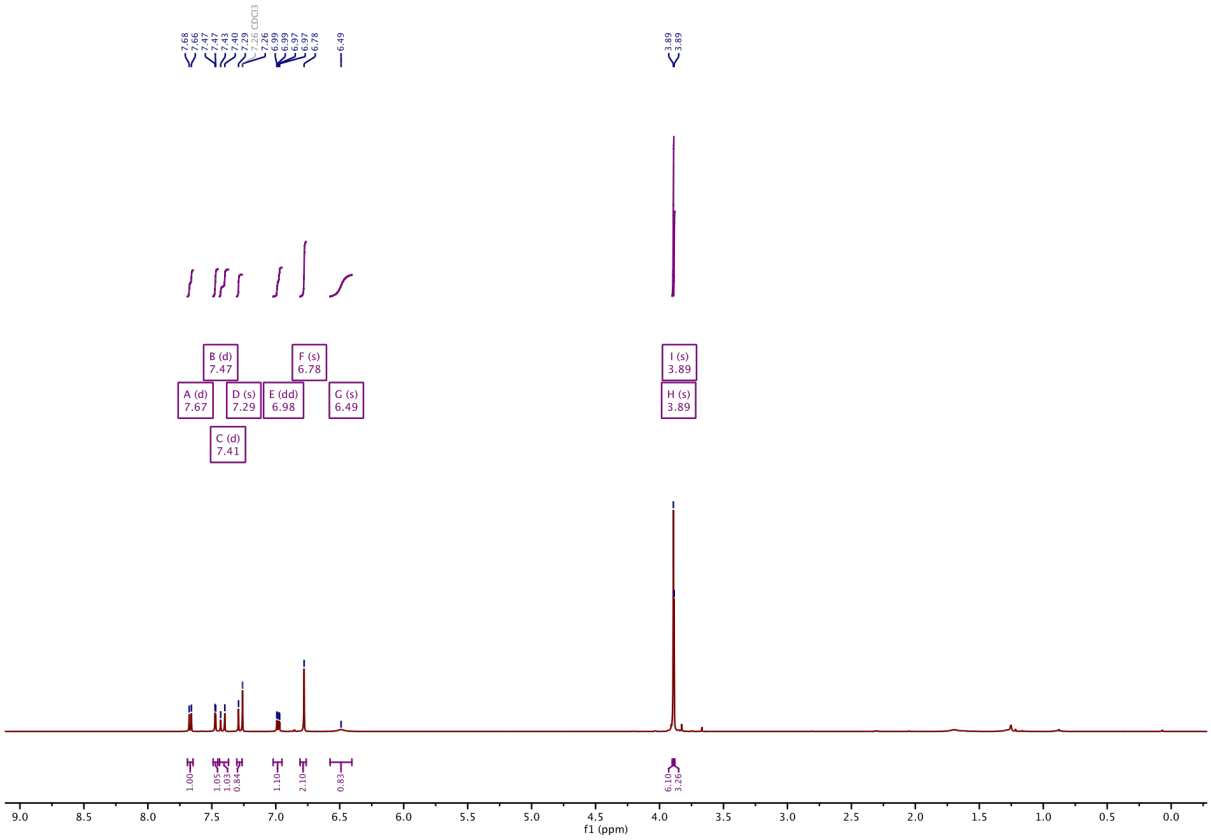

^{13}C-NMR of 4:

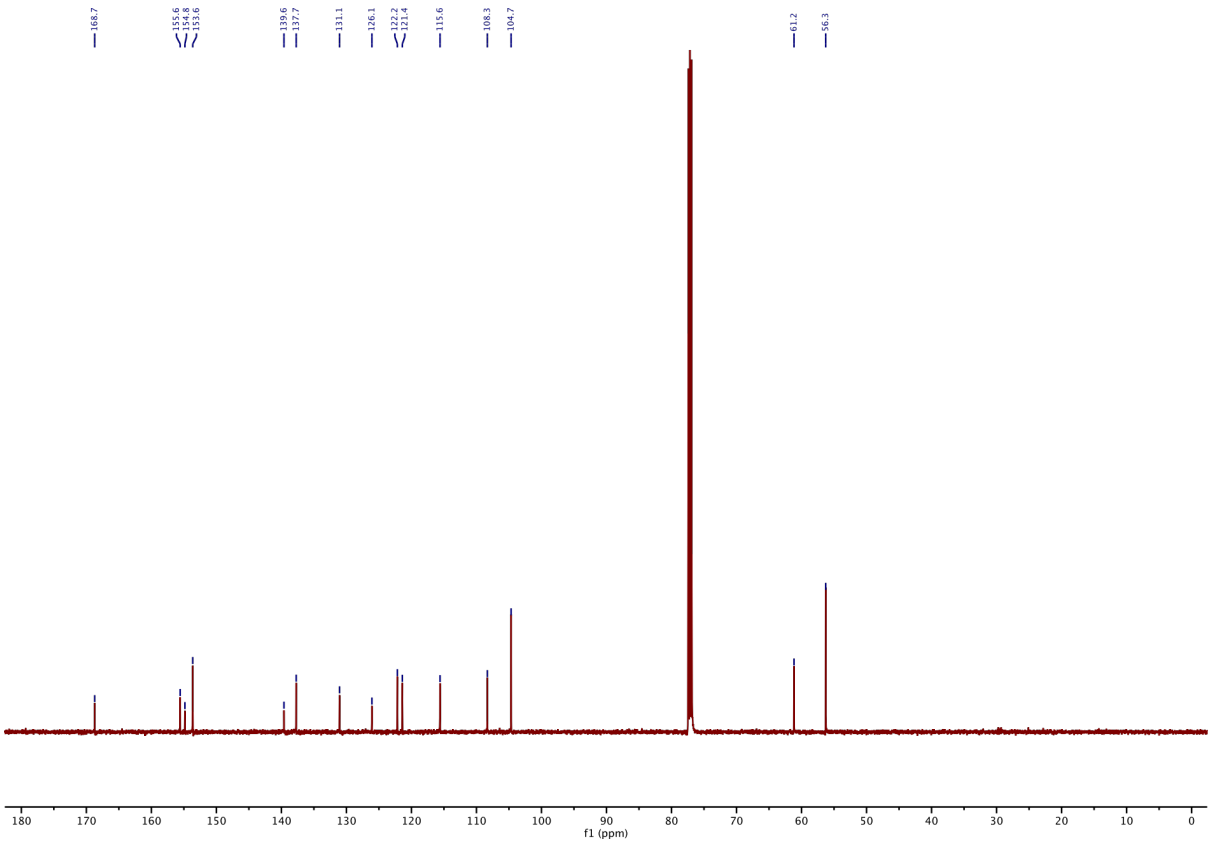

^{1}H-NMR of 5:

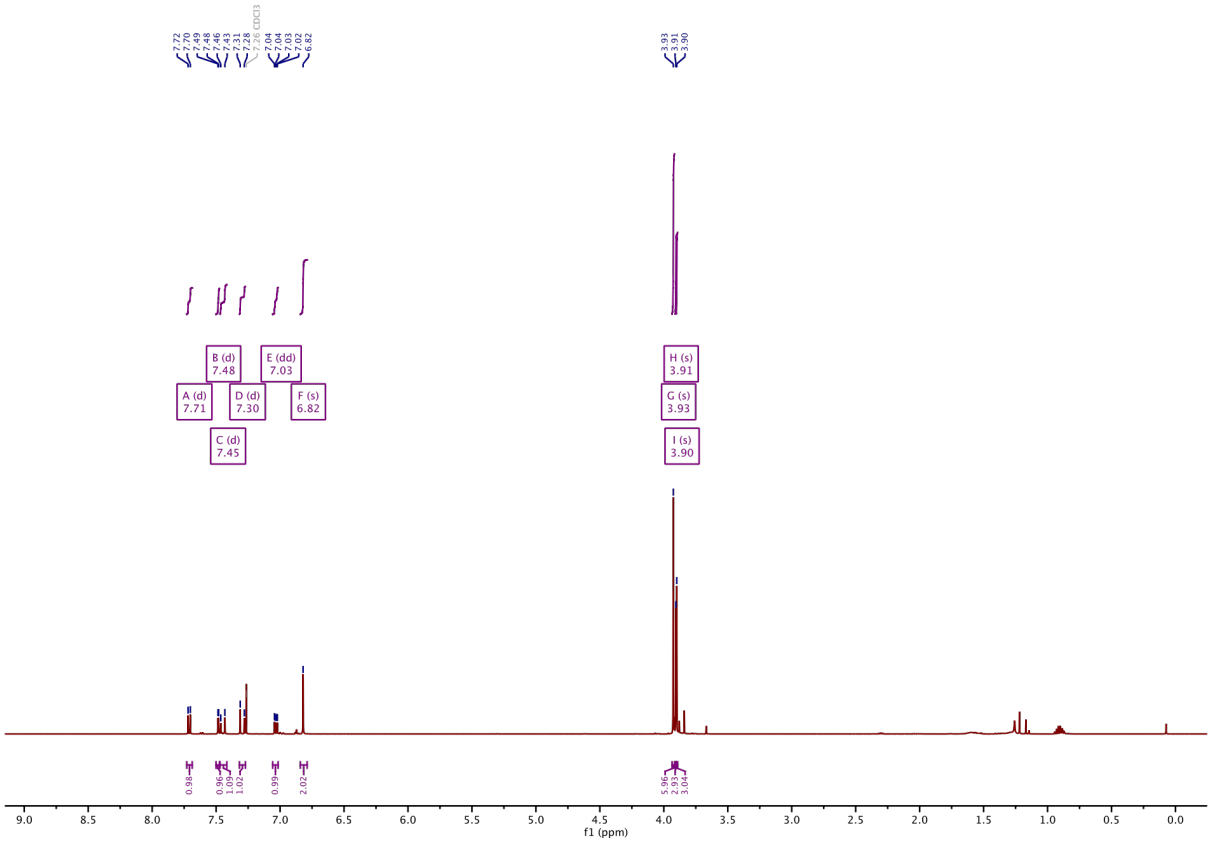

^{13}C-NMR of 5:

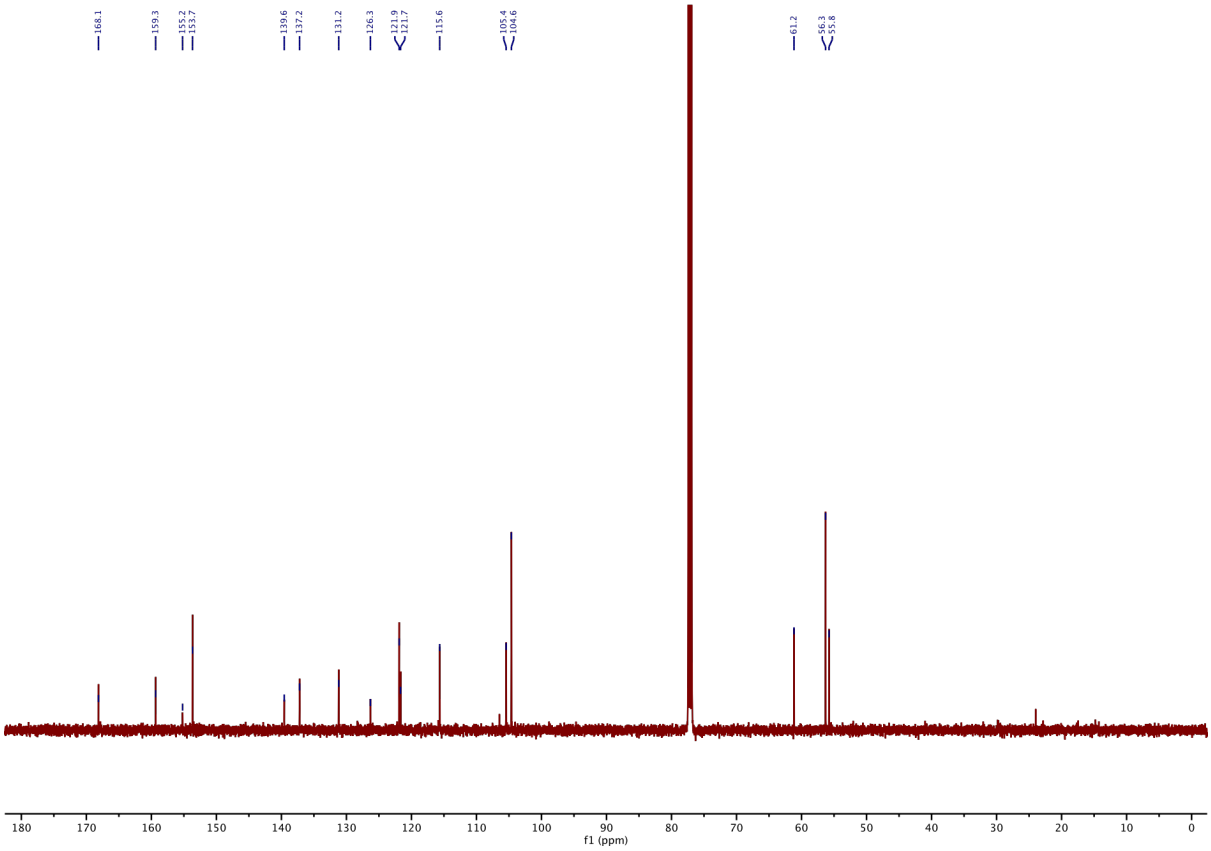

^{1}H-NMR of 6:

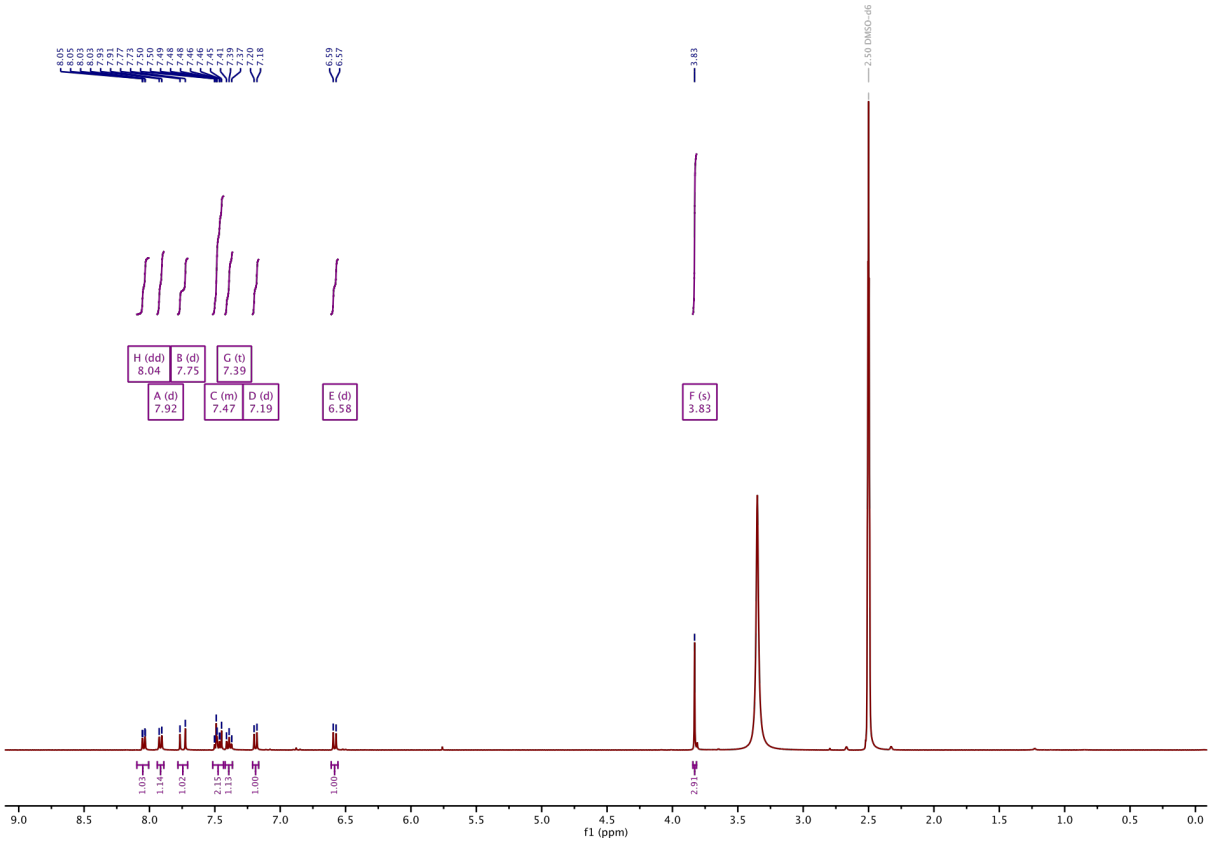

^{13}C-NMR of 6:

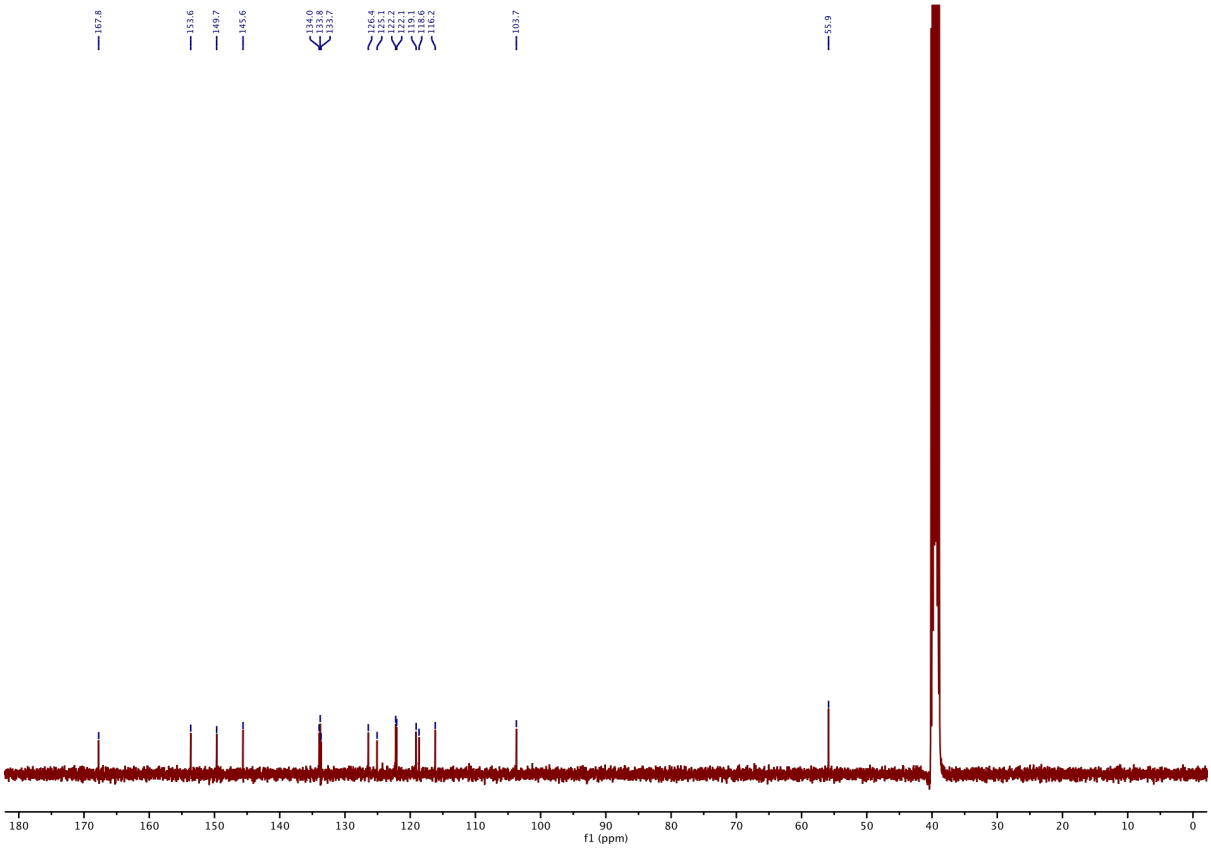

^{1}H-NMR of 7:

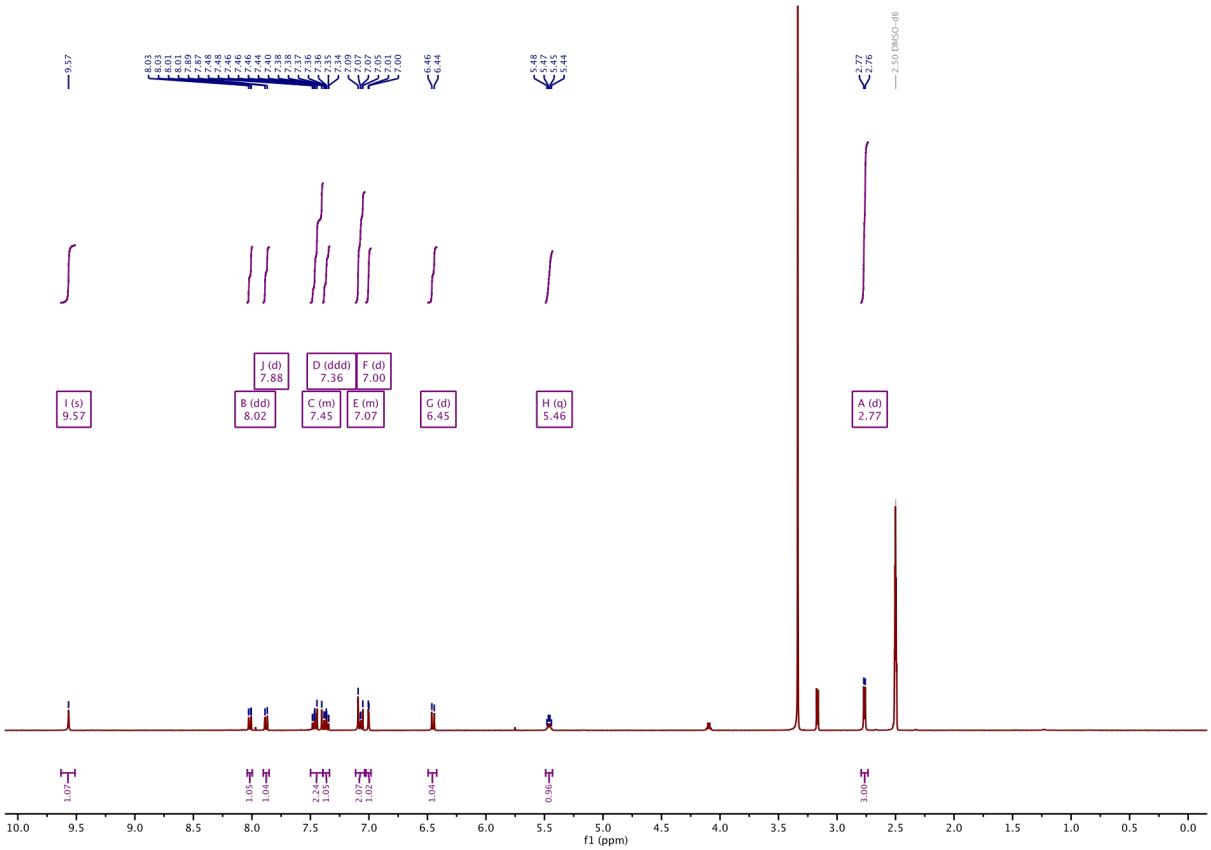

^{13}C-NMR of 7:

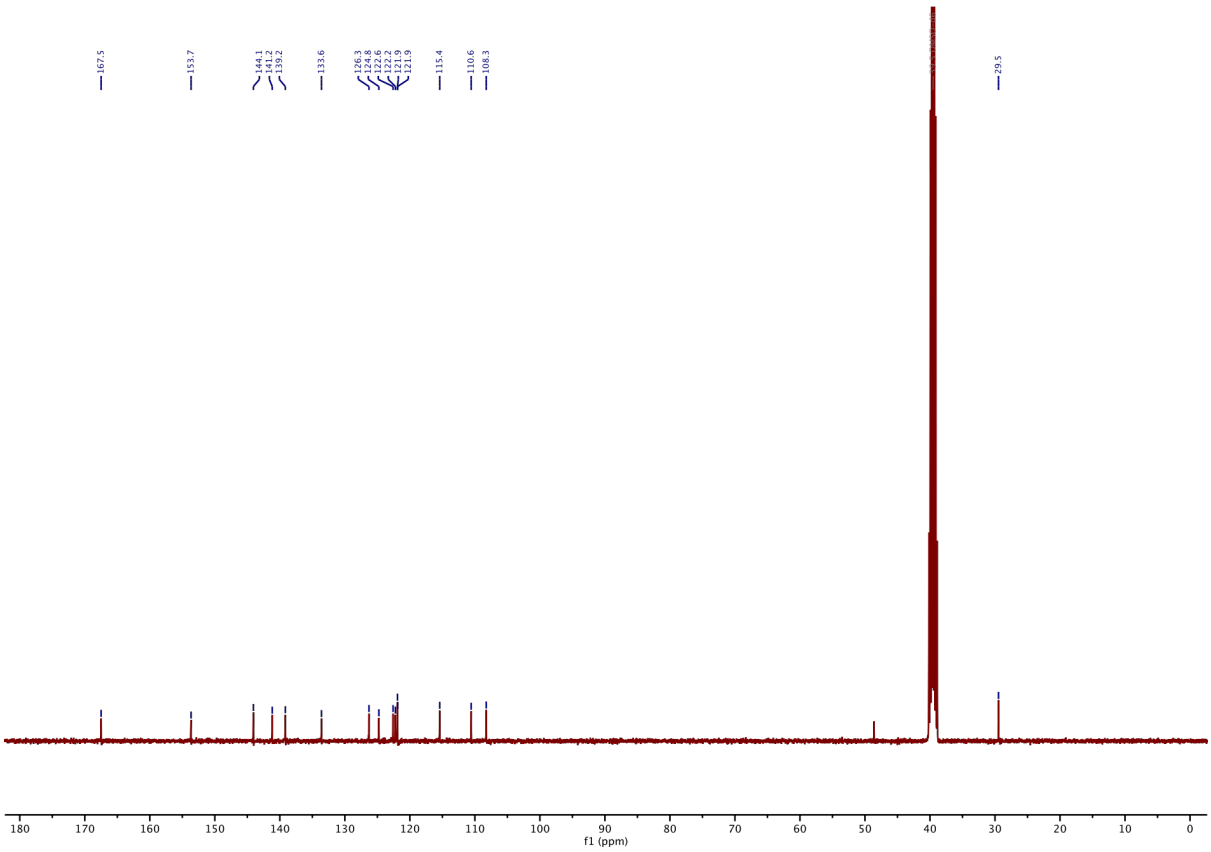

^{1}H-NMR of 8:

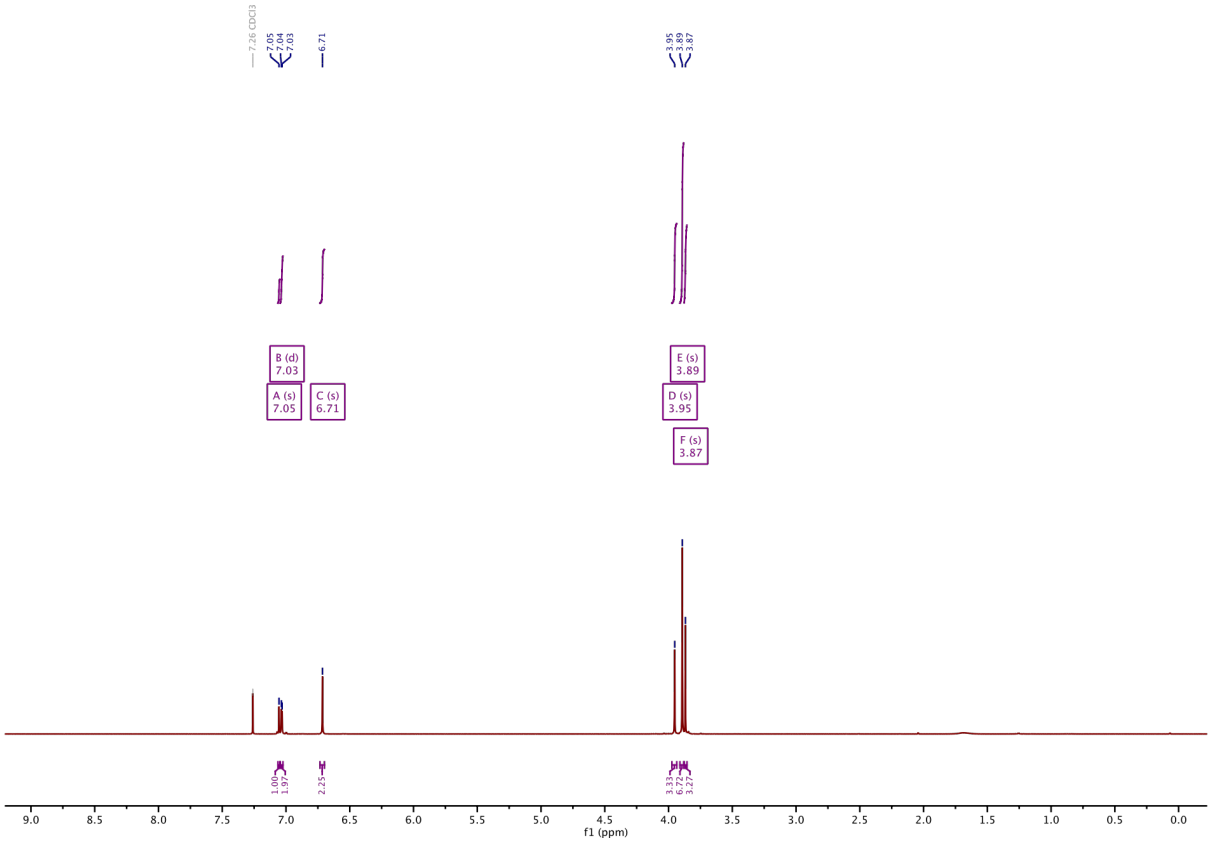

^{13}C-NMR of 8:

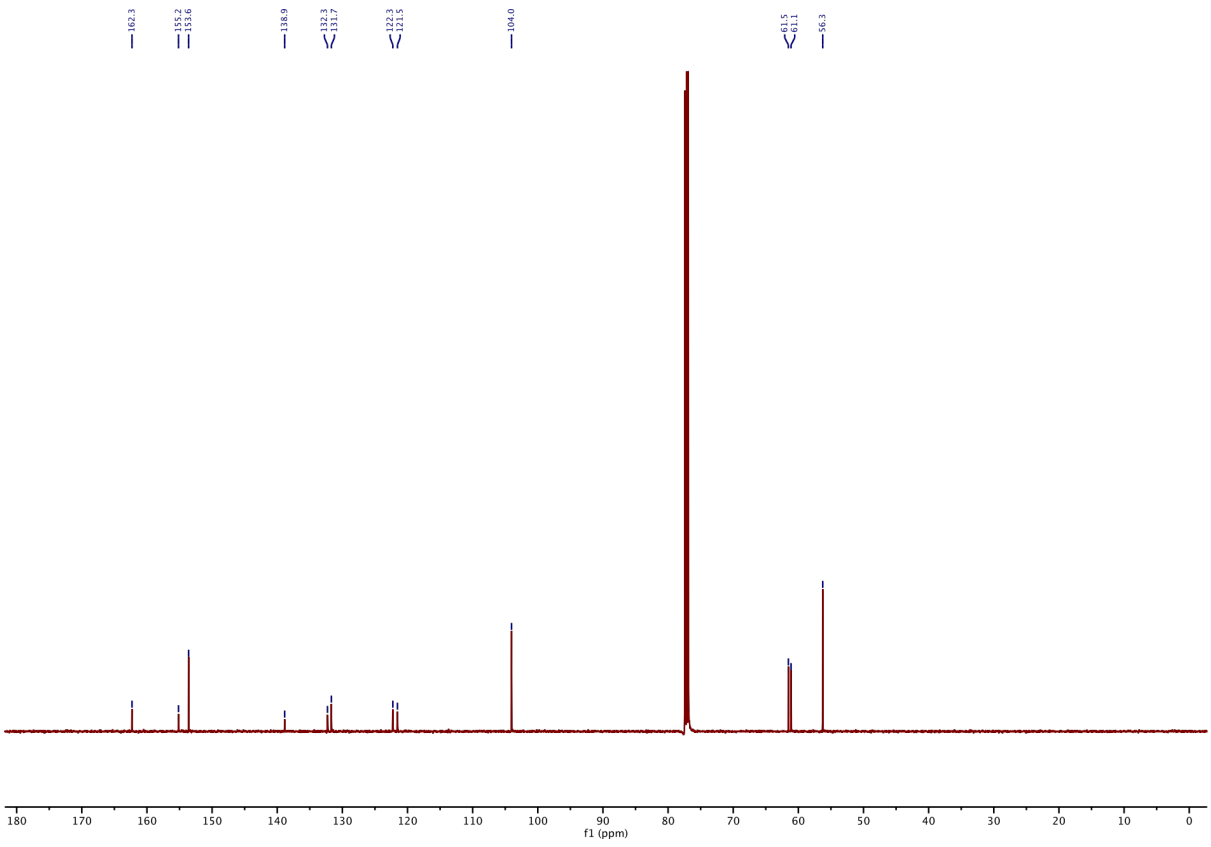

^{1}H-NMR of 9:

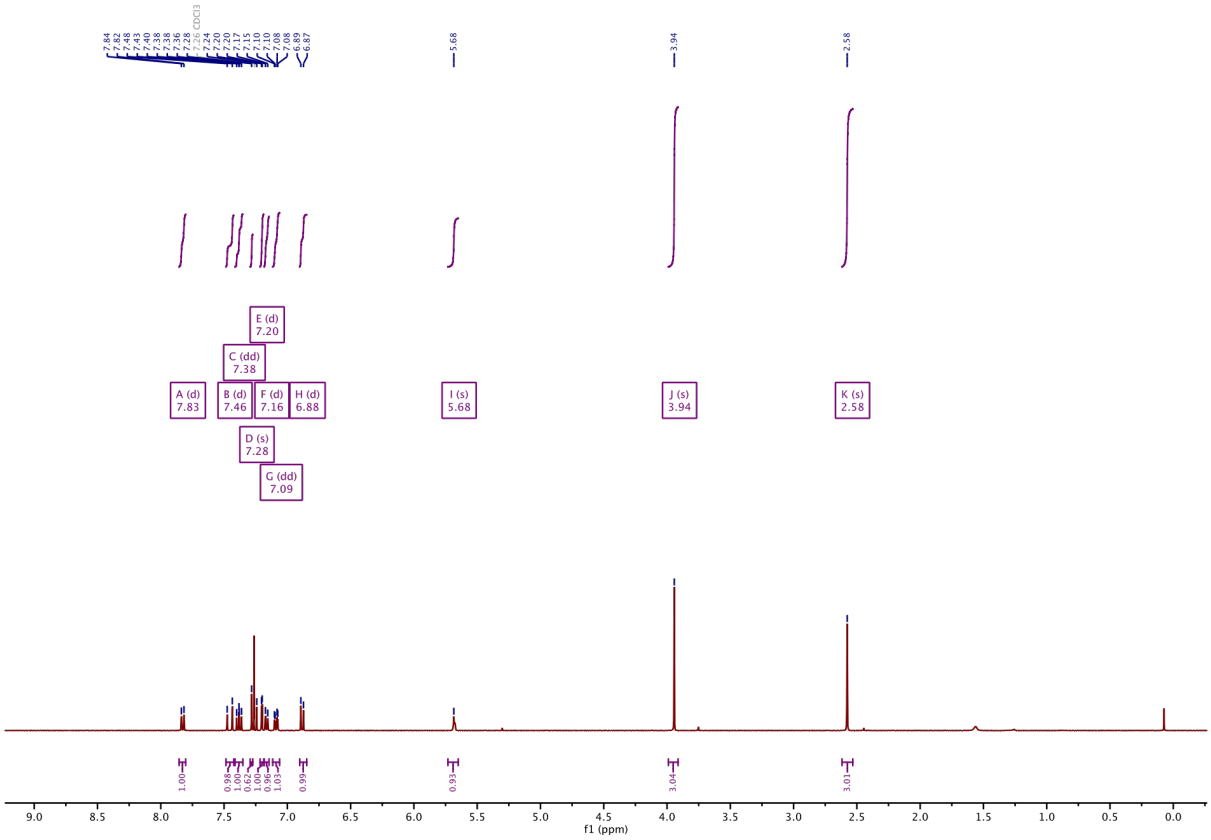

^{13}C-NMR of 9:

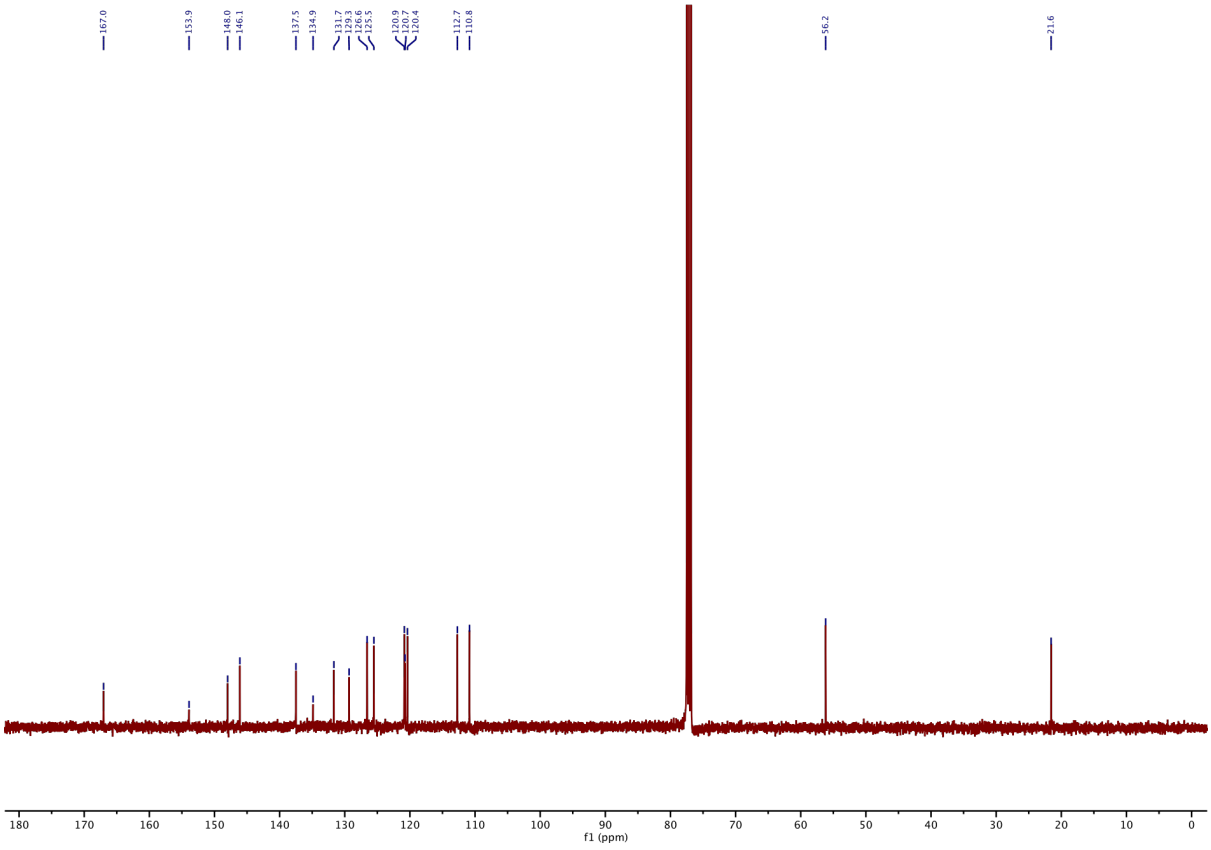

^{1}H-NMR of 10:

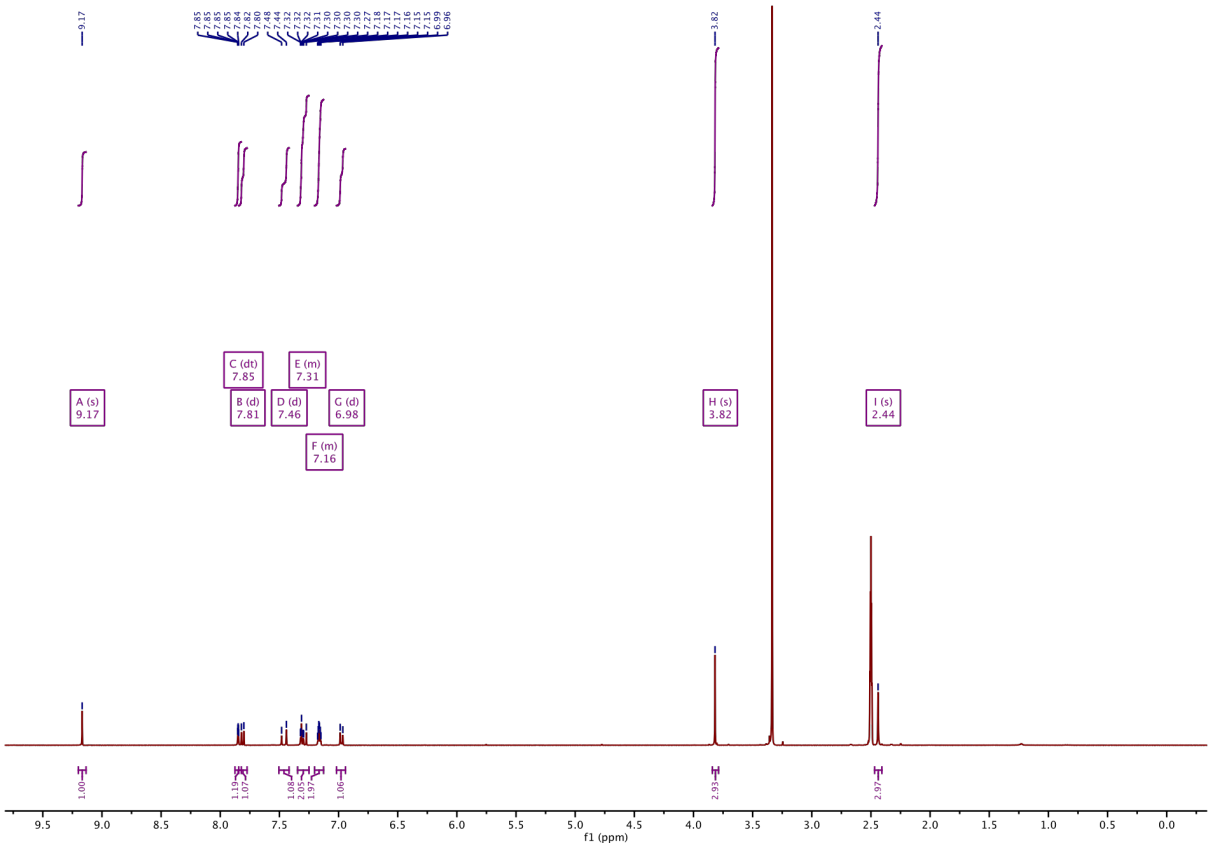

^{13}C-NMR of 10:

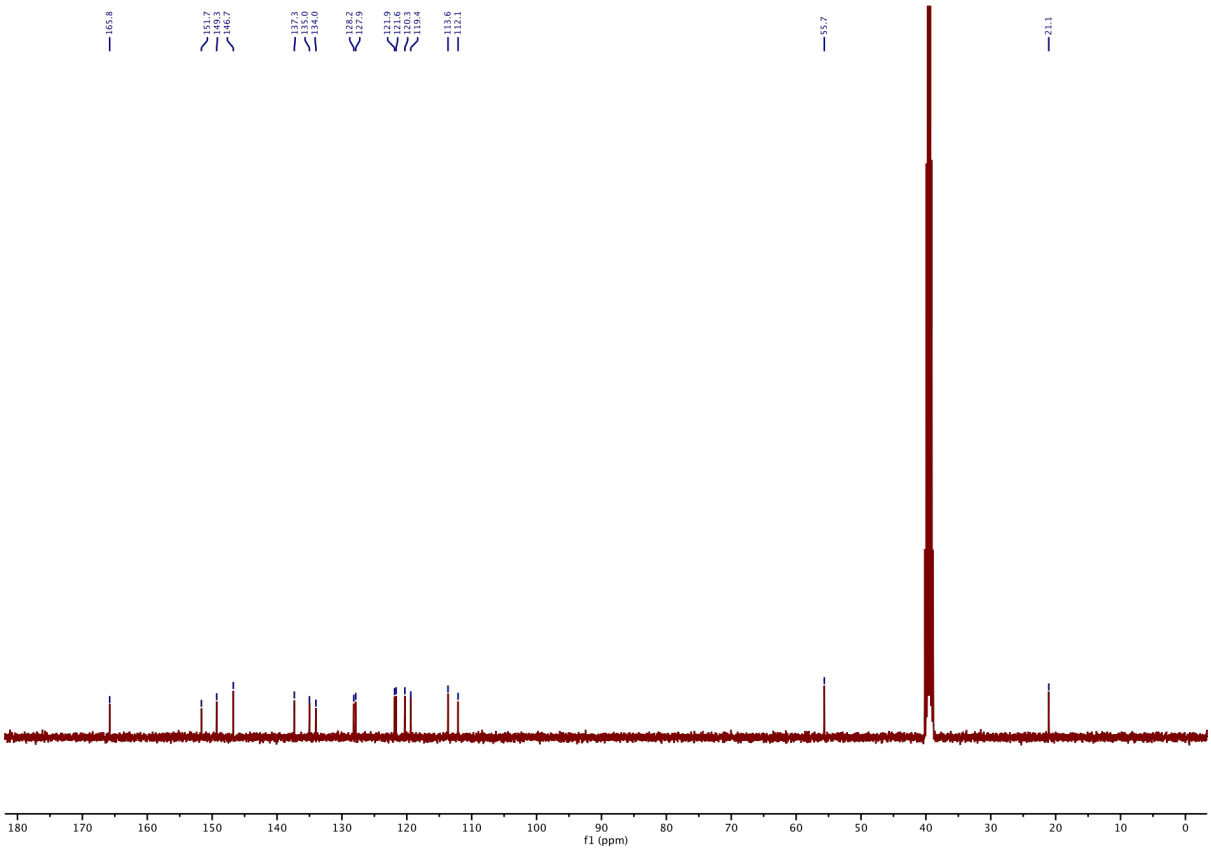

^{1}H-NMR of 11:

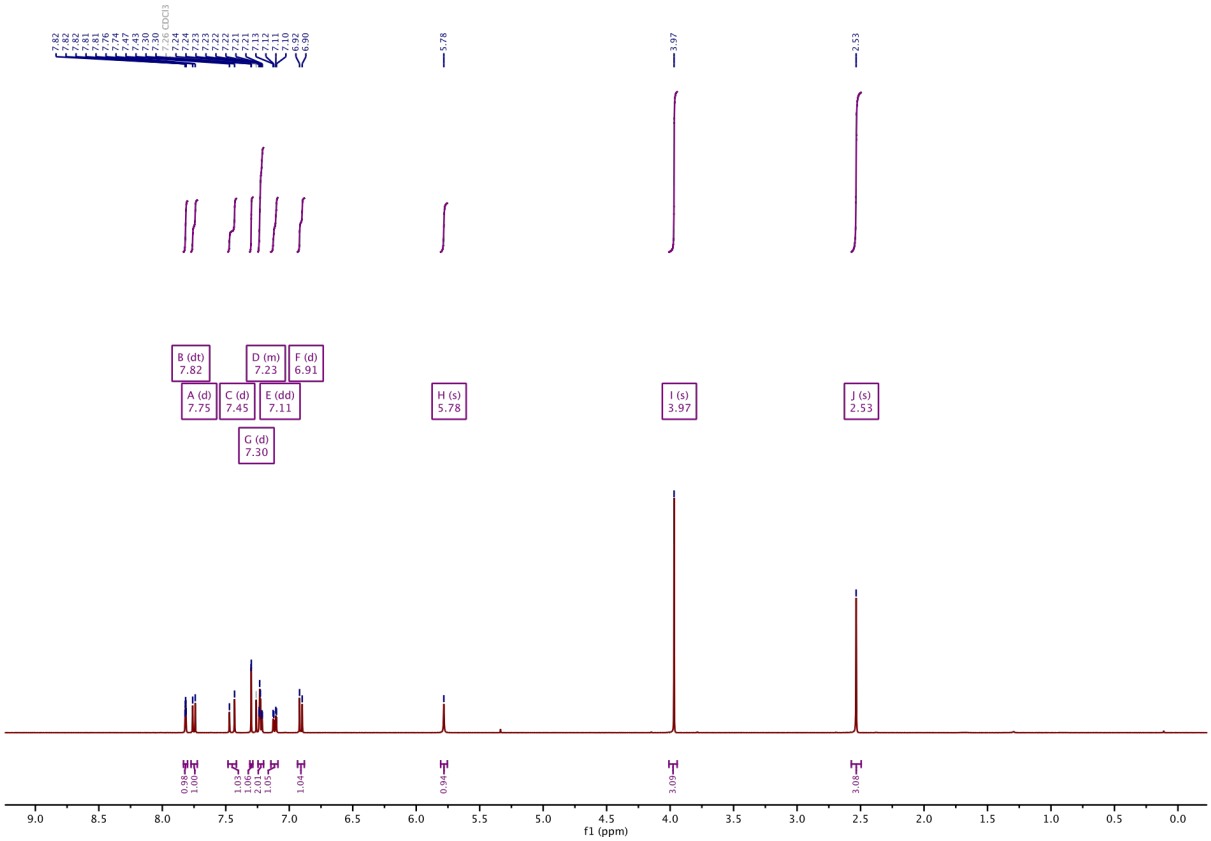

^{13}C-NMR of 11:

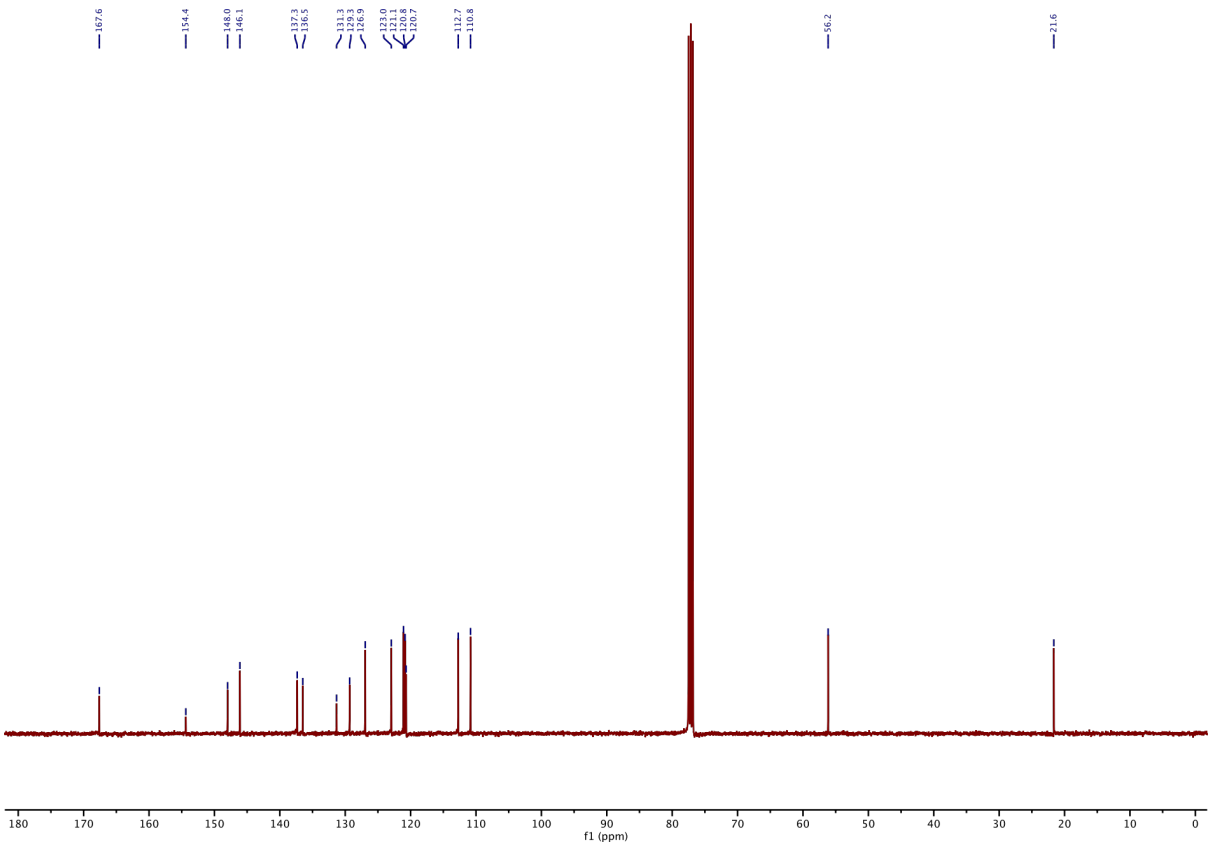

^{1}H-NMR of 12:

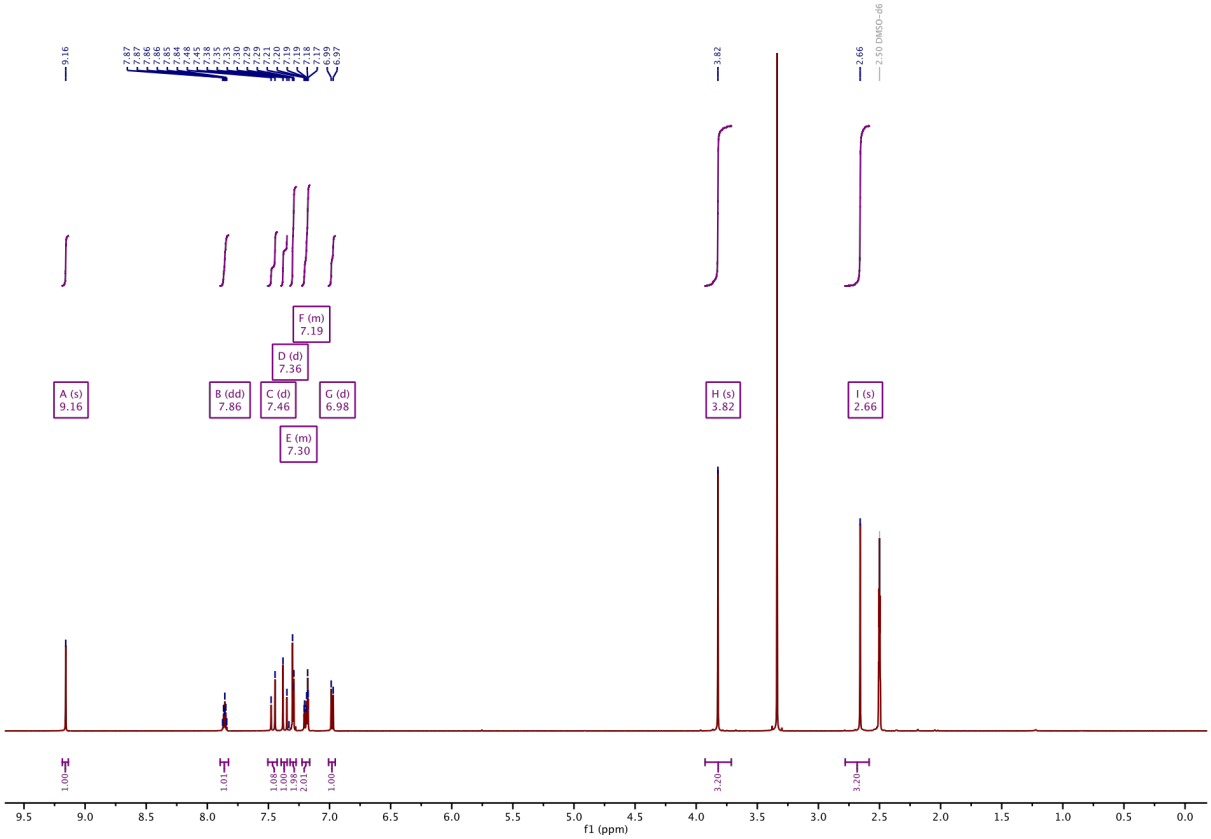

^{13}C-NMR of 12:

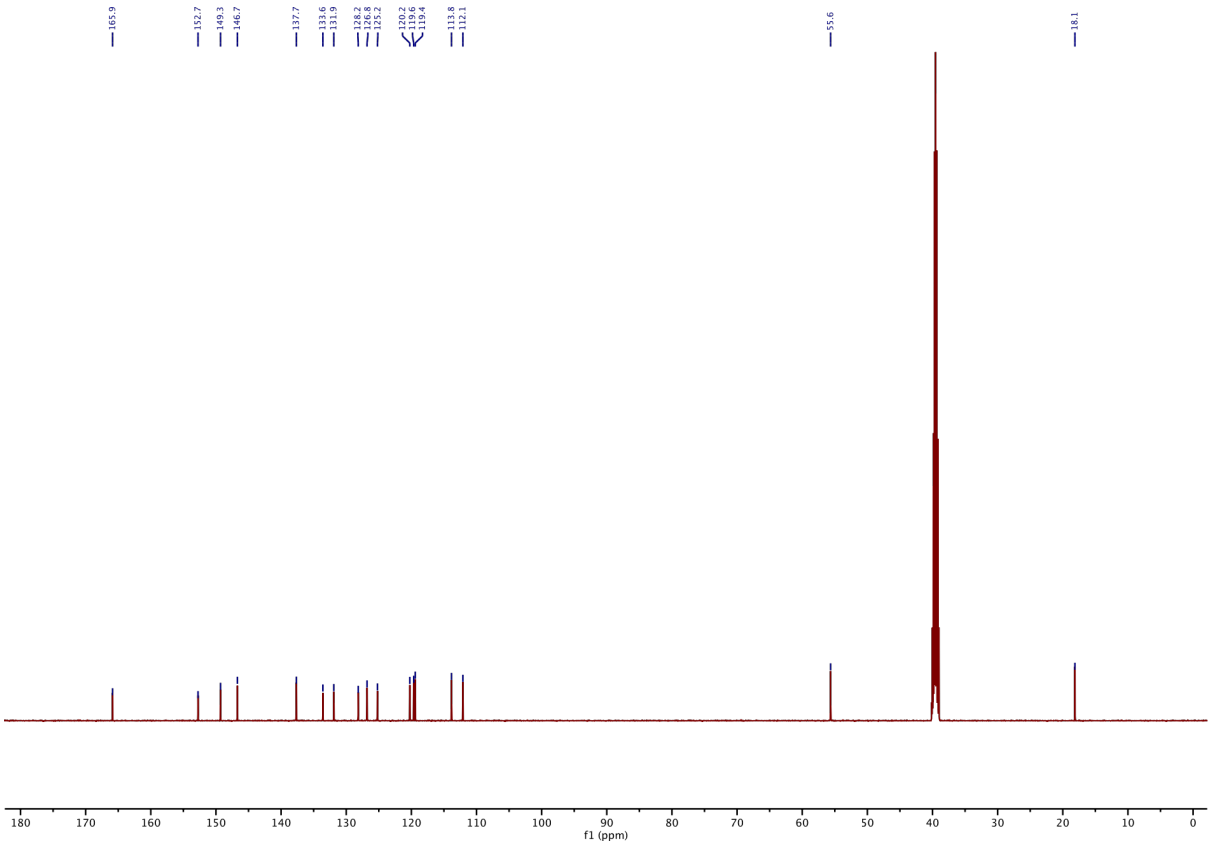

^{1}H-NMR of 13:

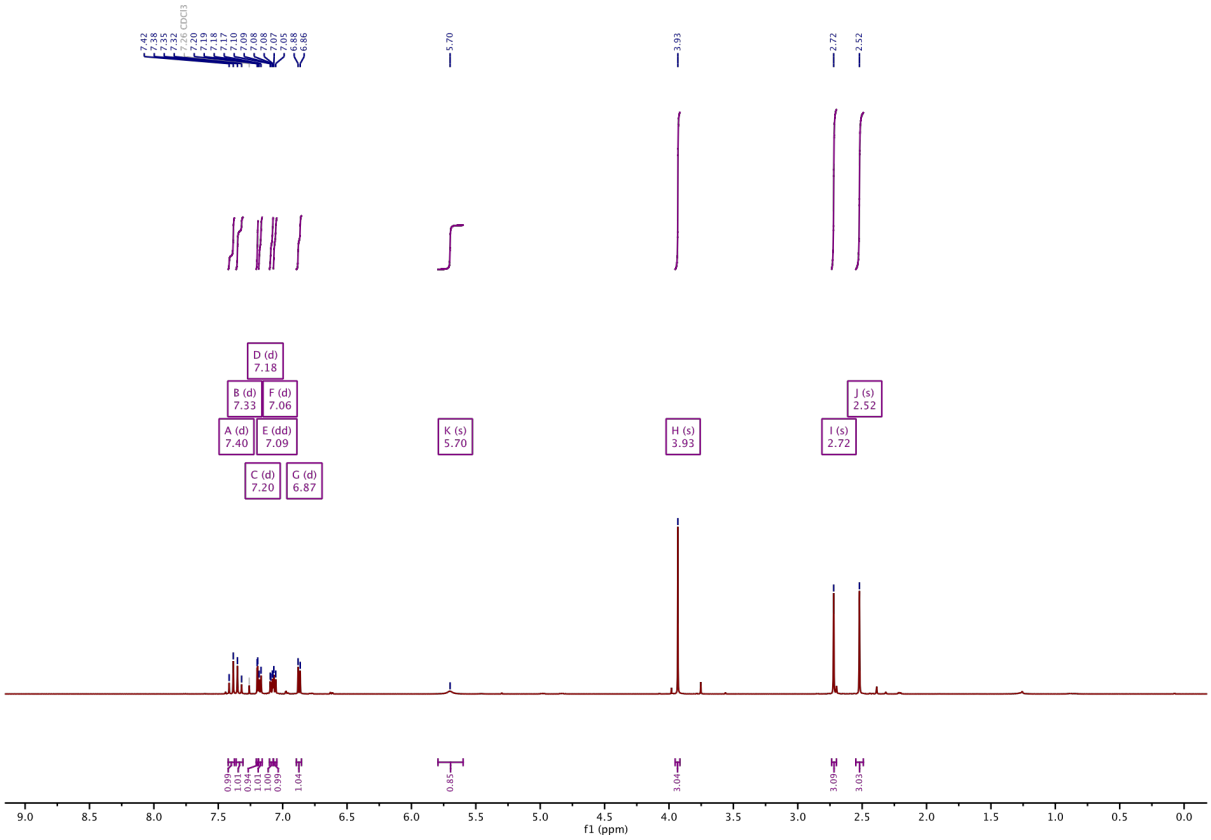

^{13}C-NMR of 13:

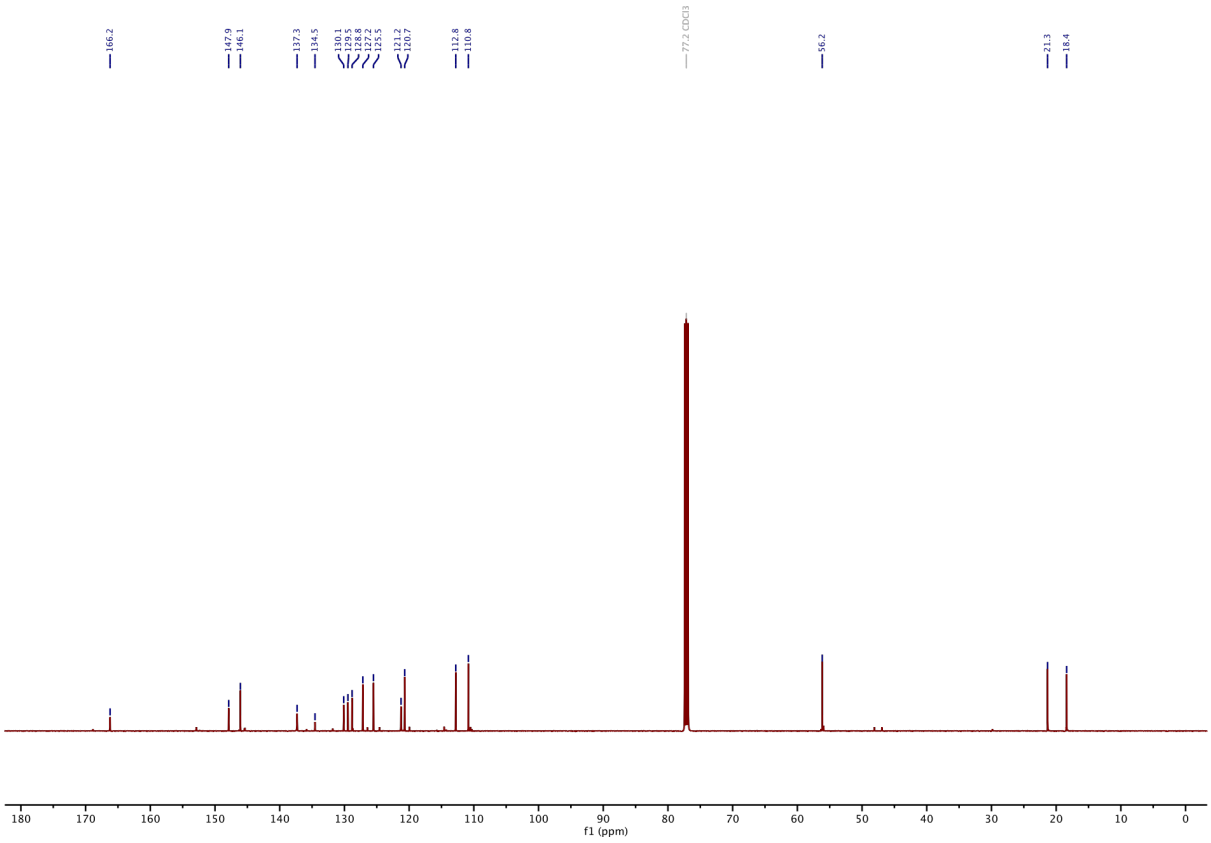

^{1}H-NMR of 14:

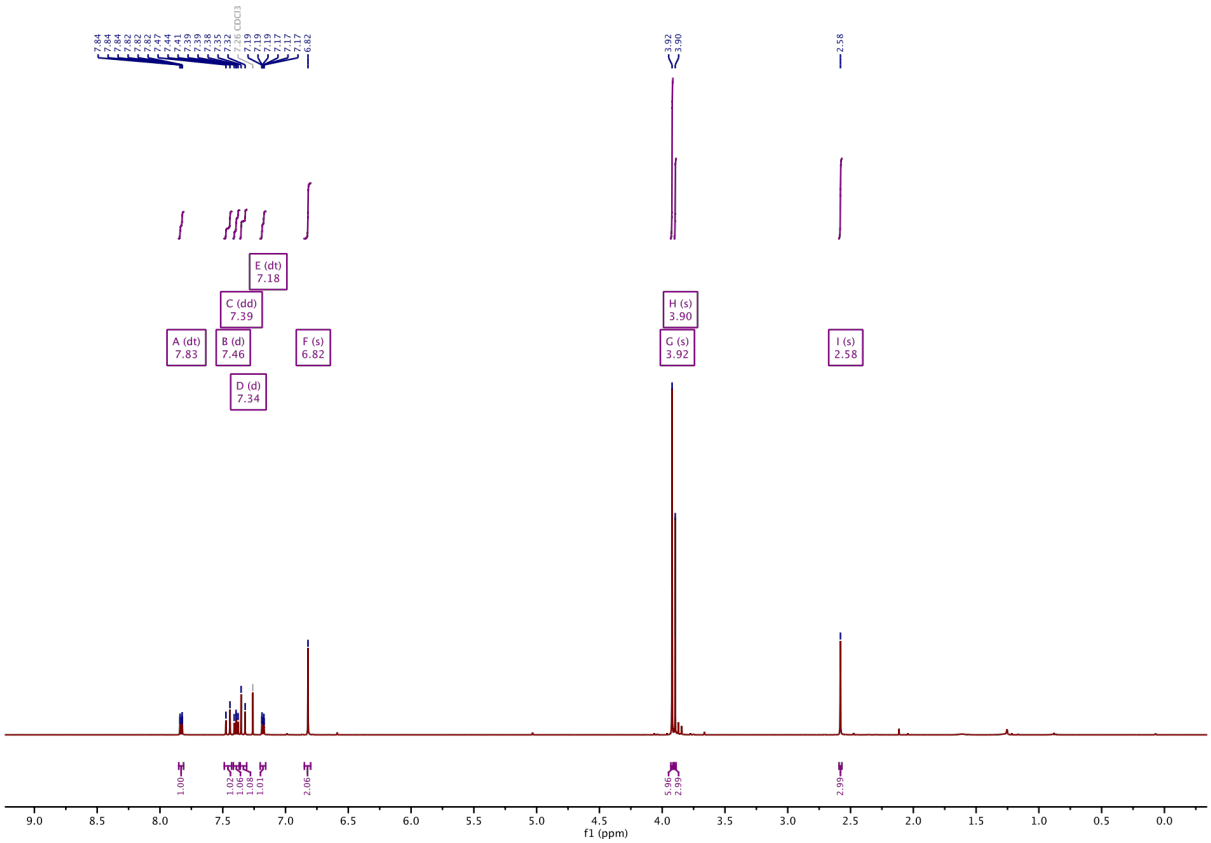

^{13}C-NMR of 14:

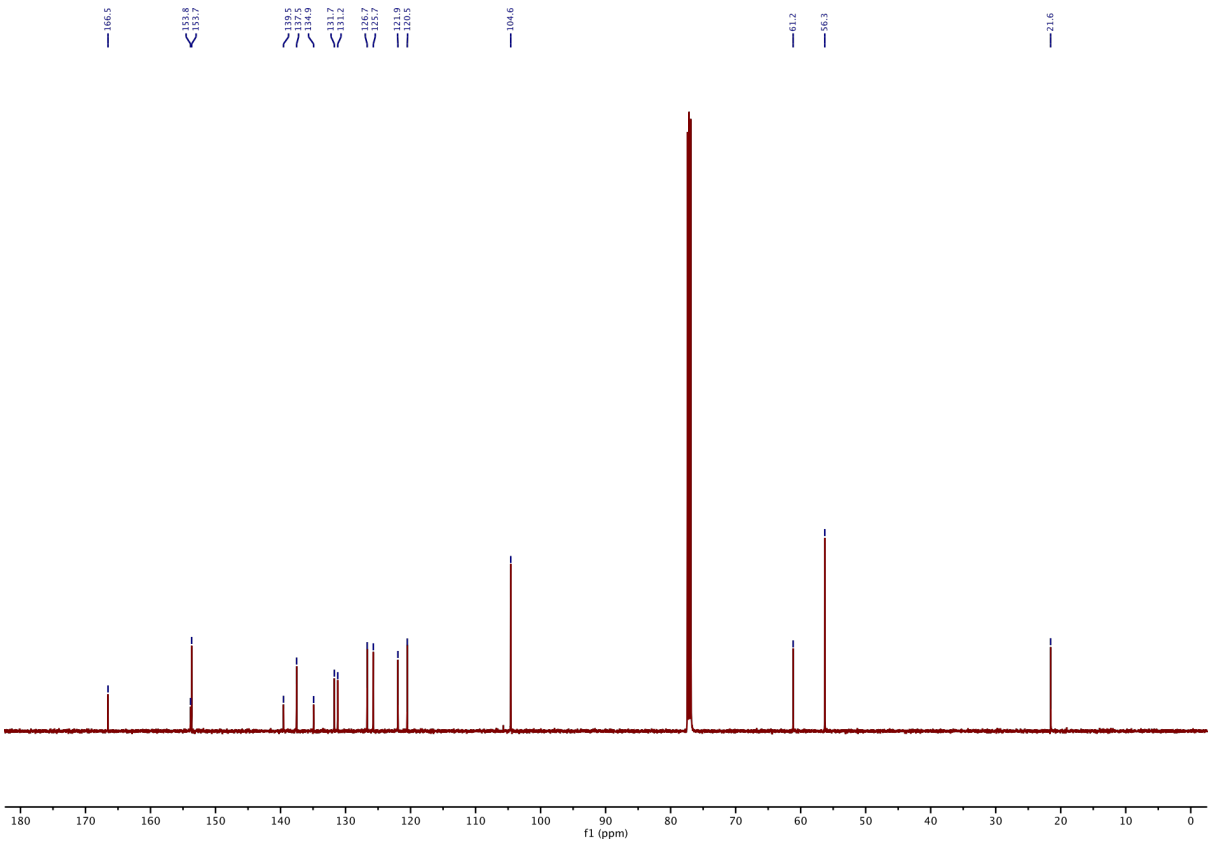

1H-NMR of SBTub2M:

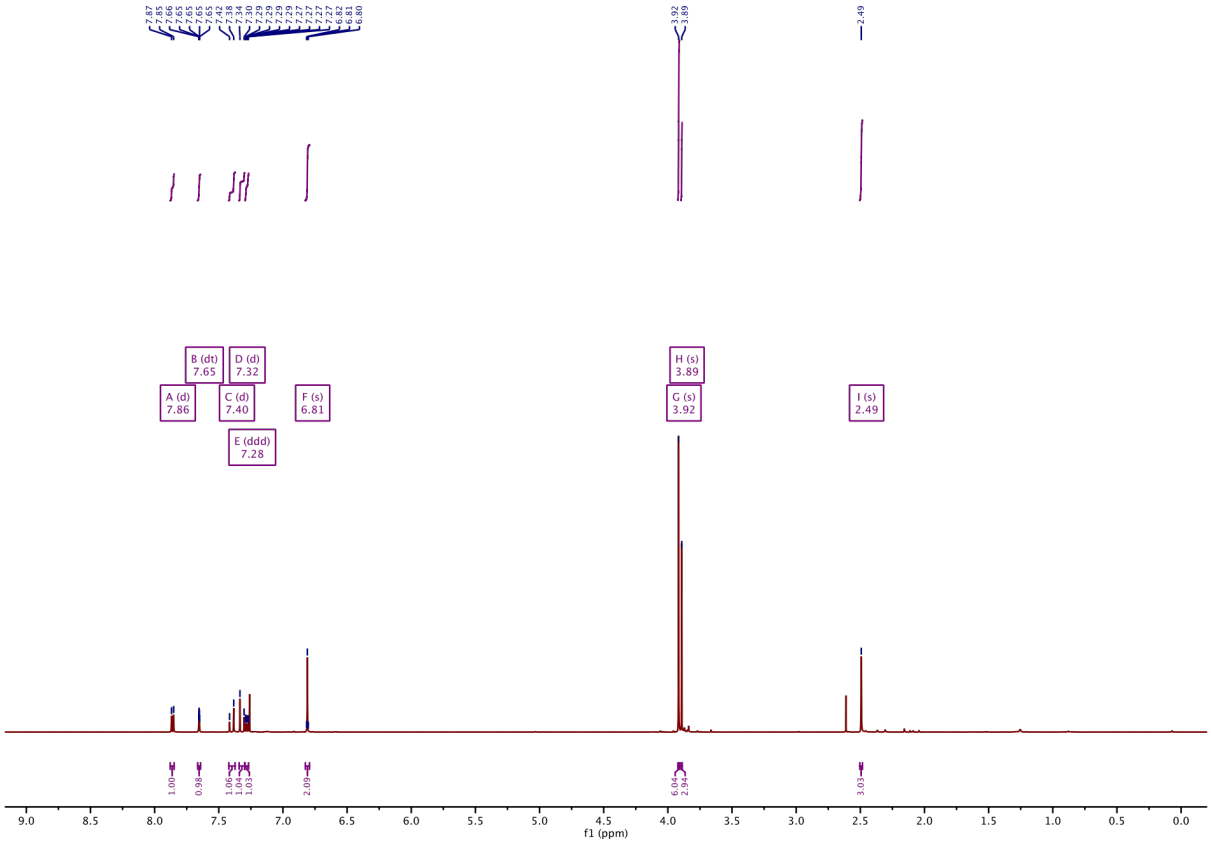

13C-NMR of SBTub2M:

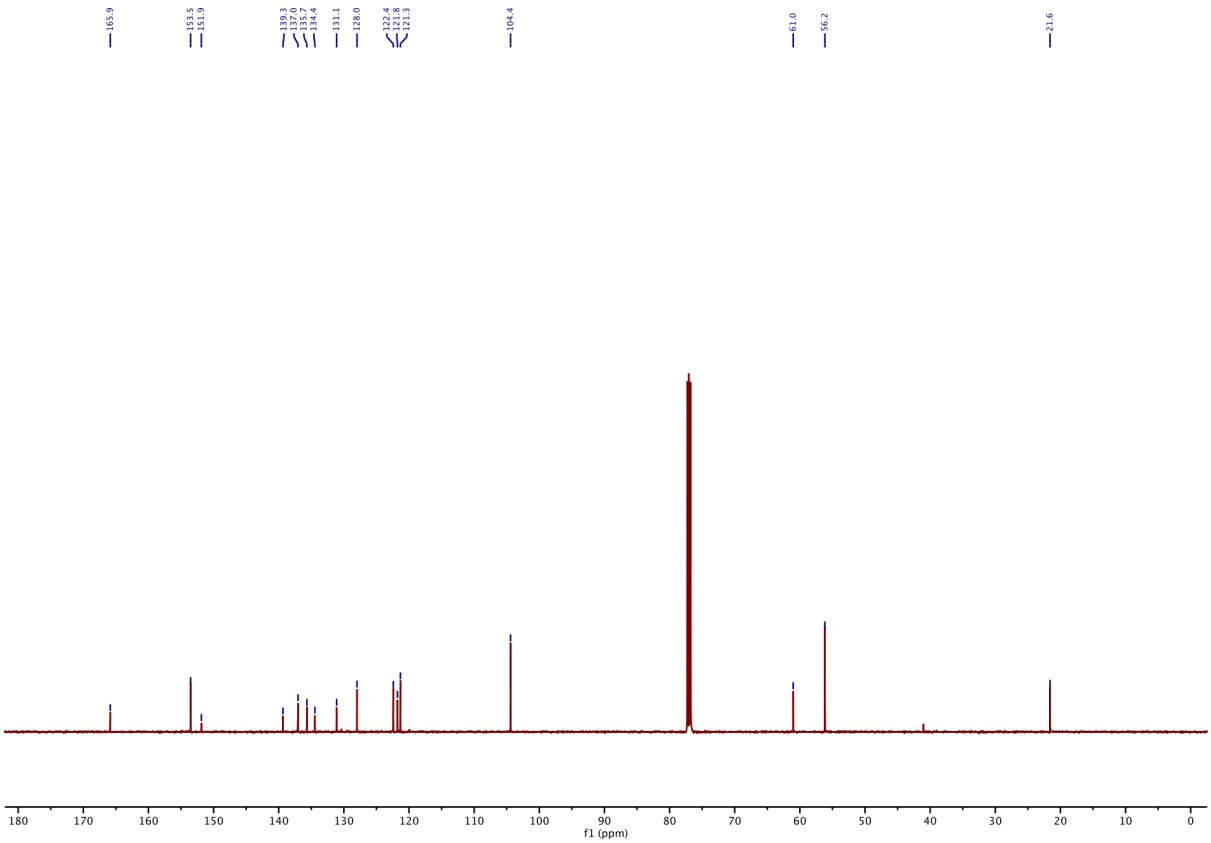

^{1}H-NMR of 16:

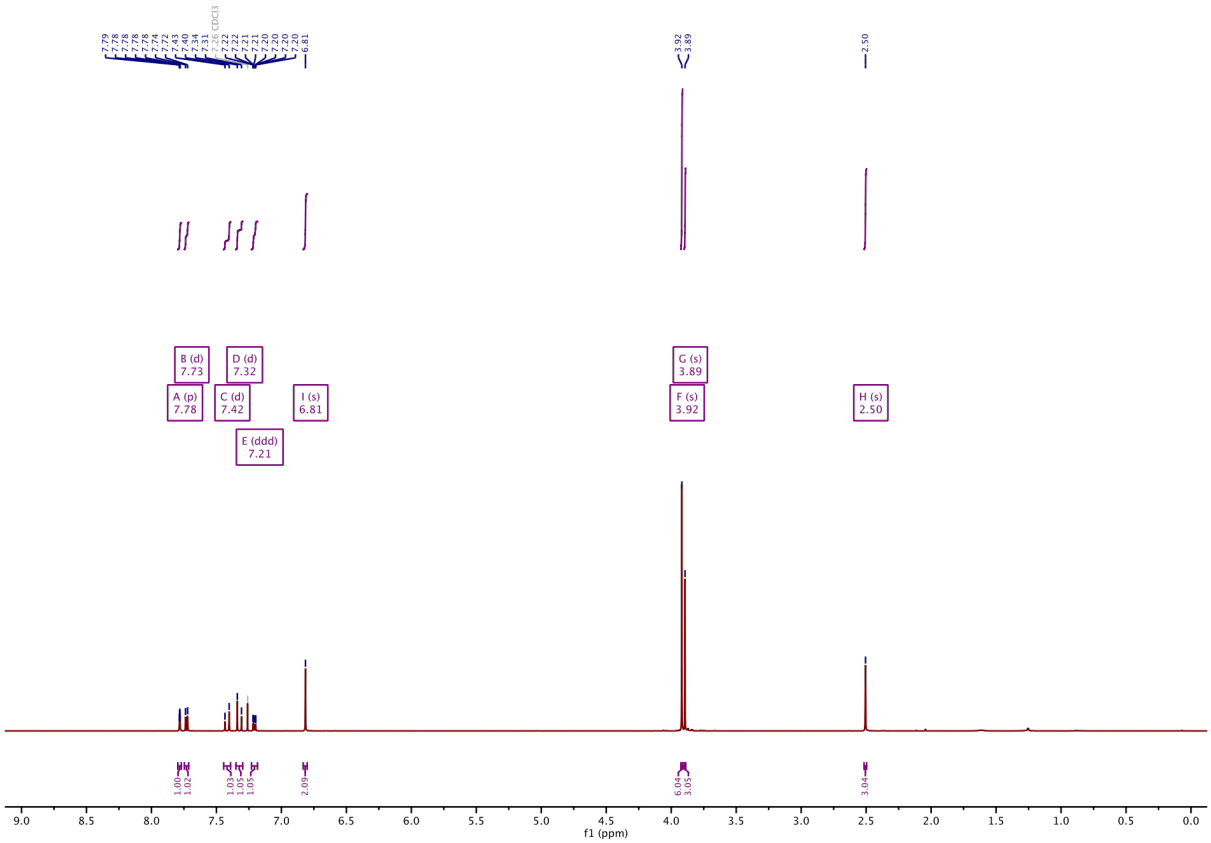

^{13}C-NMR of 16:

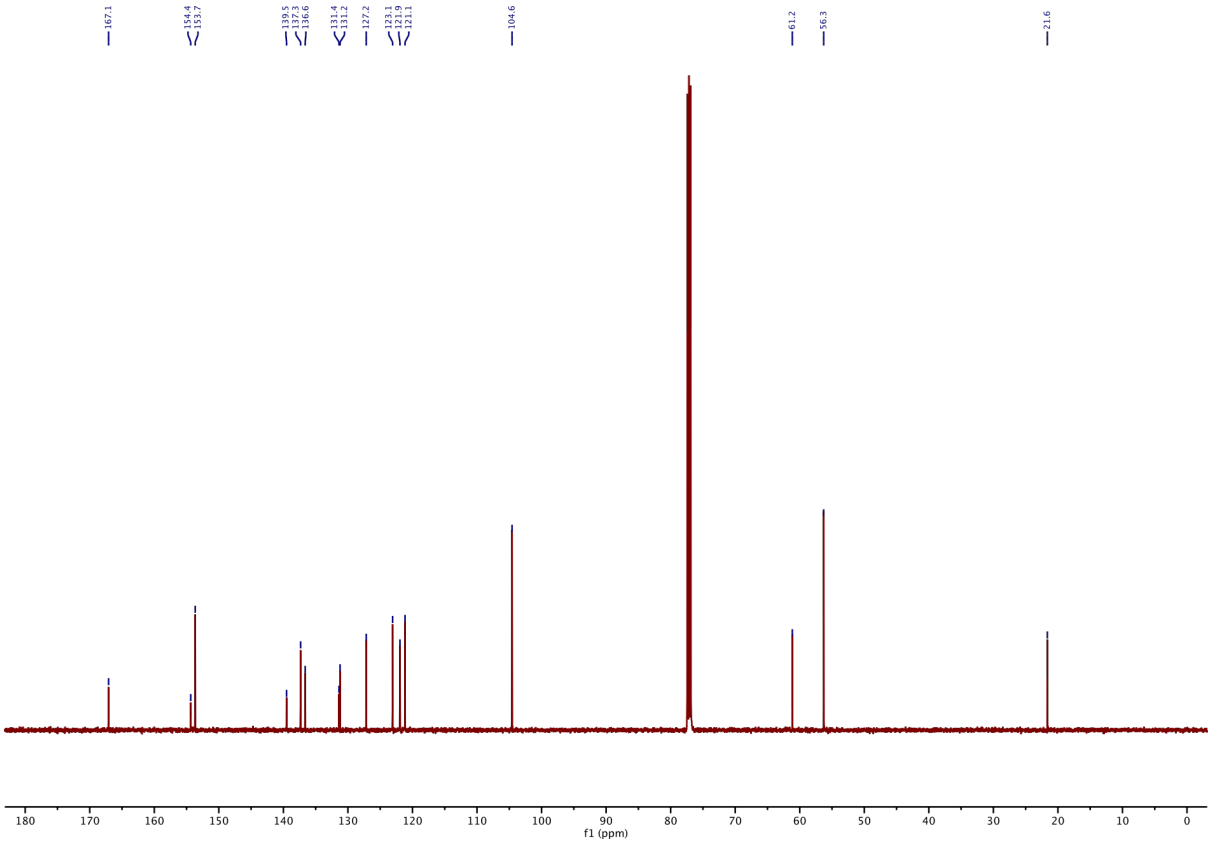

^{1}H-NMR of 17:

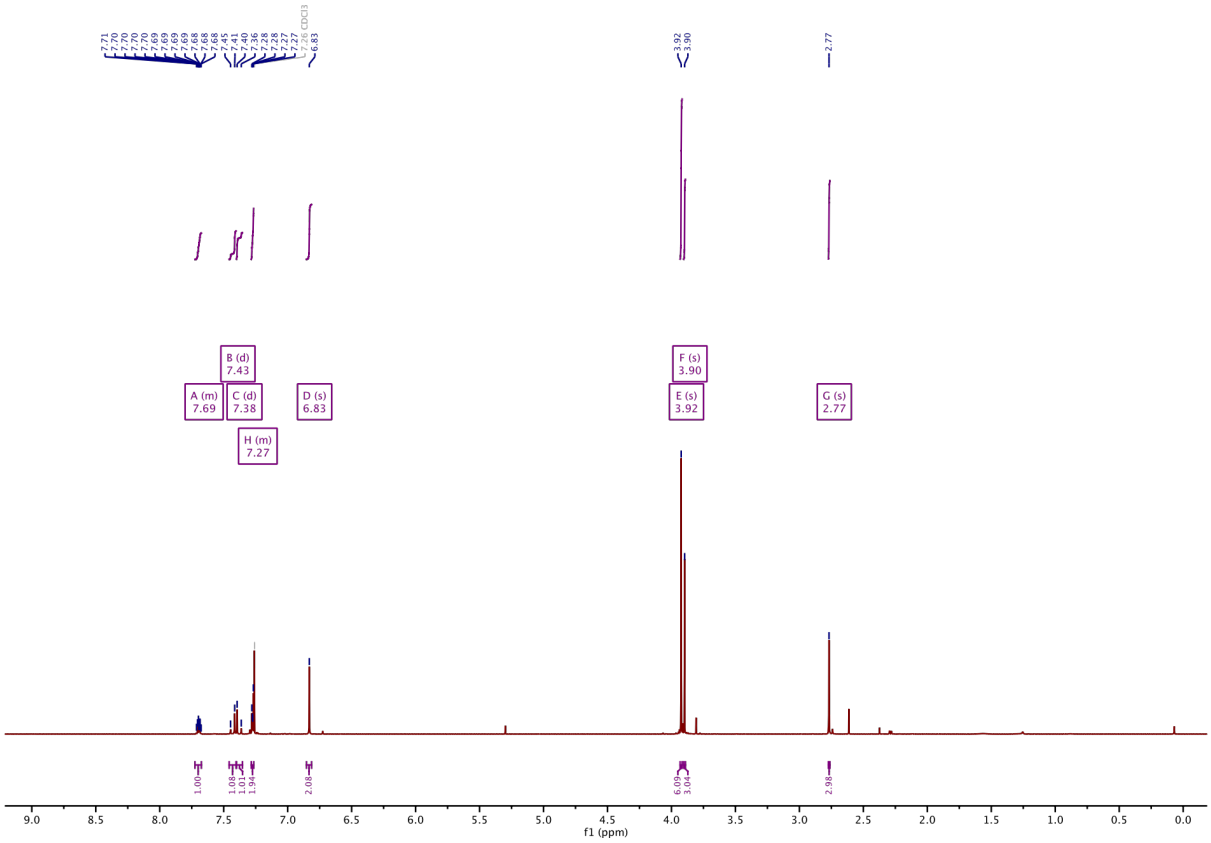

^{13}C-NMR of 17:

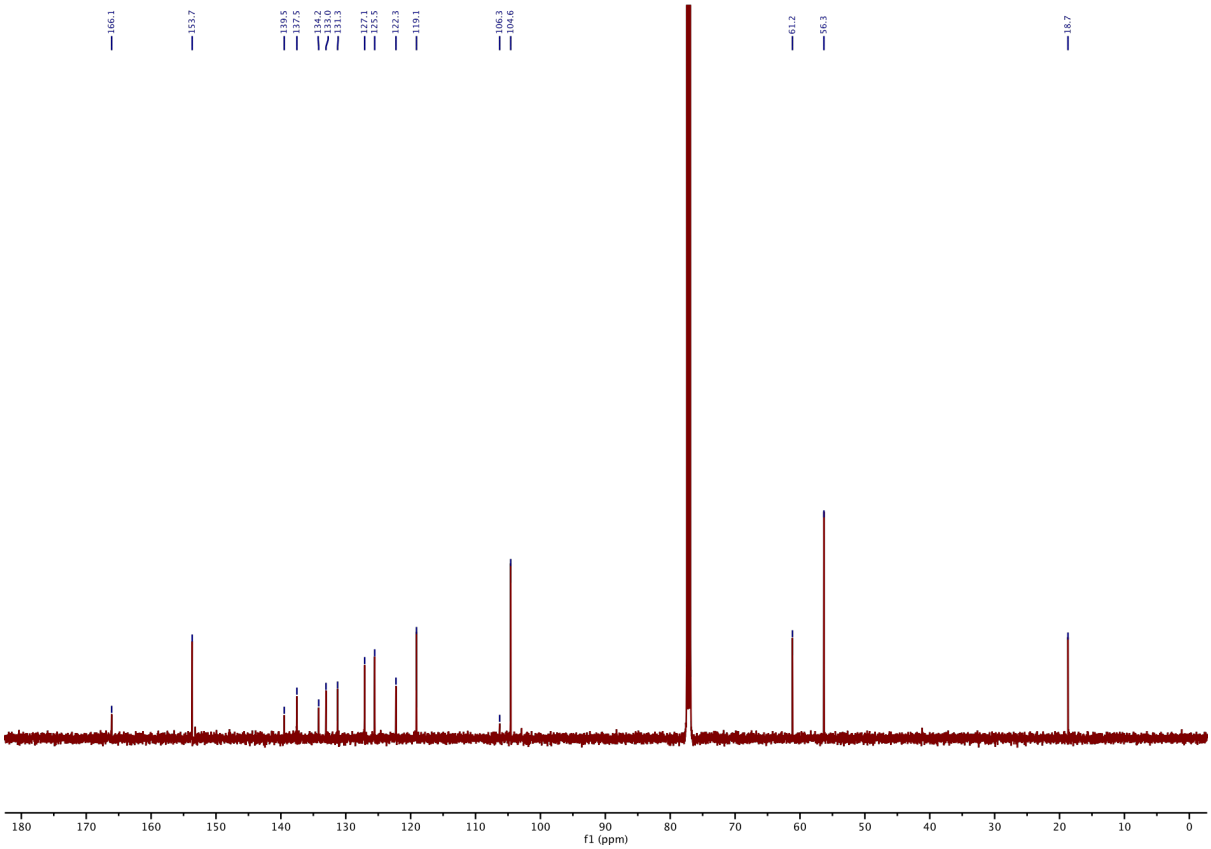

^{1}H-NMR of 18:

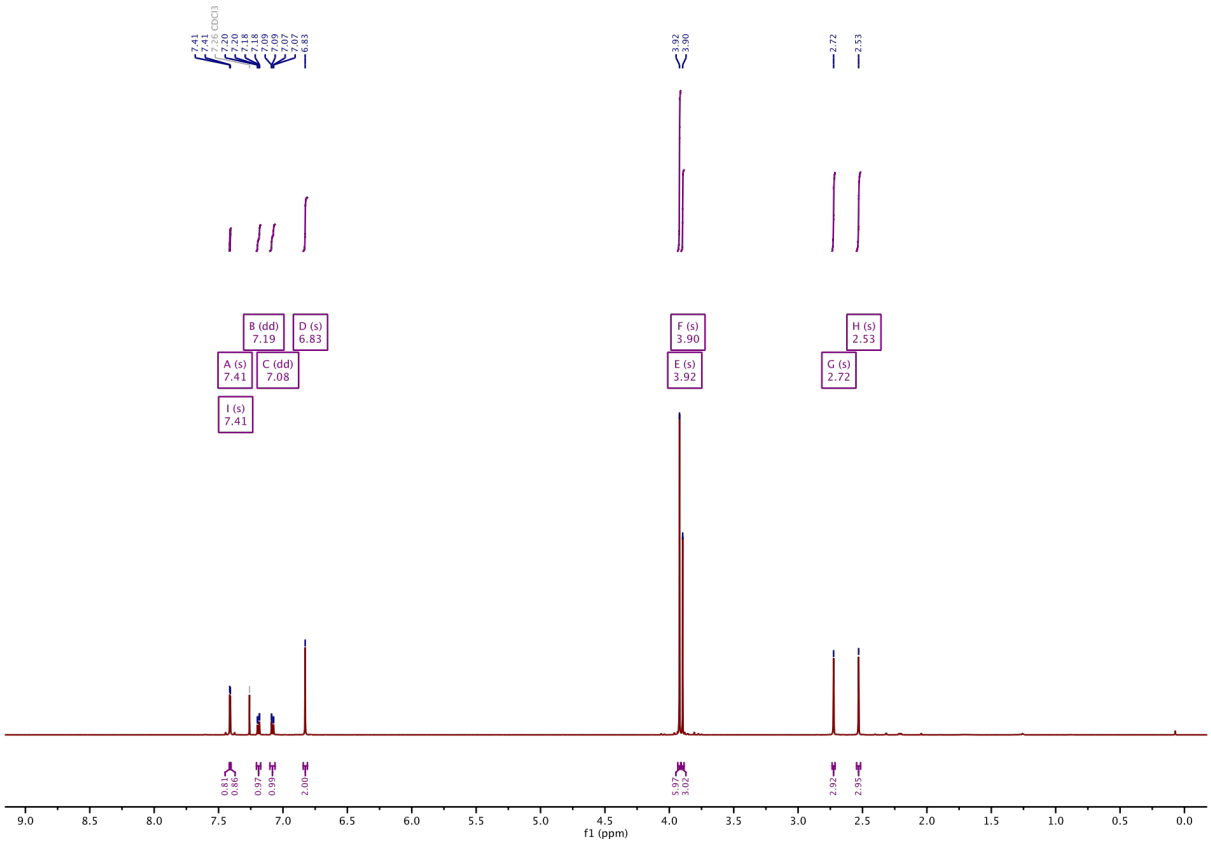

^{13}C-NMR of 18:

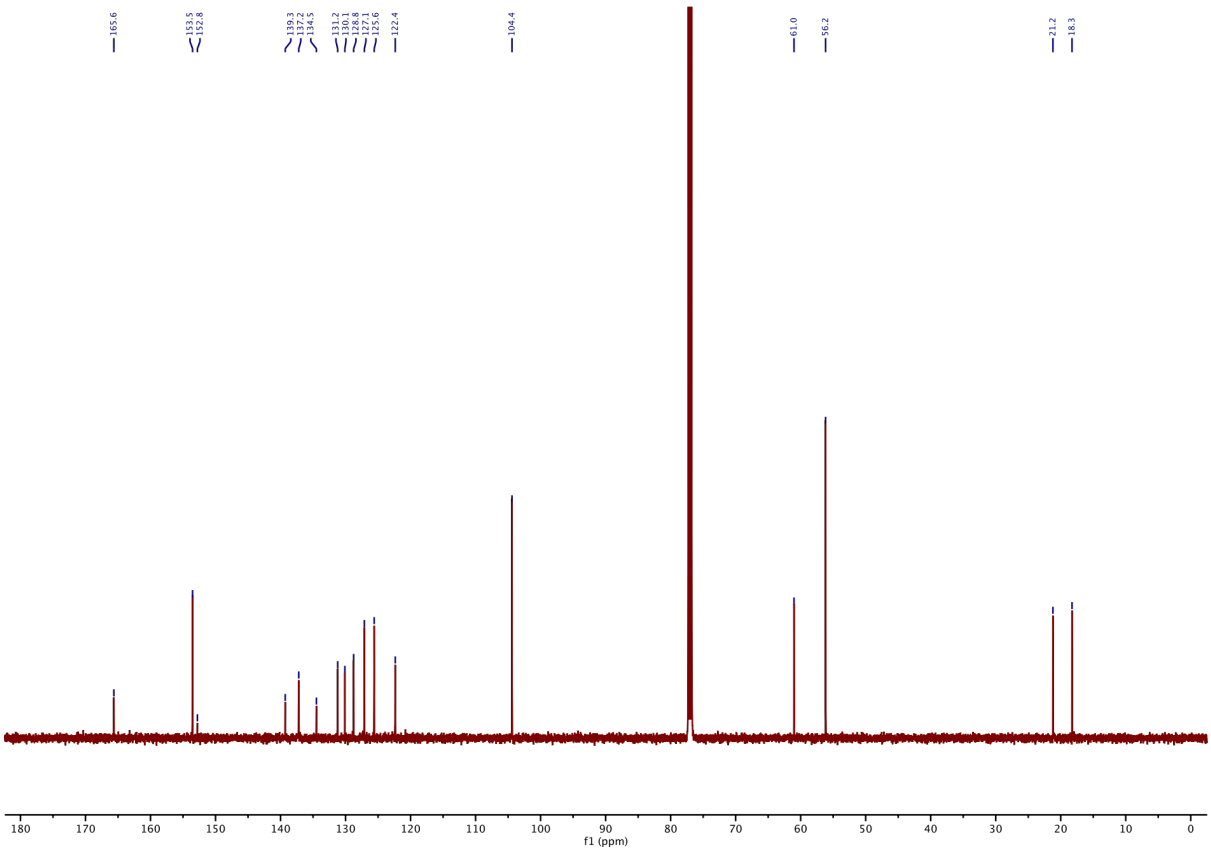

^{1}H-NMR of SBTub3P:

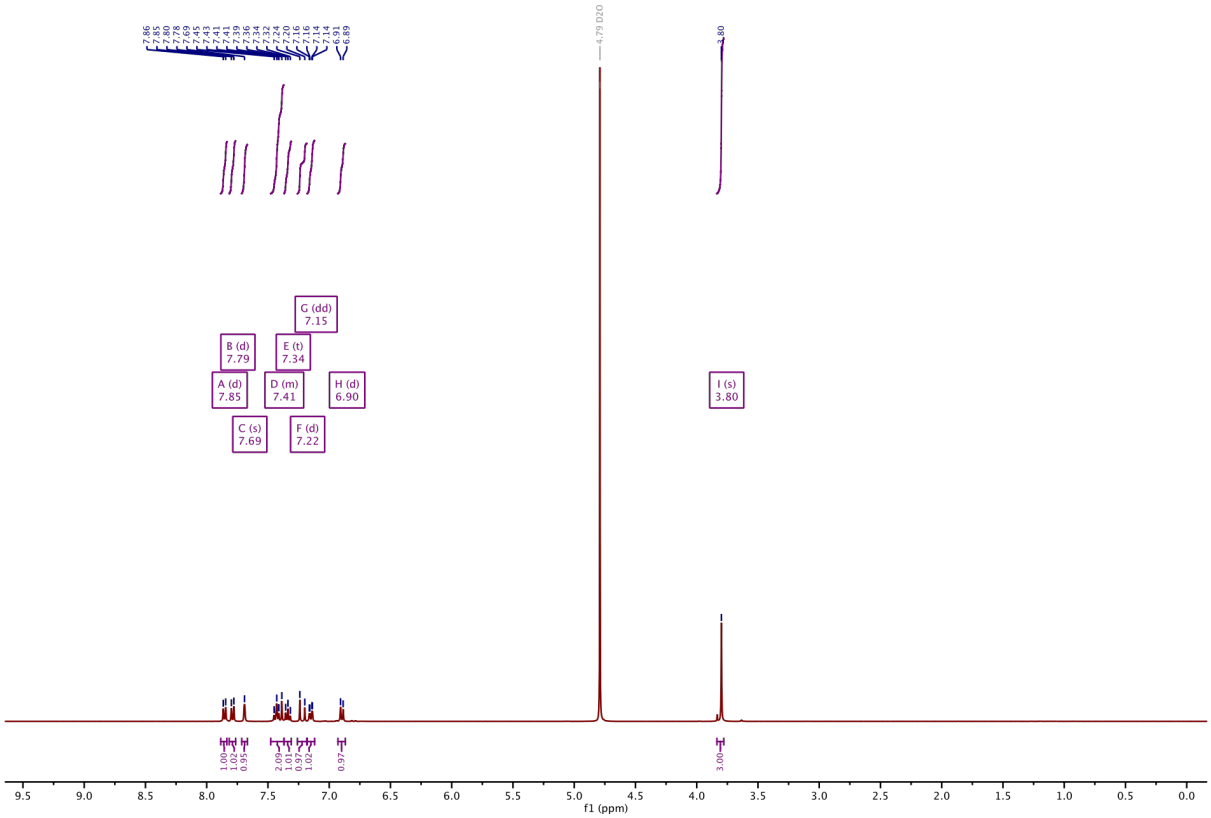

^{13}C-NMR of SBTub3P:

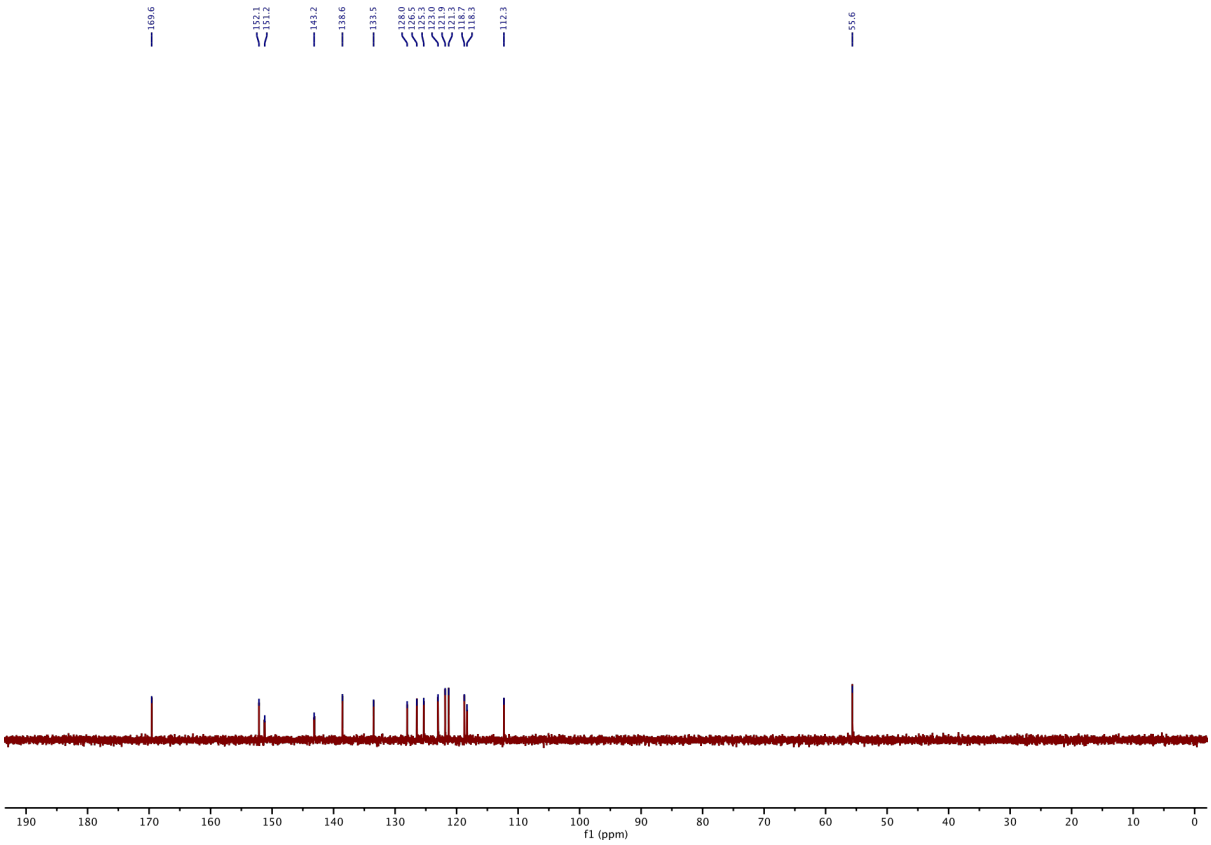

[1]H-NMR of Dibenzyl protected SBTubA4P:

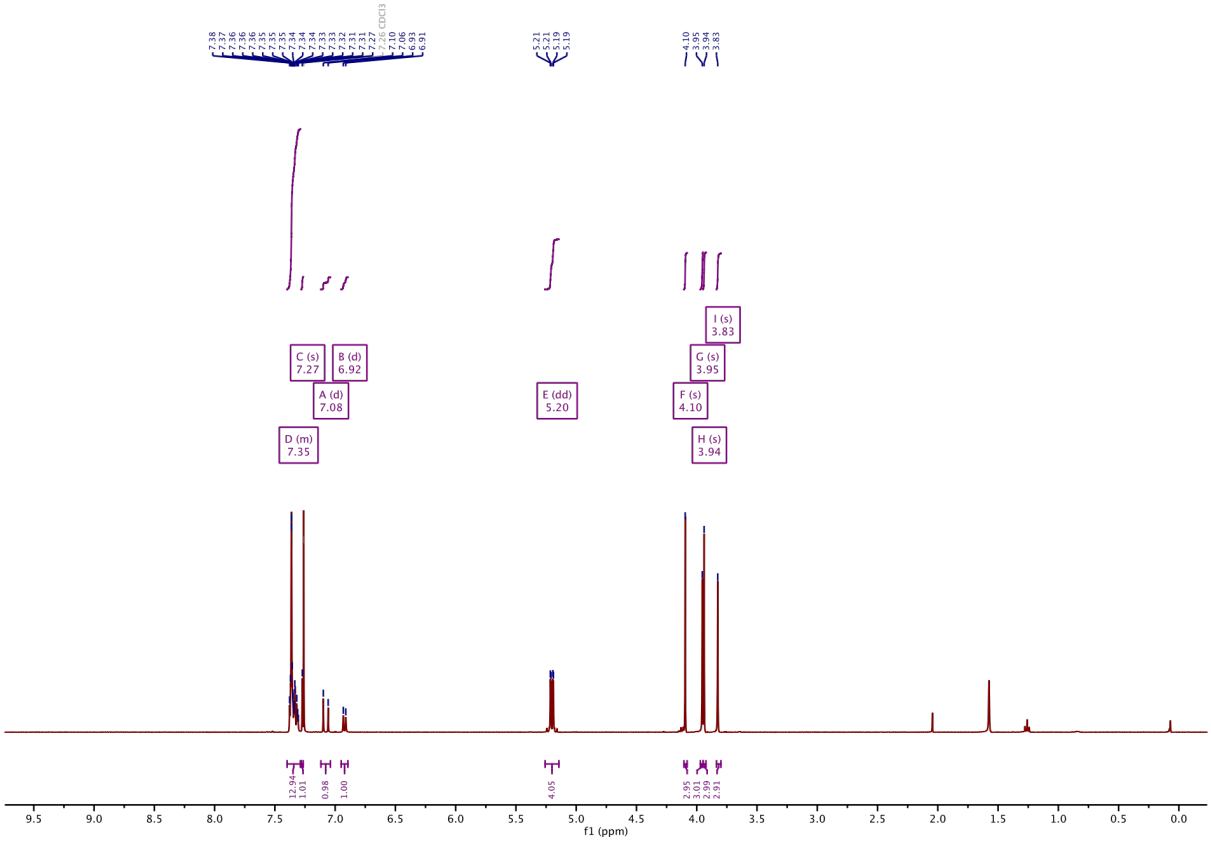

[13]C-NMR of Dibenzyl Protected SBTubA4P:

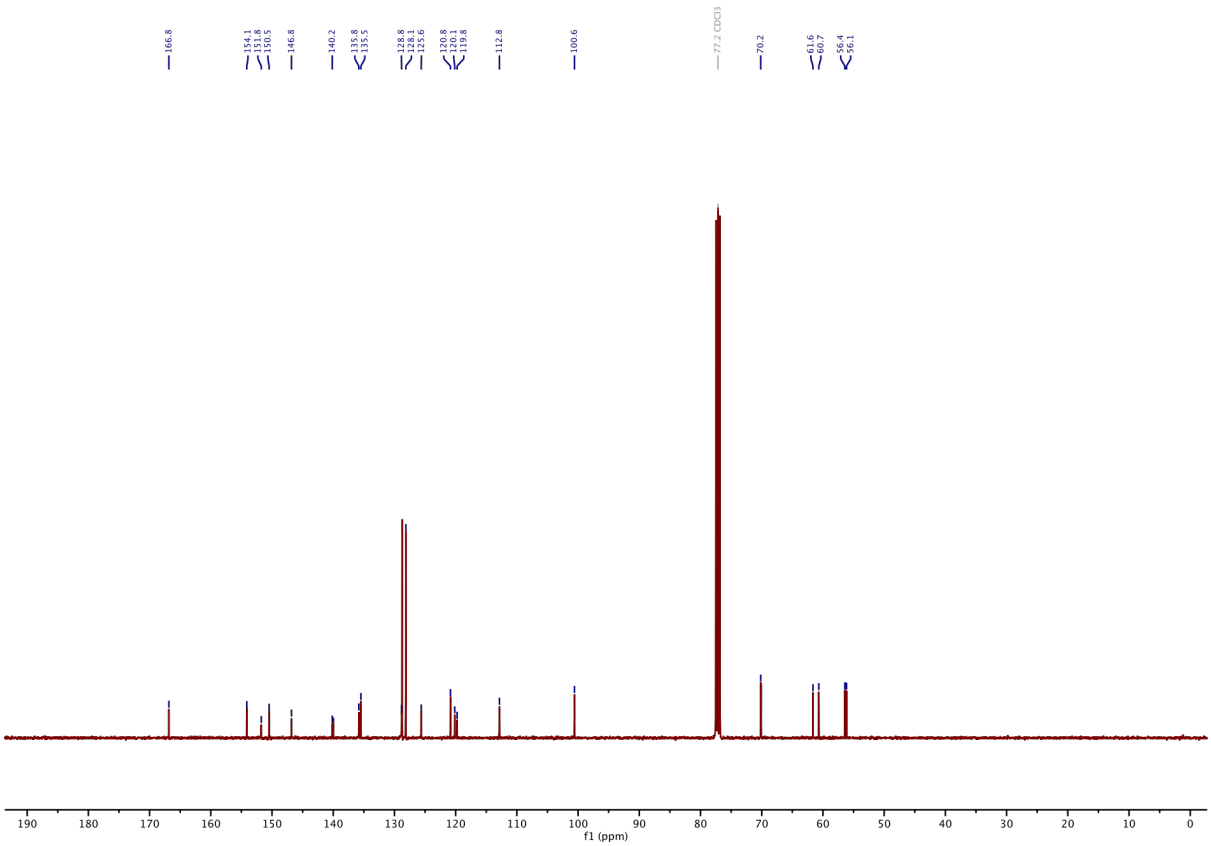

^{1}H-NMR of SBTubA4p:

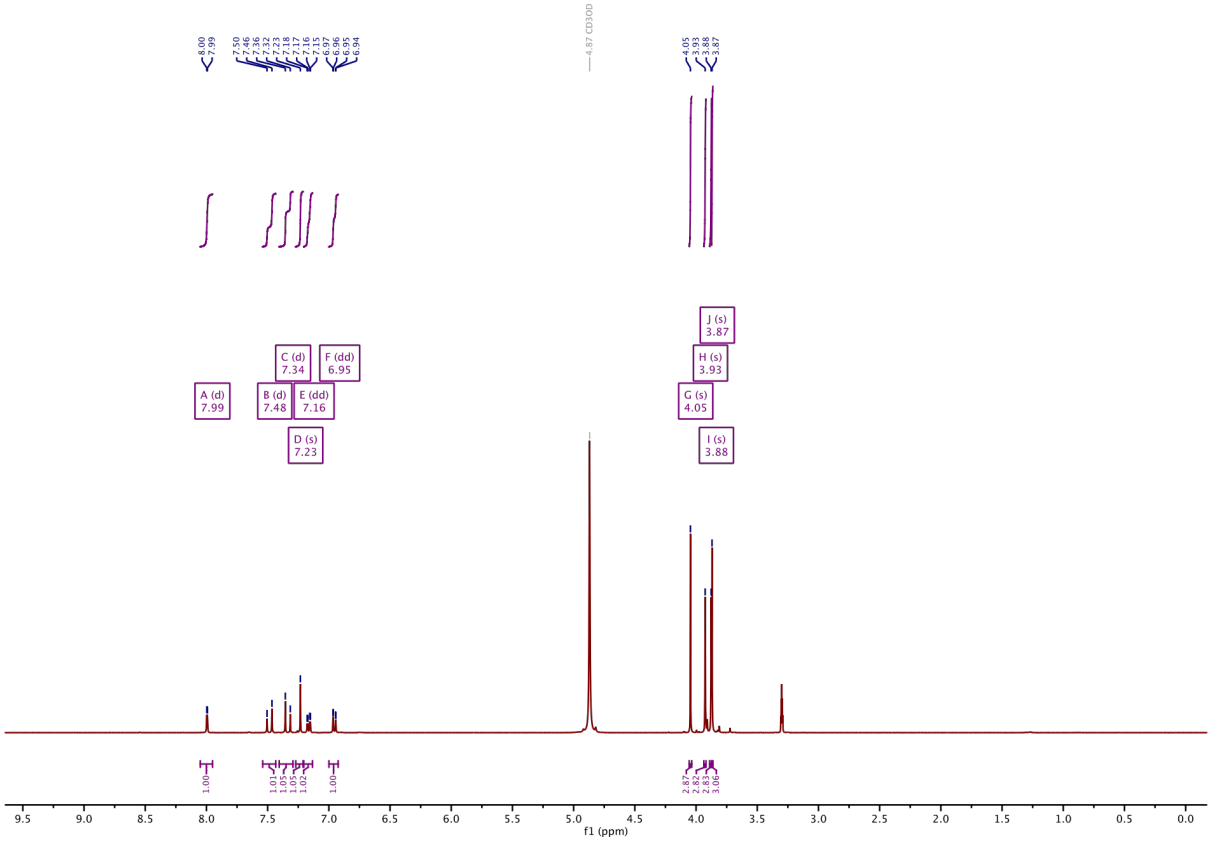

^{13}C-NMR of SBTubA4P:

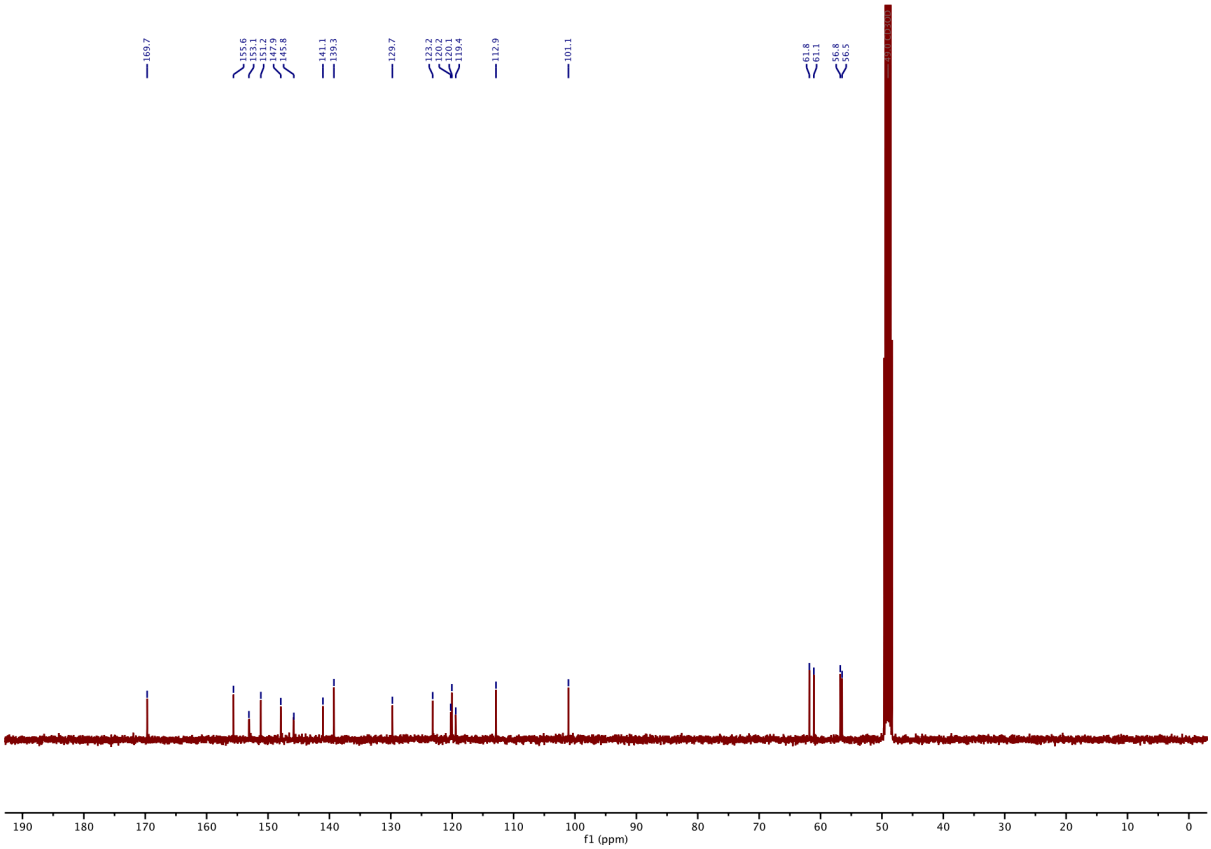

^{1}H-NMR of S1:

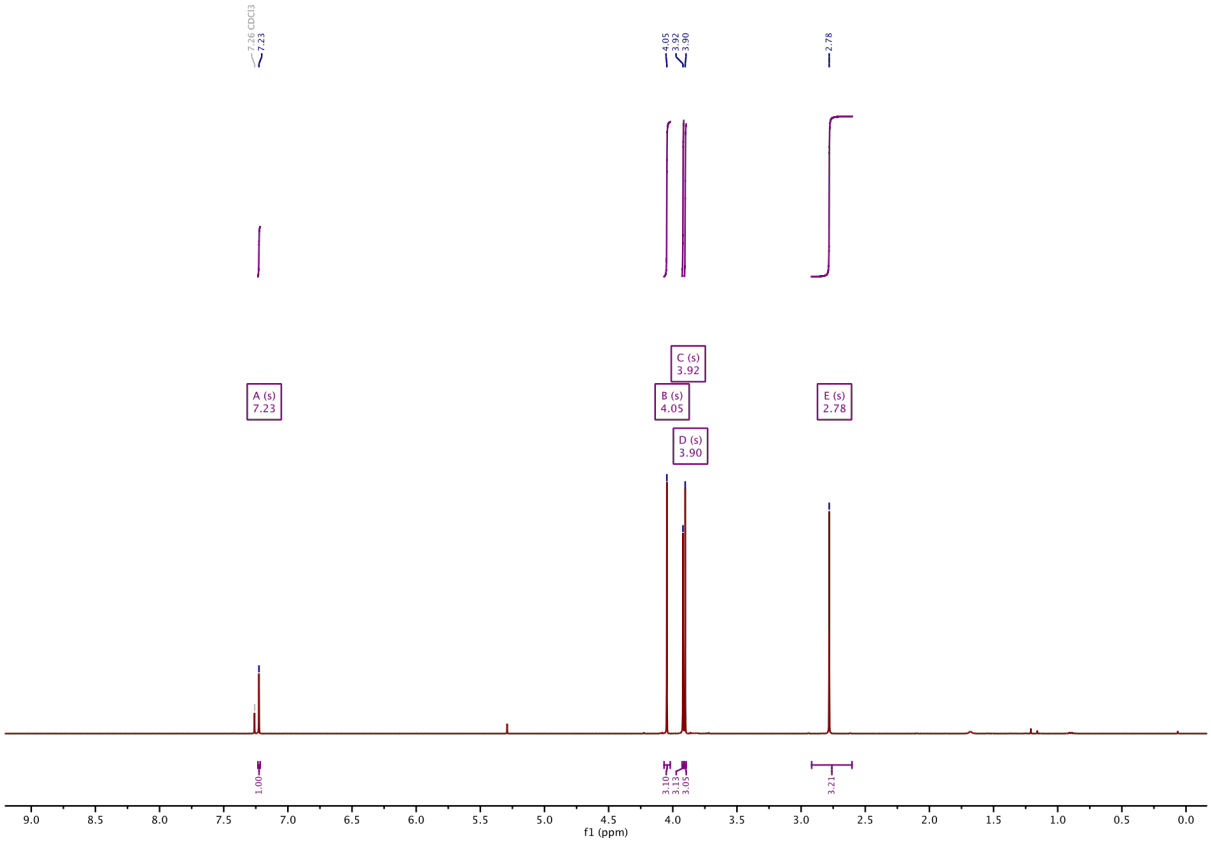

^{13}C-NMR of S1:

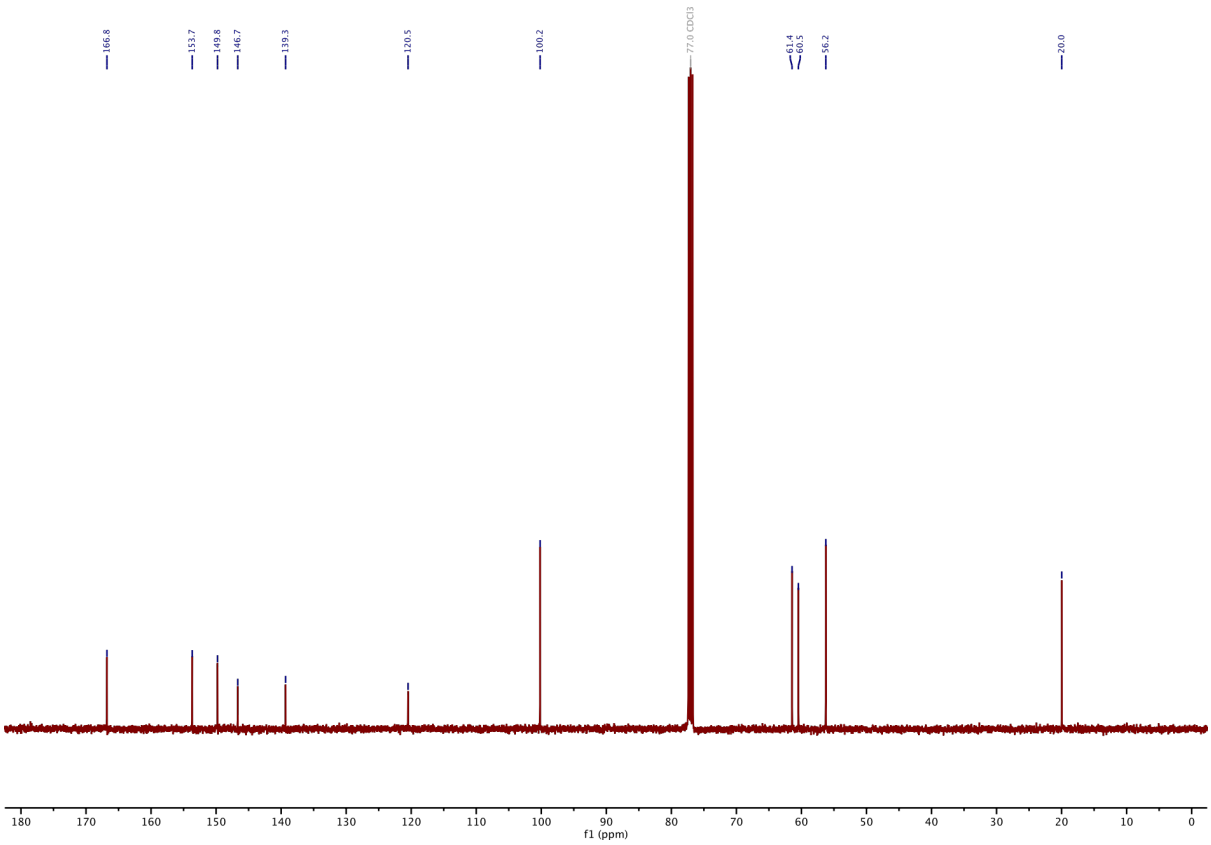

^{1}H-NMR of S2:

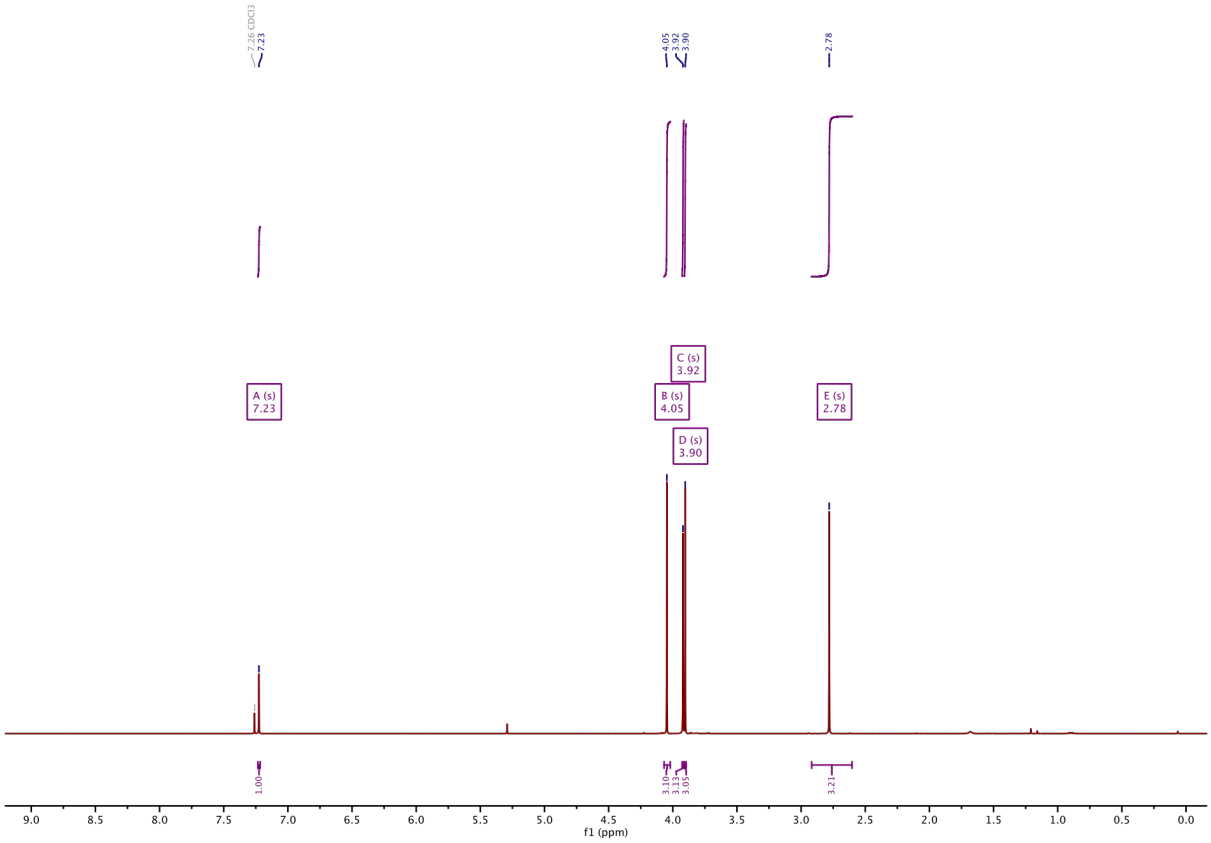

^{13}C-NMR of S2:

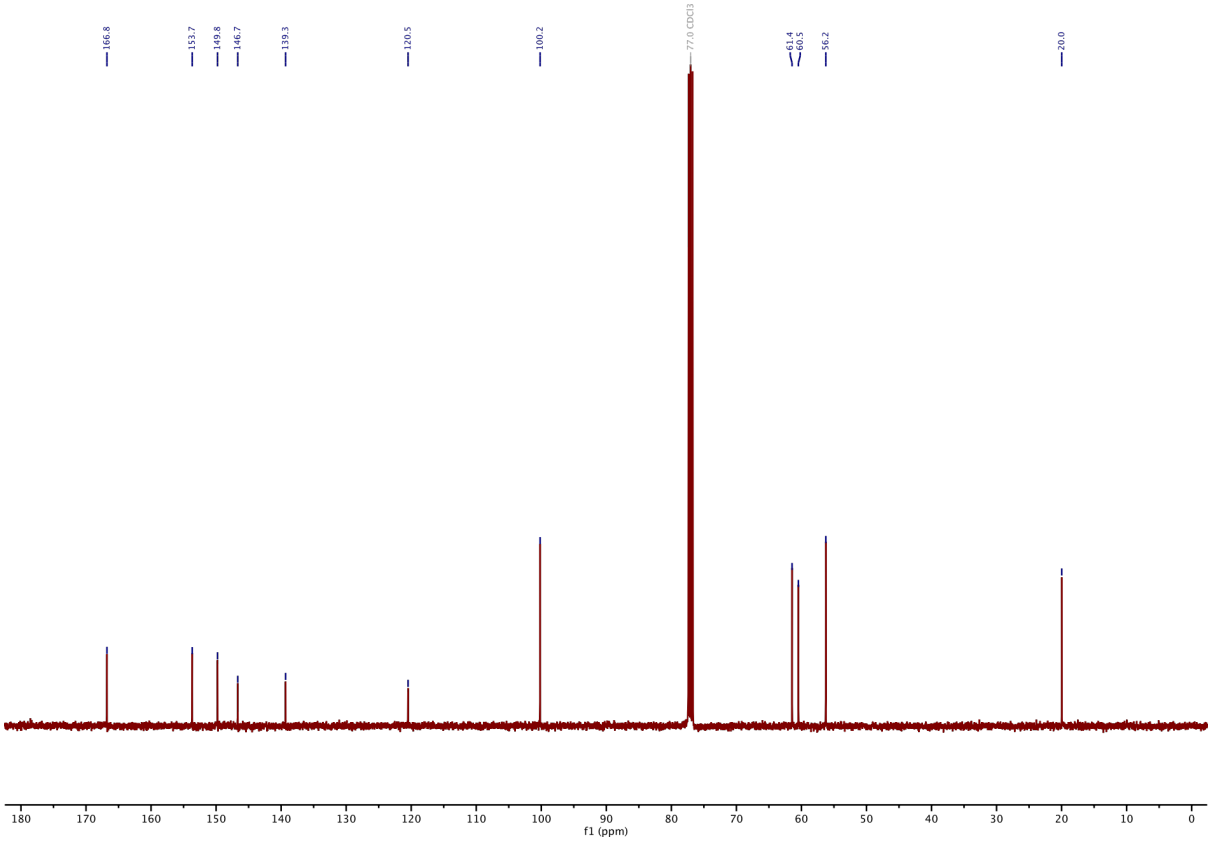

^{1}H-NMR of S3:

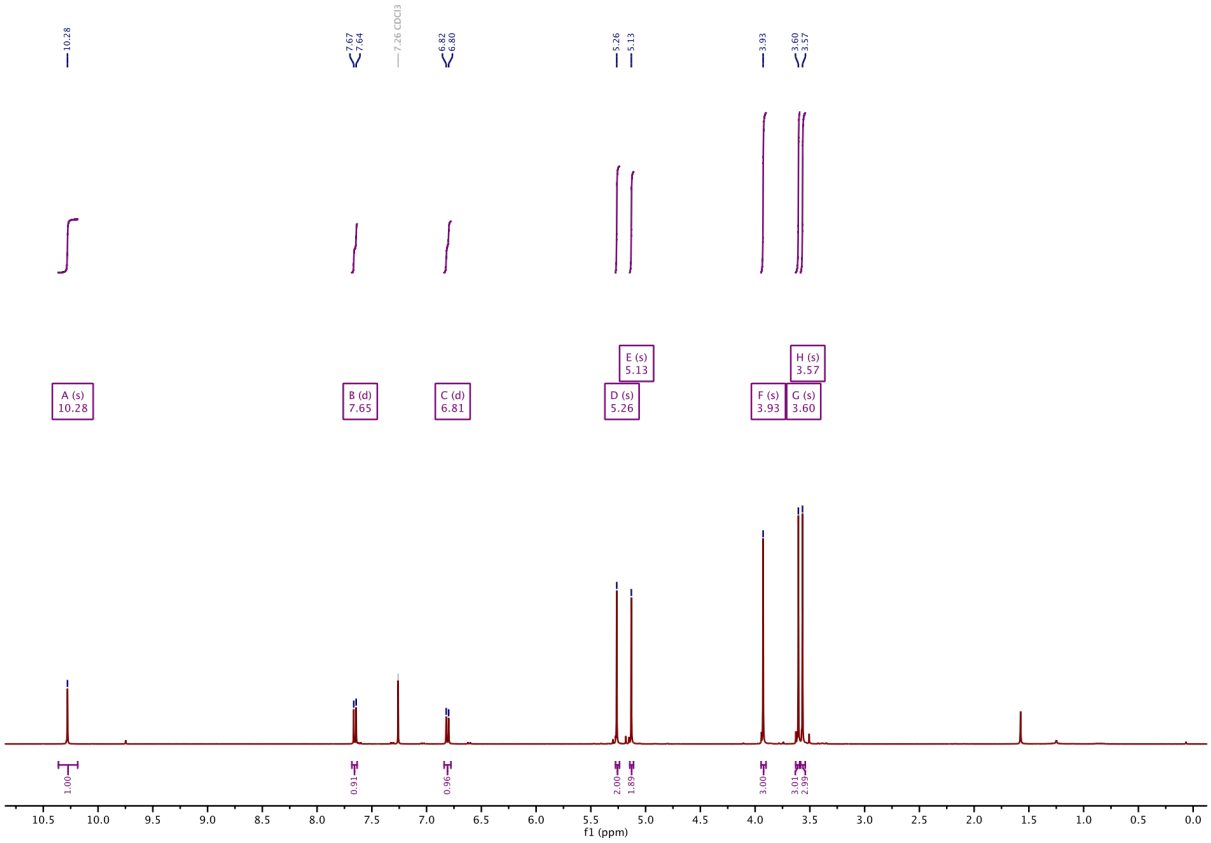

^{13}C-NMR of S3:

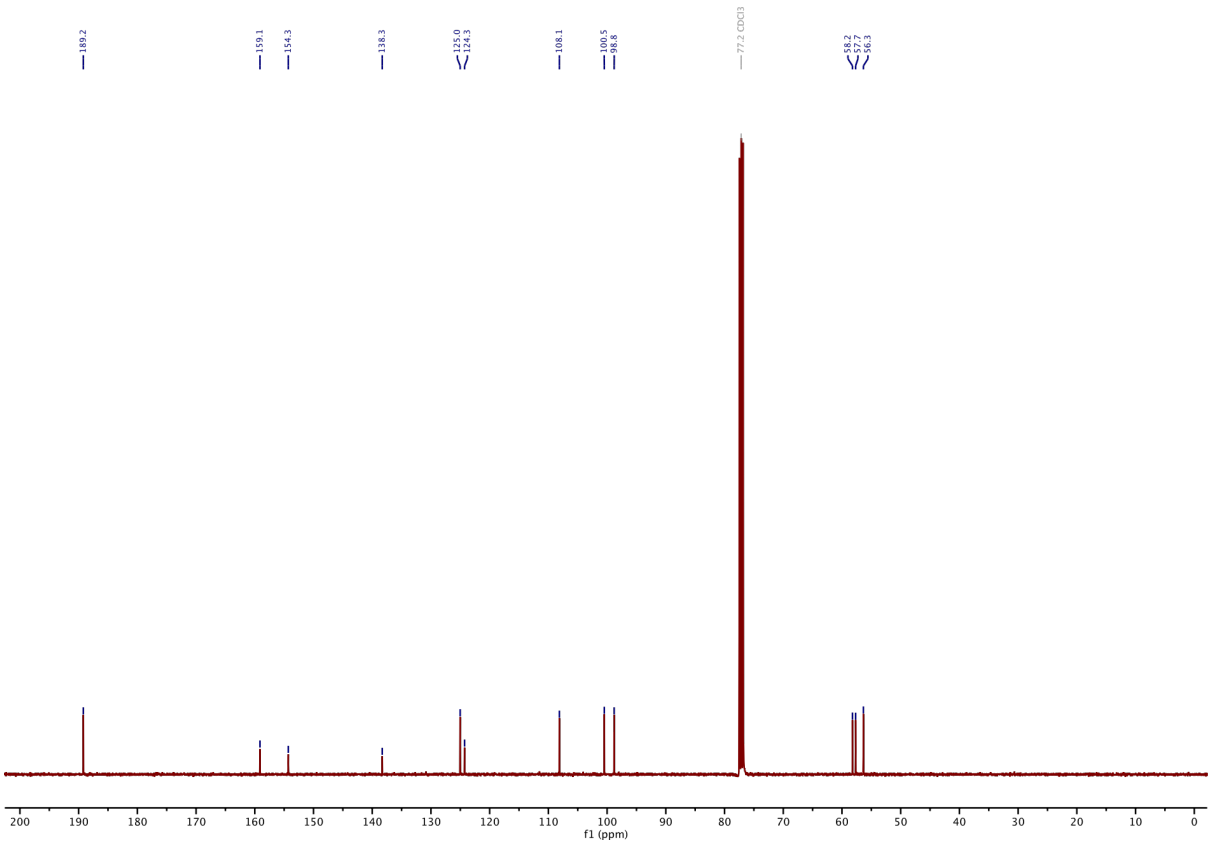

^{1}H-NMR of S4:

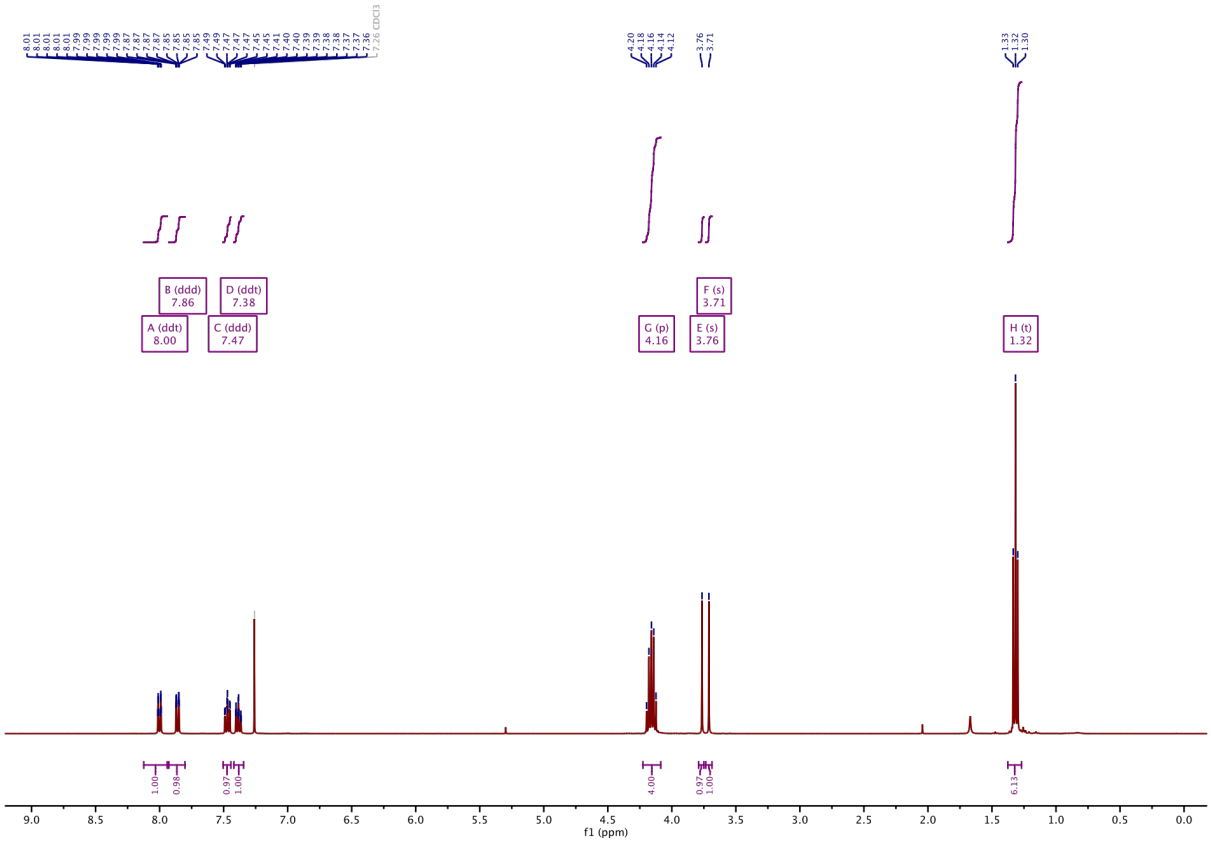

^{1}H-NMR of S5:

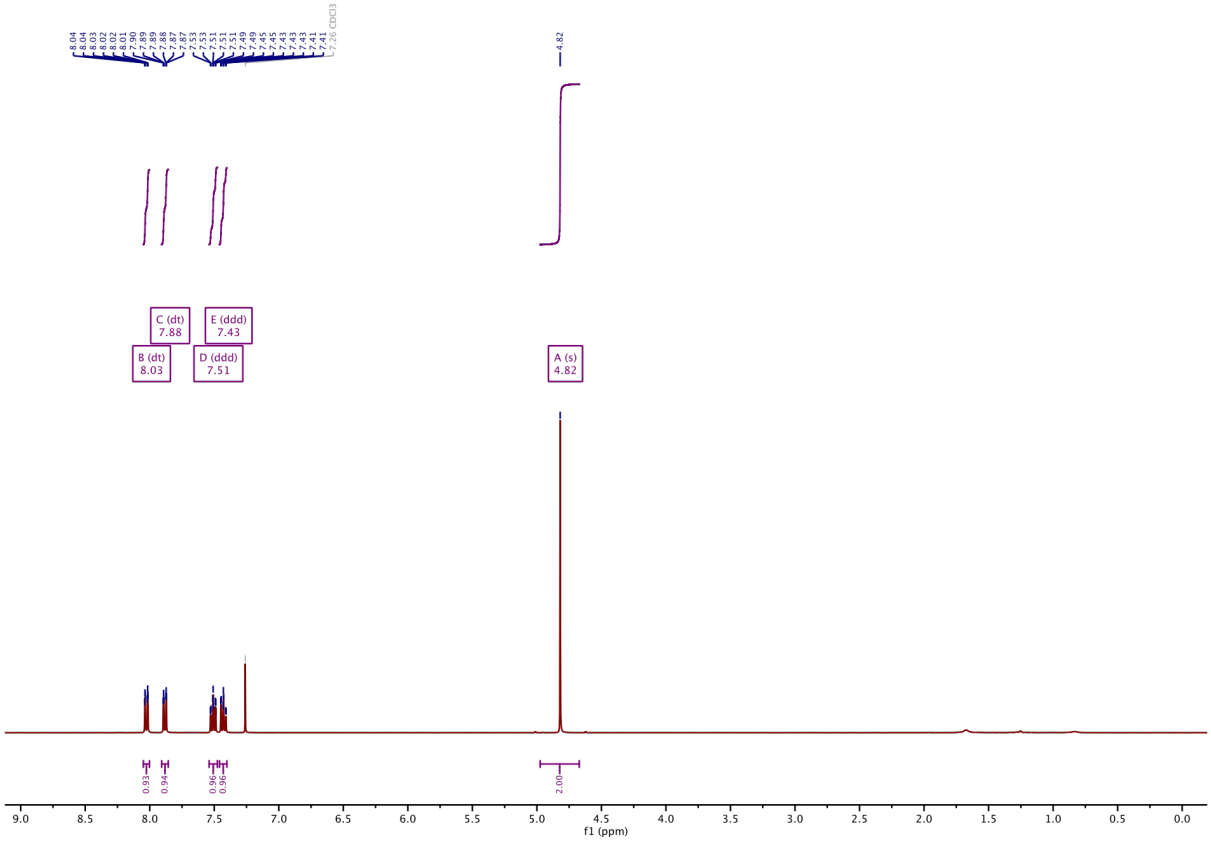

^{1}H-NMR of S6:

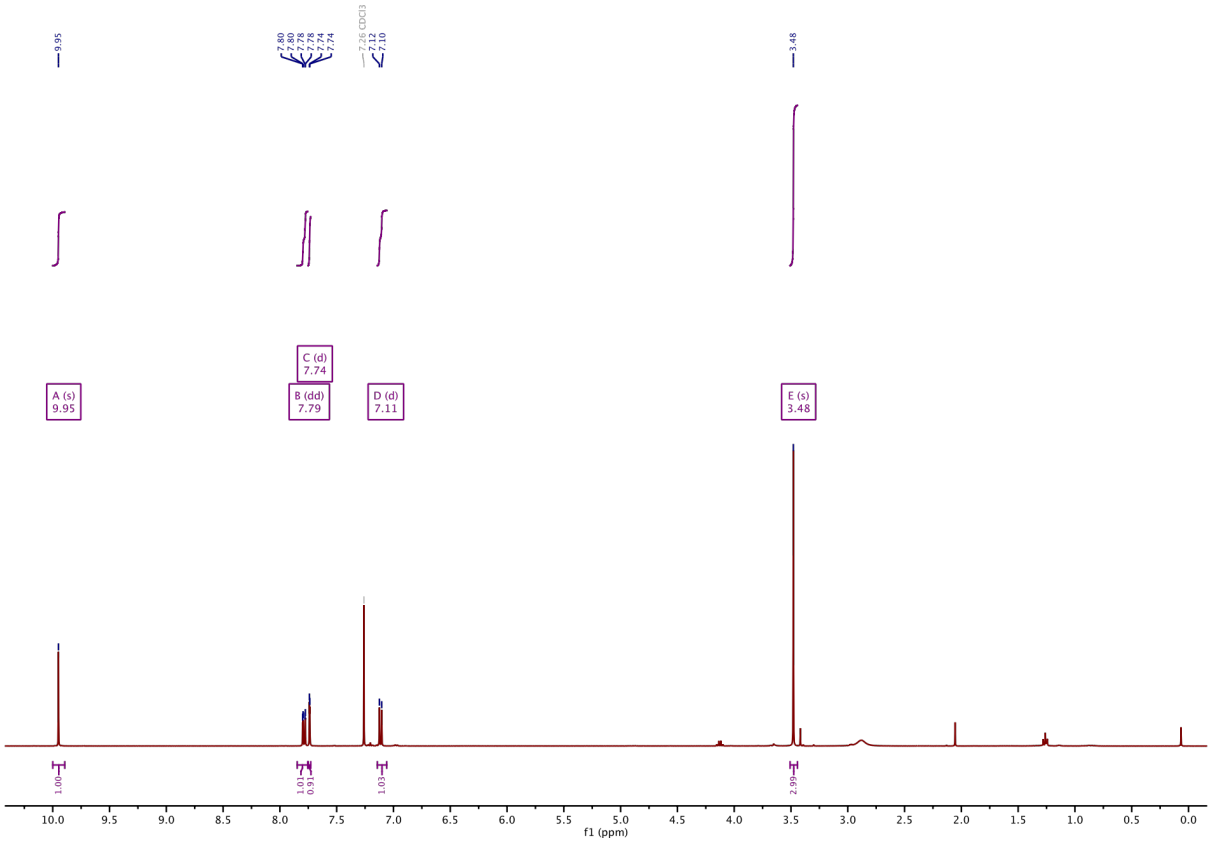

^{1}H-NMR of S7 GAO461:

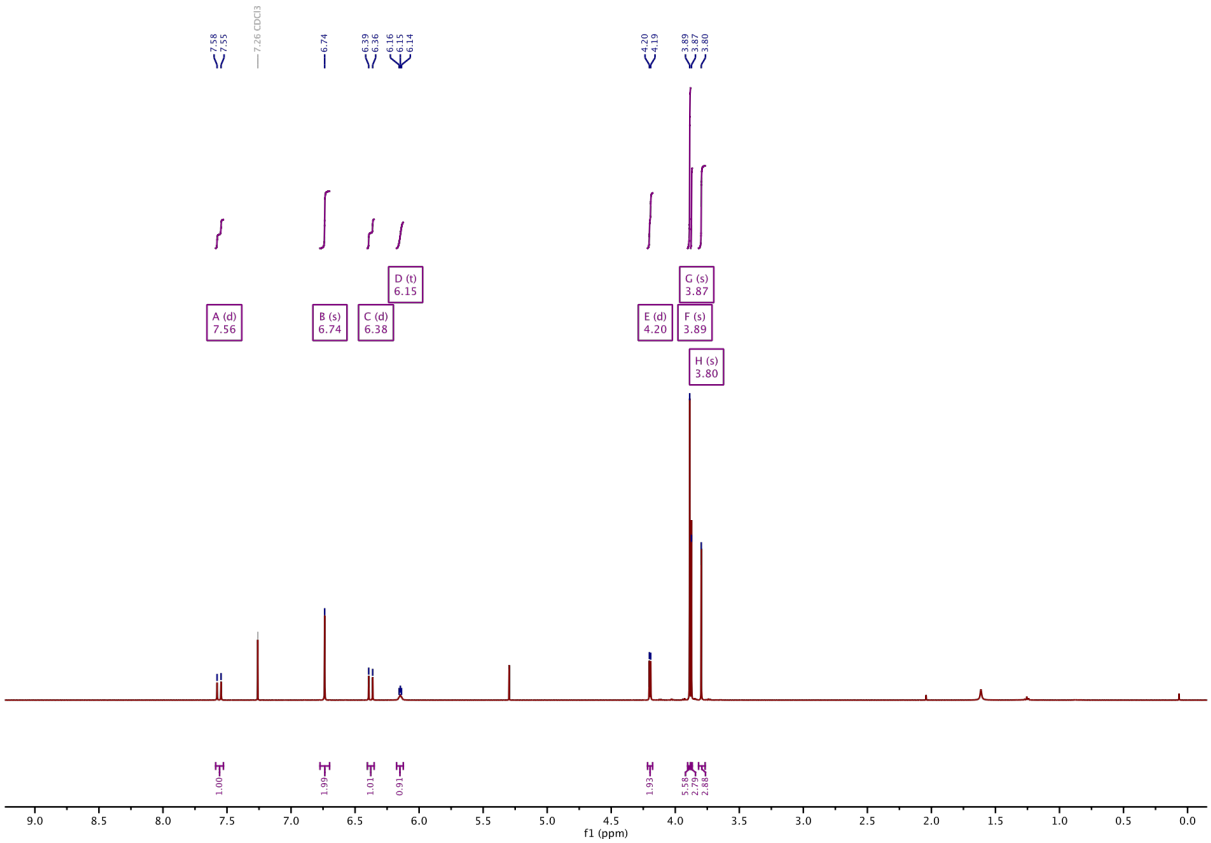

^{13}C-NMR of S7 GAO461:

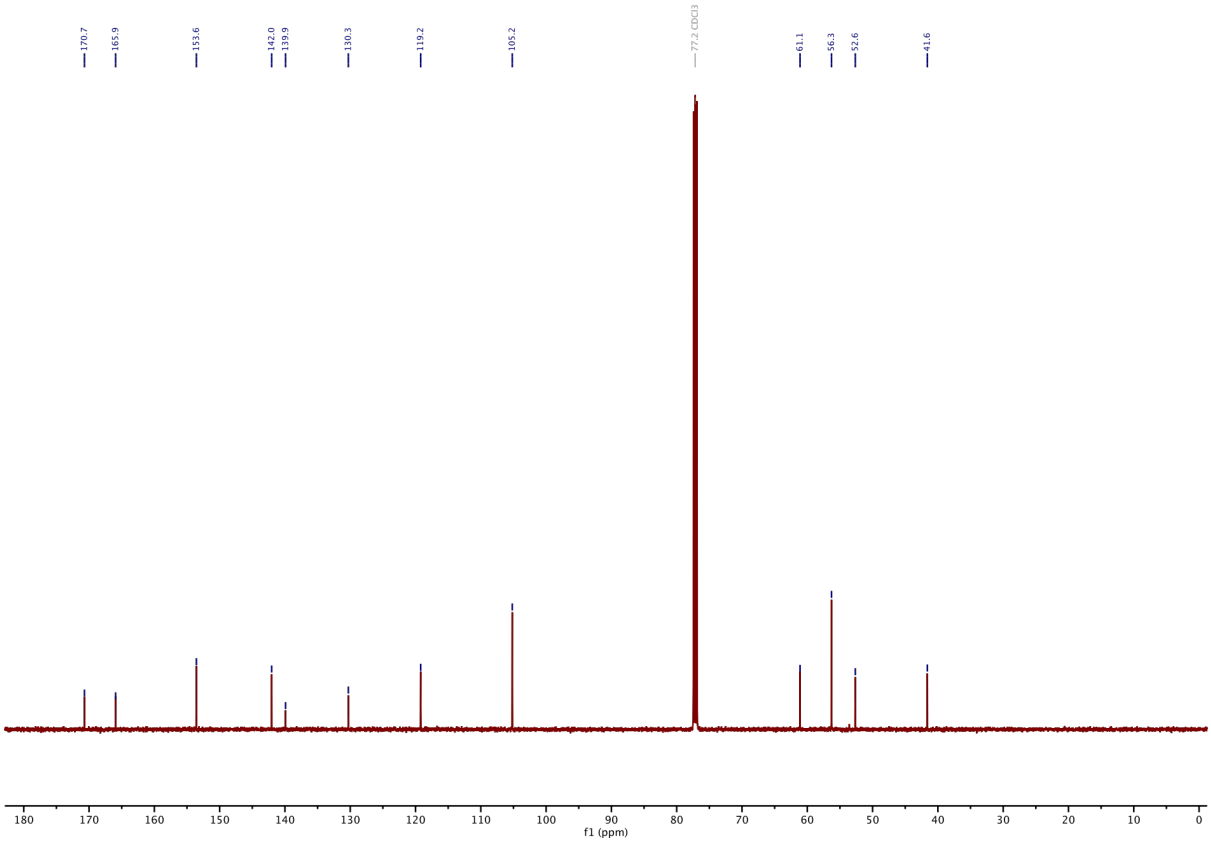

^{1}H-NMR of S8 GAO274:

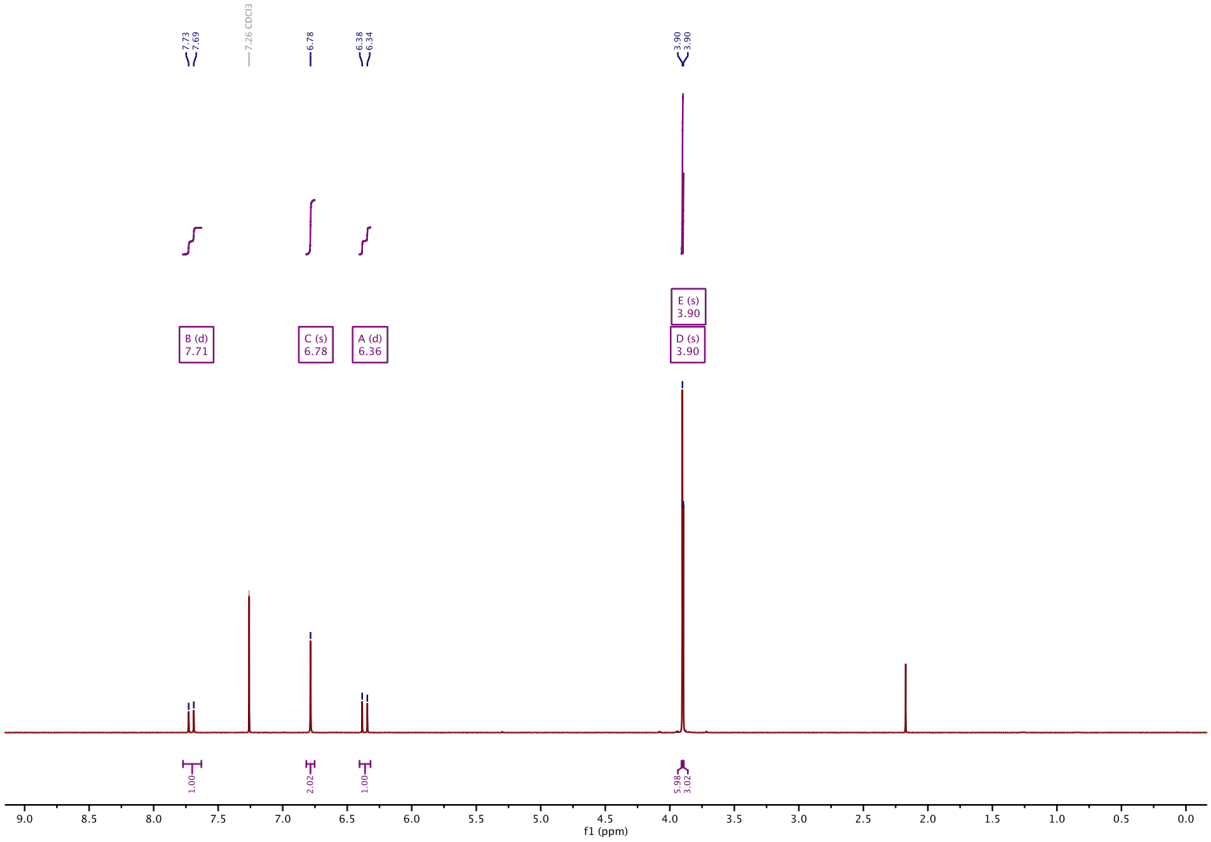

^{13}C-NMR of S8 GAO274:

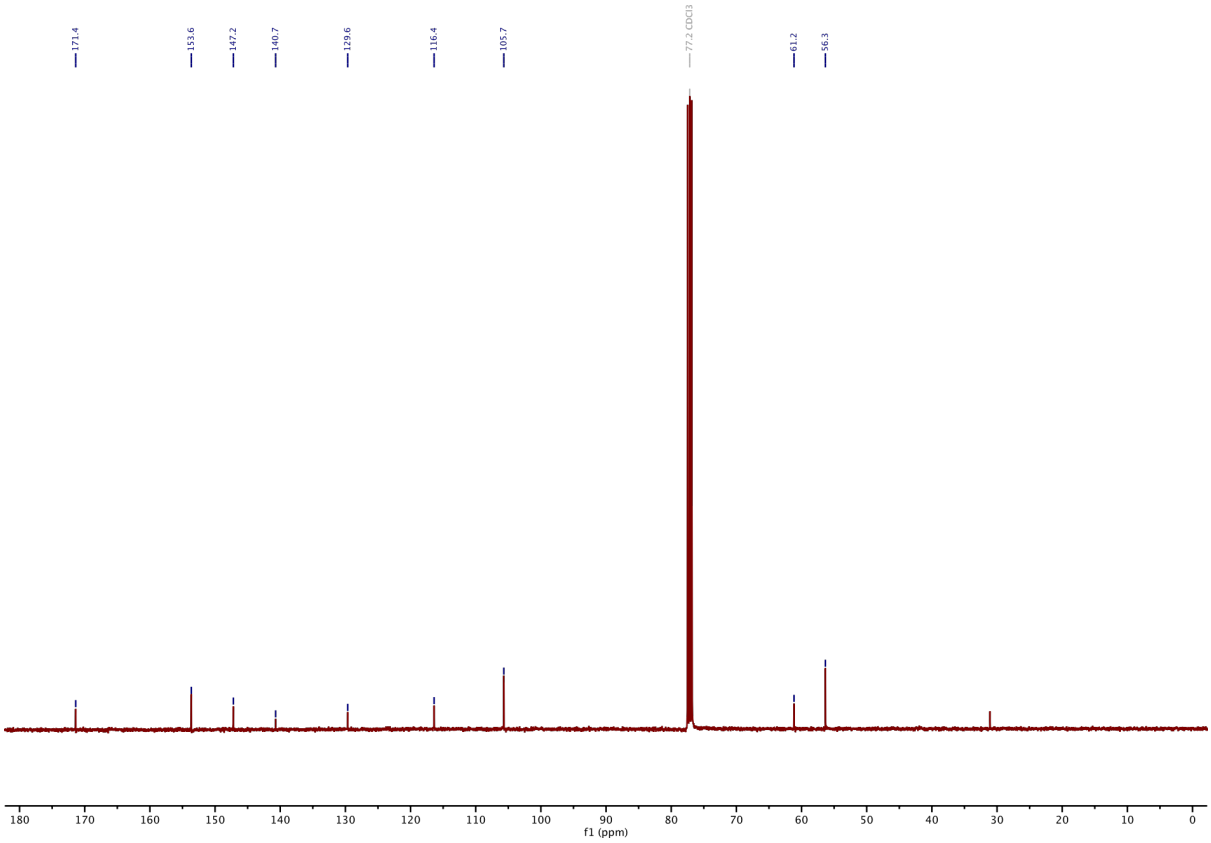

^{1}H-NMR of S9 GAO552:

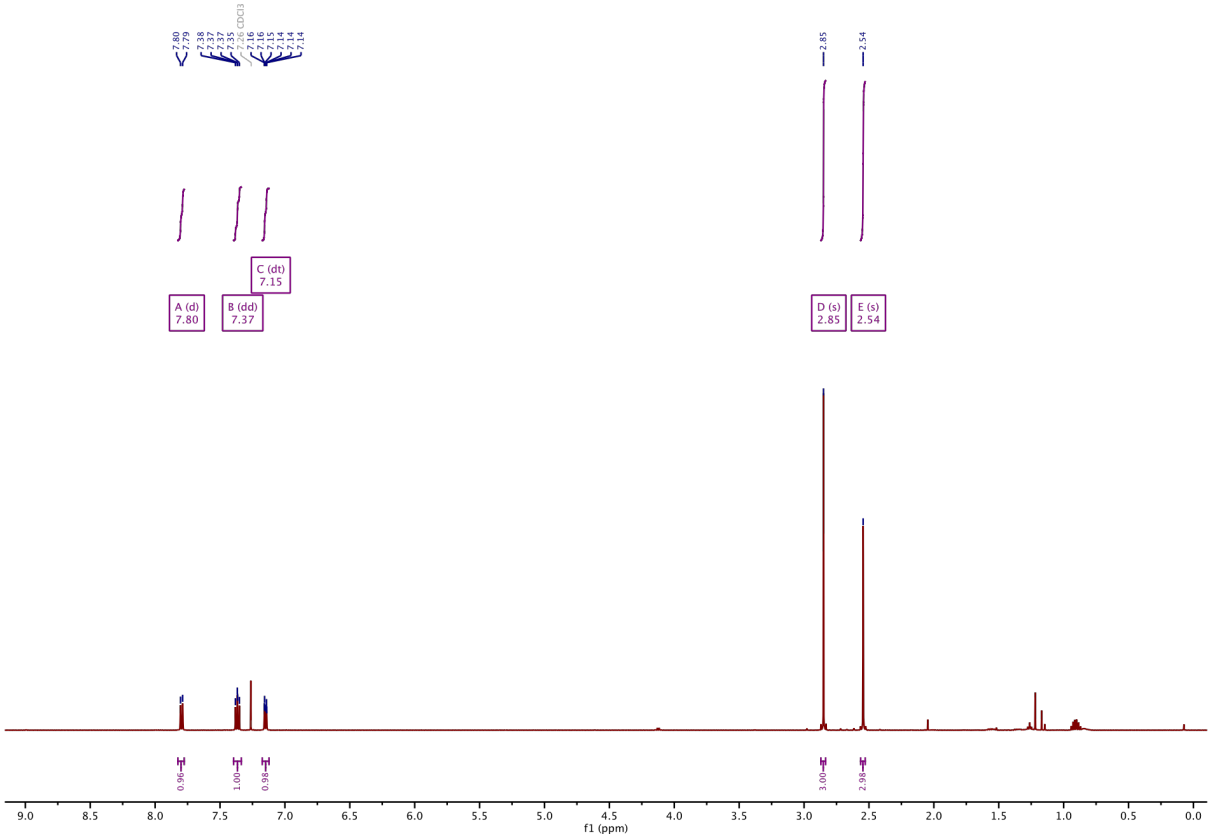

^{13}C-NMR of S9 GAO552:

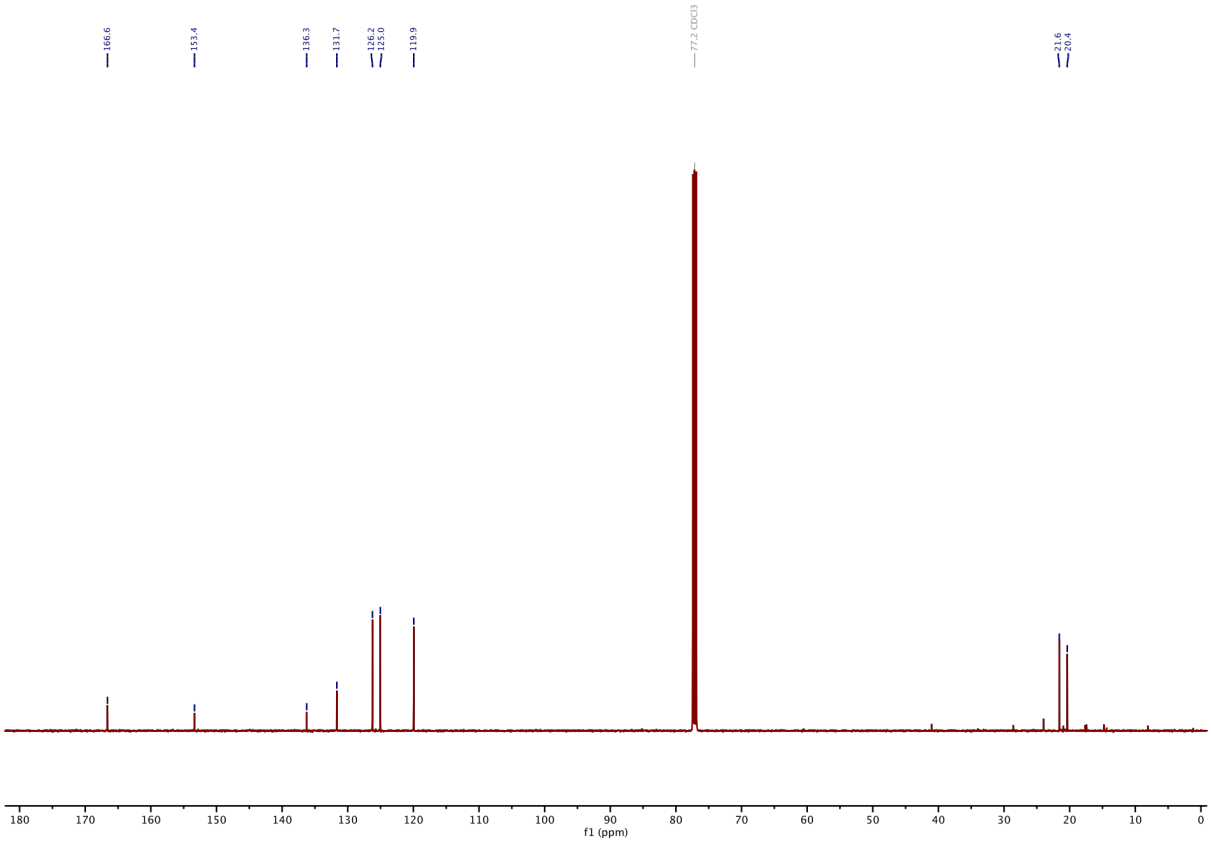

^{1}H-NMR of S10 GAO491:

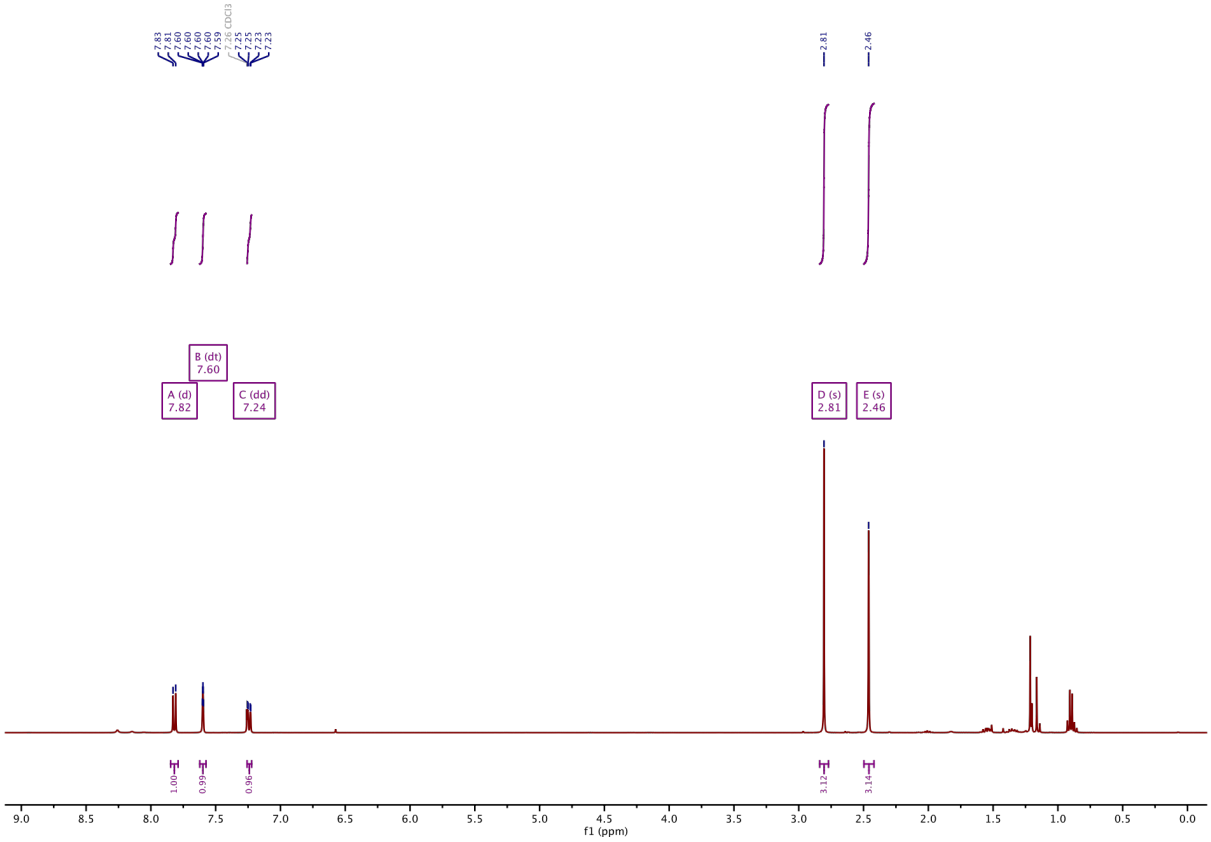

^{1}H-NMR of S11 GAO553:

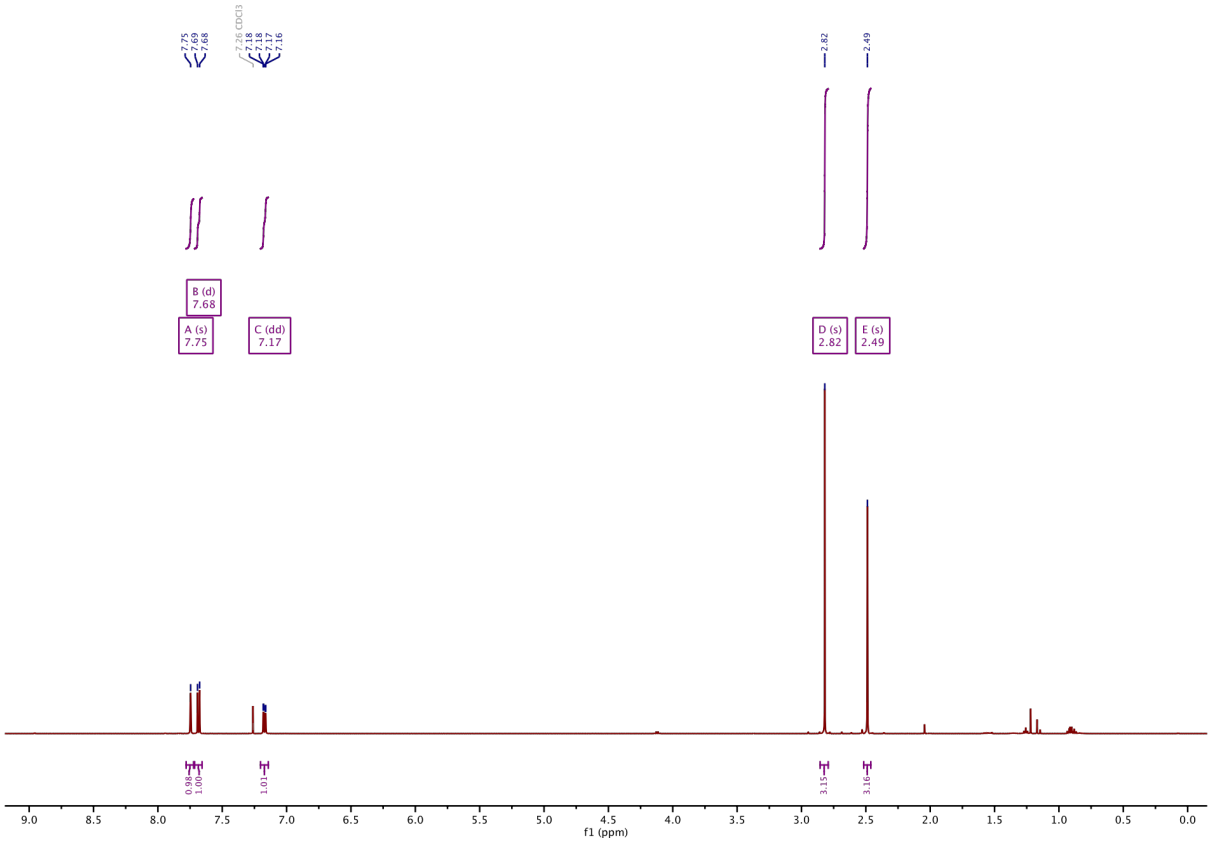

^{13}C-NMR of S11 GAO553:

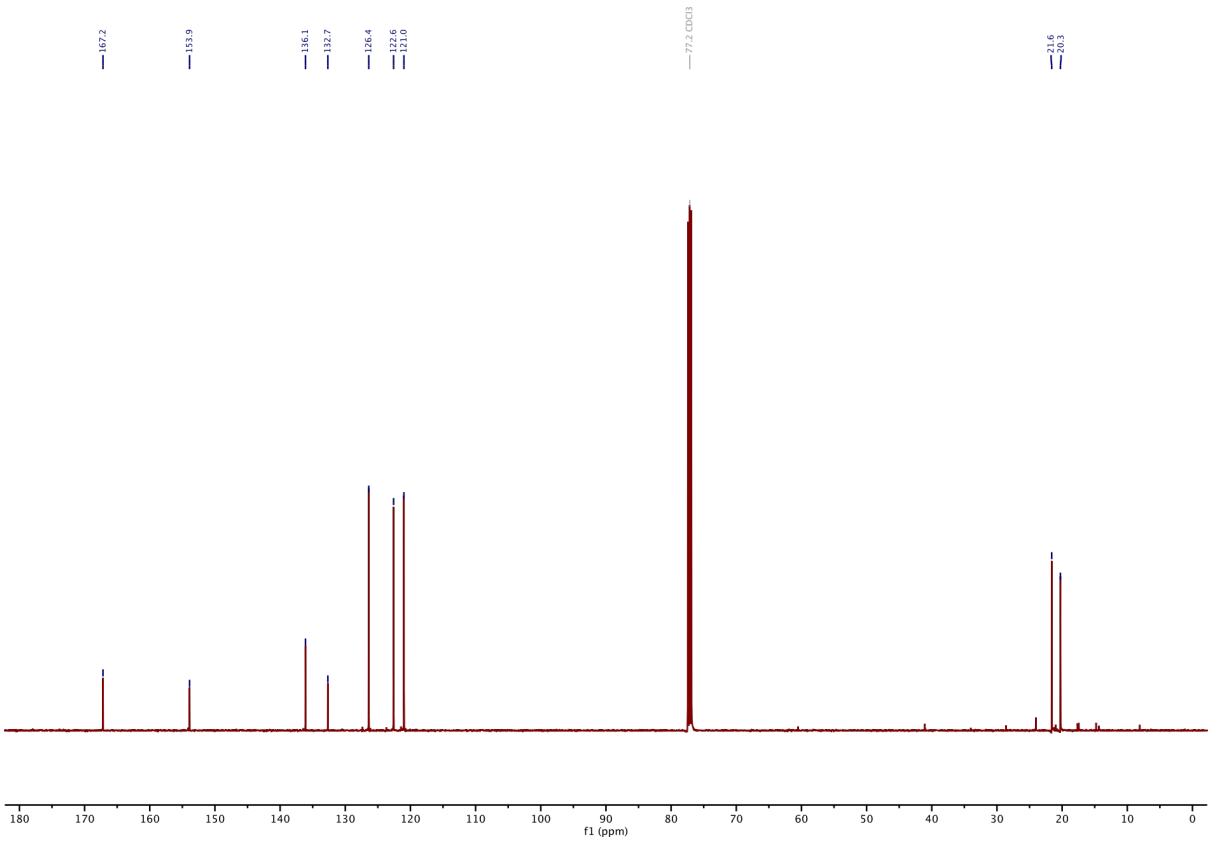

^{1}H-NMR of S12 GAO437:

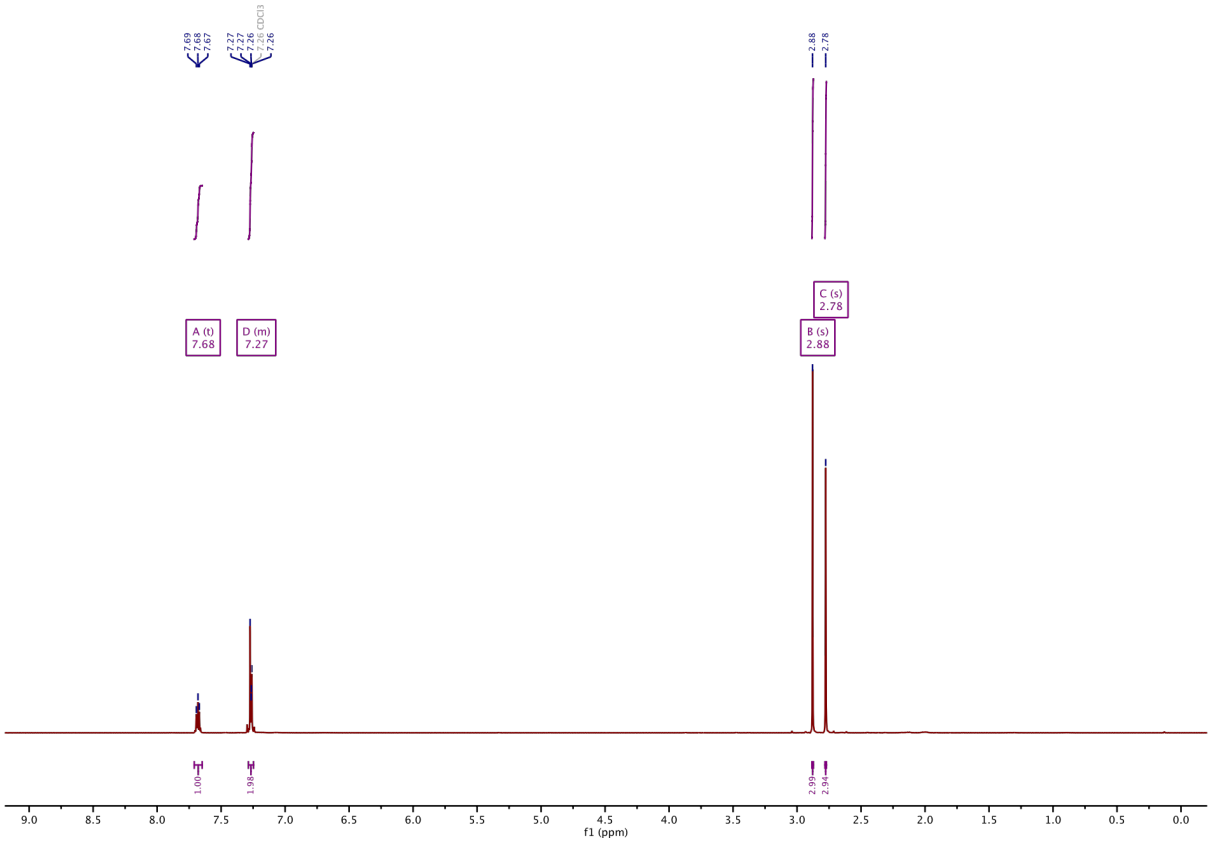

^{13}C-NMR of S12 GAO437:

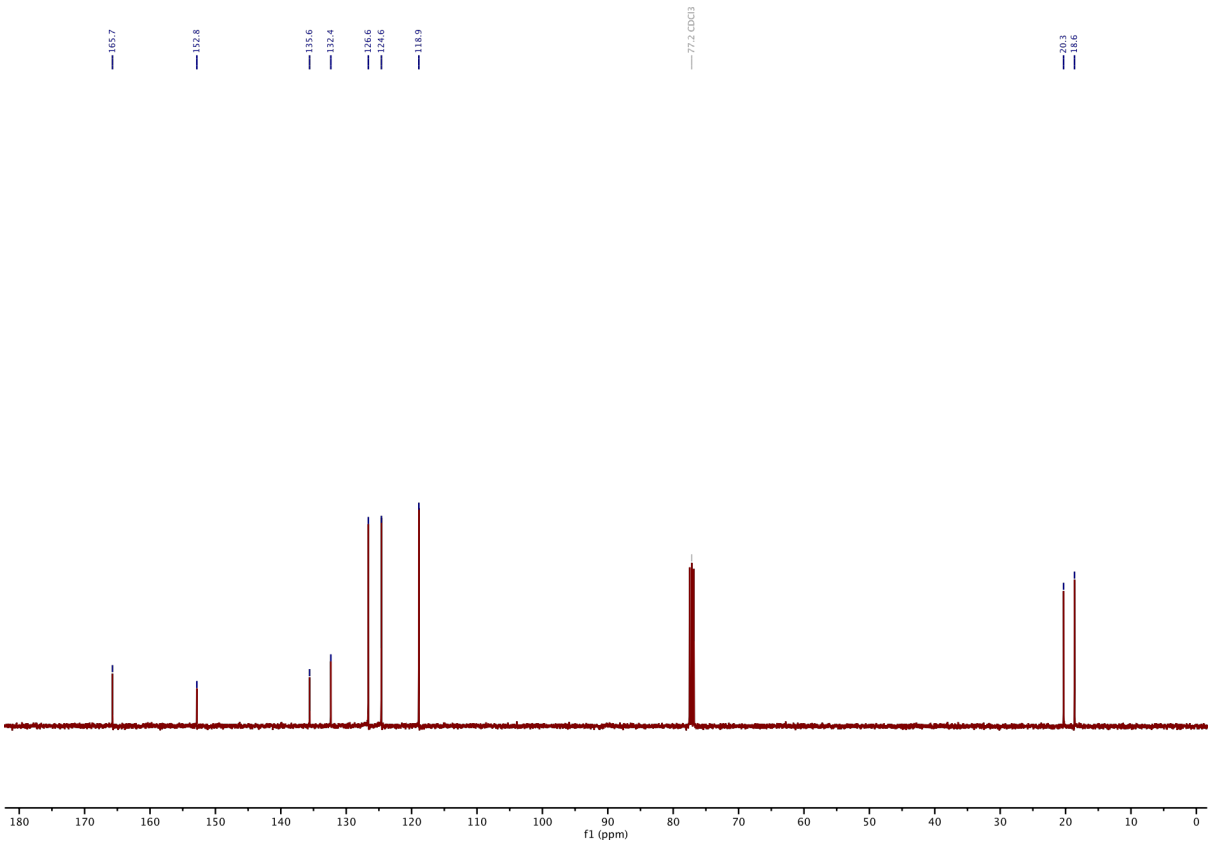

^{1}H-NMR of S13 GAO490:

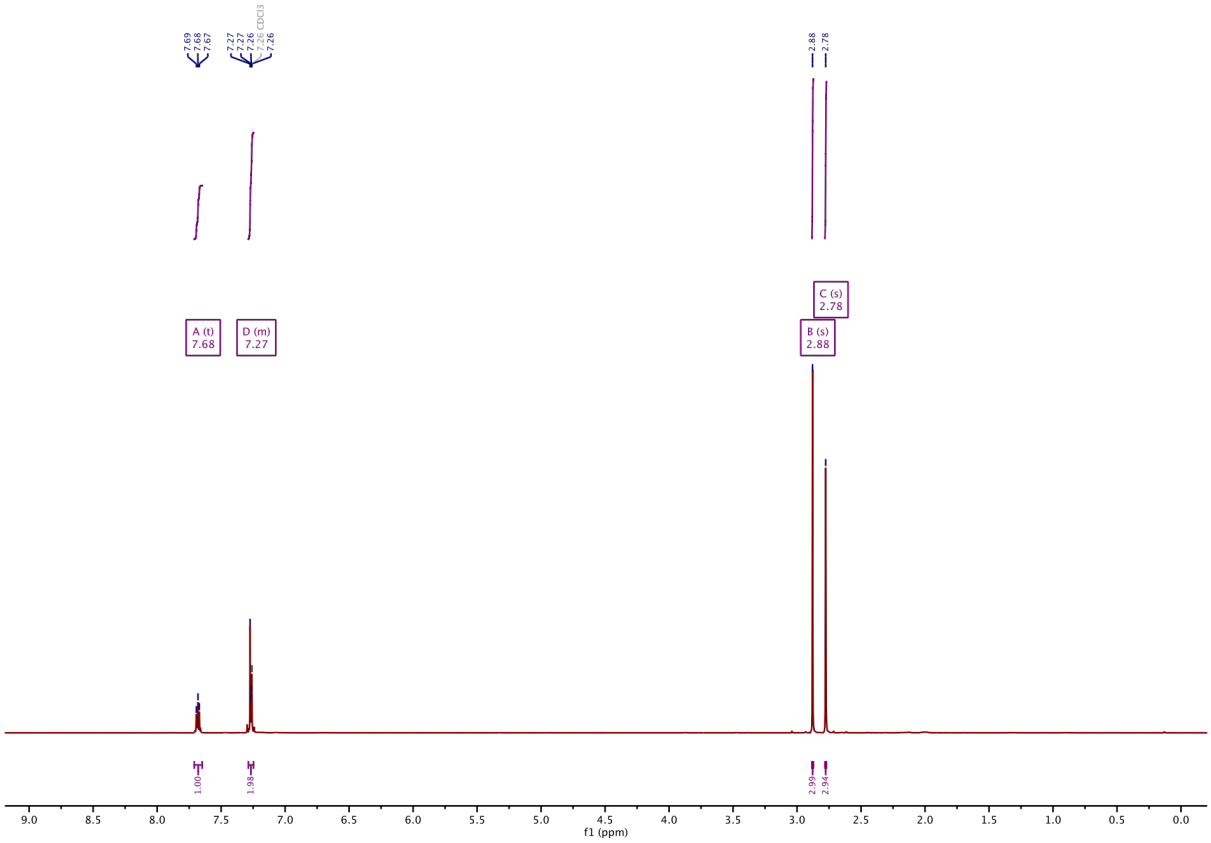

^{13}C-NMR of S13 GAO490:

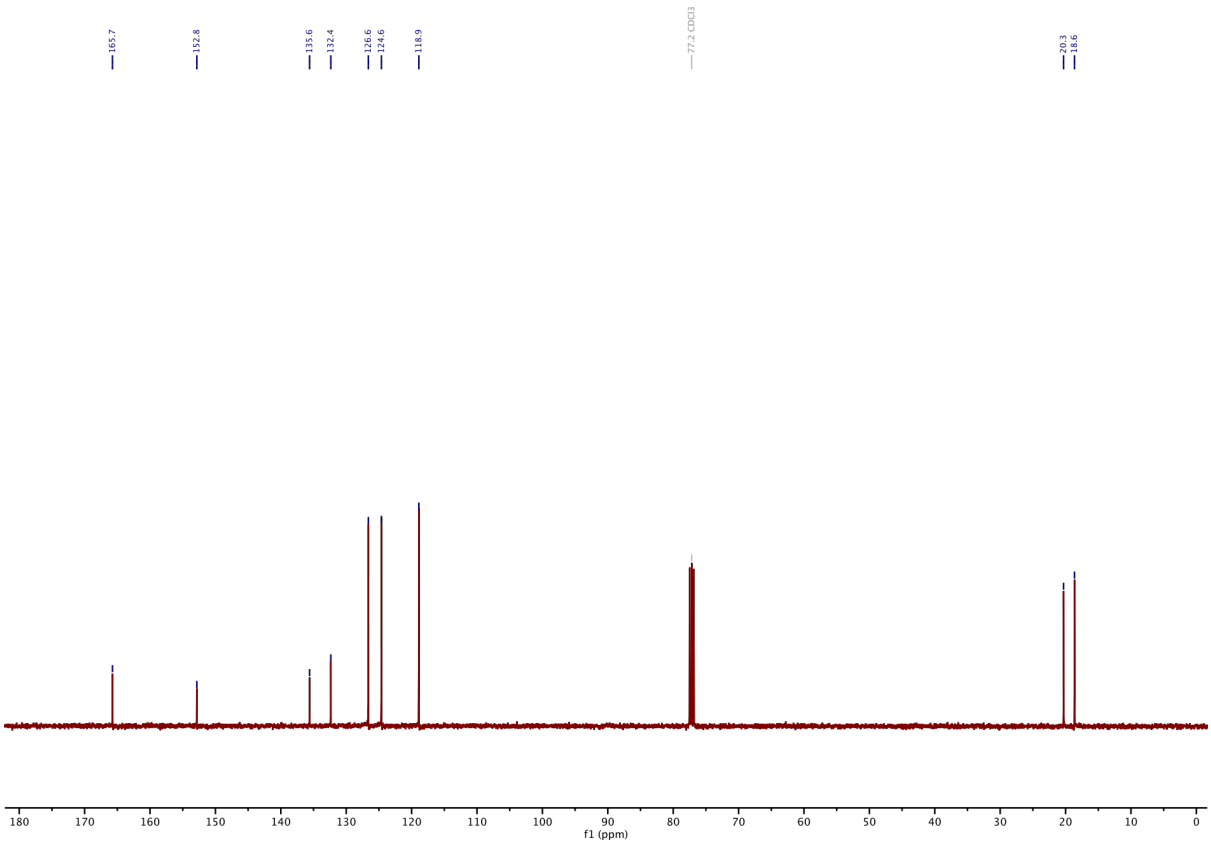

Part F: Bibliography

(1) Fulmer, G. R.; Miller, A. J.; Sherden, N. H.; Gottlieb, H. E.; Nudelman, A.; Stoltz, B. M.; Bercaw, J. E.; Goldberg, K. I. NMR Chemical Shifts of Trace Impurities: Common Laboratory Solvents, Organics, and Gases in Deuterated Solvents Relevant to the Organometallic Chemist. *Organometallics* **2010**, *29* (9), 2176–2179.

(2) Ma, D.; Xie, S.; Xue, P.; Zhang, X.; Dong, J.; Jiang, Y. Efficient and Economical Access to Substituted Benzothiazoles: Copper-Catalyzed Coupling of 2-Haloanilides with Metal Sulfides and Subsequent Condensation. *Angew. Chem. Int. Ed.* **2009**, *48* (23), 4222–4225. https://doi.org/10.1002/anie.200900486.

(3) Jiang, L.; Zhang, M.; Tang, L.; Weng, Q.; Shen, Y.; Hu, Y.; Sheng, R. Identification of 2-Subsituted Benzothiazole Derivatives as Triple-Functional Agents with Potential for AD Therapy. *RSC Adv.* **2016**, *6* (21), 17318–17327. https://doi.org/10.1039/C5RA25788C.

(4) Sawyer, J. S.; Baldwin, R. F.; Rinkema, L. E.; Roman, C. R.; Fleisch, J. H. Optimization of the Quinoline and Substituted Benzyl Moieties of a Series of Phenyltetrazole Leukotriene D4 Receptor Antagonists. *J. Med. Chem.* **1992**, *35* (7), 1200–1209. https://doi.org/10.1021/jm00085a005.

(5) Petrov, O. I.; Kalcheva, V. B.; Antonova, A. T. C-Formylation of Some 2 (3H)-Benzazolones and 2H-1, 4-Benzoxazin-3 (4H)-One. *Collect. Czechoslov. Chem. Commun.* **1997**, *62* (3), 494–497.

(6) Haydl, A. M.; Hartwig, J. F. Palladium-Catalyzed Methylation of Aryl, Heteroaryl, and Vinyl Boronate Esters. *Org. Lett.* **2019**, *21* (5), 1337–1341. https://doi.org/10.1021/acs.orglett.9b00025.

(7) Gao, L.; Meiring, J. C. M.; Kraus, Y.; Wranik, M.; Weinert, T.; Pritzl, S. D.; Bingham, R.; Ntouliou, E.; Jansen, K. I.; Olieric, N.; Standfuss, J.; Kapitein, L. C.; Lohmüller, T.; Ahlfeld, J.; Akhmanova, A.; Steinmetz, M. O.; Thorn-Seshold, O. A Robust, GFP-Orthogonal Photoswitchable Inhibitor Scaffold Extends Optical Control over the Microtubule Cytoskeleton. *Cell Chem. Biol.* **2020**, *0* (0). https://doi.org/10.1016/j.chembiol.2020.11.007.

(8) Sailer, A.; Ermer, F.; Kraus, Y.; Bingham, R.; Lutter, F. H.; Ahlfeld, J.; Thorn-Seshold, O. Potent Hemithioindigo-Based Antimitotics Photocontrol the Microtubule Cytoskeleton in Cellulo. *Beilstein J. Org. Chem.* **2020**, *16*, 125–134. https://doi.org/10.3762/bjoc.16.14.

(9) Sailer, A.; Meiring, J.; Heise, C.; Pettersson, L.; Akhmanova, A.; Thorn-Seshold, J.; Thorn-Seshold, O. Pyrrole Hemithioindigo Antimitotics with Near-Quantitative Bidirectional Photoswitching Photocontrol Cellular Microtubule Dynamics with Single-Cell Precision. *ChemArxiv* **2021**. https://doi.org/10.26434/chemrxiv.14130107.v1.

(10) Folkes, L. K.; Christlieb, M.; Madej, E.; Stratford, M. R. L.; Wardman, P. Oxidative Metabolism of Combretastatin A-1 Produces Quinone Intermediates with the Potential To Bind to Nucleophiles and To Enhance Oxidative Stress via Free Radicals. *Chem. Res. Toxicol.* **2007**, *20* (12), 1885–1894. https://doi.org/10.1021/tx7002195.

(11) Gao, L.; Meiring, J. C. M.; Kraus, Y.; Wranik, M.; Weinert, T.; Pritzl, S. D.; Bingham, R.; Ntouliou, E.; Jansen, K. I.; Olieric, N.; Standfuss, J.; Kapitein, L. C.; Lohmüller, T.; Ahlfeld, J.; Akhmanova, A.; Steinmetz, M. O.; Thorn-Seshold, O. A Robust, GFP-Orthogonal Photoswitchable Inhibitor Scaffold Extends Optical Control over the Microtubule Cytoskeleton. *Cell Chem. Biol.* **2021**, *28* (2), 228-241.e6. https://doi.org/10.1016/j.chembiol.2020.11.007.

(12) Schindelin, J.; Arganda-Carreras, I.; Frise, E.; Kaynig, V.; Longair, M.; Pietzsch, T.; Preibisch, S.; Rueden, C.; Saalfeld, S.; Schmid, B.; Tinevez, J.-Y.; White, D. J.; Hartenstein, V.; Eliceiri, K.; Tomancak, P.; Cardona, A. Fiji: An Open-Source Platform for Biological-Image Analysis. *Nat. Methods* **2012**, *9* (7), 676–682. https://doi.org/10.1038/nmeth.2019.

(13) Linnemann, J. R.; Miura, H.; Meixner, L. K.; Irmler, M.; Kloos, U. J.; Hirschi, B.; Bartsch, H. S.; Sass, S.; Beckers, J.; Theis, F. J.; Gabka, C.; Sotlar, K.; Scheel, C. H. Quantification of Regenerative Potential in Primary Human Mammary Epithelial Cells. *Development* **2015**, *142* (18), 3239–3251. https://doi.org/10.1242/dev.123554.
(14) Buchmann, B.; Meixner, L. K.; Fernandez, P.; Hutterer, F. P.; Raich, M. K.; Scheel, C. H.; Bausch, A. R. Mechanical Plasticity of the ECM Directs Invasive Branching Morphogenesis in Human Mammary Gland Organoids. *bioRxiv* **2019**, 860015. https://doi.org/10.1101/860015.
(15) Cabernard, C.; Prehoda, K. E.; Doe, C. Q. A Spindle-Independent Cleavage Furrow Positioning Pathway. *Nature* **2010**, *467* (7311), 91–94. https://doi.org/10.1038/nature09334.
(16) Rusan, N. M.; Peifer, M. A Role for a Novel Centrosome Cycle in Asymmetric Cell Division. *J. Cell Biol.* **2007**, *177* (1), 13–20. https://doi.org/10.1083/jcb.200612140.
(17) Pearl, E.; Morrow, S.; Noble, A.; Lerebours, A.; Horb, M.; Guille, M. An Optimized Method for Cryogenic Storage of Xenopus Sperm to Maximise the Effectiveness of Research Using Genetically Altered Frogs. *Theriogenology* **2017**, *92*, 149–155. https://doi.org/10.1016/j.theriogenology.2017.01.007.
(18) Roberts, A.; Borisyuk, R.; Buhl, E.; Ferrario, A.; Koutsikou, S.; Li, W.-C.; Soffe, S. R. The Decision to Move: Response Times, Neuronal Circuits and Sensory Memory in a Simple Vertebrate. *Proc. R. Soc. B Biol. Sci.* **2019**, *286* (1899), 20190297. https://doi.org/10.1098/rspb.2019.0297.
(19) Borowiak, M.; Nahaboo, W.; Reynders, M.; Nekolla, K.; Jalinot, P.; Hasserodt, J.; Rehberg, M.; Delattre, M.; Zahler, S.; Vollmar, A.; Trauner, D.; Thorn-Seshold, O. Photoswitchable Inhibitors of Microtubule Dynamics Optically Control Mitosis and Cell Death. *Cell* **2015**, *162* (2), 403–411. https://doi.org/10.1016/j.cell.2015.06.049.
(20) An, Y.; Chen, C.; Zhu, J.; Dwivedi, P.; Zhao, Y.; Wang, Z. Hypoxia-Induced Activity Loss of a Photo-Responsive Microtubule Inhibitor Azobenzene Combretastatin A4. *Front. Chem. Sci. Eng.* **2020**, *14* (5), 880–888. https://doi.org/10.1007/s11705-019-1864-6.
(21) Gao, L.; Meiring, J. C. M.; Kraus, Y.; Wranik, M.; Weinert, T.; Pritzl, S. D.; Bingham, R.; Ntouliou, E.; Jansen, K. I.; Olieric, N.; Standfuss, J.; Kapitein, L. C.; Lohmüller, T.; Ahlfeld, J.; Akhmanova, A.; Steinmetz, M. O.; Thorn-Seshold, O. A Robust, GFP-Orthogonal Photoswitchable Inhibitor Scaffold Extends Optical Control over the Microtubule Cytoskeleton. *Cell Chem. Biol.* **2021**, *28*, 1–14. https://doi.org/10.1016/j.chembiol.2020.11.007.
(22) Gavin, J.; Ruiz, J. F. M.; Kedziora, K.; Windle, H.; Kelleher, D. P.; Gilmer, J. F. Structure Requirements for Anaerobe Processing of Azo Compounds: Implications for Prodrug Design. *Bioorg. Med. Chem. Lett.* **2012**, *22* (24), 7647–7652. https://doi.org/10.1016/j.bmcl.2012.10.014.
(23) Matera, C.; Gomila, A. M. J.; Camarero, N.; Libergoli, M.; Soler, C.; Gorostiza, P. Photoswitchable Antimetabolite for Targeted Photoactivated Chemotherapy. *J. Am. Chem. Soc.* **2018**, *140* (46), 15764–15773. https://doi.org/10.1021/jacs.8b08249.
(24) Distel, M.; Hocking, J. C.; Volkmann, K.; Köster, R. W. The Centrosome Neither Persistently Leads Migration nor Determines the Site of Axonogenesis in Migrating Neurons in Vivo. *J. Cell Biol.* **2010**, *191* (4), 875–890. https://doi.org/10.1083/jcb.201004154.
(25) Distel, M.; Wullimann, M. F.; Köster, R. W. Optimized Gal4 Genetics for Permanent Gene Expression Mapping in Zebrafish. *Proc. Natl. Acad. Sci.* **2009**, *106* (32), 13365–13370. https://doi.org/10.1073/pnas.0903060106.
(26) Pecqueur, L.; Duellberg, C.; Dreier, B.; Jiang, Q.; Wang, C.; Plückthun, A.; Surrey, T.; Gigant, B.; Knossow, M. A Designed Ankyrin Repeat Protein Selected to Bind to Tubulin Caps the Microtubule plus End. *Proc. Natl. Acad. Sci.* **2012**. https://doi.org/10.1073/pnas.1204129109.

(27) Weinert, T.; Olieric, N.; Cheng, R.; Brünle, S.; James, D.; Ozerov, D.; Gashi, D.; Vera, L.; Marsh, M.; Jaeger, K.; Dworkowski, F.; Panepucci, E.; Basu, S.; Skopintsev, P.; Doré, A. S.; Geng, T.; Cooke, R. M.; Liang, M.; Prota, A. E.; Panneels, V.; Nogly, P.; Ermler, U.; Schertler, G.; Hennig, M.; Steinmetz, M. O.; Wang, M.; Standfuss, J. Serial Millisecond Crystallography for Routine Room-Temperature Structure Determination at Synchrotrons. *Nat. Commun.* **2017**, *8* (1), 1–11. https://doi.org/10.1038/s41467-017-00630-4.

(28) La Sala, G.; Olieric, N.; Sharma, A.; Viti, F.; de Asis Balaguer Perez, F.; Huang, L.; Tonra, J. R.; Lloyd, G. K.; Decherchi, S.; Díaz, J. F.; Steinmetz, M. O.; Cavalli, A. Structure, Thermodynamics, and Kinetics of Plinabulin Binding to Two Tubulin Isotypes. *Chem* **2019**, *5* (11), 2969–2986. https://doi.org/10.1016/j.chempr.2019.08.022.

(29) Kabsch, W. XDS. *Acta Crystallogr. D Biol. Crystallogr.* **2010**, *66* (Pt 2), 125–132. https://doi.org/10.1107/S0907444909047337.

(30) Tickle, I. J.; Flensburg, C.; Keller, P.; Paciorek, W.; Sharff, A.; Smart, O.; Vonrhein, C.; Bricogne, G. *STARANISO Anisotropy & Bayesian Estimation Server*; Global Phasing Ltd: Cambridge, United Kingdom, 2018.

(31) Smart, O. S.; Womack, T. O.; Flensburg, C.; Keller, P.; Paciorek, W.; Sharff, A.; Vonrhein, C.; Bricogne, G. Exploiting Structure Similarity in Refinement: Automated NCS and Target-Structure Restraints in BUSTER. *Acta Crystallogr. D Biol. Crystallogr.* **2012**, *68* (4), 368–380. https://doi.org/10.1107/S0907444911056058.

(32) Adams, P. D.; Afonine, P. V.; Bunkoczi, G.; Chen, V. B.; Davis, I. W.; Echols, N.; Headd, J. J.; Hung, L.-W.; Kapral, G. J.; Grosse-Kunstleve, R. W.; McCoy, A. J.; Moriarty, N. W.; Oeffner, R.; Read, R. J.; Richardson, D. C.; Richardson, J. S.; Terwilliger, T. C.; Zwart, P. H. PHENIX: A Comprehensive Python-Based System for Macromolecular Structure Solution. *Acta Crystallogr. Sect. D* **2010**, *66* (2), 213–221. https://doi.org/10.1107/S0907444909052925.

(33) Emsley, P.; Cowtan, K. Coot: Model-Building Tools for Molecular Graphics. *Acta Crystallogr. Sect. D* **2004**, *60* (12 Part 1), 2126–2132. https://doi.org/10.1107/S0907444904019158.

7. Part Three: Photoswitchable epothilone-based microtubule stabilizers

In this work we have rationally designed a set of photopharmaceutical reagents to stabilize microtubule structure and inhibit microtubule dynamics with micron-scale spatial resolution and second-scale temporal precision, that are applicable to cell-free and to cellular uses.

Building on the design Müller-Deku et al.[59] previously used for azobenzene derivatives, we transferred the SBT photoswitch concept out of the well-established colchicine domain binding site to the taxane scaffold with unfortunately low antiproliferative potency and photoisomer-dependent bioactivity.

We therefore decided to switch away from the taxane scaffold, and to explore epothilone-based photopharmaceuticals instead. Based on X-ray studies we rationalized a photoswitch extension site on the heterocyclic side-chain that would isomer-dependently interfere with the stabilization of the β-tubulin M-loop and its crucial H-bonding.

We apply the styrylthiazole (ST) photoswitch, which has not been reported for photopharmacology before, in an ST-extension approach to rationally exploit the ST's unique feature of a photoswitchable hydrogen-bond-accepting nitrogen that interacts with β-tubulin's Thr276 residue, a key determinant of epothilone *potency* (not binding affinity) because it induces folding of a key partially-disordered loop, that then establishes and stabilizes protein-protein interactions inside the microtubule. Our study both rationally exploits this H-bonding in our lead compound (**STEpo2**), and also controls for its relevance (**STEpo4**), by creating designs to isomer-dependently permit this H-bond to form.

By a stringent combination of high-resolution protein manipulation experiments, providing both short-term and long-term mechanistic proofs in both cell-free and cellular contexts, we deliver robust evidence supporting that our rationally designed reagents maintain their tubulin-inhibiting mechanism of action in all settings. **STEpos** have up to 100 times higher potency than the only previously-reported microtubule stabilizing photopharmaceuticals compounds and they are the only GFP-imaging-compatible microtubule stabilizing photopharmaceuticals.

Outstanding challenges for the ongoing development of **STEpos** include accessing the high potency epoxide-bearing derivative **STEpo1** in better yields and to improve the speed of photoactivation at the 405 nm laser line by slightly redshifting the ST absorption bands.

Photoswitchable epothilone-based microtubule stabilisers allow GFP-imaging-compatible, optical control over the microtubule cytoskeleton

Li Gao[1,†], Joyce C. M. Meiring[2,†], Constanze Heise[1], Ankit Rai[2], Adrian Müller-Deku[1], Anna Akhmanova[2], Julia Thorn-Seshold[1], Oliver Thorn-Seshold[1,3,*]

[1] Department of Pharmacy, Ludwig-Maximilians University of Munich, Munich 81377, Germany

[2] Cell Biology, Neurobiology and Biophysics, Department of Biology, Faculty of Science, Utrecht University, Utrecht 3584, Netherlands

[3] Lead Contact

[†] these authors contributed equally

*Correspondence: oliver.thorn-seshold@cup.lmu.de

***Keywords**: microtubule dynamics; cytoskeleton; photopharmacology; tubulin polymerisation inhibitor; optical control; epothilone; antimitotic; cell division; cell cycle; spatiotemporal control; photoswitch.*

Abstract

Optical methods to modulate microtubule stability and dynamics are promising approaches to reach the micron- and millisecond-scale resolution needed to decrypt the diverse roles of the microtubule cytoskeleton in biology. However, such optical methods have until now focussed nearly exclusively on microtubule destabilisation. Here, we introduce "STEpos" as light-responsive epothilone reagents, designed to photoswitchably bind to tubulin and stabilise lateral contacts in the microtubule lattice. Using a novel styrylthiazole photoswitch, designed to allow the hydrogen-bonding that is key to epothilone potency, we have created the first set of GFP-orthogonal photoswitchable microtubule stabilisers. The STEpos can photocontrol microtubule polymerisation, cell division, and cellular microtubule dynamics with micron- and second-scale spatiotemporal precision. STEpos offer substantial improvements of potency, solubility, and ease-of-use compared to the only previous photopharmaceuticals for microtubule stabilisation. The intriguing structure-photoswitching-activity relationship insights from this work will also assist future developments of improved STEpo reagents, and we anticipate that these will contribute greatly to high-precision cytoskeleton research across the fields of biophysics, cargo transport, cell motility, cell division, development, and neuroscience.

Introduction

All cellular processes depend on spatiotemporal regulation of protein function. Molecular tools to modulate protein function with the micrometre spatial precision and millisecond temporal precision inherent to these processes, are extremely valuable for precise biological research.[1,2] Cytoskeleton biology in particular would benefit from such tools, since hundreds of cellular processes rely simultaneously on the cytoskeletal scaffolding networks, with tight spatial regulation and with temporally dynamic response to changing conditions. Therefore, spatiotemporally-specific tools to modulate e.g. the microtubule and actin cytoskeleton, offer unique opportunities to decrypt and modify many different classes of biological functions.[3,4]

Microtubules (MTs) are giant, hollow, tube-like noncovalent polymers of α/β-tubulin heterodimers.[5] They are formed into a spatially structured network extending throughout the cell, that is rapidly remodelled through regulated cycles of growth and shrinkage in order to fulfil their spatiotemporally-regulated functions. These functions include acting as scaffolding for cell shape and for mechanical processes, as tracks for cargo transport by motor proteins, and as an organising system for proteins and structures within the cell. This makes MT network structure and remodelling dynamics vital in diverse fields, including cell migration, cell division and development (e.g. by supporting the segregation of chromosomes), and neuroscience (e.g. supporting the formation and maintenance of specialized extensions like axons and dendrites).[6,7]

Drugs that modulate MT stability and/or de/polymerisation dynamics are prime research tools for all these fields, being useful to nonspecifically suppress MT-dependent cellular processes. Archetypical MT stabilisers (polymerisers) include taxanes, epothilones, and laulimalide; while notable destabilisers (depolymerisers) include colchicine analogues, vinca alkaloids, auristatins/dolastatins, and maytansines (**Fig 1a**). While both MT destabilisers and MT stabilisers can be used to suppress MT polymerisation dynamics in cell culture, they enable different biological applications particularly *in vivo*. For example, MT stabilisation in damaged mature neurons seems to promote axonal regeneration by reducing the formation of retraction bulbs and modulating glial scar formation, which is relevant to spinal cord injury.[8,9] Conversely, colchicinoid MT destabilisers currently seem to show promise in reducing Covid-19 mortality[10] by suppressing inflammatory responses, via a complex mechanism that is initiated by reducing microtubule polymer mass. Both MT stabilisers and destabilisers have substantial societal impact, with several, such as the taxanes, epothilones, and vinca alkaloids, having reached blockbuster status as cancer therapeutics due to their ability to interfere with cell proliferation.[11,12]

As research tools however, the lack of spatiotemporal precision with which these drugs can be applied has been a major hurdle for manipulation experiments that would ideally localise their activity on the scale of µm and ms. Indeed, spatiotemporally-specific approaches to modulate the stability and dynamics of the MT cytoskeleton are still in their infancy. Irreversibly photouncaged derivatives of MT inhibitors e.g. taxol and combretastatin A-4[13] have been developed to improve the spatiotemporal precision of drug application in research, , although these are not widely used. We are aware of only one optogenetic tool system for MTs, the photo-inactivatable π-EB1 system from Wittmann[14], which can reversibly light-suppress MT polymerisation.

In contrast, reversibly photoswitchable analogues of taxane and colchicinoid MT-inhibiting drugs have been developed recently, that do offer cell-specific spatial precision and sub-second-scale temporal precision (**Fig 1a**). These photopharmaceuticals have practical advantages compared to photouncaging, such as fast light response, absence of phototoxic byproducts, easier handling and reduced potential for degradation. Additionally, although there is no directly comparable optogenetic system, the ability to apply these photopharmaceuticals across diverse model organisms, particularly in early developmental stages, is a strong advantage over genetic approaches. In general, optically controlled MT stabilisers are a particularly attractive target for use in cell culture and early development research, since the biological functions of the MT cytoskeleton essentially depend on stabilised or growing MTs. However, only one family of photoswitchable MT stabilisers has

been reported; the azobenzene-based "AzTax" taxane analogues, which allowed fast, spatiotemporally precise, reversible control of MT dynamics, with a degree of subcellular control in neurons.[15] In contrast, work on photoswitchable colchicinoid MT depolymerisers has explored a diversity of photoswitch scaffolds, from azobenzene (PST reagents),[3,16], to hemithioindigo (HOTub/HITub),[17,18], spiropyran-merocyanin[19]), and styrylbenzothiazole or "SBT" (SBTub reagents), each with their own drawbacks and advantages (**Fig 1a**).[20]

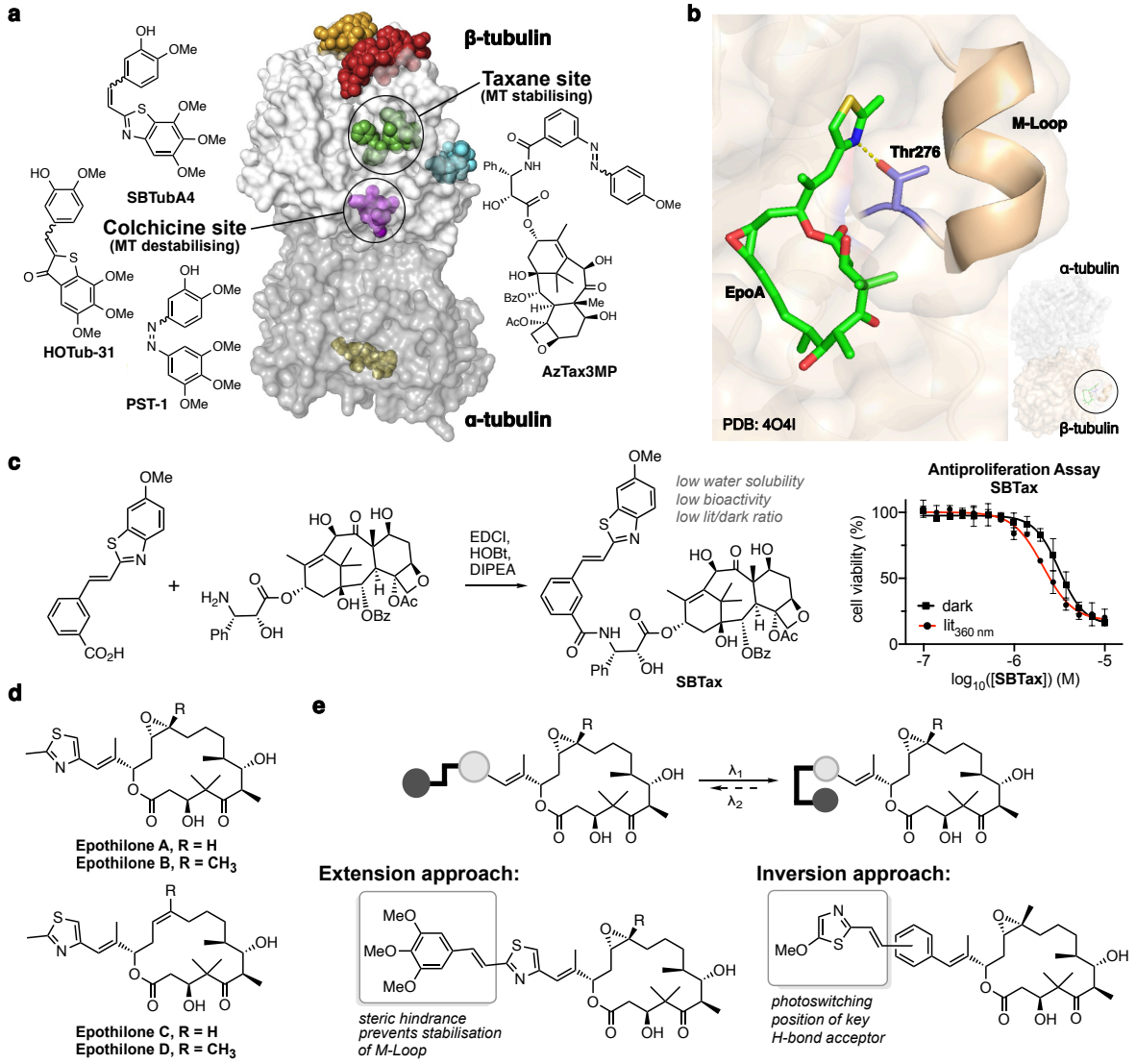

Figure 1: Microtubule stabiliser photopharmacology. (a) α/β-tubulin heterodimer with major drug binding sites coloured, and representative structures of the major photopharmaceutical chemotypes (figure from Steinmetz and Prota[21]). **(b)** Epothilone binding to β-tubulin stabilises the M-loop, which stabilises tubulin-tubulin lateral contacts and thus stabilises the MT. A key interaction is the hydrogen bond from Thr276 to the thiazole nitrogen.[adapted from PDB 4o4i][22] **(c)** Synthesis and biological evaluation of an SBT photoswitch scaffold based Taxol derivative **(d)** Principal epothilones. The epoxide of EpoA/B is a structural feature and is dispensible for binding (EpoC/D). **(e)** A peripheral photoswitch attachment strategy for epothilone, using the styrylthiazole (ST) photoswitch, was designed to photoswitchably impact the stabilisation of the M-loop and/or the position of an H-bond acceptor.

Notably, the SBT photoswitch offered a particularly attractive combination of advantages for biological research use: (1) The SBT scaffold is completely unaffected by standard GFP imaging at ca. 490 nm excitation, so biological assays can be imaged with common fluorescent proteins or markers without compromising the photopharmaceutical. This is a crucial factor for usability. The vast majority of biological models use GFP or closely-related fluorescent proteins, so GFP-orthogonal photoswitches are needed if researchers are to apply photopharmacology without having to change model (which is particularly problematic with

transgenic animal lines that can take years to breed and validate). GFP-orthogonality is also needed to keep imaging channels free for the multiplexed readouts that are increasingly standard in cutting-edge research.[23] (2) The SBT's C=C chromophore is ideally situated for efficient photoswitching at 405 nm or 442 nm, so matching the typical photoactivation lasers installed in microscope - again a crucial feature for practical impact. (3) SBT is highly metabolically stable, and avoids biochemical photoswitch scission. This scission is generally problematic for both azobenzene isomers, but they also suffer from faster *Z*-isomer scission, that further complicates assay readouts[24,25]. More problematically still, in typical photopharmaceutical uses, photoswitches are built onto the molecular periphery (as they were in the AzTax reagents), so if either isomer suffers scission, it releases a non-photoswitchable fragment that is typically more potent than the photopharmaceutical and further compromises assay readout (discussed further elsewhere[20]). Taken together, these advantages of the SBTs proved crucial in allowing SBTubs to succeed as MT photoswitches in tissue and animal applications across a variety of animal models, while photopharmaceuticals based on the other photoswitches have not generally succeeded in moving beyond 2D cell culture or early embryo applications.[23]

We were therefore motivated to bring the powerful advantages of the SBT photoswitch to bear on the attractive class of microtubule stabilisers, to generate novel optically-controlled MT-stabilisers with improved practical applicability and scope. We now report the development of such GFP-orthogonal photopharmaceutical MT stabilisers, based on epothilone (**Fig 1b**).

Results

Initial approach: SBT-taxanes

We had initially applied the metabolically resistant, GFP-orthogonal SBT photoswitch to the taxane scaffold. We used the same design as we had previously used for the metabolically labile, non-GFP-orthogonal photoswitch azobenzene,[15] deprotecting the sidechain 3'-amine of docetaxel and coupling it to a SBT-carboxylic acid to give SBT-taxane **SBTax** (**Fig 1c**). However, **SBTax** had poor solubility, unsatisfactory cellular antiproliferative potency, and its bioactivity was not significantly photoisomer-dependent (**Fig 1c**). This may simply reflect the taxanes' weaknesses for photopharmaceutical adaptation, including their 'ball and sidechain' structure (with no obvious basis for rational introduction of isomer-dependent potency), low solubility, already high molecular weight, and structural and chemical complexity that limit reasonable synthetic modifications.

Final approach: design of ST-epothilones (STEpos)

We therefore decided to switch away from the taxane scaffold, and to explore epothilone-based photopharmaceuticals instead. Epothilones are a structurally simpler class of microtubule stabilisers, that share the same binding pocket as taxanes (**Fig 1b**) but feature higher binding affinity and potency.[26,27] Epothilones have proven particularly useful as research reagents, in that their greater solubility, bioavailability, and ability to cross the blood-brain barrier, allow applications inaccessible to taxanes: such as systemic (rather than local) administration for stabilising axons, to regenerate the central nervous system after injury.[28] The synthetic tractability of the epothilones has enabled extensive drug analogue campaigns (**Fig 1d**), clarifying structure-activity relationship (SAR) features;[29,30] and a range of epothilone derivatives have undergone advanced clinical trials, with ixabepilone being FDA-approved for treatment of metastatic breast cancer. A further advantage of the chemically simpler epothilone is that late-stage modifications that preserve binding activity while altering chemically or biologically problematic groups are known; in our case, this would later prove to be removal of the C12/C13 epoxide of epothilone B, to give the *Z*-alkene epothilone D. The SAR of epothilones suggests that while aryl-aryl substituents are not tolerated around C12/C13,[31] even relatively large heterocycles can be tolerated in place of the thiazole, with potent thiazole, purine, quinoline and benzothiazole derivatives all being known, and larger rings particularly tolerated in epothilone D derivatives.[29]

X-ray studies also reveal the critical role of the epothilones' nitrogen-containing aryl ring in forming and orienting the β-tubulin M-loop, so that this loop stabilises tubulin-tubulin lateral

contacts, which in turn stabilise microtubules (**Fig 1b**). As well as sterics, the hydrogen bond from Thr276 to the ring nitrogen is a key interaction for this loop formation,[22] which is underlined by e.g. the 20- to 100-fold potency loss on going from 2-pyridine to near-isosteric 3- and 4-pyridine epothilone analogues.[32]

Using an SBT-like photoswitch to replace the thiazole of epothilones therefore seemed attractive as a rational design principle (**Fig 1e**). (i) The size of the photoswitch would seem to be tolerated, yet sterics around the attachment site play a significant role in bioactivity, giving hope that E/Z isomerisation would influence tubulin-binding potency. (ii) The epothilone scaffold seemed sufficiently water-soluble to support the photoswitch, without incurring the limitations seen with the taxanes. (iii) Finally, the photoswitch's ring nitrogen raises the exciting opportunity, that photoisomer-dependently repositioning the thiazole portion could modulate its H-bond-accepting capacity, and therefore drastically influencing its M-loop-stabilising activity, and biological potency.

To minimise the overall size and insolubility of the photoswitch, we chose to work with our recently developed styrylthiazole (ST) photoswitches instead of SBTs. STs are isosteric to azobenzenes, but feature similar electronics and absorption spectra as the GFP-orthogonal, metabolically-resistant SBTs (see also below).[20] We explored two design strategies. Firstly, an "extension approach" aimed to project the photoswitch into the M-loop as the *trans* isomer, alleviating steric pressure as the *cis* isomer, and therefore designing towards a *cis*-active photopharmaceutical (NB: the *cis* isomer of SBTs always places the nitrogen atom accessibly towards the outside,[20] therefore we did not anticipate that the *cis* isomer would be incapable of acting as an H-bond acceptor). As elsewhere in our work, we chose a trimethoxyphenyl group for this approach, as we find that the combination of the out-of-plane orientation of the central methoxy group that reduces π-stacking, and the additional hydrophilicity of the three extra OMe groups, contribute greatly to water solubility. Secondly, an "inversion approach" tested whether photoswitching could bring an H-bond accepting ring nitrogen sufficiently close to Thr276 to favour *cis*-specific binding (**Fig 1e**). We decided to compare *meta* with *para* photoswitch connection in this inverted approach. We anticipated that the *meta*-connection could bring the thiazole nitrogen close enough to be effective, and although the *para*-connected switch might sterically clash too greatly with the M-loop in both isomers, it could serve as a useful control for e.g. phototoxicity and solubility. As far as we are aware, there is no systematic study of the dependency of ST photochemistry on substituents; but we reasoned that, analogously to azobenzenes, raising the electron density in the thiazole by including an OMe substituent should help shift ST absorption bands towards the visible. It should also be noted that by retaining the vinyl substituent, both extension and inversion designs benefit from an additional shift towards the visible.

Synthesis of STEpos

Horner-Wadsworth-Emmons olefination of the epothilone methyl ketone **1** is a flexible, established route to attach diverse aryl rings to epothilones,[33] and we determined to use it to install pre-formed styrylthiazoles (STs). Starting from epothilone B, we cleaved the double bond by ozonolysis[34] then TES-protected the free OH groups to give protected methyl ketone **2** (**Fig 2a**). The ST photoswitch phosphonates **8** and **12a/b** were synthesised by Arbuzov reaction from the chlorides, which in turn had been accessed from heterocyclic ring closure of the cinnamic acid derivatives (**6** and **10a/b**, **Fig 2b-c**). Initially, methyl ketone **2** was olefinated with phosphonate **12a**, giving inversion photoswitch **STEpo1** after deprotection (**Fig 2d**). Although Mulzer has shown that the epoxide tolerates various basic, oxidative, reductive and electrophilic reagents,[35] the loss of scarce material by epoxide opening under dilute acid conditions prompted us to deoxygenate the epoxide instead,[36] which still preserves bioactivity in the epothilone series.[37] We therefore targeted ST derivatives of epothilone D, and deoxygenated **2** with WCl_6[38] to give TES-protected methyl ketone **3** (**Fig 2a**) in good yields. Olefination with ST phosphonates, then deprotection, yielded extension design **STEpo2** and inversion designs **STEpo3** and **STEpo4** in milligram quantities (**Fig 2e**) (see Supporting Information for details).

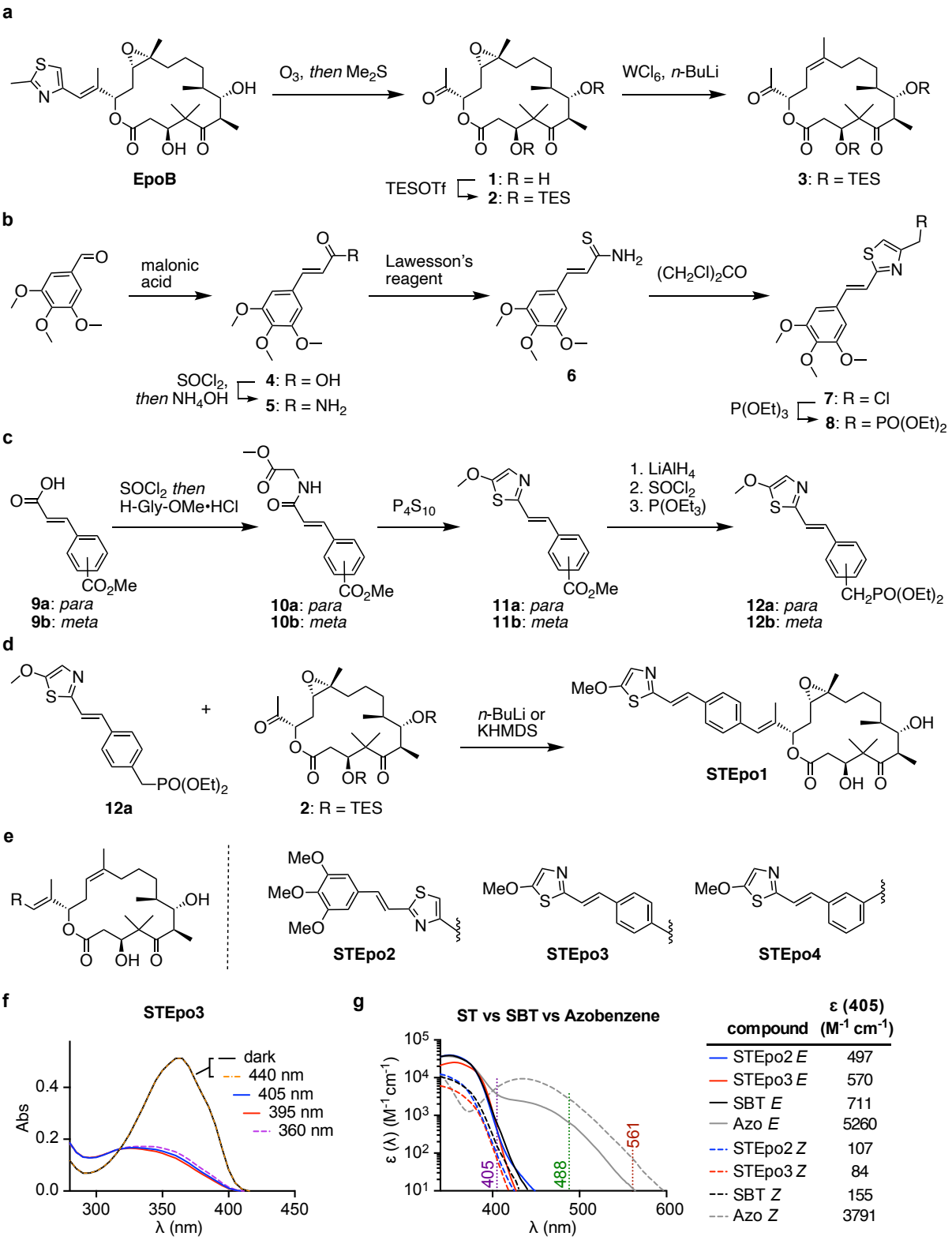

Figure 2: Synthesis and photocharacterisation of STEpo photopharmaceuticals. (a) route to epothilone methyl ketones **2** and **3**. **(b)** route to ST phosphonate **8**. **(c)** route to ST phosphonates **12a** and **12b**. **(d)** Epothilone B inversion design derivative, **STEpo1**. **(e)** Epothilone D derivatives **STEpo2** (extension) and **STEpo3**/**STEpo4** (inversion). **(f)** Photostationary state (PSS) equilibrium UV-Vis spectra of **STEpo3** during sequential irradiations starting from the dark state (all-*E*) shows no response to 440 nm light, efficient isomerisation to mostly-*Z* by wavelengths from 405—360 nm, and no degradation under this illumination. **(g)** Comparison of absorption spectra of *E* and *Z* isomers of **STEpos** with an SBT and a typical *para*-methoxylated azobenzene. At 405 nm, the **STEpos** have approx two thirds of the absorption coefficient of an SBT photoswitch. The log scale plot highlights the full orthogonality of the ST (and SBT) photoswitches to 488 nm (GFP) or 561 nm (RFP) imaging, whereas the azobenzene is still responsive to high-intensity focused imaging lasers at these wavelengths. See Supporting Information for details.

Photoisomerisation and GFP-orthogonality of STEpos

The STEpos' performance regarding photoisomerisation and photostability was characterised by UV-Vis spectroscopy. Similarly to SBTs,[20] the STEpos could be reproducibly photoisomerised to majority-*Z* photostationary states (PSSs) by near-UV light (360-410 nm; ca. 85% *Z*; see Supporting Information) (**Fig 2f, Fig S1a-b**). We observed gradual degradation with illumination below 340 nm, presumably by [2+2] cycloaddition, though not by illumination above this wavelength. The vinylthiazole photoswitch **STEpo2** was blueshifted by ca. 10 nm compared to the methoxythiazole (inversion) photoswitches. Surprisingly, the STs were blueshifted by only ca. 10 nm compared to the benzannulated SBTs (**Fig S1d**). The *Z*-STs were thermally stable, giving <1% relaxation to *E*-STs in solution at 37°C after 8 h (**Fig S1c**).

Typically, the major *E*-ST absorption band was centred around 355 nm; the 20%-of-maximum intensity was at ca. 392 nm, with a sharp cutoff above this wavelength (ε dropping by a factor of 10 every 12 nm). The major *Z*-ST absorption band was centred around 325 nm; the 20%-of-maximum intensity was at 382 nm, also with a sharp cutoff above this wavelength (ε dropping by a factor of 10 every 16 nm) (**Fig 2g**). These sharp cutoffs are crucial features. These are responsible for the ST's absorption being effectively zero above 440 nm, which should ensure that it is entirely unaffected by GFP imaging either with lasers (488 nm) or with broader filtered excitation sources (typically 490±25 nm). This is in sharp contrast to azobenzene photoswitches, particularly those that benefit from polymethoxylation, which are significantly impacted by imaging of GFP, YFP, and even RFP (**Fig 2g**).[20]

STEpos give photoisomer-dependent cellular bioactivity

We first evaluated the GFP-orthogonal, photoswitchable STEpos for their photoisomer-dependent antiproliferative activity in cells in culture, which MT inhibitors cause by blocking mitosis. We incubated HeLa cervical cancer cells with *E*-STEpos in the dark (all-*E*) or lit by non-phototoxic pulsed illuminations from low-power 360 nm LEDs (<1 mW/cm^2; <1% duty cycle; *in situ* photoswitching to mostly-*Z*) as described previously,[3,20] and assessed cell viability 44 h later.

All compounds showed antiproliferative activity in the submicromolar range, and all compounds had reproducibly light-dependent bioactivity with up to ca. 8-fold potency shift upon isomerisation (**Fig 3a**). The epothilone B *para*-inversion analogue **STEpo1** (IC_{50}(lit) ca. 3 nM, IC_{50}(dark) ca. 12 nM) was ca. 100-fold more potent than its epothilone D inversion counterpart **STEpo3**, and ca. 35-fold more than epothilone D extension analogue **STEpo2**, which were likewise lit-active with similar 4-fold photoswitchability of bioactivity. Interestingly, epothilone D *meta*-inversion analogue **STEpo4** was instead dark-active, with *Z*-**STEpo4** being equipotent to *E*-**STEpo3**, and *E*-**STEpo4** being equipotent to *Z*-**STEpo3**. This reversal suggests an intriguing structural basis for photoisomer-dependent activity in the STEpo series, which is an ongoing challenge in our research. It also highlights the absence of phototoxicity from either the ST or the illumination protocols, since this would otherwise result in consistent lit-toxic effects.

We did not continue with **STEpo1** due to its lower synthetic availability, and since **STEpo2** offered an identical photoswitchability of bioactivity (ratio of apparent cellular activity, comparing limiting illumination conditions) while not facing solubility problems. Since lit-active photopharmaceuticals present the greatest practical advantage for biological use, we also did not continue with **STEpo4**.

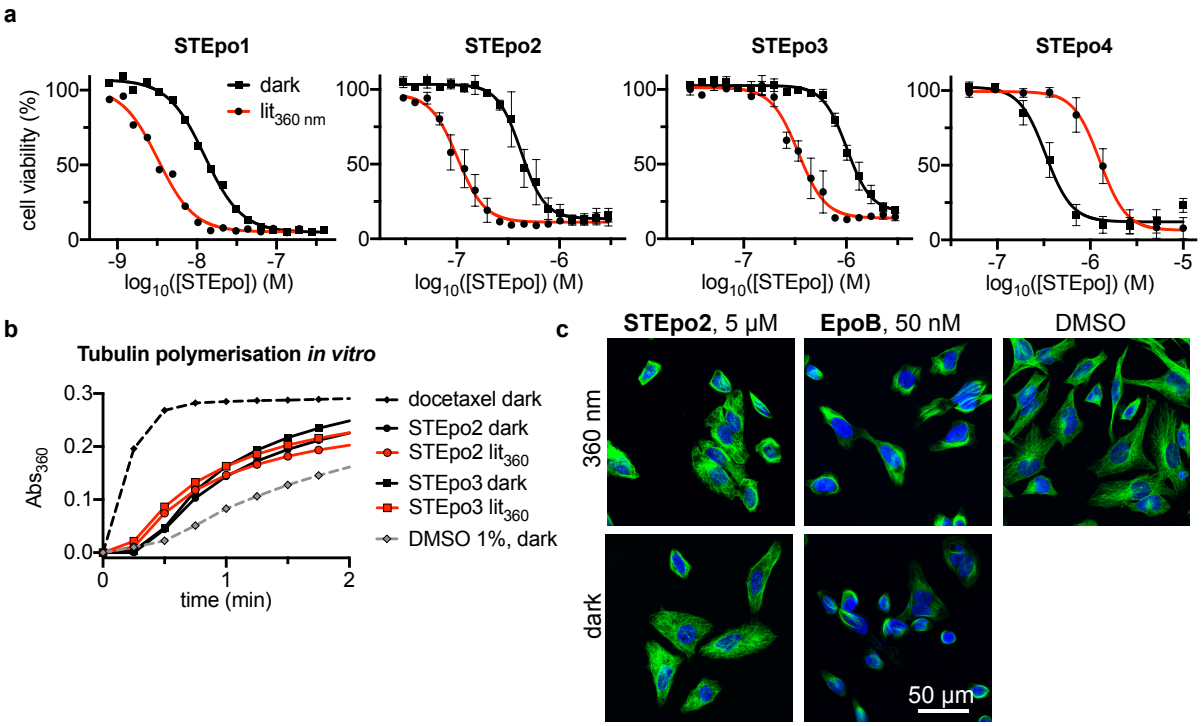

Figure 3: Cellular bioactivity and mechanism of action of STEpos. (a) STEpos have potent and light-dependent antiproliferative activity (HeLa cells, 44 h incubation; all-*E* dark conditions versus mostly-*Z* UV-lit conditions; **STEpo1**: one representative of three independent experiments shown; **STEpo2-4**: three replicates, mean+SD). **(b) STEpo2/3** promote tubulin polymerisation (turbidimetric *in vitro* assay; greater absorbance corresponds to a greater degree of polymerisation; time to onset of polymerisation should be examined) with a small light-dependency visible (earlier onset). **(c)** Immunofluorescence imaging of cells treated with **STEpo2** shows breakdown of MT architecture and mitotic arrests under lit conditions (mostly-*Z*), but nearly no disorganization in the dark (all-*E*) (HeLa cells, 20 h incubation; α-tubulin in green, DNA stained with DAPI in blue).

Mechanism of action of STEpo

To begin testing their molecular mechanism of light-dependent bioactivity in a simplified cell-free system, we assayed the photoswitchably cytotoxic, lit-active **STEpo2/3** for light-dependent enhancement of polymerisation of purified tubulin (polymerisation in bulk). Both isomers were polymerisation enhancers, indicating that they act directly on tubulin as do the epothilones; and the time to polymerisation onset was noticeably shorter with pre-lit mostly-*Z* stocks, than with all-*E* stocks: matching their cellular activity pattern (**Fig 3b**).

Next, we imaged the network architecture of the MT cytoskeleton in cells incubated with **STEpo2/3** to examine their cellular mechanism of isomer-dependent bioactivity. Dark (all-*E*) assays showed markedly less impact on the MT network architecture than *in situ* lit assays (mostly *Z*-isomer) (**Fig 3c**). The mitotic arrests and MT depolymerisation that are particularly visible on the lit assays are hallmarks of MT inhibitors, matching the assumption that their photoisomer-dependent cytotoxicity arises from their *Z*-isomers more potently inhibiting MT dynamics and stability in cells.

Finally, we studied the capacity of **STEpo2** to permit *in situ* photocontrol over microtubule polymerisation in cell-free settings: with spatial resolution on the µm scale allowing us to optically target *individual microtubules*, and with temporal resolution on the scale of seconds.

We used TIRF microscopy to image a reconstituted microtubule polymerisation system. This uses the non-hydrolysable GTP analogue GMPCPP to form stable microtubule "seeds" that are fixed to a glass surface for spatially-localised imaging; free tubulin is then applied together with the drug under testing and as well as MT plus end-tracking protein EB3, added to improve visualization of dynamic MT tips (**Fig 4a**)[39,40]; finally, GTP is supplied and the seeds initiate normal cycles of growth and shrinkage using the free tubulin in the mixture. Using the labelled seed of each MT as a static reference point, kymographs tracking the growing and shrinking tips of the MT reveal the frequency of shrinkage events as the "spikes" in the kymograph. Typically, MTs depolymerise back to the seed before restarting polymerisation. MT-stabilising drugs decrease the frequency of shrinkage events and can stabilize a shrinking

MT before the seed is reached (known as a rescue). In the event that the drug stabilises a different protofilament number of MT than the seeds have (14 for GMPCPP), stable rescue sites will be observed, while if the drug stabilizes the protofilament number matching the seed, rescues will occur stochastically at different sites along the microtubule,[39] so offering mechanistic insights into the nature of MT stabilisation. As epothilones are 14-protofilament MT stabilisers, we expected that if our **STEpos** retained the same MT-stabilising properties with *Z*-specific potency, they would permit these MT rescues after illumination (**Fig 4b**): which we aimed to apply with spatial specificity to regions near single selected MT tips.

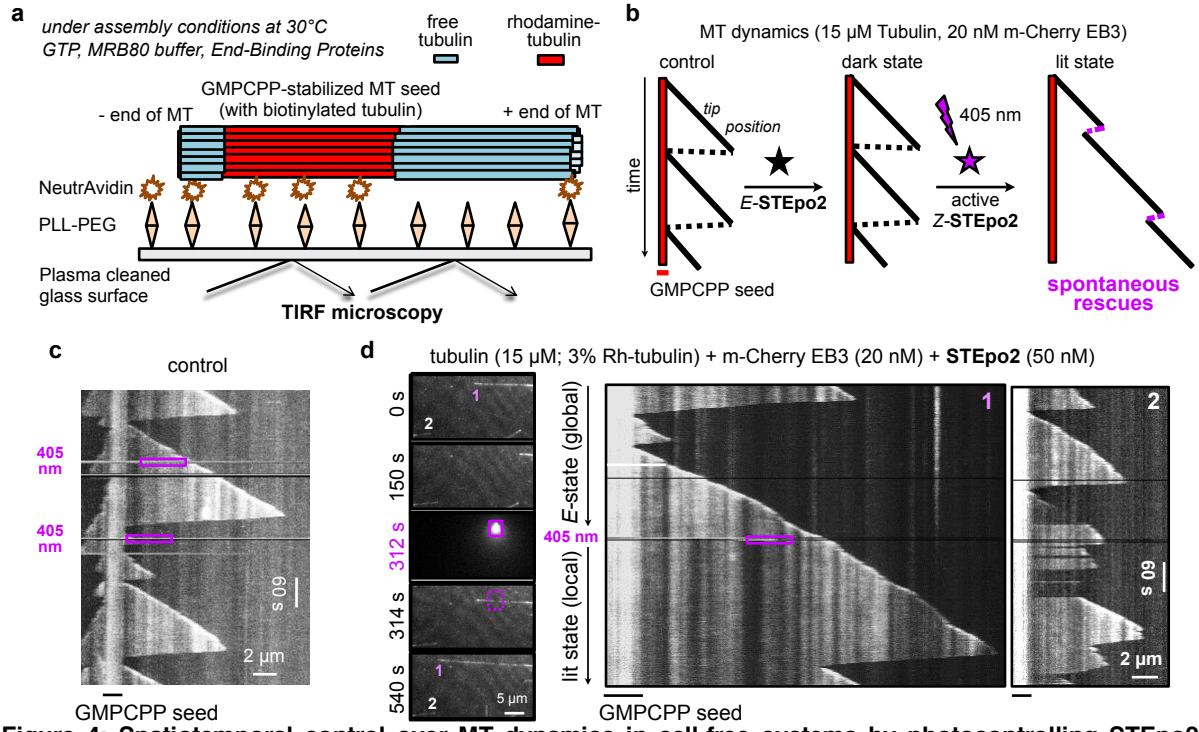

Figure 4: Spatiotemporal control over MT dynamics in cell-free systems by photocontrolling STEpo2: **(a)** Schematic of the *in vitro* MT dynamics imaging assay, and **(b)** cartoon of kymographs illustrating MT growth and catastrophe patterns during normal conditions, then expected patterns for **SBEpo2** as a 405 nm-dependent 14-protofilament MT stabiliser. **(c)** No-drug control kymograph showing MT shrinkage frequency and polymerisation restarts at the seed (405 nm illuminations in the purple dotted boxes). **(d)** Time-lapse images at left, showing two microtubules in the field of view (labelled 1 and 2), with their kymographs at right. 405 nm illumination at 312 s is in the purple box region of time-lapse panel/kymographs (0.01% of the total field of view).

During control assays, kymographs revealed that shrinkage events proceeded all the way down to the seed before polymerisation restarted, as expected, and this MT behaviour was unaffected by 405 nm illumination (**Fig 4c**, **Fig S2a**). When *E*-**SBEpo2** was added at 50 nM concentration, MT shrinkage events were similar to control conditions, reaching the GMPCPP seeds before restart (first 5 min, **Fig 4d**), although higher concentrations predictably caused MT stabilisation (**Fig S2b**). Local 405 nm illumination near a single selected microtubule (labelled "1" in **Fig 4d**) stabilised it, increasing MT length and showing rescue. By contrast, other MTs which were further from the illumination zone (e.g. "2") maintained similar shrinkage frequency as before, though with some spontaneous rescues (next 5 min, **Fig 4d**; **Movie S1**; see too **Fig S2c**). These stringent assays confirm that **STEpo2** is an epothilone-like, *Z*-isomer-specific stabiliser of 14-protofilament MTs, which can be spatiotemporally targeted in cell-free settings with micron-and-second scale precision.

Live cell photocontrol with STEpo

To test the STEpos' ability to enable *in situ* photocontrol of MT dynamics with spatiotemporal precision, we imaged **STEpo2**-treated cells transfected with the fluorescently-labelled MT end binding protein EB3-GFP. EB3 marks the GTP cap region of MTs, thus revealing the dynamics of polymerising MT plus ends as dynamic "comets";[41] and EB3

imaging is an effective spatiotemporally-resolved readout for isomerisation-dependent control of MT dynamics by photoswitchable inhibitors.[20]

Cells were therefore imaged continually with excitation at 488 nm. Imaging was begun before **STEpo2** application to establish baseline MT dynamics. Low intensity 405 nm pulsing was applied, inducing negligible comet count reduction. Then **STEpo2** was applied at 0.6 µM, again resulting in no noticeable change of EB3 statistics. That 488 nm imaging of **STEpo2**-treated cells did not induce inhibition of MT dynamics (unlike the performance of azobenzene-based photopharmaceuticals)[20] matches their design for GFP-compatibility by absorption cut-off. However, in a fourth phase, 405 nm photoactivation pulses were additionally applied, and now MT dynamics were rapidly suppressed (EB3 comet count halved within seconds; $P < 0.0001$) (**Fig 5**; **Movie S2**). These assays show that *in situ* photoswitching of **STEpo2** is an effective approach to precise, noninvasive MT control in cellular settings.

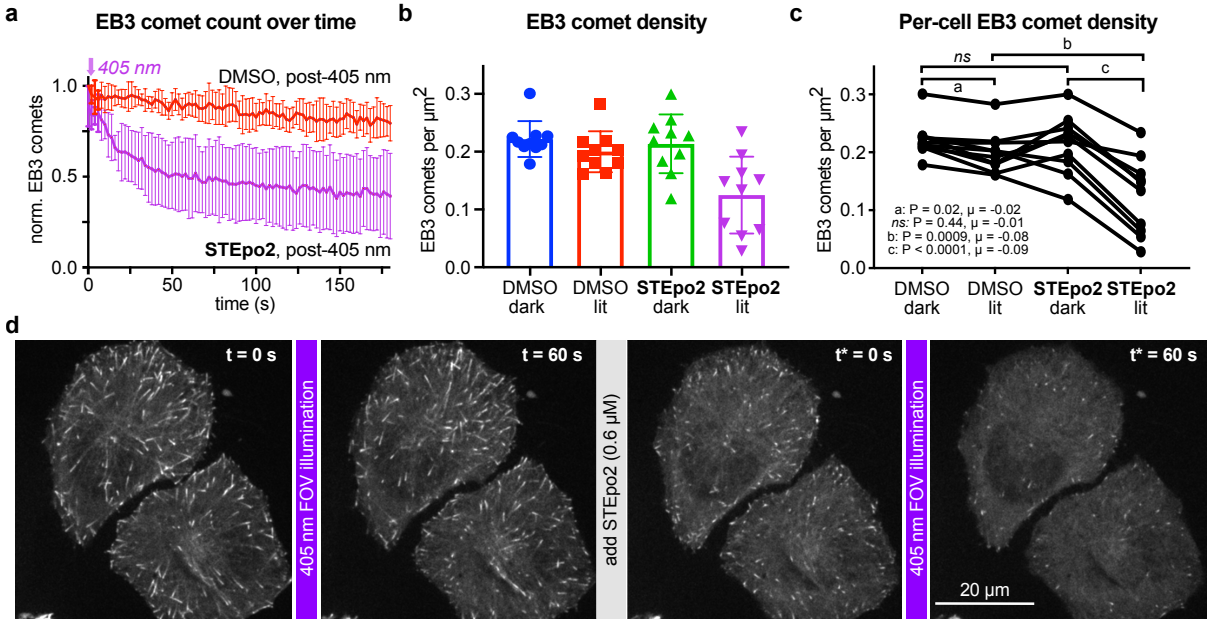

Figure 5: Spatiotemporal control over cellular MT dynamics with STEpo2: Live cell EB3-GFP "comets" during GFP imaging with 488 nm (HeLa cells). MT inhibition with **STEpo2** is initiated upon 405 nm illumination (cells first treated with 1% DMSO, then imaged for 60 s for baseline, then photoactivated from time t = 0 with 405 nm during imaging over 3 min; then an additional 0.6 μM *E*-**STEpo2** was applied, and 405 nm/imaging applied from time t* = 0. 10 cells acquired). **(a)** mean ± SD comet count (each cell normalised to t=0 of the DMSO control). **(b-c)** Comet density statistics show large and significant differences upon **STEpo2** photoactivation (dark at t = 0 or t* = 0, lit at t = 60 s or t* = 60 s; **b** shows pooled data, **c** shows longitudinal traces per cell; P-values and μ mean differences as annotated). **(d)** Stills from representative movie (data related to **Movie S2**).

Conclusions

Methods to modulate biological processes with the spatiotemporal resolution appropriate to their endogenous functioning, have become increasingly powerful and effective over recent years. Photopharmacology in particular is rapidly evolving into an elegant technique for high-precision, non-invasive biological control in fast-response and/or spatially-localised applications from neuroscience[42,43] to cytoskeleton research[3,4]. As the optical instrumentation of biological research becomes ever more sophisticated and widespread, the value of robust optically-controlled tools will continue to rise: particularly for studies of inherently (sub)cellularly- and subsecond-resolved processes, such as those that the microtubule cytoskeleton supports.[44]

In this work we report the first photopharmaceuticals based on the epothilone MT stabiliser scaffold. The mid-nanomolar potencies, reliable solubility, and the robust photoswitchability of bioactivity of all the **STEpos** in this work are very promising features for future research, and can be favourably compared to the micromolar potencies, solubility problems, and variable photoswitchability of bioactivity we have found here and previously[15]

for photoswitch-derivatised taxanes. We feel that designing towards isomer-dependent interference with a partially disordered structural element (here, the tubulin M-loop) represents an exciting general principle for photopharmacology, which currently focusses on relatively rigid steric clashes that may be unrealistic to identify and photocontrol. By exploring uncommonly large epothilone derivatives, we have also revealed aspects of epothilone SAR that can lead to identifying which steric and polarity aspects determine **STEpo** binding and/or M-loop orientation, and so will inspire the rational design of still-more-potent systems with still greater photoswitchability of bioactivity.

This is also, we believe, the first use of the compact styrylthiazole (ST) as a photoswitch scaffold for biology: one that is isosteric to azobenzene, yet offers significant practical benefits. Here we highlight its GFP-orthogonality, that enables easy imaging, and its intriguing and biologically relevant potential to act as an H-bond acceptor, which matched the requirements of the epothilone system. We feel that GFP-orthogonality is currently an under-appreciated goal amongst chemical reagent makers. The race toward NIR-capable photoswitches for deep tissue photoisomerisation is understandable, even though deep tissue isomerisation has to contend with significant spatial scattering of illumination (as is seen by shining a red laser pointer through a finger) and so may sacrifice the spatial precision that is one of photopharmacology's greatest advantages. A recent design shift, driven by biologists, is however underway: emphasising biochemically stable, imaging-orthogonal photoswitch scaffolds that can be easily employed in tissue slice and embryo/early animal research across a variety of models.[20,23] This shift has great potential to serve the biological research community with a valuable palette of rapid-response, non-phototoxic, byproduct-free reagents for studies in diverse fields. To continue this progress will rely on expanding our scope of photopharmaceutical design principles and of photoswitch scaffolds. In this context, unlocking a useful new photoswitch scaffold, may prove as valuable as unlocking a new drug or binding site for a key, central biological player.

There are several challenges for the ongoing development of **STEpos**. Topics in focus in our group include: (i) To understand and to harness the greater potency seen for the epoxide-bearing derivative with milder chemical routes. (ii) To improve the speed of photoactivation at the 405 nm laser line by slightly redshifting the ST absorption bands (just a 15 nm shift would produce a 10-fold rate enhancement due to the steepness of absorption cutoff). We have elsewhere achieved this with increasing substituent donor strength (e.g. *para*-NMe_2Ph- instead of Ph- for the extension design)[23]; for the inverted design, further photochemical exploration of the ST scaffold will be needed, although again we anticipate that increasing the electron donating capacity of the thiazole will be key. (iii) To achieve bidirectional photoswitching with a photoswitch offering the GFP-orthogonality of an ST (and the metabolic robustness of an SBT). This requires increasing the separation between the absorption bands of the *E* and *Z* isomers, which is an object of ongoing study.

In conclusion, the **STEpos** are reliably soluble, easy to apply, GFP-orthogonal, potent MT-stabilising photoswitches for cell culture, and should also easily find applications through to *in vivo* GFP/multiplexed imaging experiments in near-surface settings. These **STEpos**, or future reagents, will undoubtedly bring great value to cytoskeleton research across fields from development and motility to transport and cell division. In particular we expect that the **STEpo** toolset will benefit research into axonal repair following injury, which can be favoured by MT stabilisers, though by still-unknown mechanisms whose elucidation has so far been stymied by poor spatiotemporal precision of MT stabilisation.[8,9,15,28] Lastly, we are optimistic that by contributing to innovations in the realms of photoswitch scaffold chemistry and of rational photopharmaceutical design, the **STEpos** are a promising advance not only for high-precision microtubule biology, but also towards the refinement of high-performance photopharmacology against other protein targets.

Acknowledgements

This research was supported by funds from the German Research Foundation (DFG: Emmy Noether grant number 400324123; SFB 1032 project B09 number 201269156; SFB TRR 152 project P24 number 239283807; and SPP 1926 project number 426018126 to

O.T.-S.). J.C.M.M. acknowledges support from an EMBO Long Term Fellowship. We thank Jan Huebner and Bayer for the gift of EpoB, Dirk Trauner for enabling the material transfers, Monique Preusse for early cell viability testing, and Rebekkah Hammar for performing the tubulin polymerisation assay. We are grateful to Henrietta Lacks, now deceased, and to her surviving family members for their contributions to biomedical research.

Author contributions

L.G. designed and performed the epothilone syntheses, performed photocharacterisation and cell viability assays, and coordinated data assembly. J.C.M.M. performed live cell EB3 imaging during photoswitching and coordinated data assembly. C.H. performed cell viability assays, immunofluorescence staining, and cell cycle analysis. A.M.-D. synthesised the SBT-taxane. A.A. supervised EB3 imaging. J.T.-S. performed cell cycle analysis, coordinated data assembly and supervised all other cell biology. O.T.-S. designed the concept and experiments, supervised all other experiments, coordinated data assembly and wrote the manuscript.

Declaration of interests

The authors declare no competing interests.

References

(1) Goglia, A. G.; Toettcher, J. E. A Bright Future: Optogenetics to Dissect the Spatiotemporal Control of Cell Behavior. *Curr Opin Chem Biol* **2019**, *48*, 106–113. https://doi.org/10.1016/j.cbpa.2018.11.010.

(2) Hoorens, M. W. H.; Szymanski, W. Reversible, Spatial and Temporal Control over Protein Activity Using Light. *Trends In Biochemical Sciences* **2018**, *43* (8), 567–575. https://doi.org/10.1016/j.tibs.2018.05.004.

(3) Borowiak, M.; Nahaboo, W.; Reynders, M.; Nekolla, K.; Jalinot, P.; Hasserodt, J.; Rehberg, M.; Delattre, M.; Zahler, S.; Vollmar, A.; Trauner, D.; Thorn-Seshold, O. Photoswitchable Inhibitors of Microtubule Dynamics Optically Control Mitosis and Cell Death. *Cell* **2015**, *162* (2), 403–411. https://doi.org/10.1016/j.cell.2015.06.049.

(4) Borowiak, M.; Küllmer, F.; Gegenfurtner, F.; Peil, S.; Nasufovic, V.; Zahler, S.; Thorn-Seshold, O.; Trauner, D.; Arndt, H.-D. Optical Manipulation of F-Actin with Photoswitchable Small Molecules. *JACS* **2020**, *142* (20), 9240–9249. https://doi.org/10.1021/jacs.9b12898.

(5) Akhmanova, A.; Steinmetz, M. O. Tracking the Ends: A Dynamic Protein Network Controls the Fate of Microtubule Tips. *Nat Rev Mol Cell Biol* **2008**, *9* (4), 309–322. https://doi.org/10.1038/nrm2369.

(6) Glotzer, M. The 3Ms of Central Spindle Assembly: Microtubules, Motors and MAPs. *Nat Rev Mol Cell Biol* **2009**, *10* (1), 9–20. https://doi.org/10.1038/nrm2609.

(7) Kapitein, L. C.; Hoogenraad, C. C. Building the Neuronal Microtubule Cytoskeleton. *Neuron* **2015**, *87* (3), 492–506. https://doi.org/10.1016/j.neuron.2015.05.046.

(8) Hellal, F.; Hurtado, A.; Ruschel, J.; Flynn, K. C.; Laskowski, C. J.; Umlauf, M.; Kapitein, L. C.; Strikis, D.; Lemmon, V.; Bixby, J.; Hoogenraad, C. C.; Bradke, F. Microtubule Stabilization Reduces Scarring and Causes Axon Regeneration After Spinal Cord Injury. *Science* **2011**, *331* (6019), 928. https://doi.org/10.1126/science.1201148.

(9) Sengottuvel, V.; Leibinger, M.; Pfreimer, M.; Andreadaki, A.; Fischer, D. Taxol Facilitates Axon Regeneration in the Mature CNS. *J Neurosci* **2011**, *31* (7), 2688–2699. https://doi.org/10.1523/jneurosci.4885-10.2011.

(10) Deftereos, S. G.; Giannopoulos, G.; Vrachatis, D. A.; Siasos, G. D.; Giotaki, S. G.; Gargalianos, P.; Metallidis, S.; Sianos, G.; Baltagiannis, S.; Panagopoulos, P.; Dolianitis, K.; Randou, E.; Syrigos, K.; Kotanidou, A.; Koulouris, N. G.; Milionis, H.; Sipsas, N.; Gogos, C.; Tsoukalas, G.; Olympios, C. D.; Tsagalou, E.; Migdalis, I.; Gerakari, S.; Angelidis, C.; Alexopoulos, D.; Davlouros, P.; Hahalis, G.; Kanonidis, I.; Katritsis, D.; Kolettis, T.; Manolis, A. S.; Michalis, L.; Naka, K. K.; Pyrgakis, V. N.;

Toutouzas, K. P.; Triposkiadis, F.; Tsioufis, K.; Vavouranakis, E.; Martinèz-Dolz, L.; Reimers, B.; Stefanini, G. G.; Cleman, M.; Goudevenos, J.; Tsiodras, S.; Tousoulis, D.; Iliodromitis, E.; Mehran, R.; Dangas, G.; Stefanadis, C.; on behalf of the GRECCO-19 investigators. Effect of Colchicine vs Standard Care on Cardiac and Inflammatory Biomarkers and Clinical Outcomes in Patients Hospitalized With Coronavirus Disease 2019: The GRECCO-19 Randomized Clinical Trial. *JAMA Network Open* **2020**, *3* (6), e2013136–e2013136. https://doi.org/10.1001/jamanetworkopen.2020.13136.

(11) Peterson, J. R.; Mitchison, T. J. Small Molecules, Big Impact: A History of Chemical Inhibitors and the Cytoskeleton. *Chemistry Biology* **2002**, *9* (12), 1275–1285. https://doi.org/10.1016/S1074-5521(02)00284-3.

(12) Steinmetz, M. O.; Prota, A. E. Microtubule-Targeting Agents: Strategies To Hijack the Cytoskeleton. *Trends In Cell Biology* **2018**, *28* (10), 776–792. https://doi.org/10.1016/j.tcb.2018.05.001.

(13) Wühr, M.; Tan, E. S.; Parker, S. K.; Detrich III, H. W.; Mitchison, T. J. A Model for Cleavage Plane Determination in Early Amphibian and Fish Embryos. *Current Biology* **2010**, *20* (22), 2040–2045. https://doi.org/10.1016/j.cub.2010.10.024.

(14) van Haren, J.; Charafeddine, R. A.; Ettinger, A.; Wang, H.; Hahn, K. M.; Wittmann, T. Local Control of Intracellular Microtubule Dynamics by EB1 Photodissociation. *Nature Cell Biology* **2018**, *20* (3), 252–261. https://doi.org/10.1038/s41556-017-0028-5.

(15) Müller-Deku, A.; Meiring, J. C. M.; Loy, K.; Kraus, Y.; Heise, C.; Bingham, R.; Jansen, K. I.; Qu, X.; Bartolini, F.; Kapitein, L. C.; Akhmanova, A.; Ahlfeld, J.; Trauner, D.; Thorn-Seshold, O. Photoswitchable Paclitaxel-Based Microtubule Stabilisers Allow Optical Control over the Microtubule Cytoskeleton. *NComm* **2020**, *11* (1), 4640. https://doi.org/10.1038/s41467-020-18389-6.

(16) Engdahl, A. J.; Torres, E. A.; Lock, S. E.; Engdahl, T. B.; Mertz, P. S.; Streu, C. N. Synthesis, Characterization, and Bioactivity of the Photoisomerizable Tubulin Polymerization Inhibitor Azo-Combretastatin A4. *OL* **2015**, *17* (18), 4546–4549. https://doi.org/10.1021/acs.orglett.5b02262.

(17) Sailer, A.; Ermer, F.; Kraus, Y.; Lutter, F. H.; Donau, C.; Bremerich, M.; Ahlfeld, J.; Thorn-Seshold, O. Hemithioindigos for Cellular Photopharmacology: Desymmetrised Molecular Switch Scaffolds Enabling Design Control over the Isomer-Dependency of Potent Antimitotic Bioactivity. *CBC* **2019**, *20* (10), 1305–1314. https://doi.org/10.1002/cbic.201800752.

(18) Sailer, A.; Ermer, F.; Kraus, Y.; Bingham, R.; Lutter, F. H.; Ahlfeld, J.; Thorn-Seshold, O. Potent Hemithioindigo-Based Antimitotics Photocontrol the Microtubule Cytoskeleton in Cellulo. *BJOC* **2020**, *16*, 125–134. https://doi.org/10.3762/bjoc.16.14.

(19) Rastogi, S. K.; Zhao, Z.; Gildner, M. B.; Shoulders, B. A.; Velasquez, T. L.; Blumenthal, M. O.; Wang, L.; Li, X.; Hudnall, T. W.; Betancourt, T.; Du, L.; Brittain, W. J. Synthesis, Optical Properties and in Vitro Cell Viability of Novel Spiropyrans and Their Photostationary States. *Tet* **2021**, *80*, 131854. https://doi.org/10.1016/j.tet.2020.131854.

(20) Gao, L.; Meiring, J. C. M.; Kraus, Y.; Wranik, M.; Weinert, T.; Pritzl, S. D.; Bingham, R.; Ntouliou, E.; Jansen, K. I.; Olieric, N.; Standfuss, J.; Kapitein, L. C.; Lohmüller, T.; Ahlfeld, J.; Akhmanova, A.; Steinmetz, M. O.; Thorn-Seshold, O. A Robust, GFP-Orthogonal Photoswitchable Inhibitor Scaffold Extends Optical Control over the Microtubule Cytoskeleton. *Cell Chemical Biology* **2021**, *28*, 1–14. https://doi.org/10.1016/j.chembiol.2020.11.007.

(21) Steinmetz, M. O.; Prota, A. E. Microtubule-Targeting Agents: Strategies To Hijack the Cytoskeleton. *Trends In Cell Biology* **2018**. https://doi.org/10.1016/j.tcb.2018.05.001.

(22) Prota, A. E.; Bargsten, K.; Northcote, P. T.; Marsh, M.; Altmann, K.-H.; Miller, J. H.; Díaz, J. F.; Steinmetz, M. O. Structural Basis of Microtubule Stabilization by Laulimalide and Peloruside A. *Angewandte Chemie International Edition* **2014**, *53* (6), 1621–1625. https://doi.org/10.1002/anie.201307749.

(23) Gao, L.; Meiring, J. C. M.; Varady, A.; Ruider, I. E.; Heise, C.; Wranik, M.; Velasco, C. D.; Taylor, J. A.; Terni, B.; Standfuss, J.; Cabernard, C. C.; Llobet, A.; Steinmetz, M. O.; Bausch, A. R.; Distel, M.; Thorn-Seshold, J.; Akhmanova, A.; Thorn-Seshold, O. In Vivo Photocontrol of Microtubule Dynamics and Integrity, Migration and Mitosis, by the Potent GFP-Imaging-Compatible Photoswitchable Reagents SBTubA4P and SBTub2M. *bioRxiv* **2021**, 2021.03.26.437160. https://doi.org/10.1101/2021.03.26.437160.

(24) An, Y.; Chen, C.; Zhu, J.; Dwivedi, P.; Zhao, Y.; Wang, Z. Hypoxia-Induced Activity Loss of a Photo-Responsive Microtubule Inhibitor Azobenzene Combretastatin A4. *Frontiers Of Chemical Science Engineering* **2020**, *14* (5), 880–888. https://doi.org/10.1007/s11705-019-1864-6.

(25) Gavin, J.; Ruiz, J. F. M.; Kedziora, K.; Windle, H.; Kelleher, D. P.; Gilmer, J. F. Structure Requirements for Anaerobe Processing of Azo Compounds: Implications for Prodrug Design. *BMCL* **2012**, *22* (24), 7647–7652. https://doi.org/10.1016/j.bmcl.2012.10.014.

(26) Bollag, D. M.; McQueney, P. A.; Zhu, J.; Hensens, O.; Koupal, L.; Liesch, J.; Goetz, M.; Lazarides, E.; Woods, C. M. Epothilones, a New Class of Microtubule-Stabilizing Agents with a Taxol-like Mechanism of Action. *Cancer Res* **1995**, *55* (11), 2325–2333.

(27) Höfle, G.; Bedorf, N.; Steinmetz, H.; Schomburg, D.; Gerth, K.; Reichenbach, H. Epothilone A and B—Novel 16-Membered Macrolides with Cytotoxic Activity: Isolation, Crystal Structure, and Conformation in Solution. *Angewandte Chemie International Edition* **1996**, *35* (13 - 14), 1567–1569. https://doi.org/10.1002/anie.199615671.

(28) Ruschel, J.; Hellal, F.; Flynn, K. C.; Dupraz, S.; Elliott, D. A.; Tedeschi, A.; Bates, M.; Sliwinski, C.; Brook, G.; Dobrindt, K.; Peitz, M.; Brustle, O.; Norenberg, M. D.; Blesch, A.; Weidner, N.; Bunge, M. B.; Bixby, J. L.; Bradke, F. Axonal Regeneration. Systemic Administration of Epothilone B Promotes Axon Regeneration after Spinal Cord Injury. *Science* **2015**, *348* (6232), 347–352. https://doi.org/10.1126/science.aaa2958.

(29) Altmann, K.-H.; Schinzer, D. Chemistry and Biology of Epothilones. In *Natural Products in Medicinal Chemistry*; Methods and Principles in Medicinal Chemistry; Wiley-VCH, 2014; Vol. 60, pp 81–126. https://doi.org/10.1002/9783527676545.ch03.

(30) Nicolaou, K. C.; Roschangar, F.; Vourloumis, D. Chemical Biology of Epothilones. *Angewandte Chemie International Edition* **1998**, *37* (15), 2014–2045. https://doi.org/10.1002/(SICI)1521-3773(19980817)37:15<2014::AID-ANIE2014>3.0.CO;2-2.

(31) Reiff, E. A.; Nair, S. K.; Henri, J. T.; Greiner, J. F.; Reddy, B. S.; Chakrasali, R.; David, S. A.; Chiu, T.-L.; Amin, E. A.; Himes, R. H.; Vander Velde, D. G.; Georg, G. I. Total Synthesis and Evaluation of C26-Hydroxyepothilone D Derivatives for Photoaffinity Labeling of β-Tubulin. *JOC* **2010**, *75* (1), 86–94. https://doi.org/10.1021/jo901752v.

(32) Nicolaou, K.; Scarpelli, R.; Bollbuck, B.; Werschkun, B.; Pereira, M.; Wartmann, M.; Altmann, K.-H.; Zaharevitz, D.; Gussio, R.; Giannakakou, P. Chemical Synthesis and Biological Properties of Pyridine Epothilones. *Chemistry Biology* **2000**, *7* (8), 593–599. https://doi.org/10.1016/S1074-5521(00)00006-5.

(33) Nicolaou, K. C.; Rhoades, D.; Wang, Y.; Bai, R.; Hamel, E.; Aujay, M.; Sandoval, J.; Gavrilyuk, J. 12,13-Aziridinyl Epothilones. Stereoselective Synthesis of Trisubstituted Olefinic Bonds from Methyl Ketones and Heteroaromatic Phosphonates and Design, Synthesis, and Biological Evaluation of Potent Antitumor Agents. *JACS* **2017**, *139* (21), 7318–7334. https://doi.org/10.1021/jacs.7b02655.

(34) Höfle, G.; Glaser, N.; Leibold, T.; Sefkow, M. Epothilone A-D and Their Thiazole-Modified Analogs as Novel Anticancer Agents. *Pure Applied Chemistry* **1999**, *71* (11), 2019–2024. https://doi.org/10.1351/pac199971112019.

(35) Martin, H. J.; Drescher, M.; Mulzer, J. How Stable Are Epoxides? A Novel Synthesis of Epothilone B. *Angewandte Chemie International Edition* **2000**, *39* (3), 581–583.

https://doi.org/10.1002/(SICI)1521-3773(20000204)39:3<581::AID-ANIE581>3.0.CO;2-W.

(36) Johnson, J.; Kim, S.-H.; Bifano, M.; DiMarco, J.; Fairchild, C.; Gougoutas, J.; Lee, F.; Long, B.; Tokarski, J.; Vite, G. Synthesis, Structure Proof, and Biological Activity of Epothilone Cyclopropanes. *OL* **2000**, *2* (11), 1537–1540. https://doi.org/10.1021/ol0058240.

(37) White, J. D.; Carter, R. G.; Sundermann, K. F.; Wartmann, M. Total Synthesis of Epothilone B, Epothilone D, and *Cis* - and *Trans* -9,10-Dehydroepothilone D. *JACS* **2001**, *123* (23), 5407–5413. https://doi.org/10.1021/ja010454b.

(38) Sharpless, K. B.; Umbreit, M. A.; Nieh, M. T.; Flood, T. C. Lower Valent Tungsten Halides. New Class of Reagents for Deoxygenation of Organic Molecules. *JACS* **1972**, *94* (18), 6538–6540. https://doi.org/10.1021/ja00773a045.

(39) Rai, A.; Liu, T.; Glauser, S.; Katrukha, E. A.; Estévez-Gallego, J.; Rodríguez-García, R.; Fang, W.-S.; Díaz, J. F.; Steinmetz, M. O.; Altmann, K.-H.; Kapitein, L. C.; Moores, C. A.; Akhmanova, A. Taxanes Convert Regions of Perturbed Microtubule Growth into Rescue Sites. *Nature Materials* **2020**, *19* (3), 355–365. https://doi.org/10.1038/s41563-019-0546-6.

(40) Bieling, P.; Laan, L.; Schek, H.; Munteanu, E. L.; Sandblad, L.; Dogterom, M.; Brunner, D.; Surrey, T. Reconstitution of a Microtubule Plus-End Tracking System in Vitro. *Nature* **2007**, *450* (7172), 1100–1105. https://doi.org/10.1038/nature06386.

(41) Roostalu, J.; Thomas, C.; Cade, N. I.; Kunzelmann, S.; Taylor, I. A.; Surrey, T. The Speed of GTP Hydrolysis Determines GTP Cap Size and Controls Microtubule Stability. *eLife* **2020**, *9*. https://doi.org/10.7554/eLife.51992.

(42) Laprell, L.; Tochitsky, I.; Kaur, K.; Manookin, M. B.; Stein, M.; Barber, D. M.; Schön, C.; Michalakis, S.; Biel, M.; Kramer, R. H.; Sumser, M. P.; Trauner, D.; Van Gelder, R. N. Photopharmacological Control of Bipolar Cells Restores Visual Function in Blind Mice. *Journal Of Clinical Investigation* **2017**, *127* (7), 2598–2611. https://doi.org/10.1172/JCI92156.

(43) Leinders-Zufall, T.; Storch, U.; Bleymehl, K.; Mederos y Schnitzler, M.; Frank, J. A.; Konrad, D. B.; Trauner, D.; Gudermann, T.; Zufall, F. PhoDAGs Enable Optical Control of Diacylglycerol-Sensitive Transient Receptor Potential Channels. *Cell Chemical Biology* **2018**, *25* (2), 215-223.e3. https://doi.org/10.1016/j.chembiol.2017.11.008.

(44) Castle, B. T.; Odde, D. J. Optical Control of Microtubule Dynamics in Time and Space. *Cell* **2015**, *162* (2), 243–245. https://doi.org/10.1016/j.cell.2015.06.064.

Supplemental Information

Photoswitchable epothilone-based microtubule stabilisers allow GFP-imaging-compatible, optical control over the microtubule cytoskeleton

Li Gao[1,†], Joyce C. M. Meiring[2,†], Constanze Heise[1], Ankit Rai[2], Adrian Müller-Deku[1], Anna Akhmanova[2], Julia Thorn-Seshold[1], Oliver Thorn-Seshold[1,3,*]

[1] Department of Pharmacy, Ludwig-Maximilians University of Munich, Munich 81377, Germany
[2] Cell Biology, Neurobiology and Biophysics, Department of Biology, Faculty of Science, Utrecht University, Utrecht 3584, Netherlands
[3] Lead Contact
[†] these authors contributed equally
* Correspondence: oliver.thorn-seshold@cup.lmu.de

ORCID: O.T.-S. 0000-0003-3981-651X

***Keywords**: microtubule dynamics; cytoskeleton; photopharmacology; tubulin polymerisation inhibitor; optical control; colchicine; antimitotic; cell division; cell migration; development; photoswitch.*

Table of Contents

Part A: Chemical Synthesis

Conventions

Abbreviations: The following abbreviations are used: Hex – distilled isohexanes, EA – ethyl acetate, DCM – dichloromethane, Et – ethyl, Ac – acetyl, Me – methyl, MeCN – acetonitrile, DMSO – dimethylsulfoxide, PBS – phosphate buffered saline, FA – Formic Acid, TFA – trifluoro acetic acid, TEA – triethyl amine, LR – Lawesson's reagent.

Safety Hazards: no unexpected or unusually high safety hazards were encountered.

Reagents and Conditions: Unless stated otherwise, (1) all reactions and characterizations were performed with unpurified, undried, non-degassed solvents and reagents, used as obtained, under closed air atmosphere without special precautions; (2) "hexane" used for chromatography was distilled from commercial crude isohexane fraction by rotary evaporation; (3) "column" and "chromatography" refer to manual flash column chromatography on Merck silica gel Si-60 (40−63 μm); (4) MPLC flash column chromatography refers to purification on a Biotage Isolera Spektra, using prepacked silica cartridges from Biotage; (5) procedures and yields are unoptimized; (6) yields refer to isolated chromatographically and spectroscopically pure materials, corrected for residual solvent content; (7) all eluent and solvent mixtures are given as volume ratios unless otherwise specified, thus "1:1 Hex:EA" indicates a 1:1 (v/v) mixture of hexanes and ethyl acetate; (8) chromatography eluents e.g. "0→25% EA:Hex" indicate a linear gradient of eluent composition.

Thin-layer chromatography (TLC) was run on 0.25 mm Merck silica gel plates (60, F-254), typically with Hex:EA eluents, except where indicated. UV light (254 nm) was used as a visualizing agent, with cross-checking by 365 nm UV lamp. Compounds not containing chromophores were stained with cerium ammonium molybdate instead. TLC characterizations are abbreviated as $\mathbf{R_f}$ = 0.64 (EA:Hex = 1:1).

NMR: Standard NMR characterization was by ^{1}H- and ^{13}C-NMR spectra on a Bruker Ascend 400 (400 **MHz** & 100 **MHz** for ^{1}H and ^{13}C respectively) or a Bruker Ascend 500 (500 **MHz** & 125 **MHz** for ^{1}H and ^{13}C, respectively). Known compounds were checked against literature data and their spectral analysis is not detailed unless necessary. Chemical shifts (δ) are reported in ppm calibrated to residual non-perdeuterated solvent as an internal reference[1]. Peak descriptions singlet (s), doublet (d), triplet (t), quartet (q) and multiplet (m).

Analytical HPLC and Mass Spectra: Analytical HPLC-MS measurements were performed on an Agilent 1100 SL coupled HPLC-MS system with (a) a binary pump to deliver H_2O:MeCN eluent mixtures containing 0.1% formic acid at a 0.4 mL/min flow rate, (b) Thermo Scientific Hypersil GOLD™ C18 column (1.9 μm; 3 × 50 mm) maintained at 25°C, whereby the solvent front eluted at t_{ret} = 0.5 min, (c) an Agilent 1100 series diode array detector used to acquire peak spectra of separated compounds/isomers in the range 200-550 nm after manually

baselining across each elution peak of interest to correct for eluent composition effects, (d) a Bruker Daltonics HCT-Ultra mass spectrometer used in ESI mode at unit mass resolution. Run conditions were a linear gradient of H_2O:MeCN eluent composition from the starting ratio through to 10:90, applied during the separation phase (first 5 min), then 0:100 maintained until all peaks of interest had been observed (typically 2 min more); the column was equilibrated with the H_2O:MeCN eluent mixture for 2 minutes before each run. HRMS was carried out by the Zentrale Analytik of the LMU Munich using ESI or EI ionization as specified. LRMS was carried out on an expression CMS by Advion with either APCI or ESI as ionization source.
Preperative HPLC (prep-HPLC): Prep-HPLC purification was carried out on a 1260 Infinity II Preparative LC System by Agilent using an Agilent reversed phase Prep-HT C18 column (21.2 x 250 mm, 10 µm) at a 20 mL/min flow rate.

Synthesis of STEpos

TES protected STEpo1:

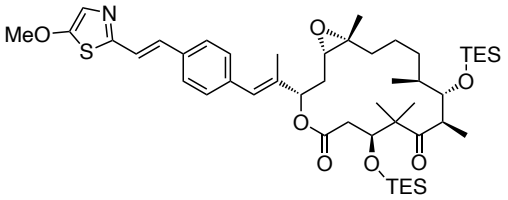

To a solution of styrylthiazole phosphonate **12a** (50 mg, 0.14 mmol, 2.5 eq) in dry THF (1.5 mL) was added sodium bis(trimethylsilyl)amide (2 M in THF, 50 µL, 0.10 mmol, 1.8 eq) and the solution was stirred at –78°C for 30 min. A solution of methyl ketone **2** (35 mg, 55 µmol, 1 eq) in THF (1 mL) was added dropwise, and the red reaction mixture was stirred for 2 h at –78°C. Then the reaction mixture was quenched with sat. aq. NH_4Cl (2 mL), and allowed to warm to room temperature. The two phases were separated, and the aqueous layer was extracted with EA (3 × 5mL). The combined organic layers were dried over Na_2SO_4 and concentrated under reduced pressure. The obtained residue was purified by normal phase MPLC (0→20% EA:Hex, elutes at 17% EA) to afford TES protected **STEpo1** (8.3 mg, 9.7 µmol, 18%) as colorless oil.

^{1}H-NMR (500 MHz, $CDCl_3$): δ = 7.45 (d, *J* = 8.2 Hz, 2H), 7.29 (d, *J* = 8.0 Hz, 2H), 7.15 – 7.05 (m, 3H), 6.55 (s, 1H), 5.29 (dd, *J* = 8.9, 2.8 Hz, 1H), 4.14 (dd, *J* = 7.2, 4.8 Hz, 1H), 3.95 (s, 3H), 3.91 (d, *J* = 9.1 Hz, 1H), 3.09 – 3.00 (m, 1H), 2.84 (dd, *J* = 9.9, 3.6 Hz, 1H), 2.73 – 2.60 (m, 2H), 2.22 (dt, *J* = 14.9, 3.2 Hz, 1H), 1.93 (d, *J* = 1.4 Hz, 3H), 1.92 – 1.84 (m, 1H), 1.74 (dt, *J* = 12.5, 6.0 Hz, 1H), 1.44 – 1.31 (m, 4H), 1.28 (s, 3H), 1.25 (s, 1H), 1.21 (s, 1H), 1.18 (s, 3H), 1.14 (s, 3H), 1.10 (d, *J* = 6.8 Hz, 3H), 1.00 – 0.97 (m, 12H), 0.93 (t, *J* = 8.0 Hz, 9H), 0.64 (dd, *J* = 16.5, 8.1 Hz, 12H) ppm. **^{13}C-NMR (125 MHz, $CDCl_3$):** δ = 215.4, 170.8, 162.3, 155.1, 137.1,

136.8, 134.5, 131.7, 129.6, 127.0, 126.6, 122.6, 121.7, 79.8, 77.1, 75.7, 62.5, 62.1, 61.4, 53.5, 48.1, 39.9, 36.7, 33.9, 32.2, 31.3, 29.7, 24.9, 23.8, 22.4, 19.6, 17.5, 14.1, 7.2, 7.0, 5.5, 5.3 ppm. **R_f** = 0.48 (EA:Hex = 2:8). **HRMS (ESI, positive):** calc. for $C_{47}H_{76}NO_7SSi_2^+$ $[M+H]^+$ 854.4876, found 854.4864.

STEpo1:

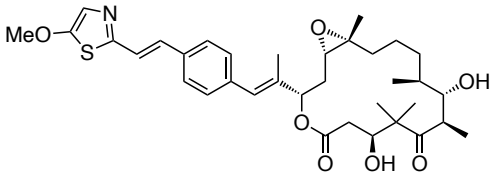

TES protected **STEpo1** (8.3 mg, 9.7 µmol, 1 eq) was dissolved in dry THF (1 mL) and cooled to 0°C. HF•pyr (70%, 40 µL, excess) was added and the reaction mixture was allowed to warm to room temperature. After 5 h, the reaction mixture was carefully quenched with sat. aq. $NaHCO_3$ (10 mL). The two layers were separated, and the aqueous layer was extracted with EA (3 × 10 mL). The combined organic layers were dried over Na_2SO_4 and concentrated under reduced pressure. Purification by prep-HPLC (40→100% MeCN:H_2O) afforded **STEpo1** (1 mg, 1.6 µmol, 16%) as colorless solid.

^{1}H-NMR (500 MHz, $CDCl_3$): δ = 7.46 (d, *J* = 8.3 Hz, 2H), 7.28 (d, *J* = 8.4 Hz, 2H), 7.13 – 7.05 (m, 3H), 6.58 (s, 1H), 5.48 (dd, *J* = 7.0, 4.0 Hz, 1H), 4.08 (dd, *J* = 9.3, 3.1 Hz, 1H), 3.95 (s, 3H), 3.81 (t, *J* = 4.4 Hz, 1H), 3.35 – 3.26 (m, 1H), 2.83 (dd, *J* = 7.2, 5.5 Hz, 1H), 2.57 (dd, *J* = 14.7, 9.6 Hz, 1H), 2.48 (d, *J* = 3.5 Hz, 1H), 2.35 (s, 1H), 2.13 – 2.03 (m, 2H), 2.02 – 1.92 (m, 5H), 1.70 (dd, *J* = 15.1, 7.9 Hz, 3H), 1.57 – 1.43 (m, 3H), 1.35 (s, 3H), 1.30 (s, 3H), 1.18 (d, *J* = 7.0 Hz, 3H), 1.11 (s, 3H), 1.01 (d, *J* = 7.0 Hz, 3H) ppm. **R_f** = 0.24 (EA:Hex = 6:4). **HRMS (ESI, positive)**: calc. for $C_{35}H_{48}NO_7S^+$ $[M+H]^+$ 626.3146, found 626.3144.

TES protected STEpo2:

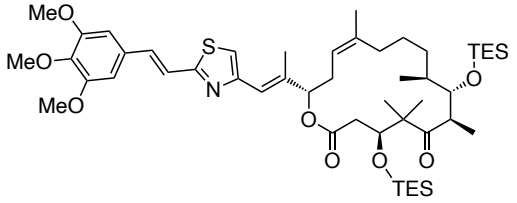

To a solution of styrylthiazole phosphonate **8** (45 mg, 0.11 mmol, 3.5 eq) in dry THF (1.5 mL) was added *n*-BuLi (2.5 M in hexane, 30 µL, 76 µmol, 2.5 eq) and the purple solution was stirred at –78°C for 45 min. A solution of methyl ketone **3** (19 mg, 30 µmol, 1 eq) in THF (1 mL) was added dropwise, and the reaction mixture was allowed to slowly warm to 0°C. After 2 h the orange reaction mixture was quenched with sat. aq. NH_4Cl (2 mL), and transferred to a separation funnel. The two layers were separated, and the aqueous layer was extracted with

EA (3 × 5mL). The combined organic layers were dried over Na_2SO_4 and concentrated under reduced pressure. The obtained residue was purified by normal phase MPLC (0→20% EA:Hex, elutes at 10% EA) to afford TES protected **STEpo2** (12 mg, 13 µmol, 44%) as colorless oil.

^{1}H-NMR (500 MHz, C_6D_6): δ = 7.52 (d, *J* = 16.1 Hz, 1H), 7.35 (d, *J* = 16.1 Hz, 1H), 6.78 (s, 1H), 6.62 (s, 1H), 6.53 (s, 2H), 5.33 (d, *J* = 9.8 Hz, 1H), 5.27 – 5.21 (m, 1H), 4.23 (d, *J* = 8.9 Hz, 1H), 4.15 (d, *J* = 9.4 Hz, 1H), 3.82 (s, 3H), 3.32 (s, 6H), 3.06 – 2.96 (m, 1H), 2.87 – 2.75 (m, 2H), 2.64 (ddd, *J* = 20.2, 11.8, 4.9 Hz, 2H), 2.38 (s, 3H), 2.03 (dd, *J* = 14.3, 6.3 Hz, 1H), 1.93 – 1.78 (m, 4H), 1.75 (s, 3H), 1.39 – 1.34 (m, 2H), 1.21 (d, *J* = 6.9 Hz, 3H), 1.19 (s, 3H), 1.12 – 1.07 (m, 21H), 0.86 – 0.80 (m, 6H), 0.77 (t, *J* = 7.9 Hz, 6H), 0.73 (s, 3H) ppm. **^{13}C-NMR (125 MHz, C_6D_6):** δ = 214.0, 170.9, 166.0, 154.9, 154.4, 140.6, 140.4, 139.4, 135.1, 131.4, 121.2, 120.3, 120.1, 116.7, 105.1, 80.6, 76.7, 60.6, 55.8, 53.4, 48.0, 39.4, 38.1, 32.7, 32.5, 32.0, 30.2, 28.1, 25.2, 23.4, 23.3, 19.5, 17.7, 15.3, 7.5, 7.4, 6.1, 5.9 ppm. **R_f** = 0.56 (EA:Hex = 2:8). **LRMS (APCI, positive):** calc. for $C_{49}H_{80}NO_8SSi_2$ $[M+H]^+$ 898.5138, found 899.5.

STEpo2:

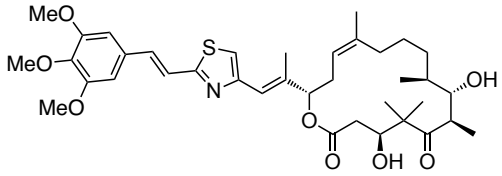

TES protected **STEpo2** (12 mg, 13 µmol, 1 eq) was dissolved in dry THF (1 mL) and cooled to 0°C. HF•pyr (70%, 75 µL, excess) was added and reaction mixture was allowed to warm to room temperature. After 1.5 h, only mono-deprotected TES **STEpo2** was observed. Another 50 µL HF•pyr was added at 0°C and stirring was continued another 2 h at room temperature. The reaction mixture was carefully quenched with sat. aq. $NaHCO_3$ (10 mL). The two layers were separated, and the aqueous layer was extracted with EA (3 × 10 mL). The combined organic layers were dried over Na_2SO_4 and concentrated under reduced pressure. Purification by prep-HPLC (40→100% MeCN:H_2O + 0.1% FA) afforded **STEpo2** (6.5 mg, 9.7 µmol, 73%) as slightly yellowish solid.

^{1}H-NMR (500 MHz, C_6D_6): δ = 7.53 (d, *J* = 16.1 Hz, 1H), 7.30 (d, *J* = 16.1 Hz, 1H), 6.85 (t, *J* = 1.4 Hz, 1H), 6.63 (s, 1H), 6.56 (s, 2H), 5.48 – 5.43 (m, 1H), 5.20 (dd, *J* = 10.2, 5.2 Hz, 1H), 4.22 (dd, *J* = 11.0, 2.8 Hz, 1H), 3.83 (s, 3H), 3.74 (dd, *J* = 4.1, 2.8 Hz, 1H), 3.34 (s, 6H), 2.97 (qd, *J* = 6.8, 2.8 Hz, 1H), 2.69 (dt, *J* = 15.0, 9.8 Hz, 1H), 2.39 (dd, *J* = 14.9, 11.0 Hz, 1H), 2.26 (d, *J* = 1.3 Hz, 4H), 2.18 – 2.10 (m, 2H), 1.81 (dt, *J* = 19.0, 5.7 Hz, 2H), 1.64 (t, *J* = 1.5 Hz, 4H), 1.28 – 1.20 (m, 3H), 1.10 (d, *J* = 6.8 Hz, 3H), 1.03 (d, *J* = 7.0 Hz, 3H), 1.01 (s, 3H), 0.97 (s, 3H) ppm. **^{13}C-NMR (125 MHz, C_6D_6):** δ = 219.6, 170.1, 166.1, 154.6, 154.4, 140.7, 139.6, 138.6, 135.2, 131.4, 121.4, 120.8, 119.7, 116.3, 105.2, 79.4, 74.5, 72.8, 60.6, 55.8, 53.6, 42.1,

40.1, 38.7, 32.8, 32.0, 31.7, 25.9, 23.2, 22.8, 18.4, 16.1, 15.9, 13.9 ppm. $\mathbf{R_f}$ = 0.31 (EA:Hex = 4:6). **HRMS (ESI, positive):** calc. for $C_{37}H_{52}NO_8S^+$ $[M+H]^+$ 670.3408, found 670.3410.

TES protected STEpo3:

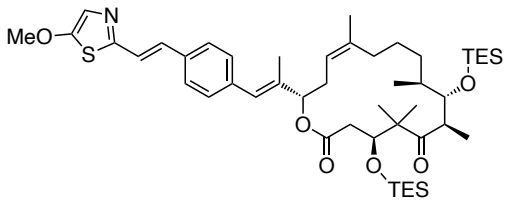

To a solution of styrylthiazole phosphonate **12a** (39 mg, 0.11 mmol, 3 eq) in dry THF (1.5 mL) was added sodium bis(trimethylsilyl)amide (2 M in THF, 44 µL, 88 µmol, 2.5 eq) and the red solution was stirred at –78°C for 50 min. A solution of methyl ketone **3** (22 mg, 35 µmol, 1 eq) in THF (1 mL) was added dropwise, and the reaction mixture was allowed to slowly warm to 0°C. After 2.5 h the reaction mixture was quenched with sat. aq. NH_4Cl (5 mL), and the reaction mixture was allowed to warm to room temperature. The two layers were separated, and the aqueous layer was extracted with EA (3 × 5mL). The combined organic layers were dried over Na_2SO_4 and concentrated under reduced pressure. The obtained residue was purified by normal phase MPLC (5→25% EA:Hex, elutes at 11%) to afford TES protected **STEpo3** (12 mg, 14 µmol, 41%) as colorless oil.

^{1}H-NMR (400 MHz, $CDCl_3$): δ = 7.47 (d, *J* = 8.2 Hz, 2H), 7.29 (d, *J* = 8.1 Hz, 2H), 7.17 (d, *J* = 6.7 Hz, 2H), 7.08 (s, 1H), 6.51 (s, 1H), 5.19 (t, *J* = 8.2 Hz, 1H), 5.12 (d, *J* = 9.9 Hz, 1H), 4.12 (dd, *J* = 8.0, 3.9 Hz, 1H), 3.97 (s, 3H), 3.94 (d, *J* = 9.0 Hz, 1H), 3.11 – 2.98 (m, 1H), 2.73 – 2.68 (m, 2H), 2.44 (d, *J* = 8.5 Hz, 1H), 2.08 (dd, *J* = 14.9, 5.7 Hz, 1H), 1.94 (s, 3H), 1.77 – 1.63 (m, 5H), 1.60 – 1.49 (m, 2H), 1.25 (s, 3H), 1.18 (s, 3H), 1.11 (d, *J* = 7.3 Hz, 6H), 0.99 (t, *J* = 7.8 Hz, 12H), 0.90 (t, *J* = 7.9 Hz, 9H), 0.67 (q, *J* = 8.0 Hz, 6H), 0.59 (q, *J* = 7.5 Hz, 6H) ppm.
^{13}C-NMR (125 MHz, $CDCl_3$): δ = 215.6, 171.1, 162.2, 155.8, 140.6, 138.1, 134.0, 129.7, 127.0, 126.1, 119.4, 80.1, 80.0, 76.1, 61.7, 53.7, 48.0, 39.7, 37.5, 32.6, 32.1, 32.1, 31.3, 29.9, 27.5, 24.4, 24.0, 23.2, 22.8, 19.3, 17.7, 14.6, 14.3, 7.3, 7.1, 5.7, 5.4 ppm. $\mathbf{R_f}$ = 0.28 (EA:Hex = 15:85).
HRMS (ESI, positive): calc. for $C_{47}H_{76}NO_6SSi_2$ $[M+H]^+$ 838.4926, 838.4926 found.

STEpo3:

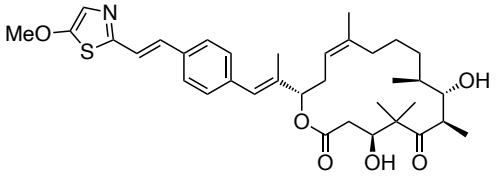

TES protected **STEpo3** (12 mg, 14 µmol, 1 eq) was dissolved in dry THF (2 mL) and cooled to 0°C. HF•pyr (70%, 100 µL, excess) was added and reaction mixture was allowed to warm to room temperature. After 5 h the reaction mixture was carefully quenched with sat. aq.

$NaHCO_3$ (10 mL). The two layers were separated, and the aqueous layer was extracted with EA (3 × 10 mL). The combined organic layers were dried over Na_2SO_4 and concentrated under reduced pressure. Purification by prep-HPLC (40→100% MeCN:H_2O + 0.1% FA) afforded desired product *E*-**STEpo3** (1.7 mg, 28 µmol, 20%) as colorless solid and *Z*-**STEpo3** (1.3 mg, 21 µmol, 25%) as colorless solid.

^{1}H-NMR (500 MHz, C_6D_6): δ = 7.27 (d, *J* = 16.1 Hz, 1H), 7.21 – 7.18 (m, 4H), 7.13 (d, *J* = 12.3 Hz, 1H), 7.03 (s, 1H), 6.72 (s, 1H), 5.45 (dd, *J* = 9.9, 2.2 Hz, 1H), 5.20 (dd, *J* = 10.1, 5.2 Hz, 1H), 4.07 (ddd, *J* = 10.4, 6.7, 2.9 Hz, 1H), 3.73 (s, 1H), 3.17 (s, 3H), 2.93 (qd, *J* = 6.8, 3.0 Hz, 1H), 2.80 (s, 1H), 2.68 (dt, *J* = 15.0, 9.9 Hz, 1H), 2.34 – 2.27 (m, 2H), 2.14 (dd, *J* = 15.3, 2.9 Hz, 1H), 2.11 – 2.07 (m, 1H), 2.00 (d, *J* = 7.0 Hz, 1H), 1.86 (s, 3H), 1.84 – 1.78 (m, 2H), 1.64 (s, 3H), 1.62 – 1.56 (m, 1H), 1.23 – 1.18 (m, 3H), 1.08 (d, *J* = 6.8 Hz, 3H), 1.02 (d, *J* = 7.1 Hz, 3H), 0.92 (s, 3H), 0.89 (s, 3H) ppm. **^{13}C-NMR (125 MHz, C_6D_6):** δ = 219.3, 170.0, 162.7, 154.8, 138.6, 137.7, 137.5, 135.0, 131.7, 129.9, 127.1, 126.8, 123.4, 122.3, 121.4, 79.7, 74.5, 73.1, 60.5, 53.2, 42.3, 40.0, 38.7, 32.7, 31.9, 30.2, 26.1, 23.2, 22.5, 18.8, 16.2, 14.9, 14.0 ppm. **R_f** = 0.43 (EA:Hex = 6:4). **HRMS (ESI, positive)**: calc. for $C_{35}H_{48}NO_6S^+$ $[M+H]^+$ 610.3197, found 610.3201.

STEpo4:

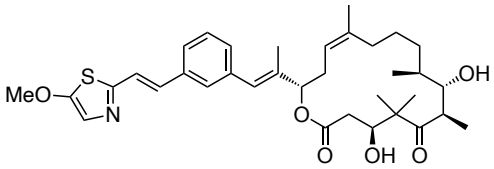

To a solution of styrylthiazole phosphonate **12b** (30 mg, 82 µmol, 4.6 eq) in dry THF (1 mL) was added *n*-BuLi (2 M in THF, 25 µL, 63 µmol, 3.5 eq) and the solution was stirred at –78°C for 1 h. A solution of methyl ketone **3** (11 mg, 18 µmol, 1 eq) in THF (1 mL) was added dropwise, and the reaction mixture was allowed to slowly warm to 0°C. Reaction progress was checked by TLC after 2.5 h, showing a weak fluorescent spot **R_f** = 0.32 (EA:Hex = 1:9). The reaction mixture was quenched with sat. aq. NH_4Cl (4 mL), and the reaction mixture was allowed to warm to room temperature. The two layers were separated, and the aqueous layer was extracted with EA (3 × 5mL). The combined organic layers were dried over Na_2SO_4 and concentrated under reduced pressure. The crude product was filtered over a short silica plug (EA:Hex =3:7) to remove phosphonate **12b** and the filtrate was concentrated. The crude was redissolved in dry THF (1 mL) and cooled to 0°C. HF•pyr (70%, 100 µL, excess) was added and reaction mixture was allowed to warm to room temperature. After 3 h the reaction mixture was carefully quenched with sat. aq. $NaHCO_3$ (10 mL). The two layers were separated, and the aqueous layer was extracted with EA (3 × 10 mL). The combined organic layers were dried over Na_2SO_4 and concentrated under reduced pressure. Purification over prep-HPLC

(40→100% MeCN:H_2O + 0.1% FA) afforded **STEpo4** (0.8 mg, 1.3 µmol, 7%) as colorless solid.

^{1}H-NMR (400 MHz, C_6D_6): δ = 7.37 (s, 1H), 7.27 (s, 1H), 7.23 (s, 1H), 7.21 (s, 1H), 7.08 – 7.04 (m, 2H), 7.01 (s, 1H), 6.73 (s, 1H), 5.46 (dd, *J* = 9.7, 2.1 Hz, 1H), 5.21 (dd, *J* = 9.8, 4.8 Hz, 1H), 4.09 (dd, *J* = 10.8, 2.4 Hz, 1H), 3.73 (t, *J* = 3.3 Hz, 1H), 3.46 (br, 1H), 3.16 (s, 3H), 2.93 (dd, *J* = 6.8, 3.0 Hz, 1H), 2.81 (br, 1H), 2.69 (dt, *J* = 14.8, 9.8 Hz, 1H), 2.32 (dd, *J* = 15.1, 10.9 Hz, 2H), 2.18 – 2.09 (m, 2H), 1.87 – 1.77 (m, 5H), 1.65 (d, *J* = 1.5 Hz, 3H), 1.60 (d, *J* = 4.0 Hz, 1H), 1.23 (s, 3H), 1.07 (d, *J* = 6.8 Hz, 3H), 1.02 (d, *J* = 7.0 Hz, 3H), 0.92 (s, 3H), 0.89 (s, 3H) ppm. **R_f** = 0.51 (EA:Hex = 6:4). **HRMS (ESI, positive):** calc. for $C_{35}H_{48}NO_6S^+$ $[M+H]^+$ 610.3197, found 610.3203.

Synthesis of epothilone methyl ketones

Synthesis of the Epothilone B/ Epothilone D methyl ketones was performed closely following previously reported protocols by Nicolaou et al[2,3] and characterization matched the literature.

Synthesis of methyl ketone 1

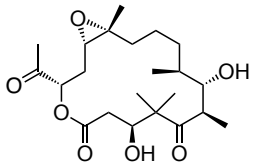

Freshly generated ozone was bubbled through a stirred solution of Epothilone B (117 mg, 230 µmol, 1.0 eq) in dichloromethane (5 mL) at −78°C. The reaction mixture was immediately quenched with dimethyl sulfide (170 µL, 2.31 mmol, 10 eq) when the color turned blue. The reaction mixture was warmed to room temperature and stirred for 1 h before the solvent was removed under reduced pressure and purified by MPLC (20→60% EA:Hex) to give methyl ketone 1 (76 mg, 184 µmol, 80%) as colorless solid and recovered starting material Epothilone B (11 mg, 22 µmol, 9%).

^{1}H-NMR (500 MHz, $CDCl_3$): δ = 5.30 (dd, *J* = 10.5, 1.9 Hz, 1H), 4.30 (dd, *J* = 10.6, 3.2 Hz, 1H), 3.69 (t, *J* = 4.3 Hz, 1H), 3.24 (qd, *J* = 6.8, 4.7 Hz, 1H), 2.82 (dd, *J* = 9.4, 3.1 Hz, 1H), 2.55 (d, *J* = 10.6 Hz, 1H), 2.52 (d, *J* = 10.6 Hz, 1H), 2.34 (dt, *J* = 15.3, 2.6 Hz, 1H), 2.28 (s, 3H), 2.25 (d, *J* = 3.0 Hz, 1H), 1.79 – 1.70 (m, 2H), 1.68 – 1.61 (m, 1H), 1.51 – 1.43 (m, 1H), 1.41 (s, 3H), 1.37 – 1.29 (m, 2H), 1.28 (s, 3H), 1.27 – 1.22 (m, 2H), 1.19 (d, *J* = 6.8 Hz, 3H), 1.08 (s, 3H), 0.98 (d, *J* = 6.9 Hz, 3H) ppm. **^{13}C-NMR (125 MHz, $CDCl_3$):** δ = 220.6, 204.9, 170.7, 76.8, 74.5, 71.6, 62.4, 62.1, 53.4, 42.7, 39.9, 37.4, 32.8, 31.2, 28.9, 26.3, 23.2, 22.5, 22.4, 18.0, 17.2, 14.4 ppm. **R_f** = 0.28 (EA:Hex = 1:1). **LRMS (ESI, positive):** calc for $C_{22}H_{37}O_7^+$ $[M+H]^+$ 413.2534, 413.3 found.

Synthesis of TES protected methyl ketone 2.

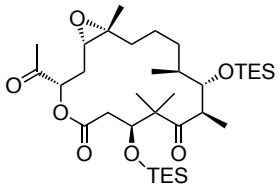

To a stirred solution of methyl ketone **1** (44 mg, 107 µmol, 1 eq) in dry dichloromethane (2 mL) was added 2,6-lutidine (37 µL, 320 µmol, 3 eq) and triethylsilyl trifluoromethanesulfonate (58 µL, 265 µmol, 2.4 eq) at –78°C. The reaction mixture was stirred for 30 min, before quenching with water (5 mL) and warming up to room temperature. The reaction mixture was transferred to a separation funnel and the organic layer was separated. The aqueous layer was extracted with EA (3 × 5 mL) and the combined organic layers were dried over Na_2SO_4. The solvent was removed under reduced pressure and purification by normal phase MPLC (10→20% EA:Hex) afforded desired compound **2** (55 mg, 85.8 µmol, 80%) as colorless foam. **^{1}H-NMR (500 MHz, $CDCl_3$):** δ = 5.01 (dd, *J* = 9.9, 2.1 Hz, 1H), 4.04 (dd, *J* = 10.0, 2.3 Hz, 1H), 3.91 (d, *J* = 9.4 Hz, 1H), 3.02 (dq, *J* = 9.2, 6.7 Hz, 1H), 2.91 (dd, *J* = 16.3, 2.4 Hz, 1H), 2.84 (dd, *J* = 10.1, 4.0 Hz, 1H), 2.75 (dd, *J* = 16.4, 10.0 Hz, 1H), 2.35 (ddd, *J* = 15.0, 4.1, 2.1 Hz, 1H), 2.22 (s, 3H), 1.70 (ddt, *J* = 18.5, 10.1, 4.9 Hz, 2H), 1.63 – 1.53 (m, 2H), 1.52 – 1.43 (m, 2H), 1.38 (d, *J* = 12.1 Hz, 1H), 1.27 (s, 3H), 1.22 (s, 3H), 1.15 (s, 3H), 1.07 (d, *J* = 6.8 Hz, 3H), 1.05 – 1.01 (m, 1H), 0.99 – 0.96 (m, 12H), 0.91 (t, *J* = 7.8 Hz, 9H), 0.64 (q, *J* = 7.8 Hz, 6H), 0.58 (q, *J* = 7.8 Hz, 6H) ppm. **^{13}C-NMR (125 MHz, $CDCl_3$):** δ = 215.2, 203.4, 171.8, 80.2, 76.5, 76.2, 62.5, 62.2, 53.4, 48.5, 39.4, 36.8, 32.0, 31.0, 30.3, 25.9, 24.9, 24.6, 23.6, 22.6, 19.6, 17.8, 7.3, 7.0, 5.7, 5.3 ppm. **R_f** = 0.53 (EA:Hex = 2:8). **LRMS (ESI, positive):** calc for $C_{34}H_{65}O_7Si_2^+$ $[M+H]^+$ 641.4263, 641.3 found.

Synthesis of deepoxidised TES protected methyl ketone 3.

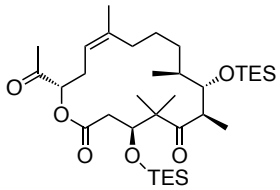

A solution of tungsten hexachloride (27 g, 0.069 mmol, 2.0 eq) in dry THF (2 mL) was cooled to –78°C and n-BuLi (2.5 M in hexanes, 55 µL, 0.137 mmol, 4.0 eq) was added dropwise. The suspension was stirred for 10 min, before the reaction mixture was warmed to 25°C and stirred another 30 min. The black suspension was cooled to –20°C, and a solution of methyl ketone **2** (0.22 mg, 0.034 mmol,1.0 eq) in tetrahydrofuran (1 mL) was added dropwise, and the reaction mixture was warmed to 0°C. After 3 h, the reaction mixture was quenched with sat. aq. NH_4Cl (5 mL), and allowed to warm to room temperature. The reaction mixture was

transferred into a separation funnel and the two phases were separated. The aqueous layer was extracted with ethyl acetate (3 × 5 mL). The combined organic layers were dried over Na_2SO_4, filtered and concentrated under reduced pressure. The obtained residue was purified by MPLC purification (0→15% EA:Hex) to afford deepoxidised methyl ketone **3** (10.6 g, 0.017 mmol, 49%) as a colorless oil.

^{1}H-NMR (500 MHz, $CDCl_3$): δ = 5.16 (t, *J* = 8.2 Hz, 1H), 4.84 (d, *J* = 9.7 Hz, 1H), 4.04 (dd, *J* = 10.4, 1.9 Hz, 1H), 3.91 (d, *J* = 9.1 Hz, 1H), 3.08 – 2.96 (m, 1H), 2.92 (dd, *J* = 15.7, 1.8 Hz, 1H), 2.76 (dd, *J* = 16.2, 10.2 Hz, 1H), 2.54 (dt, *J* = 14.7, 9.8 Hz, 1H), 2.42 (t, *J* = 11.0 Hz, 1H), 2.24 (dd, *J* = 14.7, 7.4 Hz, 1H), 2.19 (s, 3H), 1.78 – 1.69 (m, 2H), 1.69 (s, 3H), 1.55 – 1.48 (m, 2H), 1.22 (s, 3H), 1.14 (s, 3H), 1.09 (d, *J* = 6.7 Hz, 3H), 1.07 – 1.02 (m, 2H), 1.01 – 0.96 (m, 12H), 0.88 (t, *J* = 7.9 Hz, 9H), 0.65 (q, *J* = 7.9 Hz, 6H), 0.56 (q, *J* = 7.8 Hz, 6H) ppm. **R_f** = 0.58 (EA:Hex = 15:85). **LRMS (ESI, positive):** calc for $C_{34}H_{65}O_7Si_2^+$ $[M+H]^+$ 641.4263, 641.3 found.

Synthesis of styrylthiazole phosphonates

Synthesis of styrylthiazole phosphonate 8:

*General remarks: Synthesis of phosphonate photoswitches was performed with as little purification as possible for time efficiency reasons. It is recommended to remove most of the side products after synthesis of **6**.*

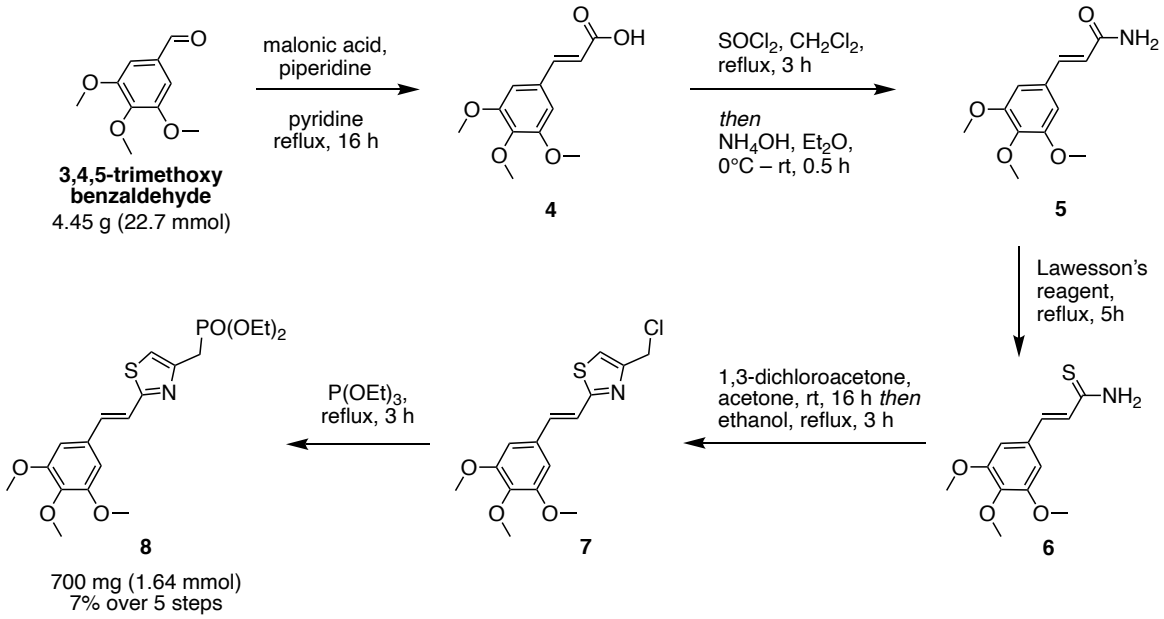

A solution of 3,4,5-trimethoxybenzaldehyde (4.45 g, 22.7 mmol, 1.0 eq.), malonic acid (2.83 g, 27.2 mmol, 1.2 eq) and piperidine (0.5 mL) in pyridine (20 mL) was stirred overnight at reflux. After cooling down to room temperature, the solvent was removed under reduced pressure and redissolved in EA (30 mL). The organic layer was washed with 2 M HCl (15 mL), water

(15 mL) and brine (15 mL), dried over $MgSO_4$ and filtered to afford cinnamic acid **4** (5.40 g, 22.7 mmol, quant.) without further purification.
^{1}H-NMR (400 MHz, $CDCl_3$): δ = 7.71 (d, *J* = 15.9 Hz, 1H), 6.78 (s, 2H), 6.36 (d, *J* = 15.9 Hz, 1H), 3.90 (s, 6H), 3.90 (s, 3H) ppm. **^{13}C-NMR (100 MHz, $CDCl_3$):** δ = 172.1, 153.6, 147.2, 140.7, 129.6, 116.5, 105.7, 61.1, 56.3 ppm. **R_f** = 0.57 (EA:Hex:FA = 1:1:0.01). **HRMS (EI, positive):** calc. for $C_{12}H_{14}O_5^{+\bullet}$ $[M]^{+\bullet}$ 238.0836, found 238.0836.

The cinnamic acid **4** (5.40 g, 22.7 mmol, 1 eq) was dissolved in dichloromethane (100 mL). Thionyl chloride (16.5 mL, 227 mmol, 10 eq.) was added slowly and the reaction mixture was stirred at reflux for 3 h. The solvent was removed under reduced pressure and redissolved in Et_2O (80 mL) and NH_4OH (10 mL) was added slowly at 0°C. Stirring was continued for 30 min. The precipitate was washed with Et_2O several times to give cinnamic amide **5** (4.95 g, 20.9 mmol, 91%).
^{1}H-NMR (400 MHz, DMSO-*d_6*): δ = 7.49 (s, 1H), 7.35 (d, *J* = 15.8 Hz, 1H), 7.06 (s, 1H), 6.88 (s, 2H), 6.57 (d, *J* = 15.8 Hz, 1H), 3.80 (s, 6H), 3.67 (s, 3H) ppm. **^{13}C-NMR (100 MHz, DMSO-*d_6*):** δ = 166.9, 153.1, 139.5, 138.7, 130.6, 121.7, 105.0, 60.2, 55.9 ppm. **R_f** = 0.23 (EA = 100%). **HRMS (ESI, positive):** calc. for $C_{12}H_{16}NO_4^+$ $[M+H]^+$ 238.1074, found 238.1075.

The cinnamic amide **5** (5.40 g, 22.7 mmol, 1 eq) was dissolved in THF (100 mL). Lawesson's reagent (4.95 g, 11.3 mmol, 0.5 eq.) was added portionwise and the reaction mixture was stirred at reflux for 5 h. The solvent was removed under reduced pressure and redissolved in dichloromethane (100 mL) transferred into a separation funnel and washed with 2M HCl (3 × 30 mL) and brine (30 mL), dried over $MgSO_4$ and filtered. All volatiles were removed by rotary evaporation and filtered. Purification by normal phase MPLC (40→60% EA:Hex, elutes at 60% EA) to remove most of the Lawesson's reagent byproducts afforded cinnamic thioamide **6** (840 mg, 3.32 mmol, 14% over 3 steps).
^{1}H-NMR (400 MHz, $CDCl_3$): δ = 7.71 (d, *J* = 15.8 Hz, 1H), 6.78 (s, 2H), 6.36 (d, *J* = 15.8 Hz, 1H), 3.90 (s, 6H), 3.89 (s, 3H) ppm. **^{13}C-NMR (100 MHz, $CDCl_3$):** δ = 172.1, 153.6, 147.2, 140.7, 129.6, 116.5, 105.7, 61.1, 56.3 ppm. **R_f** = 0.26 (EA:Hex = 1:1). **HRMS (ESI, positive):** calc. for $C_{12}H_{16}NO_3S^+$ $[M+H]^+$ 254.0845, found 254.0847.

A solution of cinnamic thioamide **6** (840 mg, 3.32 mmol, 1 eq) in acetone (25 mL) was added dropwise to a solution of 1,3-dichloroacetone (421 mg, 3.32 mg, 1 eq) in acetone (25 mL) at 50°C. The reaction mixture was allowed to cool down to room temperature and stirred overnight. The acetone was removed under reduced pressure, redissolved in ethanol (30 ml) and refluxed for 3 h. After cooling down to room temperature the solvent was removed *in*

vacuo and purified by MPLC (30→40% EA:Hex) to give compound **7** (811 mg, 2.49 mmol, 75%) as slightly yellowish solid.

^{1}H NMR (400 MHz, $CDCl_3$): δ = 7.33 (d, *J* = 16.2 Hz, 1H), 7.24 – 7.16 (m, 2H), 6.76 (s, 2H), 4.69 (d, *J* = 0.7 Hz, 2H), 3.90 (s, 6H), 3.88 (s, 3H) ppm. **^{13}C-NMR (100 MHz, $CDCl_3$):** δ = 168.0, 153.6, 152.3, 139.5, 136.0, 131.0, 120.1, 116.6, 104.5, 61.1, 56.3, 40.5 ppm. **R_f** = 0.38 (EA:Hex = 3:7). **HRMS (ESI, positive):** calc. for $C_{15}H_{17}NO_3ClS^+$ $[M+H]^+$ 326.0612, found 326.0615.

A stirred solution styrylthiazole **7** (811 mg, 2.49 mmol, 1 eq) in triethyl phosphite (6 mL, 35 mmol, 10.5 eq) was heated to 160 °C. After 3 h, the triethyl phosphite was removed under a steady flow of nitrogen gas, and the reaction mixture was allowed to cool to 25°C. The crude material was purified by normal phase MPLC (20→100% EA:Hex, elutes at 100% EA) to give stryrylthiazole phosphonate **8** (700 mg, 1.64 mmol, 66%) as yellow oil.

^{1}H-NMR (500 MHz, $CDCl_3$): δ = 7.30 (d, *J* = 16.1 Hz, 1H), 7.19 (dd, *J* = 16.1, 0.7 Hz, 1H), 7.16 (d, *J* = 3.4 Hz, 1H), 6.75 (s, 2H), 4.11 (dq, *J* = 8.3, 7.1 Hz, 4H), 3.90 (s, 6H), 3.87 (s, 3H), 3.40 (dd, *J* = 21.0, 0.8 Hz, 2H), 1.30 (t, *J* = 7.1 Hz, 6H) ppm. **^{13}C-NMR (125 MHz, $CDCl_3$):** δ = 166.5, 153.6, 147.5, 147.4, 139.1, 134.4, 131.4, 121.0, 115.6, 115.6, 104.3, 62.5, 62.4, 61.1, 56.3, 30.3, 29.1, 16.6, 16.5 ppm. **R_f** = 0.13 (EA:Hex = 9:1). **HRMS (ESI, positive):** calc. for $C_{19}H_{27}NO_6PS^+$ $[M+H]^+$ 428.1291, found 428.1293.

Synthesis of styrylthiazole phosphonate 12a

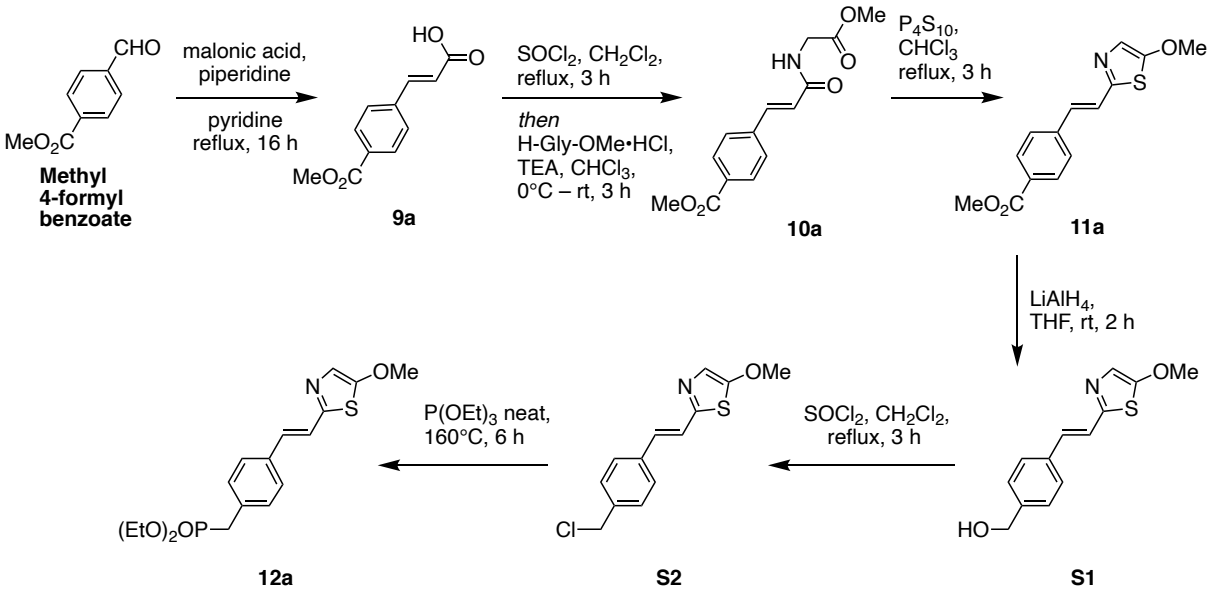

A mixture of methyl 4-formylbenzoate (1.64 g, 10 mmol, 1 eq), malonic acid (1.25 g, 12 mmol, 1.2 eq) and piperidine (99 µL, 1 mmol, 0.1 eq) in pyridine (20 mL) was refluxed overnight. The reaction mixture was cooled down to room temperature, the solvent was removed, redissolved

in EA (30 mL) and transferred into a separation funnel. The organic layer was washed with 2M HCl (2 × 20 mL), water (20 mL) and brine (20 mL). After drying over $MgSO_4$, the solvent was filtered and concentrated *in vacuo* to give crude cinnamic acid **9a** (2.06 g, 10 mmol, quant.) as colorless solid, which was directly resuspended in DCM (30 mL). $SOCl_2$ (7.25 mL, 10 mmol, 10 eq) was added in a dropwise manner. The reaction mixture was stirred at reflux for 1.5 h, cooled down to room temperature and all volatiles were removed by rotary evaporation. The residuals were redissolved in $CHCl_3$ (30 mL) and added slowly to a stirring suspension of glycine methyl ester hydrochloride (1.38 g, 11 mmol, 1.1 eq) and TEA (3.1 mL, 22 mmol, 2.2 eq) at 0°C. The reaction mixture was allowed to warm up to room temperature and stirring was continued for 3 h. The solution was transferred into a separation funnel and washed with water (20 mL) and brine (20 mL), dried over $MgSO_4$, filtered and concentrated under reduced pressure to give crude amide **10a**, which was directly redissolved in chloroform (50 mL) and phosphorus pentasulfide (4.45 g, 10 mmol, 1 eq) was added. The reaction mixture was stirred at 80°C for 3 h after cooling down to room temperature the reaction was carefully quenched with 2M NaOH (100 mL) and extracted with EA (5 x 40 mL). The combined organic layers were dried over $MgSO_4$, filtered and purified by normal phase MPLC (10→40% EA:Hex) to give styrylthiazole **11a** (678 mg, 2.46 mmol, 25% over three steps) as brown solid.
^{1}H-NMR (500 MHz, $CDCl_3$): δ = 8.02 (d, *J* = 8.4 Hz, 2H), 7.53 (d, *J* = 8.5 Hz, 2H), 7.22 (s, 1H), 7.11 (d, *J* = 16.3 Hz, 1H), 7.09 (d, *J* = 0.8 Hz, 1H), 3.95 (s, 3H), 3.91 (s, 3H) ppm. **^{13}C-NMR (125 MHz, $CDCl_3$):** δ = 166.8, 163.0, 154.3, 140.5, 130.7, 130.2, 129.8, 126.7, 125.0, 122.2, 61.6, 52.3 ppm. **R_f** = 0.29 (EA:Hex = 3:7). **HRMS (ESI, positive):** calc. for $C_{14}H_{14}NO_3S^+$ $[M+H]^+$ 276.0689, found 276.0691.

11a (552 mg, 2 mmol, 1 eq) was dissolved in dry THF (20 mL) and $LiAlH_4$ (2.21 mL, 2.21 mmol, 1.1 eq) was added dropwise at 0°C. The mixture was stirred at room temperature until complete reduction, and then cooled to 0°C, quenched with ice water, and filtered through Celite. The filtrate was dried over $MgSO_4$ and concentrated *in vacuo* to give benzyl alcohol **S1** (495 mg, 2 mmol, quant.) as colorless solid.
^{1}H-NMR (400 MHz, $CDCl_3$): δ = 7.38 (d, *J* = 8.0 Hz, 2H), 7.26 (d, *J* = 7.9 Hz, 2H), 7.01 (d, *J* = 0.9 Hz, 2H), 6.96 (s, 1H), 4.61 (s, 2H), 3.85 (d, *J* = 0.9 Hz, 3H) ppm. **^{13}C-NMR (125 MHz, $CDCl_3$):** δ = 162.4, 155.2, 141.4, 135.5, 131.9, 127.6, 127.2, 122.8, 121.8, 65.2, 61.6 ppm. **R_f** = 0.45 (EA:Hex = 1:1). **HRMS (ESI, positive):** calc. for $C_{13}H_{14}NO_2S^+$ $[M+H]^+$ 248.0740, found 248.0742.

The benzyl alcohol **S1** (495 mg, 2 mmol, 1 eq) was dissolved in DCM (20 mL) and $SOCl_2$ (0.73 ml, 10.1 mmol, 5 eq) and DMF (0.5 mL) was added at 0°C. The reaction mixture was

stirred at room temperature for 2 h before all volatiles were removed under reduced pressure and purified by normal phase MPLC (10→80% EA:Hex, elutes at 40% EA) to give benzyl chloride **S2** (460 mg, 1.73 mmol, 87%).

^{1}H-NMR (400 MHz, $CDCl_3$): δ = 7.48 (d, *J* = 8.3 Hz, 2H), 7.39 (d, *J* = 8.3 Hz, 2H), 7.12 (s, 1H), 7.11 (s, 1H), 7.08 (s, 1H), 4.59 (s, 2H), 3.96 (s, 3H) ppm. **^{13}C-NMR (125 MHz, $CDCl_3$):** δ = 162.5, 154.8, 137.7, 136.2, 131.3, 129.1, 127.1, 123.3, 121.7, 61.4, 45.9 ppm. **R_f** = 0.45 (EA:Hex = 4:6). **HRMS (ESI, positive):** calc. for $C_{13}H_{13}ClNOS^+$ $[M+H]^+$ 266.0401, found 266.0405.

The benzyl chloride **S2** (460 mg, 1.73 mmol, 1 eq) was dissolved in 2 mL triethyl phosphite and stirred at 160°C for 6 h. The solvent was removed over a steady stream of N_2 gas. And the remaining crude was purified over normal phase MPLC (10→100% EA:Hex, elutes at 100% EA) to give phosphonate **12a** (470 mg, 1.28 mmol, 74%) as a yellow oil.

^{1}H-NMR (400 MHz, $CDCl_3$): δ = 7.43 (dd, *J* = 8.4, 1.2 Hz, 2H), 7.29 (dd, *J* = 8.3, 2.5 Hz, 2H), 7.08 (s, 2H), 7.05 (s, 1H), 4.02 (dqd, *J* = 8.2, 7.1, 2.0 Hz, 4H), 3.94 (s, 3H), 3.15 (d, *J* = 21.9 Hz, 2H), 1.25 (td, *J* = 7.1, 0.5 Hz, 6H) ppm. **^{13}C-NMR (100 MHz, $CDCl_3$):** δ = 162.3, 155.0, 134.7, 134.6, 132.2, 132.1, 131.6, 131.6, 130.3, 130.2, 127.0, 127.0, 122.6, 122.6, 121.7, 62.2, 62.2, 61.4, 34.4, 33.0, 16.4, 16.4 ppm. **R_f** = 0.14 (EA:Hex = 9:1). **HRMS (ESI, positive):** calc. for $C_{17}H_{23}NO_4PS^+$ $[M+H]^+$ 368.1080, found 368.1083.

Synthesis of styrylthiazole phosphonate 12b

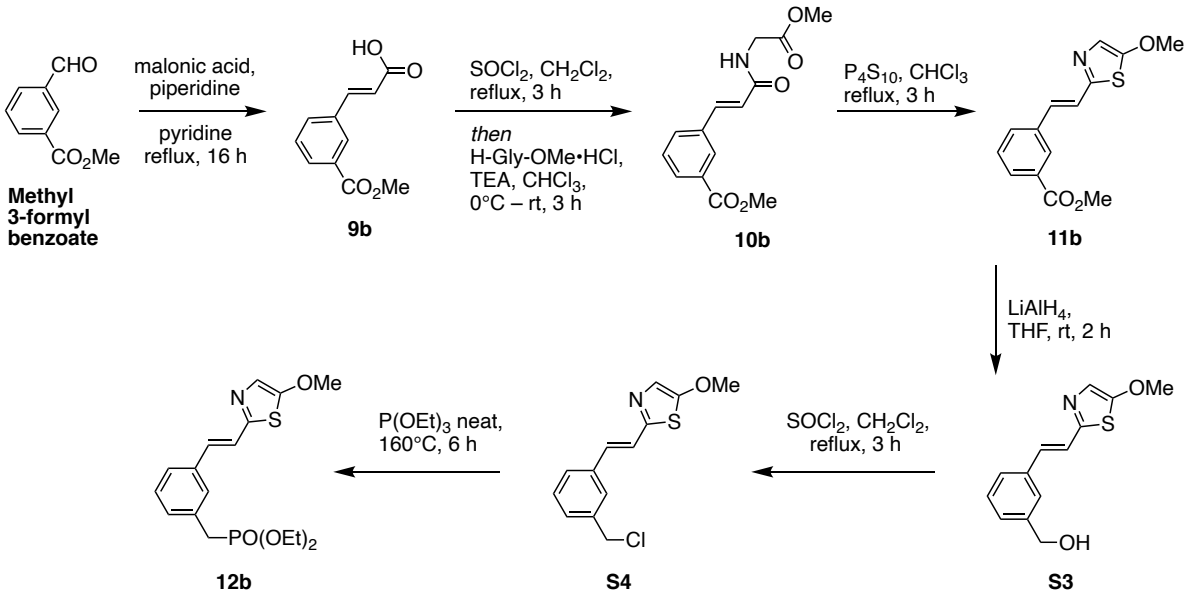

Styrylthiazole **11b** was synthesized following the same procedures for **11a**, starting from Methyl 3-formylbenzoate (2 g, 12.2 mmol, 1 eq) to give **11b** (766 mg, 2.78 mmol, 23% over three steps) as brown solid.

^{1}H-NMR (400 MHz, $CDCl_3$): δ = 8.12 (t, *J* = 1.8 Hz, 1H), 7.91 (ddd, *J* = 7.8, 1.7, 1.2 Hz, 1H), 7.64 – 7.58 (m, 1H), 7.39 (t, *J* = 7.8 Hz, 1H), 7.15 (d, *J* = 16.3 Hz, 1H), 7.08 (d, *J* = 16.3 Hz, 1H), 7.05 (s, 1H), 3.91 (s, 3H), 3.90 (s, 3H) ppm. **^{13}C-NMR (100 MHz, $CDCl_3$):** δ = 166.7, 162.6, 154.3, 136.3, 130.8, 130.8, 130.7, 129.3, 128.9, 127.9, 123.8, 121.9, 61.4, 52.2 ppm. **R_f** = 0.51 (EA:Hex = 1:1). **HRMS (ESI, positive):** calc. for $C_{14}H_{14}NO_3S^+$ $[M+H]^+$ 276.0689, found 276.0687.

Reduction of **11b** (433 mg, 2 mmol, 1 eq) following the same procedure as for benzyl alcohol **S1** gave benzyl alcohol of **S3** (367 mg, 1.48 mmol, 94%).
^{1}H-NMR (500 MHz, $CDCl_3$): δ =7.50 (s, 1H), 7.42 (d, *J* = 7.6 Hz, 1H), 7.36 (t, *J* = 7.6 Hz, 1H), 7.30 (d, *J* = 7.5 Hz, 1H), 7.13 (d, *J* = 1.8 Hz, 2H), 7.06 (s, 1H), 4.72 (s, 2H), 3.95 (s, 3H) ppm. **^{13}C-NMR (125 MHz, $CDCl_3$):** 162.5, 155.1, 141.6, 136.4, 131.9, 129.2, 127.2, 126.2, 125.4, 123.1, 121.9, 65.3, 61.6 ppm. **R_f** = 0.20 (EA:Hex = 3:7). **HRMS (ESI, positive):** calc. for $C_{13}H_{14}NO_2S^+$ $[M+H]^+$ 248.0740, found 248.0739.

Chlorination of benzyl alcohol of **S3** (330 mg, 1.33 mg, 1 eq) was obtained following the same the same procedure as for benzyl chloride **S2** to yield benzyl chloride **S4** (315 mg, 1.19 mmol, 89%).
^{1}H-NMR (400 MHz, $CDCl_3$): δ = 7.50 (d, *J* = 1.8 Hz, 1H), 7.45 (dt, *J* = 7.5, 1.6 Hz, 1H), 7.36 (t, *J* = 7.5 Hz, 1H), 7.32 (dt, *J* = 7.7, 1.6 Hz, 1H), 7.15 (d, *J* = 16.2 Hz, 1H), 7.10 (d, *J* = 16.1 Hz, 2H), 4.60 (s, 2H), 3.96 (s, 3H) ppm. **^{13}C-NMR (100 MHz, $CDCl_3$):** δ = 162.6, 154.8, 138.2, 136.7, 131.4, 129.4, 128.7, 127.1, 126.8, 123.5, 122.0, 61.6, 46.1 ppm. **R_f** = 0.49 (EA:Hex = 3:7). **HRMS (ESI, positive):** calc. for $C_{13}H_{13}ClNOS^+$ $[M+H]^+$ 266.0401, found 266.0400.

Styrylthiazole phosphonate **12b** was synthesized from the benzyl chloride of **S4** (315 mg, 1.19 mmol, 1 eq), following the same procedure as for phosphonate **12a** to obtain desired product **12b** (211 mg, 0.574 mmol, 49%) as yellow oil.
^{1}H-NMR (400 MHz, $CDCl_3$): δ = 7.43 – 7.34 (m, 2H), 7.31 (t, *J* = 7.6 Hz, 1H), 7.24 (ddt, *J* = 7.6, 2.9, 1.5 Hz, 1H), 7.10 (s, 1H), 7.10 (s, 1H), 7.06 (s, 1H), 4.03 (dqd, *J* = 8.3, 7.1, 2.1 Hz, 4H), 3.94 (s, 3H), 3.16 (d, *J* = 21.6 Hz, 2H), 1.25 (t, *J* = 7.1 Hz, 6H) ppm. **^{13}C-NMR (100 MHz, $CDCl_3$):** δ = 162.4, 154.9, 136.3, 136.3, 132.5, 132.4, 131.8, 130.1, 130.0, 129.1, 129.1, 128.4, 128.4, 125.3, 125.3, 123.0, 121.8, 62.3, 62.2, 61.5, 34.5, 33.1, 16.5, 16.5 ppm. **R_f** = 0.12 (EA:Hex = 9:1). **HRMS (ESI, positive):** calc. for $C_{17}H_{23}NO_4PS^+$ $[M+H]^+$ 368.1080, found 368.1083.

Synthesis of SBTax

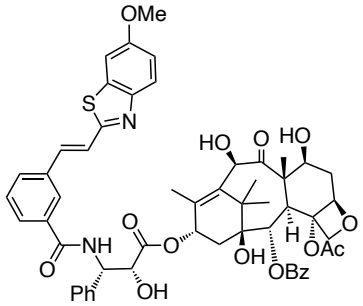

A flask was charged with docetaxel (19 mg, 24 µmol, 1 eq) and DCM (2 mL) and the solution was stirred at 0°C for 2 min. TFA (2 mL) was added and the mixture was stirred at 0°C for 1 hour. The solution was added into rapidly stirred sat. aq. $NaHCO_3$ (15 mL). Solid $NaHCO_3$ was added until all TFA was neutralized. The mixture was extracted with DCM (3 × 10 mL). The combined organic layers were washed with sat. aq. $NaHCO_3$ (10 mL), brine (10 mL), dried on Na_2SO_4, filtered and concentrated to give crude deprotected docetaxel as a colorless foam. The crude was dissolved in DMF (1 mL). The SBT photoswitch (22.4 mg, 72 µmol 3 eq) was dissolved in DMF (1 mL), HOBt•H_2O (8.1 mg, 60 µmol, 2.5 eq) and EDCI (8.4 mg, 54 µmol, 2.25 eq) were added and the solution stirred at room temperature for 5 min. DIPEA (25 µL,144 µmol, 6.0 eq) was added and stirring was continued for 10 min. The solution of crude deprotected docetaxel was added and the solution was stirred for 12 h at room temperature, then poured into 10% aq. $NaHCO_3$ (20 mL) and extracted with DCM (3 × 10 mL). The combined organic layers were washed with sat. aq. $NaHCO_3$ (10 mL), sat. aq. LiCl (10 mL), brine (10 mL), dried on Na_2SO_4, filtered and concentrated to a yellow solid. Chromatography on silica (EA:Hex = 3:7→1:1 then DCM:MeOH = 1:0→9:1) yielded **SBTax** as a colorless solid (6 mg, 6 µmol, 25%).

^{1}H-NMR (400 MHz, $CDCl_3$): δ = 8.14 (d, *J* = 7.3 Hz, 2H), 7.92 (s, 1H), 7.86 (d, *J* = 9.0 Hz, 1H), 7.73 (d, *J* = 7.8 Hz, 1H), 7.67 (d, *J* = 7.8 Hz, 1H), 7.61 (t, *J* = 7.3 Hz, 1H), 7.54 – 7.30 (m, 10H), 7.20 (d, *J* = 9.0 Hz, 1H), 7.07 (dd, *J* = 9.0, 2.5 Hz, 1H), 6.25 (t, *J* = 8.8 Hz, 1H), 5.85 – 5.79 (m, 1H), 5.69 (d, *J* = 7.1 Hz, 1H), 5.20 (s, 1H), 4.96 (d, *J* = 9.3 Hz, 1H), 4.81 (s, 1H), 4.35 – 4.17 (m, 4H), 3.93 (d, *J* = 7.1 Hz, 1H), 3.89 (s, 3H), 3.64 (s, 1H), 2.61 (dt, *J* = 14.9, 8.1 Hz, 1H), 2.42 (s, 3H), 2.31 (t, *J* = 8.8 Hz, 2H), 1.89 (t, *J* = 12.8 Hz, 1H), 1.79 (m, 5H), 1.78 – 1.71 (m, 1H), 1.22 (s, 3H), 1.13 (s, 3H) ppm. **^{13}C-NMR (100 MHz, $CDCl_3$):** δ = 211.4, 172.5, 170.9, 167.1, 166.7, 164.2, 158.3, 148.3, 138.1, 136.4, 136.3, 135.9, 135.5, 134.7, 133.9, 130.7, 130.4, 129.5, 129.3, 129.2, 128.9, 128.5, 127.7, 127.2, 125.8, 123.8, 123.6, 116.0, 104.2, 84.3, 81.4, 78.9, 74.9, 74.7, 73.6, 72.5, 72.2, 57.8, 56.0, 55.4, 46.8, 43.2, 37.3, 36.0, 29.9, 26.8, 22.7, 20.6, 14.7, 10.1 ppm. $\mathbf{R_f}$ = 0.22 (DCM:MeOH = 97:3). **HRMS (ESI, positive):** calc. for $C_{55}H_{57}N_2O_{14}S^+$ $[M+H]^+$ 1001.3525, found 1001.3517.

Synthesis of SBT photoswitch

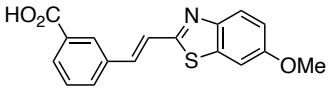

Was prepared following a procedure from Gao et al.[4] from 6-methoxy-2-methylbenzothiazole (358 mg, 2 mmol, 1 eq) and methyl 3-formylbenzoate (328 mg, 2 mmol, 1 eq). A light-yellow solid crashed out of DMSO. The precipitate was collected by filtration and washed with H_2O (2 × 50 mL), acetone (2 × 50 mL) and methanol (2 × 50 mL). No further purification was needed. The product was obtained as a light-yellow solid (468 mg, 1.49 mmol, 75%).

^{1}H-NMR (400 MHz, DMSO-*d*$_6$): δ = 8.25 (t, *J* = 1.8 Hz, 1H), 8.03 (dt, *J* = 7.9, 1.5 Hz, 1H), 7.93 (dt, *J* = 7.7, 1.3 Hz, 1H), 7.87 (d, *J* = 8.9 Hz, 1H), 7.68 (d, *J* = 2.6 Hz, 1H), 7.66 – 7.63 (m, 2H), 7.56 (t, *J* = 7.7 Hz, 1H), 7.11 (dd, *J* = 8.9, 2.6 Hz, 1H), 3.85 (s, 3H), 2.54 (s, 1H) ppm. **^{13}C-NMR (100 MHz, DMSO-*d*$_6$):** δ =167.0, 163.6, 157.7, 147.9, 135.8, 135.8, 135.3, 131.5, 131.2, 129.8, 129.2, 128.5, 123.2, 123.1, 115.9, 104.8, 55.8 ppm. **R_f** = 0.30 (DCM:MeOH = 97:3). **HRMS (EI, positive):** calc. for $C_{17}H_{12}NO_3S^+$ $[M-H]^+$ 310.0532, found 310.0521.

Part B: Photocharacterization

Absorption spectra in cuvette ("UV-Vis") were acquired on a Cary 60 UV-Vis Spectrophotometer from Agilent (1 cm pathlength). For photoisomerisation measurements, Hellma microcuvettes (HL105-200-15-40) taking 150 µL volume to top of optical window were used with the test solution concentrations of 10-20 µM. Measurements were performed in pure DMSO or in PBS/DMSO 1:1 indicated by asterisk. Photoisomerisations and relaxation monitoring (**Fig S1c**) were performed at room temperature unless indicated otherwise. Medium-power LEDs (H2A1-models spanning 360–490 nm from Roithner Lasertechnik) were used to deliver high-intensity and relatively monochromatic light (FWHM ~25 nm) into the cuvette, for rapid PSS determinations (**Fig S1a,d**) that were also predictive of what would be obtained in LED-illuminated cell culture. Spectra of pure *E* and *Z* isomers (**Fig S1b**) were acquired from the inline Diode Array Detector during analytical separation on the HPLC (injection of 5-10 µL, 5→100% MeCN:H_2O over 20 min), after a DMSO stock (0.5 – 2.5mM) was irradiated with a 395 nm LED (~ 5 min) or from the inline Diode Array Detector during **STEpo** purification on the prep-HPLC.

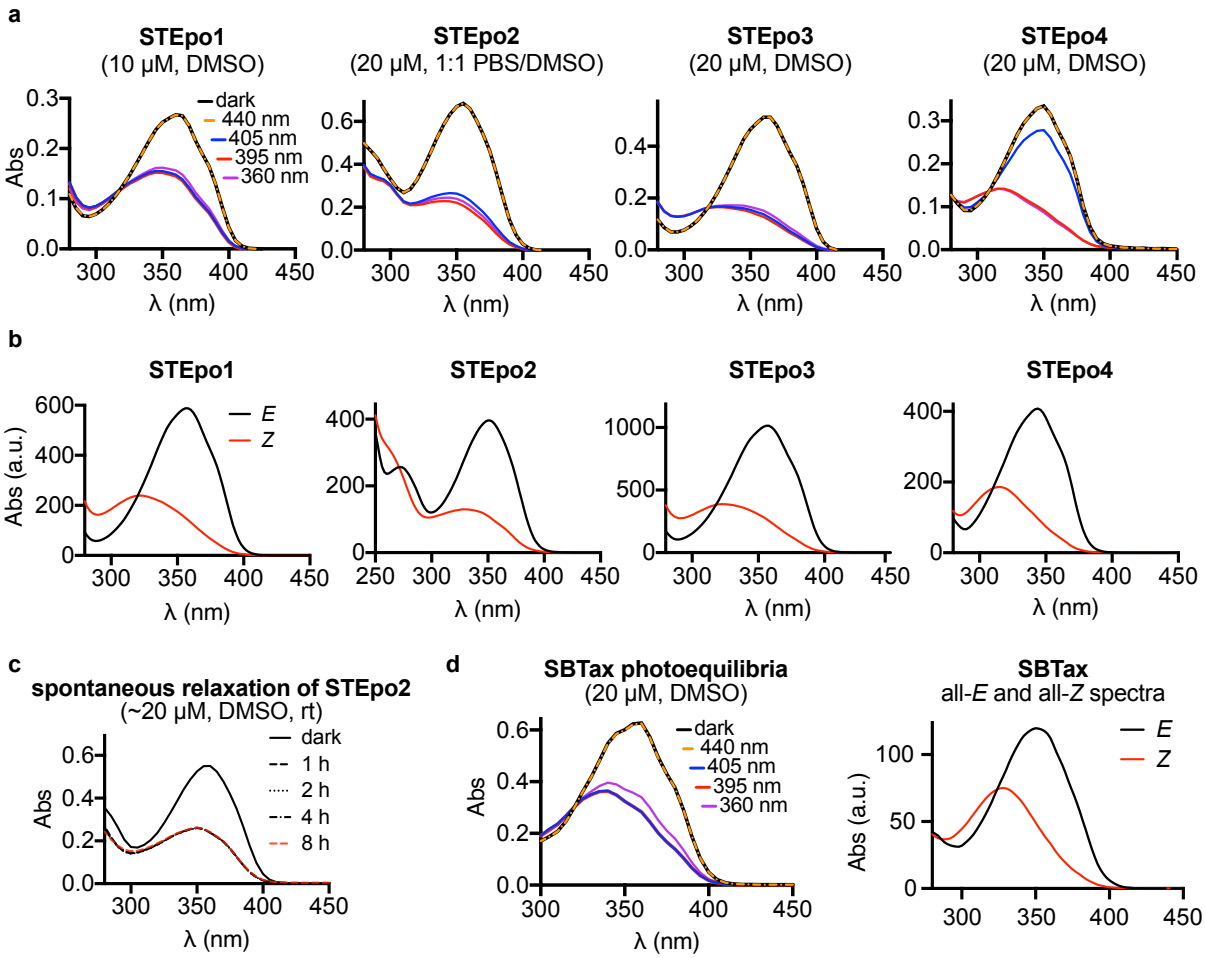

Fig S1: (a) UV-Vis spectra of **STEpo**s at various photostationary states, shows that the ST photoswitch scaffold photoisomerizes from an all-*E* isomer state to a *Z*-isomer enriched state when irradiated with UV light (~400 nm). **(b)** all-*E* and all-*Z* spectra obtained from inline HPLC-DAD show that PSS spectra of **STEpos** irradiated with 395 nm photoisomerization **(c) STEpo2** shows no spontaneous relaxation after illumination with 395 nm light at room temperature over 8 hours in DMSO. **(d)** Photocharacterization of **SBTax**.

Part C: Biological Data

Tubulin polymerisation

99% tubulin from porcine brain was obtained from Cytoskeleton Inc. (cat. #T240). The polymerisation reaction was performed at 5 mg/mL tubulin, in polymerisation buffer BRB80 (80 mM piperazine-N,N′-bis(2-ethanesulfonic acid) (PIPES) pH = 6.9; 0.5 mM EGTA; 2 mM $MgCl_2$), in a cuvette (120 µL final volume, 1 cm path length) in a Agilent CaryScan 60 with Peltier cell temperature control unit maintained at 37°C; with glycerol (10 µL). Tubulin was first incubated for 10 min at 37°C with "lit"- (395 nm-pre-illuminated; mostly-*Z*-), dark- (all-*E*) **STEpo** (final concentration 1 µM) or docetaxel (positive ctrl, 10 µM) in buffer with 3% DMSO, without GTP. Then GTP was added to achieve final GTP concentration 1 mM (with mixing), and the change in absorbance at 340 nm was monitored for 15 min, scanning at 15 s intervals.

General cell culture

HeLa and Jurkat cells were maintained under standard cell culture conditions in Dulbecco's modified Eagle's medium (DMEM; PAN-Biotech: P04-035550) supplemented with 10% fetal calf serum (FCS), 100 U/mL penicillin and 100 U/mL streptomycin. Cells were grown and incubated at 37°C in a 5% CO_2 atmosphere. Cells were typically transferred to phenol red free medium prior to assays (DMEM; PAN-Biotech: P04-03591). Substrates and cosolvent (DMSO; 1% final concentration) were added *via* a D300e digital dispenser (Tecan). Cells were either incubated under "lit" or "dark" conditions; "lit" indicates a pulsed illumination protocol was applied by multi-LED arrays to create the *Z*-isomers of the compounds in *situ* in cells and then maintain the wavelength-dependent PSS isomer ratio throughout the experiment, as described previously.[4] Typical "lit" timing conditions were 75 ms pulses of ~1 mW/cm^2 applied every 15 s. "Dark" indicates that **STEpo** biostocks were used with an all-*trans* state, as determined by analytical HPLC, kept in the dark at 4°C, applied while working under red-light conditions, and cells were then incubated in light-proof boxes to shield from ambient light, thereby maintaining the all-*E*-isomer population throughout the experiment.

Resazurin antiproliferation assay

HeLa cells were seeded in 96-well plates at 5,000 cells/well and left to adhere for 24 h before treating with test compounds. *E*-**STEpos** were added for 48 h (final well volume 100 µL, 1% DMSO; three technical replicates); the "cosolvent control" ("ctrl") indicates treatment with DMSO only. Cells were then treated with Resazurin 150 mg/mL for 3 h. Fluorescence was measured at 590 nm (excitation 544 nm) using a FLUOstar Omega microplate reader (BMG Labtech). Absorbance data was averaged over the technical replicates, then normalized to viable cell count from the cosolvent control cells (%control) as 100%, where 0% viability was assumed to correspond to fluorescence signal in PBS only with no cells. Three independent experiments were performed. Data were plotted against the log of **STEpo** concentration ($\log_{10}$([**STEpo**]) (M)) with mean ±SD.

Immunofluorescence staining

HeLa cells were seeded on glass coverslips in 24-well plates (50,000 cells/well) and treated with **STEpo2** the next day under "dark" or "lit" conditions for 24 h. Cells were washed with pre-warmed (37°C) MTSB buffer (80 mM PIPES pH 6.8; 1 mM $MgCl_2$, 5 mM ethylene glycol tetraacetic acid (EGTA) dipotassium salt; 0.5% Triton X-100) for 30 s then fixed with 0.5% glutaraldehyde for 10 min. After quenching with 0.1% $NaBH_4$ (7 min), samples were blocked with PBS + 10% FCS (30 min). The cells were treated with primary antibody (1:400 rabbit alpha-tubulin; Abcam ab18251) in PBS containing 10% FCS for 1 h and then washed with

PBS. Cells were incubated with secondary antibody (1:400 goat-anti-rabbit Alexa fluor 488; Abcam ab150077) in PBS containing 10% FCS for 1 h. After washing with PBS, the coverslips were mounted onto glass slides using Roti-Mount FluorCare DAPI (Roth) and imaged with a Zeiss LSM Meta confocal microscope (CALM platform, LMU). Images were processed using the free Fiji software. Postprocessing was only performed to improve visibility.

In vitro microtubule dynamics imaging

Reagents: GMPCPP was obtained from Jena Biosciences. Biotinylated poly(l-lysine)-[g]-poly(ethylene glycol) (PLL-PEG-biotin) was obtained from Susos AG. NeutrAvidin was obtained from Invitrogen. Ethylene glycol-bis(2-aminoethylether)-N,N,N',N'-tetraacetic acid (EGTA), potassium chloride, potassium hydroxide, κ-casein, 1,4-piperazinediethanesulfonic acid (PIPES), GTP, methylcellulose, glucose oxidase from Aspergillus niger, catalase from bovine liver, dithiothreitol (DTT), magnesium chloride and glucose were obtained from Sigma-Aldrich. Different types of labeled and unlabeled purified tubulin used in the assays were purchased from Cytoskeleton.

The *in vitro* microtubule dynamics assay was performed as described previously (Bieling et al., 2007; Rai et al., 2020)[5,6]. GMPCPP (a slowly hydrolyzable GTP analog) stabilized microtubule seeds were prepared by two rounds of polymerization and depolymerization in the presence of GMPCPP. A solution of 20 µM porcine brain tubulin mix containing 12% rhodamine-labeled tubulin and 18% biotin-labeled tubulin was polymerized in MRB80 buffer (80 mM K-PIPES, pH 6.8, 4 mM $MgCl_2$, 1 mM EGTA) in the presence of GMPCPP (1 mM) at 37°C for 30 min. After polymerization, the mixture was pelleted by centrifugation at 119,000 g for 5 min in an Airfuge centrifuge. The pellet obtained was resuspended in MRB80 buffer and microtubules were depolymerized further on ice for 20 min. The resuspended mixture was again polymerized in the presence of GMPCPP. After the second round of polymerization and pelleting, GMPCPP-stabilized microtubule seeds were stored in MRB80 in the presence of 10% glycerol.

Microscopy slides with plasma-cleaned glass coverslips were used to prepare *in vitro* flow chambers using two strips of double-sided tape. Flow chambers were sequentially incubated with 0.2 mg/mL PLL-PEG-biotin and 1 mg/mL NeutrAvidin in MRB80 buffer. The chamber was further incubated with GMPCPP stabilized microtubule seeds followed by treatment with 1 mg/ml κ-casein in MRB80 buffer. The reaction mixtures containing 15 µM porcine brain tubulin supplemented with 3% rhodamine-tubulin, 20 nM mCherry-EB3, 0.1% methylcellulose, 0.2 mg/mL κ-casein, 50 mM KCl, 1 mM GTP and oxygen scavenger mixture (50 mM glucose, 400 µg/mL glucose oxidase, 200 µg/mL catalase, and 4 mM DTT in MRB80 buffer) without or with **STEpo2** (50 nM) were added to the flow chambers after centrifugation in an Airfuge for

5 minutes at 119,000 g. The chambers were sealed with vacuum grease and microtubule dynamics was recorded at 30 °C using TIRF microscopy.

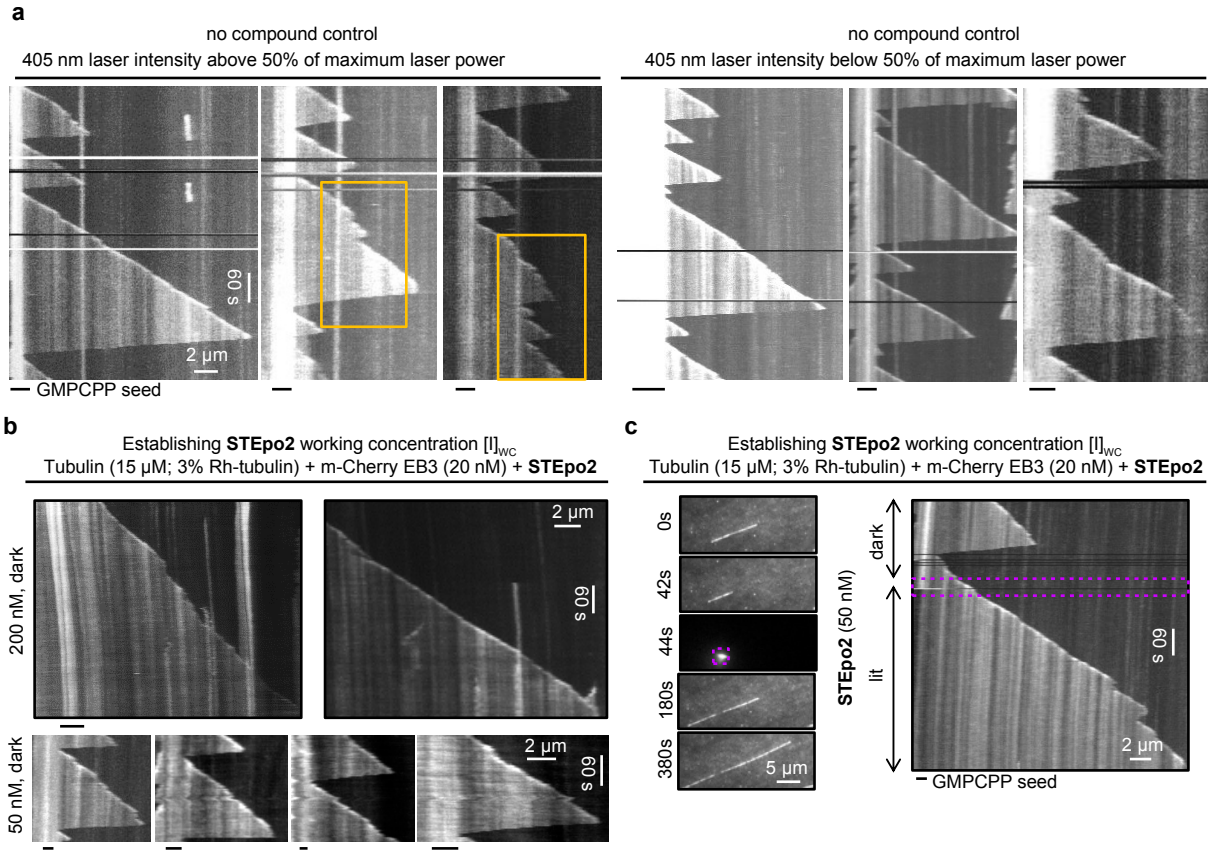

Fig S2: (a) Representative kymographs showing MT dynamics during control conditions with different laser intensities of 405 nm. The assay was performed in the presence of tubulin (15 µM supplemented with 3% of rhodamine tubulin) and 20 nM m-Cherry EB3. MT were showing some random rescues or catastrophes (yellow boxes) when the laser was used above 50% of maximum laser power. No significant change in microtubule dynamics was observed when the laser was used below 50% of maximum laser power. A laser intensity of 20-30% of maximum laser power was used for the activation of **STEpo2** (two independent experiments). **(b)** Representative kymographs (two independent experiments) showing microtubule dynamics in the presence of different concentrations of **STEpo2** without 405 nm laser illumination (dark). MT stabilizing dark activity of *E*-**STEpo2** is observed at 200 nM. When decreasing **STEpo2** concentration to 50 nM, MT behave similar to control. 50 nM of STEpo2 was selected as viable working concentration $[I]_{WC}$ for light dependent MT stabilization. **(c)** Time-lapse images and representative kymographs (from three independent experiments) show MT dynamics before (dark) and after (lit) 405 nm photoactivation (20% of maximum laser power, purple box). MT growth events were similar to control conditions in the presence of *E*-**STEpo2** (catastrophes reaching to GMPCPP seeds). After 405 nm photoactivation, MT was showing processive growth event with spontaneous rescues indicating activation of microtubule stabilization by *Z*-**STEpo2**.

Image acquisition by TIRF microscopy

Imaging was performed on a TIRF microscope setup (inverted research microscope Nikon Eclipse Ti-E) which was equipped with a perfect focus system (PFS) (Nikon) and Nikon CFI Apo TIRF 100x 1.49 N.A. oil objective (Nikon, Tokyo, Japan). The microscope was supplemented with TIRF-E motorized TIRF illuminator modified by Roper Scientific France/PICT-IBiSA Institut Curie, and a stage top incubator model INUBG2E-ZILCS (Tokai Hit) was used to regulate the temperature of the sample. Image acquisition was performed using Prime BSI sCMOS camera (Teledyne Photometrics, final magnification 0.068 µm/pixel)

and controlled with MetaMorph 7.7 software (Molecular Devices, CA). Images were captured with 1 frame/2 s in time-lapse mode.

A TIRF microscope equipped with an ILas system (Roper Scientific/PICTIBiSA) was used to photoactivate **STEpo2** with 405 nm light. A region of microtubules was illuminated using a focused laser beam. *In vitro* microtubule dynamics assay was performed in the presence of GMPCPP-stabilized microtubule seeds with 15 µM tubulin, supplemented with 3% rhodamine-tubulin without (control) or with 50 nM **STEpo2**. Kymographs representing the life history of microtubule dynamics were generated using KymoResliceWide v.0.4 (https://github.com/ekatrukha/KymoResliceWide (Katrukha, 2015)) plugin in ImageJ.

Live cell microtubule dynamics: imaging

HeLa cells were transfected with EB3-tdTomato using FuGENE 6 (Promega) according to manufacturer's instructions. Experiments were imaged on a Nikon Eclipse Ti microscope equipped with a perfect focus system (Nikon), a spinning disk-based confocal scanner unit (CSU-X1-A1, Yokogawa), an Evolve 512 EMCCD camera (Photometrics) attached to a 2.0× intermediate lens (Edmund Optics), a Roper Scientific custom-made set of Vortran Stradus 405 nm (100 mW), 488 nm (487 nm / 150 mW) and Cobolt Jive 561 nm (110 mW) lasers, a set of ET-DAPI, ET-GFP and ET-mCherry filters (Chroma), a motorized stage MS-2000-XYZ, a stage top incubator INUBG2E-ZILCS (Tokai Hit) and lens heating calibrated for incubation at 37°C with 5% CO_2. Microscope image acquisition was controlled using MetaMorph 7.7 and images were acquired using a Plan Apo VC 40× NA 1.3 oil objective. Imaging conditions were initially optimized to minimize tdTomato bleaching and phototoxicity for untreated cells. For compound treated acquisitions 0.6 µM **STEpo2** diluted in prewarmed cell medium was applied to cells in a dark room with only red ambient light, cells were protected from all ambient light after application of drug. Drug was incubated on cells for at least 1 min before commencing experiment. Comet count analysis was performed in ImageJ using the ComDet plugin (E. Katrukha, University of Utrecht, Netherlands, https://github.com/ekatrukha/ComDet).

Live cell microtubule dynamics: quantification and statistics

All relevant assays were done in independent biological replicates. All attempts at replication were successful and no data were excluded from analysis. Blinding was not performed as assay readout is mostly unbiased (plate reader, flow cytometry, Fiji/ImageJ plugins). Microscopic evaluation was performed independently by two separate scientists. Data were analysed using Prism 9 software (GraphPad). Two-tailed unpaired t tests were used in pairwise group comparisons; * was used for $P < 0.05$, ** for $P < 0.01$, *** for $P < 0.001$, **** for $P < 0.0001$.

Part D: NMR Spectra

^{1}H-NMR of TES protected STEpo1:

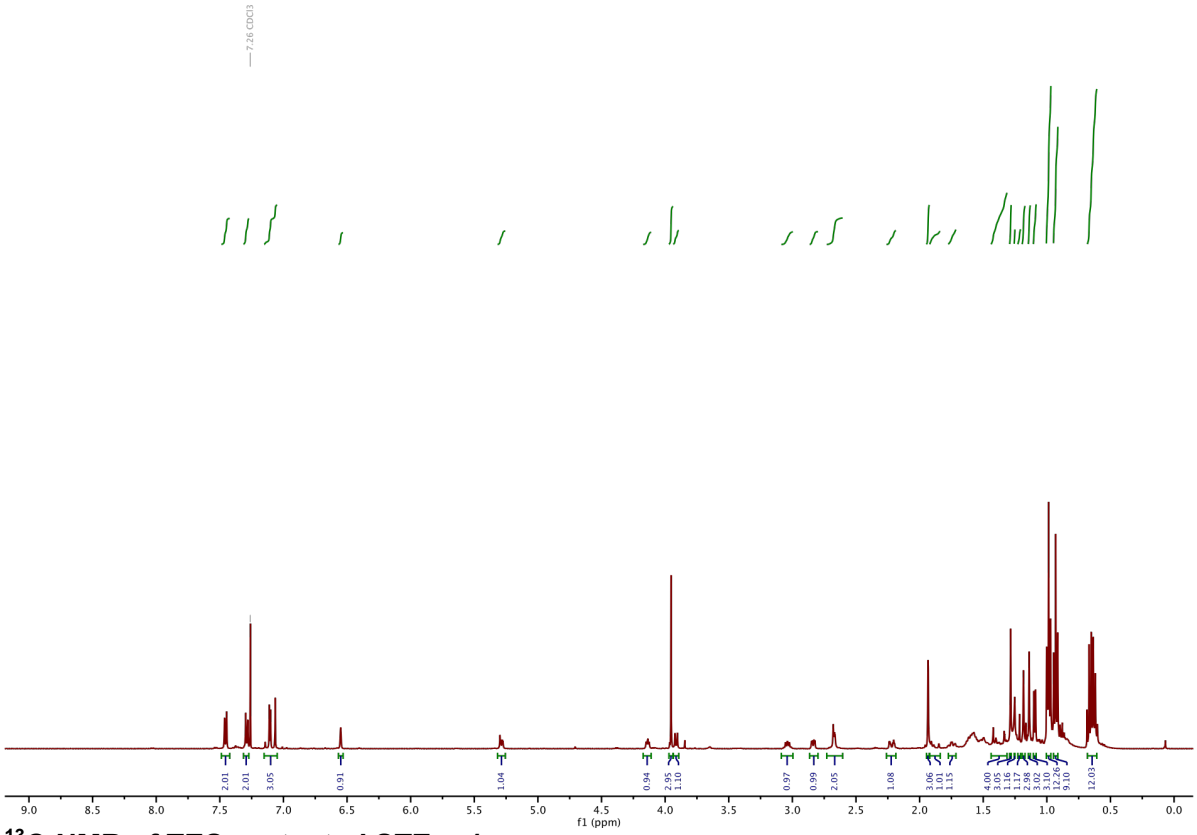

^{13}C-NMR of TES protected STEpo1:

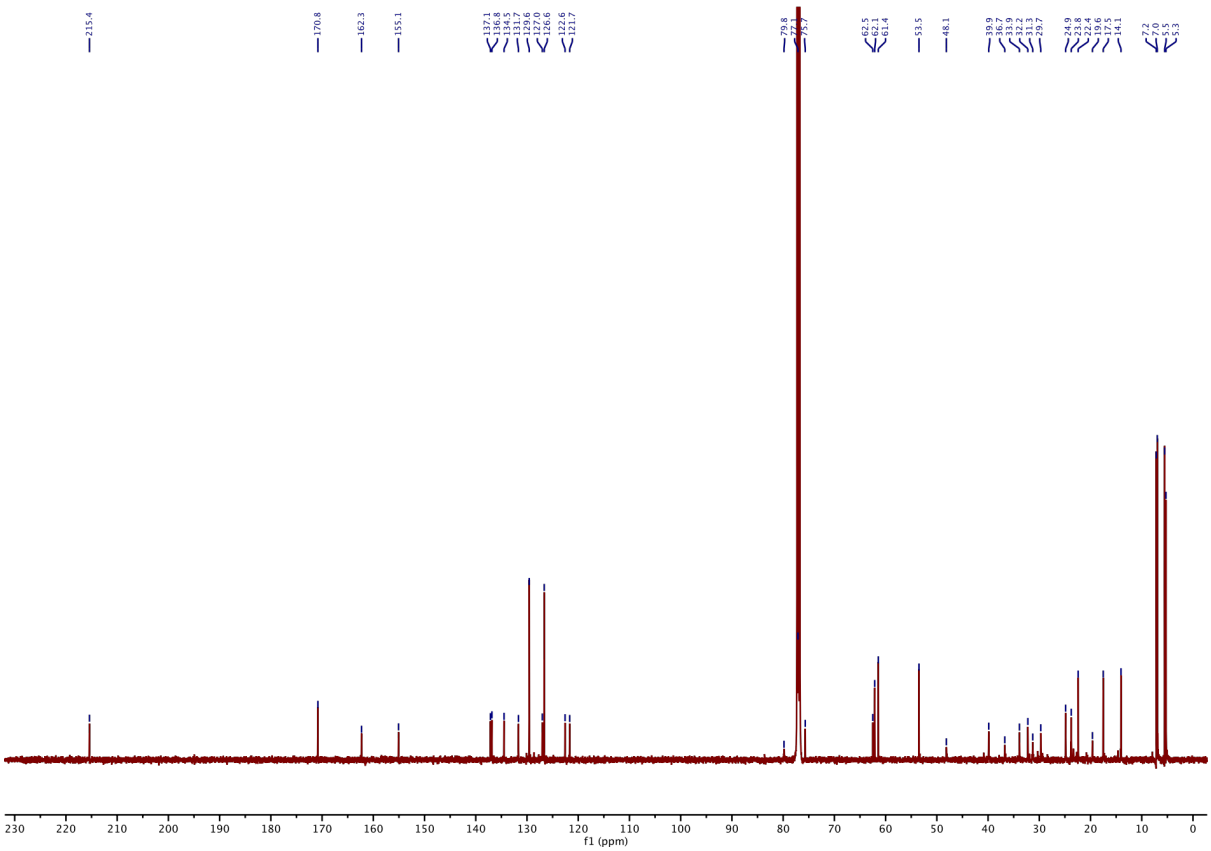

^{1}H-NMR of STEpo1:

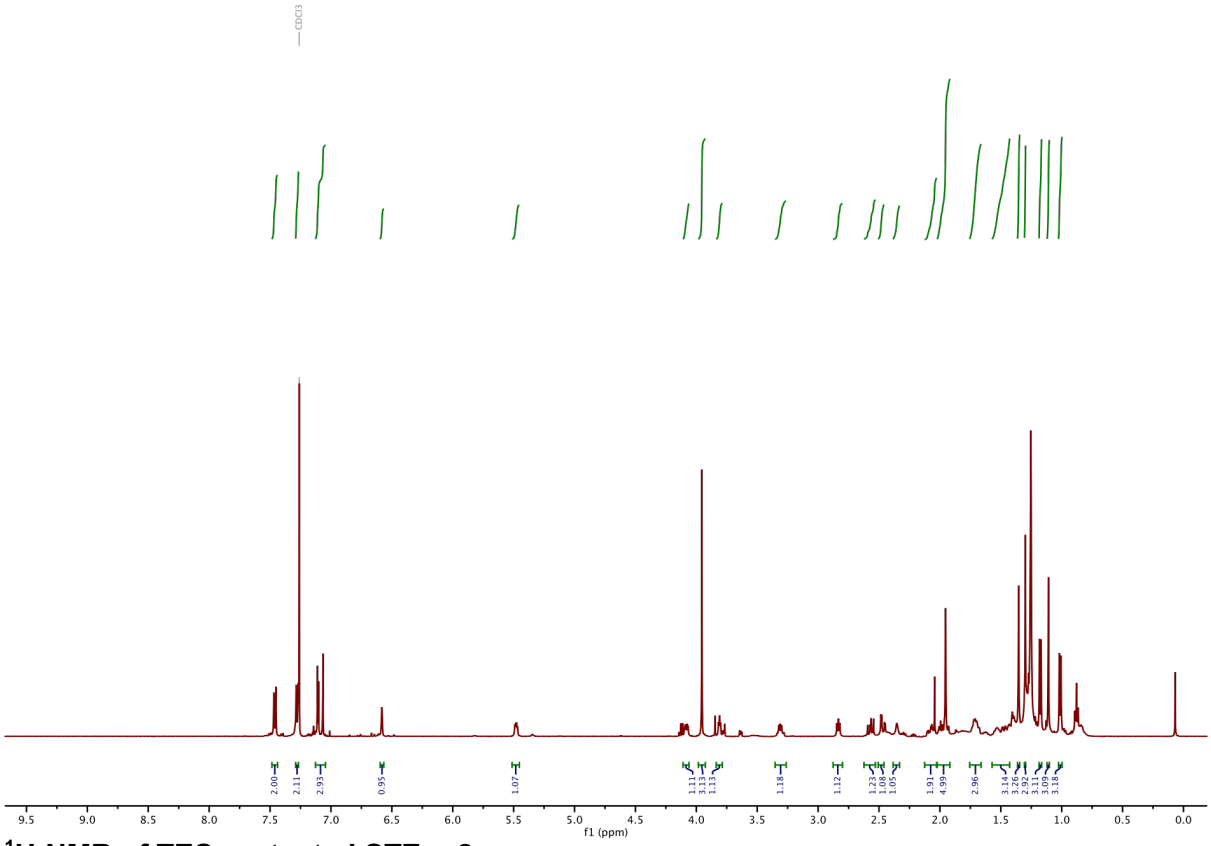

^{1}H-NMR of TES protected STEpo2:

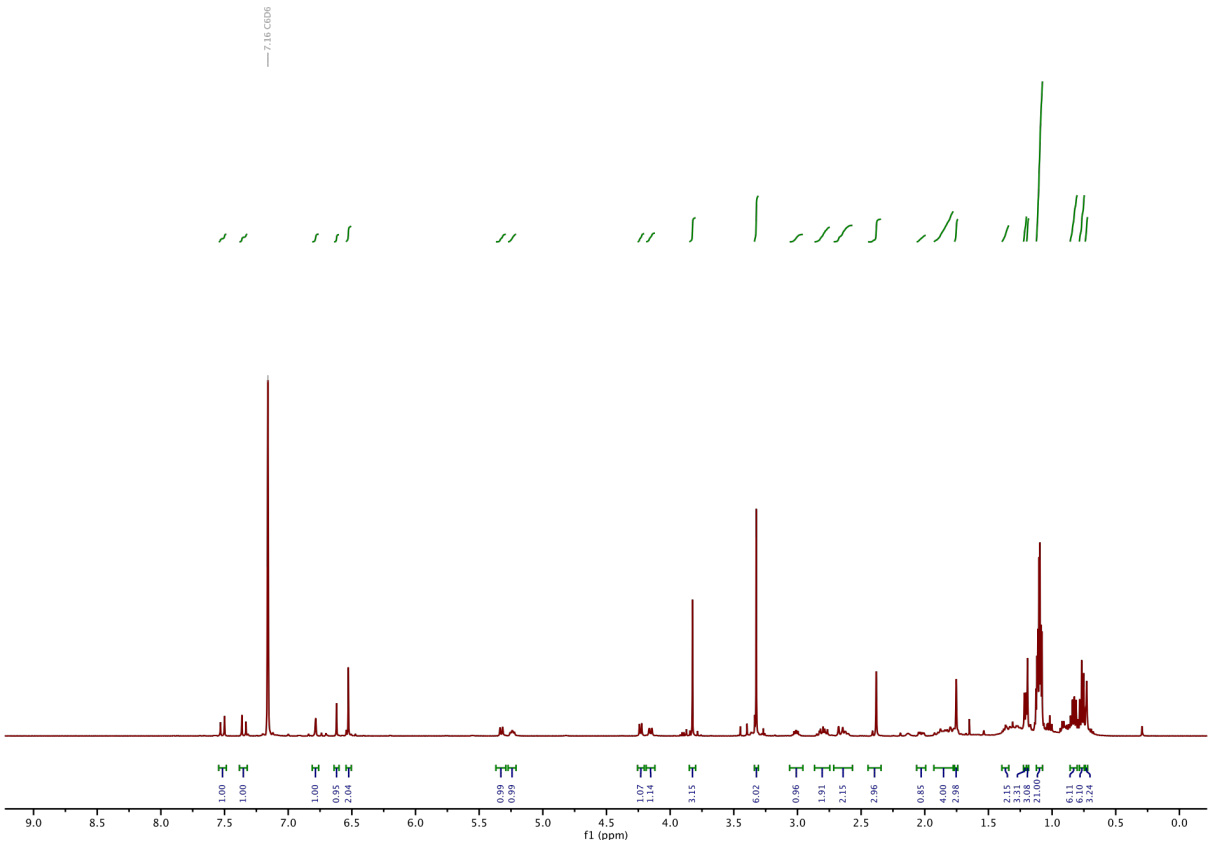

^{13}C-NMR of TES protected STEpo2:

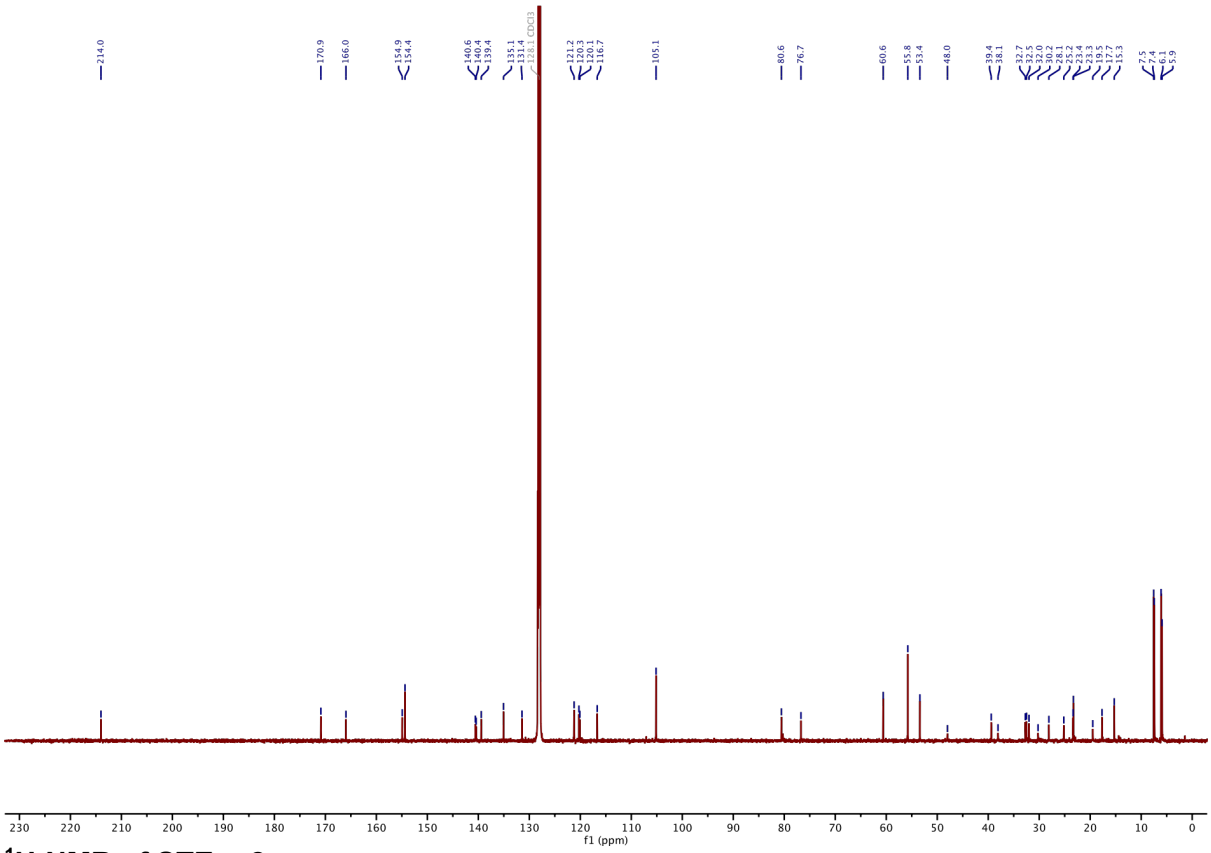

^{1}H-NMR of STEpo2:

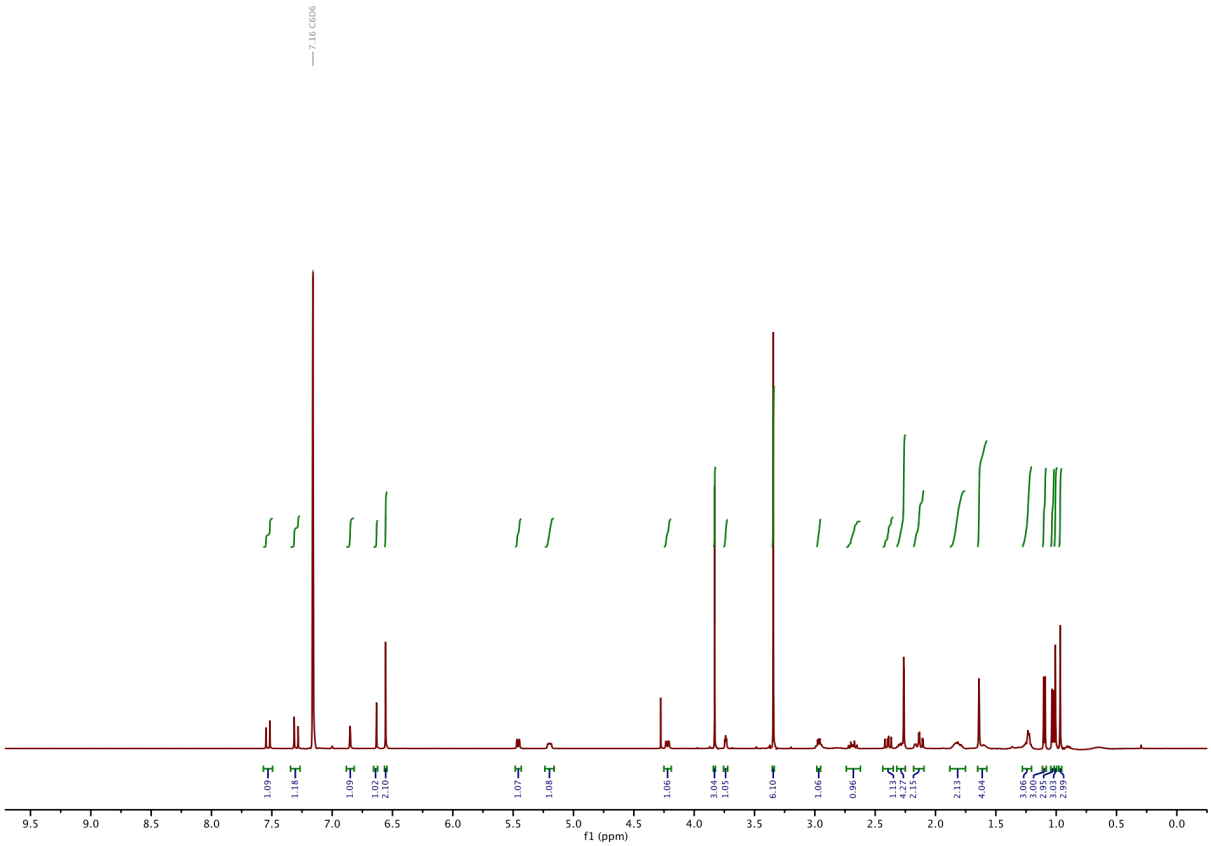

^{13}C-NMR of STEpo2:

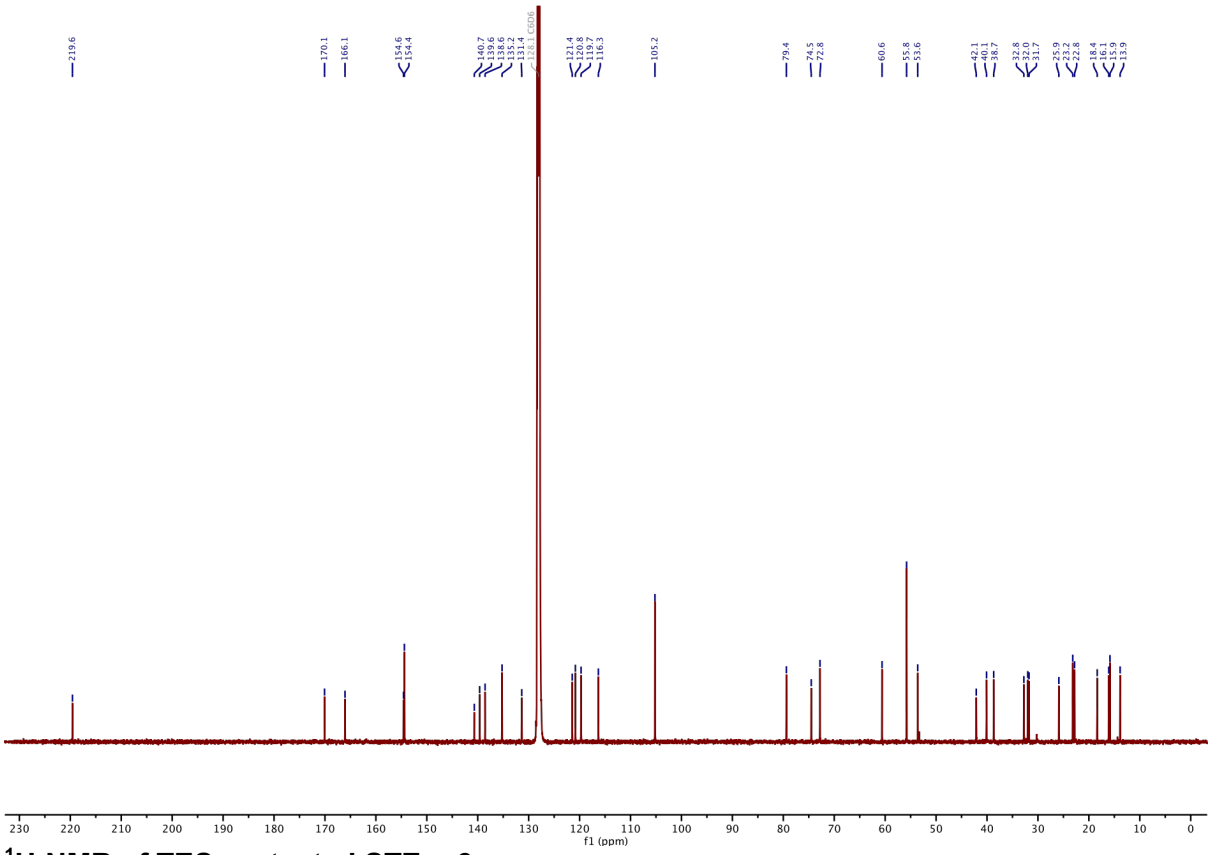

^{1}H-NMR of TES protected STEpo3:

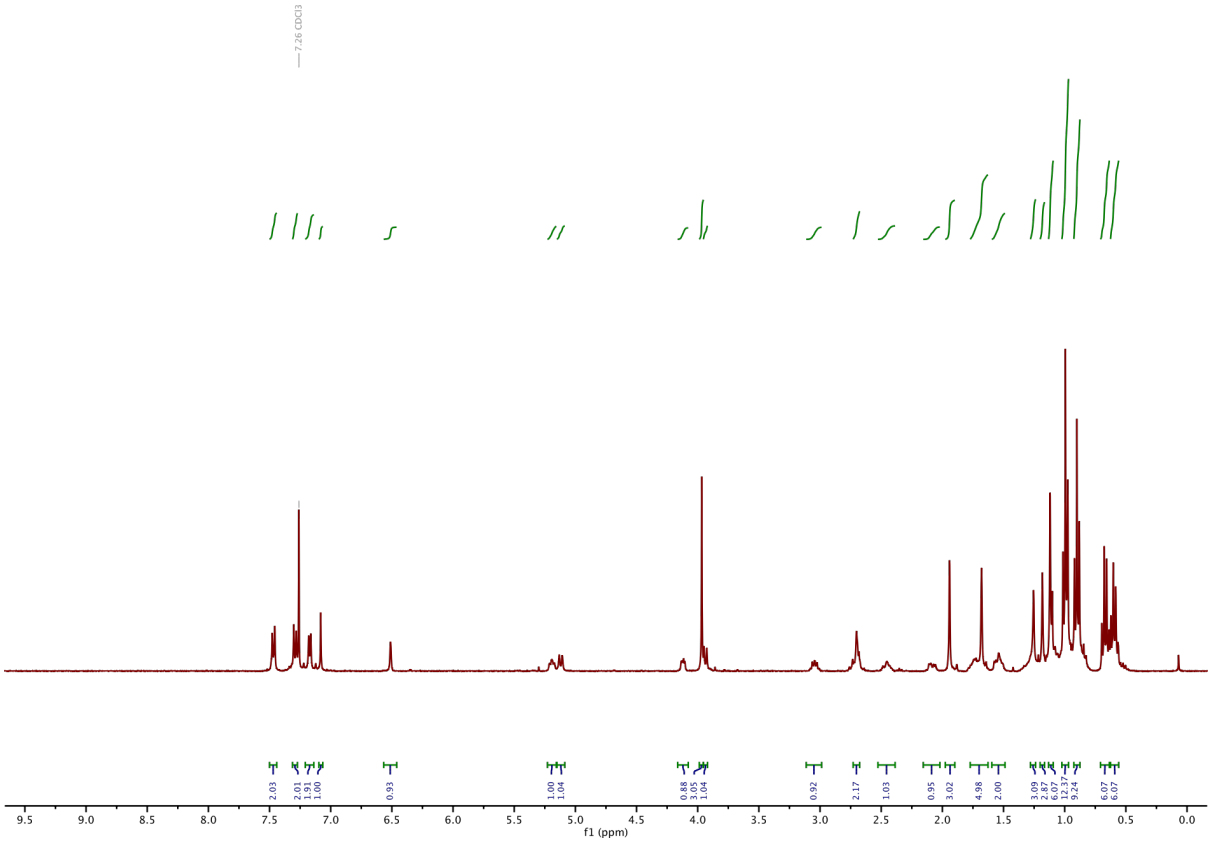

^{13}C-NMR of TES protected STEpo3:

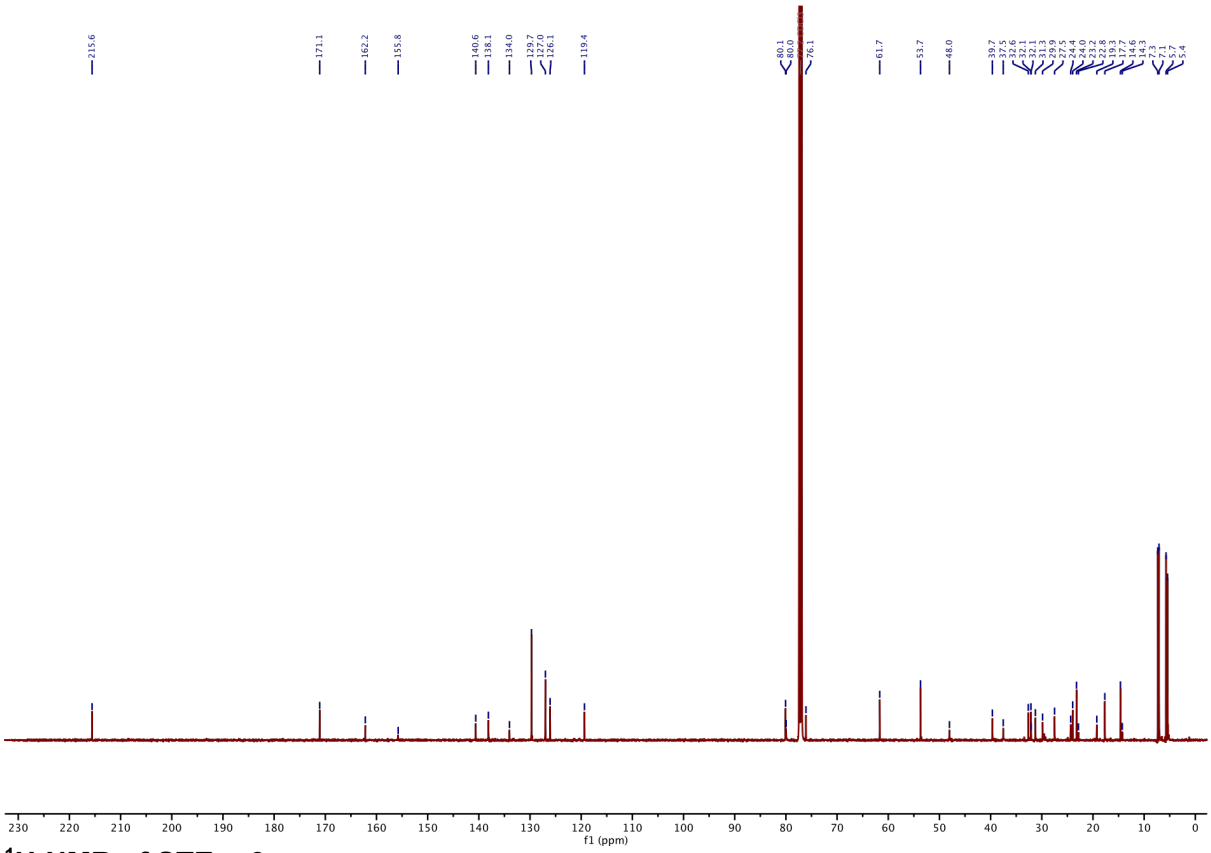

^{1}H-NMR of STEpo3:

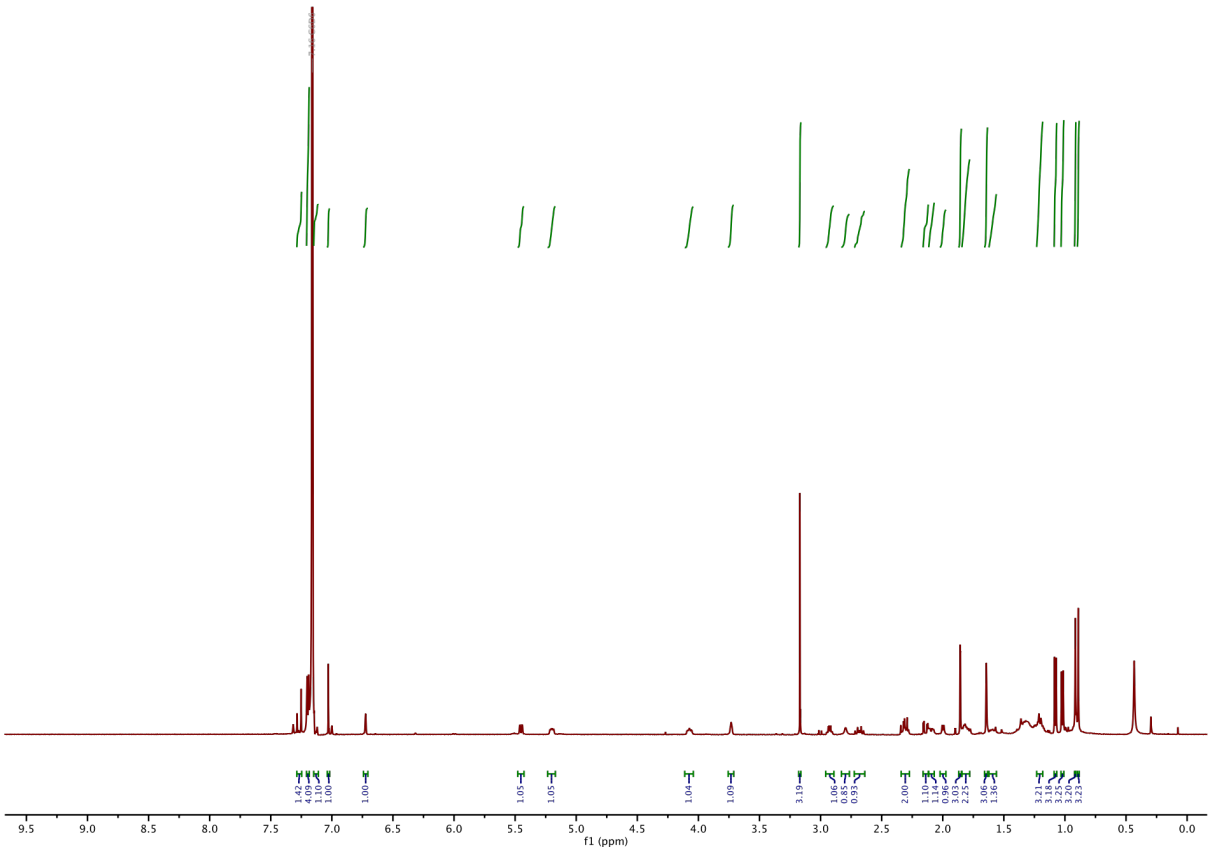

^{13}C-NMR of STEpo3:

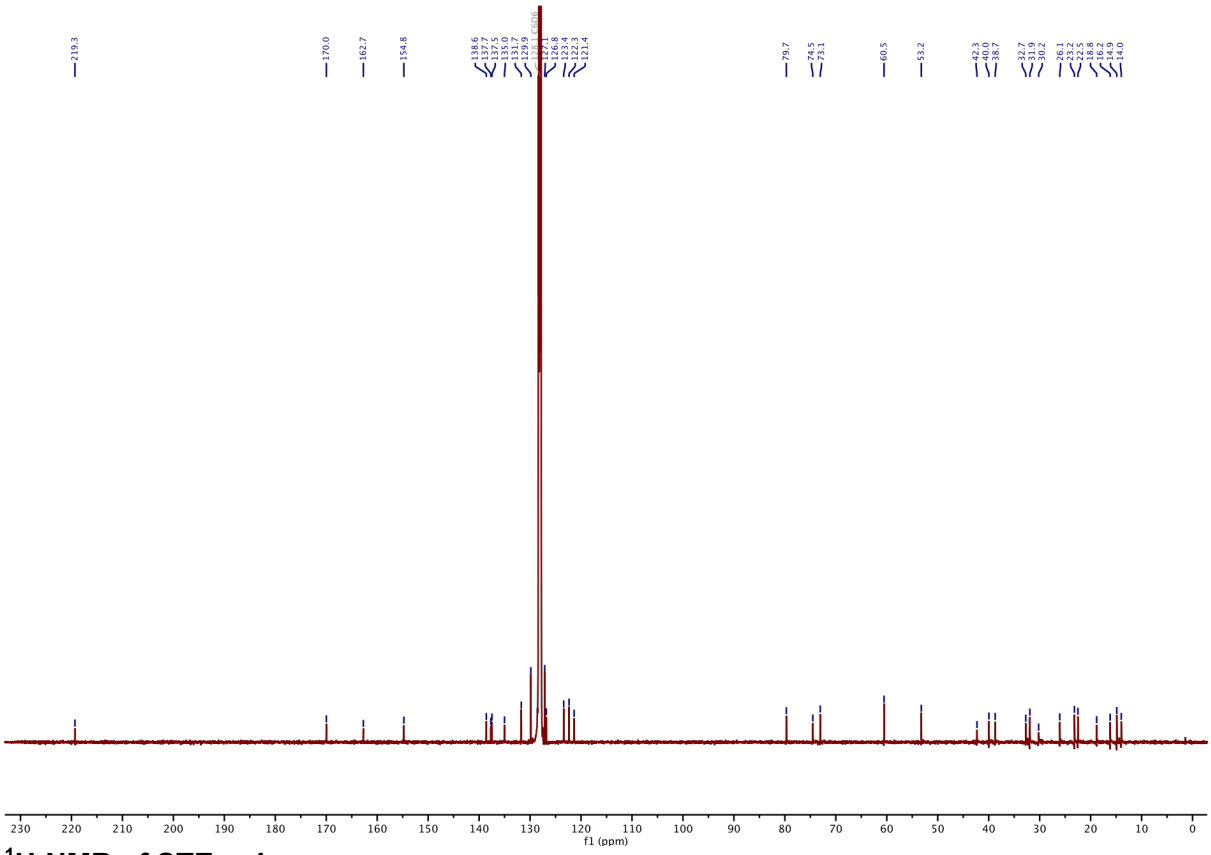

^{1}H-NMR of STEpo4:

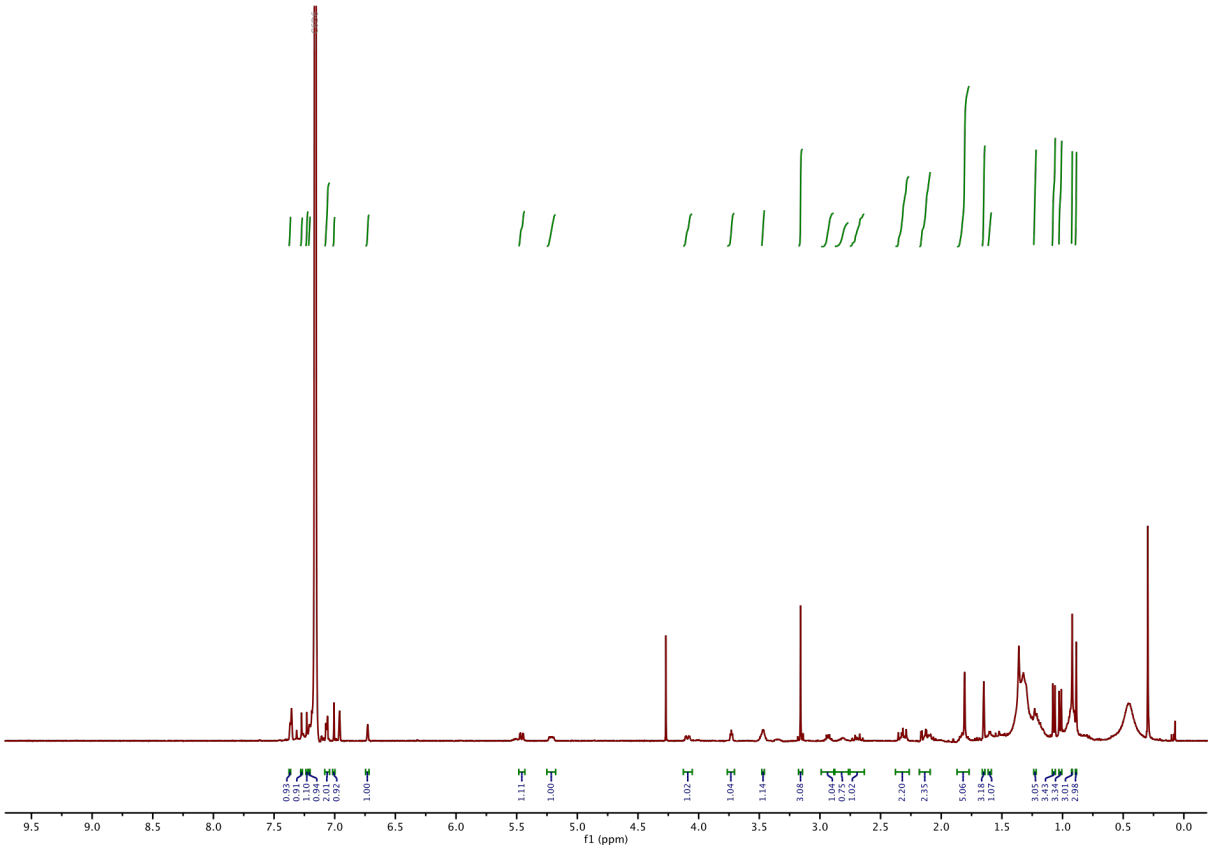

^{1}H-NMR of 1:

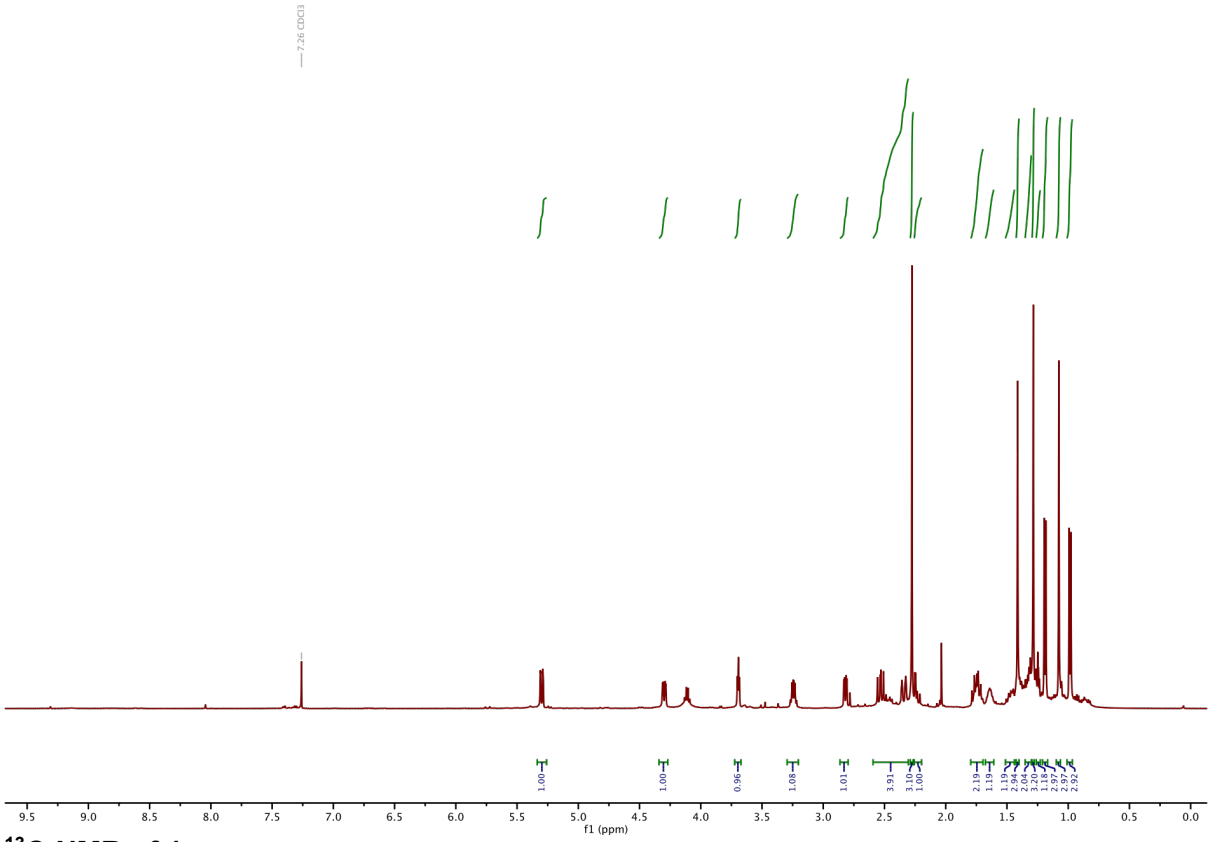

^{13}C-NMR of 1:

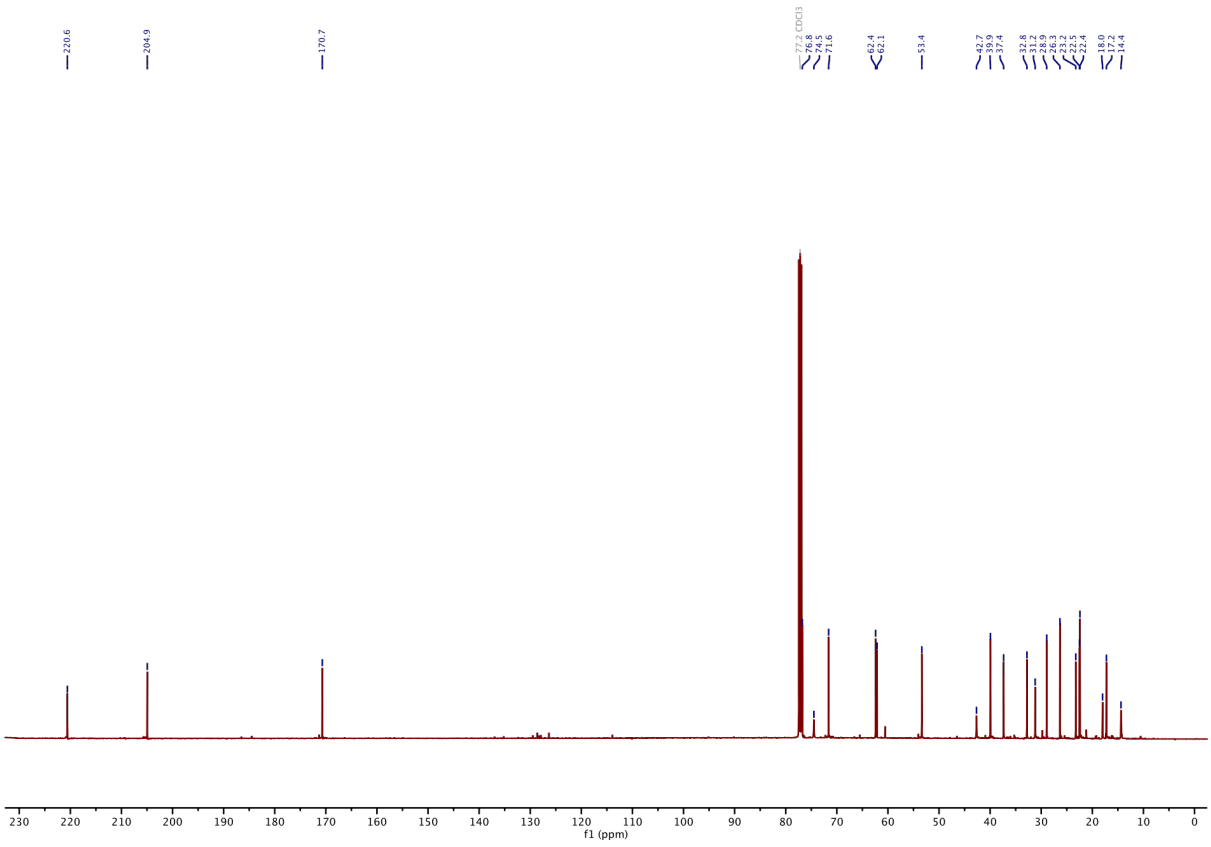

^{1}H-NMR of 2:

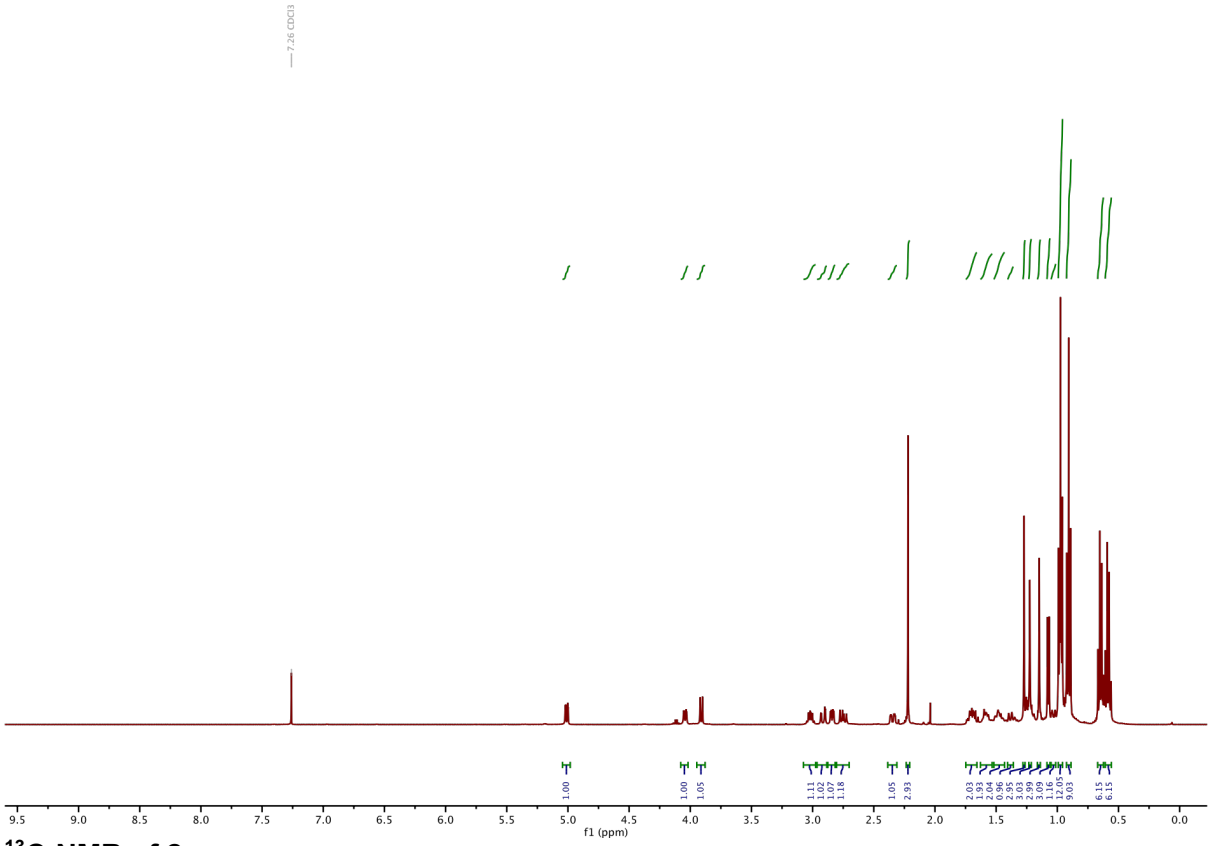

^{13}C-NMR of 2:

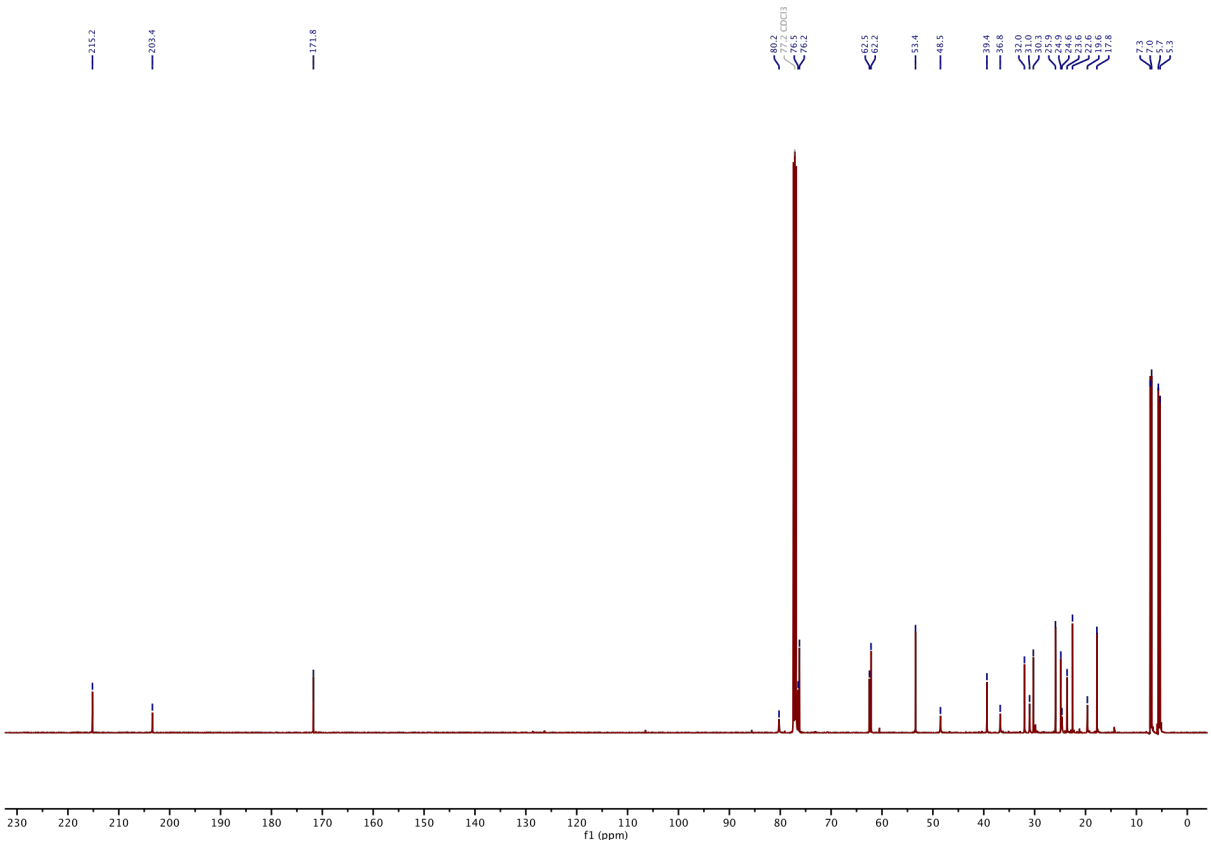

^{1}H-NMR of 3:

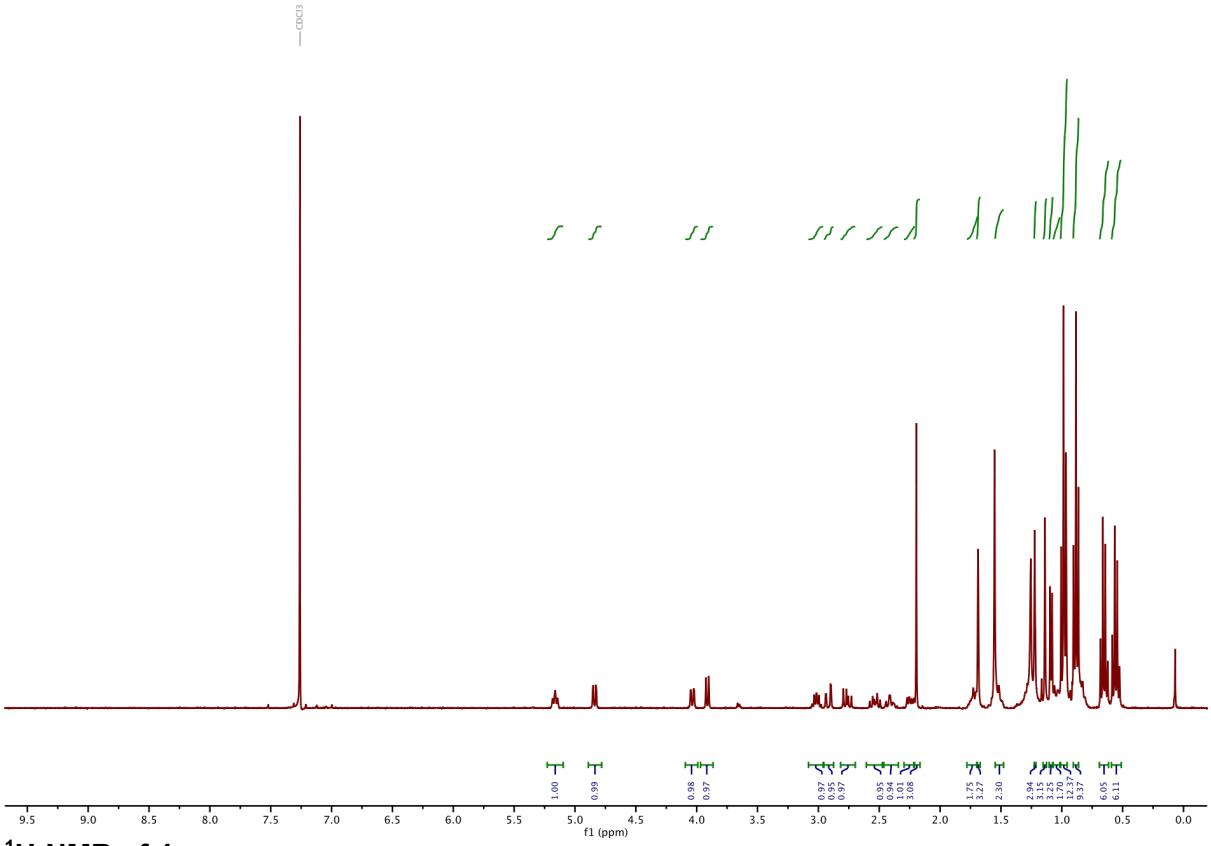

^{1}H-NMR of 4:

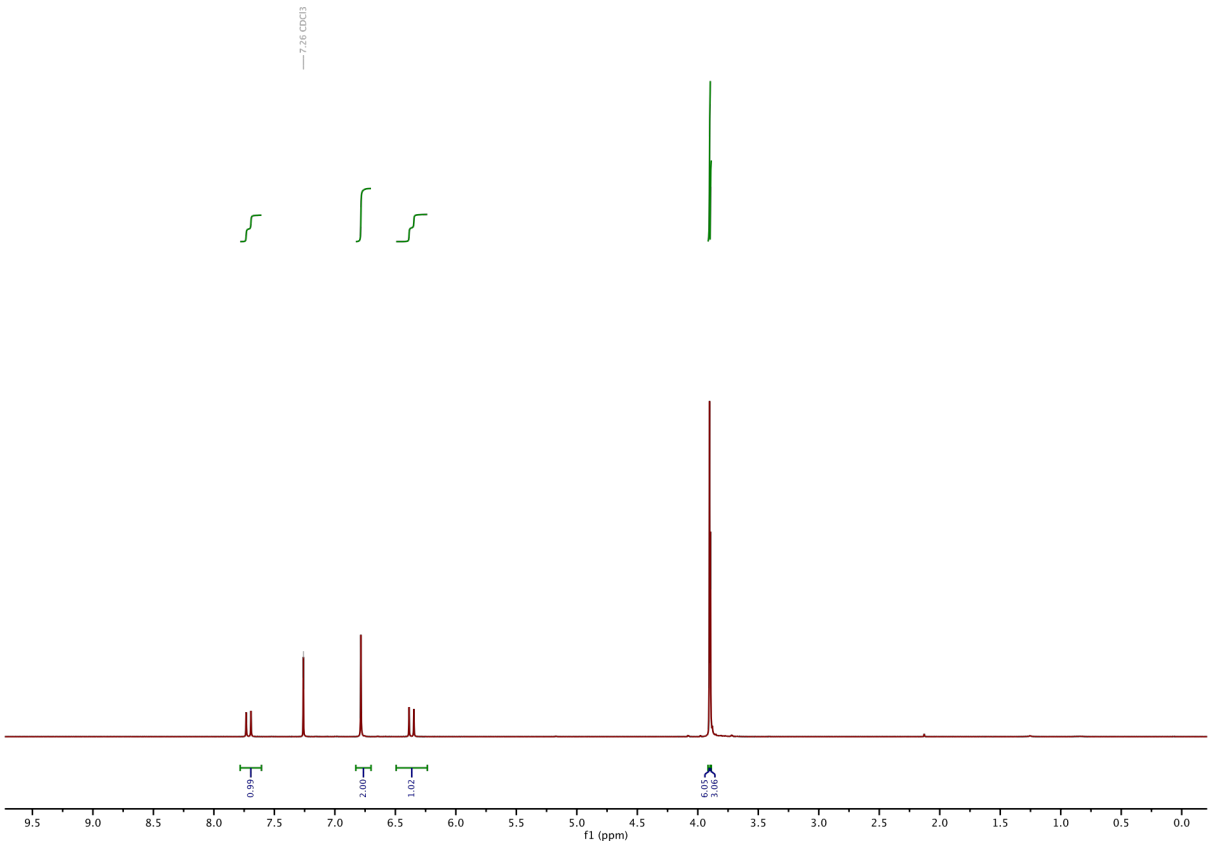

^{13}C-NMR of 4:

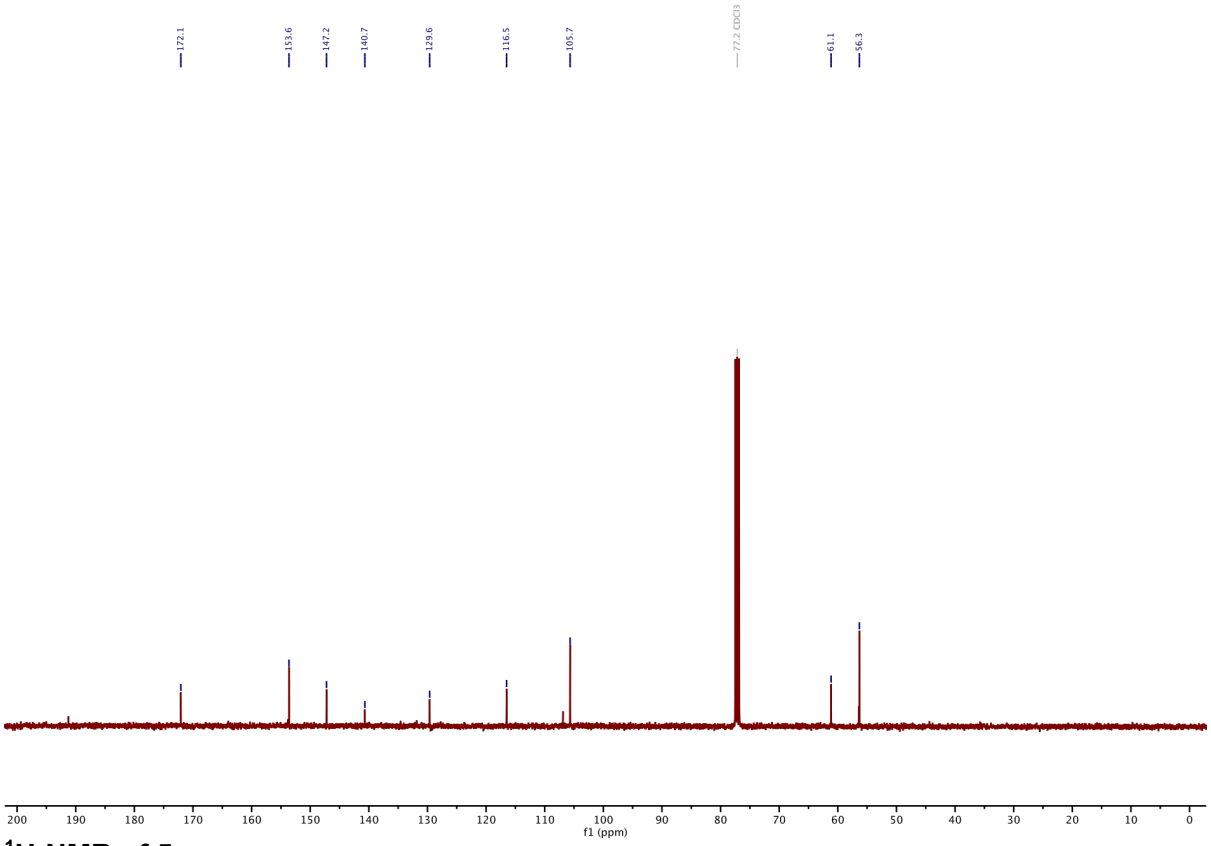

^{1}H-NMR of 5:

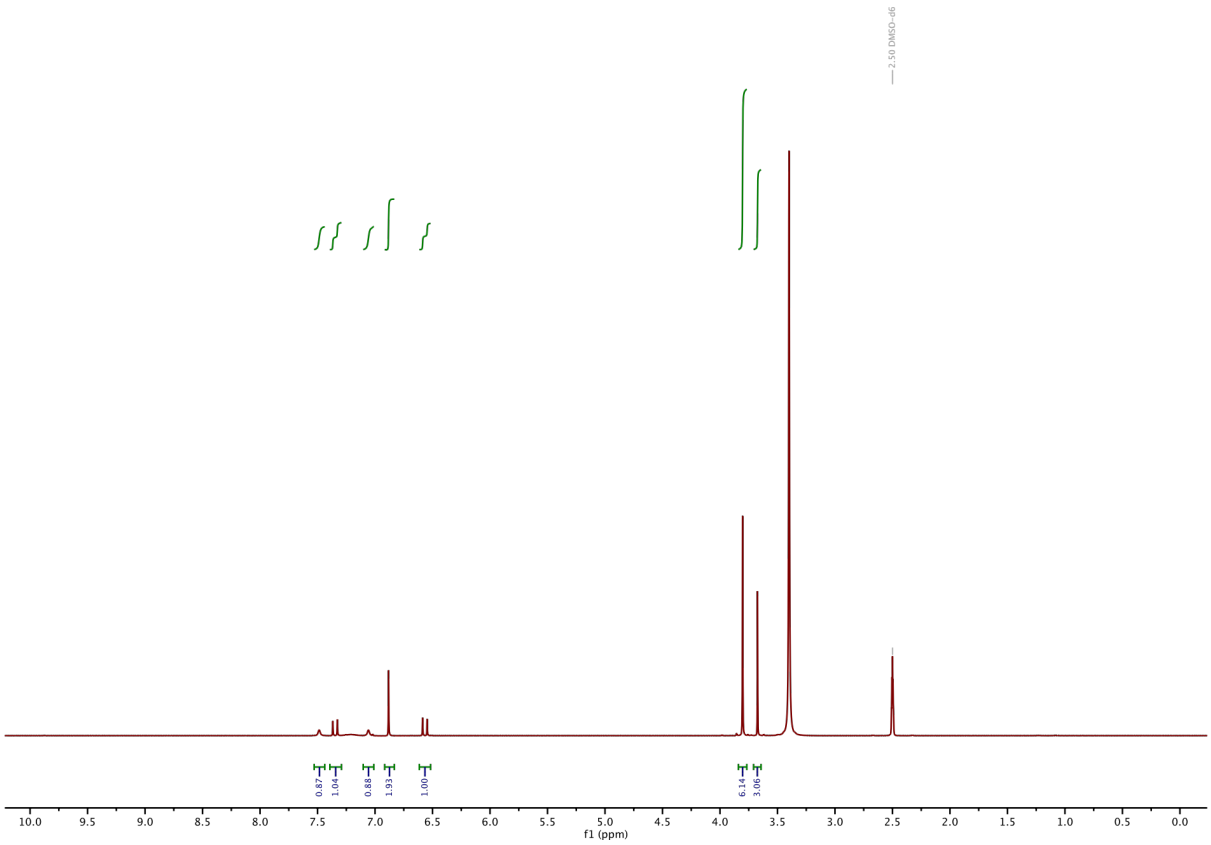

^{13}C-NMR of 5:

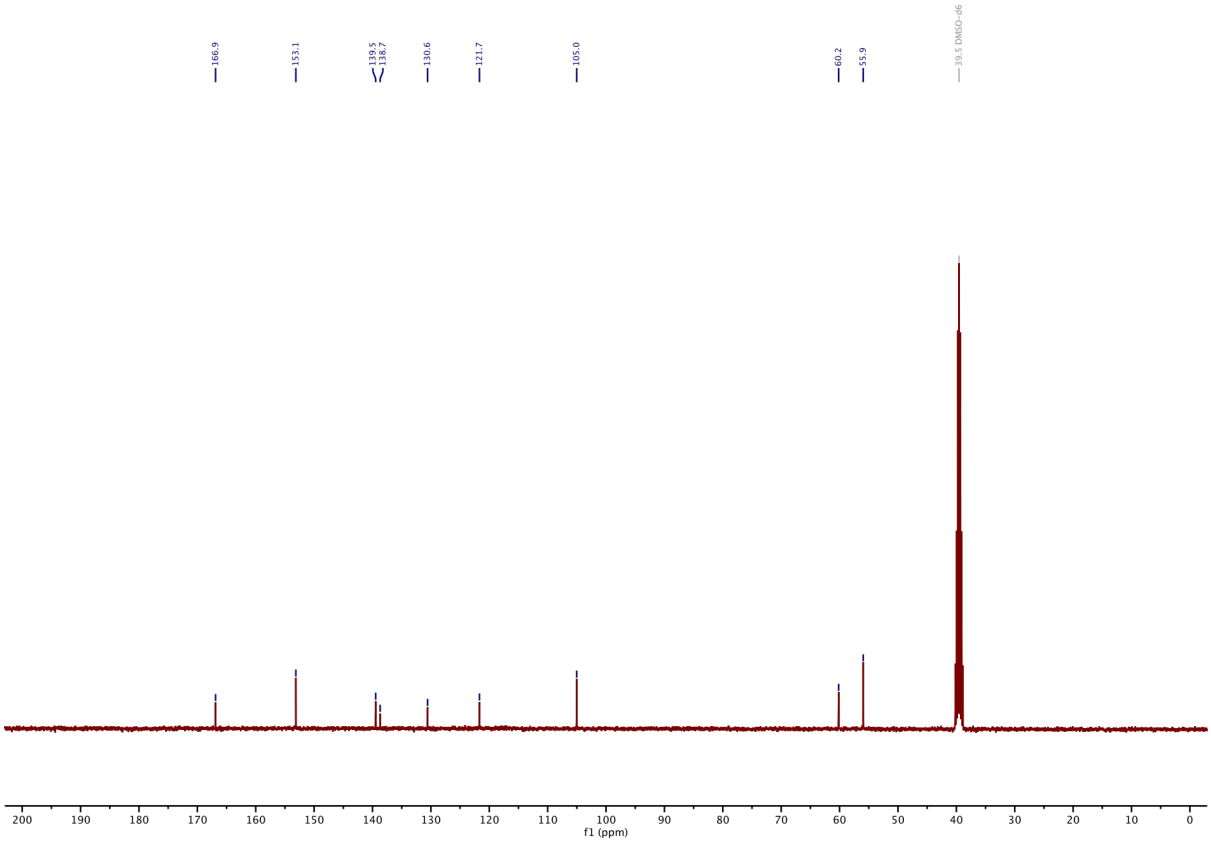

^{1}H-NMR of 6:

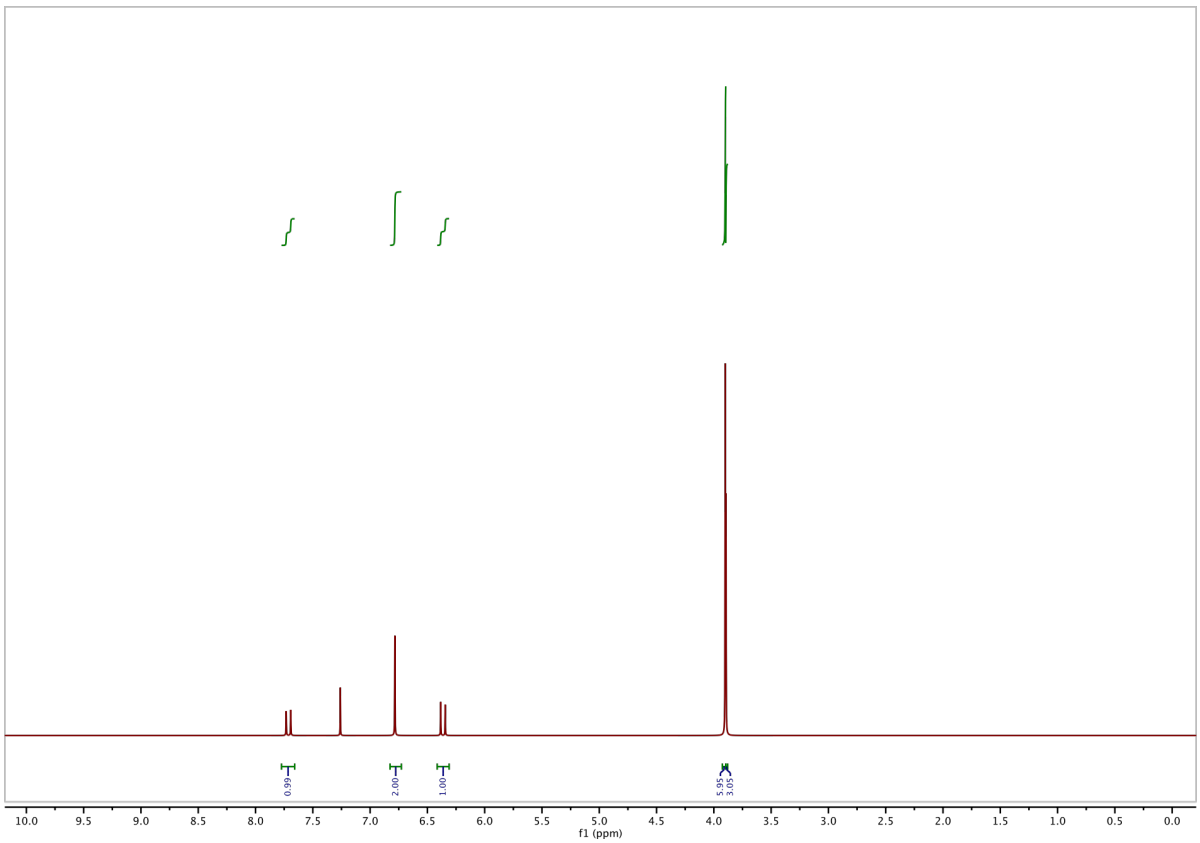

^{13}C-NMR of 6:

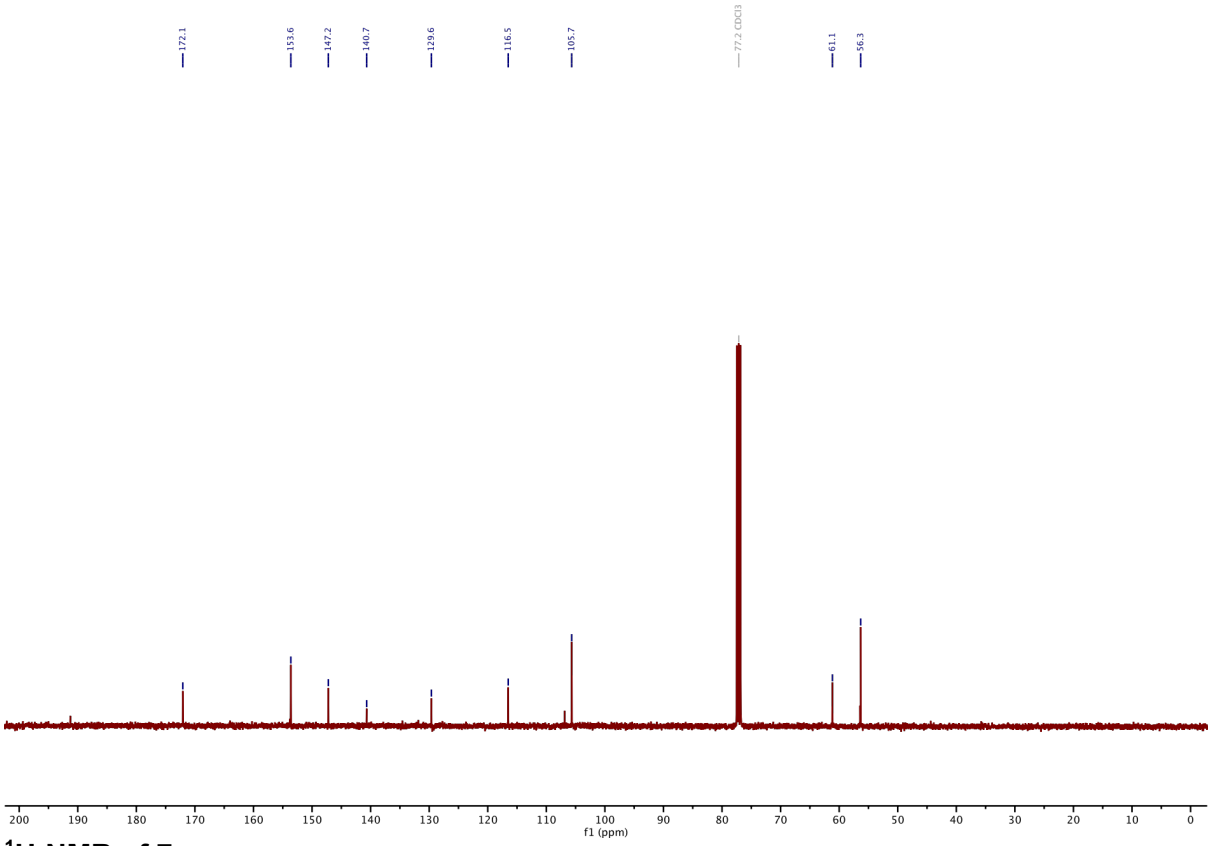

^{1}H-NMR of 7:

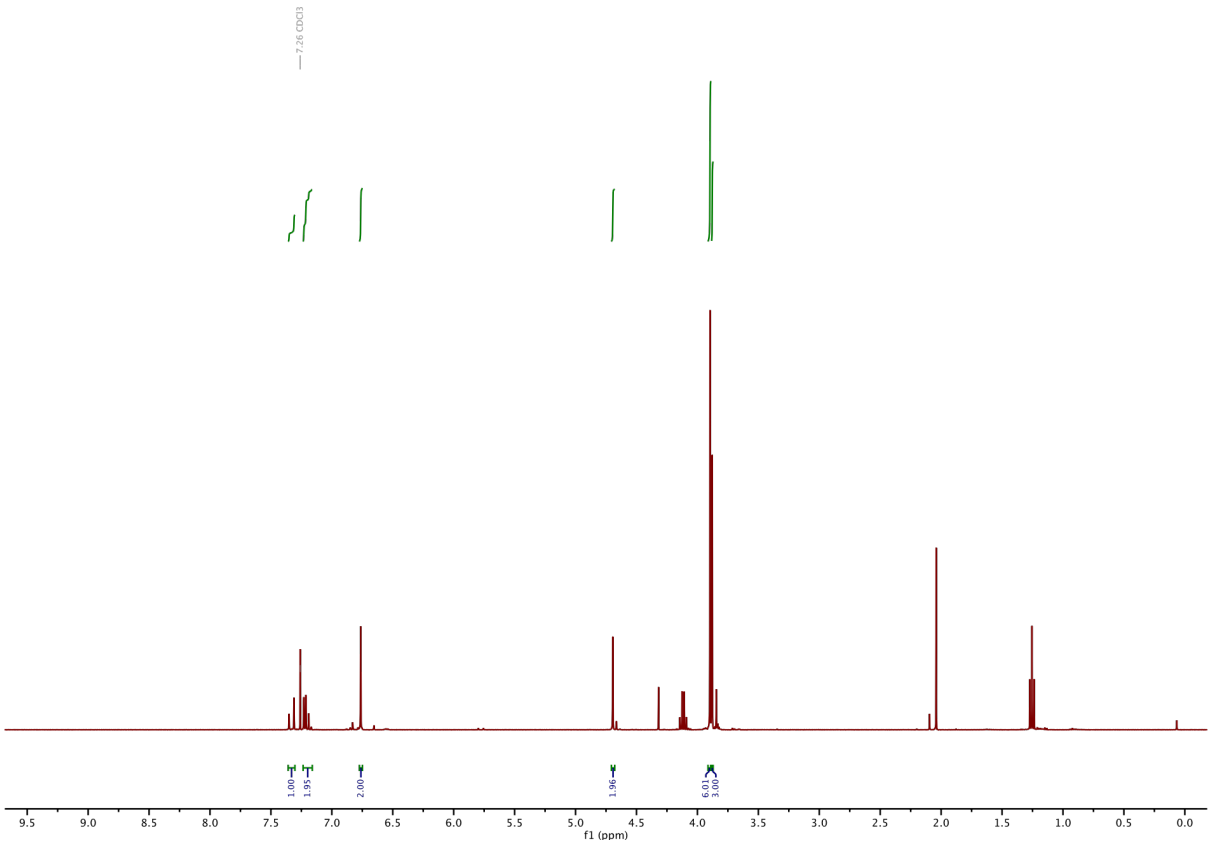

^{13}C-NMR of 7:

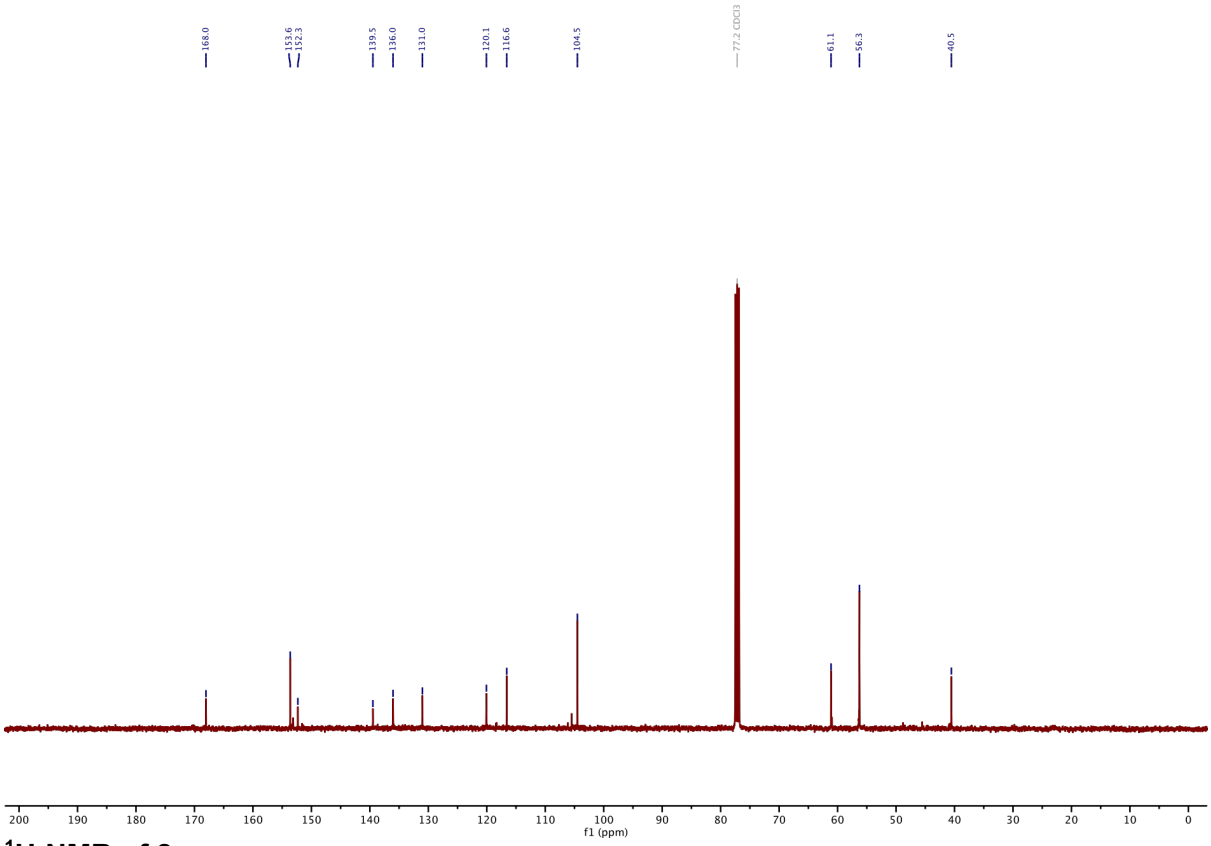

^{1}H-NMR of 8:

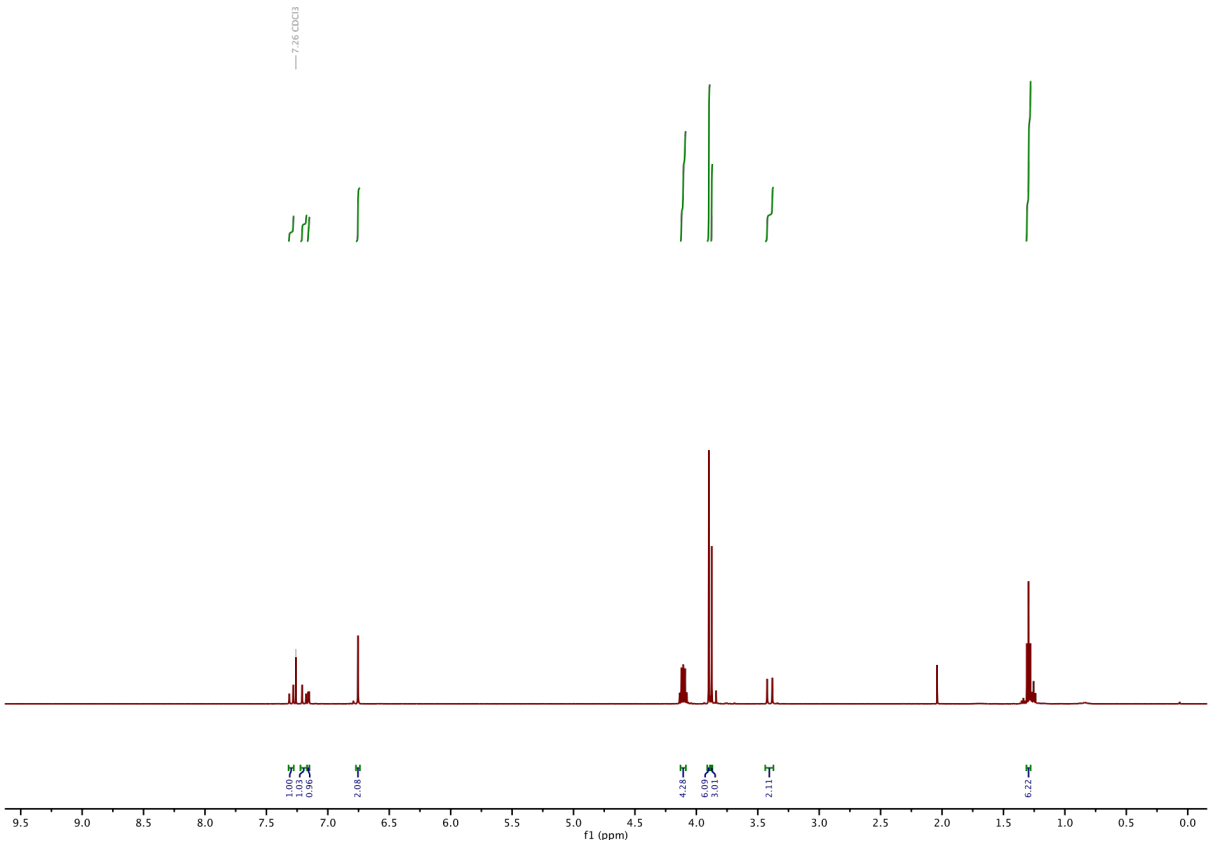

^{13}C-NMR of 8:

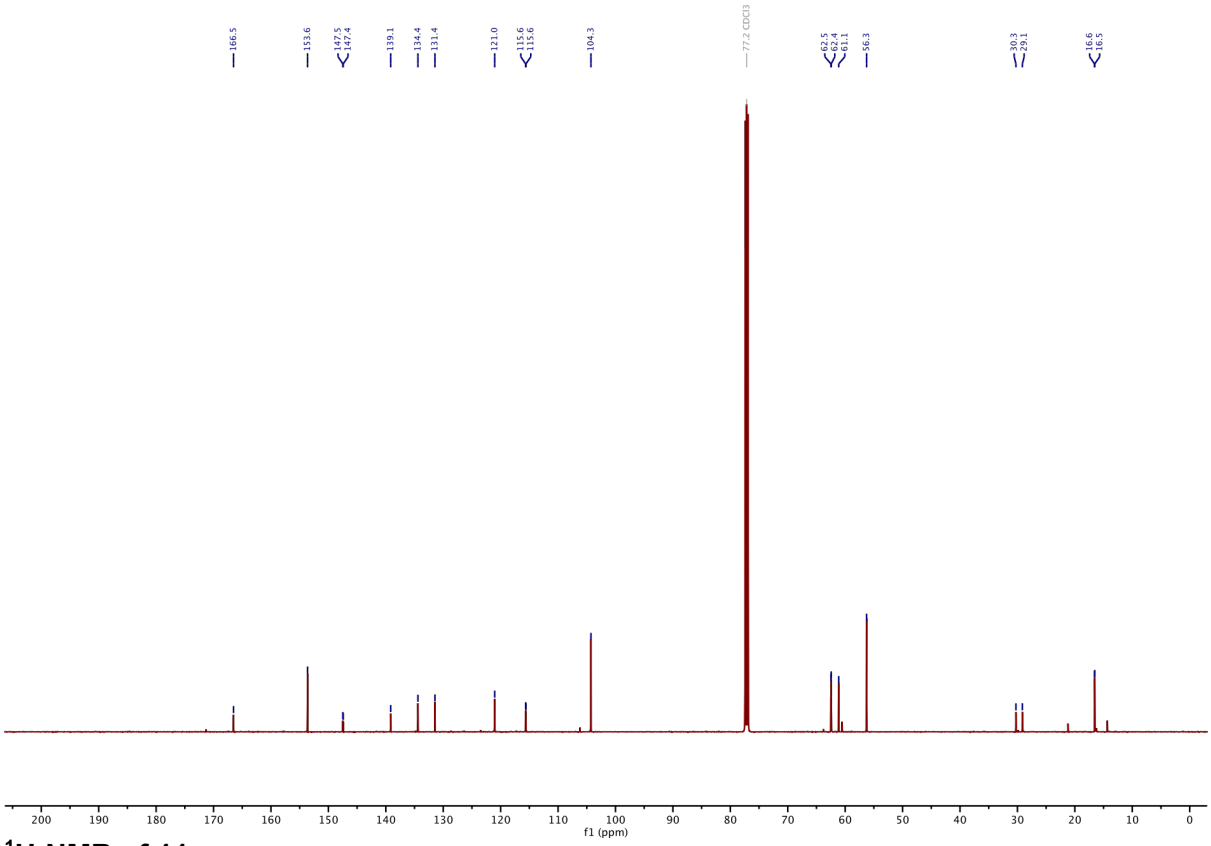

^{1}H-NMR of 11a:

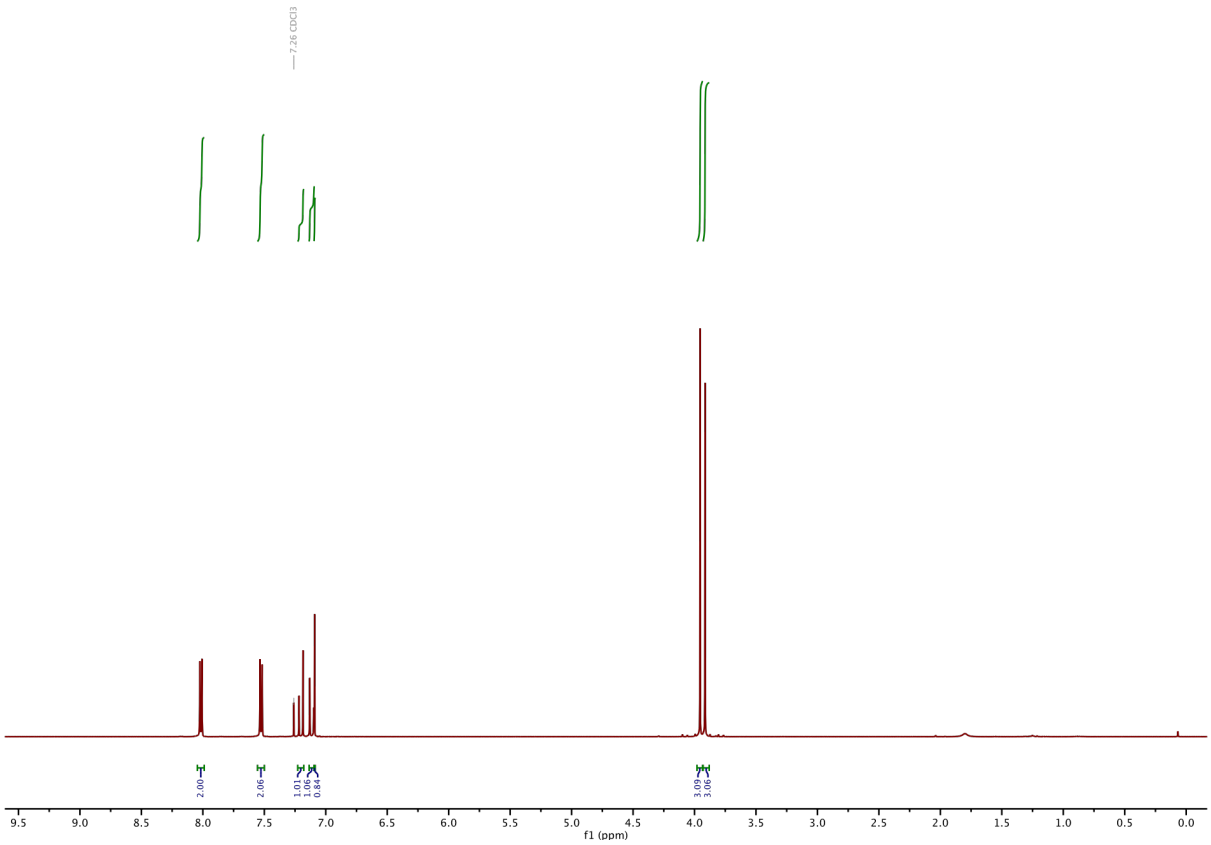

^{13}C-NMR of 11a:

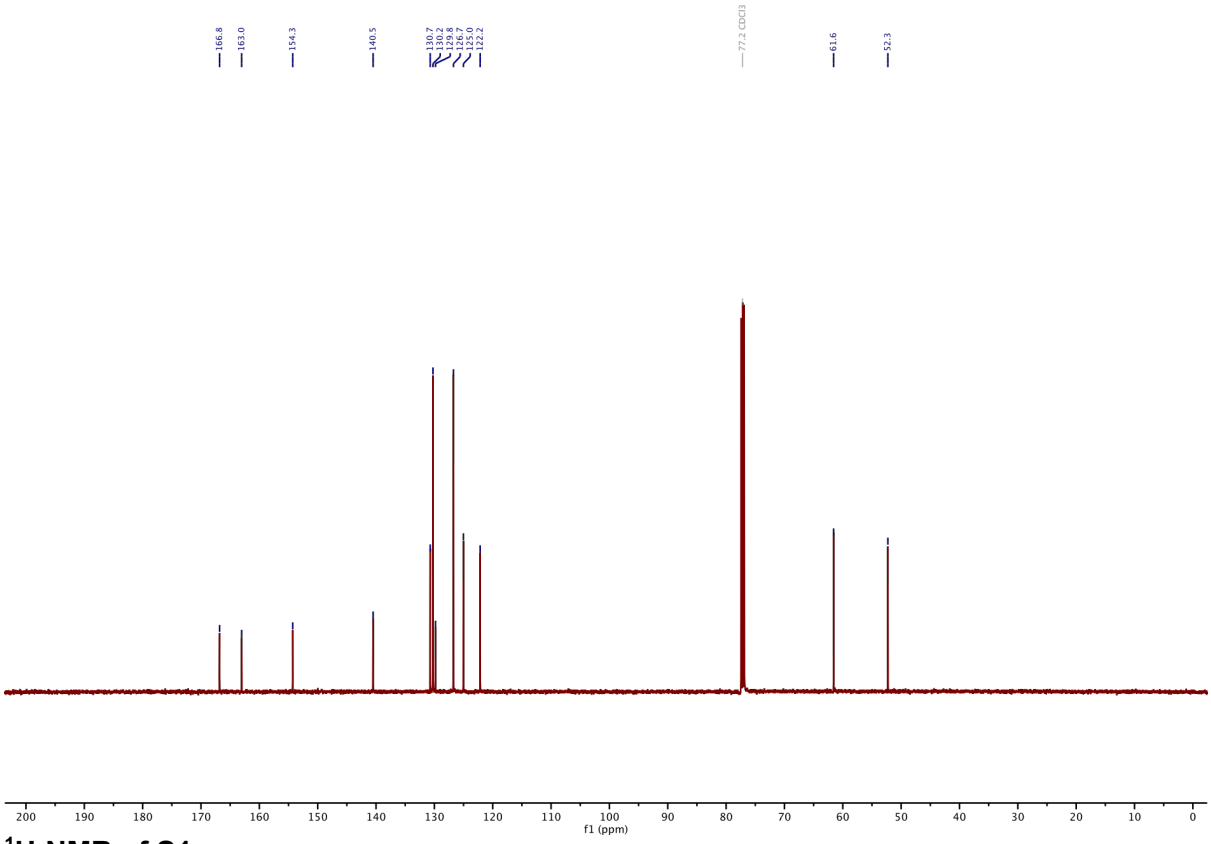

^{1}H-NMR of S1:

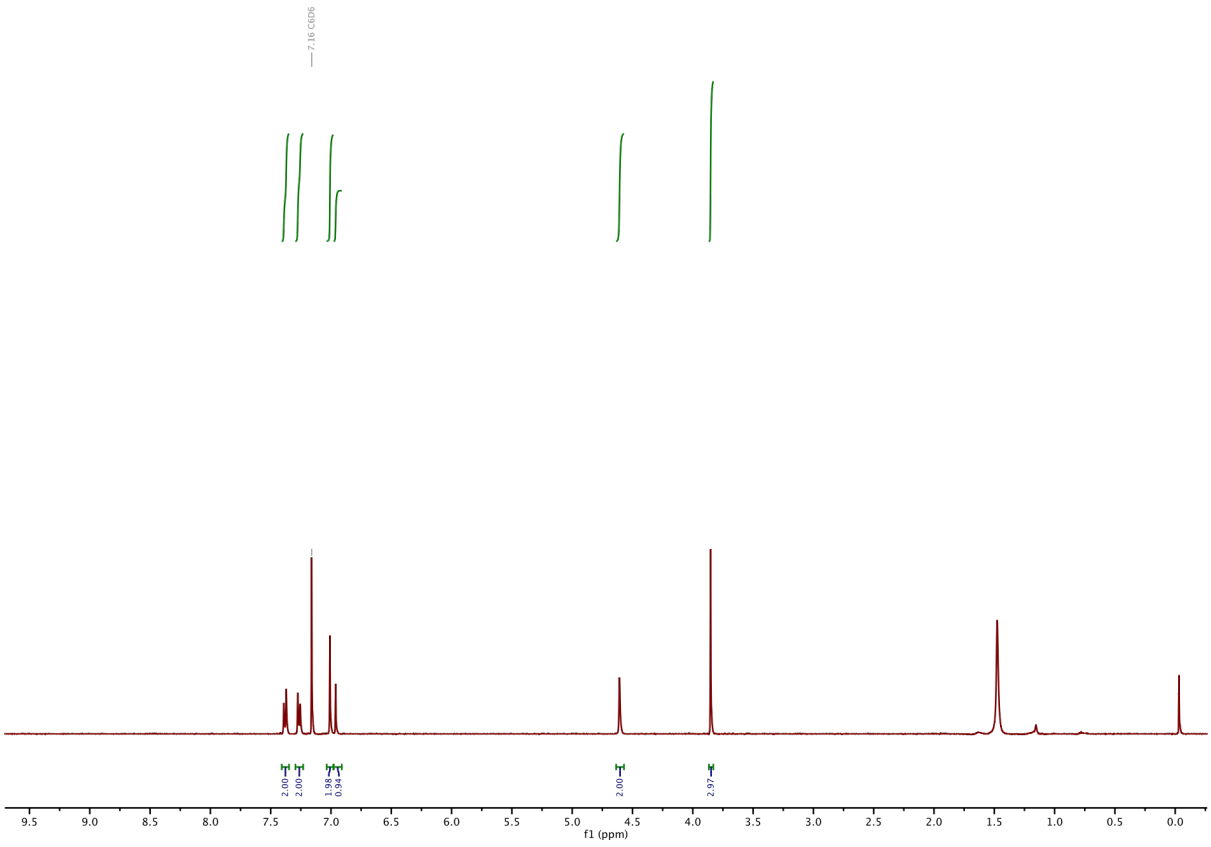

^{13}C-NMR of S1

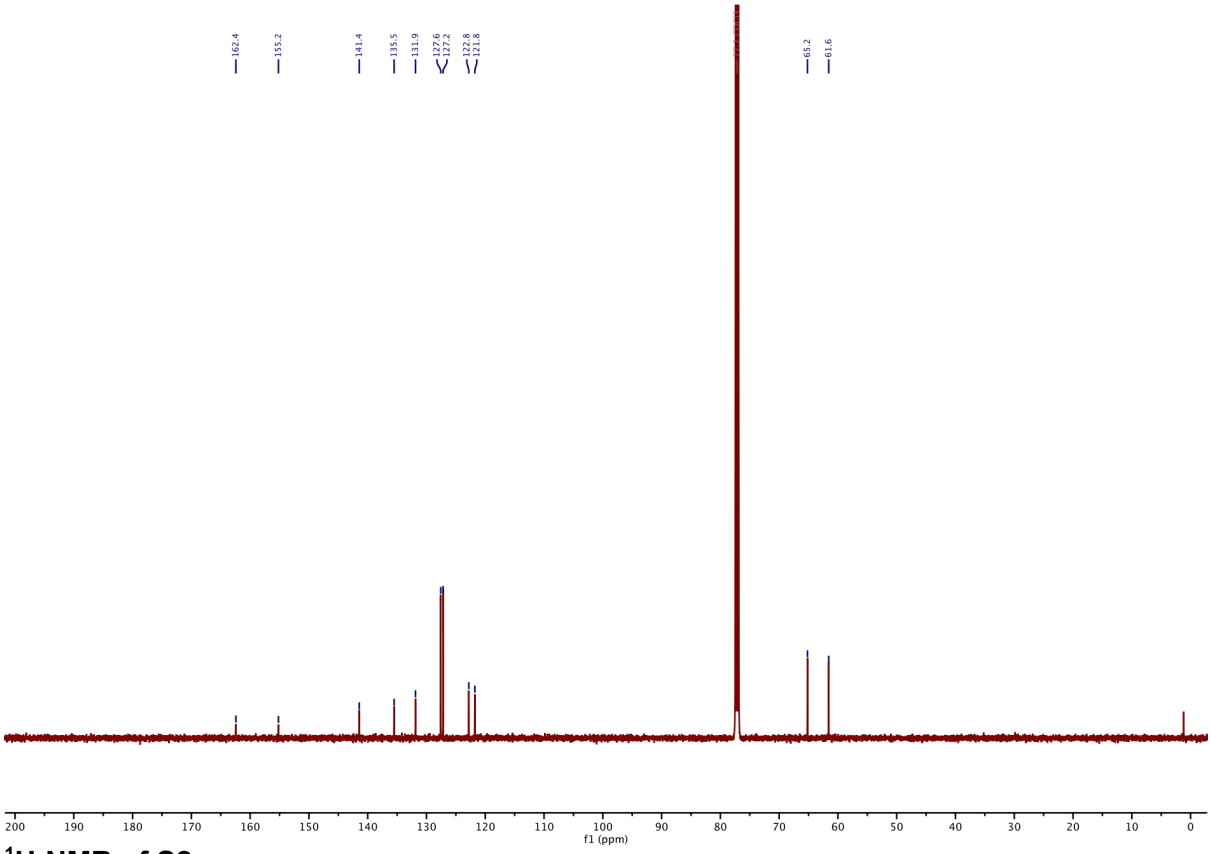

^{1}H-NMR of S2:

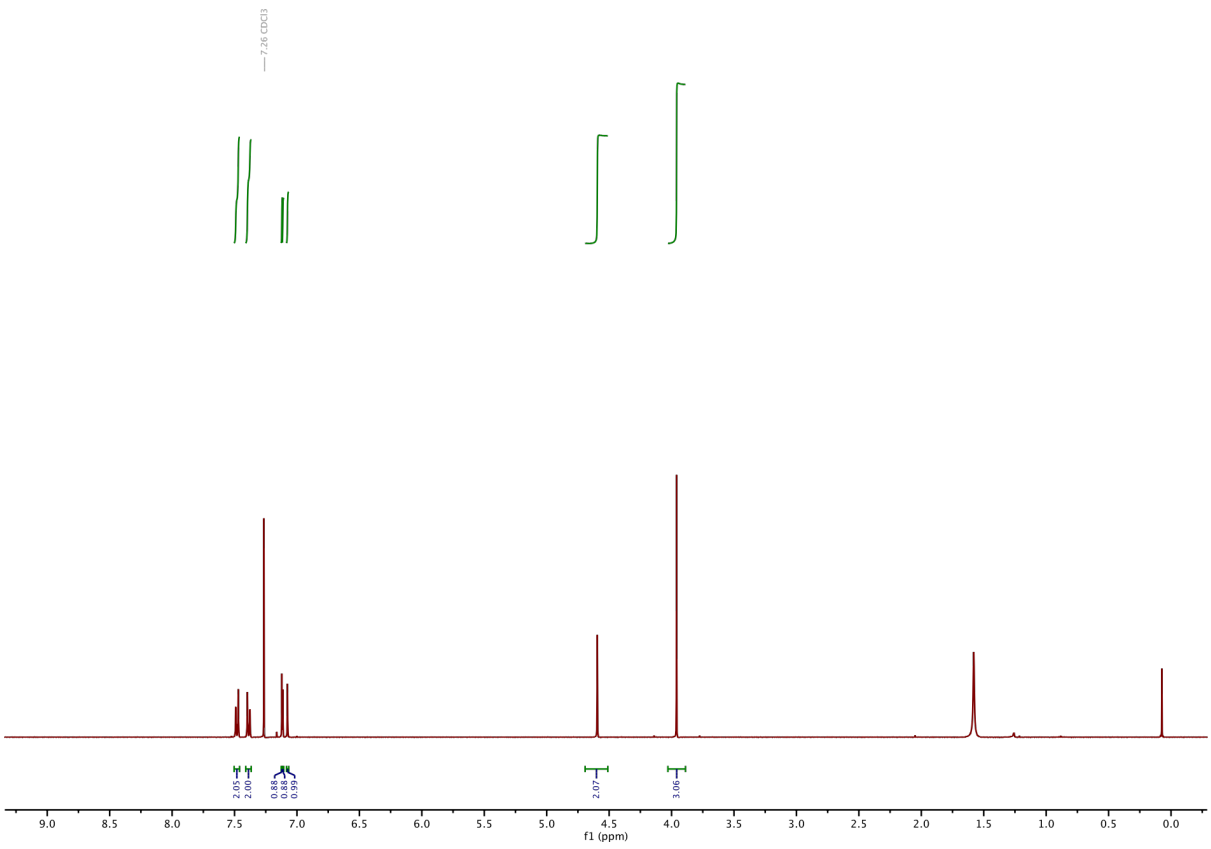

^{13}C-NMR of S2:

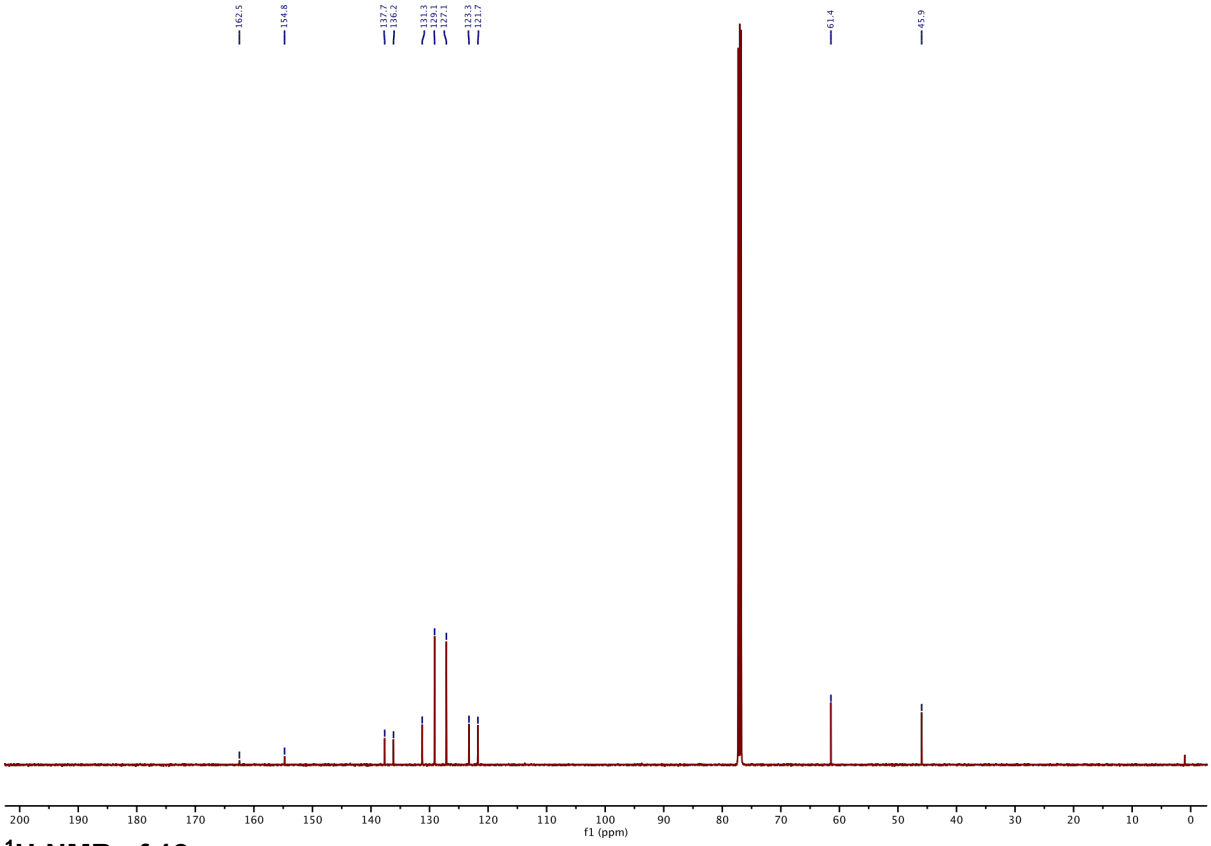

^{1}H-NMR of 12a:

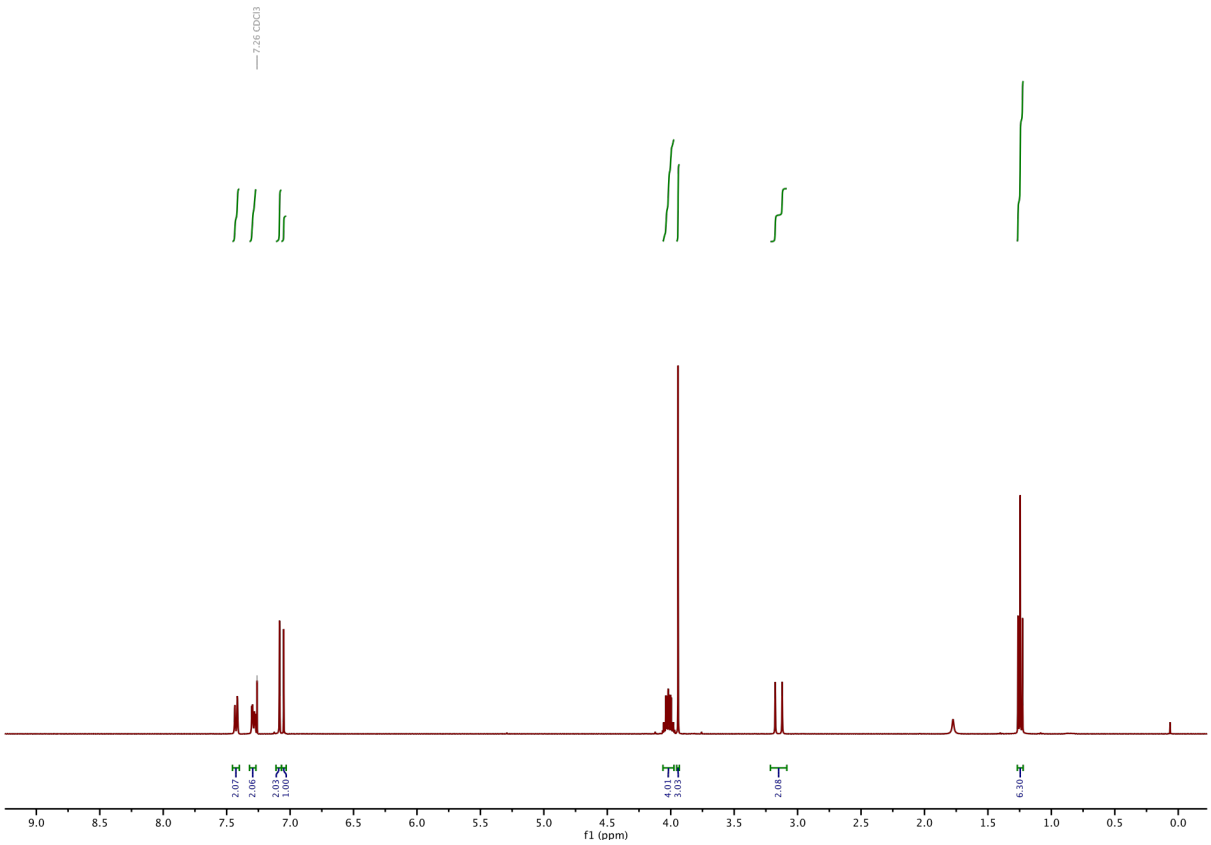

^{13}C-NMR of 12a:

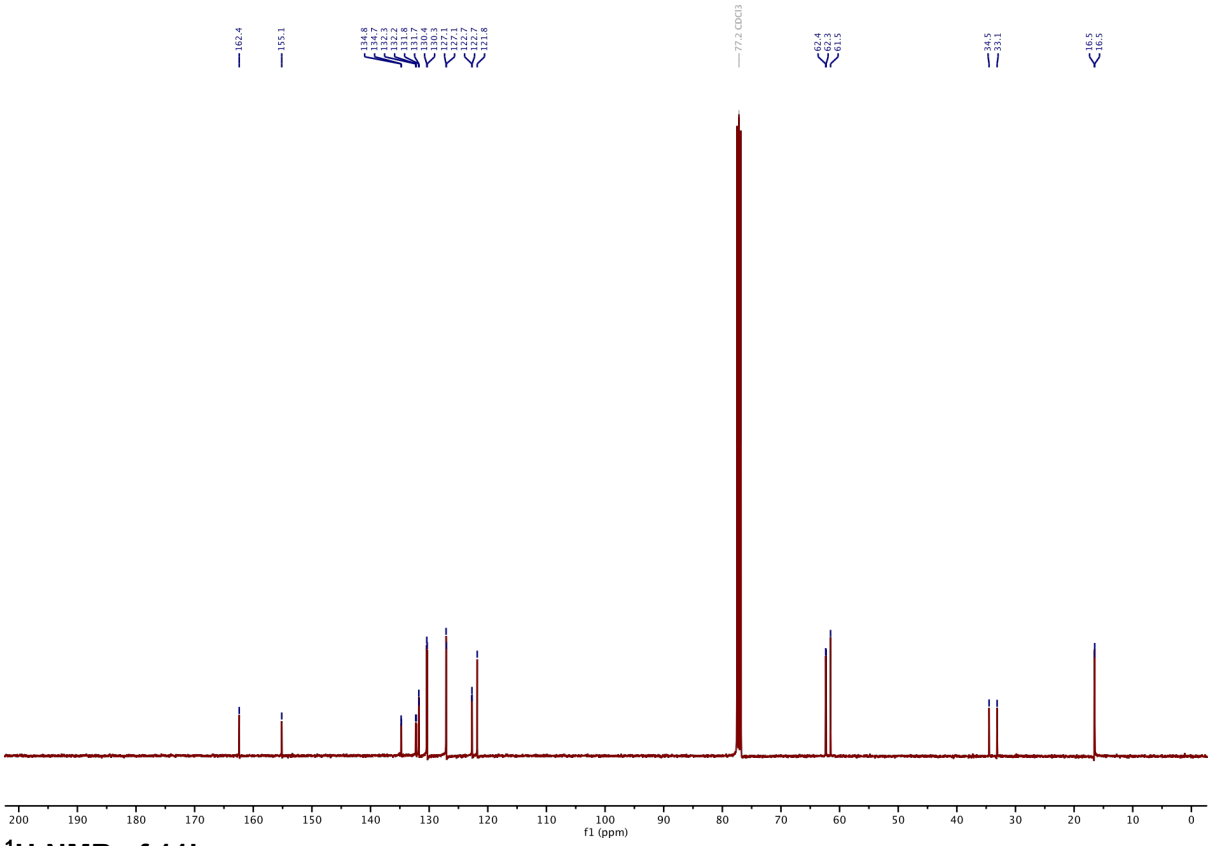

^{1}H-NMR of 11b:

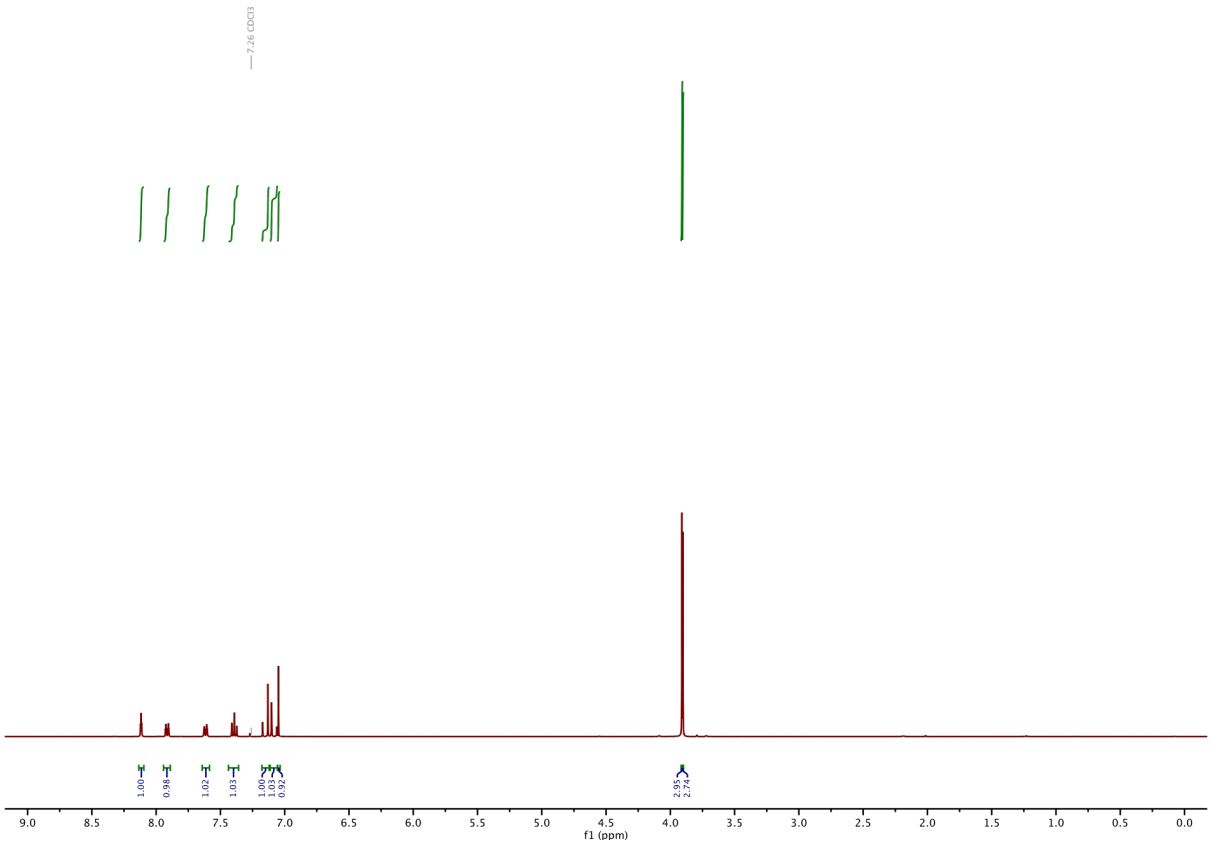

^{13}C-NMR of 11b:

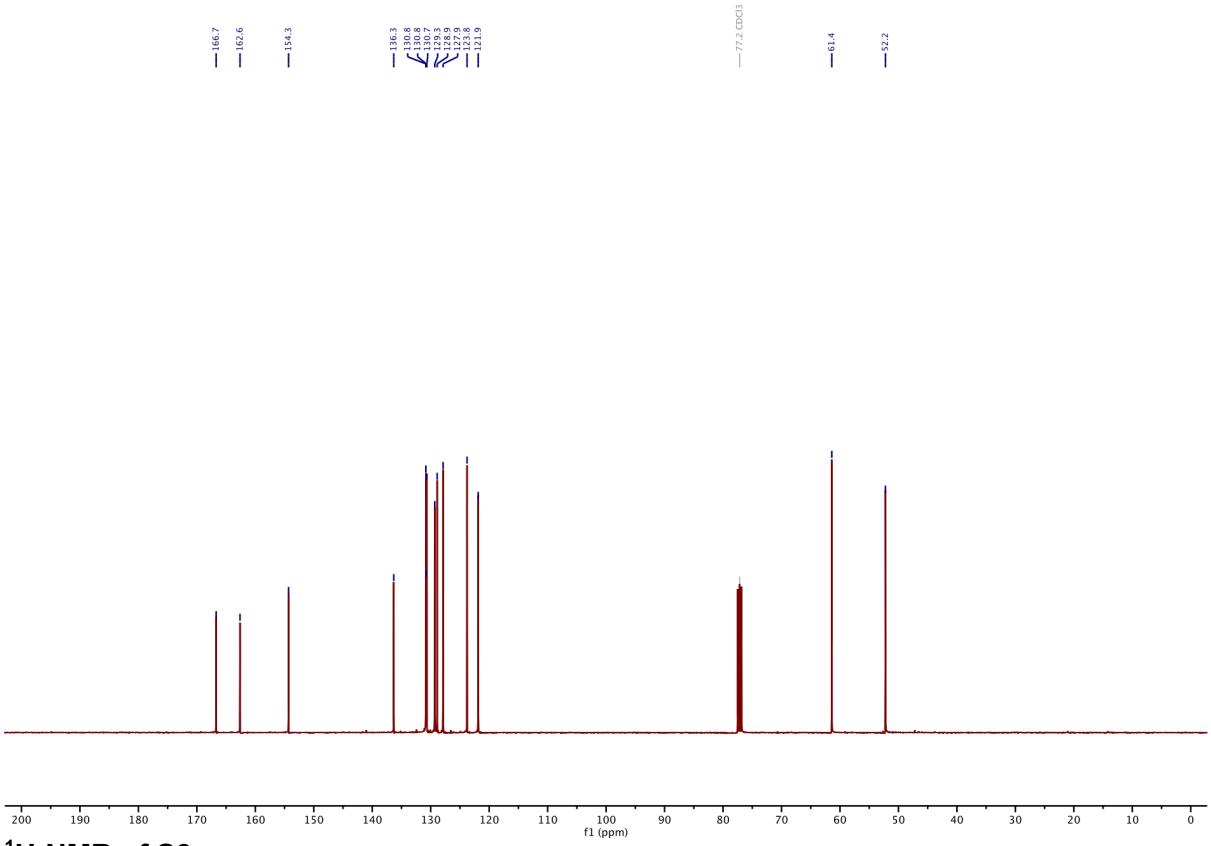

^{1}H-NMR of S3:

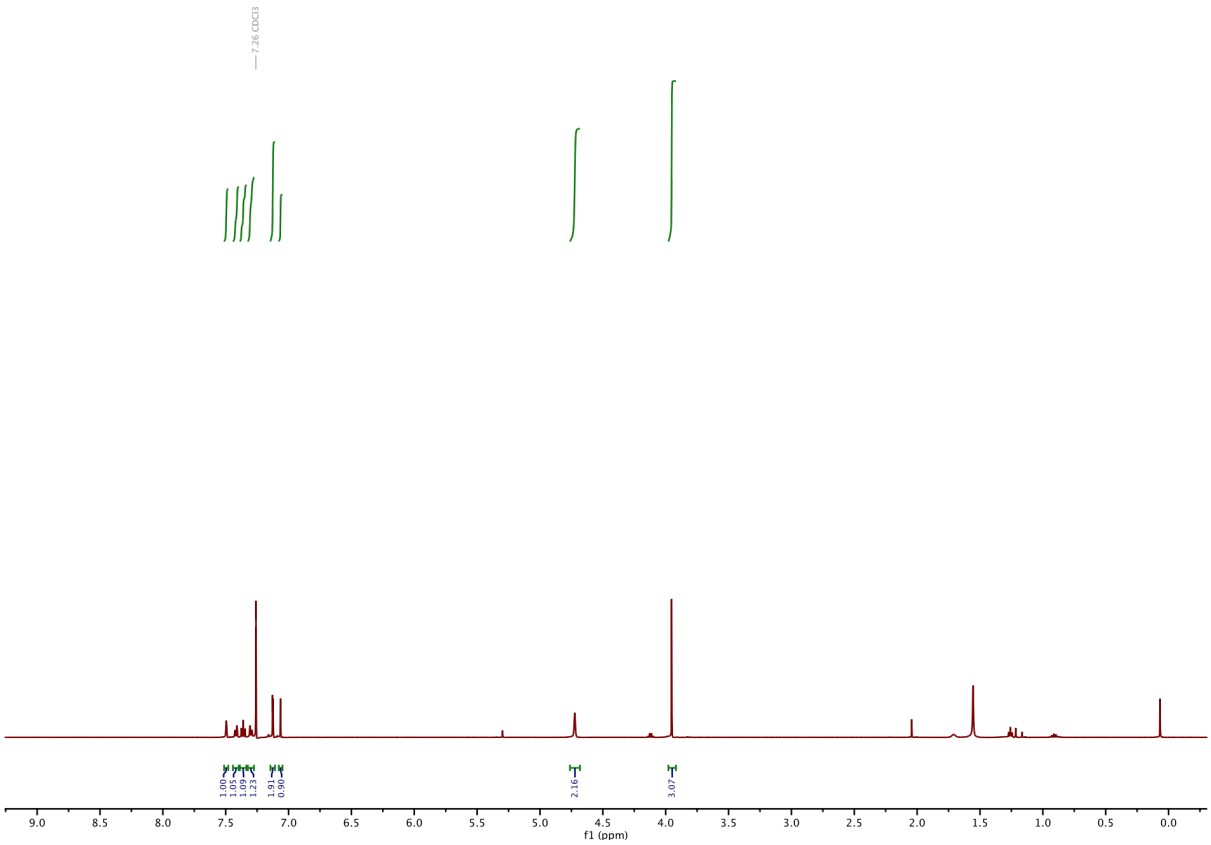

^{13}C-NMR of S3:

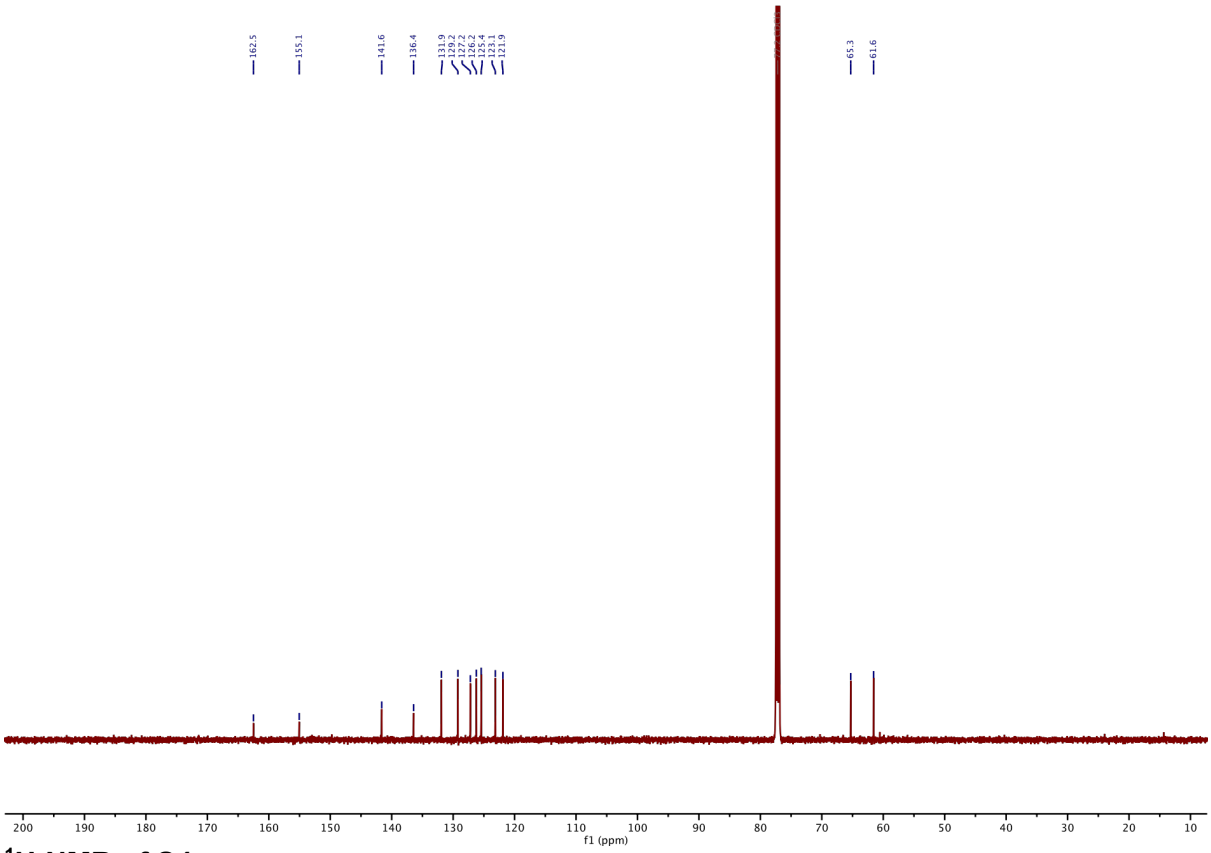

^{1}H-NMR of S4:

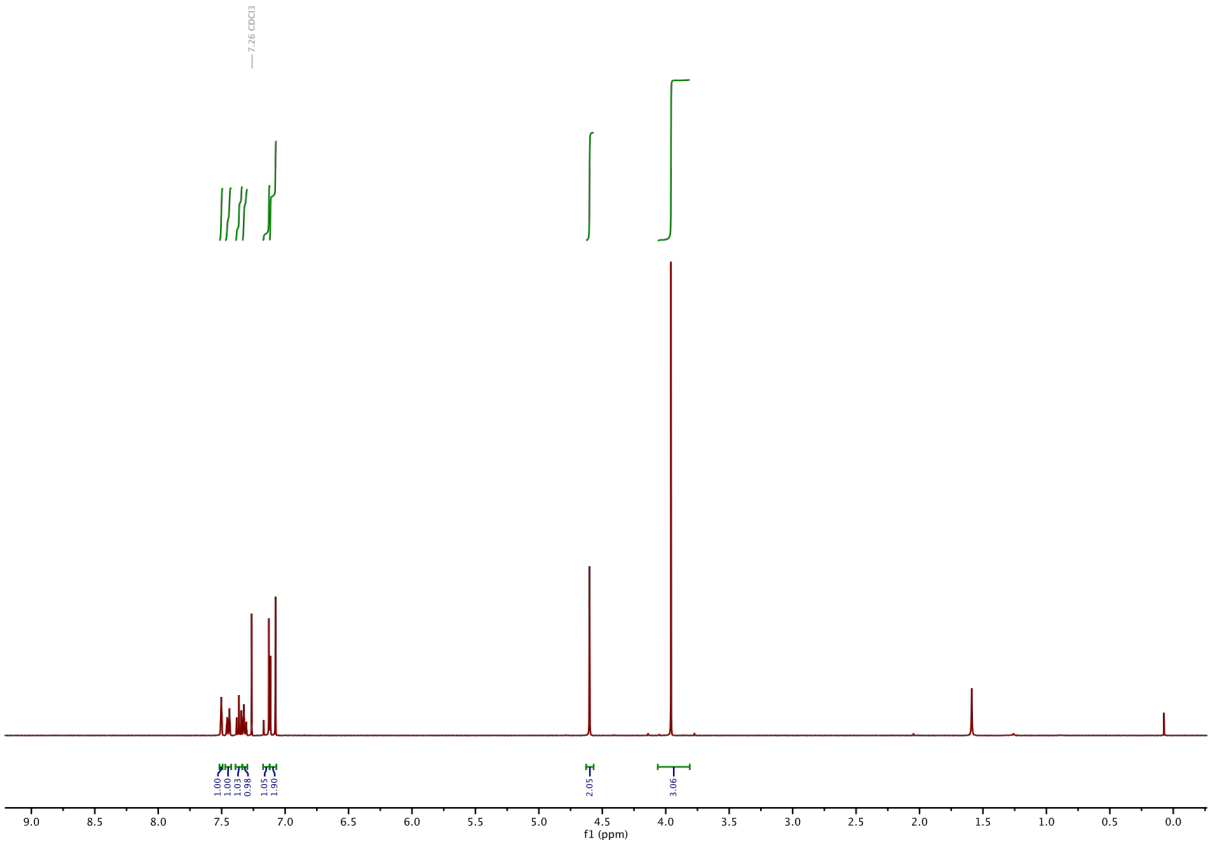

^{13}C-NMR of S4:

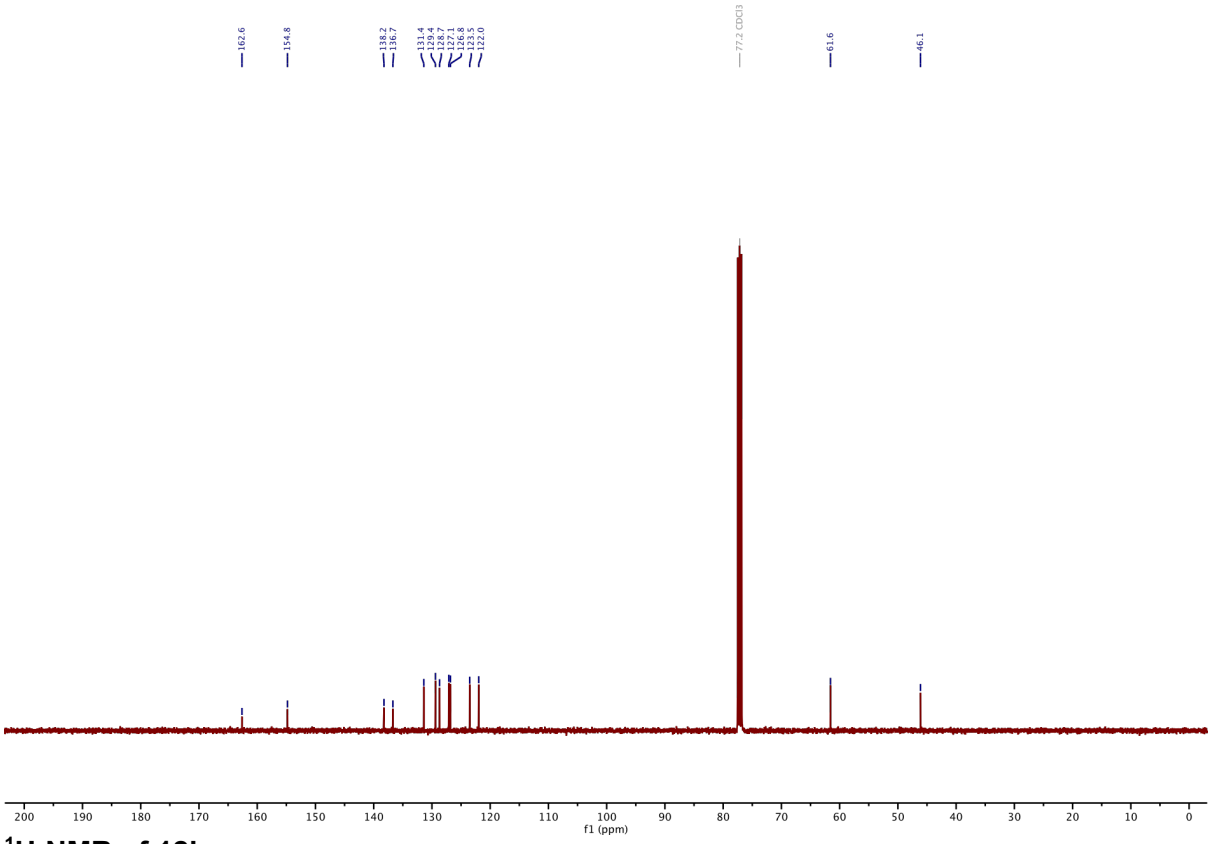

^{1}H-NMR of 12b:

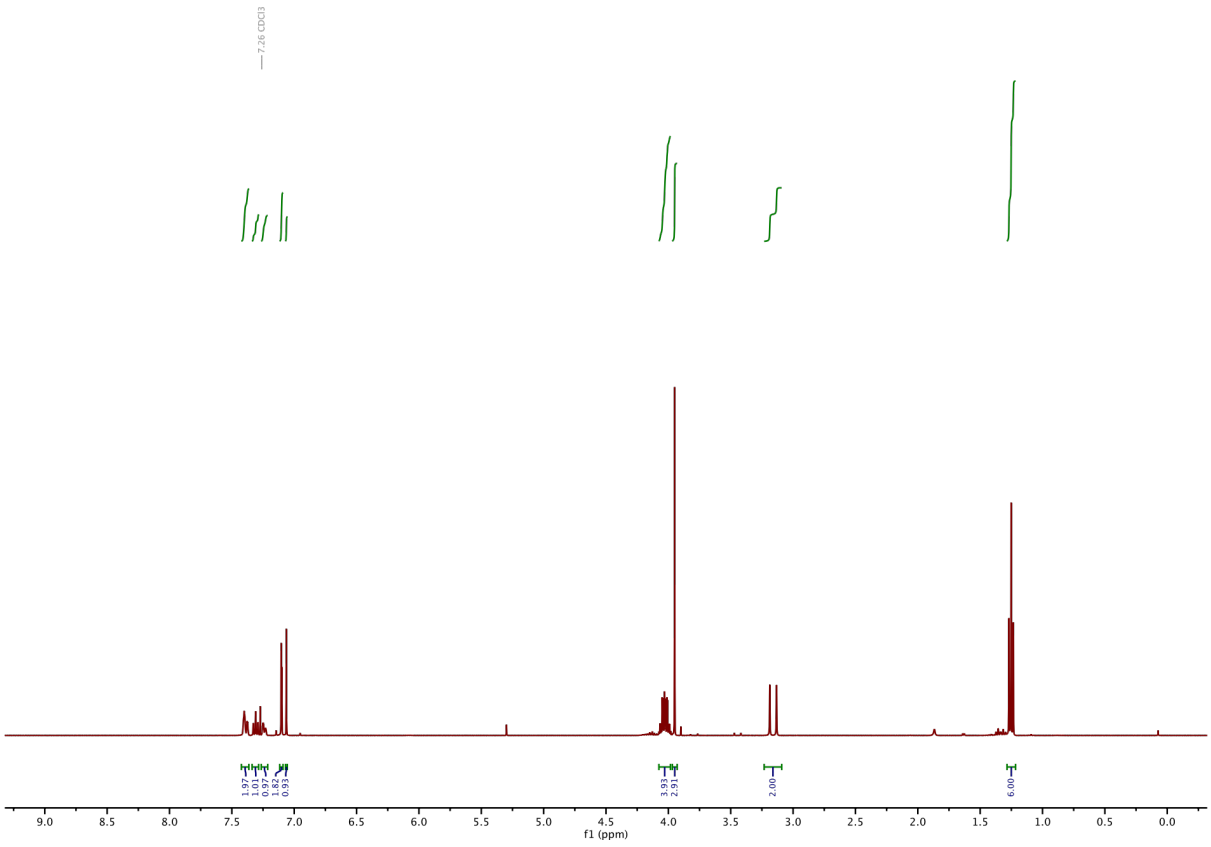

^{13}C-NMR of 12b:

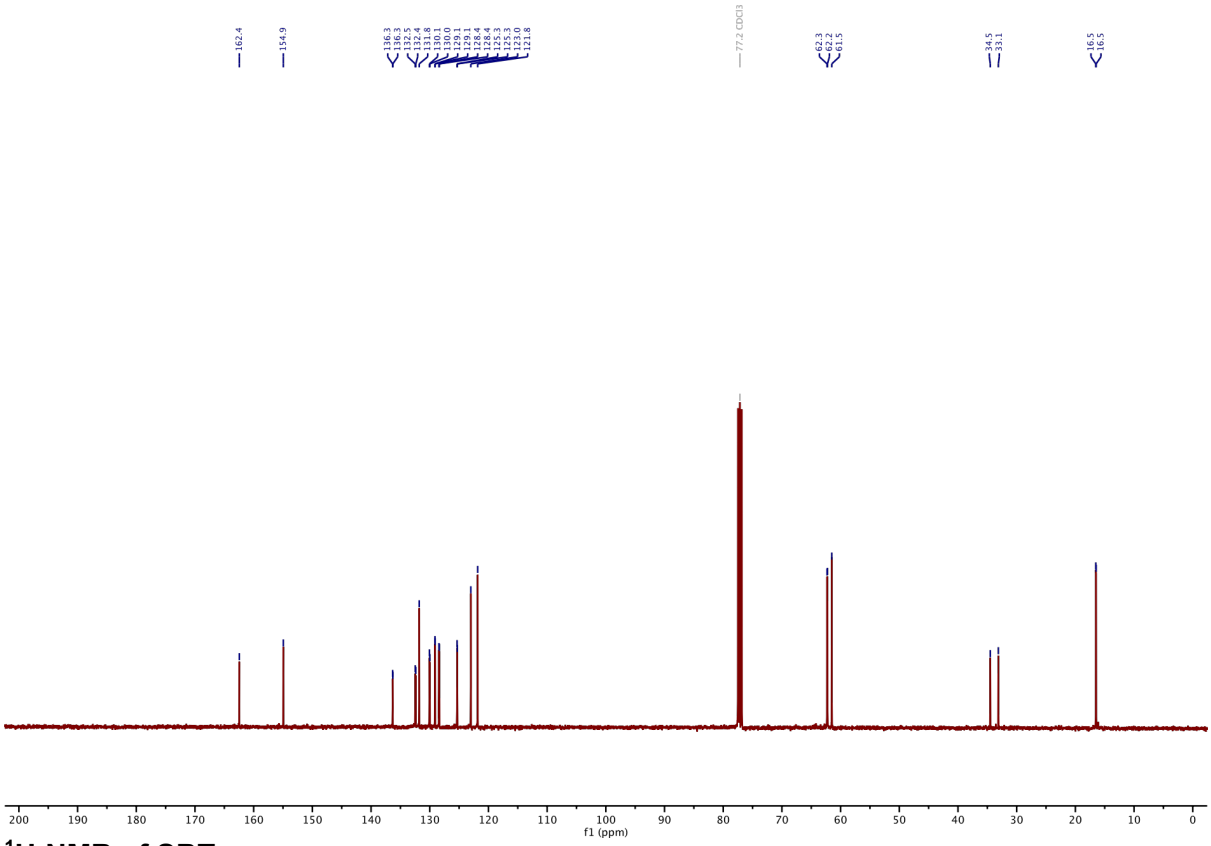

^{1}H-NMR of SBTax:

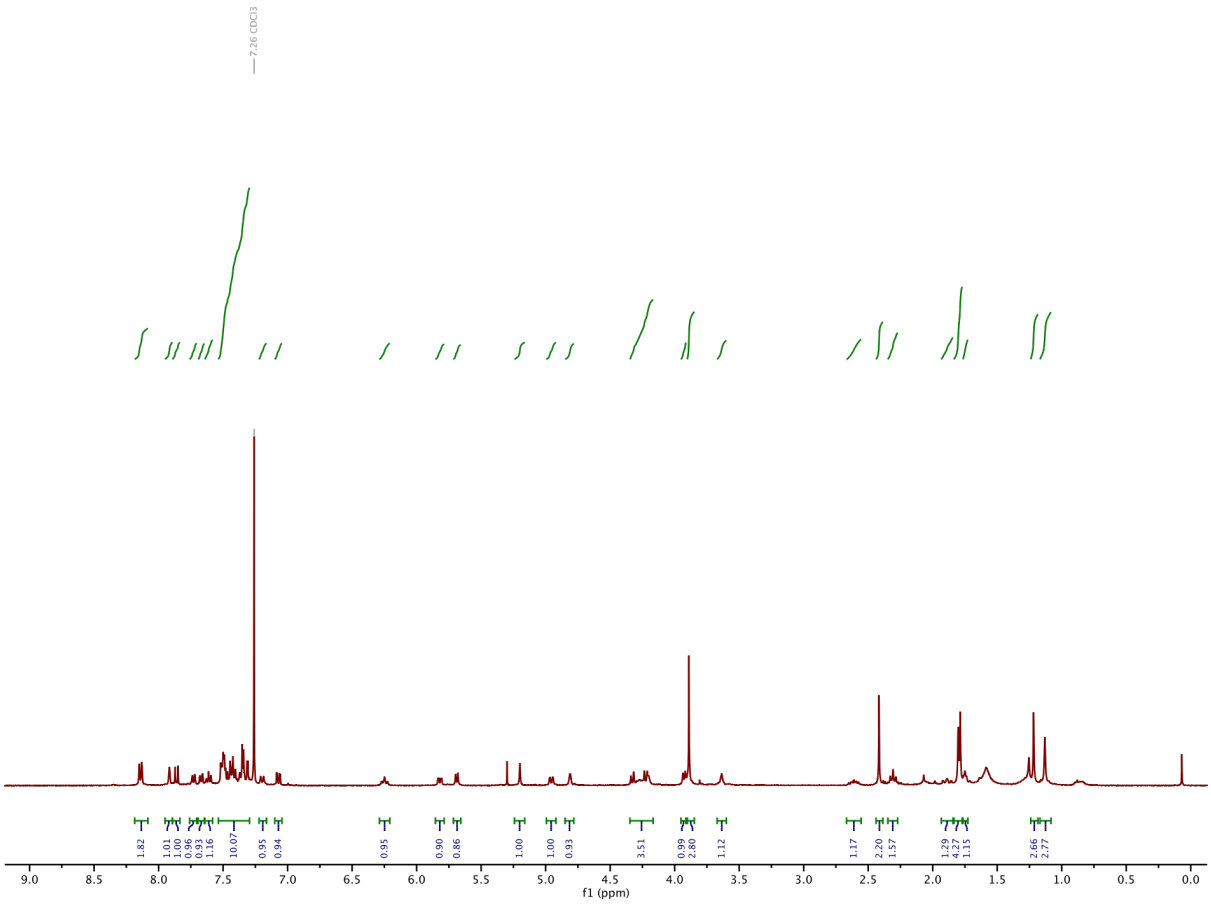

^{13}C-NMR of SBTax:

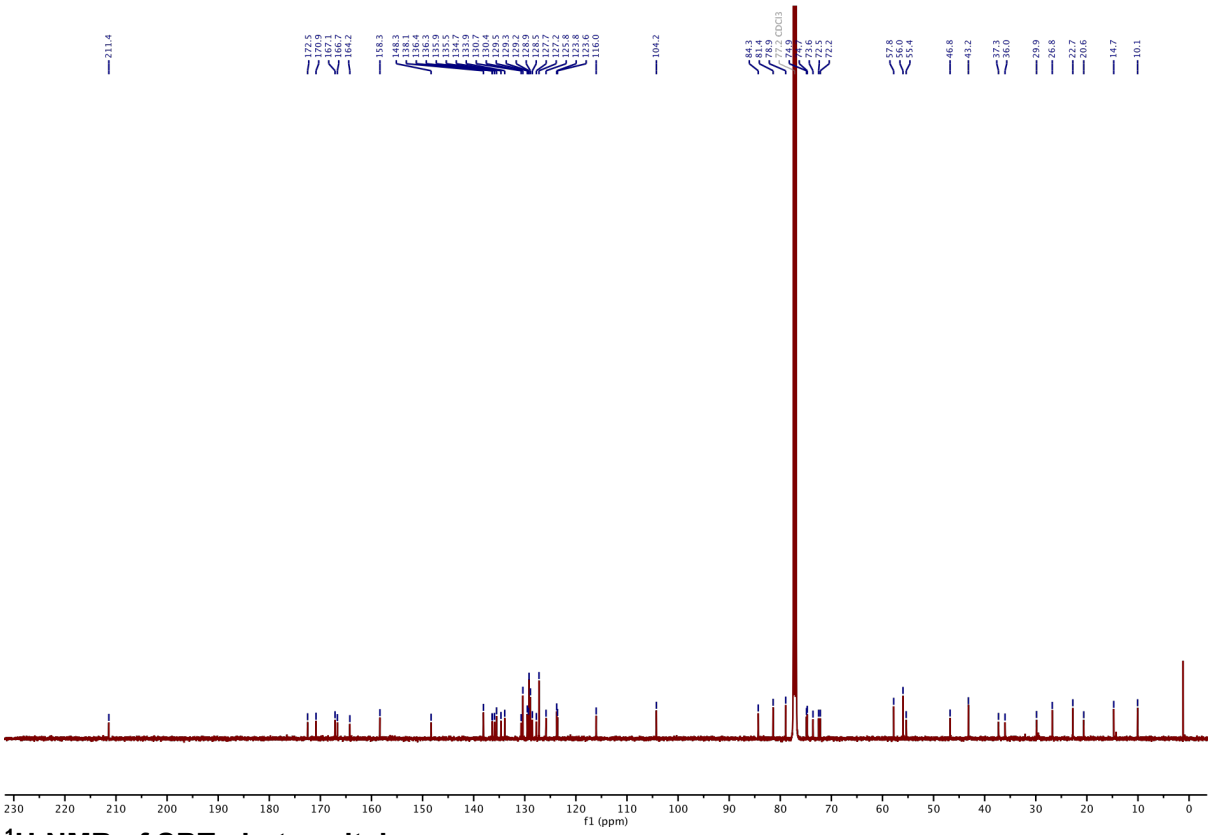

^{1}H-NMR of SBT photoswitch:

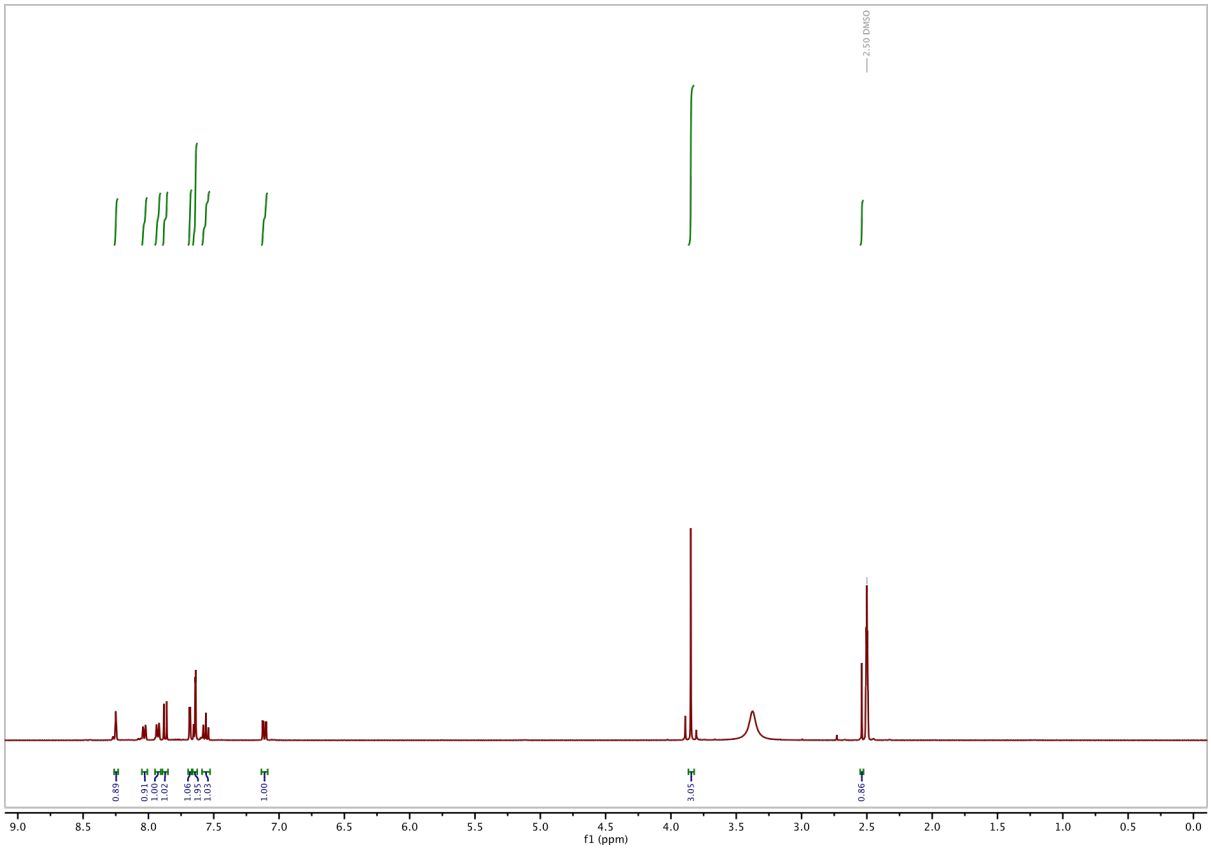

^{13}C-NMR of SBT photoswitch:

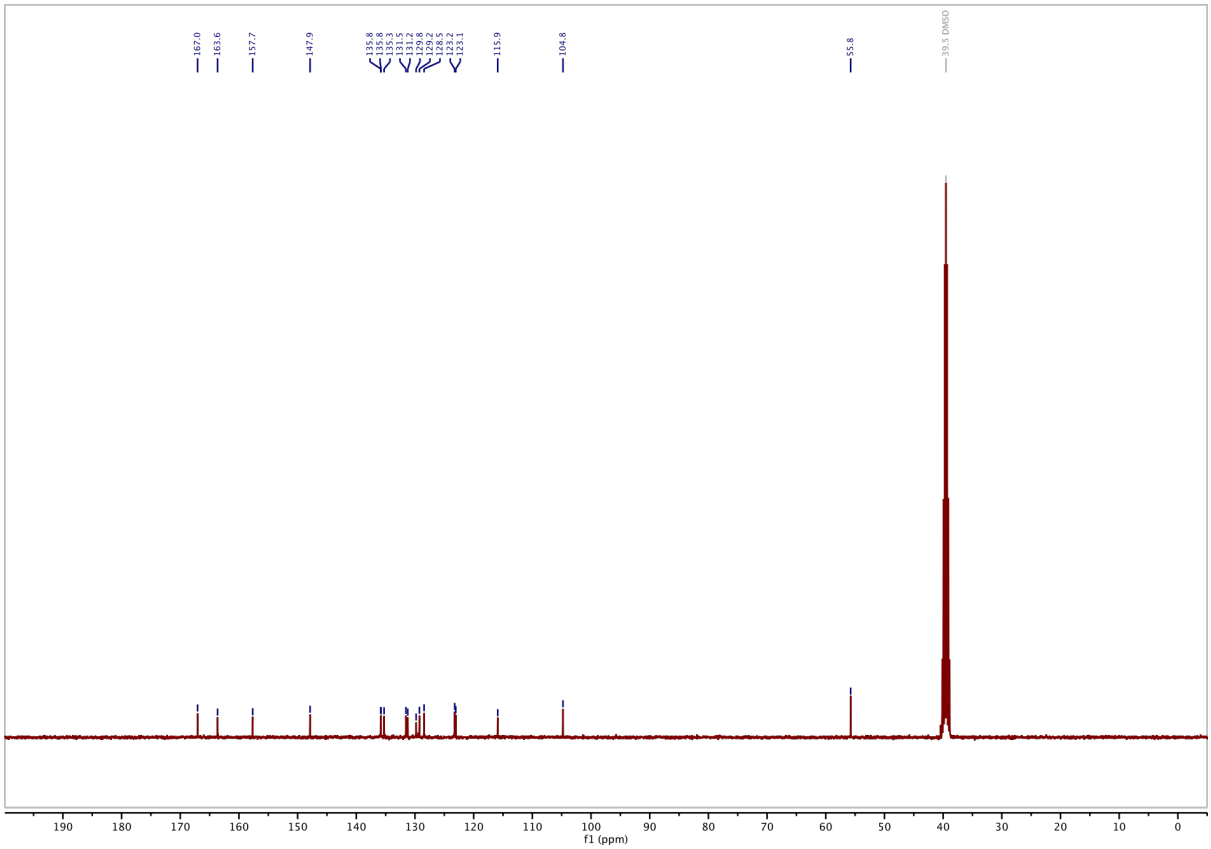

Supporting Information Bibliography

(1) Fulmer, G. R.; Miller, A. J.; Sherden, N. H.; Gottlieb, H. E.; Nudelman, A.; Stoltz, B. M.; Bercaw, J. E.; Goldberg, K. I. NMR Chemical Shifts of Trace Impurities: Common Laboratory Solvents, Organics, and Gases in Deuterated Solvents Relevant to the Organometallic Chemist. *Organometallics* **2010**, *29* (9), 2176–2179.

(2) Nicolaou, K. C.; Rhoades, D.; Wang, Y.; Bai, R.; Hamel, E.; Aujay, M.; Sandoval, J.; Gavrilyuk, J. 12,13-Aziridinyl Epothilones. Stereoselective Synthesis of Trisubstituted Olefinic Bonds from Methyl Ketones and Heteroaromatic Phosphonates and Design, Synthesis, and Biological Evaluation of Potent Antitumor Agents. *J. Am. Chem. Soc.* **2017**, *139* (21), 7318–7334. https://doi.org/10.1021/jacs.7b02655.

(3) Nicolaou, K. C.; Shelke, Y. G.; Dherange, B. D.; Kempema, A.; Lin, B.; Gu, C.; Sandoval, J.; Hammond, M.; Aujay, M.; Gavrilyuk, J. Design, Synthesis, and Biological Investigation of Epothilone B Analogues Featuring Lactone, Lactam, and Carbocyclic Macrocycles, Epoxide, Aziridine, and 1,1-Difluorocyclopropane and Other Fluorine Residues. *J Org Chem* **2020**, 53.

(4) Gao, L.; Meiring, J. C. M.; Kraus, Y.; Wranik, M.; Weinert, T.; Pritzl, S. D.; Bingham, R.; Ntouliou, E.; Jansen, K. I.; Olieric, N.; Standfuss, J.; Kapitein, L. C.; Lohmüller, T.; Ahlfeld, J.; Akhmanova, A.; Steinmetz, M. O.; Thorn-Seshold, O. A Robust, GFP-Orthogonal Photoswitchable Inhibitor Scaffold Extends Optical Control over the Microtubule Cytoskeleton. *Cell Chem. Biol.* **2021**, *28* (2), 228-241.e6. https://doi.org/10.1016/j.chembiol.2020.11.007.

(5) Bieling, P.; Laan, L.; Schek, H.; Munteanu, E. L.; Sandblad, L.; Dogterom, M.; Brunner, D.; Surrey, T. Reconstitution of a Microtubule Plus-End Tracking System in Vitro. *Nature* **2007**, *450* (7172), 1100–1105. https://doi.org/10.1038/nature06386.

(6) Rai, A.; Liu, T.; Glauser, S.; Katrukha, E. A.; Estévez-Gallego, J.; Rodríguez-García, R.; Fang, W.-S.; Díaz, J. F.; Steinmetz, M. O.; Altmann, K.-H.; Kapitein, L. C.; Moores, C. A.; Akhmanova, A. Taxanes Convert Regions of Perturbed Microtubule Growth into Rescue Sites. *Nat. Mater.* **2020**, *19* (3), 355–365. https://doi.org/10.1038/s41563-019-0546-6.

8. Outlook and Conclusions

8.1. Conclusions

8.1.1. Research summary

Photopharmaceuticals allow optical control over various biological systems with spatiotemporal precision. Small molecule photodrugs can be rapidly transitioned across different models and settings, and they can be rationally designed for various applications depending on the experimental setup and model system. To do so, various photoswitch scaffolds will be necessary to cover a wide range of the chemical drug space and photoswitch properties.

This work investigated the adaptability of the SBT photoswitch scaffold for photopharmacological applicability from 2D cell culture, to 3D culture and whole-organ explant, to systemic *in vivo* administration with local photoactivation and we compared their photoswitching properties and metabolic robustness with the classic azobenzene photoswitch and photouncaging strategies.

We showed that SBTs' photoswitching performance is chemocompatible and tunable with *o*/*p*-EDGs such as hydroxyl groups, which are often found in bioactive druglike compounds but lead to ultrafast relaxation rates of azobenzene or HTI photoswitches in intracellular (~aqueous environment) applications.

The SBT photoswitch's major advantage over classic azobenzenes are their improved metabolic robustness and their compatibility/orthogonality to fluorescence imaging tags since SBTs are efficiently photoactivated with the common 405 nm laser, but their sharp absorption cutoff leaves GFP, YFP, and RFP channels free for multiplexed imaging of fusion protein markers without risking compound photoactivation.

Based on these advantages of the SBT photoswitch scaffold we have developed **SBTubs** as robust, GFP-orthogonal photoswitchable microtubule depolymerizers for cell biology and confirmed their tubulin depolymerizing mechanism of action in several assays including immunofluorescence staining of MT architecture, cell cycle partitioning, and live cell imaging of microtubule dynamics. These consistent results across a range of models at different scales of time, length, and biological complexity, recommend the **SBTubs** as excellent and unique general-purpose tools for optically manipulating microtubule dynamics, microtubule structure, and microtubule dependent processes with high spatiotemporal precision. Current star compound **SBTubA4P** offers an alternative approach towards precisely-targeted *in vivo* applications by localized *in situ* photoactivation following systemic administration.

The **SBTubs** share photophysical properties of both azobenzene based PST-1 and photocaged CA4. They can be used as "turn-*ON*" probes with fast photoactivation kinetics like azobenzenes, but long thermal half-lives effectively make them unidirectional in cellular settings like photocaged drugs. Unlike caged CA4, the newly developed **SBTubs** do not release toxic by-products during photoactivation and they can be "inactivated" by thermal relaxation in case of accidental photoactivation, making them easier to handle than caged drugs where accidental illumination requires chemical reattachment of the cleaved photocage.

Lastly, a new photoswitchable MT stabilizer was introduced which is derived from the natural product epothilone and has advantages over the previously reported azo-taxol in terms of solubility, potency, compatibility with GFP imaging, and metabolic stability. Thus, significantly broadening the repertoire of optical tools to study the complex dynamics of the cytoskeleton. We rationally designed our lead compound **STEpo2** based on analysis of the tubulin-EpoA X-ray structure and provide mechanistical proof for their light dependent MT stabilizing effects.

8.1.2. General Conclusion

This work has shown that the SBT and ST photoswitch scaffolds can provide alternative solutions to install optical control over the MT cytoskeleton and can be translated to different binding sites other than the colchicine site and supposedly to other proteins than tubulin. The introduction of SBTs should be seen as an expansion of the toolbox of photoswitches in photopharmacology instead of a replacement of the azobenzene photoswitch. While weaknesses of the azobenzene scaffold are discussed in my thesis the azobenzene's bidirectional photoswitching is a great advantage over the SBT scaffold that guarantees that most photopharmaceutical designs will continue to use the azobenzene scaffold, especially if the target of interest is located in cell compartments with low GSH levels (e.g. the plasma membrane).

However, this work also shows that photopharmaceutical drug design should always take into account the scientific question one wants to answer and choose the right photoswitch accordingly. Therefore, it can be said that there is not a single "best photoswitch" because different purposes and circumstances will favor different photoswitch scaffolds.

The SBT photoswitch is surely a viable photoswitch in situations, where (i) readout is solely based on fluorescently tagged GFP/YFP proteins; (ii) in strong reducing environments; (iii) bidirectional switching is not absolutely needed or (iv) long-thermal half-lives are required; (v) the SBT scaffold is more isosteric to the parent drug scaffold than the azobenzene; (vi) a robust design turn-off probe is wanted.

8.2. Outlook

8.2.1. The future of SBTubs

The **SBTubs** have been introduced as photoswitchable tubulin inhibitors with proof of concept applications across various models and settings, but no new biological insights have been made yet. I believe that **SBTub**'s GFP-orthogonality opens up new possibilities to study MT-dependent processes. Proteins that are available as fluorescent fusion proteins can nearly always be found as GFP fusions. Therefore **SBTubs** can be used directly instead of having to develop an YFP or RFP fusion protein to avoid isomerization of HTI or azobenzene reagents due to photoresponse at ≤530 nm. More importantly however, since the amount of imaging channels are limited on a microscopy setup, it is crucial to have as many of them free for fluorescence imaging of the POIs in order to study the interactions of multiple proteins with each other (Fig 15a), as was shown in chapter 6 (cf. Fig 5f) where we imaged both mCherry-labeled MTs and GFP-labeled cellular structural elements after photoactivation of **SBTub2M**. This could for example allow future experiments to study repositioning/rescue behavior of various centromere proteins upon temporally precise MT depolymerization by **SBTubs** at different stages of mitosis.

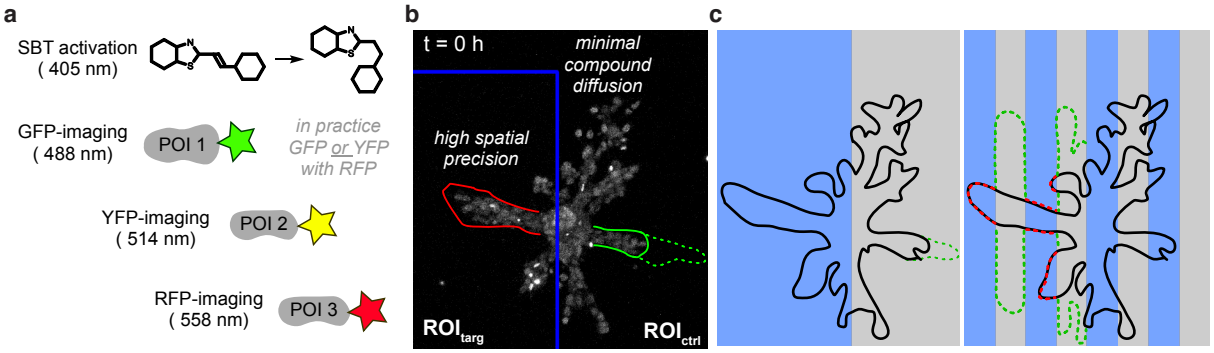

Figure 15: **(a)** Common laser lines available on microscopy stages could be used for photoswitching and imaging of multiple protein targets at the same time. **(b) SBTubs** can be photoisomerized with exquisite spatial precision in 3D organoid systems to stop branch development exclusively in the targeted area. **(c)** This could allow "inhibition patterning" on a single organoid.

While diffusion to the extracellular medium can restore MT dynamics in a 2D cell culture setting usually within 20 s, it is not an option in 3D tissues that are embedded for growth and imaging where diffusion is much slower (as seen in chapter 6 Fig 5, Fig 15b). However, this allows **SBTubs** to be photoisomerized with exquisite spatial precision in 3D organoid systems to study differentiated growth behavior within a single organoid in 3D cell culture. Our first organoid experiments were performed to compare two halves of the same organoid under different light regimes, however the local restriction of **SBTubA4P** after photoactivation could allow "inhibition patterning" on a single organoid (Fig 15c). Sample questions that could therefore be asked include: what happens if a growing branch is "severed" by photoactivating

SBTubs in the middle of it (tip-to-center communication)? How much accumulated damage does an organoid tolerate before it collapses, and is it important where that damage is located? I believe that **SBTubs** are a viable tool to study how a large conglomerate of cells communicate with each other and how they respond to spatially localized cellular damage.

Overall the long thermal halflives of **SBTubs** allow clean and robust long-term studies on MT dependent processes without having to continuously reapply light as it would be necessary for azobenzene based PST-1 and without the byproduct formation from photouncaging strategies.

8.2.1. The potential therapeutic use of SBTubA4P

Our first proof of concept in organoid and zebrafish models and **SBTub**'s inherent metabolic stability and long-thermal half-lives of the *Z*-isomer support the idea that **SBTub**s could also be used in mouse xenograft models: for example, to study the light-dependent effect of **SBTubA4P** on tumor growth and if the underlying effect is solely based on their antimitotic effect in tumor cells, or if **SBTubs** have an additional anti-angiogenic or vascular disrupting effects on the supporting vasculature.

8.2.2. Improving SBTs thermal relaxation rates

The biggest drawback of the SBT photoswitch scaffold is their lack of photoreversibility. While bidirectional SBT photoswitching may be difficult within the biologically-compatible wavelength range, accelerating thermal relaxation to the minute scale, which is probably the most appropriate scale for 3D/*in vivo* applications, may be feasible especially in the presence of *o*/*p*-electron-donating groups (Fig 16a), as was seen in chapter 5. **SBTub4** showed the influence of solvent environment on relaxation rates. If the acidity of the *para*-phenol could be further increased it might be possible to achieve minute-scale relaxation rates at 37°C.

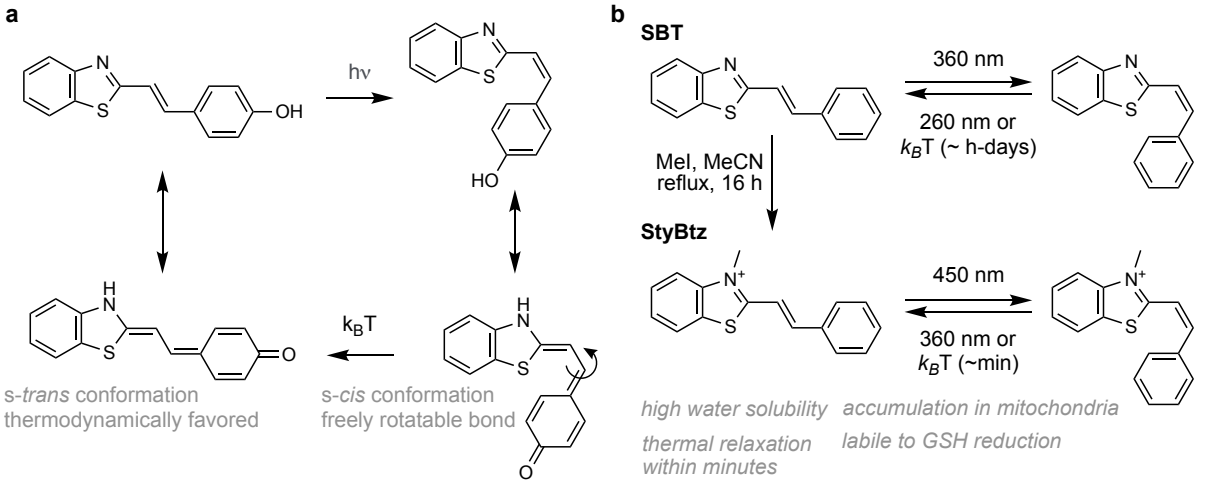

Figure 16: **(a)** SBTs with *o*/*p*-EDGs could undergo faster thermal *Z*→*E* isomerization by undergoing conformational change of the s-*cis* diene to the thermodynamically favored s-*trans* diene. **(b)** Styrylbenzothiazolium photoswitches have red-shifted isomerization wavelengths ($\lambda_{E\rightarrow Z}$ ~450 nm) and undergo thermal relaxation to the thermodynamically favored *E*-isomer within minutes.

An alternative solution to improve thermal relaxation rates which I am currently exploring is the formation of styrylbenzothiazolium ions by *N*-alkylation of the nitrogen atom from SBTs (Fig 16b).[138] This class of photoswitch has red-shifted isomerization wavelengths ($\lambda_{E\rightarrow Z}$ ~450 nm) and undergoes thermal relaxation to the thermodynamically favored *E*-isomer within minutes, depending on their substitution pattern. Additionally, they are highly water soluble due to their permanent positive charge. However, since styrylbenzothiazolium photoswitches are delocalized lipophilic cations they accumulate in mitochondria (restricted availability of protein targets) which I have observed in unpublished work not described in this thesis, where they also are likely to undergo destruction by conjugate addition of nucleophiles to their polarized C=C double bond.

8.2.3. Embracing SBT's photoswitching and physicochemical properties

I personally believe that future SBT-based photodrug design should focus on finding new application areas for the SBT scaffold, instead of trying to engineer the SBT scaffold to deliver the same performance as azobenzene, or to compete in research areas where the field is (rightfully) dominated by azobenzene photopharmaceuticals.

8.2.4. SBT based photo-antibiotics could withstand reduction by azoreductases

Because of SBTs high resistance to biochemical degradation I believe that it is better suited for the development of photo-antibiotics than the azobenzenes. There is also a large number of benzothiazole-based compounds with antibacterial activity that bind to different biological targets in bacterial cells and have been shown to be inhibitors of enzymes that are important for essential processes in bacterial cells (Fig 17a-d)[139] and "*styrylbenzothiazologization*" of these compounds could allow isomer-dependent control of their antibiotic activity. Because the bacterial cell wall plays an important role in the survival and intrinsic drug resistance of bacteria, it is one of the main target systems that has been exploited in the discovery of antibacterial compounds. One example is TCA1, an inhibitor of Decaprenyl phosphoryl-β-D-ribose 2'-epimerase (Dpre1), which is an important oxidase enzyme in the biosynthesis of arabinogalactan that is a structural component of the Mycobacterium (tuberculosis) cell wall (Fig 17a). TCA1 binds at the interface of a flavin adenine dinucleotide (FAD) binding site domain and a substrate binding domain and the benzothiazole ring is oriented roughly parallel to the isoalloxazine of FAD. Since the binding of TCA1 and the enzyme are dominated by hydrophobic and van der Waals interactions I assume that the amide bond can be replaced by a C=C double bond as long as the noncovalent interactions between the benzothiazole and the flavin are maintained, which contributes to a large fraction of the total contact surface (Fig 17b).[140]

Another prime example for "*styrylbenzothiazologization*" is PC190723[141] (Fig 17c), which is an inhibitor of FtsZ[142] - a prokaryotic homologue of tubulin that is crucial for bacterial cell division. Since styrylpyridothiazole is a highly electron deficient system I would expect a relatively blue-shifted π→π* that would complicate *E*→*Z* isomerization in the biologically tolerated optical window (> 360 nm) and making photoactivation using the common 405 nm laser on microscopy setups impossible. However, photoactivation on a microscopy stage would be highly desired for a dynamic protein like FtsZ. Haydon et al.[143] showed that benzothiazole derivatives of PC190723 maintain their nanomolar activity. In order to maintain GFP-orthogonality and photoactivation by 405 nm light, I would instead synthesize an SBT derivative of PC190723 instead of a styrylpyridothiazole.

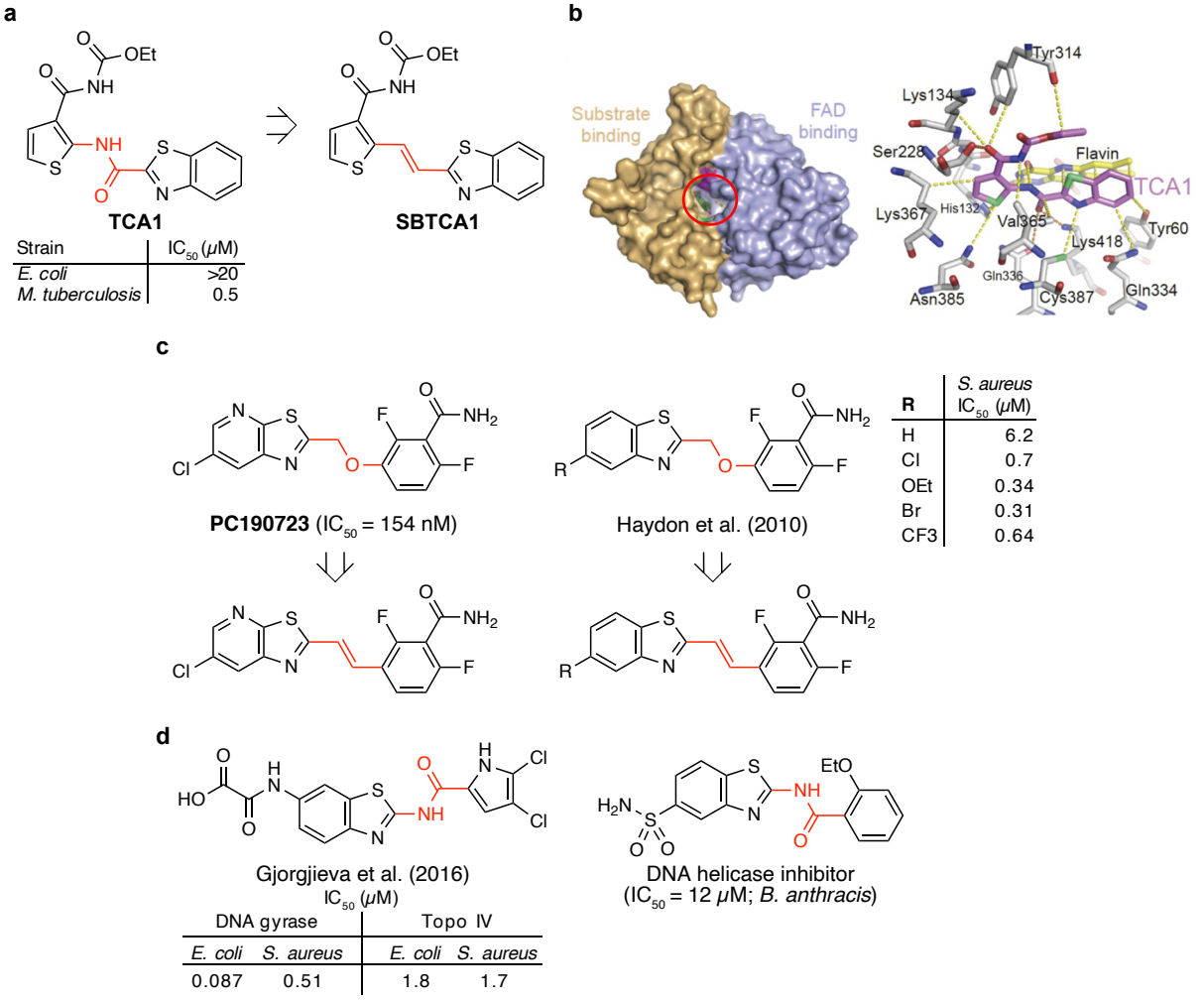

Figure 17: Possible SBT-based photo-antibiotics derived from benzothiazole containing parent drug scaffolds. The "*styrylbenzothiazologization*" site is highlighted in red. **(a)** TCA1 is an inhibitor of Decaprenyl phosphoryl-β-D-ribose 2'-epimerase 1 (DprE1), that **(b)** binds at the interface of a flavin adenine dinucleotide (FAD) binding site domain and a substrate binding domain (adapted from Wang et al.[140]). **(c)** PC190723 is an inhibitor of FtsZ - a prokaryotic homologue of tubulin. Haydon et al. showed that replacing the pyridothiazole ring with classic benzothiazoles maintains their FtsZ inhibiting mechanism of action. **(d)** Benzothiazole-based compounds with antibacterial activity that bind to DNA gyrase, bacterial Topoisomerase IV and DNA helicase.[144,145]

Other benzothiazole-based compounds with antibacterial activity bind to DNA gyrase, bacterial Topoisomerase IV and DNA helicase (Fig 17d) offering a large selection of biological targets

in bacterial cells to develop SBT-based photo-antibiotics. Because the designed compounds would be dark-active, they would be auto-deactivated when exposed to sunlight, which would reduce excessive and unwanted exposure of bacteria to the active form of the drug, and thus drastically limit the number of bacteria with engaged resistance mechanisms as it is envisioned by Szymanski and Feringa.[146]

8.2.5. Possible SBT-based photopharmaceuticals for eukaryotes

Toll-like receptors[147] (TLRs) recognize viral and bacterial pathogen associated molecular patterns (PAMPs) to activate the innate immune system. Binding of a TLR8 agonist, induces two TLR8 protomers to be brought into close proximity and initiates MYD88-dependent response and downstream activation of cytokine and chemokine releasing signaling pathways (Fig 18a).

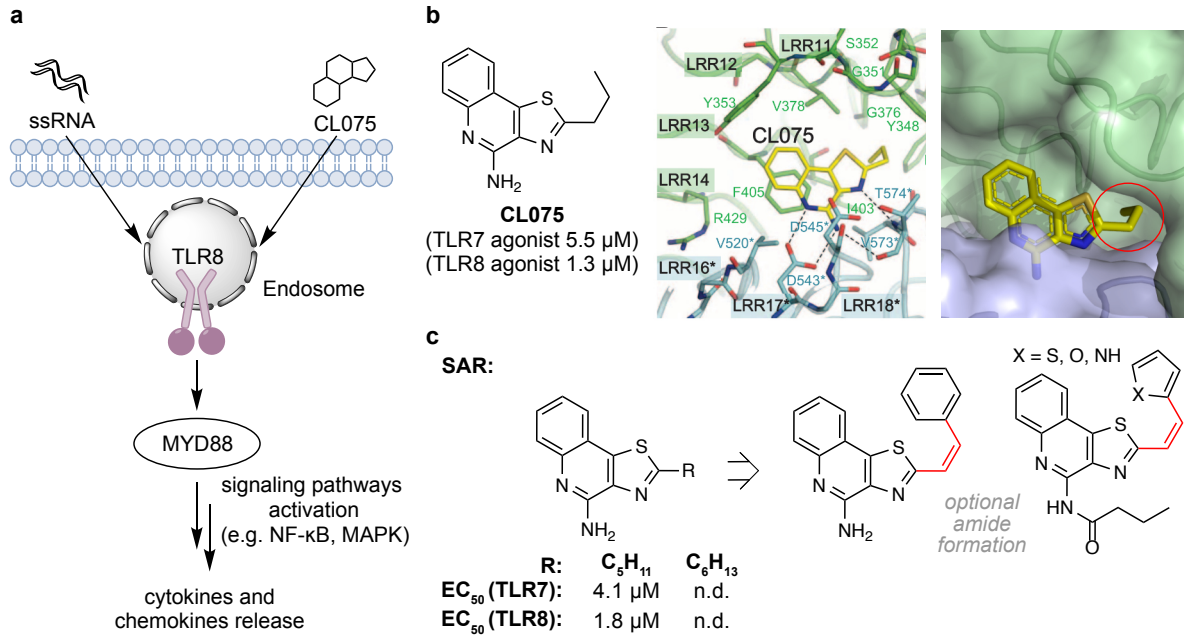

Figure 18: **(a)** Agonists bind to TLR8 and activate various cytokine and chemokine releasing signaling pathways. **(b)** TLR7/8 agonist CL075 binds in between the interface of the two TLR domains and the 2-propyl substituent that protrudes into a small hydrophobic pocket (red circle). **(c)** future TLR8 photopharmaceuticals could target that site to attach a photoswitch that extends in and out of the small pocket.

Therefore, TLR agonists have established therapeutic benefits as anticancer agents that activate immune cells in the tumor microenvironment. CL075 is a TLR8 agonist with a thiazoloquinoline core and a 2-propyl substituent that protrudes into a small hydrophobic pocket (Fig 18b)[148]. SAR studies have shown that substitution of the 2-propyl group by *n*-pentyl is well tolerated, whereas *n*-hexyl is not (Fig 18c).[149] A styryl-extension at the 2 position could install optical control over the TLR8 activity which could be used as a tumor targeted switch for immune response.

8.2.6. The SBT scaffold's potential in time-resolved serial crystallography

X-Ray free electron lasers allow serial crystallographic data collection from femtoseconds to milliseconds. This ultrafast crystallography can provide structural snapshots of proteins that can be assembled into molecular movies to visualize protein structural rearrangement dynamics.[150] To accumulate a large set of crystallographic snapshots the crystallized protein is embedded into a matrix and this jet of protein crystals is continuously extruded and hit by X-ray pulses (Fig 19). Time-resolved serial femtosecond crystallography (TR-SFX) has already been used to study structural changes in a light-driven sodium pump[151] with high spatial and temporal resolution and it could offer completely new insights into protein ligand dynamics with outstanding resolution on the molecular to atomic level using photoswitchable compounds.[152]

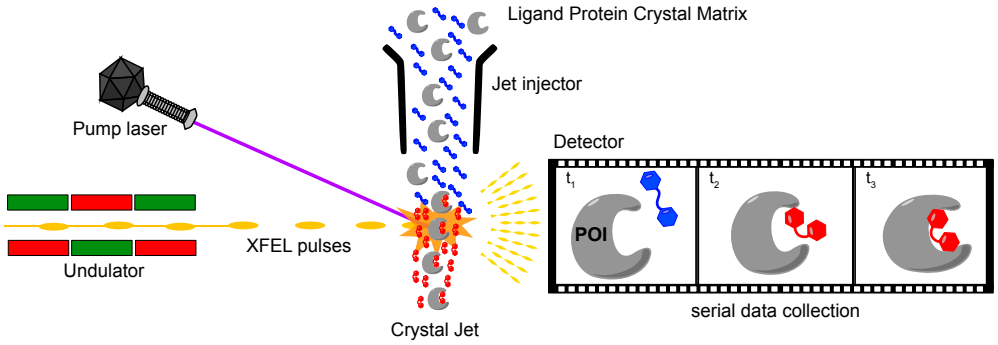

Figure 19: Schematic picture of a possible time-resolved serial femtosecond crystallography experiment using a photoswitchable ligand to study protein structural rearrangement dynamics.

Because the sample is jetted no bidirectional switching of the photodrug is required, which makes SBT an equivalent alternative to azobenzenes in these experimental settings, if not even better because the sulfur from SBT can be used to help orient the ligand position within the protein binding pocket similar to how sulfur anomalous scattering can be used for SAD[153] (single-wavelength anomalous diffraction) phasing in *de novo* phase evaluations to solve the sulfur substructure and calculate initial maps.

8.2.7. General Outlook

I expect that by supporting conceptual innovations in photoswitch scaffold chemistry and rational photopharmaceutical design, and particularly by starting to unlock the applications promise of photopharmacology for globally-administered, locally-targeted *in vivo* use, this research represents a promising advance for high-performance photopharmacology against other protein targets in general, beyond their immediate impact on microtubule biology; always with the goal to develop photopharmaceutical tools to study biological processes, instead of developing bioassays for photopharmaceuticals.

9. Acknowledgments

First of all I would like to thank my supervisor Dr. Oliver Thorn-Seshold for giving me the opportunity to pursue my doctoral thesis in his group. Thank you for all the support and trust throughout these years. It has been a great honor to be your first PhD student and to help you build up this group.

Secondly, I am very grateful to Prof. Dr. Ivan Huc for agreeing to be the second reviewer of this thesis, and I would also like to thank the rest of my defense committee: Prof. Dr. Franz Bracher, Prof. Dr. Daniel Merk, Prof. Dr. Konstantin Karaghiosoff, and Prof. Dr. Dirk Trauner, who introduced me to the wonderful world of photopharmacology early on in my studies.

I want to thank Prof. Dr. Wanner for his supervision and support during my first two years and I want to thank the Wanner group and the LMU Trauner group, especially, Janina, Maren, Heinrich, Jörg and Nils for taking me in at the beginning.

Many thanks to my lab mates Adrian, Alex, Ben and Philipp for the time we got to share in the lab and to the current TS group members - Jan, Lukas, Lena, Markus, Elena, Julia, Constanze, Annabel, Martin and Carina - as well as all the TS group alumni, especially Yelena, Petar, Longhi, Franzi, Bekkah and Monique. You are all absolutely outstanding scientists and the most wonderful bunch of people that I had the pleasure to work and party with.

I want to express my gratitude to all my collaborators, especially Joyce and Max, for the opportunity to work with all of you on these highly interdisciplinary projects - it has been a great experience to see all the science that's out there.

To my interns and students, Leonie, Vivian, Kati, Rakan, Ferdi, Sonja, Paula, Savanna, Simon and Ricky: Thank you all for your great work, wish you all the best for your studies and it was a pleasure to have been your senpai.

I am also very grateful for the great work of the members of the analytical department, especially Claudia and Lars.

Thank you Stefan for a great friendship throughout our studies and our PhDs and I thank everyone that has supported me during these years.

Lastly, thanks to my parents for everything.

10. Appendix

10.1. List of abbreviations

API	Active pharmaceutical ingredient	k_a	Association rate
BTQ	Benzothiazoloquinolinium	LOV domain	Light-oxygen-voltage domain
CA4	Combretastatin A4	MAP	Microtubule-associated protein
CDI	Colchicine domain inhibitor	MDA	Microtubule Destabilizing Agent
CENP	Centromer protein	MSA	Microtubule Stabilizing Agent
Cryo-EM	Cryogenic electron microscopy	MT	Microtubule
DNA	Deoxyribonucleic acid	MYD88	Myeloid differentiation primary response 88
Dpre1	Decaprenyl phosphoryl-β-D-ribose 2'-epimerase	NCI	National Cancer Institute
DTE	Dithienylethene	pa-Rac1	Photoactivatable Rac1
DTT	Dithiothreitol	PAMP	Pathogen associated molecular pattern
EB	End-binding (protein)	Pgp	Permeability glycoprotein
EDG	Electron donating group	POI	Protein of interest
FAD	Flavin adenine dinucleotide	RFP	Red fluorescent protein
FDA	Food and Drug Administration	ROI	Region of interest
FEL	Free-electron laser	SAD	Single-wavelength anomalous diffraction
FtsZ	Filamenting temperature-sensitive mutant Z	SBT	Styrylbenzothiazole
GDP	Guanosin diphosphate	SiR	Silicon Rhodamine
GFP	Green fluorescent protein	SPMC	Spiropyran-merocyanine
GSH	Glutathione	ST	Styrylthiazole
GSSG	Glutahtione disulfide	THC	Tetrahydrocannabinol
GTP	Guanosin triphosphate	TLR	Toll-like receptor
HDAC	Histone deacetylase	TR-SFX	Time-resolved serial femtosecond crystallography
HTI	Hemithioindigo	UV	Ultraviolet
$[I]_{WC}$	Working concentration	YFP	Yellow fluorescent protein
K-fibers	Kinetochore fibers	+TIP	Microtubule-plus-end tracking proteins
K_a	Association constant		

10.2. Bibliography

(1) Zemelman, B. V.; Lee, G. A.; Ng, M.; Miesenböck, G. Selective Photostimulation of Genetically ChARGed Neurons. *Neuron* **2002**, *33* (1), 15–22. https://doi.org/10.1016/s0896-6273(01)00574-8.

(2) Boyden, E. S.; Zhang, F.; Bamberg, E.; Nagel, G.; Deisseroth, K. Millisecond-Timescale, Genetically Targeted Optical Control of Neural Activity. *Nat. Neurosci.* **2005**, *8* (9), 1263–1268. https://doi.org/10.1038/nn1525.

(3) Boyden, E. S. A History of Optogenetics: The Development of Tools for Controlling Brain Circuits with Light. *F1000Prime Rep* **2011**, *3* (11).

(4) Nagel, G.; Szellas, T.; Huhn, W.; Kateriya, S.; Adeishvili, N.; Berthold, P.; Ollig, D.; Hegemann, P.; Bamberg, E. Channelrhodopsin-2, a Directly Light-Gated Cation-Selective Membrane Channel. *Proc. Natl. Acad. Sci.* **2003**, *100* (24), 13940–13945.

(5) Zhang, F.; Wang, L.-P.; Brauner, M.; Liewald, J. F.; Kay, K.; Watzke, N.; Wood, P. G.; Bamberg, E.; Nagel, G.; Gottschalk, A.; Deisseroth, K. Multimodal Fast Optical Interrogation of Neural Circuitry. *Nature* **2007**, *446* (7136), 633–639. https://doi.org/10.1038/nature05744.

(6) Deisseroth, K. Optogenetics. *Nat. Methods* **2011**, *8* (1), 26–29. https://doi.org/10.1038/nmeth.f.324.

(7) Huala, E.; Oeller, P. W.; Liscum, E.; Han, I.-S.; Larsen, E.; Briggs, W. R. Arabidopsis NPH1: A Protein Kinase with a Putative Redox-Sensing Domain. *Science* **1997**, *278* (5346), 2120–2123. https://doi.org/10.1126/science.278.5346.2120.

(8) Wu, Y. I.; Frey, D.; Lungu, O. I.; Jaehrig, A.; Schlichting, I.; Kuhlman, B.; Hahn, K. M. A Genetically Encoded Photoactivatable Rac Controls the Motility of Living Cells. *Nature* **2009**, *461* (7260), 104–108. https://doi.org/10.1038/nature08241.

(9) Velema, W. A.; Szymanski, W.; Feringa, B. L. Photopharmacology: Beyond Proof of Principle. *J Am Chem Soc* **2014**, *136* (6), 2178–2191. https://doi.org/10.1021/ja413063e.

(10) Broichhagen, J.; Frank, J. A.; Trauner, D. A Roadmap to Success in Photopharmacology. *Acc Chem Res* **2015**, *48* (7), 1947–1960. https://doi.org/10.1021/acs.accounts.5b00129.

(11) Deal, W. J.; Erlanger, B. F.; Nachmansohn, D. Photoregulation of Biological Activity by Photochromic Reagents, Iii. Photoregulation of Bioelectricity by Acetylcholine Receptor Inhibitors. *Proc. Natl. Acad. Sci.* **1969**, *64* (4), 1230–1234. https://doi.org/10.1073/pnas.64.4.1230.

(12) Hüll, K.; Morstein, J.; Trauner, D. In Vivo Photopharmacology. *Chem Rev* **2018**, *118* (21), 10710–10747. https://doi.org/10.1021/acs.chemrev.8b00037.

(13) Mayer, G.; Heckel, A. Biologically Active Molecules with a "Light Switch." *Angew Chem Int Ed* **2006**, *45* (30), 4900–4921. https://doi.org/10.1002/anie.200600387.

(14) Klán, P.; Šolomek, T.; Bochet, C. G.; Blanc, A.; Givens, R.; Rubina, M.; Popik, V.; Kostikov, A.; Wirz, J. Photoremovable Protecting Groups in Chemistry and Biology: Reaction Mechanisms and Efficacy. *Chem. Rev.* **2013**, *113* (1), 119–191. https://doi.org/10.1021/cr300177k.

(15) Norrish, R. G. W.; Bamford, C. H. Photo-Decomposition of Aldehydes and Ketones. *Nature* **1937**, *140* (3535), 195–196. https://doi.org/10.1038/140195b0.

(16) Beharry, A. A.; Woolley, G. A. Azobenzene Photoswitches for Biomolecules. *Chem Soc Rev* **2011**, *40* (8), 4422–4437. https://doi.org/10.1039/c1cs15023e.

(17) Hartley, G. S. The Cis-Form of Azobenzene. *Nature* **1937**, *140* (3537), 281. https://doi.org/10.1038/140281a0.

(18) Westphal, M. V.; Schafroth, M. A.; Sarott, R. C.; Imhof, M. A.; Bold, C. P.; Leippe, P.; Dhopeshwarkar, A.; Grandner, J. M.; Katritch, V.; Mackie, K.; Trauner, D.; Carreira, E. M.; Frank, J. A. Synthesis of Photoswitchable Δ^9-Tetrahydrocannabinol Derivatives Enables Optical Control of Cannabinoid Receptor 1 Signaling. *J. Am. Chem. Soc.* **2017**, *139* (50), 18206–18212. https://doi.org/10.1021/jacs.7b06456.

(19) Morstein, J.; Awale, M.; Reymond, J.-L.; Trauner, D. Mapping the Azolog Space Enables the Optical Control of New Biological Targets. *ACS Cent. Sci.* **2019**, *5* (4), 607–618. https://doi.org/10.1021/acscentsci.8b00881.

(20) Kobauri, P.; Szymanski, W.; Cao, F.; Thallmair, S.; J. Marrink, S.; D. Witte, M.; J. Dekker, F.; L. Feringa, B. Biaryl Sulfonamides as Cisoid Azosteres for Photopharmacology. *Chem. Commun.* **2021**, *57* (34), 4126–4129. https://doi.org/10.1039/D1CC00950H.

(21) Frank, J. A.; Moroni, M.; Moshourab, R.; Sumser, M.; Lewin, G. R.; Trauner, D. Photoswitchable Fatty Acids Enable Optical Control of TRPV1. *Nat. Commun.* **2015**, *6* (1), 7118. https://doi.org/10.1038/ncomms8118.

(22) Leinders-Zufall, T.; Storch, U.; Bleymehl, K.; Mederos y Schnitzler, M.; Frank, J. A.; Konrad, D. B.; Trauner, D.; Gudermann, T.; Zufall, F. PhoDAGs Enable Optical Control of Diacylglycerol-Sensitive Transient Receptor Potential Channels. *Cell Chem. Biol.* **2018**, *25* (2), 215-223.e3. https://doi.org/10.1016/j.chembiol.2017.11.008.

(23) Urban, P.; Pritzl, S. D.; Konrad, D. B.; Frank, J. A.; Pernpeintner, C.; Roeske, C. R.; Trauner, D.; Lohmüller, T. Light-Controlled Lipid Interaction and Membrane Organization in Photolipid Bilayer Vesicles. *Langmuir* **2018**, *34* (44), 13368–13374. https://doi.org/10.1021/acs.langmuir.8b03241.

(24) Frank, J. A.; Franquelim, H. G.; Schwille, P.; Trauner, D. Optical Control of Lipid Rafts with Photoswitchable Ceramides. *J. Am. Chem. Soc.* **2016**, *138* (39), 12981–12986. https://doi.org/10.1021/jacs.6b07278.

(25) Meier, H. The Photochemistry of Stilbenoid Compounds and Their Role in Materials Technology. *Angew. Chem. Int. Ed. Engl.* **1992**, *31* (11), 1399–1420. https://doi.org/10.1002/anie.199213993.
(26) Brown, E. V.; Granneman, G. R. Cis-Trans Isomerism in the Pyridyl Analogs of Azobenzene. Kinetic and Molecular Orbital Analysis. *J. Am. Chem. Soc.* **1975**, *97* (3), 621–627. https://doi.org/10.1021/ja00836a025.
(27) Fedorova, O. A.; Gulakova, E. N.; Fedorov, Y. V.; Lobazova, I. E.; Alfimov, M. V.; Jonusauskas, G. A Photochemical Electrocyclization of the Benzothiazolylphenylethenes Involving a CN Bond Formation. *J. Photochem. Photobiol. Chem.* **2008**, *196* (2), 239–245. https://doi.org/10.1016/j.jphotochem.2007.07.036.
(28) Jørgensen, K. B. Photochemical Oxidative Cyclisation of Stilbenes and Stilbenoids-the Mallory Reaction. *Molecules* **2010**, *15* (6), 4334–4358. https://doi.org/10.3390/molecules15064334.
(29) Kaupp, G.; Gründken, E.; Matthies, D. Umlagerungen und komplexe Eliminierungen mit 1,5-Benzothiazepin-4-onen. *Chem. Ber.* **1986**, *119* (10), 3109–3120.
(30) Coelho, P. J.; Castro, M. C. R.; Raposo, M. M. M. Fast (Hetero)Aryl-Benzothiazolium Ethenes Photoswitches Activated by Visible-Light at Room Temperature. *Dyes Pigment* **2015**, *117*, 163–169. https://doi.org/10.1016/j.dyepig.2015.02.015.
(31) Irie, M. Diarylethenes for Memories and Switches. *Chem. Rev.* **2000**, *100* (5), 1685–1716. https://doi.org/10.1021/cr980069d.
(32) Berdnikova, D.; Fedorova, O.; Gulakova, E.; Ihmels, H. Photoinduced in Situ Generation of a DNA-Binding Benzothiazoloquinolinium Derivative. *Chem Commun* **2012**, *48* (38), 4603–4605. https://doi.org/10.1039/c2cc30958k.
(33) Andryukhina, E. N.; Fedorova, O. A.; Fedorov, Y. V.; Panfilov, M. A.; Ihmels, H.; Alfimov, M. V.; Gromov, S. P. Electrocyclic Reaction of Crown-Containing 2-Styrylbenzothiazoles. *Russ. Chem. Bull.* **2005**, *54* (5), 1328–1330.
(34) Wiedbrauk, S.; Dube, H. Hemithioindigo—an Emerging Photoswitch. *Tetrahedron Lett.* **2015**, *56* (29), 4266–4274. https://doi.org/10.1016/j.tetlet.2015.05.022.
(35) Buback, J.; Kullmann, M.; Langhojer, F.; Nuernberger, P.; Schmidt, R.; Würthner, F.; Brixner, T. Ultrafast Bidirectional Photoswitching of a Spiropyran. *J. Am. Chem. Soc.* **2010**, *132* (46), 16510–16519. https://doi.org/10.1021/ja1062746.
(36) Halbritter, T.; Kaiser, C.; Wachtveitl, J.; Heckel, A. Pyridine–Spiropyran Derivative as a Persistent, Reversible Photoacid in Water. *J. Org. Chem.* **2017**, *82* (15), 8040–8047. https://doi.org/10.1021/acs.joc.7b01268.
(37) Abeyrathna, N.; Liao, Y. Stability of Merocyanine-Type Photoacids in Aqueous Solutions. *J. Phys. Org. Chem.* **2017**, *30* (8), e3664. https://doi.org/10.1002/poc.3664.
(38) Helmy, S.; Oh, S.; Leibfarth, F. A.; Hawker, C. J.; Read de Alaniz, J. Design and Synthesis of Donor–Acceptor Stenhouse Adducts: A Visible Light Photoswitch Derived from Furfural. *J. Org. Chem.* **2014**, *79* (23), 11316–11329. https://doi.org/10.1021/jo502206g.
(39) Hoorens, M. W. H.; Medved', M.; Laurent, A. D.; Di Donato, M.; Fanetti, S.; Slappendel, L.; Hilbers, M.; Feringa, B. L.; Jan Buma, W.; Szymanski, W. Iminothioindoxyl as a Molecular Photoswitch with 100 Nm Band Separation in the Visible Range. *Nat. Commun.* **2019**, *10* (1), 2390. https://doi.org/10.1038/s41467-019-10251-8.
(40) Fehrentz, T.; Schönberger, M.; Trauner, D. Optochemical Genetics. *Angew. Chem. Int. Ed.* **2011**, *50* (51), 12156–12182. https://doi.org/10.1002/anie.201103236.
(41) Tochitsky, I.; Trautman, J.; Gallerani, N.; Malis, J. G.; Kramer, R. H. Restoring Visual Function to the Blind Retina with a Potent, Safe and Long-Lasting Photoswitch. *Sci. Rep.* **2017**, *7* (1), 45487. https://doi.org/10.1038/srep45487.
(42) Stawski, P.; Sumser, M.; Trauner, D. A Photochromic Agonist of AMPA Receptors. *Angew. Chem. Int. Ed.* **2012**, *51* (23), 5748–5751. https://doi.org/10.1002/anie.201109265.
(43) Damijonaitis, A.; Broichhagen, J.; Urushima, T.; Hüll, K.; Nagpal, J.; Laprell, L.; Schönberger, M.; Woodmansee, D. H.; Rafiq, A.; Sumser, M. P.; Kummer, W.; Gottschalk, A.; Trauner, D. AzoCholine Enables Optical Control of Alpha 7 Nicotinic Acetylcholine Receptors in Neural Networks. *ACS Chem. Neurosci.* **2015**, *6* (5), 701–707. https://doi.org/10.1021/acschemneuro.5b00030.
(44) Barber, D. M.; Schönberger, M.; Burgstaller, J.; Levitz, J.; Weaver, C. D.; Isacoff, E. Y.; Baier, H.; Trauner, D. Optical Control of Neuronal Activity Using a Light-Operated GIRK Channel Opener (LOGO). *Chem. Sci.* **2016**, *7* (3), 2347–2352. https://doi.org/10.1039/C5SC04084A.
(45) Schönberger, M.; Trauner, D. A Photochromic Agonist for μ-Opioid Receptors. *Angew. Chem. Int. Ed.* **2014**, *53* (12), 3264–3267. https://doi.org/10.1002/anie.201309633.
(46) Pittolo, S.; Gómez-Santacana, X.; Eckelt, K.; Rovira, X.; Dalton, J.; Goudet, C.; Pin, J.-P.; Llobet, A.; Giraldo, J.; Llebaria, A.; Gorostiza, P. An Allosteric Modulator to Control Endogenous G Protein-Coupled Receptors with Light. *Nat. Chem. Biol.* **2014**, *10* (10), 813–815. https://doi.org/10.1038/nchembio.1612.
(47) Lachmann, D.; Studte, C.; Männel, B.; Hübner, H.; Gmeiner, P.; König, B. Photochromic Dopamine Receptor Ligands Based on Dithienylethenes and Fulgides. *Chem. – Eur. J.* **2017**, *23* (54), 13423–13434. https://doi.org/10.1002/chem.201702147.
(48) Pfaff, P.; Samarasinghe, K. T. G.; Crews, C. M.; Carreira, E. M. Reversible Spatiotemporal Control of Induced Protein Degradation by Bistable PhotoPROTACs. *ACS Cent. Sci.* **2019**, *5* (10), 1682–1690. https://doi.org/10.1021/acscentsci.9b00713.

(49) Reynders, M.; Matsuura, B. S.; Bérouti, M.; Simoneschi, D.; Marzio, A.; Pagano, M.; Trauner, D. PHOTACs Enable Optical Control of Protein Degradation. *Sci. Adv.* **2020**, *6* (8), eaay5064. https://doi.org/10.1126/sciadv.aay5064.
(50) Lai, A. C.; Crews, C. M. Induced Protein Degradation: An Emerging Drug Discovery Paradigm. *Nat. Rev. Drug Discov.* **2017**, *16* (2), 101–114. https://doi.org/10.1038/nrd.2016.211.
(51) Tochitsky, I.; Kienzler, M. A.; Isacoff, E.; Kramer, R. H. Restoring Vision to the Blind with Chemical Photoswitches. *Chem. Rev.* **2018**, *118* (21), 10748–10773. https://doi.org/10.1021/acs.chemrev.7b00723.
(52) Velema, W. A.; van der Berg, J. P.; Szymanski, W.; Driessen, A. J. M.; Feringa, B. L. Orthogonal Control of Antibacterial Activity with Light. *ACS Chem Biol* **2014**, *9* (9), 1969–1974. https://doi.org/10.1021/cb500313f.
(53) Velema, W. A.; van der Berg, J. P.; Hansen, M. J.; Szymanski, W.; Driessen, A. J. M.; Feringa, B. L. Optical Control of Antibacterial Activity. *Nat. Chem.* **2013**, *5* (11), 924–928. https://doi.org/10.1038/nchem.1750.
(54) Hansen, M. J.; Velema, W. A.; de Bruin, G.; Overkleeft, H. S.; Szymanski, W.; Feringa, B. L. Proteasome Inhibitors with Photocontrolled Activity. *ChemBioChem* **2014**, *15* (14), 2053–2057. https://doi.org/10.1002/cbic.201402237.
(55) Szymanski, W.; Ourailidou, M. E.; Velema, W. A.; Dekker, F. J.; Feringa, B. L. Light-Controlled Histone Deacetylase (HDAC) Inhibitors: Towards Photopharmacological Chemotherapy. *Chem. – Eur. J.* **2015**, *21* (46), 16517–16524. https://doi.org/10.1002/chem.201502809.
(56) Borowiak, M.; Küllmer, F.; Gegenfurtner, F.; Peil, S.; Nasufovic, V.; Zahler, S.; Thorn-Seshold, O.; Trauner, D.; Arndt, H.-D. Optical Manipulation of F-Actin with Photoswitchable Small Molecules. *J. Am. Chem. Soc.* **2020**, *142* (20), 9240–9249. https://doi.org/10.1021/jacs.9b12898.
(57) Borowiak, M.; Nahaboo, W.; Reynders, M.; Nekolla, K.; Jalinot, P.; Hasserodt, J.; Rehberg, M.; Delattre, M.; Zahler, S.; Vollmar, A.; Trauner, D.; Thorn-Seshold, O. Photoswitchable Inhibitors of Microtubule Dynamics Optically Control Mitosis and Cell Death. *Cell* **2015**, *162* (2), 403–411. https://doi.org/10.1016/j.cell.2015.06.049.
(58) Janke, C.; Steinmetz, M. O. Optochemistry to Control the Microtubule Cytoskeleton. *EMBO J* **2015**, *34* (16), 2114–2116. https://doi.org/10.15252/embj.201592415.
(59) Müller-Deku, A.; Meiring, J. C. M.; Loy, K.; Kraus, Y.; Heise, C.; Bingham, R.; Jansen, K. I.; Qu, X.; Bartolini, F.; Kapitein, L. C.; Akhmanova, A.; Ahlfeld, J.; Trauner, D.; Thorn-Seshold, O. Photoswitchable Paclitaxel-Based Microtubule Stabilisers Allow Optical Control over the Microtubule Cytoskeleton. *Nat. Commun.* **2020**, *11* (1), 4640. https://doi.org/10.1038/s41467-020-18389-6.
(60) Fuchter, M. J. On the Promise of Photopharmacology Using Photoswitches: A Medicinal Chemist's Perspective. *J. Med. Chem.* **2020**. https://doi.org/10.1021/acs.jmedchem.0c00629.
(61) Alberts, B.; Bray, D.; Lewis, J.; Raff, M.; Roberts, K.; Watson, J. D.; Alberts, B.; Bray, D.; Lewis, J.; Raff, M.; Roberts, K.; Watson, J. D. Chapter 16: The Cytoskeleton - Microtubules. In *Molecular Biology of the Cell*; Garland Science, 1994; pp 803–815.
(62) Mandelkow, E. M.; Schultheiss, R.; Rapp, R.; Müller, M.; Mandelkow, E. On the Surface Lattice of Microtubules: Helix Starts, Protofilament Number, Seam, and Handedness. *J. Cell Biol.* **1986**, *102* (3), 1067–1073. https://doi.org/10.1083/jcb.102.3.1067.
(63) Steinmetz, M. O.; Prota, A. E. Microtubule-Targeting Agents: Strategies To Hijack the Cytoskeleton. *Trends Cell Biol.* **2018**, *28* (10), 776–792. https://doi.org/10.1016/j.tcb.2018.05.001.
(64) Gelfand, V. I.; Bershadsky, A. D. Microtubule Dynamics: Mechanism, Regulation, and Function. *Annu. Rev. Cell Biol.* **1991**, *7* (1), 93–116. https://doi.org/10.1146/annurev.cb.07.110191.000521.
(65) Bodakuntla, S.; Jijumon, A. S.; Villablanca, C.; Gonzalez-Billault, C.; Janke, C. Microtubule-Associated Proteins: Structuring the Cytoskeleton. *Trends Cell Biol.* **2019**, *29* (10), 804–819. https://doi.org/10.1016/j.tcb.2019.07.004.
(66) Akhmanova, A.; Steinmetz, M. O. Tracking the Ends: A Dynamic Protein Network Controls the Fate of Microtubule Tips. *Nat. Rev. Mol. Cell Biol.* **2008**, *9* (4), 309–322. https://doi.org/10.1038/nrm2369.
(67) van Haren, J.; Charafeddine, R. A.; Ettinger, A.; Wang, H.; Hahn, K. M.; Wittmann, T. Local Control of Intracellular Microtubule Dynamics by EB1 Photodissociation. *Nat. Cell Biol.* **2018**, *20* (3), 252–261. https://doi.org/10.1038/s41556-017-0028-5.
(68) Stepanova, T.; Slemmer, J.; Hoogenraad, C. C.; Lansbergen, G.; Dortland, B.; De Zeeuw, C. I.; Grosveld, F.; van Cappellen, G.; Akhmanova, A.; Galjart, N. Visualization of Microtubule Growth in Cultured Neurons via the Use of EB3-GFP (End-Binding Protein 3-Green Fluorescent Protein). *J. Neurosci.* **2003**, *23* (7), 2655–2664. https://doi.org/10.1523/JNEUROSCI.23-07-02655.2003.
(69) Tolić, I. M. Mitotic Spindle: Kinetochore Fibers Hold on Tight to Interpolar Bundles. *Eur. Biophys. J.* **2018**, *47* (3), 191–203. https://doi.org/10.1007/s00249-017-1244-4.
(70) Glotzer, M. The 3Ms of Central Spindle Assembly: Microtubules, Motors and MAPs. *Nat. Rev. Mol. Cell Biol.* **2009**, *10* (1), 9–20. https://doi.org/10.1038/nrm2609.
(71) Janke, C.; Magiera, M. M. The Tubulin Code and Its Role in Controlling Microtubule Properties and Functions. *Nat. Rev. Mol. Cell Biol.* **2020**, *21* (6), 307–326. https://doi.org/10.1038/s41580-020-0214-3.
(72) Jordan, M. A.; Wilson, L. Microtubules as a Target for Anticancer Drugs. *Nat. Rev. Cancer* **2004**, *4* (4), 253–265. https://doi.org/10.1038/nrc1317.

(73) Hamel, E. Antimitotic Natural Products and Their Interactions with Tubulin. *Med. Res. Rev.* **1996**, *16* (2), 207–231. https://doi.org/10.1002/(SICI)1098-1128(199603)16:2<207::AID-MED4>3.0.CO;2-4.
(74) Dumontet, C.; Jordan, M. A. Microtubule-Binding Agents: A Dynamic Field of Cancer Therapeutics. *Nat. Rev. Drug Discov.* **2010**, *9* (10), 790–803. https://doi.org/10.1038/nrd3253.
(75) Tron, G. C.; Pirali, T.; Sorba, G.; Pagliai, F.; Busacca, S.; Genazzani, A. A. Medicinal Chemistry of Combretastatin A4: Present and Future Directions. *J Med Chem* **2006**, *49* (11), 3033–3044. https://doi.org/10.1021/jm0512903.
(76) Lu, Y.; Chen, J.; Xiao, M.; Li, W.; Miller, D. D. An Overview of Tubulin Inhibitors That Interact with the Colchicine Binding Site. *Pharm. Res.* **2012**, *29* (11), 2943–2971. https://doi.org/10.1007/s11095-012-0828-z.
(77) Graham, W.; Roberts, J. B. Intravenous Colchicine in the Management of Gouty Arthritis. *Ann. Rheum. Dis.* **1953**, *12* (1), 16–19.
(78) Pettit, G. R.; Singh, S. B.; Hamel, E.; Lin, C. M.; Alberts, D. S.; Garcia-Kendal, D. Isolation and Structure of the Strong Cell Growth and Tubulin Inhibitor Combretastatin A-4. *Experientia* **1989**, *45* (2), 209–211. https://doi.org/10.1007/BF01954881.
(79) Ravelli, R. B. G.; Gigant, B.; Curmi, P. A.; Jourdain, I.; Lachkar, S.; Sobel, A.; Knossow, M. Insight into Tubulin Regulation from a Complex with Colchicine and a Stathmin-like Domain. *Nature* **2004**, *428* (6979), 198–202. https://doi.org/10.1038/nature02393.
(80) Prota, A. E.; Bargsten, K.; Zurwerra, D.; Field, J. J.; Díaz, J. F.; Altmann, K.-H.; Steinmetz, M. O. Molecular Mechanism of Action of Microtubule-Stabilizing Anticancer Agents. *Science* **2013**, *339* (6119), 587. https://doi.org/10.1126/science.1230582.
(81) Nogales, E.; Whittaker, M.; Milligan, R. A.; Downing, K. H. High-Resolution Model of the Microtubule. *Cell* **1999**, *96* (1), 79–88. https://doi.org/10.1016/S0092-8674(00)80961-7.
(82) Wani, M. C.; Taylor, H. L.; Wall, M. E.; Coggon, P.; McPhail, A. T. Plant Antitumor Agents. VI. Isolation and Structure of Taxol, a Novel Antileukemic and Antitumor Agent from Taxus Brevifolia. *J. Am. Chem. Soc.* **1971**, *93* (9), 2325–2327. https://doi.org/10.1021/ja00738a045.
(83) Schiff, P. B.; Fant, J.; Horwitz, S. B. Promotion of Microtubule Assembly in Vitro by Taxol. *Nature* **1979**, *277* (5698), 665–667. https://doi.org/10.1038/277665a0.
(84) Menzin, A. W.; King, S. A.; Aikins, J. K.; Mikuta, J. J.; Rubin, S. C. Taxol (Paclitaxel) Was Approved by FDA for the Treatment of Patients with Recurrent Ovarian Cancer. *Gynecol. Oncol.* **1994**, *54* (1), 103.
(85) Höfle, G.; Bedorf, N.; Steinmetz, H.; Schomburg, D.; Gerth, K.; Reichenbach, H. Epothilone A and B—Novel 16-Membered Macrolides with Cytotoxic Activity: Isolation, Crystal Structure, and Conformation in Solution. *Angew. Chem. Int. Ed.* **1996**, *35* (13-14), 1567–1569. https://doi.org/10.1002/anie.199615671.
(86) Bollag, D. M.; McQueney, P. A.; Zhu, J.; Hensens, O.; Koupal, L.; Liesch, J.; Goetz, M.; Lazarides, E.; Woods, C. M. Epothilones, a New Class of Microtubule-Stabilizing Agents with a Taxol-like Mechanism of Action. *Cancer Res.* **1995**, *55* (11), 2325–2333.
(87) Höfle, G.; Bedorf, N.; Gerth, K.; Reichenbach (GBF), H. DE-B 4138 042, 1993. *Chem Abstr* **1993**, No. 120, 52841.
(88) Nicolaou, K. C.; Roschangar, F.; Vourloumis, D. Chemical Biology of Epothilones. *Angew. Chem. Int. Ed.* **1998**, *37* (15), 2014–2045. https://doi.org/10.1002/(SICI)1521-3773(19980817)37:15<2014::AID-ANIE2014>3.0.CO;2-2.
(89) Hunt, J. T. Discovery of Ixabepilone. *Mol. Cancer Ther.* **2009**, *8* (2), 275–281. https://doi.org/10.1158/1535-7163.MCT-08-0999.
(90) Mani, S.; McDaid, H.; Hamilton, A.; Hochster, H.; Cohen, M. B.; Khabelle, D.; Griffin, T.; Lebwohl, D. E.; Liebes, L.; Muggia, F.; Horwitz, S. B. Phase I Clinical and Pharmacokinetic Study of BMS-247550, a Novel Derivative of Epothilone B, in Solid Tumors. *Clin. Cancer Res. Off. J. Am. Assoc. Cancer Res.* **2004**, *10* (4), 1289–1298. https://doi.org/10.1158/1078-0432.ccr-0919-03.
(91) de Jonge, M.; Verweij, J. The Epothilone Dilemma. *J. Clin. Oncol.* **2005**, *23* (36), 9048–9050. https://doi.org/10.1200/JCO.2005.03.8844.
(92) Forli, S. Epothilones: From Discovery to Clinical Trials. *Curr. Top. Med. Chem.* **2014**, *14* (20), 2312–2321.
(93) Prota, A. E.; Bargsten, K.; Northcote, P. T.; Marsh, M.; Altmann, K.-H.; Miller, J. H.; Díaz, J. F.; Steinmetz, M. O. Structural Basis of Microtubule Stabilization by Laulimalide and Peloruside A. *Angew. Chem. Int. Ed.* **2014**, *53* (6), 1621–1625. https://doi.org/10.1002/anie.201307749.
(94) Ranjan, R.; Snedeker, J.; Chen, X. Asymmetric Centromeres Differentially Coordinate with Mitotic Machinery to Ensure Biased Sister Chromatid Segregation in Germline Stem Cells. *Cell Stem Cell* **2019**, *25* (5), 666-681.e5. https://doi.org/10.1016/j.stem.2019.08.014.
(95) Ruschel, J.; Hellal, F.; Flynn, K. C.; Dupraz, S.; Elliott, D. A.; Tedeschi, A.; Bates, M.; Sliwinski, C.; Brook, G.; Dobrindt, K.; Peitz, M.; Brüstle, O.; Norenberg, M. D.; Blesch, A.; Weidner, N.; Bunge, M. B.; Bixby, J. L.; Bradke, F. Systemic Administration of Epothilone B Promotes Axon Regeneration after Spinal Cord Injury. *Science* **2015**, *348* (6232), 347–352. https://doi.org/10.1126/science.aaa2958.
(96) Wittmann, T.; Dema, A.; van Haren, J. Lights, Cytoskeleton, Action: Optogenetic Control of Cell Dynamics. *Curr. Opin. Cell Biol.* **2020**, *66*, 1–10. https://doi.org/10.1016/j.ceb.2020.03.003.
(97) Chapman, O. L.; Smith, H. G.; King, R. W. The Structure of β-Lumicolchicine. *J. Am. Chem. Soc.* **1963**, *85* (6), 803–806. https://doi.org/10.1021/ja00889a031.
(98) Aronson, J.; Inoué, S. Reversal by Light of the Action of N-Methyl N-Desacetyl Colchicine on Mitosis. *J. Cell Biol.* **1970**, *45* (2), 470–477. https://doi.org/10.1083/jcb.45.2.470.

(99) Hamaguchi, M. S.; Hiramoto, Y. Analysis of the Role of Astral Rays in Pronuclear Migration in Sand Dollar Eggs by the Colcemid-UV Method. *Dev. Growth Differ.* **1986**, *28* (2), 143–156. https://doi.org/10.1111/j.1440-169X.1986.00143.x.
(100) Wühr, M.; Tan, E. S.; Parker, S. K.; Detrich, H. W.; Mitchison, T. J. A Model for Cleavage Plane Determination in Early Amphibian and Fish Embryos. *Curr. Biol.* **2010**, *20* (22), 2040–2045. https://doi.org/10.1016/j.cub.2010.10.024.
(101) Butler, J.; Gaukroger, K.; Hadfield, J. A.; Hamblett, I.; Hepworth, L. A.; Land, E. J.; Lawrence, N. J.; Mayalarp, S. P.; Mcgown, A. T. Substituted Stilbenes and Their Reactions. WO0250007A2, June 27, 2002.
(102) Bisby, R. H.; Botchway, S. W.; Hadfield, J. A.; McGown, A. T.; Parker, A. W.; Scherer, K. M. Fluorescence Lifetime Imaging of E-Combretastatin Uptake and Distribution in Live Mammalian Cells. *Eur. J. Cancer* **2012**, *48* (12), 1896–1903. https://doi.org/10.1016/j.ejca.2011.11.025.
(103) Pettit, G. R.; Rhodes, M. R.; Herald, D. L.; Chaplin, D. J.; Stratford, M. R.; Hamel, E.; Pettit, R. K.; Chapuis, J. C.; Oliva, D. Antineoplastic Agents 393. Synthesis of the Trans-Isomer of Combretastatin A-4 Prodrug. *Anticancer. Drug Des.* **1998**, *13* (8), 981–993.
(104) Gaspari, R.; Prota, A. E.; Bargsten, K.; Cavalli, A.; Steinmetz, M. O. Structural Basis of Cis- and Trans-Combretastatin Binding to Tubulin. *Chem* **2017**, *2* (1), 102–113. https://doi.org/10.1016/j.chempr.2016.12.005.
(105) Engdahl, A. J.; Torres, E. A.; Lock, S. E.; Engdahl, T. B.; Mertz, P. S.; Streu, C. N. Synthesis, Characterization, and Bioactivity of the Photoisomerizable Tubulin Polymerization Inhibitor Azo-Combretastatin A4. *Org Lett* **2015**, *17* (18), 4546–4549. https://doi.org/10.1021/acs.orglett.5b02262.
(106) Sheldon, J. E.; Dcona, M. M.; Lyons, C. E.; Hackett, J. C.; Hartman, M. C. T. Photoswitchable Anticancer Activity via Trans-Cis Isomerization of a Combretastatin A-4 Analog. *Org Biomol Chem* **2016**, *14* (1), 40–49. https://doi.org/10.1039/c5ob02005k.
(107) Zenker, J.; White, M. D.; Templin, R. M.; Parton, R. G.; Thorn-Seshold, O.; Bissiere, S.; Plachta, N. A Microtubule-Organizing Center Directing Intracellular Transport in the Early Mouse Embryo. *Science* **2017**, *357* (6354), 925–928. https://doi.org/10.1126/science.aam9335.
(108) Singh, A.; Saha, T.; Begemann, I.; Ricker, A.; Nüsse, H.; Thorn-Seshold, O.; Klingauf, J.; Galic, M.; Matis, M. Polarized Microtubule Dynamics Directs Cell Mechanics and Coordinates Forces during Epithelial Morphogenesis. *Nat. Cell Biol.* **2018**, *20* (10), 1126–1133. https://doi.org/10.1038/s41556-018-0193-1.
(109) Zenker, J.; White, M. D.; Gasnier, M.; Alvarez, Y. D.; Lim, H. Y. G.; Bissiere, S.; Biro, M.; Plachta, N. Expanding Actin Rings Zipper the Mouse Embryo for Blastocyst Formation. *Cell* **2018**, *173* (3), 776–791. https://doi.org/10.1016/j.cell.2018.02.035.
(110) Theisen, U.; Ernst, A. U.; Heyne, R. L. S.; Ring, T. P.; Thorn-Seshold, O.; Köster, R. W. Microtubules and Motor Proteins Support Zebrafish Neuronal Migration by Directing Cargo. *J. Cell Biol.* **2020**, *219* (10), e201908040. https://doi.org/10.1083/jcb.201908040.
(111) Kopf, A.; Renkawitz, J.; Hauschild, R.; Girkontaite, I.; Tedford, K.; Merrin, J.; Thorn-Seshold, O.; Trauner, D.; Häcker, H.; Fischer, K.-D.; Kiermaier, E.; Sixt, M. Microtubules Control Cellular Shape and Coherence in Amoeboid Migrating Cells. *J. Cell Biol.* **2020**, *219* (e201907154). https://doi.org/10.1083/jcb.201907154.
(112) Eguchi, K.; Taoufiq, Z.; Thorn-Seshold, O.; Trauner, D.; Hasegawa, M.; Takahashi, T. Wild-Type Monomeric α-Synuclein Can Impair Vesicle Endocytosis and Synaptic Fidelity via Tubulin Polymerization at the Calyx of Held. *J. Neurosci.* **2017**, *37* (25), 6043–6052. https://doi.org/10.1523/JNEUROSCI.0179-17.2017.
(113) Rastogi, S. K.; Zhao, Z.; Barrett, S. L.; Shelton, S. D.; Zafferani, M.; Anderson, H. E.; Blumenthal, M. O.; Jones, L. R.; Wang, L.; Li, X.; Streu, C. N.; Du, L.; Brittain, W. J. Photoresponsive Azo-Combretastatin A-4 Analogues. *Eur J Med Chem* **2018**, *143*, 1–7. https://doi.org/10.1016/j.ejmech.2017.11.012.
(114) Rastogi, S. K.; Zhao, Z.; Gildner, M. B.; Shoulders, B. A.; Velasquez, T. L.; Blumenthal, M. O.; Wang, L.; Li, X.; Hudnall, T. W.; Betancourt, T.; Du, L.; Brittain, W. J. Synthesis, Optical Properties and in Vitro Cell Viability of Novel Spiropyrans and Their Photostationary States. *Tetrahedron* **2021**, *80*, 131854. https://doi.org/10.1016/j.tet.2020.131854.
(115) Sailer, A.; Ermer, F.; Kraus, Y.; Lutter, F. H.; Donau, C.; Bremerich, M.; Ahlfeld, J.; Thorn-Seshold, O. Hemithioindigos for Cellular Photopharmacology: Desymmetrised Molecular Switch Scaffolds Enabling Design Control over the Isomer-Dependency of Potent Antimitotic Bioactivity. *ChemBioChem* **2019**, *20* (10), 1305–1314. https://doi.org/10.1002/cbic.201800752.
(116) Sailer, A.; Ermer, F.; Kraus, Y.; Bingham, R.; Lutter, F. H.; Ahlfeld, J.; Thorn-Seshold, O. Potent Hemithioindigo-Based Antimitotics Photocontrol the Microtubule Cytoskeleton in Cellulo. *Beilstein J. Org. Chem.* **2020**, *16*, 125–134. https://doi.org/10.3762/bjoc.16.14.
(117) Hall, N. Creating Complexity – the Beauty and Logic of Synthesis. *Chem. Commun.* **2003**, No. 6, 661–664. https://doi.org/10.1039/B212248K.
(118) The total synthesis of Taxol was pursued by some of the biggest names in Total Synthesis (e.g. Nicolaou, Danishefsky, Wender, Mukaiyama, Baran) up to this day. https://en.wikipedia.org/w/index.php?title=Paclitaxel_total_synthesis&oldid=990778314 (accessed 2021 -05 -21).

(119) Skwarczynski, M.; Noguchi, M.; Hirota, S.; Sohma, Y.; Kimura, T.; Hayashi, Y.; Kiso, Y. Development of First Photoresponsive Prodrug of Paclitaxel. *Bioorg. Med. Chem. Lett.* **2006**, *16* (17), 4492–4496. https://doi.org/10.1016/j.bmcl.2006.06.030.
(120) Morstein, J.; Awale, M.; Reymond, J.-L.; Trauner, D. Mapping the Azolog Space Enables the Optical Control of New Biological Targets. *ACS Cent. Sci.* **2019**. https://doi.org/10.1021/acscentsci.8b00881.
(121) Merino, E. Synthesis of Azobenzenes: The Coloured Pieces of Molecular Materials. *Chem. Soc. Rev.* **2011**, *40* (7), 3835–3853. https://doi.org/10.1039/C0CS00183J.
(122) Acosta-Ruiz, A.; Gutzeit, V. A.; Skelly, M. J.; Meadows, S.; Lee, J.; Parekh, P.; Orr, A. G.; Liston, C.; Pleil, K. E.; Broichhagen, J.; Levitz, J. Branched Photoswitchable Tethered Ligands Enable Ultra-Efficient Optical Control and Detection of G Protein-Coupled Receptors In Vivo. *Neuron* **2019**, *0* (0). https://doi.org/10.1016/j.neuron.2019.10.036.
(123) Morstein, J.; Hill, R. Z.; Novak, A. J. E.; Feng, S.; Norman, D. D.; Donthamsetti, P. C.; Frank, J. A.; Harayama, T.; Williams, B. M.; Parrill, A. L.; Tigyi, G. J.; Riezman, H.; Isacoff, E. Y.; Bautista, D. M.; Trauner, D. Optical Control of Sphingosine-1-Phosphate Formation and Function. *Nat. Chem. Biol.* **2019**, *15* (6), 623–631. https://doi.org/10.1038/s41589-019-0269-7.
(124) Boulègue, C.; Löweneck, M.; Renner, C.; Moroder, L. Redox Potential of Azobenzene as an Amino Acid Residue in Peptides. *ChemBioChem* **2007**, *8* (6), 591–594. https://doi.org/10.1002/cbic.200600495.
(125) Kosower, E. M.; Kanety-Londner, H. Glutathione. 13. Mechanism of Thiol Oxidation by Diazenedicarboxylic Acid Derivatives. *J. Am. Chem. Soc.* **1976**, *98* (10), 3001–3007. https://doi.org/10.1021/ja00426a054.
(126) Schehr, M.; Ianes, C.; Weisner, J.; Heintze, L.; Müller, M. P.; Pichlo, C.; Charl, J.; Brunstein, E.; Ewert, J.; Lehr, M.; Baumann, U.; Rauh, D.; Knippschild, U.; Peifer, C.; Herges, R. 2-Azo-, 2-Diazocine-Thiazols and 2-Azo-Imidazoles as Photoswitchable Kinase Inhibitors: Limitations and Pitfalls of the Photoswitchable Inhibitor Approach. *Photochem. Photobiol. Sci.* **2019**, *18* (6), 1398–1407. https://doi.org/10.1039/C9PP00010K.
(127) Fouts, J. R.; Kamm, J. J.; Brodie, B. B. Enzymatic Reduction of Prontosil and Other Azo Dyes. *J. Pharmacol. Exp. Ther.* **1957**, *120* (3), 291–300.
(128) Samanta, S.; Babalhavaeji, A.; Dong, M.; Woolley, G. A. Photoswitching of Ortho-Substituted Azonium Ions by Red Light in Whole Blood. *Angew Chem Int Ed* **2013**, *52* (52), 14127–14130. https://doi.org/10.1002/anie.201306352.
(129) Dong, M.; Babalhavaeji, A.; Samanta, S.; Beharry, A. A.; Woolley, G. A. Red-Shifting Azobenzene Photoswitches for in Vivo Use. *Acc Chem Res* **2015**, *48* (10), 2662–2670. https://doi.org/10.1021/acs.accounts.5b00270.
(130) Lei, H.; Mo, M.; He, Y.; Wu, Y.; Zhu, W.; Wu, L. Bioactivatable Reductive Cleavage of Azobenzene for Controlling Functional Dumbbell Oligodeoxynucleotides. *Bioorganic Chem.* **2019**, 103106. https://doi.org/10.1016/j.bioorg.2019.103106.
(131) Mulatihan, D.; Guo, T.; Zhao, Y. Azobenzene Photoswitch for Isomerization-Dependent Cancer Therapy via Azo-Combretastatin A4 and Phototrexate. *Photochem. Photobiol.* **2020**, *96* (6), 1163–1168. https://doi.org/10.1111/php.13292.
(132) An, Y.; Chen, C.; Zhu, J.; Dwivedi, P.; Zhao, Y.; Wang, Z. Hypoxia-Induced Activity Loss of a Photo-Responsive Microtubule Inhibitor Azobenzene Combretastatin A4. *Front. Chem. Sci. Eng.* **2020**, *14* (5), 880–888. https://doi.org/10.1007/s11705-019-1864-6.
(133) García-Amorós, J.; Velasco, D. Recent Advances towards Azobenzene-Based Light-Driven Real-Time Information-Transmitting Materials. *Beilstein J. Org. Chem.* **2012**, *8*, 1003–1017. https://doi.org/10.3762/bjoc.8.113.
(134) Garcia-Amorós, J.; Maerz, B.; Reig, M.; Cuadrado, A.; Blancafort, L.; Samoylova, E.; Velasco, D. Picosecond Switchable Azo Dyes. *Chem. – Eur. J.* **2019**, *25* (32), 7726–7732.
(135) Garcia-Amorós, J.; Díaz-Lobo, M.; Nonell, S.; Velasco, D. Fastest Thermal Isomerization of an Azobenzene for Nanosecond Photoswitching Applications under Physiological Conditions. *Angew. Chem. Int. Ed.* **2012**, *51* (51), 12820–12823. https://doi.org/10.1002/anie.201207602.
(136) Garcia, A.; Eljack, N. D.; Sani, M.-A.; Separovic, F.; Rasmussen, H. H.; Kopec, W.; Khandelia, H.; Cornelius, F.; Clarke, R. J. Membrane Accessibility of Glutathione. *Biochim. Biophys. Acta BBA - Biomembr.* **2015**, *1848* (10, Part A), 2430–2436. https://doi.org/10.1016/j.bbamem.2015.07.016.
(137) Reeßing, F.; Szymanski, W. Beyond Photodynamic Therapy: Light-Activated Cancer Chemotherapy. *Curr Med Chem* **2017**, *24* (42), 4905–4950. https://doi.org/10.2174/0929867323666160906103223.
(138) El-Hendawy, M. M.; Fayed, T. A.; Awad, M. K.; English, N. J.; Etaiw, S. E. H.; Zaki, A. B. Photophysics, Photochemistry and Thermal Stability of Diarylethene-Containing Benzothiazolium Species. *J Photochem Photobiol* **2015**, *301*, 20–31. https://doi.org/10.1016/j.jphotochem.2014.12.015.
(139) Gjorgjieva, M.; Tomašič, T.; Kikelj, D.; Mašič, L. P. Benzothiazole-Based Compounds in Antibacterial Drug Discovery. *Curr. Med. Chem.* **2018**, *25* (38), 5218–5236. https://doi.org/10.2174/0929867324666171009103327.
(140) Wang, F.; Sambandan, D.; Halder, R.; Wang, J.; Batt, S. M.; Weinrick, B.; Ahmad, I.; Yang, P.; Zhang, Y.; Kim, J.; Hassani, M.; Huszar, S.; Trefzer, C.; Ma, Z.; Kaneko, T.; Mdluli, K. E.; Franzblau, S.; Chatterjee, A. K.; Johnsson, K.; Mikusova, K.; Besra, G. S.; Fütterer, K.; Robbins, S. H.; Barnes, S. W.; Walker, J. R.; Jacobs, W. R.; Schultz, P. G. Identification of a Small Molecule with Activity against Drug-Resistant and Persistent Tuberculosis. *Proc. Natl. Acad. Sci.* **2013**, *110* (27), E2510–E2517.

(141) Andreu, J. M.; Schaffner-Barbero, C.; Huecas, S.; Alonso, D.; Lopez-Rodriguez, M. L.; Ruiz-Avila, L. B.; Núñez-Ramírez, R.; Llorca, O.; Martín-Galiano, A. J. The Antibacterial Cell Division Inhibitor PC190723 Is an FtsZ Polymer-Stabilizing Agent That Induces Filament Assembly and Condensation*. *J. Biol. Chem.* **2010**, *285* (19), 14239–14246. https://doi.org/10.1074/jbc.M109.094722.

(142) Erickson Harold P.; Anderson David E.; Osawa Masaki. FtsZ in Bacterial Cytokinesis: Cytoskeleton and Force Generator All in One. *Microbiol. Mol. Biol. Rev.* **2010**, *74* (4), 504–528. https://doi.org/10.1128/MMBR.00021-10.

(143) Haydon, D. J.; Bennett, J. M.; Brown, D.; Collins, I.; Galbraith, G.; Lancett, P.; Macdonald, R.; Stokes, N. R.; Chauhan, P. K.; Sutariya, J. K.; Nayal, N.; Srivastava, A.; Beanland, J.; Hall, R.; Henstock, V.; Noula, C.; Rockley, C.; Czaplewski, L. Creating an Antibacterial with in Vivo Efficacy: Synthesis and Characterization of Potent Inhibitors of the Bacterial Cell Division Protein FtsZ with Improved Pharmaceutical Properties. *J. Med. Chem.* **2010**, *53* (10), 3927–3936. https://doi.org/10.1021/jm9016366.

(144) Gjorgjieva, M.; Tomašič, T.; Barančokova, M.; Katsamakas, S.; Ilaš, J.; Tammela, P.; Peterlin Mašič, L.; Kikelj, D. Discovery of Benzothiazole Scaffold-Based DNA Gyrase B Inhibitors. *J. Med. Chem.* **2016**, *59* (19), 8941–8954. https://doi.org/10.1021/acs.jmedchem.6b00864.

(145) Aiello, D.; Barnes, M. H.; Biswas, E. E.; Biswas, S. B.; Gu, S.; Williams, J. D.; Bowlin, T. L.; Moir, D. T. Discovery, Characterization and Comparison of Inhibitors of Bacillus Anthracis and Staphylococcus Aureus Replicative DNA Helicases. *Bioorg. Med. Chem.* **2009**, *17* (13), 4466–4476. https://doi.org/10.1016/j.bmc.2009.05.014.

(146) Wegener, M.; Hansen, M. J.; Driessen, A. J. M.; Szymanski, W.; Feringa, B. L. Photocontrol of Antibacterial Activity: Shifting from UV to Red Light Activation. *J. Am. Chem. Soc.* **2017**, *139* (49), 17979–17986. https://doi.org/10.1021/jacs.7b09281.

(147) Gay, N. J.; Symmons, M. F.; Gangloff, M.; Bryant, C. E. Assembly and Localization of Toll-like Receptor Signalling Complexes. *Nat. Rev. Immunol.* **2014**, *14* (8), 546–558. https://doi.org/10.1038/nri3713.

(148) Tanji, H.; Ohto, U.; Shibata, T.; Miyake, K.; Shimizu, T. Structural Reorganization of the Toll-Like Receptor 8 Dimer Induced by Agonistic Ligands. *Science* **2013**, *339* (6126), 1426–1429. https://doi.org/10.1126/science.1229159.

(149) Kaushik, D.; Kaur, A.; Petrovsky, N.; Salunke, D. B. Structural Evolution of Toll-like Receptor 7/8 Agonists from Imidazoquinolines to Imidazoles. *RSC Med. Chem.* **2021**. https://doi.org/10.1039/D1MD00031D.

(150) Colletier, J.-P.; Schirò, G.; Weik, M. Time-Resolved Serial Femtosecond Crystallography, Towards Molecular Movies of Biomolecules in Action. In *X-ray Free Electron Lasers: A Revolution in Structural Biology*; Boutet, S., Fromme, P., Hunter, M. S., Eds.; Springer International Publishing: Cham, 2018; pp 331–356. https://doi.org/10.1007/978-3-030-00551-1_11.

(151) Skopintsev, P.; Ehrenberg, D.; Weinert, T.; James, D.; Kar, R. K.; Johnson, P. J. M.; Ozerov, D.; Furrer, A.; Martiel, I.; Dworkowski, F.; Nass, K.; Knopp, G.; Cirelli, C.; Arrell, C.; Gashi, D.; Mous, S.; Wranik, M.; Gruhl, T.; Kekilli, D.; Brünle, S.; Deupi, X.; Schertler, G. F. X.; Benoit, R. M.; Panneels, V.; Nogly, P.; Schapiro, I.; Milne, C.; Heberle, J.; Standfuss, J. Femtosecond-to-Millisecond Structural Changes in a Light-Driven Sodium Pump. *Nature* **2020**, *583* (7815), 314–318. https://doi.org/10.1038/s41586-020-2307-8.

(152) Schlichting, I.; Miao, J. Emerging Opportunities in Structural Biology with X-Ray Free-Electron Lasers. *Curr. Opin. Struct. Biol.* **2012**, *22* (5), 613–626. https://doi.org/10.1016/j.sbi.2012.07.015.

(153) Liu, Q.; Dahmane, T.; Zhang, Z.; Assur, Z.; Brasch, J.; Shapiro, L.; Mancia, F.; Hendrickson, W. A. Structures from Anomalous Diffraction of Native Biological Macromolecules. *Science* **2012**, *336* (6084), 1033–1037. https://doi.org/10.1126/science.1218753.